DOE/NV/25946--2416

FY 2014 Annual Report
Site-Directed Research & Development

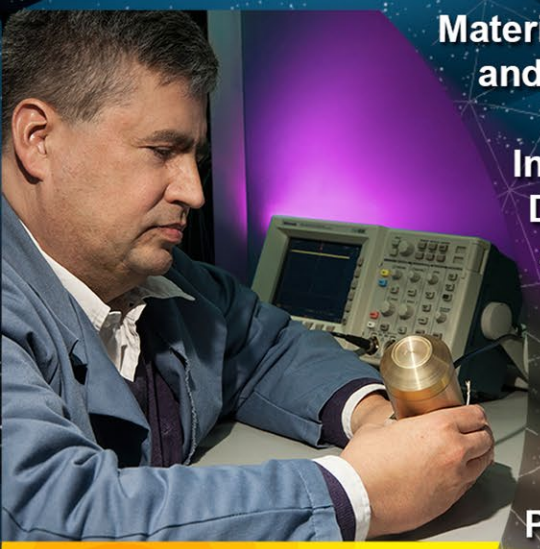

Material Studies and Techniques

Instruments, Detectors, and Sensors

Computational and Information Sciences

Photonics

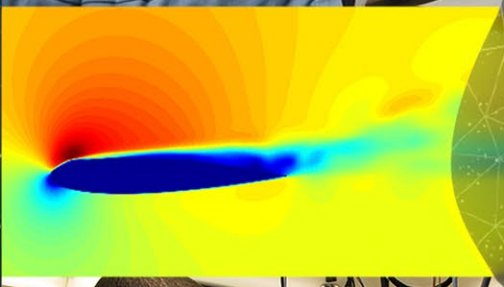

This work was done by National Security Technologies, LLC, under Contract No. DE-AC52-06NA25946, and supported by the Site-Directed Research and Development Program.
Report Date: April 2015

NNSA
Nevada National Security Site

Availability Statement

Available for sale to the public from—

U.S. Department of Commerce
National Technical Information Service
5301 Shawnee Road
Alexandria, VA 22312
Telephone: 800.553.6847
Fax: 703.605.6900
E-mail: orders@ntis.gov
Online ordering: http://www.ntis.gov/help/ordermethods.aspx

Available electronically at http://www.osti.gov/bridge

Available for a processing fee to the U.S. Department of Energy and its contractors in paper, from—

U.S. Department of Energy
Office of Scientific and Technical Information
P.O. Box 62
Oak Ridge, TN 37831-0062
Telephone: 865.576.6401
Fax: 865.576.5728
E-mail: reports@adonis.osti.gov
Online ordering: http://www.osti.gov/reportform.html

Cover images: (top) Paul Guss from the Remote Sensing Laboratory (Nellis) examines a new radiation detection package; (center) cartoon of fluid flow across an airfoil, part of the cartoon-texture decomposition technique; (bottom) Manuel Manard from the Special Technologies Laboratory works with the quadrupole mass spectrometer.

DOE/NV/25946–2416

Nevada National Security Site

Site-Directed Research and Development

Fiscal Year 2014 Annual Report

This work was done by National Security Technologies, LLC, under Contract No. DE-AC52-06NA25946 with the U.S. Department of Energy, and supported by the Site-Directed Research and Development Program.

Report Date: April 2015

Contents

“Two and a half percent; we all applaud.”

Dr. Juzaitis’ commitment to raise the Site-Directed Research and Development (SDRD) funding rate opens more opportunities. We cannot let him down though, because this was a bold move, especially when budgets are so austere. *We must deliver*. As you know, I like to look at our mission as “Ground Truth and Discovery,” but we must also think about *ownership*. This increase in SDRD funding will enable us to set and follow our own strategic plans. Already, we have initiated two strategic FY 2015 SDRDs, one for dynamic material studies and another for radiation detectors for unmanned aerial systems.

Another great example of ownership occurred in January 2015. National Security Technologies, LLC (NSTec), submitted a solo R&D 100 Award. We have received a few awards in partnership with the laboratories over the last few years, but our submission of the Urchin Platform developed at the Special Technologies Laboratory is our first wholly NSTec-owned submission.

It will be a little time before we know whether we have actually received the award, but I am proud that NSTec submitted its own R&D 100 proposal. Of course, Urchin was developed under SDRD, so an award would be a doubly great achievement. In addition, Urchin, as a compact, low-power sensor platform, will be an ideal technology to demonstrate “Ground Truth and Discovery” in future experiments at the Nevada National Security Site (NNSS).

In last year’s Foreword, we identified four actions to help strengthen SDRD. Listed below are the steps we achieved this year on that path:

1. Grew the program size—SDRD funding increased to 2.5% this year.
2. Improved transparency—Proposal preparers are now given feedback.
3. Assessed project selection—We conducted independent external reviews to verify quality in the selection process.
4. Strategically invested—We introduced two FY 2015 strategic SDRD projects.

Achieving these goals could not have been done without the excellent leadership of SDRD, the support of our administrative and review team, the insight of the external advisory board, and the successful innovations that you all continue to deliver.

Thank you!

Christopher Deeney
Chief Technology Officer
Vice President for Program Integration

This page left blank intentionally

“It’s people, it’s mission, it’s impact...”

This simple statement captures the essence of our R&D enterprise. Each year our annual report begins with program highlights about the people, the mission, and the overall impact of our efforts. But what does each of these mean? How exactly do people, mission, and impact help us achieve the best possible R&D? In 2014, termed the “year of reviews,” we looked very carefully at processes and products to ensure good stewardship of Site-Directed Research and Development (SDRD) investment. Three different, but highly introspective, reviews provided a comprehensive assessment of SDRD’s state of health—the overall diagnosis was that the program is resoundingly strong and potent. These separate activities—the External Advisory Board (EAB) meeting, the U.S. Department of Energy, National Nuclear Security Administration (NNSA) program review, and the SDRD annual project review—yielded insight that went well beyond the sum of their parts.

In April of 2014 members of the SDRD EAB met to assess the state of SDRD and status progress against recommendations made roughly two years prior. Many of the achievements we reported in the previous two annual reports were covered in depth and presented as evidence of the program improvements and transformative impact of our R&D. Thanks to the efforts of our technical staff and principal investigators, the SDRD program team, and the EAB members themselves, we are engaged in continuous improvement in a meaningful way. Ongoing dialogue between advisors, staff, and management is having a profound and lasting effect on the way we conduct R&D.

The 2nd annual integrated **year-end review of SDRD projects** was held in September 2014 and has become firmly established as the venue for presenting results

The Year in Review

*The **SDRD External Advisory Board** (EAB) met in April 2014 to evaluate performance and gauge progress since our inaugural meeting in October 2011. This was a comprehensive review examining our overall process for conducting SDRD and the impact of our research. We analyzed the initial EAB recommendations and how SDRD matched up in many of the areas of concern to the board.*

“. . .a vigorous program contributing new ideas in science and technology, and aiding recruiting.”
—D. Giovanielli

“. . .the effectiveness of the SDRD program has grown substantially, and the program has become a vital element of the S&T base. . .important new institutional capabilities and competencies have emerged for the SDRD investment.”
—R. James

Principal Investigator Craig Kruschwitz presents his research on neutron detectors (see pages 131–137) at the 2nd annual integrated year-end review of SDRD projects

and assessing technical challenges. What was particularly noteworthy was the level of quality of the projects being presented, as well as each Principal Investigator's (PI's) ability to convey why their work is important and what innovations they are uniquely bringing to the forefront.

An **NNSA review of SDRD** was conducted in July 2014. Individuals from NSTec and NNSA interacted to discuss program performance and overall R&D effectiveness (see table). Communication has always been key, and this effort strengthened the dialogue among technical staff and program management, who contributed ideas and suggestions for maximizing our R&D investment. This assessment of SDRD focused on our co-developed "contributing factors" that describe the performance of SDRD and its impact around strategy, relevance, quality, and workforce development and capabilities.

Performance factors attributable to SDRD program effectiveness

Strategy	Relevance	Quality	Workforce/Capabilities
A robust research strategy has been implemented, emphasizing a systems approach to planning	Technical accomplishments show impact to national security areas	External Advisory Board validates our direction and outcomes	SDRD provides a unique opportunity for technical staff to exercise creativity and leverage talent
NSTec strategic plan and implementing guidance ensures alignment with national priorities	Continuous emphasis on key challenges relevant to national security and focus talent and investments to bring solutions	Number and quality of published articles in high-impact journals in key areas of science and technology, and external awards	Skills and competencies developed in pursuit of independent R&D are often unparalleled
The annually updated NNSS *Technology Needs Assessment* dovetails with the strategic plan to provide detailed science, technology, and engineering requirements to our technical staff	SDRD process and leadership emphasize performance, relevance, and quality from proposal stage through project execution, and tangible outcomes during and after project life cycles	Adoption of SDRD-developed technologies is indicative of quality and relevance of efforts undertaken	SDRD provides a unifying element for the workforce across our multi-disciplinary and geographically diverse organization
Our research emphasis areas are broadly categorized: nuclear security, information security, high-energy density diagnostics, integrated experiments, advanced analysis, improvised explosive device, threat reduction, and safeguarded energy	Strong peer review, technical advising, and support from experts in national security science and technology ensure relevance to critical areas	Projects are evaluated on a quarterly basis to provide consistent checks on performance (some projects are terminated when deemed to not meet criteria)	Evidence proves SDRD helps to retain individuals and attract new talent to support the NNSS mission for national security

Development of a Three-Dimensional Seismic Velocity Model

NSTec geologists Lance Prothro, Margaret Townsend, Heather Huckins-Gang, Sig Drellack, and Dawn Reed, teaming with Todd Kincaid and Kevin Day of GeoHydros, LLC, have shown that it may be possible to convert a 3-D hydrostratigraphic framework model (HFM) of the Yucca Flat area of the Nevada National Security Site (NNSS) to a 3-D seismic-attribute framework model (SFM). The research is being pursued as a two-year SDRD project (NLV-24-14, Three-Dimensional Seismic-Attribute Model for Yucca Flat, 225–231).

The U.S. has a significant national security interest in improving its ability to detect and locate underground nuclear explosions (UNEs) that may be conducted anywhere in the world.[1] One of the primary methods to monitor for UNEs is through the analysis of seismic waves generated by the explosions. Seismic waves, whether generated by UNEs or other man-made or natural events, propagate through different rock types at differing speeds and with unique characteristics that depend largely on various rock properties and the presence of other geologic features. Current NNSS projects are studying the physics of the creation and propagation of seismic waves and have expressed interest in using the new SFM.

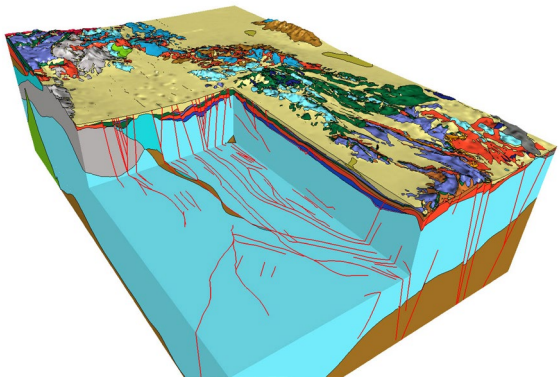

Looking northeast at a cutaway 3-D perspective view of the Yucca Flat HFM. Colored layers are hydrostratigraphic units; red lines are faults.

The Yucca Flat HFM[2] was originally developed to model groundwater flow. The Yucca Flat HFM depicts the distribution of subsurface geologic units according to their ability to transmit groundwater. Many of the rock properties and geologic structures that control groundwater flow also influence seismic wave transmission, so the team reasoned that the Yucca Flat HFM could be modified to create an SFM.

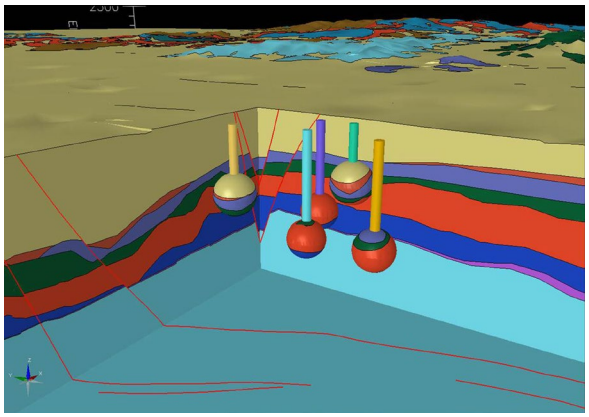

Cutaway 3-D perspective view of the Yucca Flat HFM showing how collapse chimneys (vertical columns) and damage zones (colored spheres) will appear in the Yucca Flat seismic-attribute model. For reference, the light-blue column is ~500 m tall.

Abundant geologic and geophysical data were collected in support of historic nuclear testing in Yucca Flat, and a significant effort was made to compile and evaluate these data for use in the model conversion. Then, using a subset of the data, a separate preliminary velocity model, independent of the HFM, was constructed to explore its potential to aid in evaluating the HFM. Initial assessments of the preliminary velocity model indicate that it can provide an additional and efficient method to evaluate visually and analytically the 3-D distribution of velocity volumes beneath Yucca Flat and the seismic character of model layers.

The investigators also evaluated the potential for demarcating collapse rubble chimneys and damage zones associated with UNEs in Yucca Flat. These features likely consist of rocks with altered seismic properties, and thus their demarcation would be a valuable addition to a Yucca Flat SFM. Fortunately, all the specifications necessary to digitally construct 3-D perspectives for these features for all the UNEs in Yucca Flat are available.

[1] Snelson, C. M., R. E. Abbott, S. T. Broome, R. J. Mellors, H. J. Patton, A. J. Sussman, M. J. Townsend, W. R. Walter, "Chemical explosion experiments to improve nuclear test monitoring," *Eos, Trans. American Geophysical Union* **94**, 27 (July 2013) 237–239.

[2] Bechtel Nevada, *A Hydrostratigraphic Model and Alternatives for the Groundwater Flow and Contaminant Transport Model of Corrective Action Unit 97: Yucca Flat–Climax Mine, Lincoln and Nye Counties, Nevada*, Bechtel Nevada, Las Vegas, Nevada, January 2006.

Contributed by L. Prothro and M. Townsend

SDRD to Stockpile Stewardship Success: Stereo Borescope Imaging

The stereo borescope was a two-year SDRD project in FY 2006 [1] *and FY 2007*.[2] *The stereo borescope records images over a time sequence of a metal surface shocked by high explosives. The stereo images can then be cross correlated to produce a 3-D image of the shocked surface. Ideally, we scale the 3-D image to provide dimensional coordinates on the optical Z-axis for scaled depth perception to the reconstructed 3-D image. Single line-of-sight borescope diagnostics have been fielded on previous experiments at other laboratories and the Leda subcritical experiment in U1a at the NNSS. Single line-of-sight imaging is very limited in depth perception. Going to a stereo view can provide better depth perception on the shocked surface and will potentially provide dimensional information for a shock wave traveling across a surface.*

During the SDRD project, we designed and acquired a stereo imaging bundle and custom micro-lenses for a 3 mm coherent image bundle to view both the left and right stereo images of the 3-D surface. The stereo images were then recorded on a camera system. We initially recorded static 3-D objects to investigate close proximity photogrammetry image correlation techniques. The image bundle and framing camera used to record dynamic high-explosives shock images degrade image quality with image distortion and noise. We acquired stereo framing images of shocked copper coupons with notch grooves cut to produce significant jets of material emitted from the grooves during shock. The images produce 3-D depth perception when viewed.

This diagnostic has been selected to support the upcoming suite of subcritical experiments under the name of Dynamic Stereo Surface Imaging. Custom imaging and illumination probes are being designed to view the surface in the experiment, and the stereo imaging will be combined with multiplexed photonic Doppler velocimetry [3] *to provide a wealth of diagnostic information.*

[1] Baker, S. A., S. Wu, "Stereoscopic Borescope," in *Nevada Test Site–Directed Research and Development*, FY 2006, National Security Technologies, LLC, Las Vegas, Nevada, 2007, 287–294.

[2] Baker, S. A., "Stereo Borescope," in *Nevada Test Site–Directed Research and Development*, FY 2007, National Security Technologies, LLC, Las Vegas, Nevada, 2008, 225–232

[3] Daykin, E., C. Perez, A. Rutkowski, C. Gallegos, "Advanced PDV Techniques: Evaluation of Photonic Technologies," in *Nevada National Security Site–Directed Research and Development*, FY 2010, National Security Technologies, LLC, Las Vegas, Nevada, 2011, 205–214.

Contributed by S. Baker

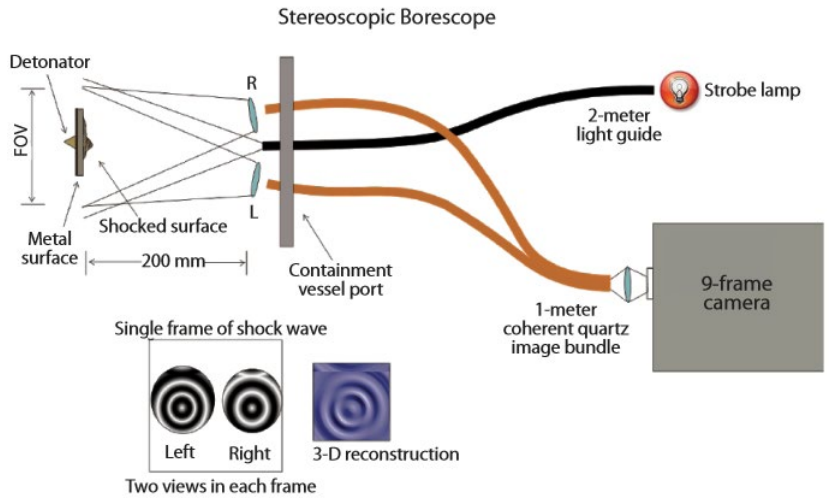

Stereo borescope schematic diagram

FY 2015 New Initiatives and FY 2014 Project Selection

This past fiscal year marked the 12th anniversary of Congressional authorization of the SDRD program. During the last decade, the program has grown and matured, becoming a vital and integral part of our technical base. As the primary source for new discovery and innovation in support of national security needs, the program has no equal and provides unparalleled return on investment. Based on numerous and high-impact successes, coupled with timely conditions, the program is well poised to achieve even greater results.

Together with the Strategic Development Office, and the organizational alignment with the Chief Technology Office (CTO) as mentioned in our last annual report, SDRD has a much improved venue for the program to execute on critical long-term strategic initiatives for the NNSS and our overall national security mission. In concert with these changes and in order to fully leverage SDRD, we created a new element or class of "strategic opportunity" R&D that will be closely aligned with the long-term strategy and corporate vision. In some aspects this element is similar to directed research at the NNSA national laboratories. A white paper, published in July 2012, titled "Leveraging SDRD to Its Fullest Extent," describes our concept for expansion of the program and has since been our roadmap and architecture for developing advanced capabilities and solutions. In FY 2014 we specially requested proposals with enhanced strategic emphasis around key challenge areas in stockpile stewardship and global security relevant to NNSS mission focus. The two themes chosen were dynamic materials and unmanned aerial sensor platforms.

For the first time in program history we have raised the investment level on SDRD to adopt and fund this new class of strategic research going forward in FY 2015. An increase of 0.5% will be applied in FY 2015 to fund these projects, above and beyond the approximate 2% utilized for the exploratory research projects that have thus far formed the core of our program. Overall, this will bring our SDRD investment rate to 2.5%, yielding a program size of approximately $9M. For the current year, FY 2014, costs were up slightly over the previous year

Developments in Optical Diagnostics

In previous reports we have highlighted the progress in optical velocimetry and probes using SDRD and other sources to mature this technology (Site-Directed Research and Development, FY 2013, National Security Technologies, LLC, Las Vegas, Nevada, 2014, x). By leveraging many major advancements in telecommunication components, we have brought new capability to measure dynamic shock phenomena, which had heretofore been impossible.

Optical diagnostics have the advantage over historical electrical-based diagnostics in that they are nonintrusive to the surface or material being measured. Measurements include velocity, displacement, thermal, images, holography, ejecta, and shock arrival.

Integrating optical diagnostics into dynamic shock experiments has been an ongoing development effort. Probe development has grown from being bulky single-channel units to smaller multichannel units. Current dynamic shock tests now produce more data from one experiment than all the data combined from all past experiments.

Future probes will continue to get smaller and be able to withstand very high temperatures and very high pressures. Probes of the future will also become highly integrated systems to support several different types of measurements through the same probe.

Contributed by V. Romero

An advanced optical probe used with multiplexed photonic Doppler velocimetry (MPDV) for dynamic material experiments

The Need for Fundamental Dynamic Materials Research

There are many applications of importance to the weapons programs of the U.S. Departments of Defense and Energy where materials are exposed to high-rate impulsive loading conditions. For example, any time a material (such as a metal) is driven by high-explosive loading, it will respond by moving and deforming at a very high strain rate. Past research has shown us that for such applications it is necessary to make fundamental physics measurements of how this deformation process occurs to be able to successfully model it, and that such fundamental properties must in some cases be made at the appropriately high strain rates.

The most fundamental property that must be captured is the equation of state (EOS) of the material of interest (see inset Ga example). If the material has phase changes that can occur under the real dynamic loading conditions, then a multi-phase EOS must be developed. Pure phase EOSs do not depend upon strain rate in the experimental technique used to determine them. But the location of transitions from one phase to another will be strain rate–dependent. This means that phase boundary information must be collected using the appropriate experimental technique, which, for high strain rates, is dynamic compression. For example, if a solid-solid phase change takes milliseconds to occur, and your process only takes microseconds, then this phase change will not be observed. One place where strain rate is important is in the strength and yielding process, both in compression and in tension. Most compressive strength data used to constrain models in large-scale computer codes derives from Kolsky bar (or similar) techniques, where strain rates near 10^4/s can be realized. For shock compression events that occur at 10^5–10^6/s, these data may not be completely relevant. So it is important to also obtain data using shock compression methods to be able to construct a wide-range strength model.

To be sure that our computer simulation predictions of complex dynamic events maintain high fidelity, we need embedded physics models for EOS and strength that capture the relevant stress, strain, and rate of strain. We also need to do such complex experiments, and directly compare to simulations to know that our simulations are representing physical reality well.

Contributed by R. Hixson

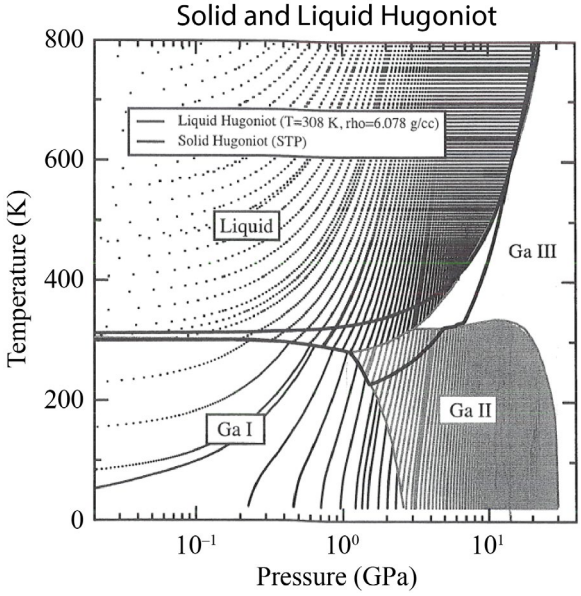

This example of the Ga EOS (based on Crockett [1]) shows the complex nature of the phase space around the Hugoniot, which translates into complex wave profiles derived from the underlying fundamental physics

[1] Crockett, S. D., C. W. Greeff, "A gallium multiphase equation of state," *AIP Conf. Proc.* **1195,** 1 (2009) 1191–1194.

based on increased number of projects, costs associated with the EAB, and funding applied to critical feasibility studies. Total expenditures were approximately $7.5M, and average project size was $240K.

Projects selected in FY 2014 came from a diverse set of proposals covering a broad spectrum of our mission areas and some stretch ideas in energy security. Innovation was particularly high with some notable potential solutions to difficult problems. Geoscience and techniques for detecting underground nuclear events has been a strong area, and this year was no exception. A renewed emphasis on some common issues surrounding stockpile science brought new ideas for advancing neutron sources and neutron detection. In other needs, new techniques to capture signatures of proliferation and simplify nuclear forensics were offered in these recurrent challenges.

In total, 120 proposals were submitted, which was a slight decrease over FY 2013 (approximately 10%). This was primarily caused by one of our sites experiencing programmatic issues that limited their ability to submit. Nonetheless, the quality was extremely high and selection was as competitive as ever. Technical review of proposals remains firmly grounded in peer review with established and comprehensive criteria. Our internal review team, supplemented by external advisors and subject matter experts, conducted an exhaustive review of all submissions. Proposals were evaluated on technical merit and innovation, probability of success balanced with technical risk, potential for mission benefit, and alignment with our mission directives to achieve the best possible outcomes.

Another first for FY 2014 was the introduction of feedback reports to individual lead PIs on all non-selected proposals. We beta-tested this concept at a single site last year and, based on suggestions received, we implemented a better model for the report with selected reviewer comments and added comprehensive

Empowering Staff: New Tools for Effective R&D

To further empower our technical staff, we have launched several initiatives that will help integrate our efforts and leverage R&D investment as much as possible.

A technical leadership team has been assembled from our multiple divisions to oversee strategic directions and facilitate communication across technical disciplines. A new technical capability database has been built to easily identify where competencies exist and how best to find them. Enhanced communication channels have been established through team networking centralized on our information systems, both CTO and SDRD websites. This also includes the first-of-its kind article/publication database. And ongoing network analysis tools have been utilized to see where clusters of internal technical capability exist and where improvements can be achieved in establishing new collaborations. We are also exploring advanced concept groups to further enhance our ability to deal with emerging areas and unchartered mission territory.

The NSTechipedia portal, one of several new R&D tools implemented in 2014

Optical Ranging for Shocked Surfaces

In an FY 2014 feasibility study, researchers Bruce Marshall and Brandon La Lone of the NSTec Special Technologies Laboratory (STL) developed a fiber optic–based system that simultaneously measures position and velocity of a dynamically moving target. The system will continue to be refined in an FY 2015 SDRD study (STL-04-15, Optical Ranging for Shocked Surfaces).

Although photonic Doppler velocimetry (PDV) systems have become an important tool in shock wave experiments, there are many instances where position data are needed but cannot be obtained by integrating the PDV velocity. PDV data cannot determine material position when the angle between the PDV probe and the target motion is unknown or changing. This is presently one of the most urgent issues being discussed in the shock compression community, especially for experiments where material position is critical.

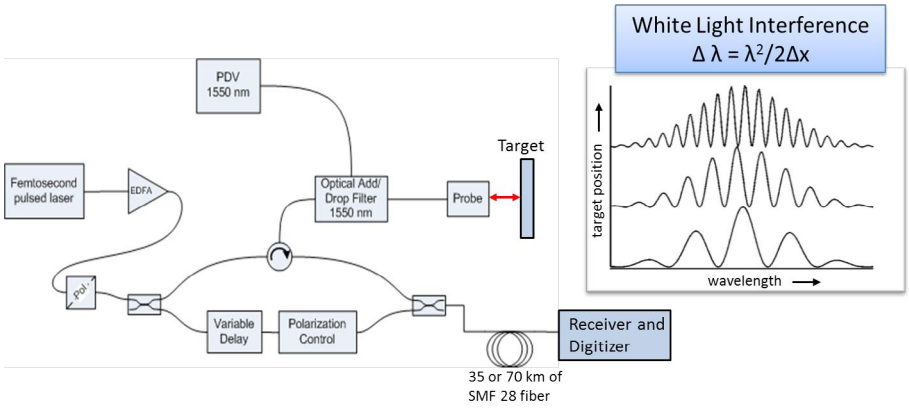

The optical ranging system prototype functions like a white-light Mach-Zehnder interferometer in which one leg reflects from the target and one leg is a fixed reference. The spectral domain is converted to the time domain using a short-pulse laser and 35 or 70 km of optical fiber for dispersion. Distance spectrograms can be constructed from collected data.

A new optical technique for time-resolved distance measurement was recently described by Xia and Zhang.[1] Their system has many advantages over other ranging systems in that it is insensitive to the Doppler shift, has high sampling rates (100 MHz), is accurate to <10 µm, and can handle very low target return light. Target reflection losses of –40 to –60 dB are typical for shock experiments. Although Xia and Zhang only applied the technique to measurements over a very small range of about 20 µm on a vibrating speaker cone, the STL researchers recognized its potential use for tracking material in shock experiments over a much larger range of at least several centimeters. The system could also be multiplexed with a PDV to simultaneously measure velocity and position from the same fiber probe.

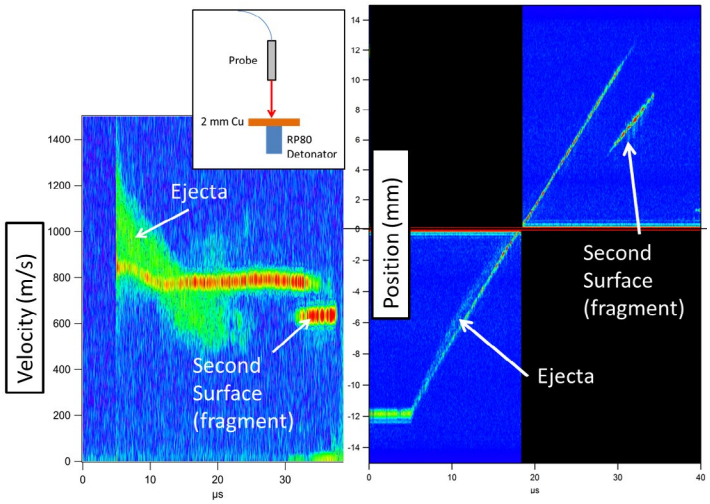

Velocity and position spectrograms of a shocked copper surface, ejecta formation and recollection, and a second copper surface late in time are observed in velocity and position. For the first time, their true time-dependent positions are quantifiable.

Optical Ranging for Shocked Surfaces (continued)…

In the feasibility study, a prototype ranging system was constructed and used in several experiments.[2] The system can be thought of as a white-light Mach-Zehnder interferometer, where one leg reflects from the target and one leg is a fixed reference. Target distance is determined from the spacing of constructively interfering wavelengths in the spectral domain. The key to the system working in a dynamic environment is that it converts the spectral domain to the time domain so that the interference frequency is proportional to distance. Distance spectrograms can be constructed from the recorded data, much like velocity spectrograms are constructed during the analysis of PDV data.

The velocity and distance spectrograms from an experiment on an explosively driven copper sample demonstrate the system's capabilities. The copper surface, ejecta formation and recollection, and a second copper surface late in time are all observed in both the velocity and the position spectrograms. These features have been observed for years in velocity spectrograms, and for the first time their true time-dependent positions are now quantifiable. Researchers at Los Alamos National Laboratory and NSTec are now considering experiments that were never before thought possible because of this diagnostic development.

[1] Xia, H., C. Zhang, "Ultrafast and Doppler-free femtosecond optical ranging based on dispersive frequency-modulated interferometry," *Optics Express* **18**, 5 (2010) 4118–4129.

[2] La Lone, B. M., B. R. Marshall, E. K. Miller, G. D. Stevens, W. D. Turley, L. R. Veeser, "Simultaneous broadband laser ranging and photonic Doppler velocimetry for dynamic compression experiments," *Rev. Sci Instrum.* **86** (2015) 023112.

Contributed by B. Marshall and B. La Lone

program manager feedback with recommendations for future efforts. So far we have seen a very positive response and believe this has filled a much needed gap in our program to provide objective evaluation of strengths and weaknesses in proposals.

FY 2014 Annual Report Synopsis

The reports that follow are for project activities that occurred from October 2013 through September 2014. Project life cycle is indicated under the title as well as the original proposal number (in the following format: site abbreviation--ID #--originating fiscal year; e.g., STL-03-14). Each of the reports describes in detail the discoveries, achievements, and challenges encountered by our principal investigators. As SDRD, by definition, invests in "high-risk" and hopefully "high-payoff" research, the element of uncertainty is inherent. While many of our efforts are "successful" and result in positive outcomes or technology utilization, some fall short of expectations, but cannot be construed as "failure" in the negative sense. The latter is a natural and valid part of the process of advanced research and often leads to unforeseen new pathways to future discovery. Regardless, either result advances our knowledge base and increases our ability to identify solutions and/or avoid costly and unwarranted paths for future challenges.

In summary, the SDRD program continues to provide an unfettered mechanism for innovation that returns multifold to our customers, to national security, and to the general public. The program is a vibrant R&D innovation engine, benefited by its discretionary pedigree, enhanced mission spectrum, committed resources, and sound competitiveness to yield maximum taxpayer benefit. The 25 projects described exemplify the creativity and ability of a diverse scientific and engineering talent base. The efforts also showcase an impressive capability and resource that can be brought to find solutions to a broad array of technology needs and applications relevant to the NNSS mission and national security. Further SDRD performance metrics can be found in the appendix at the end of this report.

Howard A. Bender III
SDRD Program Manager

This page left blank intentionally

National Security Technologies–Operated Sites

Los Alamos Operations (LAO)
182 East Gate Drive
Los Alamos, New Mexico 87544

Livermore Operations (LO)
P.O. Box 2710
Livermore, California 94551-2710

North Las Vegas (NLV)
P.O. Box 98521
Las Vegas, Nevada 89193-8521

Nevada National Security Site (NNSS)
P.O. Box 98521
Las Vegas, Nevada 89193-8521

Remote Sensing Laboratory–Andrews Operations (RSL-A)
P.O. Box 380
Suitland, Maryland 20752-0380
(Andrews Air Force Base)

Remote Sensing Laboratory–Nellis Operations (RSL-N)
P.O. Box 98521
Las Vegas, Nevada 89193-8521
(Nellis Air Force Base)

Sandia Operations (SO)
Sandia National Laboratories
P.O. Box 5800
Mail Stop 1193
Albuquerque, New Mexico 87185

Special Technologies Laboratory (STL)
5520 Ekwill Street
Santa Barbara, California 93111-2352

This page left blank intentionally

Acronyms and Abbreviations

A

AC	alternating current
ACE	Advanced Configuration Environment
A/D	analog to digital
ADC	analog-to-digital converter
Ag	silver
AGC	automatic gain control
AGW	acoustic gravity waves
Al	aluminum
ALEGRA	an MHD simulation code (SNL)
AlO	aluminum monoxide
Al_2O_3	aluminum oxide
Al_2O_3:Cr	ruby (chromium-doped aluminum oxide)
^{241}Am	americium-241
$^{241}AmBe$	americium-241/beryllium
AMS	Aerial Measuring System
ANSI	American National Standards Institute
Ar(g)	argon
ASCII	American Standard Code for Information Interchange
ASI	Applied Spectra, Inc.
ASTER	Advanced Spaceborne Thermal Emission and Reflection Radiometer
ATD	arrival time distribution
Au	gold
AWG	arbitrary waveform generator
AXI	advanced eXtensible interface (arbiter)

B

^{10}B	boron-10
BaF_2	barium fluoride
BaO	barium oxide
BaTiO4	barium titanate
$Ba_2TiSi_3O_8$	fresnoite
BCB	bisbenzocyclobutene
BEEF	Big Explosives Experimental Facility

BLE	Bluetooth low energy
BPI	byte peripheral interface
BS	beam-splitting cube

C

CAD	computer-aided design
Caltech	California Institute of Technology
$CaMoO^4$	calcium molybdate
CaO	calcium oxide
$CaWO^4$	calcium tungstate
CBRNE	chemical, biological, radiological, nuclear, and explosives
CCD	charge-coupled device
CCFET	capacitive coupled field-effect transistor
CCSD(T)	coupled-cluster singles and doubles plus perturbative triples method
Ce	cerium
CERN	European Organization for Nuclear Research
^{252}Cf	californium-252
CF	CompactFlash (card)
CH_4	methane
CJ	Chapman-Jouguet
^{35}Cl	chlorine-35
CLLB	$Cs_2LiLaBr_6:Ce_{0.5\%}$
CLLBC:Ce	$Cs_2LiLa(Br_6)_{90\%}(Cl_6)_{10\%}:Ce$
CLLC	$Cs_2LiLaCl_6:Ce_{0.5\%}$
CLYB	$Cs_2LiYBr_6:Ce_{0.5\%}$
CLYC	$Cs_2LiYCl_6:Ce_{0.5\%}$
^{57}Co	cobalt-57
^{60}Co	cobalt-60
CPU	central processing unit
Cr	chromium
^{133}Cs	cesium-133
^{137}Cs	cesium-137
CT	computerized tomography
CTBT	Comprehensive Test Ban Treaty
CTBTO	Preparatory Commission for the Comprehensive Nuclear-Test-Ban Treaty Organization

CTH	An SNL-developed radiation-diffusion hydrodynamics code derived from the 1-D 1969 "Chart D," which was extended to two dimensions in 1975 (and named CSQ = (Chart D)^2), and then to three dimensions in 1987 (and renamed CTH = (CSQ)$^{3/2}$).
CTO	Chief Technology Office
CVL	core-to-valence luminescence

D

DAC	diamond anvil cell
DBS	dichroic beam splitter
DC	direct current
D-D	deuterium-deuterium
DDR3	double data rate type 3 dynamic random access memory
DFT	density functional theory
DNT	2,4-Dinitrotoluene
DOE	U.S. Department of Energy
DPF	dense plasma focus
DPRK	Democratic People's Republic of Korea
DSSI	dynamic stereo surface imaging
DSSS	direct-sequence spread-spectrum (modulation)
D-T	deuterium-tritium
DU	depleted uranium

E

EAB	External Advisory Board (SDRD)
EBSD	electron backscattered electron microscopy
EEPROM	electrically erasable programmable read-only memory
EIA	electronic industries alliance
EM	electromagnetic
EMP	electromagnetic pulse
ENOB	effective number of bits (in digital oscilloscope)
EOS	equation-of-state
EPROM	erasable programmable read-only memory
^{152}Eu	europium-152
Eu^{3+}	europium
Eu_2O_3	europium oxide

F

FAR	false-alarm rate
FAT	file allocation table
FEA	finite element analysis
FEM	finite element method
FET	field-effect transistor
FFT	fast Fourier transform
FMC	FPGA mezzanine card
FOM	figure of merit
FOV	field of view
FPGA	field-programmable gate array
FWHM	full-width at half-maximum
FY	fiscal year

G

Ga	gallium
GaAs	gallium arsenide
GATOR	grating-actuated transient optical recorder
GCC	GNU compiler collection
GEANT4	particle simulation software
GEE_n	gamma equivalent energy (for thermal neutrons)
GeO	germanium oxide
GIS	geographic information system
GNSS	Global Navigation Satellite System
GPIO	general purpose input/output
GPS	global positioning system
GUI	graphical user interface

H

H_2	hydrogen
H_2O	water
H_2WO_4-GO	tungstic acid/graphene oxide
^3He	helium-3
^4He	helium-4
HE	high explosive
HCl	hydrogen chloride
HCP	hexagonal close packed

HEDP	high-energy density physics
HEL	Hugoniot elastic limit
HET	High Explosive Testing (campaign: June 2014)
HFM	hydrostratigraphic framework model
Hg-Ar	mercury-argon
HRTEM	high-resolution transmission electron microscopy
HSU	hydrostratigraphic unit

I

IAR	ionospheric Alfvén resonator
I^2C	inter-integrated circuit
ICV-E	integrity check value in EPROM
ICV-P	integrity check value in processor
IF	intermediate frequency
InGaAs	indium gallium arsenide
InP	indium phosphide
InSb	indium antimonide
I-NVM	invisible non-volatile memory
I/O	input/output
IpFFT	interpolated fast Fourier transform
IR	infrared

J

JASPER	Joint Actinide Shock Physics Experimental Research (facility)
JTAG	Joint Test Action Group

K

K	potassium
KUT	potassium, uranium, and thorium

L

LANL	Los Alamos National Laboratory
LAO	Los Alamos Operations
LC/APC	latched connector/angle-polished connector
LDRD	Laboratory-Directed Research and Development
LED	light-emitting diode
^6Li	lithium-6
$LiBaF_3$	lithium barium fluoride

$LiBaF_3$:Ce,Rb	cerium-rubidium-doped lithium barium fluoride
LIBS	laser-induced breakdown spectroscopy
LiF	lithium fluoride
LiF/ZnS:Ag^+	silver-doped lithium fluoride zinc sulfide
LiI:Eu^{2+}	europium-doped lithium iodine
$LiInSe_2$	lithium indium selenide
linac	linear accelerator
LLNL	Lawrence Livermore National Laboratory
LO	Livermore Operations
LPA	local polynomial approximation
LSO:Ce	cerium-doped lutetium oxyorthosilicate
LSP	large-scale plasma simulation code (Alliant Techsystems Operations, LLC)

M

MC	Monte Carlo
MCMC	Markov Chain Monte Carlo
MCNP	Monte Carlo N-Particle
MCNPX	Monte Carlo N-Particle Extended
MCP	microchannel plate
MESFET	metal-semiconductor field-effect transistor
MH	Metropolis-Hastings
MHD	magneto-hydrodynamic (code)
MLE	maximum likelihood estimate
MPDV	multiplexed photonic Doppler velocimetry
MPIC	Max Planck Institute of Chemistry
MPU	microprocessor unit
MT	Mechanical Transfer
M-Z	Mach-Zehnder

N

Na	sodium
Na_2WO_4-GO	sodium-tungstate/graphene oxide
NaCl	sodium chloride
NaI	sodium iodide
NaI:Tl	thallium-doped sodium iodide
NASA	National Aeronautics and Space Administration

ND	nanodisk
NDSE	Neutron-Diagnosed Subcritical Experiment
Nd:YAG	neodymium-doped yttrium aluminum garnet (laser)
NFO	Nevada Field Office
NH_3	ammonia
NIF	National Ignition Facility
NLV	North Las Vegas
NM	nitromethane
NNSA	U.S. Department of Energy, National Nuclear Security Administration
NNSS	Nevada National Security Site
NO_2	nitrogen dioxide
NRAT	Nuclear/Radiological Advisory Team
NSCRAD	Nuisance-Rejection Spectral Comparison Ratio Anomaly Detection
NSTec	National Security Technologies, LLC
NToF	neutron time of flight
NTP	network timing protocol
NURE	National Uranium Resource Evaluation

O

1-D	one-dimensional
O_2	molecular oxygen
OFHC	oxygen-free, high-conductivity
OMA	optical multichannel analyzer

P

PAS	power automation system
PC	personal computer
PCB	printed circuit board
PCD	photoconductive device
PD	photodiode
PDE	partial differential equation
PHD	pulse height discrimination
phe	PMT photoelectrons
PHY	physical (layer)
PIC	particle-in-cell (code)
PMT	photomultiplier tube

POD	proper orthogonal decomposition
ppm	parts per million
PSD	pulse shape discrimination
PSF	point spread function
^{239}Pu	plutonium-239
PVD	photonic Doppler velocimetry
P-wave	seismic compressional wave
PXRD	powder x-ray diffraction

R

R&D	research and development
RAM	random access memory
RAP	Radiological Assistance Program
RBU	radiological background unit
RF	radio frequency
RGB	red, green, blue
rGO	reduced graphene oxide
RINEX	Receiver Independent Exchange
RISC	reduced instruction set computing
RMD	Radiation Monitoring Devices, Inc.
rms	root mean square
ROI	region of interest
ROM	reduced order model
RPI	Rensselaer Polytechnic Institute
RRC	raised-root cosine (filter)
RSL-A	Remote Sensing Laboratory–Andrews

S

S&T	science and technology
SBA	super bialkali
SBSF	statistics-based spline fitting
SCADA	supervisory control and data acquisition
SD	secure digital (card)
SDRD	Site-Directed Research and Development
SEM	scanning electron microscopy
SFM	seismic-attribute framework model

SFP	small form-factor pluggable
Si	silicon
SiN	silicon nitride
SiO_2	synthetic silicon
Si_3O_6	trisilicon hexaoxide
SiO_2H_2O	hydrous silicon dioxide
SNL	Sandia National Laboratories
SNR	signal-to-noise ratio
SPE	Source Physics Experiment
SPH	smoothed-particle hydrodynamics
SPI	serial peripheral interface
$SrI_2:Eu^{2+}$	europium-doped strontium iodide
SSU	seismo-stratigraphic unit
STL	Special Technologies Laboratory

T

2-D	two-dimensional
3-D	three-dimensional
TBP	tributyl phosphate
Tc	technetium
^{99}Tc	technetium-99
^{99m}Tc	metastable technetium
TCXO	temperature-compensated crystal oscillator
TEC	total electron current
TEM	transmission electron microscopy
Th	thorium
THOR	Texas High-Intensity Optical Research Laser
TiO_2	titanium dioxide
TRL	technology readiness level

U

U	uranium
^{235}U	uranium-235
^{238}U	uranium-238
UART	universal asynchronous receiver/transmitter
UCSB	University of California, Santa Barbara

UGTA	Underground Test Area
UNE	underground nuclear explosion
UNLV	University of Nevada, Las Vegas
UNPE	underground nuclear proliferation experiment
UO_2	uranium dioxide
U_3O_8	triuranium octoxide
UQ	uncertainty quantification
U.S.	United States
USAF	United States Air Force
USB	universal serial bus
USGS	U.S. Geological Survey
UTC	coordinated universal time (French: temps universel coordonné)
UV	ultraviolet

V

VASP	Vienna *ab-initio* simulation package
VCTCXO	voltage-controlled, temperature-compensated crystal oscillator
VISAR	velocity interferometer system for any reflector
VITA	VMEbus International Trade Association
V-NVM	visible non-volatile memory
VTK	Visualization Toolkit

W

WAVRAD	Wavelet Assisted Variance Reduction for Anomaly Detection
WO_3	tungsten trioxide
WO_3-rGO	tungsten oxide/reduced graphene oxide
WP	working point
WTP	weapons testing program

X

XRD	x-ray diffraction
XRF	x-ray fluorescence
XUV	extreme ultraviolet

Y

YAG:Ce	cerium-doped yttrium aluminum garnet
Y_2O_3:Eu	europium-doped yttrium oxide

Z

0-D	zero-dimensional

Material Studies and Techniques

Grain-Selective MPDV Experiments

NLV-08-14 | Continued in FY 2015 | Year 1 of 2

Edward Daykin,[1,a] Mike Grover,[b] Robert S. Hixson,[c] Brandon La Lone,[b] Carlos Perez,[a] Gerald Stevens,[b] and Dale Turley[b]

Tin samples of varying thickness and grain size were subjected to planar impacts using the NSTec Special Technologies Laboratory's gas gun to investigate yield strength, spall strength, phase change, and sound speed non-uniformity as a function of grain orientation at differing spatial locations. Multiplexed photonic Doppler velocimetry (MPDV) methods were used to measure velocity at 32 spatial locations and obtain wave profiles from individual grains in large-grain samples. For these measurements samples with grain sizes larger than the sample thickness maximized velocity heterogeneities. The largest velocity differences between the grains were observed in the amplitude of the elastic precursor of the profile; results suggest that the yield strength of tin depends on the crystallographic orientation. Little to no velocity differences were observed in the phase change or spall strength signatures. Experiments on small-grain tin samples were also conducted for comparison, and no heterogeneities were detected. Similar investigations of multi-dimensional and mesoscale impact phenomena have been conducted with line-VISAR; however, to the best of our knowledge, this is the first such application of MPDV to quantify heterogeneities in shock structure across a 2-D area. In FY 2015 some topics we investigate may be spall strength and grain size-to-sample thickness dependency for tin, quantification of measurement uncertainty due to stochastic effects, validation and amplification of previous VISAR measurements on large-grain iron, and exploration of mesoscale boundary effects in material mixtures.

[1] daykinep@nv.doe.gov, 702-295-0681
[a] North Las Vegas; [b] Special Technologies Laboratory; [c] Los Alamos Operations

Background

Multiplexed photonic Doppler velocimetry (MPDV) is a new fiber-optic interferometry system that allows many channels (~100s) of time-resolved velocimetry measurement at user-defined spatial locations in a single experiment. The combination of MPDV and fiber-coupled optical probes offers opportunities to diagnose experiments in "high definition" to explore both macroscopic and mesoscale behaviors simultaneously with spatial resolution on the order of 10 microns and temporal resolution of several nanoseconds. Additionally, MPDV is capable of recording multiple surface velocities and/or dispersive behavior such as ejecta within any single measurement point, as well as accommodating a very large dynamic range (~40 dB) in signal return. Application of MPDV to relevant topics in shock physics promises to improve and complement existing experimental techniques such as VISAR. Velocity non-uniformities thought to result from grain structure heterogeneity, defects, and the stochastic nature of material failure have been measured using VISAR; however, this technique tends to fail in the presence of large variations in signal return or multiple velocities. We have begun to investigate the shock wave behavior of metals with heterogeneous grain structure under planar shock loading using a 32-channel MPDV system.

Non-uniformities in shock structure and sound speed are seldom studied despite their importance to weapons modeling. A long-standing question in experimental shock compression research on polycrystalline metals is how flat the shock wave really is. Rules of thumb exist for the planarity of shock waves that have traversed some number of grains in a polycrystalline sample, but detailed measurements have been lacking. This question is important especially in experiments where the sample thickness or the number of grains is very small, such as can be the case for laser-driven shock wave experiments. This project is focused on finding quantitative answers to some of these questions.

The average size of grains in a polycrystalline metal depends on parameters such as purity, fabrication method (wrought or cross-rolling), and thermal history (annealing). For highly pure metals, macroscopic grains can have sizes that are on the order of centimeters. We are investigating high-purity (99.9999%) polycrystalline tin with grains comparable in size to the target thickness. We measured surface velocity of tin under planar shock loading to determine whether variations in the velocimetry profiles could be observed to correlate with observed grain orientations across a 2-D area (~24 mm^2) under investigation. We also varied sample thickness to investigate differences in shock profiles as a function of the grain size-to-thickness ratio. Several sample disks of large-grain cast tin were cut to thicknesses of 0.5, 1.0, and 2.0 mm and diamond turned to produce a very flat surface (free of machining grooves), which allowed us to visually observe individual grains under illumination from polarized white light. Tin was chosen for this research because we have a considerable body of knowledge on shock properties with small-grain polycrystalline samples, and we know how to make samples with large grains. A downside to using tin is that it has a relatively complex tetragonal structure. Future efforts will be devoted to finding a good candidate cubic metal for research.

Practical application of many optical velocimetry channels requires fiber-optically coupled probes. This can be a bottleneck. For instance, an experiment with 32 MPDV channels might require 32 discrete probes (~$150 per probe) to be individually mounted, aimed, glued, and then characterized (metrology includes determining position, spot size, pointing direction). This fabrication can take days and can be imprecise.

Much of the initial work in this project was development of precise, repeatable, low-cost optical probes as well as metrology methods necessary for widespread application of MPDV techniques. Our intention is to present an economical and practical methodology to obtain many channels of shock wave data from experiments using MPDV, in effect to make MPDV a more useful tool for shock wave experimentation. Currently, optical velocimetry techniques use discrete fiber-optic probes or complex and costly custom optical systems. Because these probes are almost always destroyed during an experiment, a more economical approach is needed. Also, both discrete probes and custom optical systems require significant effort to metrologize each target spot, a practical limitation to employing many tens to hundreds of MPDV velocimetry measurements on a routine basis. We have identified several approaches using commercially available fiber-optic components along with inexpensive imaging systems to allow for rapid (couple hours) and inexpensive (~$800) probe assembly and metrology for application to MPDV experiments requiring channel counts from 30 to 50.

We completed the first year of this project with an experimental campaign of four gas gun experiments on large- and small-grain tin shocked to pressures appropriate to either induce phase change or emphasize the elastic precursor. The 1" diameter tin target samples were shocked via a ½" diameter copper impactor using the NSTec Special Technologies Laboratory (STL) “mini” gas gun platform. An 8 × 4 grid of 32 velocimetric measurement points was applied to the target sample using an integrated fiber-optic probe (one of several above-mentioned options) uniformly distributed across an area of approximately 7.5 × 3.25 mm. MPDV data were recorded and analyzed, allowing correlation of velocity and time-of-arrival data to pre-shot recorded relative grain locations. (Note: Crystallographic orientation of the grains was not

performed.) Observed shock wave profiles indicative of both phase change and material elastic properties were analyzed and are detailed in the remainder of this report.

Project

Optical Probe and Metrology Development

In this project, we have developed several alternatives for some of the most common platforms and sample sizes employed in shock physics experiments. We produced three alternative fiber-coupled probes defined as having "coarse," "medium," and "fine" sample densities. Commercially available optical components can be used to construct a free-space optical relay system. The rail systems and achromatic doublet lenses were procured from Thorlabs for less than $500 per set (two lenses, rails, and x-y translation mounts). Choosing from various focal lengths commonly made by vendors allows users to select magnifications ranging from 1:1 to 5:1; imaging results were modeled via ray-tracing software.

The coarse probe sampling is provided by a 3-D-printed 1" disc with inserts specific to commercially available latched connector/angle-polished connector (LC/APC) fiber-optic connectors (including keyed orientation to account for 8° fiber polish). The fine sampling option was accomplished using close-packed fiber arrays built with a commercially available honeycomb. We used the medium sampling density probes provided by commercially available MT fiber-optic connectors. An MT fiber-optic connector can be selected with a grid of 1 × 12, 2 × 12, or 4 × 12, and each fiber location is known to within 1.5 microns. This allows for a highly repeatable and easily metrologized target grid. We used the 4 × 12 MT connectors metrologized by visible illumination of four corners of the target grid. The MT connector was then mated to the probe rail system using 3-D-printed receptacle discs mounted into commercially available opto-mechanical components. Figure 1 shows one of these multi-fiber probes mounted to the gas gun barrel within the target chamber.

Material Samples and Surface Preparation

Material samples of cast, large-grain tin were acquired from Los Alamos National Laboratory (LANL) as 1" diameter bar stock. Samples were cut and diamond turned to thicknesses of 0.5, 1.0, and 2.0 mm. The vendor performed two machining methods of diamond turning: fly-cut on a mill and turned on a lathe. Interestingly, the fly-cut samples provided much greater visual contrast of grain boundaries than the lathe-prepared samples.

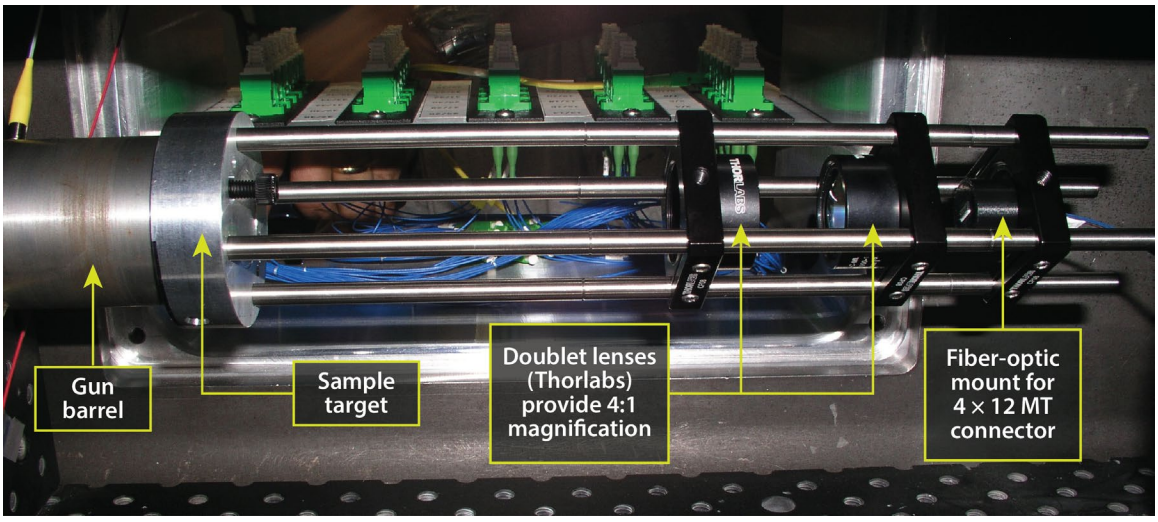

Figure 1. Gas gun target chamber including gun barrel (projectile travels from left to right) capped with tin target sample mount. Shock wave profiles of the sample are measured with a 32-channel fiber-optically coupled optical imaging system (i.e., probe). The probe was expended during the course of the experiment.

Small-grain, cross-rolled tin was acquired commercially. Cross-rolled preparation of tin effectively crushed and randomized the tin grains so that the sample appearance was that of sand—randomly distributed grains with sizes ranging from 10s to 100s of microns. An experiment using small-grain tin was conducted with the presumption that the many, small, randomly oriented grains would average out grain orientation effects and provide a uniform shock front with identical behavior across the region of interest. This information might provide an accurate measure of impactor angle (or tilt) via gradients in the shock front time of arrival. Typical images of both large-grain and small-grain tin are shown in Figure 2.

Following sample inspection and photographic cataloging of grain structure, the diamond-turned surfaces of the tin samples were manually roughed using Scotchbrite pads. This caused the incident illumination to be reflected by the surface within an angular cone of ~10°. We anticipated that a specular (diamond-turned) surface would produce dramatic variations in signal return of reflected light should surface tilt occur. Following surface preparation, the samples were glued onto a gas gun target flange and attached to the opto-mechanical probe assembly. The probe-target package was then metrologized for target spot locations by visible illumination of the target area. Finally, the assembled and metrologized target package was mounted to the gun barrel within the target chamber.

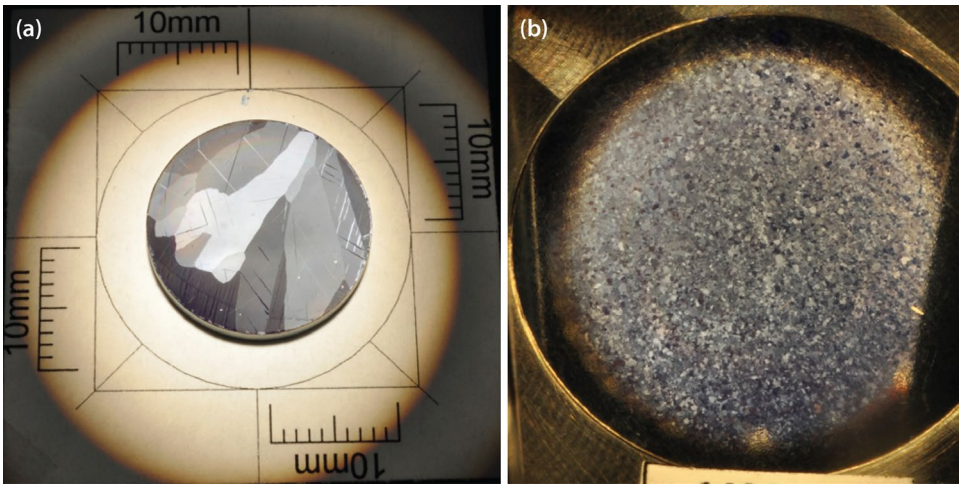

Figure 2. (a) Large- and (b) small-grain tin samples; photographs were taken using polarization-dependent white-light illumination

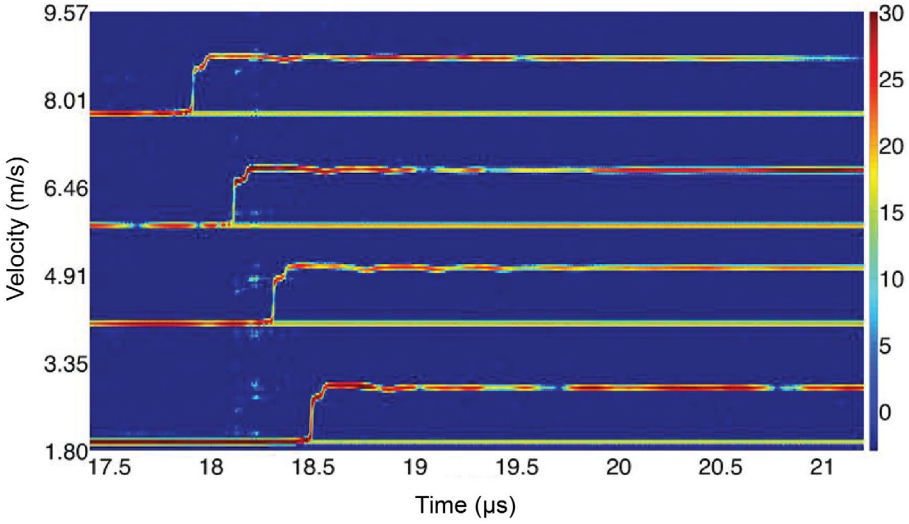

Figure 3. Typical MPDV frequency multiplexed data (four signal traces) from a tin experiment demonstrating high-fidelity signal returns. Relative offsets in trace jump-off times are due to fiber-optic delays incorporated into the diagnostic system to allow for time stagger of simultaneous signals.

Planar Shock Experiments

Four experiments were conducted on the STL gas gun using ½" diameter copper impactors:

- Two experiments on large-grain tin, thickness = 2.0 mm, shocked to 12.1 GPa
- One experiment on small-grain tin, thickness = 2.1 mm, shocked to 12.0 GPa
- One experiment on large-grain tin, thickness = 1.0 mm, shocked to ~5 GPa

Upon compression, tin undergoes a solid-solid phase transition at approximately 9 GPa (Mabire 2000), so the shots performed at 12 GPa were anticipated to have three distinct features in the rising edge: (1) a low-amplitude elastic wave, (2) a plastic wave (P1), and (3) a phase transition wave (P2). The three 12 GPa experiments were performed to investigate heterogeneities in the phase transition amplitude, or shape of the transition wave. Such heterogeneities would suggest a crystallographic orientation dependence on this transition. The experiment at ~5 GPa is below the phase transition and was designed to investigate heterogeneities in the elastic wave, which would indicate an orientation dependence of the material strength.

MPDV was used to measure 32 velocimetry profiles at discrete locations across a 2-D region of the tin samples. The NSTec prototype Gen-1 MPDV was employed for these experiments with multiplexing in both frequency (4x) and time (2x), resulting in eight data traces per digitizer record. Laser illumination of approximately 10 mW was applied at each target location. Reflected Doppler-shifted illumination was collected and transmitted by the fiber-optic probe to the MPDV system. Four traces (measurement points) from a typical data record are shown in Figure 3.

To quantify heterogeneities in shock front time of arrival, it was necessary to first correct for any systematic influences due to impactor tilt. Given our new diagnostic capability and allowing a high sample density of measurement points, we chose to investigate whether a global average of jump-off times could be used to infer impactor tilt, our hypothesis being that localized (distance ~1 mm) variations in arrival times due to heterogeneities would average out over areas much greater than the grain size. Our data seem to confirm this hypothesis; we observed systematic trends on each experiment that we attributed to tilt. Impactor tilt was corrected for each experiment prior to further analysis of grain orientation effects. An example of the data and analysis for the small-grain tin experiment is shown in Figure 4.

Data from large- and small-grain tin experiments shocked to 12 GPa were analyzed for variations in phase-transition signature as well as shock breakout time of arrival. Breakout time of arrival is a difficult parameter to extract from frequency-multiplexed MPDV signals. We automated the extraction of breakout times using a recently developed FFT analysis technique that compares discontinuous step-widths of a shock with the width governed by the uncertainty principle. Due to placement of the MPDV sampling grid, the outermost measurement points were observed to differ (at ~200 ns after start of motion) from the remaining measurements; this was attributed to impactor edge release waves. Otherwise, velocimetric signatures for these data sets were identical to within measurement precision. This is a somewhat surprising result, and needs to be compared with predictions from measured sound speed. This also indicates a need to measure grain orientation if possible. Velocity time-histories and time-of-arrival correlation to grain locations are shown on Figures 5a and 5b for the 2 mm thick large-grain tin.

Our final experiment sought to determine whether the material strength as measured by the elastic precursor exhibited any correlation to grain orientation. In Figure 6a, the elastic precursor can be seen as the small step-like velocity signature occurring just prior to the principal jump in surface velocity. To emphasize the precursor signature, the shock pressure was reduced by lowering the impactor velocity. At the lower stress, there is more time separation between the elastic and plastic waves, making the elastic precursor easier to

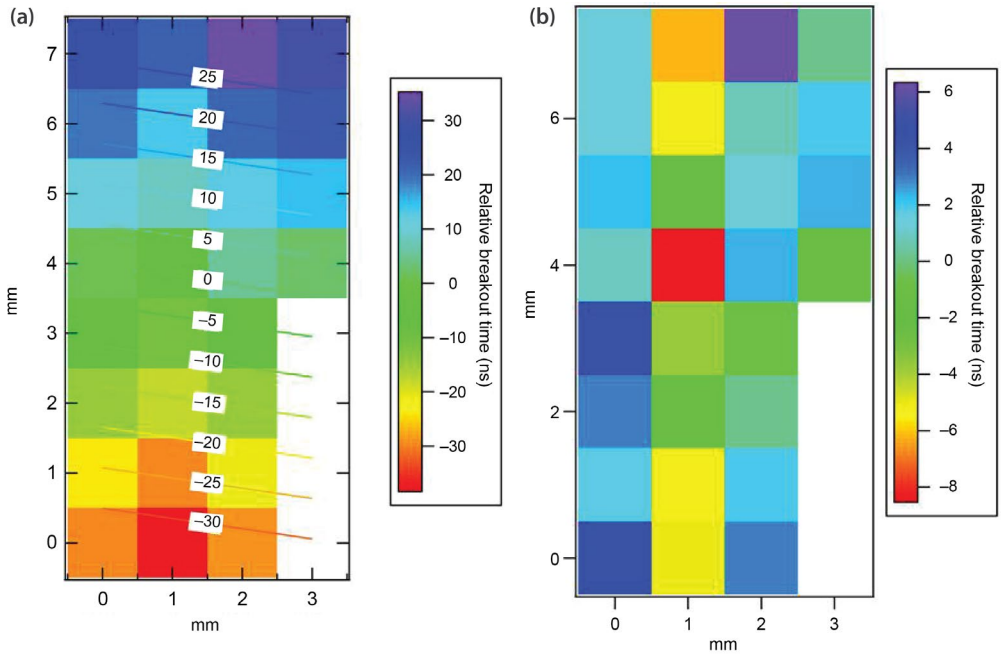

Figure 4. (a) Raw and (b) corrected shock wave breakout time-of-arrival data for small-grain tin experiment demonstrating measured impactor tilt. Thirty-two MPDV measurement locations were made across an 8 × 4 grid of the tin sample (approximate grid spacing of 1 mm). Tilt of approximately 8 mrad was measured and corrected, resulting in a time-of-arrival standard deviation of 3.5 ns.

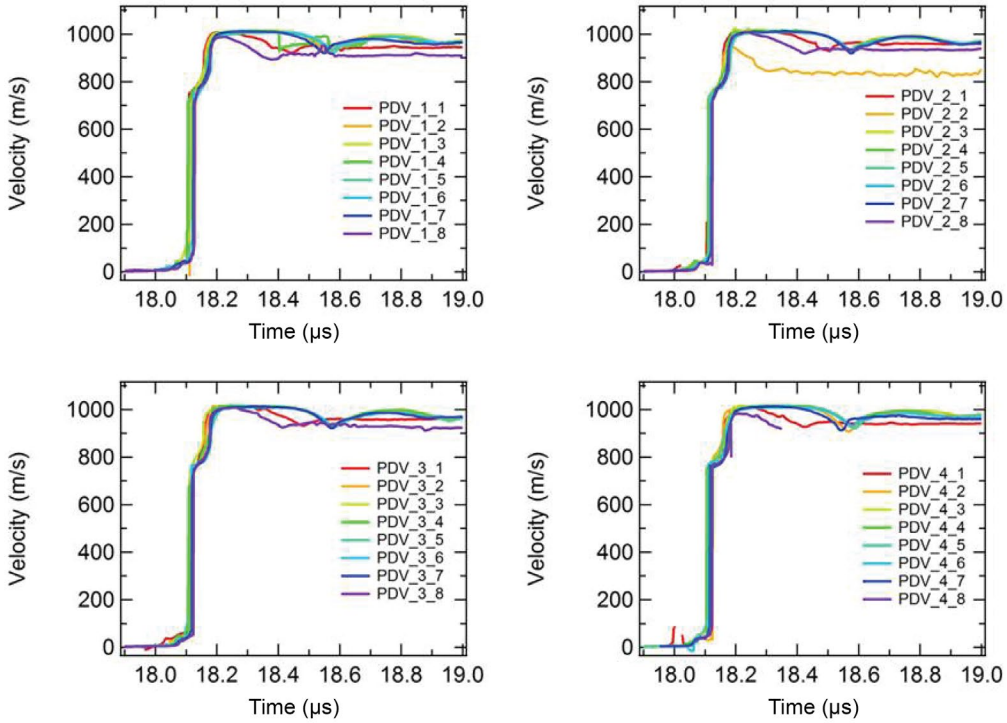

Figure 5a. Raw data from large-grain tin phase-transition experiment. Shock-front time-of-arrival and phase-change signature are identical, except for the outermost (edge) measurement points (red, yellow, and purple traces), and these differences are attributed to edge release waves. There does *not* appear to be any correlation between grain orientation and phase-transition signature.

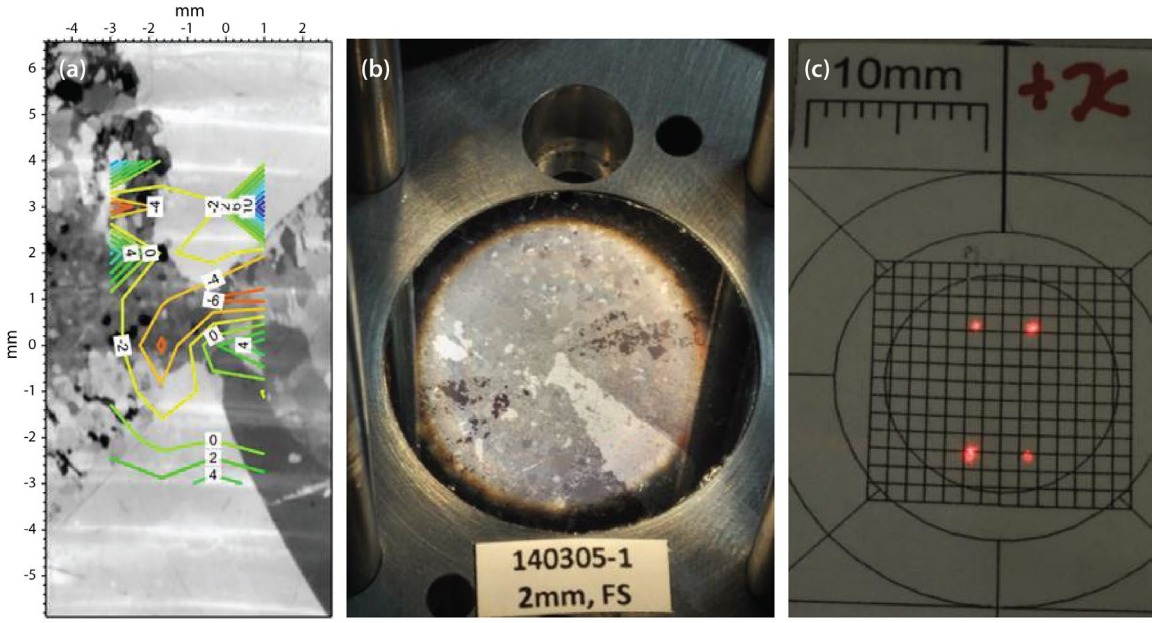

Figure 5b. (a) Shock wave breakout time-of-arrival contours (tilt corrected) for a large-grain tin experiment, (b) photograph of large-grain tin demonstrating variations in grain orientation, and (c) MPDV target grid corner locations for velocimetry measurements. Shock front time of arrival does not appear to correlate with grain locations.

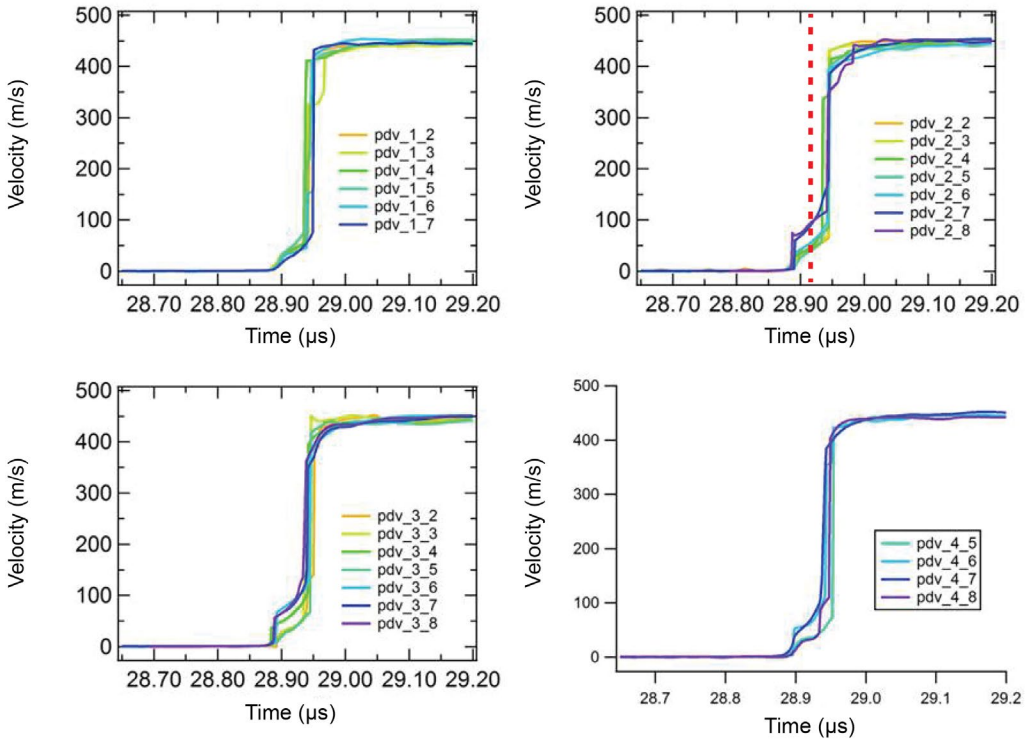

Figure 6a. Large-grain tin material strength experiment (5 GPa) velocimetry profiles. The elastic precursor is the low amplitude foot of the rising edge of the wave profiles. Variations in the elastic precursor signatures are apparent, with certain locations exhibiting double the amplitude of other locations. The precursor amplitudes correlate with grain location as shown in Figure 6b. Precursor amplitude was taken in the middle of the precursor step (indicated by the red dashed line in the upper right figure).

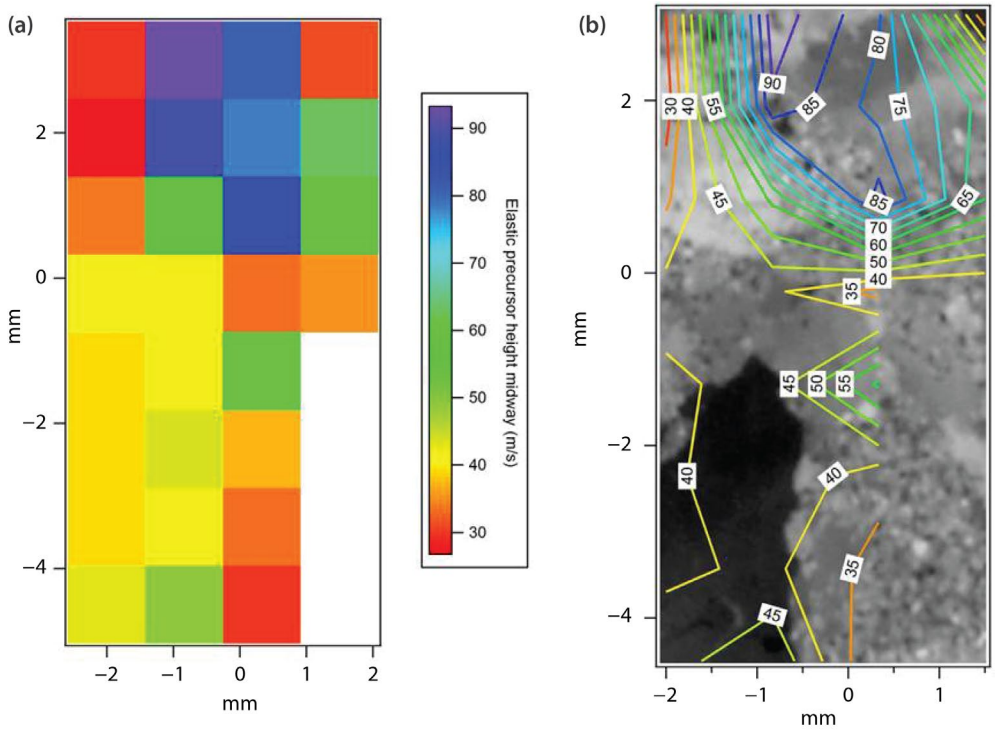

Figure 6b. Large-grain tin material strength experiment. (a) A map of precursor amplitudes measured by the array of probes is shown and (b) a contour plot of these amplitudes is overlaid on a polarized image of the surface. Variations in elastic precursor amplitude appear to correlate with grain locations, with the largest amplitudes observed for the grain at the upper right.

resolve than in the high-stress experiments. In this experiment, we observed variation in the amplitude of the elastic precursor that does suggest dependency on grain orientation. However, the elastic precursor is still somewhat difficult to resolve with PDV due to circulator bleed through of the up-shifted heterodyne laser. The variations in tin strength, as measured by the value at the middle of the precursor rise (~30 ns after first motion), do appear to correlate with the grain locations. This provides some indirect evidence that grain orientations were different. Raw data and elastic precursor half-amplitude are shown in Figures 6a and 6b.

Conclusion

We have developed both the methodology for efficient execution of shock wave experiments using MPDV diagnostics and acquired dynamic data demonstrating grain orientation effects for large-grain tin. Key to the methodology was development of many-channel, fiber-optic probe options that are economical and readily metrologized. We applied these enabling developments to a series of shock wave, planar impact gas gun experiments on both large- and small-grain tin to explore effects of heterogeneous grain orientation. Thirty-two MPDV measurements were made across a 24 mm^2 area of large- and small-grain tin to determine grain orientation effects on material parameters such as phase change and sound speed. The high spatial density of measurement points was also leveraged to determine (and correct for) impactor angle by analyzing the average shock front time of arrival over the sampled area. Phase-change behavior was observed to be independent of grain orientation; however, variations in the elastic properties of tin did appear to correlate with the grain structure. Similar investigations of materials with heterogeneous grain orientations have been made using line-VISAR, but we believe this is the first data providing behavior across a 2-D region of material under test using MPDV.

This project will continue in FY 2015. Future investigations of interest include spall strength and grain size-to-sample thickness dependency for tin, quantification of measurement uncertainty due to stochastic effects, validation and amplification of previous VISAR measurements on large-grain iron, and exploration of mesoscale boundary effects in material mixtures.

Acknowledgments

We would like to thank Rusty Gray (LANL) for his contributions to this work.

Reference

Mabire, C., P. L. Héreil, "Shock induced polymorphic transition and melting of tin," in *Shock Compression of Condensed Matter–1999, AIP Conf. Proc.*, M. D. Furnish, L. C. Chhabildas, R. S. Hixson, eds., **505** (2000) 93–96.

This page left blank intentionally

New Methods to Quantify Thermodynamic and Phase Properties of Shocked Materials

STL-22-14 | Year 1 of 1

Brandon La Lone,[1,a] Dale Turley,[a] Gerald Stevens,[a] Gene Capelle,[a] Eric Larson,[a] Mike Grover,[a] Lynn Veeser,[b] Oleg Fatyanov,[c] and Paul Asimow[c]

We have developed methods that use shock-wave compression followed by laser heating to accomplish two important goals. The first goal was to use long-pulse laser heating to locate high pressure and temperature phase transitions in metals. The second goal was to use short-pulsed laser heating to determine thermal transport properties of shock-compressed materials. Both goals are critical for equations-of-state development for the Stockpile Stewardship Program. Continuous laser irradiance near 1 MW/cm² is needed for the phase boundary identification measurements. To demonstrate the feasibility of the long-pulsed laser heating technique, ambient pressure-heating measurements were performed in which the surface of tin was melted in <1 μs. Also, gas gun pyrometry experiments were performed without laser heating to show that pyrometric temperatures of <400 K could be measured in a shock-wave experiment. Both measurements were critical to the future demonstration of the long-pulsed heating method.

The short-pulsed laser heating technique for thermal transport measurements was developed in an FY 2012 SDRD project (La Lone 2013b) and refined in FY 2013 (La Lone 2014a). This year, experiments were performed on explosively compressed tin and subsequently published (La Lone 2014b). The short-pulse laser heating technique was transitioned to the California Institute of Technology two-stage light gas gun to perform high-pressure thermal transport measurements on shocked lithium fluoride. A single experiment was performed but was unsuccessful in synchronizing the laser pulse with the impact event, so the thermal transport information was not obtained.

[1] lalonebm@nv.doe.gov, 805-681-2046
[a] Special Technologies Laboratory; [b] Keystone International, Inc.; [c] California Institute of Technology

Background

Weapons simulations require material properties over an extensive range of high pressure, temperature, and strain rate conditions. Of particular importance for simulations is the location (pressure-volume-temperature) of phase boundaries under high strain–rate loading because the phase of the material (i.e., solid vs. liquid) influences how the material flows in an imploding weapon. To study high-pressure and temperature states in the laboratory, dynamic compression techniques are used, such as plate impact, explosive detonation, magnetically driven compression, and high-energy laser-driven shock waves. These dynamic compression techniques attain extreme pressures and temperatures that are inaccessible by other laboratory methods. However, they also typically access a somewhat narrow range of thermodynamic states

between the principal isentrope (ramp compression) and the shock Hugoniot (shock compression), and relevant phase boundaries can be far removed from these paths. Simply accessing a particular thermodynamic state is of little use without a measurement (stress, volume, temperature, and phase) of that state. Therefore, the measurements, as well as the experimental platforms, are of great importance to the weapons physics and the high-pressure physics communities as a whole. Traditionally, only stress and volume are determined experimentally (through the careful analysis of measured velocity profiles), while temperature and phase are calculated from theory, as they are difficult to measure. Temperatures are rarely measured, material phases are difficult to identify, and most dynamic compression methods access a limited range of thermodynamic states. Consequently, the phase boundaries at high pressure for most materials are poorly constrained by experiments.

Temperature measurements in dynamic compression experiments are particularly difficult for opaque, low emissivity materials such as metals, because thermal equilibration with an in situ gauge material is not likely to occur in experiments that typically last <1 μs. The most widely used temperature measurement technique is optical pyrometry as it is a fast response (<10 ns) non-contact method. In a typical pyrometry experiment on an opaque material, a dynamically compressed sample is backed with a transparent window that holds the sample-window interface at an elevated stress and temperature until the arrival of edge rarefaction or other release waves. The thermal radiance emitted from the sample-window interface is recorded with a pyrometer, and Planck's law is used to relate the radiance spectrum to the interface temperature. By combining radiance and emissivity measurements, interface temperatures have been determined with 20 K uncertainty (out of ~1200 K) with the pyrometric technique in dynamic compression experiments (La Lone 2013a). However, it is the temperature in the interior of the sample that is most useful for thermodynamic studies, and the interface temperature differs from the interior temperature for several reasons (Grover 1974, Tan 1990, 2001). One reason is that shock-wave interactions on a roughened surface or a gap at the interface can heat the surface to temperatures higher than the interior. A second reason, which is addressed in this work, is that the differing thermodynamic properties of the shocked sample and window cause them to have different temperatures near the interface after the passage of the shock wave. Therefore, heat flows across the boundary, and the interface temperature will be an intermediate value between the bulk sample and window temperatures (Grover 1974). The thermal transport properties of both the sample and window are needed to relate the surface temperature to the interior temperature.

Previous investigators (Gallagher 1996, Ahrens 1998, Holland 1998) have attempted to measure thermal transport properties in dynamic compression experiments. They used a window-metal film-window sandwich method, which has several limitations (Tan 2001, La Lone 2013a). In the FY 2012 and FY 2013 projects (La Lone 2013b, 2014a), we explored an alternative approach using a pulsed laser to rapidly heat a thin layer of material at the interface between the metal of interest and a window. The temperature rise and decay of the heat pulse is recorded with pyrometry and the thermal effusivity, a key thermal transport property, is extracted from the shape of the pulse. In this year's work, we applied the technique to experiments on explosively compressed tin and subsequently published our findings (La Lone 2014b). We also used the technique on a two-stage light gas gun experiment at the California Institute of Technology (Caltech).

Phase boundary identification in dynamic compression experiments is complicated because the states are difficult to access experimentally, and phase changes are difficult to identify with velocity-profile measurements. Therefore, alternatives to traditional shock- and ramp-wave experimental techniques are being explored, such as sample preheating, powder compaction, and complex loading, in order to access a broader range of thermodynamic states. Also, new phase diagnostics such as x-ray diffraction (Washington State University, Los Alamos National Laboratory, Lawrence

Livermore National Laboratory) and optical reflectance (NSTec's Special Technologies Laboratory [STL]) are being developed to identify phase transitions. All of these techniques have limitations, and there is an ongoing search for complementary methods of phase-change identification and experimental phase-boundary locators.

We have been developing a technique for identifying phase boundaries that uses shock-wave compression with explosives or plate impact followed by continuous laser heating (as opposed to pulsed laser heating) of the sample-window interface for the duration of the experiment. Analogous to differential scanning calorimetry, phase boundaries are expected to cause a change in the rate of temperature increase as heat is applied. This technique accesses temperatures that traditional shock and ramp compressions cannot and, unlike x-ray diffraction or reflectance, both the pressure and the temperature of the phase boundary can be determined. Simulations of this technique were first performed in FY 2013 (La Lone 2014a), and a laser capable of irradiance on the order of 1 MW/cm^2 (necessary for these measurements) was acquired. In this work, both ambient pressure laser-heating experiments and gas gun shock-wave pyrometry experiments (without laser heating) were performed as crucial steps toward the simultaneous shock-wave and laser heating experiment.

Project

Long-Pulsed Laser Heating for Phase Boundary Identification

The temperature response of a surface to rapid heating is dependent on the conductivity of heat away from the surface (the thermal conductivity) and the temperature change that corresponds to a change in the internal energy (the heat capacity). The heat capacity increases dramatically at a first-order phase transition, such as a melt boundary, because most of the thermal energy is consumed by the phase transformation, as opposed to raising the temperature. Therefore, analogous to differential scanning calorimetry, if constant heating is applied to the surface with a laser, the rate of temperature increase should undergo a discontinuity at a phase boundary (Figure 1). Laser powers near 1 MW are needed to increase the surface temperature enough to cross a melt boundary on the timescale of a shock-wave experiment that lasts <1 µs. A high-power laser was located at NSTec's Los Alamos

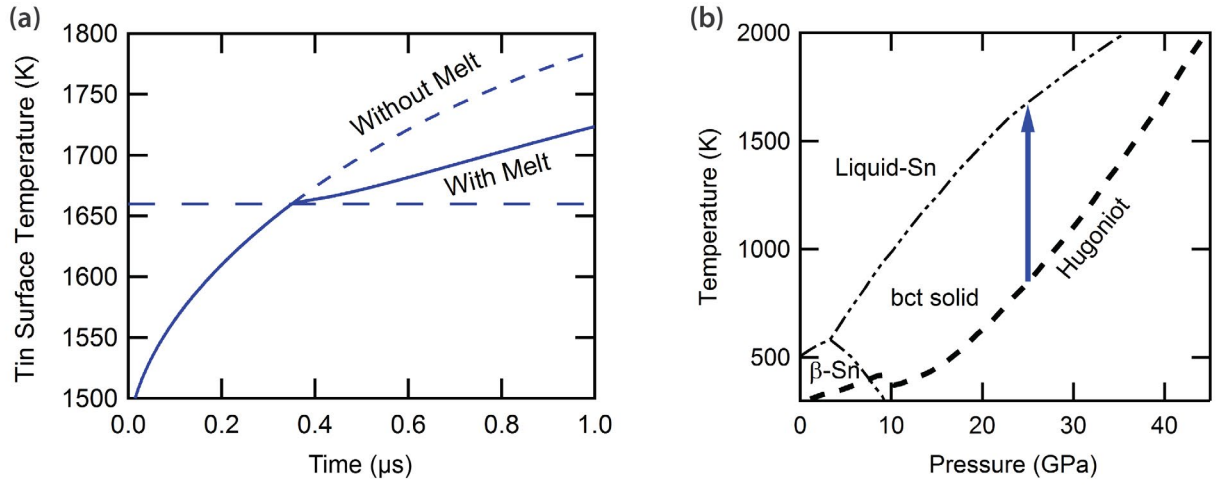

Figure 1. (a) Calculated surface temperature for tin undergoing heating from continuous laser irradiation at 1.8 MW/cm^2. Calculations were performed with (solid line) and without (dashed line) a melt boundary at 1660 K (long-dashed line). The melt temperature is identified as a break in the slope of the temperature-time curve. (b) The blue arrow indicates the path in phase space taken for tin that was shock compressed to 25 GPa and laser heated toward the melt boundary. The pressure-temperature path is overlaid on the theoretical phase diagram developed by Mabire and Héreil (2000).

Operations and transferred to STL (La Lone 2014a). During SDRD projects in FY 2012 and FY 2013, considerable effort was undertaken to restore the laser; it was not fully functional until late into FY 2014.

Ambient Pressure Long-Pulse Laser Heating

As an important step toward making the dynamic measurement, we performed ambient pressure laser heating experiments on a sample of chromium (Cr)-coated tin. A schematic diagram of the experimental arrangement is shown in Figure 2. The laser, with a power of approximately 100 kW, a beam diameter of 5 mm, and a pulse length of 1 µs, heats the surface of the sample. The thermal radiance from the surface is directed into a pyrometer using a pair of off-axis parabolic mirrors. The time-resolved temperature of the surface is monitored with a single-channel pyrometer consisting of a 3.6 µm long pass filter, a liquid-nitrogen-cooled indium antimonide (InSb) detector with an active area of 0.05 mm^2, and a custom-built (at STL) transimpedance amplifier. The voltage from the transimpedance amplifier is recorded on a high-speed digitizing oscilloscope, and the signals are converted to temperature using calibration data that were previously recorded with a black body source. This pyrometer is capable of recording temperatures (emissivity = 1) below 350 K with a response time of <5 ns, but, of course, its lower limit is reduced for lower sample emissivities. The Cr coating has a higher emissivity than bare tin, enabling us to record temperatures below 400 K on the sample. Prior to the experiment, we performed a reflectance measurement on the Cr-coated tin sample and estimated an emissivity of 0.20 at the wavelengths to which the pyrometer is sensitive (3.6–5.2 µm), much higher than the bare tin, which has an emissivity of 0.04 at these wavelengths. Also, we verified that the 3.6 µm long pass filter adequately rejected the 1.06 µm laser light by replacing the target with a gold mirror. The gold mirror heats very little, and we detected only a negligible signal.

Temperatures recorded with both laser heating and immediately after the laser is turned off are shown in Figures 3a and 3b, respectively. The measured temperatures may be slightly off if the emissivity

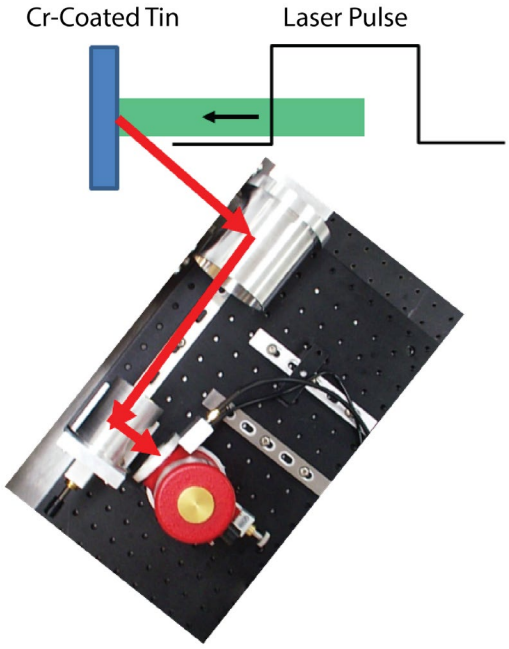

Figure 2. Diagram of the long-pulse laser heating experiment at ambient pressure. The surface of a tin sample with an emissive Cr coating was laser heated. The temperature of the heated spot was monitored with a single-channel InSb pyrometer.

changes during the experiment. The melting point of tin at 505 K is shown for comparison. In Figure 3a, the temperature increases rapidly until near the melting point of tin, above which the temperature continues to increase, but at a slower rate. While this was the anticipated behavior, the laser irradiance is not steady near the change in slope, which complicates the interpretation of the results. Immediately after the laser is turned off (Figure 3b), the surface cools rapidly as heat diffuses into the bulk tin. A clear break in the rate of cooling is observed in the temperature-time profile near the melting point as the melted interfacial material re-solidifies. The effect of the melt boundary is less ambiguous in the cooling signal with the laser off than it was in the rising signal with the laser on, because the rates are not complicated by fluctuations in laser power. While these preliminary ambient pressure results are encouraging, we intend to revisit this measurement early in FY 2015 in an effort to record the change in the temperature rate with the laser on at a time when the laser power is relatively flat. Nonetheless, these results demonstrate

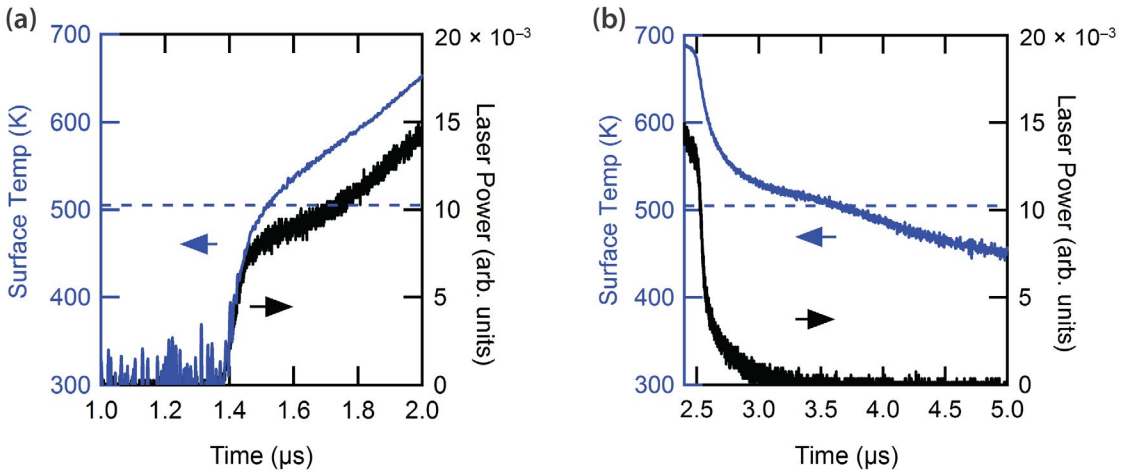

Figure 3. Surface temperature (blue curves) of the laser-heated tin sample during (a) heating and (b) cooling. The monitored laser power is shown as a black curve in each plot. The dashed blue line represents the melting temperature of tin (505 K).

our ability to heat a surface by several hundred Kelvin in less than 1 μs, which is necessary for the dynamic experiment to be successful.

Gas Gun Experiments with Indium Antimonide Pyrometer

The ultimate goal of this work is to perform long-pulsed heating measurements under shock-wave compression at the STL gas gun. To verify that we could make a pyrometry measurement on the gas gun, where the shock-wave temperatures are relatively low, two experiments were performed with the InSb detector previously described. For the first experiment, we used a tin sample backed by a sapphire window attached with glue. For the second experiment, we used a tin sample backed by a lithium fluoride (LiF) window separated by a 1 μm vacuum gap. The tin samples were 2 mm thick and were impacted with a 10 mm diameter copper disk traveling at 0.8 km/s. In both experiments the initial shock stress in tin was 12 GPa. This re-shocked to 16 GPa when the shock wave reflected off of the higher impedance (relative to the wave impedance of tin) sapphire window in the first experiment, and it released to 9 GPa upon reflection from the lower impedance LiF window in the second experiment. A photograph and schematic diagram of the experimental setup is shown in Figure 4. Thermal radiance emitted from the sample-window interface is reflected from a gold mirror and directed through a sapphire port window in the side of the gas gun target chamber. A pair of off-axis parabolic mirrors images the sample-window interface onto the InSb detector. To collect as much radiance as possible, no optical filters were used in these experiments.

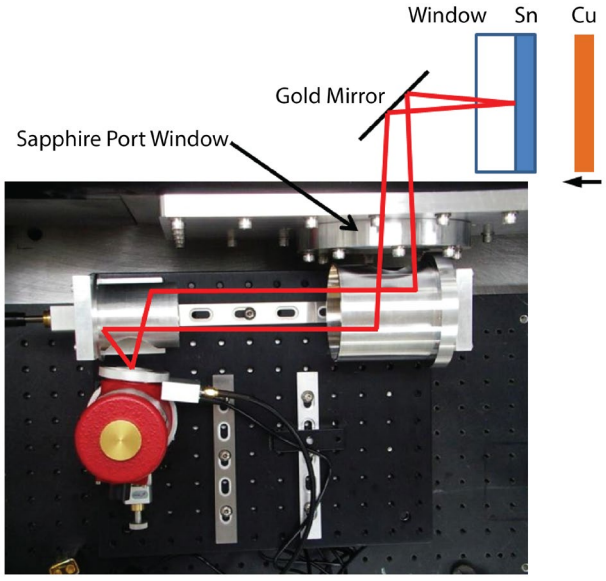

Figure 4. Diagram of the low-temperature pyrometry experiments on the STL gas gun. A tin sample backed by either a sapphire or LiF window was impacted with a copper flyer. Thermal radiance from the tin-window interface was directed through a port window in the target chamber and imaged onto the InSb pyrometer using a pair of off-axis parabolic mirrors.

The recorded temperature history from the first experiment with the sapphire window is shown in Figure 5. The temperatures were converted from the measured radiance using a previously published emissivity value of 0.22 for shocked tin at 5 µm wavelength (Turley 2011). Also shown is the stress history at the interface calculated using a prior velocity measurement on 2 mm thick tin impacted by a copper impactor at 0.8 km/s (Daykin 2015). The two-wave structure in the stress history is a result of the 9 GPa solid-solid phase transition in tin. The temperature history mimics the stress history at the interface as observed in prior pyrometry experiments (La Lone 2013a). Peak temperatures were approximately 460 K. The experiment with the LiF window is also shown in Figure 5. Because the stresses at the interface were lower, the temperatures were lower, and the signal-to-noise ratio was not as good. The wave structure is not as clear in the temperature history, and only a slowly rising signal is present. We estimated peak temperatures to be near 390 K. However, since the peak interface stress is near the solid-solid phase boundary, the material phase and emissivity are less certain than in the sapphire window experiment.

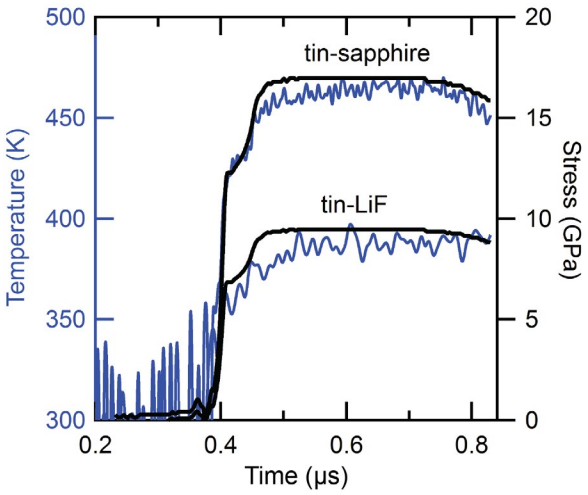

Figure 5. Measured temperature histories (blue curves) of the interface between shock-wave-compressed tin and a sapphire window (upper) or a LiF window (lower) using an emissivity of 0.22 (Turley 2011). The black curves are calculated stress histories from a prior experiment (Daykin 2015).

The successful experiments demonstrate that low-temperature pyrometry on the STL gas gun is possible. However, the time when the temperatures are steady in these experiments is less than 300 ns, which will make the laser heating measurement challenging. This measurement may be better suited for a larger-bore gas gun that can hold the peak shock pressures at the interface longer. Because of the importance of this diagnostic to the Stockpile Stewardship Program, we intend to perform gas gun experiments with long-pulse laser heating in FY 2015.

Short-Pulsed Laser Heating for Thermal Transport Measurements (Boom Box)

The pulsed laser technique for thermal effusivity measurement is based on a method by Beck (2007) for measuring thermal diffusivity in static, high-pressure experiments, and is similar to other flash-heating methods for thermal transport measurements (Zammit 2011). We originally developed the method in FY 2012 (La Lone 2013b) and refined it in FY 2013 (La Lone 2014a). This year, the refined technique was used on experiments at the STL Boom Box to investigate the thermal effusivity of shock-compressed tin. The experimental methods and results of this work have been published elsewhere (La Lone 2014b) and are not discussed here. The measurements suggested that the thermal effusivity of tin, at a stress of 25 GPa and temperature of 1300 K, is nearly a factor of two higher than the ambient value and likely (though not yet definitively) reflects a thermal conductivity increase of 2–4 times relative to the ambient value. These are the first published measurements on the thermal effusivity of a metal in the dynamically compressed state.

Short-Pulsed Laser Heating for Thermal Transport Measurements (Caltech Two-Stage Gun)

At stresses above ~40 GPa, the glue used to bond transparent windows to metal samples in pyrometry experiments loses transparency. Because of this, experiments at high stresses cannot use glue, thus leaving the metal in direct contact with the optical window. (Unless the metal can be coated to the window, there will be a small gap of >1 µm [Urtiew 1974].) In such

experiments, thermal transport information of both the window and the metal sample will be needed to relate interface temperatures to the interior metal temperatures. To investigate window thermal-transport properties, we performed an experiment on LiF at the Caltech Lindhurst Laboratory for Experimental Geophysics. LiF was chosen because it is one of the most common optical-window materials in shock-wave experiments, as it remains transparent over a wide range of shock stresses (from 0 to 200 GPa) (Rigg 2014).

The experimental arrangement used is depicted in Figure 6. A 1 in. long and 1 in. diameter Lexan projectile with a 2.5 mm thick by 19 mm diameter aluminum impactor is launched from the Caltech two-stage light gas gun at a velocity of 5.2 km/s. The target consists of a sandwich of two pieces of LiF separated by a 10 µm thick vacuum gap, and the back piece is coated with a 0.15 µm thick layer of Cr. The front LiF piece was 2 mm thick by 38 mm diameter and the rear piece was 5 mm thick by 38 mm diameter. The impact sends a 60 GPa shock into the LiF, and the emissive Cr layer quickly equilibrates to the surrounding LiF temperature, which is heated by the shock wave. The presence of the gap causes the material near the interface in the left LiF piece to undergo a shock→release→re-shock cycle, and heats this thin layer to a higher temperature than the single-shock temperature. Because a small gap could not be avoided, we intentionally made the gap large so that this hot layer would be thick enough that the cooler single-shocked material to the left of this layer would not communicate to the Cr/LiF interface during the experiment. The goal was to have a nearly constant interface temperature prior to the laser pulse. Thermal radiance from the emissive Cr layer was collected from the center of the sample via a 600 µm optical fiber, which directed the radiance outside the target chamber and into a two-channel pyrometer. The laser pulse was brought in normal to the surface; a 1180 nm dichroic optical splitter separated the laser light from the thermal radiance, as shown in Figure 6.

The two-channel pyrometer used for this experiment was a modified version of the pyrometer used in the prior Boom Box experiments (La Lone 2014b) and was built specifically for this effort. One channel (1500+) monitored the thermal radiance from 1500 to 1700 nm, while the other channel (1500−) monitored the thermal radiance from 1180 to 1500 nm. Both detectors were 300 µm diameter indium gallium arsenide (InGaAs) photodiodes from Fermionics, and the photodiode outputs were amplified using transimpedance amplifiers (Terahertz Technologies, Inc.). Signals were recorded on high-speed digitizers.

The thermal radiance recorded from the two-stage gun experiment is shown in Figure 7. The calculated pressure history (simulated in CTH, a Sandia National Laboratories–developed hydrodynamics code) for this experiment is also indicated in the figure. Cross-timing lasers and diagnostics on a two-stage gun is difficult; our laser did not receive trigger signals at the correct times, so it did not fire. The earliest signal (at ~0.5 µs)

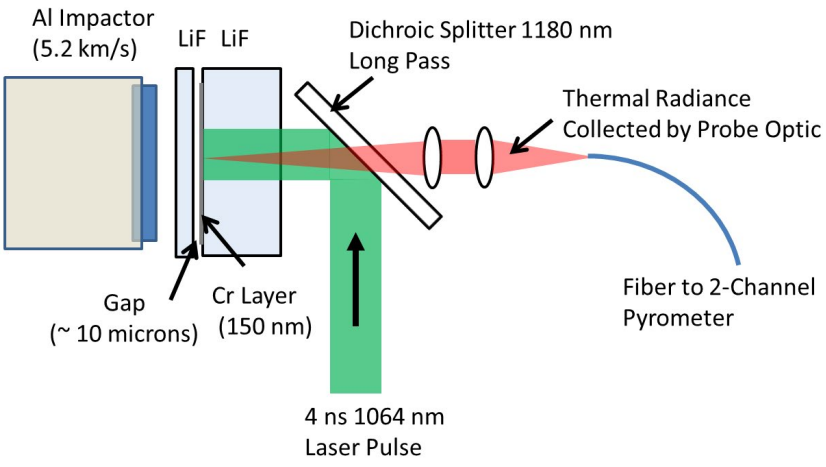

Figure 6. Schematic diagram of the short-pulsed laser heating experiment at the Caltech two-stage light gas gun. A LiF target with an embedded Cr layer is impacted with an aluminum flyer. The laser light is directed onto the target with a dichroic splitter. The thermal radiance of the Cr layer is monitored with a fiber-coupled, two-channel pyrometer.

originates from the light flash that occurs at the aluminum-LiF impact surface as a small amount of trapped gas is superheated (termed impact flash). Some of this light passes through the Cr coating and is collected by the pyrometer detectors. Prior to performing the measurement, contamination of light from the impact flash was a major concern. However, the impact flash is a short-lived signal (~10 ns) and decays long before the shock arrives at the Cr layer, so it does not contaminate the measurement of interest. The shock reaches the Cr layer at about 0.7 µs, causing a nearly discontinuous increase in the radiance signals. The signals were larger than anticipated and saturated the 1500+ channel for the first 100 ns and the 1500− channel for the first 500 ns after shock arrival. The signal immediately following the shock arrival has a slow decay component until the arrival of the release wave from the back of the impactor (1.1 µs), after which the signal decay is more rapid. The signals then flatten at the bottom of the release, which is at 32 GPa, not zero, because the aluminum impactor was backed with Lexan plastic instead of a vacuum. A new source of light appears at ~1.5 µs, which is consistent with the time expected for the rear LiF window to spall, so this late-time light is probably not thermal but more likely fractoluminescence (Turley 2013). Before the rear window spallation, the signals qualitatively track the pressure history at the Cr layer but with an additional slowly decaying component. This decay is predicted by simulations, as discussed below.

CTH was used to calculate the initial spatial temperature profile near the LiF-gap–Cr-LiF interface a few nanoseconds after passage of the shock wave. This somewhat complex profile, shown in Figure 8, is strongly dependent on material equation of state, so it is likely only giving qualitative temperatures and spatial locations. The left-most temperatures near 1700 K (a), which extend for >30 µm from the interface, result from the shock→release→re-shock cycle in this material due to closure of the vacuum gap in our sample. Just left of the Cr layer (b) is an even hotter (~2300 K) region in LiF that is ~1 µm thick, again resulting from a shock→release→re-shock cycle. However, here the re-shock was initially to a higher stress because the Cr layer has

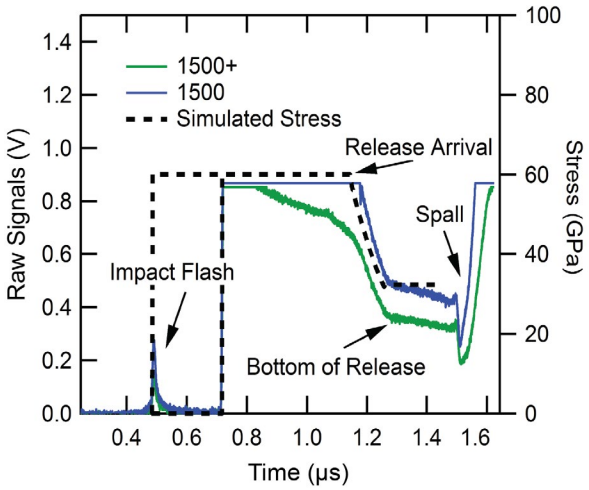

Figure 7. Raw radiance signals from the Caltech two-stage gun experiment on a shocked LiF target with an embedded Cr layer. The 1500+ pyrometer channel is the blue curve and the 1500− pyrometer channel is the green curve. The stress history (simulated in CTH) is the dashed black curve. Interesting features in the radiance histories are labeled within the figure.

a higher wave impedance than LiF. This hot, thin region of material was not considered prior to the experiment, and is the reason the temperatures were higher than expected. Also, the time-dependent decay of this layer, as its heat diffuses into the bulk, is responsible for the slowly decaying signals in the measurement. The Cr layer is labeled as (c) in Figure 8. Immediately to the right of the Cr layer, extending <1 µm, is a region (d) that underwent a shock→ring-up process due to the presence of the Cr layer; this is the coolest region near the interface at <1000 K. At the far right and extending for the remainder of the sample is the single-shock temperature in LiF (e), 1100 K at 60 GPa.

Figure 9 shows simulated temperature histories of the Cr layer, with and without laser heating, and the experimental temperature histories. The simulated histories were calculated using the spatial temperature profile given by CTH (Figure 8) and the calculated pressure history (Figure 7), combined with the MATLAB code thermalconduct (LaLone 2014b) to simulate the heat conduction and laser heating. The experimental temperatures, also shown in Figure 9,

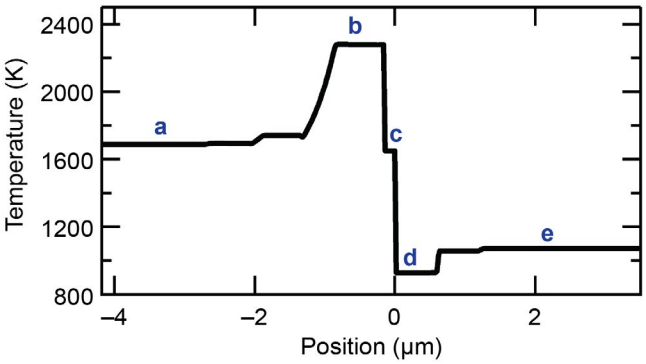

Figure 8. Simulated spatial profile of temperatures in the shocked LiF near the embedded Cr layer a few nanoseconds after shock-wave arrival in the Caltech two-stage gun experiment. The profile was simulated with CTH. The interesting features labeled within the figure are discussed in the text.

were calculated from the thermal radiance signals using a black-body calibration of the detectors and an assumed Cr emissivity of 0.54, which is the measured static value. The emissivity of Cr coatings has been measured to have negligible pressure dependence to shock stresses up to 25 GPa (La Lone 2013b), but this has not been verified at 60 GPa. The temperatures of both the 1500– and 1500+ detectors are in good agreement when both are on scale, and are about 100 K higher than the simulated temperatures.

Overall, the simulation without laser heating captures the qualitative features in the temperature history remarkably well. The gross temperature features that mimic the calculated pressure history at the Cr layer combined with the decaying signal from thermal diffusion of a thin and hot layer near the interface are apparent in both the simulations and the experiment. This shows that the measured radiance from the Cr layer is thermal and represents the LiF temperatures near the interface. Therefore, with a successful laser trigger, the thermal transport measurement is possible. The simulation with laser heating shows what is expected for a successful measurement. Triggering the laser at the correct time remains an experimental challenge. We hope to capture this event in future measurements.

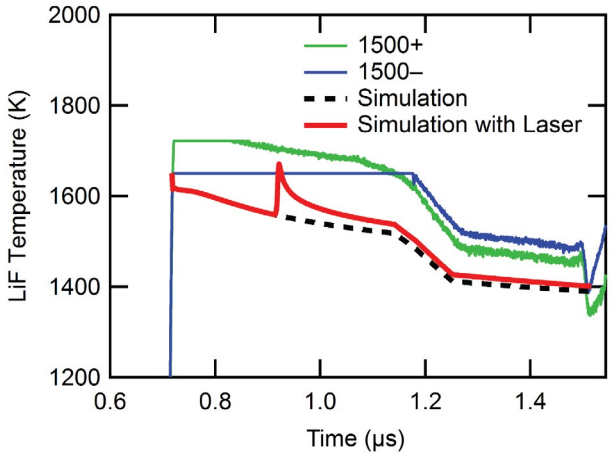

Figure 9. Experimental (blue and green curves) and theoretical (dashed black and red curves) temperatures for the embedded Cr layer in the shocked LiF target. The two experimental curves are the two different pyrometer channels. Temperature simulations were performed with (theoretical) and without (experimental) pulsed laser heating of the Cr layer.

Conclusion

An explosively driven shock-wave followed by short-pulsed laser heating was used to investigate thermal transport properties of tin in a high-pressure and temperature state. Short-pulse laser heating was also attempted on shock-compressed LiF at the Caltech two-stage gun, but laser heating was not achieved due to inadequate cross-timing. Nonetheless, an interesting temperature history of shocked LiF was recorded, and we demonstrated that the measurement is possible.

We have advanced a long-pulsed laser heating technique for identifying phase boundaries in shock-compression experiments. The technique was demonstrated on a tin target at ambient pressure. We also performed low-temperature pyrometry experiments on the STL gas gun, which is an important step toward using the long-pulsed laser-heating technique on future shock-wave experiments.

Future Work

We plan to use both the long-pulse and short-pulse laser heating techniques on future shock-wave experiments. Long-pulse laser heating experiments on shock-compressed tin will be performed on the new 1.5 in. diameter gas gun at STL. These will be low pressure-temperature (<10 GPa and <1000 K) experiments near to or below the solid-solid transition in tin, and the laser heating will drive the tin at the interface across the low-pressure melt boundary. At low pressures, the melt boundary is only a few hundred degrees above the shock Hugoniot and should be within reach of our laser heating diagnostic on the short timescale of the shock experiment.

We also plan to continue the short-pulse laser heating experiments on LiF at Caltech. The main difficulty encountered in the first experiment was triggering of the pulsed laser at the correct time relative to the impact event. We plan to transition the experiment from Caltech's two-stage gas gun to their 40 mm propellant gun, which has more triggering options and simplifies the laser timing. The larger impact area also increases the time that the interface is held under shock compression (before edge-wave release), which should allow for a more accurate measurement. The main drawback is that the maximum shock pressure achievable in LiF on the powder gun is less than 50 GPa.

References

Ahrens, T. J., K. G. Holland, G. Q. Chen, "Shock temperatures and the melting point of iron," *AIP Conf. Proc.* **429** (1998) 133–136.

Beck, P., A. F. Goncharov, V. V. Struzhkin, B. Militzer, H. Mao, R. J. Hemley, "Measurement of thermal diffusivity at high pressure using a transient heating technique," *Appl. Phys. Lett.* **91**, 18 (2007) 181914-1–181914-3.

Daykin, E., M. Grover, R. S. Hixson, B. La Lone, C. Perez, G. Stevens, W. D. Turley, "Grain-selective MPDV experiments," in *Site-Directed Research and Development*, FY 2014, National Security Technologies, LLC, Las Vegas, Nevada, 2015,1–9.

Gallagher, K. G., T. J. Ahrens, "Ultra-high pressure thermal-conductivity measurements of griceite and corundum," in *Shock Waves: Vol. 2*, B. Sturtevant, J. E. Shepherd, H. G. Hornung, eds., World Scientific, Singapore, 1996, 1401–1406.

Grover, R., P. A. Urtiew, "Thermal relaxation at interfaces following shock compression," *J. Appl. Phys.* **45**, 1 (1974) 146–152.

Holland, K. G., T. J. Ahrens, "Properties of LiF and Al_2O_3 to 240 GPa for metal shock temperature measurements," *Geophys. Monogr.* **101** (1998) 335–343.

La Lone, B. M., G. D. Stevens, W. D. Turley, D. B. Holtkamp, A. J. Iverson, R. S. Hixson, L. R. Veeser, "Release path temperatures of shock-compressed tin from dynamic reflectance and radiance measurements," *J. Appl. Phys.* **114**, 6 (2013a) 063506-1–063506-14.

La Lone, B. M., W. D. Turley, G. D. Stevens, G. A. Capelle, M. Grover, "Dynamic conductivity of shocked materials," in *Site-Directed Research and Development*, FY 2012, National Security Technologies, LLC, Las Vegas, Nevada, 2013b, 21–30.

La Lone, B. M., G. A. Capelle, W. D. Turley, G. D. Stevens, M. Grover, R. S. Hixson, O. V. Fatyanov, P. Asimow, L. Veeser, "Detection of phase transitions and effusivity changes through isobaric heating of shock-compressed materials," in *Site-Directed Research and Development*, FY 2013, National Security Technologies, LLC, Las Vegas, Nevada, 2014a, 11–18.

La Lone B. M., G. Capelle, G. D. Stevens, W. D. Turley, L. R. Veeser, "Thermal transport in shock wave–compressed solids using pulsed laser heating," *Rev. Sci. Instrum.* **85**, 7 (2014b), 073903-1–073903-7.

Mabire, C., P. L. Héreil, "Shock induced polymorphic transition and melting of tin," in *Shock Compression of Condensed Matter–1999, AIP Conf. Proc.*, M. D. Furnish, L. C. Chhabildas, R. S. Hixson, eds., **505** (2000) 93–96.

Rigg, P. A., M. D. Knudson, R. J. Scharff, R. S. Hixson, "Determining the refractive index of shocked [100] lithium fluoride to the limit of transmissibility," *J. Appl. Phys.* **116**, 3 (2014) 033515-1–033515-12.

Tan, H., T. J. Ahrens, "Shock temperature measurements for metals," *High Pressure Res.* **2**, 3 (1990) 159–182.

Tan, H., C. Dai, "Problems of shock temperature measurements for metals by using optical radiometry method," *High Pressure Res.* **21**, 3–4 (2001) 183–214.

Turley, W. D., D. B. Holtkamp, L. R. Veeser, G. D. Stevens, B. R. Marshall, A. Seifter, R. B. Corrow, J. B. Stone, J. A. Young, M. Grover, "Infrared emissivity of tin upon release of a 25 GPa shock into a lithium fluoride window," *J. Appl. Phys.* **110**, 10 (2011) 103510-1–103510-8.

Turley, W. D., G. D. Stevens, G. A. Capelle, M. Grover, D. B. Holtkamp, B. M. La Lone, L. R. Veeser, "Luminescence from edge fracture in shocked lithium fluoride crystals," *J. Appl. Phys*. **113**, 13 (2013) 133506-1–133506-5.

Urtiew, P. A., R. Grover, "Temperature deposition caused by shock interactions with material interfaces," *J. Appl. Phys.* **45**, 1 (1974) 140–145.

Zammit, U., M. Marinelli, F. Mercuri, S. Paoloni, F. Scudieri, "Invited review article: Photopyroelectric calorimeter for the simultaneous thermal, optical, and structural characterization of samples over phase transitions," *Rev. Sci. Instrum*. **82**, 12 (2011) 121101-1–121101-22.

This page left blank intentionally

Plastic Deformation Study Using a Light Gas Gun

NLV-33-13 | Continued from FY 2013 | Year 2 of 2

Michael Peña,[1,a] Robert S. Hixson,[b] Steven Becker,[a] Edward Daykin,[a] Michael E. Walling,[a] Carlos Perez,[a] Eric Machorro,[a] Rand Kelly,[a] Brendan O'Toole,[c] Mohamed Trabia,[c] Shawoon Roy,[c] Richard Jennings,[c] Muna Slewa,[c] and Melissa Matthes[c]

In FY 2013, two-stage light gas gun experiments were performed with cylindrical Lexan projectiles with velocities ranging from 4.5 to 5.8 km/s impacting A36 steel plates. Velocimetry data were collected using a multiplexed photonic Doppler velocimetry diagnostic system to obtain time-resolved particle velocity information from the back surface of the target plates during impact. The objectives of these experiments were to develop an understanding of the plastic deformation of A36 steel under ballistic impact conditions, as well as to develop accurate computational models to predict this kind of behavior. This research showed that additional information on the α↔ε phase transition of A36 steel above 13 GPa pressure was needed to fully understand the dynamic behavior from velocimetry data and to update the computational models accordingly. Therefore, the FY 2014 experiments were designed to complement those done on A36 steel and used two different types of steel plates: 304L (which does not have any known phase transition) and HY100 (with a phase transition). Experiments were simulated using a Lagrangian-based smoothed particle hydrodynamics solver in LS-DYNA and the Eulerian-based CTH hydrocode. Simulation results agree reasonably well with experimental results. Furthermore, the α↔ε phase transition of A36 steel plates was confirmed by electron backscatter diffraction. Hence, the computational model of A36 steel plate was modified to account for the reversible α↔ε phase transition in CTH hydrocode.

[1] penamt@nv.doe.gov, 702-295-3242
[a] North Las Vegas; [b] Los Alamos Operations; [c] University of Nevada, Las Vegas

Background

High-velocity impact research has been conducted using light gas guns over several decades in a wide variety of fields, including characterizing materials under shock conditions. In FY 2013 (Becker 2014), extensive gas gun experiments were performed using the two-stage light gas gun at the University of Nevada, Las Vegas (UNLV) to study the plastic deformation behavior of A36 steel plates. Projectiles were fired over a velocity range from 4.5 to 5.7 km/s to generate extreme pressure and create deformation in the A36 steel target plates. A high-fidelity data acquisition system, multiplexed photonic Doppler velocimetry (MPDV), was used to collect time-resolved velocimetry data. Target plates were also measured to obtain impact crater and bulge details after experiments. Finally, target plates were sectioned to get the details of spalling inside the target material.

Because a major objective of this research was to better understand the strengths and weaknesses of modeling such dynamic events, computational models were developed to simulate the projectile-target interaction using two complementary approaches: (1) Lagrangian-based smoothed particle hydrodynamics (SPH) solver

in LS-DYNA and (2) Eulerian-based hydrocode in CTH. One principal goal of this research was to identify the parameters of the material model and the equation of state (EOS) that can best model the shock phenomenon, and to assess the strengths and weaknesses of each modeling approach. Both simulation models used the same Johnson-Cook material model, Grüneisen EOS, and spall treatment. Results from the simulation models agreed reasonably well with the data in terms of the crater and bulge details. Also, simulated velocity profiles were shown to capture both the elastic precursor and overall shape of the experimental free surface velocity profiles fairly well. However, while the experimental and simulation results showed some differences, major signatures in free surface velocity profiles did match. These differences can be reduced if the material models used could better account for the behavior of the metallic plates under shock.

Ever since Bancroft (1956) introduced the concept of high-pressure phase transition in iron, researchers have investigated iron and iron-based alloys to study such polymorphism (Barker 1974, Duvall 1977, Murr 1983, Hammond 2004). All the simulations of A36 steel were originally performed without considering phase change models. One of the intriguing points in the experiments conducted in FY 2013 was the possibility that a polymorphic phase transition of A36 steel occurs. Simple flyer plate experiments in pure iron and iron-based alloys indicated that it occurs at around 13 GPa (Minshall 1955, Hammond 2004). In FY 2014, it became important to settle this issue of polymorphic phase change in shock-impacted A36 steel to further refine our simulations. Therefore, gas gun experiments were designed with two new types of steel as target materials: HY100 steel (which is known to have the phase change) and 304L (which is known not to have the phase change). The objective was to study velocimetry data from these two steel targets, and at the same time, to develop computational models for 304L steel and HY100 steel targets with the same type of projectile-target interactions. Our principal objective was to find the direct and indirect evidence of the phase transition in impacted A36 steel target plates and, henceforth, improve all the simulation models of A36 steel including phase transition effect. We specifically wished to identify signature(s) in the data for the phase transition.

Project

The UNLV gas gun was described in last year's report (Becker 2014). A brief description is included here to summarize some details of the gas gun operation. The gun at UNLV (Figure 1) was manufactured by Physics Applications, Inc. Major components of this gun are the propellant breech, pump tube, central breech, launch tube, blast tank, drift tube, and target chamber. The cartridge filled with gunpowder is fired with a solenoid pin. Gunpowder (IMR 4064) in the powder breech then burns, which drives a cylindrical piston (20 mm diameter and 120 mm length) in the pump tube. Hydrogen or helium gas is used as a propellant in the pump tube. The moving piston pressurizes the propellant gas, which eventually bursts the petal valve. High-pressure gas then accelerates the projectile in a launch tube through the blast tank and drift tube until it impacts the target in the target chamber.

Materials

As mentioned above, we chose two steel target materials for study in FY 2014: HY100 and type 304L stainless steel. All the target plates had a dimension of 152.4 × 152.4 × 12.7 mm. Cylindrical Lexan projectiles of 0.22 caliber and 0.375 caliber were shot over a range of impact velocities, the highest being more than 6.5 km/s. Target plates were bolted on a mounting plate inside the target chamber assembly of the gun.

MPDV System

Three different types of MPDV probe arrays were used in gas gun experiments: 11-, 12-, and 32-probe arrangements focused on the back side of the target plate to capture the velocimetry data. The 11- and 32-probe arrays were set up in a grid pattern, whereas the 12-probe array was arranged in a cross-hair pattern (Figure 2). The probes were placed in such a way to get velocimetry data from points as close to the impact center as possible. An intervalometer

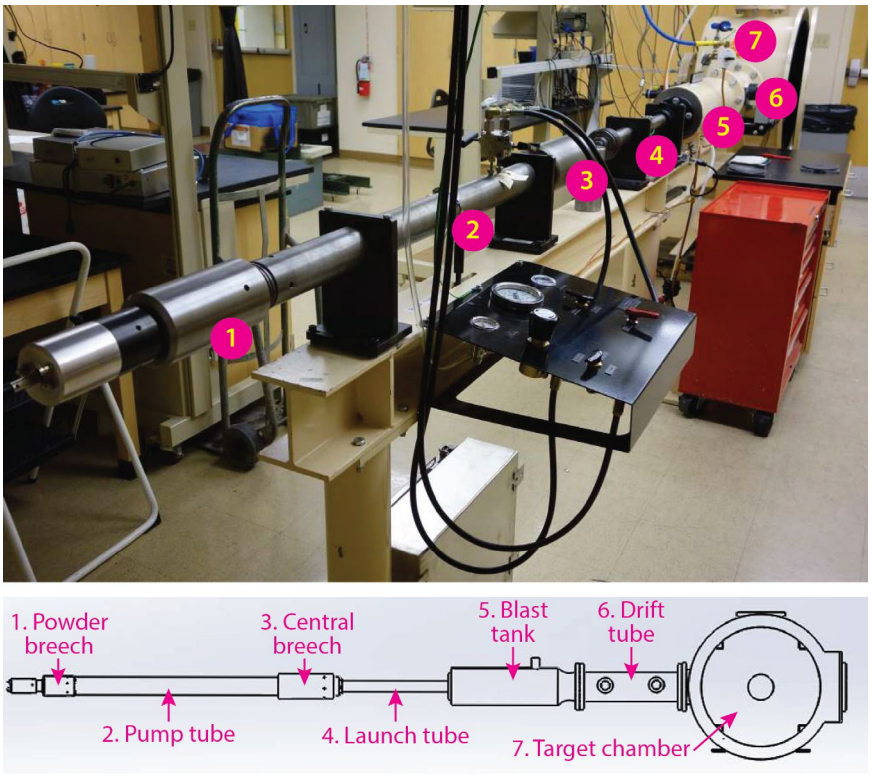

Figure 1. Schematic of UNLV two-stage gas gun

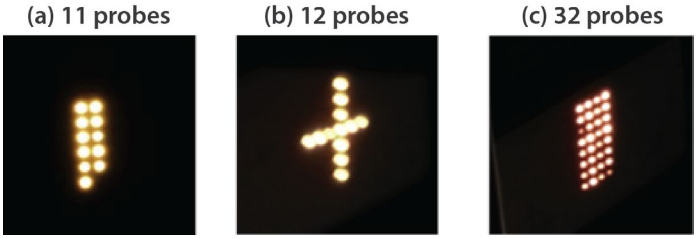

Figure 2. Typical MPDV probe array arrangements on a target plate

system measured the projectile velocity by measuring the time taken to traverse two lasers set a certain distance apart. The MPDV system was triggered by one of these intervalometer lasers. The delay time in the MPDV system was based on the trigger of the laser unit assembly (i.e., projectile velocity). A schematic of the MPDV arrangement is shown in Figure 3. The MPDV systems were fielded by NSTec staff. Data were collected at a sampling rate of 20 GSa/s in all cases. Raw data were processed using a sliding FFT analysis to obtain the velocity profile.

Results

In all experiments, a small crater with a bulge on the back side of the target plate was created as a result of impact (Figure 4). Cross sections of the target plates showed spall due to release wave interactions. Projectiles disintegrated due to the enormous stress and resulting heat generated upon impact with the target surface.

Physical Measurements

Each target plate was examined after impact for crater and bulge details. The distance between the flat rear surface of the plate and peak point of the bulge was taken to be the height of the bulge. Similarly, the distance between the flat front surface of the target plate and the deepest point of the crater is taken to be the crater depth. An average value for multiple measurements of crater diameter, depth

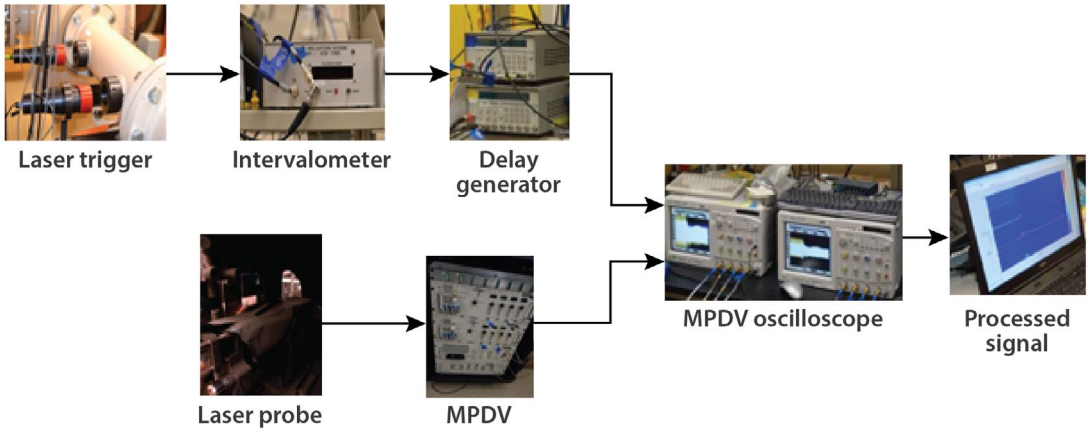

Figure 3. Schematic of MPDV data acquisition

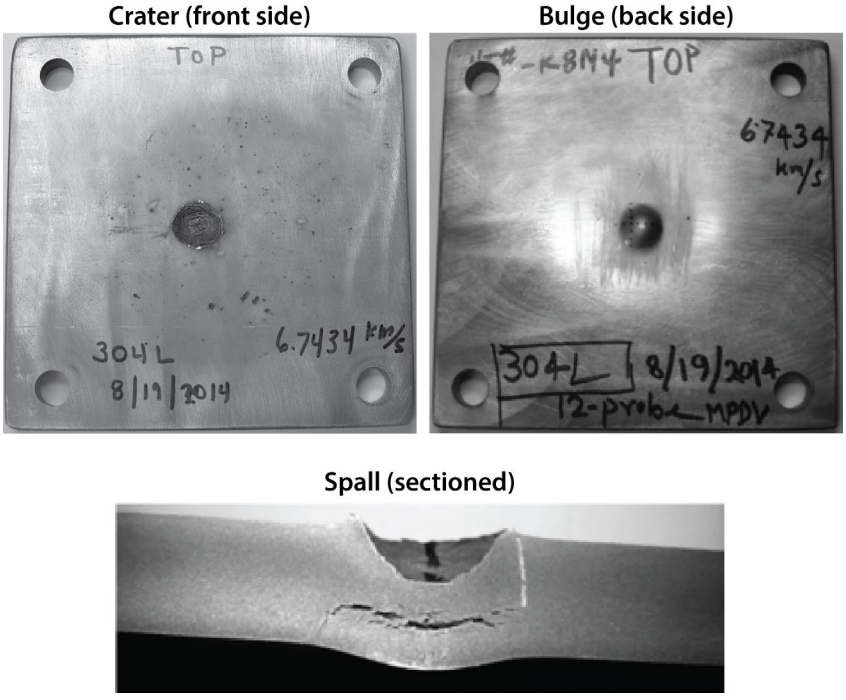

Figure 4. Typical target plates after 0.22-caliber Lexan projectile impact (here, a 304L target is shown)

of penetration, and bulge were taken as the final measurement. Table 1 lists physical information of impact craters from a few of the shots.

Free Surface Velocity Measurement

Figures 5 and 6 show typical velocity profiles from 304L stainless steel and HY100 steel experiments for 0.22-caliber Lexan projectile impacts. In general, 304L stainless steel shows a two-wave structure profile in compression: a typical elastic wave and a sharp rise in the plastic wave. Supposedly, all low carbon–alloy steels should show another wave rise after the plastic wave due to the $\alpha \leftrightarrow \varepsilon$ phase transition (Hammond 2004) similar to what was observed in shocked iron (Jensen 2006, 2009). However, for HY100 steel, the signature of $\alpha \leftrightarrow \varepsilon$ phase transition is not prominent in our gas gun experiments at the rear surface. We

Table 1. Physical measurement of impact crater and bulge

Shot Date	Caliber	MPDV Probe Arrangement	Material	Impact Velocity (km/s)	Crater Diameter (mm)	Penetration (mm)	Bulge (mm)
7/18/14	0.22	11-probe	304L	6.5832	17.33	6.35	2.44
7/18/14			HY100	6.6989	16.48	6.36	2.96
8/19/14	0.22	12 -probe	304L	6.7434	15.45	4.50	3.30
8/20/14			HY100	6.7583	15.46	3.85	3.18
8/20/14	0.375	12-probe	A36	3.3750	21.06	8.06	2.71
8/21/14				3.4715	21.86	8.37	2.68
8/21/14				3.2391	21.94	7.57	2.57
8/21/14	0.375	12-probe	304L	3.9948	23.55	9.46	3.13
8/21/14				3.9636	22.79	9.54	2.83
9/09/14	0.375	32-probe	304L	3.7398	22.44	8.40	2.81
9/11/14	0.375	32-probe	HY100	4.0968	22.94	8.14	2.74
9/11/14				4.0211	22.47	8.18	2.72
9/11/14				3.9379	21.85	7.54	2.71

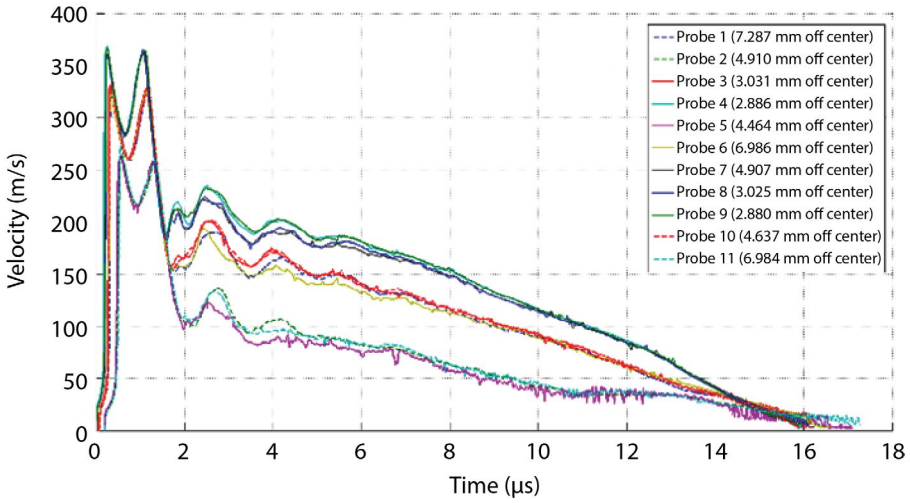

Figure 5. Typical free surface velocity profiles for a 304L stainless steel plate with 0.22-caliber Lexan projectile (impact velocity: 6.5832 km/s)

suspect this could be due to the complex, axisymmetric nature of the stress wave at that location in the target plate, and the relatively low stress amplitude of the wave at the rear surface of the target plate. Fundamental shock compression experiments that do observe the phase transition wave have all been done with a condition of uniaxial strain, which is not the case for the stress wave we observe. MPDV data show that the initial shock wave typically arrives at various probe locations in time order according to the distance from the impact point. Figure 7 shows free surface velocity profiles for 0.375-caliber Lexan shots. Velocity profiles are significantly different from the 0.22-caliber shots at the beginning because of large-diameter projectiles.

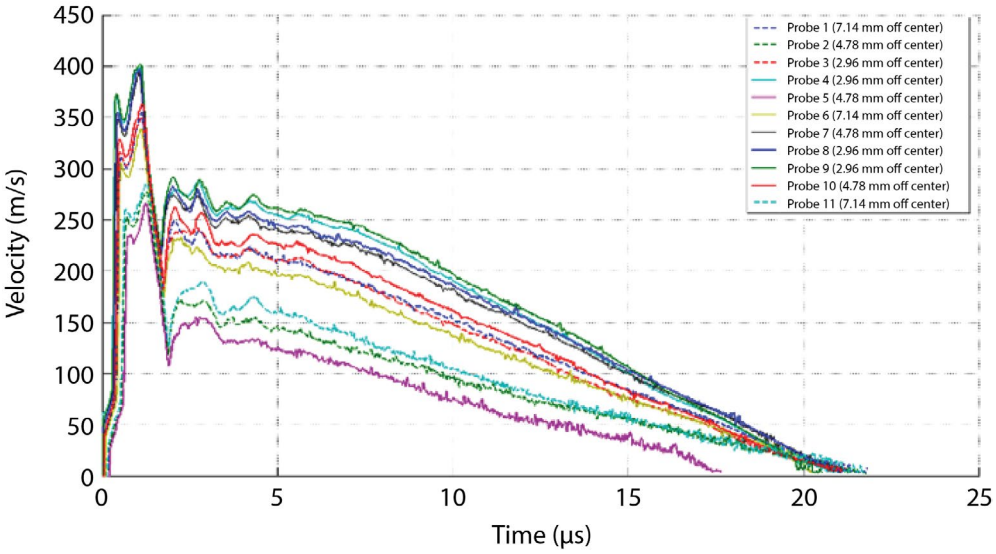

Figure 6. Typical free surface velocity profiles for an HY100 steel plate with 0.22-caliber Lexan projectile (impact velocity: 6.6989 km/s)

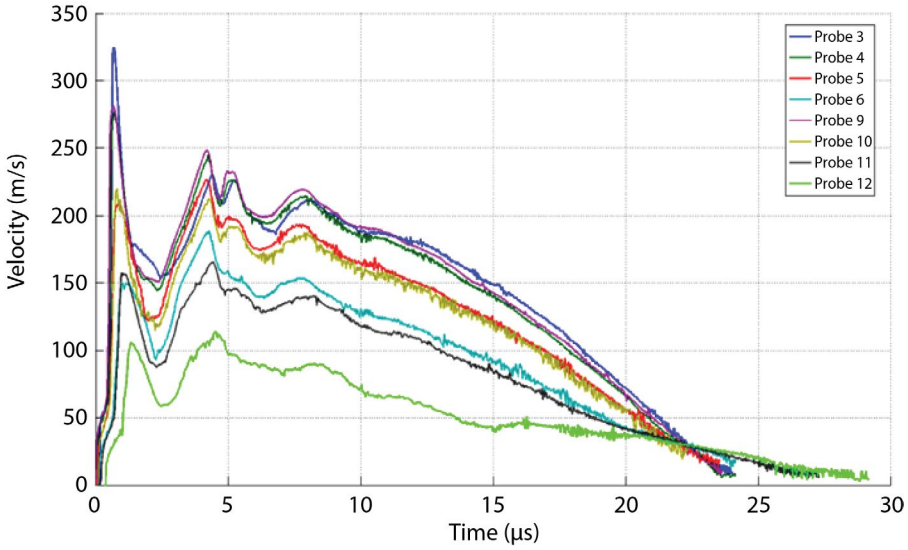

Figure 7. Typical free surface velocity profiles for an A36 steel plate with 0.375-caliber Lexan projectile (impact velocity: 3.4472 km/s)

Simulation of the Experiments

Under extremely high pressure and temperature, solid materials behave like a fluid but retain their initial strength properties. Therefore, projectile-target interactions were simulated using two different types of hydrocode approaches: (1) Lagrangian-based SPH in LS-DYNA and (2) Eulerian-based hydrocode in CTH. Both programs are capable of simulating the experiments. Better understanding the strengths and weaknesses of both approaches is one of the principal motivations for this research.

Material Models

When performing dynamic simulations of this kind, material models must be chosen for each material in the simulation. Both computational techniques used in this study consisted of choosing three material

Table 2. *EOS_GRUNEISEN parameters

Material	ρ (kg/m³)	C_0 (m/s)	S_1	γ
Lexan (Steinberg 1996)	1190	1933	1.42	0.61
304L (Danyluk 2010)	7900	4570	1.49	1.93
HY100 (Banerjee 2004)	7746	3574	1.92	1.69

Table 3. PTRAN parameters for iron (CTH library)

Material	ρ (kg/m³)	C_0 (m/s)	S_1	γ
α- iron	7850	4605	1.456	1.65
ε- iron	8219	4587	1.494	2.40

models: (1) EOS, (2) material strength in compression, and (3) material strength in tension. All the material models chosen for this project are described below.

Equation of State (EOS)

All materials in this kind of simulation require definition of an EOS. Materials under shock-wave loading need a shock model that can account for the sudden pressure, temperature, internal energy, and density changes in front of shock waves. Different forms of the EOS can be used to describe different materials and how they respond to compression or expansion. Mie-Grüneisen EOS models were chosen for all materials used in this work. This choice is limiting in regions of the EOS that are not constrained directly by shock compression data, but it is a good starting point. Future studies might benefit from choosing another EOS form, such as a tabular SESAME EOS. In both LS-DYNA and CTH, different sets of EOS parameters are available to simulate different phenomena. To simulate Lexan and 304L steel under high-impact loading, the *EOS_GRUNEISEN card was used in LS-DYNA and CTH.

$$P = \frac{\rho_0 C^2 \mu \left[1 + \left(1 - \frac{\gamma_0}{2}\right)\mu - \frac{a}{2}\mu^2\right]}{\left[1 - (S_1 - 1)\mu - S_2 \frac{\mu^2}{\mu + 1} - S_3 \frac{\mu^3}{(\mu + 1)^2}\right]^2} + (\gamma_0 + a\mu) E, \quad (1)$$

where, P is the pressure; S_1, S_2, and S_3 are the coefficients of slope of shock and particle velocity curve; γ is Grüneisen coefficient; a is the volume correction factor; ρ is the density; C is the Hugoniot intercept of the metal; and $\mu = \frac{\rho}{\rho_o} - 1$.

As HY100 steel has a polymorphic phase change, a two-state EOS system (called the PTRAN model) for iron was used in CTH. We believe this is a good approximation for low alloy steels such as HY100. In LS-DYNA, the *EOS_GRUNEISEN card used for HY100 steel as a reversible PTRAN model was not available; this means that in those simulations, the material did not undergo any phase transition. Grüneisen parameters for Lexan, 304L stainless steel, and HY100 steel are listed in Table 2, while the reversible PTRAN model parameters for iron are listed in Table 3.

Strength in Compression

The Johnson-Cook material model is one of the most effective and commonly used material models for simulating compressive strength in high strain and large deformation problems (Katayama 1995, Seidt 2007, Littlewood 2010, Elshenawy 2013). In the Johnson-Cook material model of plasticity, flow stress can be expressed as

$$\sigma_y = \left[A + B\left(\varepsilon^p\right)^n\right]\left[1 + C\, In\left(\varepsilon^{\cdot *}\right)\right]\left[1 - \left(T^*\right)^m\right], \quad (2)$$

where σ_y is the flow stress; A, B, C, n, and m are material constants; ε^p is the effective plastic strain; and $\varepsilon^{\cdot *}$ is

the effective total strain-rate normalized by quasi-static strain rate. T^* is the homologous temperature, which can be defined as

$$T^* = \frac{T - T_r}{T_m - T_r}, \quad (3)$$

where T_r and T_m are room temperature and melting temperature, respectively.

Johnson-Cook model parameters for Lexan, 304L, and HY100 steel are given in Table 4. No Johnson-Cook damage model was incorporated in simulation models as a pressure cutoff value (P_{min}) was used to allow spalling and damage.

Strength in Tension (Spall Model)

The spall strength of HY100 and 304L steels has been calculated using Equation 4. This equation was strictly derived for a 1-D shock wave with the concept of pullback signal:

$$\sigma_{spall} = \frac{1}{2} \Delta U_{fs} \rho_0 c_b. \quad (4)$$

Here, σ_{spall} is the spall strength, ρ_0 is the reference density, c_b is the bulk speed of sound in material, and ΔU_{fs} is the difference between the peak velocity and pullback velocity of free surface. Although these experiments were not uniaxial, calculating spall strength as described above still seems to give a reasonable value. Based on the literature, the P_{min} value for the Lexan projectiles was taken as 160 MPa (Steinberg 1996). From velocity profiles, the spall strengths of 304L and HY100 were calculated to be 3.2 GPa and 3.0 GPa (average), respectively. These values are fairly close to the earlier works done on these materials by other researchers (Rajendran 1995, Garrett 1996, Alexander 2002, Gray 2010, Pavlenko 2012). In both LS-DYNA and CTH, spall failure is invoked when the tensile stress exceeds a certain pressure cutoff (i.e., P_{min}) value.

LS-DYNA Simulation

As mentioned previously, the SPH solver was used to simulate all these experiments in LS-DYNA. SPH is a meshless numerical technique used to model the fluid equations of motion (i.e., large distortions). A 2-D axisymmetric SPH model was created for both projectiles and target plates. The SPH particle distance of the target plate was 0.08 mm, while distance in the projectile was selected by matching the SPH particle mass of the projectile with the SPH particle mass of the target plate. No boundary conditions were implemented, as the impact is a localized phenomenon.

CTH Simulation

CTH is an Eulerian hydrodynamics computer code developed and maintained by Sandia National Laboratories. CTH simulations were also done using a 2-D axisymmetric (cylindrical) geometry. Tracer particles were placed at various target locations to collect physics information, including close to the back surface of the target where the velocimetry data are collected. Tracers were set slightly off center radially to stay away from on-axis numerical instabilities, and to match MPDV probe locations. A zone size of 0.05 × 0.05 mm was chosen for all CTH simulations.

Finite Element Analysis (FEA) Results Comparison

The computationally predicted deformation after impact along with the target plate back surface velocity both agree well with experimental data. Crater and bulge measurements were taken in all FEA simulations to compare with the physical measurements. Table 5

Table 4. Johnson-Cook material model strength parameters

Material	*A* (MPa)	*B* (MPa)	*C*	*m*	*n*
Lexan (Littlewood 2010)	75.8	68.9	0	1.85	1.004
304L (Xue 2003)	110	1500	0.014	1	0.36
HY100 (Holmquist 1987)	752	402	0.014	1.13	0.36

Table 5. Typical comparison of physical measurements in 0.22-caliber shots

	Material	Impact Velocity (km/s)	Crater Diameter (mm)	Penetration (mm)	Bulge (mm)
Experiment	304L	6.5832	17.3	6.4	2.4
LS-DYNA	304L	6.5832	17.0	7.4	2.6
CTH	304L	6.5832	18.0	7.0	2.3
Experiment	HY100	6.6989	16.5	6.3	3.0
LS-DYNA	HY100	6.6989	20.0	7.1	2.7
CTH	HY100	6.6989	20.0	7.0	2.4

shows a comparison of crater and bulge details with 10 µs LS-DYNA and CTH simulations. The results show that the software closely matches the experiments.

To compare the difference between simulation codes and experimental results, we will discuss the salient features of the velocity signature, namely (1) the elastic precursor and Hugoniot elastic limit (HEL), (2) the plastic wave, (3) the peak velocity, (4) the second plastic wave, and (5) the spall signatures, and narrow down the discussion to the velocity at the first 4 µs after impact where most important features occur.

Figure 8 shows a comparison of the free velocity profile of LS-DYNA and CTH simulations from data obtained by the probe nearest the impact center in 304L steel in 0.22-caliber Lexan projectile shot. Impact velocity for this case was 6.5832 km/s. Results showed:

- Both LS-DYNA and CTH simulations captured the elastic precursor in a two-peak velocity profiles–like experiment. However, both of these simulations showed lower HEL.
- The CTH simulation captured the sharp rise in plastic wave, similar to the experimental result, whereas the LS-DYNA simulation showed a softer rise in plastic wave. This may be due to the higher value for linear artificial viscosity used in the LS-DYNA simulation (1.0 vs. 0.1).
- Both simulations registered higher peak velocities for the first peak velocity in the experiment. For the second peak velocity observed in the experiment, CTH showed a much higher peak and LS-DYNA showed a lower peak. But both simulations showed a delayed response for the second peak, with LS-DYNA being the slowest of all. The second velocity peak in LS-DYNA was almost 0.5 µs delayed from the experimental velocity peak.
- Both simulations were able to capture the pullback velocity signal after the second peak velocity, which determines spall strength of the material. But the magnitude of the pullback velocity signal was significantly different from that of the experiment. Hence, the spall strength values used in both CTH and LS-DYNA simulation profiles were different than the initial choice of spall strength made from the experimental profile with a 1-D assumption. Further simulation needs to be done to be able to develop a better spall strength model.

These differences in simulation profiles described above may be due to the material model parameters used for multi-dimensional shock simulation.

Similarly, Figure 9 shows a comparison of a typical HY100 steel velocity profile with corresponding LS-DYNA and CTH simulations. The impact velocity of this shot was 6.6989 km/s. As mentioned earlier, the LS-DYNA simulation was done without any phase transition model because a phase transition model is not part of LS-DYNA. The CTH simulation of the HY100 experiment was done with a reversible phase

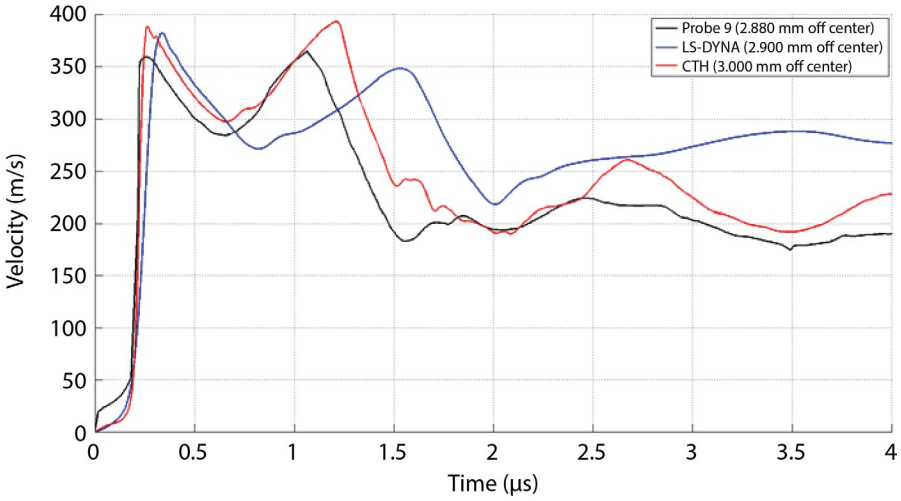

Figure 8. Typical comparison of free surface velocity profile of 304L steel in 0.22-caliber Lexan shot (6.5832 km/s) showing a "two peaks" wave structure

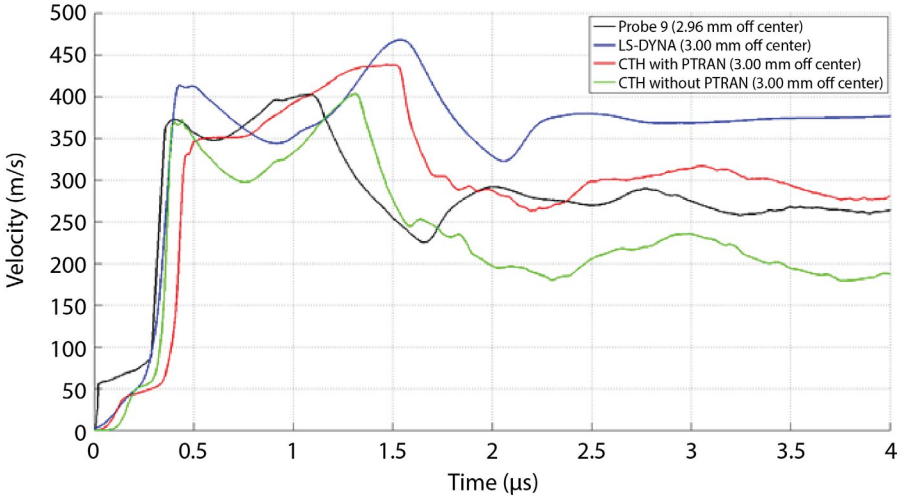

Figure 9. Typical comparison of free surface velocity profile of HY100 steel in 0.22-caliber Lexan shot (6.6989 km/s) showing a flat plateau at peak velocity point in the experiment

transition model, PTRAN. Figure 9 also presents the velocity profile from a CTH simulation done without incorporating the phase transition model. The results showed that:

- The three simulations are still softer than the experimental data during the elastic precursor. CTH without PTRAN had the slowest response. All of these simulations showed lower HEL as compared to the experimental result.
- LS-DYNA and CTH without PTRAN had slopes similar to that of the plastic wave observed from the experimental data. CTH with PTRAN was markedly slower during this phase.
- The LS-DYNA simulation showed a higher peak velocity than experimental results. CTH without PTRAN was the most accurate in capturing the peak velocity.
- The LS-DYNA simulation had a much slower response in the loading-unloading wave compared to the experimental data. The CTH without PTRAN simulation profile showed a slower response for the second peak velocity. Interestingly, the CTH with PTRAN model profile had a flat plateau following the first plastic wave. A second plastic wave rise was seen after the flat plateau, and the second peak velocity was delayed and had a higher magnitude than that of the experiment.

- All simulations were able to capture the pullback velocity signal but with different velocity magnitude. Hence, spall strength from simulation profiles will vary with our initial selection of spall strength for HY100 steel (like 304L).

Each simulation profile showed its advantages and shortcomings; none was perfect. Further refinement of simulation models is still needed to get better agreement with the experimental data.

Evidence of Phase Transition in A36 Steel

A36 steel targets were examined after impact with electron back-scattered diffraction (EBSD) to find metallurgical evidence for the stress-induced α↔ε phase change as observed in pure iron at about 13 GPa (Minshall 1955). As expected, the microstructure was significantly changed due to high-impact loading. One observation was the presence of shock-induced "twinning" (Figure 10). Twinning was present closer to the impact area, and gradually dissipated away further from the impact zone. More twinning was present in the higher-speed impact samples than the lower-speed impact samples. The twinning was most significant during the testing of the samples from the 5.80 km/s speed impact experiment. Another observation from the samples as observed with EBSD imaging (post-impact) was that the grains were significantly compressed and plastically distorted closer to the impact area. Further away from the impact area, the grain size was less affected and resembled pre-impact sizes. This trend of grain distortion was prominent in higher-impact velocity samples.

More research is needed in order to examine different orientations to observe how the twinning is formed in relation to the impact area. Observing different orientations will also provide further insight on the decreasing grain size around the immediate impact area. Another point of interest would be to test hardness, pre- and post-impact, in order to find evidence of phase change–induced hardening as previously observed (Gray 2000).

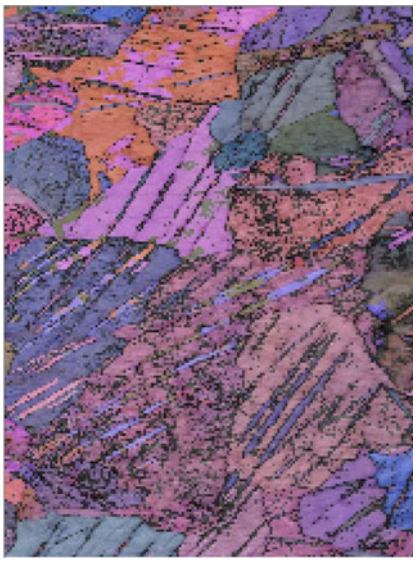

Figure 10. Typical EBSD image of A36 steel showing twinning (impact velocity: 5.834 km/s)

The presence of hexagonal closed packed (HCP) crystals (post-impact) leads to the probable conclusion of an increase in brittleness, and the probability that A36 steel does have the phase transition. It has been previously observed that pure iron has no retained high-pressure phase material (HCP), but alloyed steels can have small amounts only if the phase transition happens in the shock compression event (Gray 2014).

Conclusion

Gas gun experiments were performed to observe the plastic deformation of two different steel plates after hypervelocity impact. Free surface velocity of the back surface of the plate was measured using MPDV systems. MPDV data explained the polymorphic phase transition behavior of HY100 in free surface velocity profiles and encouraged us to revisit velocimetry data of A36 steel from FY 2013. We see some evidence from the CTH simulations of the HY100 experiment that inclusion of the phase transition leads to better agreement between experiment and simulation, although this would benefit from more research. Simulation models developed in the LS-DYNA SPH solver and CTH hydrocode were used to simulate the experiments. Simulation results are in reasonable

agreement with experimental data in terms of crater details, bulge, and free velocity profiles. Also, initial evidence of the α↔ε phase transition in A36 steel was found. Therefore, simulating the A36 steel models with the phase transition will further improve previous computational models.

References

Alexander, D. J., D. L. Robbins, "Laser-driven planar impact of miniature specimens of HY-100 steel," *AIP Conf. Proc.* **620**, 1 (2002) 630–633.

Bancroft, D., E. L. Peterson, S. Minshall, "Polymorphism of iron at high pressure," *J. Appl. Phys.* **27**, 3 (1956) 291–298.

Banerjee, B., "Material point method simulations of fragmenting cylinders," *Proc. 17th ASCE Engineering Mechanics Conference* **1** (2004) 1–15.

Barker, L. M., R. E. Hollenbach, "Shock wave study of the α↔ε phase transition in iron," *J. Appl. Phys.* **45**, 11 (1974) 4872–4887.

Becker, S., et al., "Plastic deformation study using a light gas gun," in *Site-Directed Research and Development*, FY 2013, National Security Technologies, LLC, Las Vegas, Nevada, 2014, 37–49.

Danyluk, J., *An Analysis of Multi-Material Plates Under Explosive Loading*, Master of Engineering Degree Thesis, Rensselaer Polytechnic Institute, 2010.

Duvall, G. E., R. A. Graham, "Phase transitions under shock-wave loading," *Rev. Mod. Phys.* **49**, 3 (1977) 523–579.

Elshenawy, T., Q. M. Li, "Influences of target strength and confinement on the penetration depth of an oil well perforator," *Int. J. Impact Eng.* **54** (April 2013) 130–137.

Garrett, R. K., A. M. Rajendran, H. R. Last, "Modeling spall in HY100, HY130, and AF1410 steels," *AIP Conf. Proc.* **370** (1996) 323–326.

Gray, G. T., D. B. Hayes, R. S. Hixson, "Influence of the shock-induced α-ε transition in Fe on its post-shock substructure evolution and mechanical behavior," *Journal of Physics IV France* **10** (2000) 755–760.

Gray, G. T., N. K. Bourne, K. S. Vecchio, J. C. F. Millett, "Influence of anisotropy (crystallographic and microstructural) on spallation in Zr, Ta, HY-100 steel, and 1080 eutectoid steel," *International Journal of Fracture* **163**, 1–2 (2010) 243–258.

Gray, G. T., private communication, 2014.

Hammond, R. I., W. G. Proud, "Does the pressure-induced α–ε phase transition occur for all low-alloy steels?" *Proceedings of the Royal Society of London. Series A: Mathematical, Physical and Engineering Sciences* **460**, 2050 (2004) 2959–2974.

Holmquist, T. J., *Strength and Fracture Characteristics of HY-80, HY-100, and HY-130 Steels Subjected to Various Strains, Strain Rates, Temperatures, and Pressures*, NSWC TR 88-252, Naval Surface Warfare Center, 1987, http://www.dtic.mil/dtic/tr/fulltext/u2/a233061.pdf, accessed October 1, 2014.

Jensen, B. J., P. A. Rigg, M. D. Knudson, R. S. Hixson, G. T. Gray, B. H. Sencer, F. J. Cherne, "Dynamic compression of iron single crystals," *AIP Conf. Proc.* **845** (2006) 232–235.

Jensen, B. J., G. T. Gray, R. S. Hixson, "Direct measurements of the α-ε transition stress and kinetics for shocked iron," *J. Appl. Phys.* **105**, 10 (2009) 103502-1–103502-7.

Katayama, M., S. Kibe, S. Toda, "A numerical simulation method and its validation for debris impact against the whipple bumper shield," *Int. J. Impact Eng.* **17**, 4–6 (1995) 465–476.

Littlewood, D. J., "Simulation of dynamic fracture using peridynamics, finite element modeling, and contact," *ASME 2010 International Mechanical Engineering Congress and Exposition* **9** (2010) 209–217.

Minshall, S., "Investigation of a polymorphic transition in iron at 130 kb," *Phys. Rev.* **98** (1955) 271.

Murr, L. E., M. A. Meyers, "Metallurgical effects of shock and pressure waves in metals," in *Explosive Welding, Forming and Compaction*, T. A. Blazynski, ed., Applied Science Publishers, London, 83–121, 1983.

Pavlenko, A., S. Malugina, D. N. Kazakov, Y. N. Zuev, A. E. Shestakov, D. A. Belyaev, "Plastic deformation and spall fracture of structural 12Cr18Ni10Ti steel," *AIP Conf. Proc.* **1426**, 1 (2012) 1137–1140.

Rajendran, A. M., H. R. Last, R. K. Garrett, *Plastic Flow and Failure in HY100, HY130 and AF1410 Alloy Steels Under High Strain Rate and Impact Loading Conditions*, ARL-TR-687, Army Research Laboratory, Watertown, Massachusetts, 1995.

Seidt, J. D., A. Gilat, J. A. Klein, J. R. Leach, "High strain rate, high temperature constitutive and failure models for EOD impact scenarios," in *Proc. 2007 SEM Annual Conference and Exposition on Experimental and Applied Mechanics*, Society for Experimental Mechanics, Inc., Springfield, Massachusetts, 2007.

Steinberg, D. J., *Equation of State and Strength Properties of Selected Materials*, UCRL-MA-106439, Change 1, Lawrence Livermore National Laboratory, Livermore, California, 1996.

Xue, Q., V. F. Nesterenko, M. A. Meyers, "Evaluation of the collapsing thick-walled cylinder technique for shear-band spacing," *International Journal of Impact Engineering* **28**, 3 (2003) 257–280.

This page left blank intentionally

Dynamic Temperature and Pressure Measurements with Rare-Earth Doped Phosphors

STL-03-14 | Year 1 of 1

Gerald Stevens,[1,a] Gene Capelle,[a] Brandon La Lone,[a] Rachel Posner,[a] Mike Grover,[a] and Dale Turley[a]

The luminescence from rare-earth doped phosphor materials exhibits features (line widths, wavelengths, intensities, and lifetimes) that are directly related to the temperature and pressure of the material. This fluorescence light may be used to remotely determine the properties of shocked materials beneath windows/anvils. We selected an appropriate phosphor and investigated its behavior at high pressure and temperature in shock experiments, as well as in a diamond anvil cell. Our study indicates that our technique may be suitable for higher temperature shock physics experiments, and might be extended to lower temperatures by choosing a different phosphor material.

[1] stevengd@nv.doe.gov, 805-681-2219
[a] Special Technologies Laboratory

Background

There is an ongoing need to measure temperatures in shock wave experiments for equations-of-state (EOS) development. While optical pyrometry is a useful tool for measuring the temperatures of opaque samples, it is unsuitable for most transparent (non-emissive) samples such as epoxies and anvils. Our goal in this project was to develop a technique to measure temperatures of shocked materials, specifically transparent epoxies, using an embedded fluorescent sensor with a temperature-dependent lifetime; the sample temperature is inferred from a fluorescence lifetime measurement of the sensor, and can be used with both transparent and opaque samples. Choosing the appropriate sensor for this measurement was critical. Determining the shocked glue temperature helps relate the temperature of a metal/glue interface to the bulk metal temperature, a key property used to develop accurate EOSs for weapons codes. Our team has made a great deal of progress measuring shock temperatures with a combination of thermal radiance and reflectivity measurements (La Lone 2013). An estimate of the glue temperature would allow us to constrain the correction required to infer a bulk metal temperature—one of the remaining sources of uncertainty in our measurements.

Ruby (Al_2O_3:Cr) is a common fluorescent material that has widespread applications, from lasers to temperature and pressure gauges. In the late 1970s, H. K. Mao (1976) calibrated the wavelength shift in the R1 fluorescence line of ruby as a function of pressure (up to 100 GPa), creating a standard widely used by the diamond anvil cell (DAC) community. The ruby R1 line's fluorescence lifetime is τ = 3.2 ms at room temperature, and it drops precipitously above room temperature to about 0.5 ms at 500 K. Temperature probes have been fabricated that utilize this behavior by attaching a small ruby sample to the end of an optical fiber, and using a modulated laser for lifetime determination. Ruby is not, however, an ideal pressure sensor at higher temperatures, due to thermal quenching of its fluorescence.

We have previously used cerium-doped lutetium oxyorthosilicate (LSO:Ce) and cerium-doped yttrium aluminium garnet (YAG:Ce) to measure the residual temperature (after shock and release) of copper plates. LSO:Ce and YAG:Ce phosphors have luminescence decay times of τ = 40 and 100 ns at room temperature, respectively. Their quantum yields are excellent—both close to 1—and, along with pulsed nitrogen lasers, we have used these phosphors in shock experiments. Both materials continue to fluoresce after being shocked and released to ambient pressure (Stevens 2004). However, these phosphors will not operate at the predicted temperature of shocked Loctite 326 epoxy (predicted to reach about 725 K when shocked with PBX 9501 high explosive). While there is information in the literature about the spectrum of these phosphors at pressure, no one has published decay times of phosphors at high pressure and temperature.

We began our study focusing on europium-doped yttrium oxide (Y_2O_3:Eu), one of many phosphors we characterized for thermometry over 20 years ago with collaborators from Oak Ridge National Laboratory (review article: Allison 1997). This phosphor is one of the most widely used and oldest of the cathode ray–tube phosphors being used primarily for red pixels in color televisions. As an inorganic oxide, it is robust with regards to aging and thermal decomposition or melting (melting point >2400°C) and, more importantly, recent publications on its behavior under pressure suggest that it may be suitable for our experiments (Wang 2009, Dai 2010).

An energy level diagram (adapted from Allison 1997) representing some of the processes and decay paths that contribute to the lifetime of Y_2O_3:Eu^{3+} is shown in Figure 1. For this phosphor, the dopant europium takes the place of an ytterbium ion within the host crystal. A UV (or blue) laser pulse (purple arrow) is used to excite the Eu^{3+} either indirectly or directly to a $^5D_{j=0-4}$ state. Populations within the vibrational states are temperature-dependent and governed by Maxwell–Boltzmann statistics, and the lifetime τ of each state is inversely related to the radiative and non-radiative rates k_r and k_{nr} by

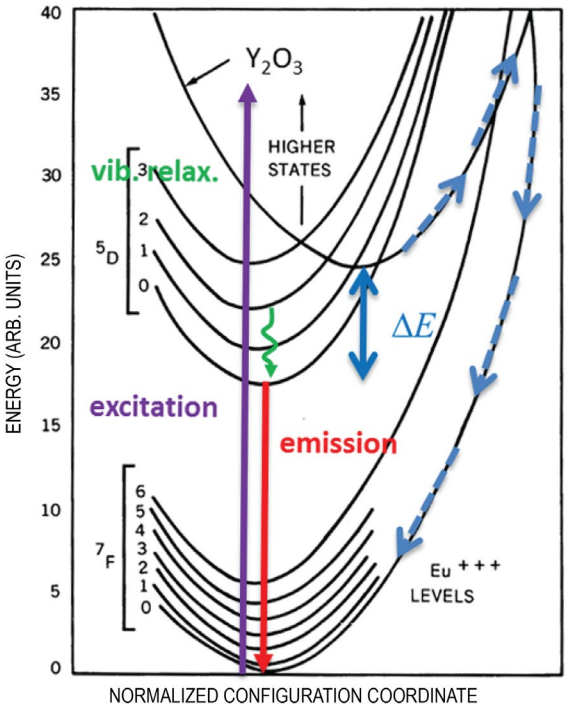

Figure 1. Energy level diagram showing some of the processes (excitation, vibrational relaxation, emission) involved in the fluorescence of Y_2O_3:Eu^{3+} (adapted from Allison 1997). The Y_2O_3 host charge transfer state is separated in energy from the lowest vibrational excited state $^5D_0$ by ΔE. This state provides a non-radiative path (dashed blue lines) to the ground state, influencing the lifetime of the phosphor.

$$\tau = \left(k_r + k_{nr} \left[e^{\frac{-(b \cdot P + \Delta E) h \cdot c}{k \cdot T}} \right] \right)^{-1} . \quad (1)$$

This equation is a simple empirical form that shows the temperature, T, and pressure, P, dependencies of the lifetime. For our purposes, an ideal phosphor will have weak pressure dependence (small coefficient b). Figure 2 shows the measured fluorescence spectrum with transitions identified.

Two sets of experiments are required to make a temperature measurement with a phosphor: DAC experiments for calibration and dynamic experiments to shock-heat a sample under study. A heated DAC allows us to characterize fluorescence lifetimes and spectra as a function of temperature at a given

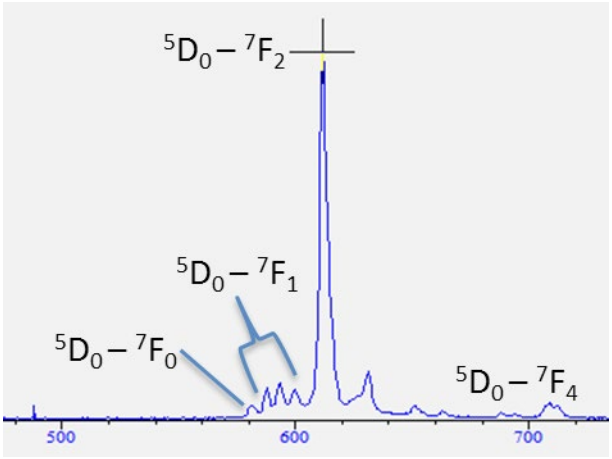

Figure 2. Fluorescence spectrum of Y_2O_3:Eu^{3+}, with Eu^{3+} transitions identified

pressure, and these data can be used along with velocimetric pressure determination in order to measure the temperature of shocked Loctite 326.

Project

Diamond Anvil Cell Measurements

We began our phosphor characterization by assembling a heated DAC optical system to measure fluorescence spectra and lifetimes of Y_2O_3:Eu^{3+}. For this investigation we chose a micron-sized phosphor powder from Sylvania (Y_2O_3:Eu^{3+} doped with 5% Eu). We used a gas membrane–driven, heated Almax easyLab Diacell HeliosDAC capable of reaching 100 GPa and 1000°C. A phosphor sample was taken from a hot-pressed powder sample that was near normal density and placed within a 100 µm diameter hole in a 75 µm thick INCONEL gasket that is sandwiched between the diamond anvils. A ~20 µm diameter ruby sphere was also placed in the hole in the gasket for pressure calibration. The left-hand inset image of Figure 3 shows the sample with the ruby sphere visible in the upper right-hand corner.

Phosphor excitation was performed using a modulated, single-mode, fiber-coupled 20 mW 405 nm laser from OZ Optics Ltd. This laser was collimated and sent through a 50/50 beam-splitting cube and focused again down to a ~50 µm spot on the phosphor sample within the DAC. A CCD camera was used to observe alignment and sample position during pressure and heating cycles. A 500 nm long-pass filter reduces the amount of laser light incident on the camera. On the other (fluorescence) side of the DAC, a similar optical setup was used, but with a 405 nm Semrock StopLine notch filter, and a 567 nm long-pass dichroic beam splitter (DBS). A Beck-Schwartzchild 15x f2.8 reflective objective was used to collect fluorescence light. It was chosen primarily for its achromatic properties. The collected fluorescence was sent alternately to either an

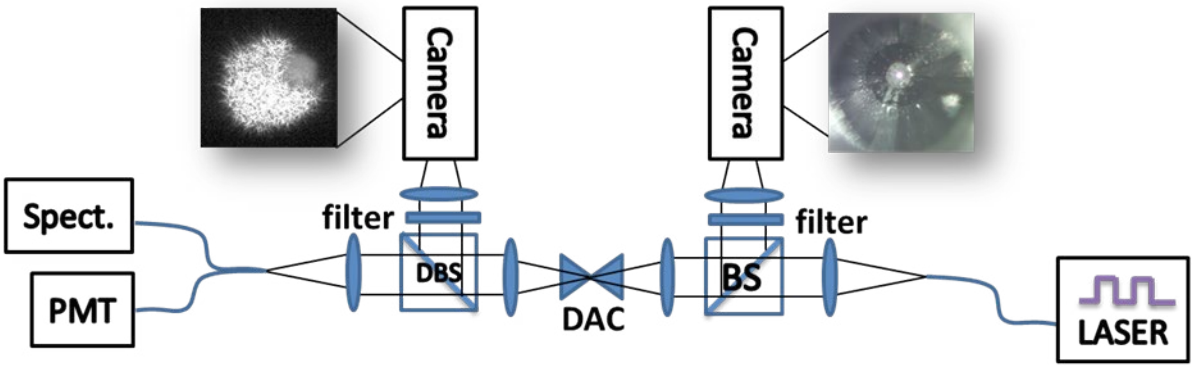

Figure 3. Schematic of experimental setup for DAC measurements. The fiber-coupled laser (right side of figure) gets collimated by a lens, and sent through a 50/50 beam-splitting (BS) cube, and focused onto the sample within the DAC. The fluorescence from the sample and ruby sphere is collimated by a lens (left of the DAC) and imaged into a fiber that goes to a spectrometer and a PMT. A DBS sends light at wavelengths shorter than 567 nm to an imaging camera. The inset left-hand image shows the glowing phosphor, with the sphere located in its upper right corner.

Ocean Optics USB4000 spectrometer or a photomultiplier tube (PMT), depending on the measurement. The laser was operated in continuous wave mode, or modulated at 20 Hz with a 5 ms pulse width. Current from the PMT was dropped through a 50 k ohm resistor on an oscilloscope, and data were averaged 256 times. The fluorescence lifetime at each temperature was determined by fitting the oscilloscope decay data with a single exponential decay. Pressure was determined by fitting the position of the ruby R1 line (measured at 694.6 nm at ambient pressure) with a Gaussian function.

Because ruby pressure determination fails at high temperatures, we chose first to pressurize the cell up to a desired ~20 GPa at ambient temperature. The Y_2O_3:Eu^{3+} 710 nm $^5D_0$–$^7F_4$ peak next to the 695 nm ruby line perturbed our quick-pressure determination, and when accounted for, we ended up with a maximum pressure of about 15 GPa. Measured lifetimes are shown in Figure 4 as a function of temperature and pressure. We observed a change in lifetime at ambient temperature from τ = 975 µs at ambient pressure to 750 µs at 12 GPa. This gives a slope of about −20 µs/GPa, significant but not indicative of too large a pressure dependence to the lifetime. Incrementally elevating the temperature up to 1076 K, we observed the phosphor lifetime "turning on" above 950 K (Figure 4) as indicated by the change in the temperature-time slope. The ruby-derived pressure of the sample is shown by the color scale in this figure. Thermal expansion of the cell causes a small increase in pressure that is correlated with temperature.

The fluorescence spectrum is shown as a function of pressure in Figure 5. The $^5D_0$–$^7F_1$ peak is a magnetic dipole transition, and its position is insensitive to pressure. The dominant $^5D_0$–$^7F_2$ peak at 611 nm is a forced dipole transition, and is very sensitive to pressure and the surrounding host crystal structure. It is parity-forbidden and requires a crystal host to break symmetry and allow the transition. As we increase pressure, we see a peak at 635 nm become the dominant fluorescence peak. Between 7 and 18 GPa, Y_2O_3:Eu^{3+} undergoes a polymorphic phase transition

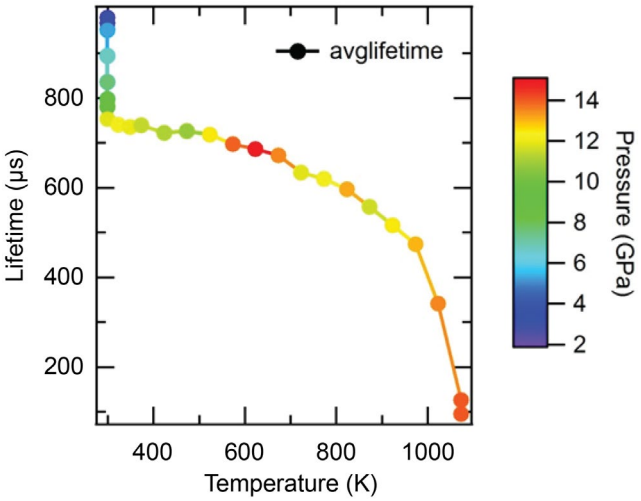

Figure 4. Lifetime of the 611 nm fluorescence, measured in the DAC, vs. temperature and pressure (color scale)

from cubic to monoclinic (Wang 2009), and the 635 nm peak we observed is the $^5D_0$–$^7F_2$ transition within the new monoclinic lattice. The observed temperature behavior is reminiscent of the phosphor at ambient pressure, despite having undergone a phase transition. It was important to characterize the phosphor in its high-pressure phase prior to shock experiments, as we had no idea what effect the transition would have on the lifetime.

Dynamic Fluorescence Measurements

For dynamic experiments, we used a Big Sky pulsed-YAG excitation laser, capable of operating in doubled (532 nm) or quadrupled (266 nm) mode. We characterized various Eu dopant concentration samples under ambient conditions and excitation at each of these wavelengths using a Thorlabs PDA36A photodetector (filtered by two KV550 long-pass filters), or an Andor gated optical multichannel analyzer (OMA, with a KV389 long-pass filter to prevent second-order diffraction peaks). UV excitation (266 nm) produces a short-lived blue fluorescence component that lasts less than 100 ns. This prompt fluorescence was initially deemed not to be a concern for dynamic experiments because we could spectrally filter the majority of this emission, and we could also excite the phosphor many microseconds prior to shock heating (temporally separating the

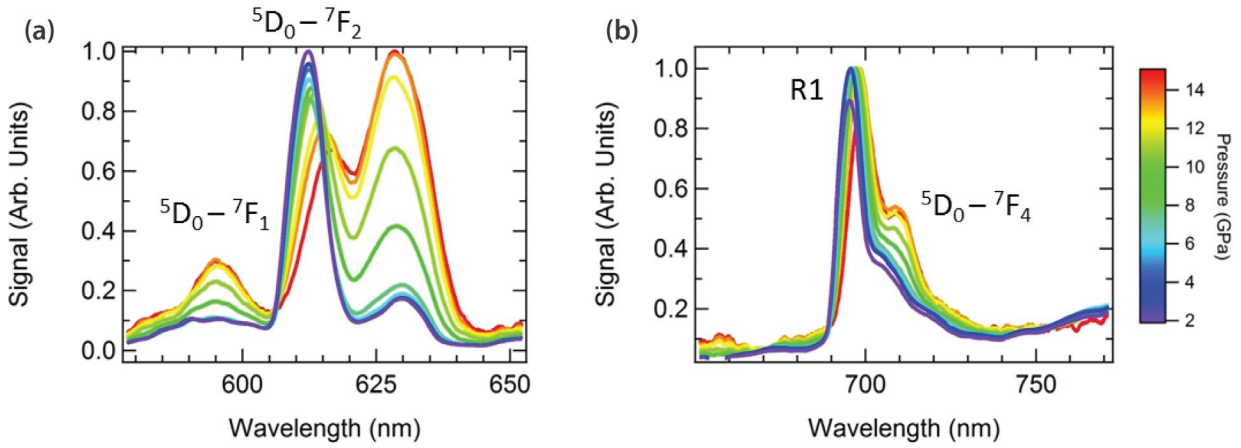

Figure 5. (a) Spectra from Y_2O_3:Eu^{3+} phosphor as a function of pressure in the DAC. Vibrational transitions at 595 and 611 nm are identified. The peak at 635 nm is the $^5D_0$–$^7F_2$ transition after a polymorphic phase transition. (b) Ruby R1 line and another Eu^{3+} vibrational transition that needs to be considered for ruby pressure determination.

prompt emission from the shock measurement). The effects of epoxy on the fluorescence spectrum were, however, a concern.

Ambient pressure and temperature measurements were made of the phosphor mixed with Loctite 326 epoxy (our preferred glue for bonding shock anvils to metal samples under study). The fluorescence spectrum of the mixed sample (black trace) at early time (t = 0 µs), and later (red, t = 25 µs) after the prompt light has decayed away, is shown in Figure 6. The prompt blue fluorescence of the glue is problematic, as it has a long spectral tail reaching all the way to the phosphor peaks of interest near 600 nm. This unwanted light decays away in less than a microsecond; however, the prompt fluorescence signal was orders of magnitude brighter than our long-lived (ms) fluorescence under study. We stacked two KV550 filters to help with rejection, but were unable to use a PMT because the ~100 V prompt peak forced our scope into a self-protection mode at high-sensitivity settings (<100 mV/division). To remedy this, we used an amplified photodiode with limited (but adequate) bandwidth and gain.

Our dynamic experiment was assembled in the Special Technologies Laboratory Boom Box explosive containment vessel. A diagram of the experiment is shown in Figure 7. The phosphor mixed with Loctite 326 glue was used to bond a tin sample to a lithium fluoride (LiF) window. Detonation of a ½" by ½" cylinder of PBX 9501 explosive was used to drive a shock wave into the tin-glue-LiF assembly. A sapphire port window in the side of the Boom Box was used to transmit the 266 nm pulsed laser. This light was weakly focused to about a 6 mm diameter spot on the phosphor/glue sample. Photonic Doppler velocimetry (PDV) was performed at ~20° relative to the shock direction, and fluorescence was collected at a similar angle. A fiber collimator was

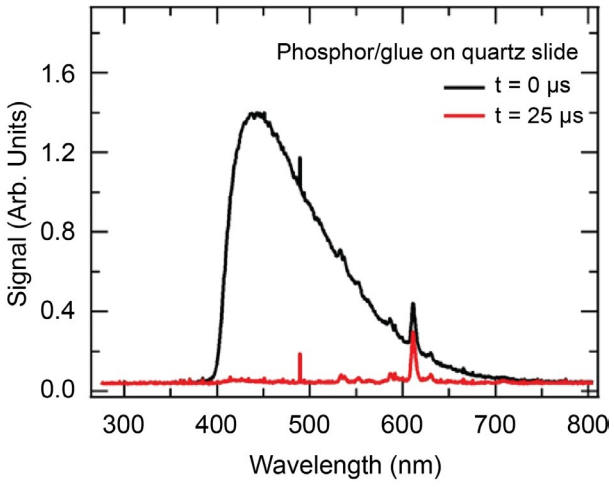

Figure 6. Prompt fluorescence spectrum of Y_2O_3:Eu^{3+} phosphor embedded in glue at two different times after excitation under ambient conditions

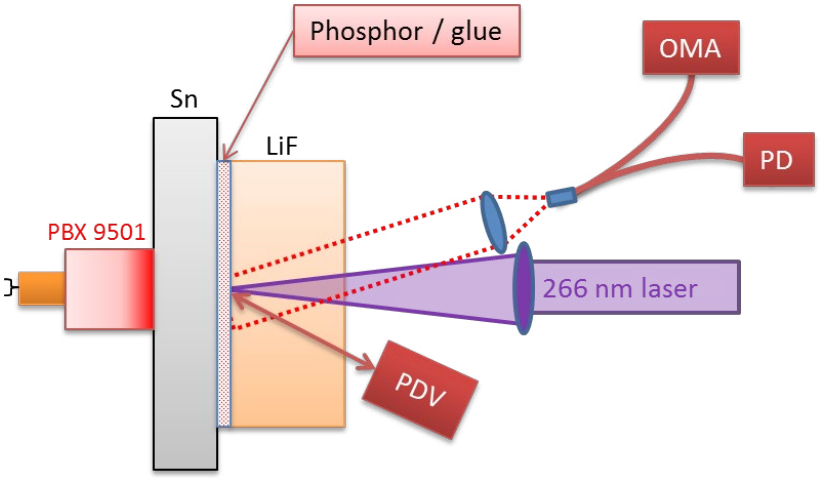

Figure 7. Shock-wave test setup. A layer of epoxy mixed with phosphor powder (red dots) binds a LiF window to a tin sample. This layer is probed by a pulsed 266 nm laser, and fluorescence is collected by an OMA and a photodiode (PD) detector.

used for light collection, providing us with a setup that is weakly dependent on the position of the phosphor/glue as it moves in time. Light from the collimator was split and sent to a gated OMA and a photodiode.

Time-varying signals from an experiment are shown in Figures 8 and 9. The laser was triggered 0.2 ms before the explosive was detonated. The large prompt fluorescence peak may be seen at about −0.2 ms in Figure 8—followed by fluorescence decay—and a large peak of unwanted LiF fracture light near t = 0 ms. Figure 9 shows the fluorescence signal during the short duration of the shock experiment and the measured velocity profile of the tin-glue-LiF interface. The shock arrives at t = 2 µs, after which there is a gradual release in pressure from the Taylor wave release of the explosive, until just after 3.5 µs when the shock arrives at the rear of the LiF (seen as a discontinuous step in the velocity profile). The experiment ends when the shock breaks out the rear of the LiF window because the window undergoes spall, loses transparency, and begins to emit fractoluminescence (Turley 2013). Also shown is a fit of the decay time (blue trace) of the phosphor in a pre-shot measurement. Had the lifetime changed from τ = 1 ms to less than 10 µs, we would have observed a change in decay slope over the short duration of the experiment. However, given the small (1.5 mV) signal level and the degree of noise, we did not observe a quantifiable change in decay time. This suggests that our phosphor's sensitivity to high temperatures does not match the temperatures reached by our experiment and that the glue temperatures are probably less than 1100 K. We determined that shocked tin in similar experiments was about 1300 K (La Lone 2013), and clearly the glue did not reach such a temperature.

Figure 10 shows the spectrum of light collected during the 1.5 µs at which the glue was under pressure. The shocked spectrum had very poor signal-to-noise ratio, and has been significantly smoothed. The ambient

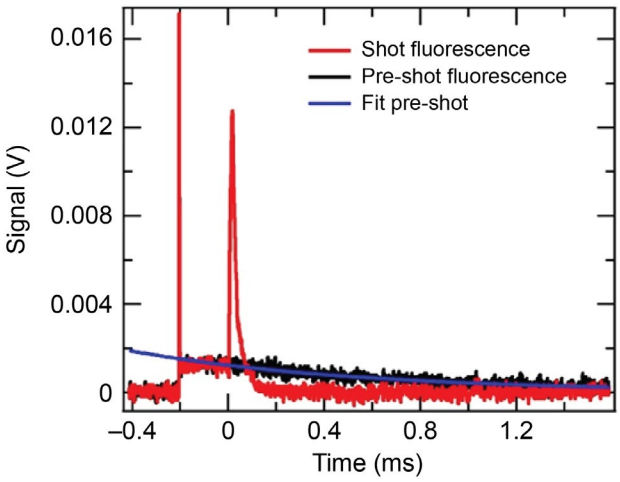

Figure 8. Pre-shot fluorescence decay (black), with an exponential fit (blue) and the fluorescence of the shocked glue/phosphor (red). Prompt fluorescence appears at t = −0.2 ms, and light produced by fracture of the LiF appears near t = 0 ms. An expanded view of the region near shock-wave arrival, from 1 to 6 µs, is shown in Figure 9.

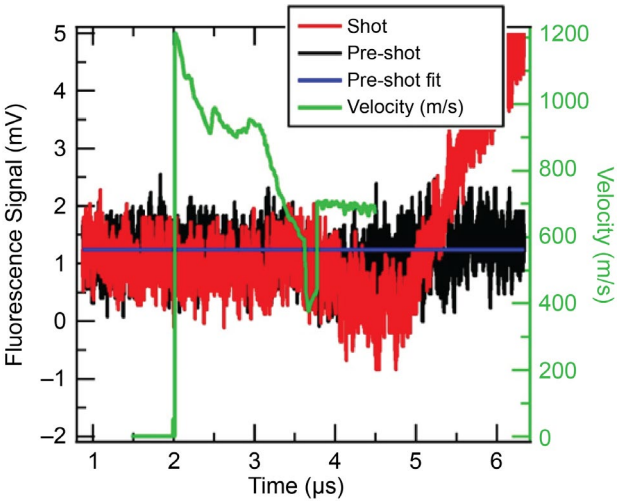

Figure 9. Expanded detail of Figure 8, near shock-wave arrival. The velocity of the tin-glue interface is shown in green, with a peak velocity of 1200 m/s and pressure of 21.4 GPa. The pressure and temperature at the interface drop for about 1.5 μs, at which point the shock arrives at the back surface of the LiF anvil ending the measurement. The fit lifetime of the pre-shot fluorescence gives τ = 0.923 ms.

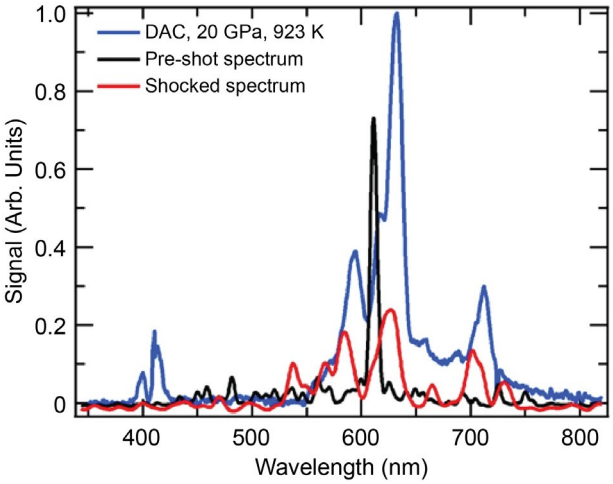

Figure 10. Pre-shot spectrum (black), shocked spectrum (red), and a DAC spectrum (blue) for comparison. The shocked spectrum had very poor signal-to-noise ratio, and has been significantly smoothed. The multiple peaks and peak shifts, and the emergence of the 630 nm peak, indicate that the sample was at pressure for the duration of the experiment.

spectrum and a DAC spectrum, taken at 20 GPa and 923 K, are shown for comparison. The multiple spectral peaks and the peak shifts in the shocked spectrum are similar to the DAC measurement, indicating that the phosphor was under high shock pressures at the time the spectrum was recorded. Given the poor signal levels, it is difficult to draw any other conclusions from the shocked spectrum.

Conclusion

As an illustrative measure of our system's sensitivity, we fit the fluorescence decay time from 3.5 to 4.5 μs, which gives τ = 4 μs. This apparent decay, however, is either due to LiF issues or simply electrical ringing; it is not obviously indicative of high temperatures due to the time at which it occurs. We might have been able to observe a 10 μs decay time, or less, during our experiment, corresponding to ~1100 K. The shocked epoxy likely did not reach this temperature. We have previously measured the glue temperature to be about 750 K using mid-wave IR pyrometry with an estimated (unknown) glue emissivity (Turley 2011).

We have demonstrated that the overall phosphor temperature measurement technique appears to be sound, and modifications to it (such as electrically shunting the prompt light signal or exciting at longer wavelengths to inhibit glue fluorescence) are obvious improvements to pursue for future applications. Shocked porous materials reach high temperatures, and Y_2O_3:Eu^{3+} may be an appropriate choice for temperature measurements of compressed porous samples. Also, it may provide an alternate temperature measurement for cross-comparison with Raman and radiance measurements to validate thermometric techniques on a single experiment.

Acknowledgments

The authors would like to thank Nenad Velisavljevic and Chris Seagle for help with the substantial issues we encountered with our DAC.

References

Allison, S. W., G. T. Gillies, "Remote thermometry with thermographic phosphors: Instrumentation and applications," *Rev. Sci. Instrum.* **68** (1997) 2615–2650.

Dai, R., Z. Wang, Z. Zhang, Z. Ding "Photoluminescence study of SiO_2 coated Eu^{3+}:Y_2O_3 core-shells under high pressure," *J. Rare Earths* **28**, Supplement 1 (December 2010) 241–245.

La Lone, B. M., G. D. Stevens, W. D. Turley, D. B. Holtkamp, A. J. Iverson, R. S. Hixson, L. R. Veeser, "Release path temperatures of shock-compressed tin from dynamic reflectance and radiance measurements," *J. Appl. Phys.* **114** (2013) 063506.

Mao, H. K., P. M. Bell, "High-pressure physics: The 1-megabar mark on the ruby r1 static pressure scale," *Science* **191**, 4229 (February 1976) 851–852.

Stevens, G. D., S. S. Lutz, W. D. Turley, C. D. Adams, R. M. Boat, L. M. Hull, "Optical response of cerium-doped lutetium oxyorthosilicate coatings at shocked surfaces," *Rev. Sci. Instrum.* **75** (2004) 462.

Turley, W. D., D. B. Holtkamp, L. R. Veeser, G. D. Stevens, B. R. Marshall, A. Seifter, R. B. Corrow, J. B. Stone, J. A. Young, M. Grover, "Infrared emissivity of tin upon release of a 25 GPa shock into a lithium fluoride window," *J. Appl. Phys.* **110** (2011) 103510.

Turley, W. D., G. D. Stevens, G. A. Capelle, M. Grover, D. B. Holtkamp, B. M. La Lone, L. R. Veeser, "Luminescence from edge fracture in shocked lithium fluoride crystals," *J. Appl. Phys.* **113** (2013) 133506-1–133506-5.

Wang, L., Y. Pan, Y. Ding, W. Yang, W. L. Mao, S. V. Sinogeikin, Y. Meng, G. Shen, H. K. Mao, "High-pressure induced phase transitions of Y_2O_3 and Y_2O_3:Eu^{3+}," *Appl. Phys. Lett.* **94** (2009) 061921.

Dynamic Recompression of Damaged Materials

STL-05-13 | Continued from FY 2013 | Year 2 of 2

Dale Turley,[1,a] Gerald Stevens,[a] Ellen Cerreta,[b] Edward Daykin,[c] George T. Gray III,[b] Robert S. Hixson,[d] Darcie Dennis-Koller,[b] Brandon La Lone,[a] Carlos Perez,[c] Paulo Rigg,[b] Veronica Livescu,[b] and Lynn Veeser [e]

We have investigated the spall mechanism for small, nearly planar explosive-driven shocks; this has not been studied extensively and is of great importance to our mission. When a metal sample is subjected to a tension wave in a shock experiment, a damaged layer can form in the sample when the tension exceeds the spall strength. In many such cases a spall scab separates from the bulk of the sample, but sometimes the explosive gases driving the shock wave can continue to accelerate the sample sufficiently to cause it to impact the spall scab several microseconds or more after spall. We set out to determine (a) whether this late-time impact can be intense enough to recompress or even collapse the spall plane or the incipient spall voids or damage features, and (b) can such recompression obscure or complicate quantification of the features of the initial damage in the recovered samples. We used diagnostics that include time-resolved velocimetry, x-ray radiography, and post-shot sample recovery with metallurgical analysis to characterize the damage process and samples. In this second year of the project, we improved the sample recovery methods and added multiplexed photonic Doppler velocimetry to determine the kinetics of the damage as a function of radial position in the sample to learn more about the stress dependence of the damage and recompression processes. We are attempting to reconcile the time-resolved data and the microstructural information from recovered samples.

[1] turleywd@nv.doe.gov, 805-681-2239
[a] Special Technologies Laboratory; [b] Los Alamos National Laboratory; [c] North Las Vegas; [d] Los Alamos Operations;
[e] Keystone International, Inc.

Background

Tensile damage formed in materials subjected to dynamic loads remains an important field of study (Curran 1987, Gray 2000). To study the spall, damage evolution, and failure phenomena, conditions of tension leading to spall are frequently created in the laboratory using shock-wave experiments utilizing either flat-top or triangular-wave profiles. A flat-top shock results from a uniform impactor, usually from a gun, striking the target. Triangular shocks can be generated by a suitably layered impactor but are more commonly produced by detonating a high explosive (HE) in contact with the sample, where the Taylor wave shock decay results in a triangular wave. The principal reasons for differences in the effects of the tension produced by flat-top and triangular shock waves are the amount of time the sample material spends at increased pressure and the magnitudes of the loading and unloading applied strain rates. The time under stress is important because the work hardening in a ductile metal depends upon the time available for plastic processes, such as dislocation multiplication and glide, to occur (Gray 2003, 2004). The longer stress times that occur for flat-top shocks allow increased substructural development in the form of increased

dislocation generation and storage. These dislocations are correlated to increased shock hardening (Gray 1988, 1993; Johnson 1999) via increased work hardening, which has been linked to lower spall strengths in some materials. The occurrence of these processes at high pressure before the shock releases is known as preconditioning. For triangular wave shapes, relatively less time is spent at peak stress, reducing the time for nucleation and growth of damage and possibly leading to a higher spall strength (Hixson 2004, Koller 2005). The degree of spall and damage formation is known to depend on the peak stress, tensile strain rate, material microstructure, and locations of impurities (Meyers 1983, Gray 2010).

Hixson (2004) and Koller (2005) have reported that copper targets subjected to compressive and tensile loading from gas gun flyer impacts producing flat-top and triangular shocks can sometimes exhibit free surface velocity profiles indicative of spall, depending on the details of the exact stress-time history applied. When there is complete spall or a very extensive, continuous plane of damage in a sample, an acoustic wave is trapped in the spall scab and reflects back and forth, leading to a sample free surface velocity profile that is roughly flat but with oscillations that damp out. The ringing period is typically twice the thickness of the spall scab divided by the sound speed. Post-shock metallurgical analysis of copper samples for various experimental stresses and release rates reveals a variety of conditions ranging from plastic strain without damage to complete spall. When the free surface velocity profile shows a spall signature, the location of the damage plane, whatever the extent of the damage, is consistent with the ringing period. For samples that do not spall or damage extensively, there can be similar ringing, but in this case the period is usually consistent with the full sample thickness. In most spall experiments the ringing in the velocity profile is a good indicator of the location of the damage plane, but these observations suggest that a free surface velocity measurement is not always a reliable indicator of complete spall separation.

Such an apparent anomalous result was reported for direct triangle wave loading of copper with the explosive Baratol (Koller 2006). No ductile voids, evidence of voids, or crack coalescence were observed in the recovered copper samples in spite of the fact that the measured wave profiles showed a ringing signature indicative of a spall plane. Instead there were localized plastic strain features and high dislocation densities where the spall damage was geometrically expected in the sample cross section upon postmortem metallurgical analysis. Subsequent experiments (Koller 2006) with a more energetic explosive, PBX 9501, showed multiple spall and damage layers consistent with the velocity profile. It was postulated that different Taylor release strain rates and/or local plastic deformation sufficient to alter the local impedance of the material to foster a wave reflection may provide an explanation for the metallurgy results, but this does not appear to easily explain the observed velocity profiles. It is, however, well known that sound wave reflections can readily occur in the absence of a free surface. For example, such reflections are observed in layers of sea water of differing temperature and salinity possessing different wave speeds that accordingly serve as wave guides in the ocean. It is also worth noting that the soft recovery technique exhibits the result of the entire process that the sample has been subjected to, from the moment the shock enters the sample until it is recovered. Recovery techniques are not capable of providing time resolution of the sample loading and unloading history, and great care is needed to prevent the sample from being shocked when it is decelerated within the recovery material.

Becker et al. (2007) suggested that the damaged zone could be recompressed during a gas gun experiment designed to have compression waves that arrive after the initial tension is generated. They hypothesized that if a sufficiently strong recompression wave follows the tension, the recompression can drive the damaged layers back together, causing the voids to collapse. Also, these authors postulated that collapsed voids might not be readily apparent in subsequent metallurgical analysis of the soft recovered sample. They constructed a gas gun experiment with a layered flyer plate to drive a recompression shock into the spalled target, and their results support their hypothesis. They found highly strained material where the

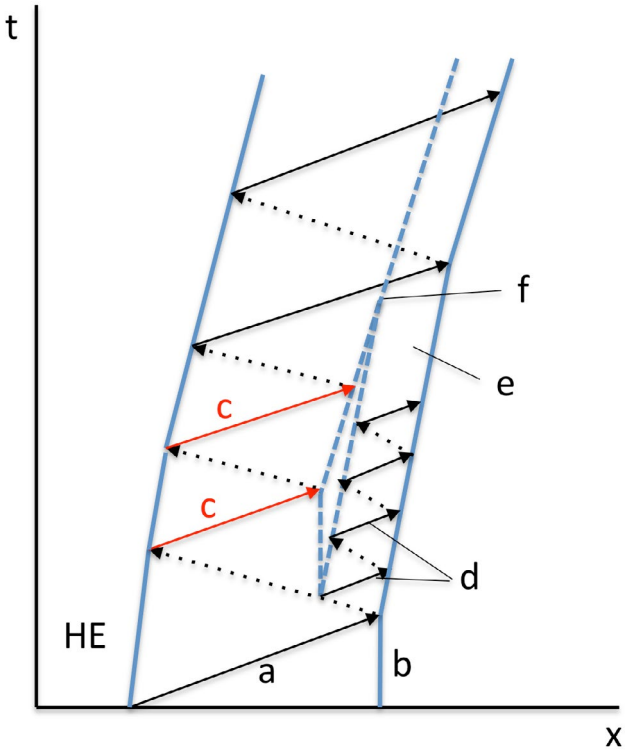

Figure 1. Notional time (t) versus position (x) diagram for metal driven by HE. HE-metal and metal-vacuum boundaries are solid blue lines and metal-spall layer boundaries are dashed blue lines. Shocks are shown as solid black or red arrows and rarefaction fronts are dotted. (a) Detonation wave from HE; (b) free surface; (c) recompression waves; (d) initial ringing in spall scab; (e) scab; (f) spall surface at time of recompression.

spall plane was expected, but there were no remaining voids in the optical images. More detailed analysis using electron backscatter diffraction (EBSD) revealed highly localized plastic deformation and the remnants of what was interpreted to be collapsed voids.

For HE drive, complete spall separation may occur while the sample is still being accelerated by the detonation gases. The tension producing the spall will pull the spall scab away from the sample. If the sample eventually moves fast enough relative to the scab, it can impact the scab and may cause a recompression shock to be formed. In addition there may be a trapped wave in the sample similar to the one in the spall scab, although if there is considerable damage within the sample, this wave may damp out relatively quickly. Figure 1 is a notional schematic time vs. position diagram of these processes for an HE-driven experiment, with the trapped recompression waves shown in red. The initial shock front (a) is reflected at the free surface (b) as a release wave and interacts with the still oncoming Taylor wave release, creating tension and spall. A trapped wave (d) in the spall scab (e) causes the characteristic ringing in free surface velocity profiles, but on average the scab travels with a constant speed. A trapped wave (c) rings in the remainder of the sample, which continues to accelerate because the HE product gases are still under pressure. Eventually the sample catches up to and impacts (f) the spall scab and recompresses the spall plane. After recompression both trapped waves (c) and (d) may be able to pass through the spall plane.

Project

Description

We have executed a set of explosive experiments in parallel with detailed 2-D hydrocode simulations (hydrodynamics code CTH, McGlaun 1990) to determine whether HE detonation gases can be made to accelerate a spalled copper target sufficiently to produce recompression of the spall zone in a manner similar to a layered flyer plate. The spall and recompression processes were studied using free surface optical velocimetry and pulsed x-ray radiography. We recovered several of the samples and analyzed them using traditional 2-D metallographic techniques (optical and electron microscopy) as well as 3-D x-ray microtomography. We conducted nine experiments. Table 1 shows the copper sample thicknesses, HE drive, and shock parameters.

The experimental configuration is shown schematically in Figure 2. Samples were shocked in three ways to produce shocks similar to Baratol, which is no longer readily available. The first method used a 5- or 6-layer stack of 25 mm diameter sheets of Detasheet, about 10 mm total thickness, which produces a peak shock stress very close to that of Baratol. (The Detasheet thickness varies a little from sample to sample, so we are unable to reproduce the shock stress exactly in each experiment.) The second method utilized a 25 mm

Table 1. Parameters for the explosive experiments

Shot No.	Experiment	HE	Thickness (mm)	Stripper	MPDV	Peak stress (GPa)	Spall strength (GPa)
1	130109	Detasheet	2.00	Control. Solid sample with no momentum trapping ring; not recovered.			
2	130306	Detasheet	1.89	No	No	21.0	2.9
3	130813-1	Detasheet	1.63	Yes	No	23.0	2.8
4	130813-2	Detasheet	1.61	Yes	No	23.0	3.2
5	130313	PBX 9501	2.00	Yes	No	33.0	2.9
6	140522	Detasheet	1.89	Yes	Yes	22.4	2.8
7	140523	Detasheet	4.27	Yes	Yes	16.8	2.7
8	140424	Nitromethane	2.20	Yes	Yes	15.3	2.0
9	140425	Nitromethane	4.18	Yes	Yes	13.9	2.1

diameter by 14 mm thick sample of nitromethane (NM) sensitized with 0.2% diethylenetriamine. Its shock stress is less than for Detasheet or Baratol. The third method used a sample of PBX 9501 that is 8.9 mm thick by 25 mm in diameter to produce a higher shock stress. In all cases the HE was axially detonated with an RP-1 detonator, yielding a slightly divergent shock wave in the sample. There is also a small decrease in shock stress with increasing radial distance from the center of the sample because the detonation waves farther from center traverse a longer path in the HE and sample.

To minimize the effects of wave releases from the edge of the 25 mm diameter HE drive, we used only the center 10 mm of the target for analysis. The copper target is a 10 mm diameter disk press fit into a guard ring (Stevens 1972) (40 mm outer diameter, 10 mm inner diameter) of similar copper with an interference fit and no measureable gap. After assembly the target is polished flat to a final thickness of 2 to 4 mm. The guard ring forms a momentum trap for edge releases, allowing planar compression but not radial tension in the central sample, and thereby minimizing 2-D perturbations. Often momentum-trapping rings used on gas gun experiments require several components (Gray 1989). Because our HE drive has a slightly curved shock front, we were able to use 2-D hydrocode simulations to design a ring that quickly pulls away from the sample, leaving a gap between the sample and ring while the sample remains relatively flat. All targets were prepared from 99.999% pure oxygen-free, high-conductivity (OFHC) copper. The center 10 mm portion was fabricated from a copper sample annealed under vacuum at 600°C for 1 hour, resulting in an average grain size of 40 µm.

Photonic Doppler velocimetry (PDV) (Strand 2006) was used to measure the free surface velocity profiles of the shocked samples for 30 µs or longer. A velocimetry probe on the first five experiments (performed in FY 2013) allowed us to record a VISAR (Barker 1972) measurement with the PDV. For the final four experiments we omitted the VISAR, which always agreed with the PDV, and added 11 more PDV channels to determine the radial dependence of the shock, spall, and recompression. For this multiplexed PDV (MPDV), the probe images 12 laser spots at equal spacings ~1.2 mm apart in a line through the center of the sample. Eight spots are located on the sample itself, and the outer two at each end of the line are on the guard ring. The focal plane for the laser spots was located several millimeters in front of the sample, so after the shock emerges, the free surface moves through the focus and beyond. Spot sizes are ~45 µm in diameter in this region.

The MPDV records were multiplexed, three to a digitizer channel, so that a single 4-channel digitizer could record all 12 PDV channels. To multiplex the PDVs we used three lasers with frequencies differing by 200 and

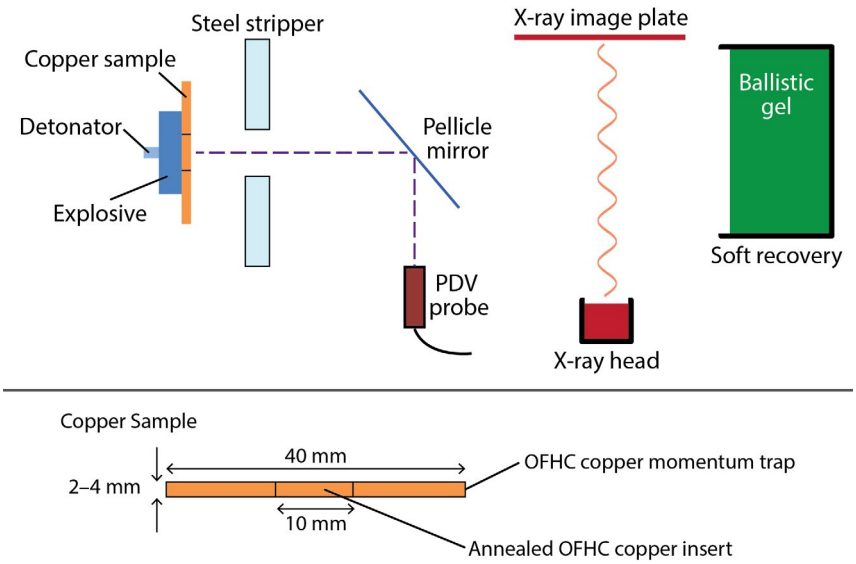

Figure 2. Schematic diagram of the experimental setup with blow up of sample assembly and dimensions

400 GHz, respectively, to enable wavelength separation. Twelve single-mode optical fibers carry the light from the lasers to the experiment and the reflected light back to the MPDV chassis. There the multiplexing is done by combining reflected light from three of the optical fibers, each with a different laser, and sending the combined light to a single detector and high-bandwidth digitizer channel. We added a local oscillator signal to each laser signal and tuned the oscillators so that the beat frequency of each laser differed from the other beat frequencies by about 2.5 and 5 GHz, respectively. This difference is more than the largest Doppler beat frequency we encountered (about 1 GHz), and it leaves the signals within the detector and oscilloscope response bandwidths but well separated from each other.

A single-pulse flash x-ray system provides a radiographic image of the target about 100 µs after detonation to verify shape and trajectory of the 10 mm center of the target, which flies free of the surrounding copper ring and is stopped in ballistic gel in the soft recovery chamber. A steel stripper, added to Shots 3–9, keeps the momentum ring fragments away from the soft-recovery gel. Subsequent metallographic characterization of the damage evolved in the recovered samples includes optical microscopy, EBSD, and orientation imaging microscopy (Adams 1992).

Velocimetry

Detasheet-Driven Experiments

We conducted six copper experiments using Detasheet HE. Shots 1–4 helped us develop the soft recovery system and test the momentum trapping, which, to our knowledge, had not been done previously with center-initiated HE. They were described in last year's SDRD Annual Report, along with Shot 5, which was driven with PBX 9501 (Turley 2014).

This year we upgraded the PDV to a 12-channel multiplexed version, omitted the VISAR, and changed from wetted felt to ballistic gel to recover the samples for metallurgy with less deceleration damage. With this improved system we fielded experiments with copper sample thicknesses of 1.89 and 4.27 mm (Shots 6 and 7) as well as two NM experiments, Shots 8 and 9, also with nominally 2 and 4 mm samples. The different sample thicknesses allow the Taylor wave decay to proceed to different states and produce different stresses upon shock release.

In Figure 3 are shown velocimetry data at the various positions on the free surface for Shot 6, the 1.89 mm thick sample driven with Detasheet. Curves are presented in pairs at symmetric positions on either side

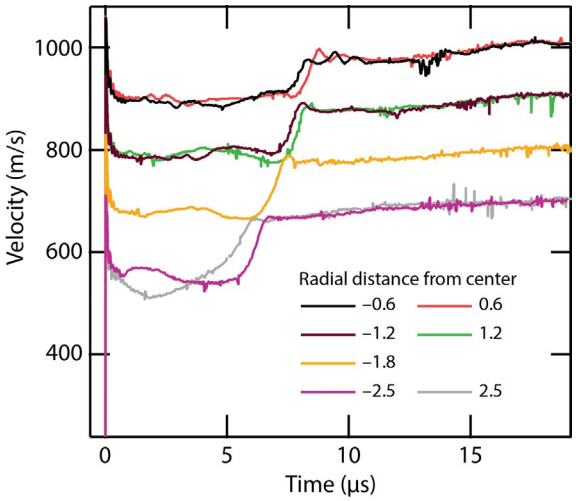

Figure 3. Velocities at various positions in a line across Shot 6, the 1.89 mm Detasheet-driven sample. Except for the two upper curves, pairs of curves at symmetric positions are offset vertically by a multiple of 100 m/s so that the curves do not all lie on top of one another. The data for one of the points 2.7 mm from center were lost because of a broken optical fiber in the probe. Radial distances in mm for the velocimetry are indicated in the annotation. Incipient spall occurs at Time = 0, and the recompression is 6 to 8 μs later. Farther from center, where the shock is relatively weaker, recompression is earlier and has a longer rise time, suggesting that it may be more gentle.

of the center of the sample, and pairs of curves farther from center are offset vertically (by integral multiples of 100 m/s) to make them easier to see. The recompressions vary considerably with position on the sample. Because the HE is center-initiated, the shock stress farther from center decreases and the recompression waves occur earlier and rise more slowly. We do not show the outer four channels, two on either side of center. They are imaged onto the guard ring, which does not travel along a line to the probe.

Figure 4 shows similar data for Shot 7, the 4.27 mm sample, also driven with Detasheet. Here there is no recompression, even in the center. Note that the peak shock stress in the center of the sample, 16.8 GPa, is lower than for the outer regions of Shot 6. In the

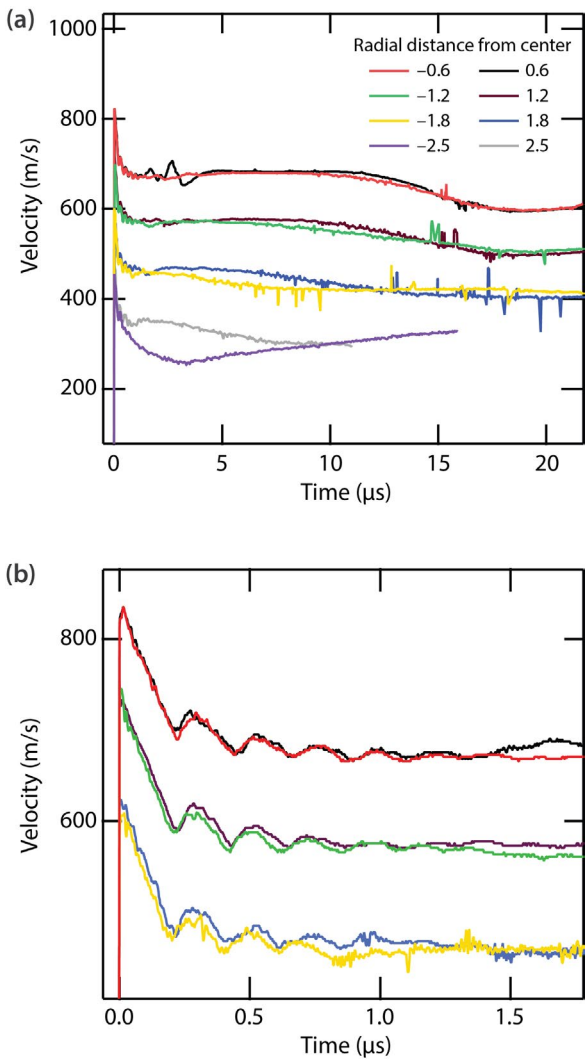

Figure 4. Velocities at various positions in a line across Shot 7, the 4.27 mm Detasheet-driven sample. Except for the two upper curves, pairs of curves at symmetric positions are offset vertically by a multiple of 100 m/s so that the curves do not all lie on top of one another. Radial distances in mm for the velocimetry are indicated in the annotation. Sharp peaks and dips at late times are artifacts caused by the PDV dropping the signal temporarily. (b) The ringing indicates spall at about 0.2 μs; there is no indication of recompression.

Radiography section, below, we show an x-ray radiograph of the spall scab flying free of the sample for Shot 7 (Figure 11).

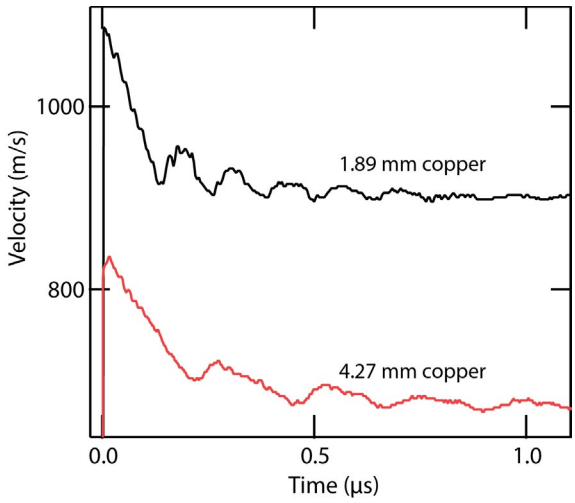

Figure 5. Comparison of the early time velocimetry near the center for Shots 6 and 7. The thicker sample's peak velocity is lower because of the increased Taylor wave decay. Also, the release rate is slower and the ringing period is longer, indicating a thicker spall scab.

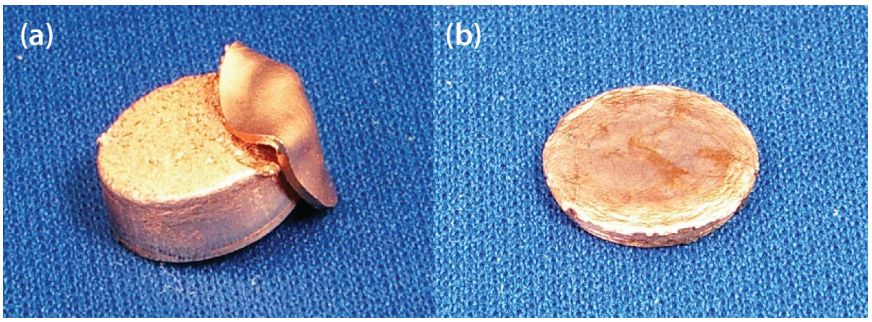

Figure 6. Samples recovered from (a) Shot 7 and (b) Shot 6. The bottoms of the samples, seen here, are the sides impacted by the HE.

The early parts of the signals for Shots 6 and 7 are compared in Figure 5. The thicker sample, which has lower peak stress at the free surface, has a slower stress decay upon shock breakout and a longer ringing period (indicating a thicker spall scab). Nevertheless, the spall strengths (see Table 1) measured for the two shots are nearly identical.

Figure 6 is a photograph of the recovered samples for Shots 6 and 7. For Shot 7 one edge of the sample struck the scab in the soft recovery vessel.

Nitromethane-Driven Experiments

We fielded two NM-driven experiments, Shot 8 with a 2.20 mm thick copper sample and Shot 9 with a 4.18 mm sample. Figure 7 shows the velocimetry data for the 2.20 mm sample. The peak free surface velocity, 760 m/s, indicates a peak shock stress of 15.3 GPa in the center of the sample, and the peak stress drops off to 13.5 GPa at 3.9 mm from the center. As with the Detasheet experiments, there is ringing in the velocity during the first microsecond after shock breakout. From the change in free surface velocity between peak and the first spall minimum we measure a peak copper spall strength of 1.9 GPa, lower than for Detasheet, which produces higher stress, but higher than for flat-top shocks reported by Hixson (2004) and Koller (2006). From the ringing period near the center of the sample, 190 ns, we estimate that the damaged region is about 450 µm from the free surface. Near the edges, where the ringing is faster, the damage is closer to the free surface. Recompression occurs around 4 µs after shock breakout for the five velocimetry points closest to center of the shock. Because of the shock asymmetry, recompression can occur at slightly different times on opposite sides of the center. For the outermost points there is no recompression shock, but instead there is slow, steady recompression. After the recompression there is very minimal evidence of longer period (~900 ns) ringing that would be expected for a sound wave reflecting from the

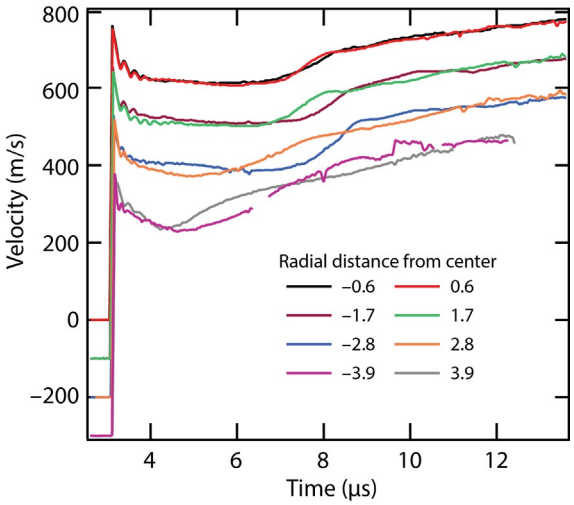

Figure 7. Velocities at various positions in a line across the 2.2 mm NM-driven sample, Shot 8. Radial distances in mm are indicated in the annotation. Curves are offset vertically in pairs for velocities at symmetric positions so that they do not all lie on top of one another. All curves except the upper two have been moved by a multiple of 100 m/s.

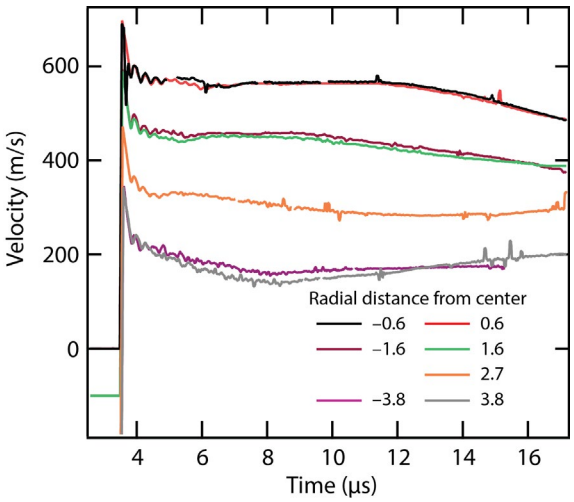

Figure 8. Velocities at various positions in a line across the 4.18 mm NM-driven sample, Shot 9. Curves are offset vertically in pairs for velocities at symmetric positions so that they do not all lie on top of one another. All curves except the upper two have been moved by a multiple of 100 m/s. Radial distances in mm are indicated in the annotation. The data for one of the points 2.7 mm from center were lost because of a broken optical fiber in the probe.

surfaces of a 2.2 mm sample. In the three channels without a recompression shock, there is no late time ringing at all.

Figure 8 shows the PDV velocity data for the 4.18 mm sample. The peak free surface velocity, 695 m/s, indicates a peak shock stress of 13.8 GPa in the center of the sample, and the stress drops off to 12.6 GPa at 3.8 mm from the center. The pullback shows a spall strength of 2.0 GPa. The ringing period during and after spall is similar to but slightly slower than the 2.2 mm sample, and it indicates a spall scab thickness of 720 μm. There is no sign of recompression at this lower shock stress, but the sample remained intact and was recovered. Recovered samples for Shots 8 and 9 are shown in Figure 9.

Comparison of Shots 7 and 8

It is of interest to compare the data from Shots 7 and 8. These were, respectively, a 4.27 mm copper sample driven by a Detasheet shock and a 2.20 mm sample driven by NM. As can be seen from the velocimetry data in Figure 10, the shock stresses are nearly identical, 16.73 and 15.88 GPa, and the release rates are also similar. Consequently we expect that the initial

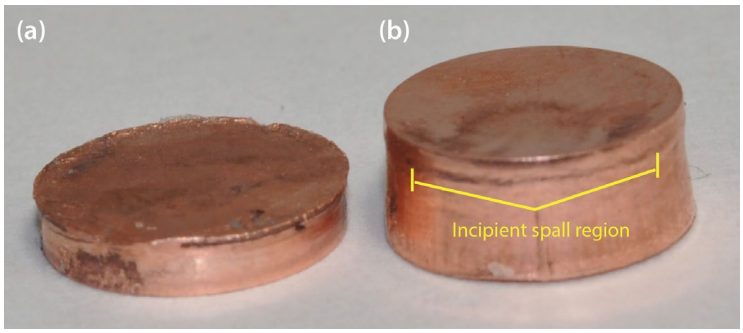

Figure 9. The recovered samples from (a) Shot 8 and (b) Shot 9. Free surface sides are up in the picture. In image (b) it is possible to see the edge of the incipient spall region on the circumference, a short distance from the top.

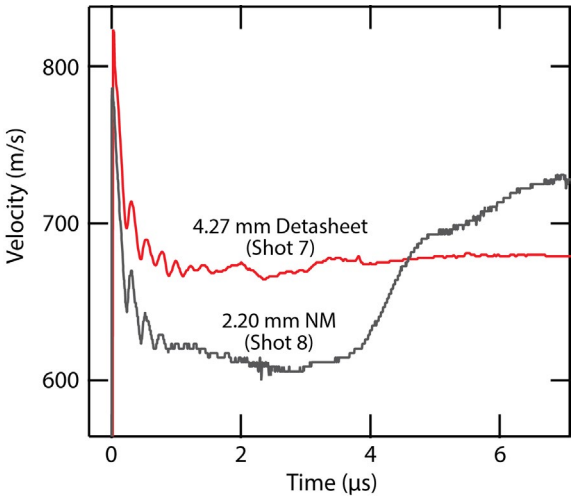

Figure 10. Velocimetry measurements near the centers of Shots 7 and 8; Shot 7 spalled, but 8 did not.

damage should be similar as well. Shot 7 spalled, while Shot 8 did not. One difference is that Shot 8 had a recompression wave while 7 did not, even though their peak stresses were nearly identical.

Radiography

Shown in Figure 11 are x-ray radiographs from three of the experiments. Image (a) shows Shot 2, for which there is no stripper (see Figure 2) to catch the momentum trap fragments. Although the momentum trap scheme nicely separates out the sample center, considerable debris from the guard ring flies behind and can cause sample damage during soft recovery. The center image, taken for Shot 3, with the stripper in place, shows a much better result, with only an intact sample in the field of view. The other target debris is trapped behind the stripper and will not interfere with the recovery process. Both of these shots had nominally 2 mm thick samples. Image (c) shows Shot 7, the 4.27 mm sample. In this case the spall scab has completely separated from the sample. Eventually one edge of the sample struck the scab in the soft recovery gel.

Metallography

Metallurgical analysis of the recovered, shock-loaded samples has proven to be a powerful tool in understanding the details of the material response to such loading. This provides a valuable complement to the time-resolved data obtained from VISAR or PDV. These analyses were done on all experiments except Shot 1. Last year's report (Turley 2014) describes the

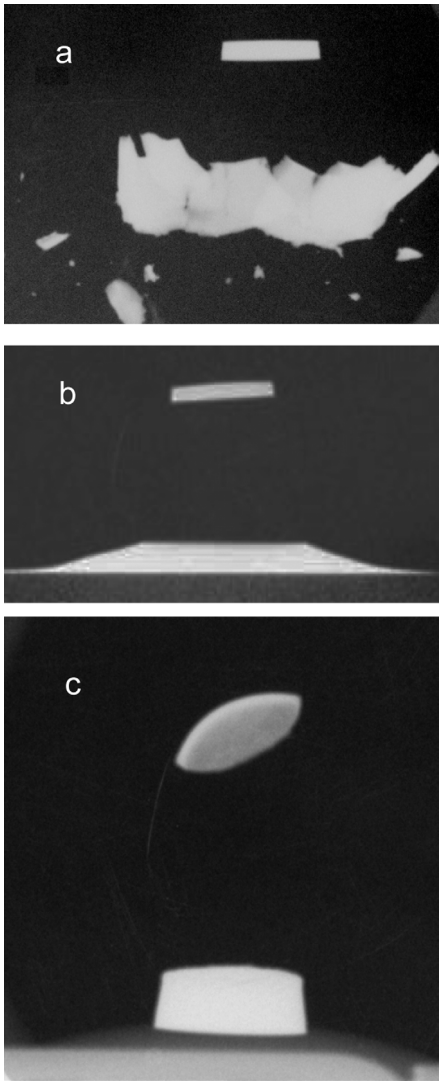

Figure 11. Flash x-ray radiographs of the target taken about 100 μs after detonation. Motion is upward. (a) Shot 2 (1.89 mm), with no stripper. The material behind the sample consists of fragments of the guard ring, which has been distorted by the diverging shock wave. (b) Shot 3 (1.63 mm), with a stripper to remove the debris, passed only the sample center through the stripper hole. (c) A 4.27 mm sample, Shot 7, with its spall scab flying ahead. The scab has begun to rotate, perhaps because it has struck the 45° pellicle used for the PDV signals.

metallurgy that was complete at the time the report was written. This year's data, described here, featured our improved soft recovery system, and there was considerably less damage caused by the sudden deceleration in the recovery process. Also the MPDV velocimetry allows us to see how the shock stress varies with radial position on the samples.

Detasheet Drive with MPDV and Improved Recovery

Experiments were conducted using Detasheet with sample thicknesses of nominally 2 and 4 mm. These experiments were guided by hydrocode simulations that predicted for Detasheet:

- 2 mm sample: Spall would occur, followed by recompression caused by the remaining target being accelerated by a continuous push from the HE product gases.
- 4 mm sample: Spall would occur but no recompression would occur, as the remaining target material is too massive to be accelerated enough to catch the spall scab.

These predicted results are consistent with the subsequently observed velocimetry as shown in the ***Velocimetry*** section. Samples were soft recovered and collected, and microstructural analyses were done. Both 2 mm and 4 mm thick samples were collected, but only the 2 mm sample was analyzed. The 4 mm thick sample completely spalled, and a spall scab separated from the bulk. For the 2 mm sample, images are shown in Figures 12–14.

Figures 12 and 13 are optical images of a cross section through the recovered sample for Shot 6. The observed microstructural features (bands) are most prominent at a distance from the free surface of the specimen that is consistent with the ringing in velocimetry records. In addition to the most prominent band, we see similar bands over a significant volume of the sample. Very similar bands were observed in previous work (Becker 2007). However, the consistency of the velocimetry and postmortem results still leaves two major questions in this work unanswered: (1) what deformation process caused these bands? and (2) when during shock loading did they form? More specifically, did this specimen ever contain a spalled surface within it? Were voids or spall surfaces welded back together in a way that is consistent with this microstructure and local plasticity as reflected by the local misorientations evolved in the local regions surrounding the damage region? This question is discussed further in the conclusion.

Nitromethane Drive with MPDV and Improved Recovery

We also recorded measurements with NM-driven 2 and 4 mm thick samples. The HE drive and center-detonation geometry were similar to the Detasheet, but the shock stress was lower. We were unable to do precise simulations for NM because of a lack of a good EOS model. The data clearly show that Detasheet is much more energetic, with a higher Chapman-Jouguet (CJ) state, and that the reshock wave carried more stress for Detasheet than for NM. Furthermore, the lower NM detonation speed leads to a more curved shock front. Both samples were collected and analyzed.

Results for the 2.20 mm sample (Shot 8) are shown in Figure 14. The damaged region in the sample begins about 550 μm back from the free surface (top). There are voids at this location and considerable void formation throughout the damaged region below that location. Notice that there is minimal damage at the outer radius of this sample. This is consistent with the velocimetry, which shows muted ringing on a continuously decreasing velocity followed by an early recompression event. This result may be consistent with incomplete recompaction of the damage created in the tensile event.

Higher-magnification images of the damaged region, as shown in Figure 15, reveal extensive void nucleation at grain boundary triple points and along numerous grain boundaries as well. Additionally, band features, similar to those observed in Figure 12 and in the Baratol data, link voids within the microstructure. Note that while such a combination of void and band features is observed frequently under plate impact conditions in tantalum (Zurek 1996), it is not typically observed

Figure 12. Optical image of the full cross-sectional area of recovered 1.89 mm sample with Detasheet drive, Shot 6. A microstructural feature, observed close to the free surface (top), appears to be very similar to that seen for the Baratol experiment, shown in Figures 8 and 9 of last year's report (Turley 2014).

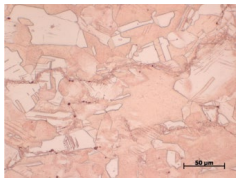

Figure 13. Higher magnification optical image from the center of the cross-sectioned sample of Figure 12 showing details of the microstructural features

Figure 14. Optical image of the cross-sectioned 2.20 mm copper sample with NM drive (Shot 8)

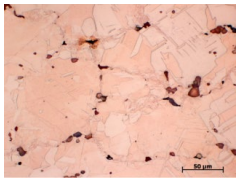

Figure 15. Higher-magnification optical image of the voids in Figure 14

Figure 16. Optical image of the cross-sectioned 4.18 mm NM-driven copper sample (Shot 9). The regions of shear localization linking voids along 45° to the sample outer diameter are consistent with late time, radial release–induced damage evolution.

under plate impact conditions in copper (Escobedo 2012). The features shown in this study therefore may be consistent with either a recompression event or the change in shear stress component caused by the HE drive. We expect the metallurgists to study the samples at higher magnification in the hope that the results will improve our understanding of the process.

Finally, characterization of the 4.18 mm thick NM-driven sample (Shot 9) was performed and yielded similar results to that observed in the 2.20 mm sample. One major difference was that significantly more void formation is observed in the 4.18 mm specimen. This can be seen in Figure 16. Higher-magnification details appear to be similar to that observed above for the 2.20 mm sample, namely void nucleation being primarily concentrated at grain boundaries and grain boundary triple points, except with considerably more porosity present. Here, too, higher magnification metallurgy will be helpful.

Conclusion

This research has focused on a previously identified issue in directly driving metal plates with high explosives in 1-D and nearly 1-D geometries. These HE drives, as well as sweeping waves (Gray 2009, 2012), result in the metal sample being subjected to triangular wave loading and unloading. When such a wave shape arrives at a free surface, tension develops immediately, and it can be very large in amplitude. The amount of tension and the rate at which it develops are proportional to the CJ state of the HE and the Taylor wave release rate for a given HE and sample thickness.

Velocimetry and hydrocode simulations indicate that the resulting tension for Detasheet and for NM in the central region produces damage sufficient to cause a spall plane to form that can reflect sound waves in a layer near the free surface. In the velocimetry data we see clear evidence for ringing of a trapped acoustic wave in the spall scab. The HE product gases then continue to accelerate the sample, and in some experiments the sample impacts the spall scab, which was moving with a constant velocity. This causes

a subsequent recompression wave, which passes through the damaged region and reaches the free surface.

We note that changing the driven sample thickness from 2 to 4 mm with a Detasheet drive was predicted by simulations to stop this recompaction process from happening, and the predicted free surface profile agreed with the measured. This absence of recompaction is caused by the change in mass of the base sample after the spall scab is formed. However, whether or not a spalled or incipiently spalled sample gets recompressed depends on other factors as well, including the peak shock stress and its release properties. In comparing Shots 7 (4.27 mm sample with Detasheet drive) and 8 (2.20 mm sample with NM drive) we saw nearly identical shock conditions, but the 2.20 mm had a recompression wave and the other, the more massive sample, did not.

The recovered samples have been examined using several microstructural tools, and the results show a band of perturbed microstructure at the location indicated to be a spall region by the velocity data and the simulations. However, it is not clear whether this feature in the microstructural results is consistent with spall damage occurring and then being recompacted by a subsequent recompression event, or whether it is caused by shear localization. Reconciling what we believe to be the physics effects in these experiments as determined by velocity data with the metallurgical analyses of the recovered samples is an ongoing process. Recompacting significant spall damage or complete spall should lead to significant lateral plastic deformation and perhaps heat-affected regions, which we do not see. Instead, we observe very localized plastic deformation. Given that the recompaction event occurs only microseconds after damage, the damaged region may still be residually heated and thus have less strength than the ambient material. Perhaps, therefore, less energy is required to collapse the damaged region than one would predict for a cold copper sample at ambient temperature and pressure, and consequently the region of plastic deformation caused by recompression may be smaller. It should be noted that the deformation band we observe in these experiments is very similar to that shown previously (Becker 2007, Figure 6) using gas gun experiments.

Our physics hypothesis is that in all of these experiments, considerable damage was done in the target immediately following the reflection of the triangular-shaped shock wave at the copper sample free surface. It would be very surprising if this wave reflection process did not cause damage, given the peak stresses involved (20–40 GPa) and the relatively low spall strength of annealed OFHC copper (1.4–3.5 GPa). We hypothesize that this damage zone is then recompressed a few microseconds later because the spall scab is moving at a constant velocity while the remaining target material (for some target thicknesses) is still being accelerated by the HE detonation gases; this is directly supported by the time-resolved data. The recompression event, as clearly observed in the velocimetry, causes the sample to strike the scab, which in turn causes heating and may cause localized recrystallization in the damaged regions.

For the highest performance HE used (PBX 9501, with a CJ pressure of ~37.5 GPa), the recompression event is very minor and does not completely "weld" the sample and scab back together because of the relatively high velocity imparted to the spall scab. For lower-pressure HE, Detasheet, and Baratol (Koller 2006), the difference in speeds between the spall scab and sample were higher (except for very thick targets), and the resulting recompression impact was more intense. The thin NM-driven sample had very similar drive conditions to the Detasheet-driven thick sample, but because the NM-driven sample was lighter, we observed a recompression wave that was not present for Detasheet.

This is a compelling story, *but it still requires unambiguous reconciliation of the velocimetry with the post-mortem metallurgical analysis*. Therefore, we plan to continue this line of research and conduct gun-driven, double-shock experiments to attempt to repeat these results in a planar geometry. Our goal is to reconcile the results we see from the velocimetry with the metallurgical evidence from the recovered

samples. A manuscript has been prepared and will be submitted to the *Journal of Dynamic Behavior of Materials* for consideration (Turley 2015).

Acknowledgments

We are grateful to Mike Grover for his extensive help in fielding the experiments.

References

Adams, B. L., S. I. Wright, K. Kunze, "Orientation imaging: The emergence of a new microscopy," *Metallurgical Trans. A* **24A** (1992) 819–831.

Barker, L. M., R. E. Hollenbach, "Laser interferometer for measuring the high velocities of any reflecting surface," *J. Appl. Phys.* **43** (1972) 4669.

Becker, R., M. M. LeBlanc, J. U. Cazamias, "Characterization of recompressed spall in copper gas gun targets," *J. Appl. Phys.* **102**, 9 (2007) 093512.

Curran, D. R., L. Seaman, D. A. Shockey, "Dynamic failure of solids," *Phys. Reports* **147** (1987) 253.

Escobedo, J. P., E. K. Cerreta, D. Dennis-Koller, B. M. Patterson, R. A. Lebensohn, C. A. Bronkhorst, "Effects of microstructure and shock loading conditions on the damage behavior of polycrystalline copper," DYMAT 2012, 10th International Conference on the Mechanical and Physical Behaviour of Materials under Dynamic Loading, Freiburg, Germany, September 2–7, 2012, EPJ Web of Conferences **26** (2012) 02008-1–02008-6.

Gray, G. T., P. S. Follansbee, "Influence of peak pressure and pulse duration on substructure development and threshold stress measurements in shock-loaded copper," in *Impact Loading and Dynamic Behavior of Materials, Vol. 2*, C. Y. Chiem, H.-D. Kunze, L. W. Meyer, eds., Deutsche Gesellschaft für Metallkunde, 1988, 541–548.

Gray, G. T., P. S. Follansbee, C. E. Frantz, "Effect of residual strain on the substructure development and mechanical response of shock-loaded copper," *Mech. Sci. Eng. A* **111** (1989) 9–16.

Gray, G. T., "Influence of shock-wave deformation on the structure/property behavior of materials," in *High-Pressure Shock Compression of Solids*, J. R. Asay and M. Shahinpoor, eds., Springer-Verlag, New York, 1993, 187–216.

Gray, G. T., *ASM Handbook Volume 8: Mechanical Testing and Evaluation*, H. Kuhn, D. Medlin, eds., ASM International, Materials Park, Ohio, 2000, 530.

Gray, G. T., N. K. Bourne, B. L. Hendrie, J. C. F. Millett, "Influence of shock-wave profile shape (triangular - "Taylor-wave" versus square-topped) on the spallation response of 316L stainless steel," *J. Phys. IV* **110** (2003) 773–778.

Gray, G. T., N. K. Bourne, J. C. F. Millett, M. F. Lopez, "Influence of shock-wave profile shape ("Taylor-wave" versus square-topped) on the shock-hardening and spallation response of 316L stainless steel," *AIP Conf. Proc.* **706** (2004) 461–464.

Gray, G. T., L. M. Hull, J. R. Faulkner, M. E. Briggs, E. K. Cerreta, F. L. Addessio, N. K. Bourne, "The effects of shockwave profile shape and shock obliquity on spallation: kinetic and stress-state effects on damage evolution," *AIP Conf. Proc.* **1195** (2009) 1097–1102.

Gray, G. T., N. K. Bourne, K. S. Vecchio, J. C. F. Millett, "Influence of anisotropy (crystallographic and microstructural) on spallation in Zr, Ta, HY-100 steel, and 1080 eutectoid steel," *Int. J. Fracture* **163**, 1 (2010) 243–258.

Gray, G. T., L. M. Hull, V. Livescu, J. R. Faulkner, M. E. Briggs, E. K. Cerreta, "Influence of sweeping detonation-wave loading on shock hardening and damage evolution during spallation loading in tantalum," DYMAT 2012, 10th International Conference on the Mechanical and Physical Behaviour of Materials under Dynamic Loading, Freiburg, Germany, September 2–7, 2012, EPJ Web of Conferences **26** (2012) 02004-1–02004-6.

Hixson, R., G. T. Gray, P. A. Rigg, L. B. Addessio, C. A. Yablinsky, "Dynamic damage investigations using triangular waves," *AIP Conf. Proc.* **706** (2004) 469–472.

Johnson, J. N., G. T. Gray III, N. K. Bourne, "Effect of pulse duration and strain rate on incipient spall fracture in copper," *J. Appl. Phys.* **86** (1999) 4892.

Koller, D. D., R. S. Hixson, G. T. Gray III, P. A. Rigg, L. B. Addessio, E. K. Cerreta, J. D. Maestas, C. A. Yablinsky, "Influence of shock-wave profile shape on dynamically induced damage in high-purity copper," *J. Appl. Phys.* **98**, 10 (2005) 103518.

Koller, D. D., R. S. Hixson, G. T. Gray III, P. A. Rigg, L. B. Addessio, E. K. Cerreta, J. D. Maestas, C. A. Yablinsky, "Explosively driven shock induced damage in OFHC copper," *AIP Conf. Proc.* **845** (2006) 599.

McGlaun, J. M., S. L. Thompson, M. G. Elrick, "CTH: A three-dimensional shock wave physics code," *Int. J. Impact Eng.* **10** (1990) 351–360.

Meyers, M. A., C. T. Aimone, "Dynamic fracture (spalling) of metals," *Progress in Materials Science* **28** (1983) 1–96.

Stevens, A. L., O. E. Jones, "Radial stress release phenomena in plate impact experiments: Compression-release," *J. Appl. Mech.* **39**, 2 (1972) 359–366.

Strand, O. T., D. R. Goosman, C. Martinez, T. L. Whitworth, W. W. Kuhlow, "Compact system for high-speed velocimetry using heterodyne techniques," *Rev. Sci. Instrum.* **77**, 8 (2006) 083108.

Turley, D., R. S. Hixson, B. La Lone, G. Stevens, L. Veeser, E. Cerreta, D. Dennis-Koller, P. Rigg, R. Gray, "Understanding damage anomalies in shocked metals," in *Site-Directed Research and Development*, FY 2013, National Security Technologies, LLC, Las Vegas, Nevada, 2014, 25–35.

Turley, D., et al., "Recompression of high-explosive-induced shock damage in copper," *J. Dynamic Behavior of Materials*, in preparation, March 2015.

Zurek, A. K., W. R. Thissell, J. N. Johnson, D. L. Tonks, R. Hixson, "Micromechanics of spall and damage in tantalum," *J. Materials Processing Technology* **60** (1996) 261–267.

Instruments, Detectors, and Sensors

Development of Fluorescent Technetium Compounds as a Radioactive Distributed Source

RSLN-25-14 | Continued in FY 2015 | Year 1 of 3

Wendy Chernesky,[1,a] Erik Johnstone,[b] Rosendo Borjas,[b] William Kerlin,[b] Matthew Ackerman,[b] Kiah Mayo,[b] Eunja Kim,[b] Frederic Poineau,[b] and Ken Czerwinski[c]

Many types of radioactive sources are used for training at the NNSS. Due to its relatively short half-life, gamma emission, and commercial availability, the metastable isotope technetium-99 (^{99m}Tc) is an attractive radionuclide for training and evaluation. However, the ground state ^{99}Tc has low specific activity, but the ability to detect the host material containing technetium would provide a means to ensure that its fate and transport remain consistent with the original, non-technetium–containing mineral's behaviors. Incorporating ^{99m}Tc into a chemical form that fluoresces in the visible from UV stimulation provides a means to track the technetium. Natural fluorescent minerals based on silicate species can provide a robust host matrix for technetium that is stable and benign in the environment. Two goals of this 3-year project are to prepare a number of fluorescent silicates with technetium incorporated into the matrix and to evaluate the resulting compound stability for each silicate compound. Our primary focus in the first year was preparation of fluorescent compounds. Materials and synthetic routes were identified to prepare fresnoite ($Ba_2TiSi_3O_8$), calcium tungstate ($CaWO_4$), and calcium molybdate ($CaMoO_4$), which we successfully obtained as 2-gram samples and as millimeter-sized particles. These products were characterized by powder x-ray diffraction and shown to fluoresce. Work also began early on a second-year task, the incorporation of rhenium and technetium into the silicate matrix. In this case, computational examinations were utilized. These calculations indicated that the formation of interstitial technetium in $CaWO_4$ and $CaMoO_4$ will be feasible for future work. In the second year of the project, technetium will be incorporated into the fluorescent materials as ammonium pertechnetate-99 (NH_4TcO_4) or total carbon dioxide (TCO_2). The resulting compounds will then be evaluated for efficiency of the technetium incorporation into the sample matrix.

[1] chernewj@nv.doe.gov, 702-295-8625
[a] Remote Sensing Laboratory–Nellis; [b] University of Nevada, Las Vegas; [c] North Las Vegas

Background

The focus of this 3-year project is the incorporation of the metastable isotope technetium-99 (^{99m}Tc) into a robust, fluorescent material for operational radiation detection training. The low-energy gamma decay of ^{99m}Tc (142 keV, $t_{1/2}$ = 6.01 hours) allows for small amounts of the nuclide to be added to a host phase and dispersed. Following its decay to ^{99}Tc, which is a pure β-emitter (214 keV, $t_{1/2}$ = 210,000 years) (Schwochau 2000), a dramatic decrease in the activity of the material occurs, and detection by standard techniques becomes operationally challenging for field responders. However, by incorporating the technetium into a fluorescent material, training can be extended to longer time frames, as the dispersed fluorescent sample would be visible under UV black light.

Ideal characteristics of the fluorescing material include resistance to chemical and environmental degradation, resistance to UV damage from the sun, and optimal synthetic parameters (i.e., one-pot synthesis, absence of atmospheric oxygen in reaction system, short reaction time, synthetic temperatures below 1000°C, low cost, and availability of starting products) required for material generation. In FY 2014, we began investigating how to incorporate technetium into minerals of choice. In future years, technetium will be added to the phases in various amounts and then assessed by examining the resulting amount incorporated and the structural phases present within the material.

Project

Benitoite Synthesis and Characterization

Benitoite can be readily synthesized using two different methods. The first is a solid-state reaction of oxide powders of barium oxide (BaO), titanium dioxide (TiO_2), and trisilicon hexaoxide (Si_3O_6). The addition of germanium oxide (GeO) has been noted to help in the formation of benitoite (Takahashi 2008). This reaction takes place under an inert atmosphere at elevated temperature. The second method is a sol-gel method. In this case, the material is precipitated from a solution of barium acetate, titanium tetrachloride, and orthosilicate. The precipitated gel is dried and then treated at 1000°C (Rase 1955). This method can also be performed hydrothermally. Benitoite fluoresces as a blue phosphor. For this project, benitoite was synthesized using a method similar to that reported by Takahashi (2008) and a gel method from Rase (1955); the gel method did not produce fluorescent material.

Powders of BaO, TiO_2, and synthetic silicon ($SiO_{2)}$-H_2O were weighed and added into a vial based on desired molar ratios. The powders were homogenized using a sonicator. The temperature was then thermally increased due to formation of $Ba(OH)_2$ from water. Samples (~5 g) of the blended powders were then removed from the vial and placed into a platinum crucible. This platinum crucible was then inserted in a ceramic crucible (Figure 1).

Figure 1. Reaction vessel consisting of a platinum crucible inserted into a ceramic crucible containing powdered reactants

The crucible and contents were placed into a high-temperature MTI furnace, and the system was flushed with Ar(g) for 15 minutes. The system was ramped (4.5°C/min) to the desired temperatures (i.e., 1300°C, 1400°C, 1450°C, or 1500°C) and held for 2 hours. Reactions below 1300°C were also performed, but no significant fusion of the material was present within the material. After heating, powder volume was significantly reduced. The resulting materials were hard, circular pucks or aggregates. The pucks were analyzed for fluorescent behavior under a handheld UV lamp (Figure 2) and also characterized by powder x-ray diffraction (PXRD). All of the materials produced from 1300°C to 1500°C fluoresced under the UV lamp. Notably, the samples synthesized at higher temperatures (1450°C and 1500°C) contained non-fluorescent inclusions, whereas the sample at 1400°C did not.

PXRD was performed on the samples synthesized at 1300°C (previously pretreated at 1200°C), 1400°C, 1450°C, and 1500°C. Representative areas from each puck were manually removed and ground with a mortar and pestle. The samples were then blended with a silicon metal standard and distributed on a low-background silicon wafer PXRD sample holder. These

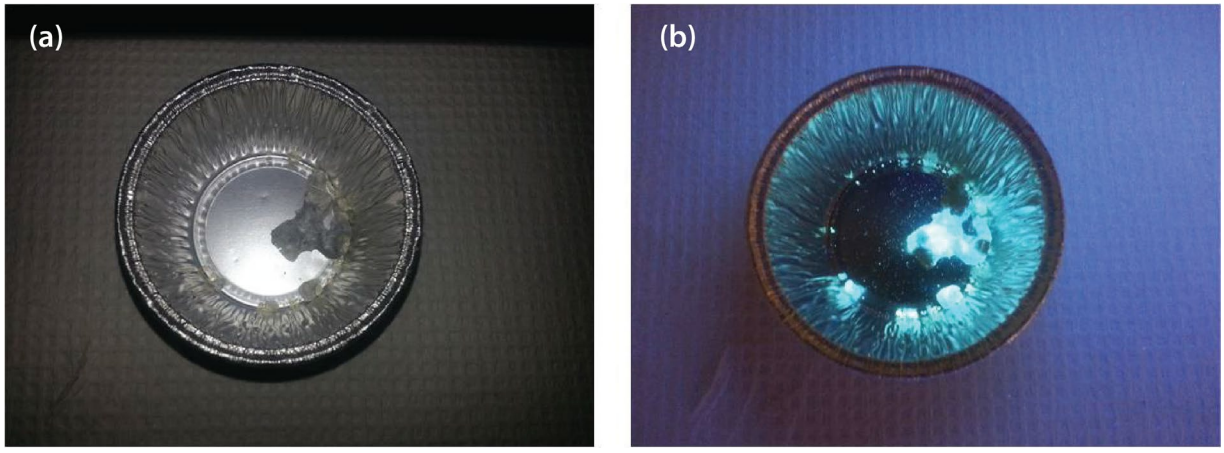

Figure 2. Reaction of powders of BaO, TiO_2, and SiO_2 at 1300°C after pretreatment at 1200°C; (a) aggregate material under normal lighting conditions and (b) aggregate material under UV lamp

Table 1. Summary of PXRD analysis of powders synthesized in the reactions of BaO_4, TiO_2, and SiO_2 at 1300°C–1500°C

Synthesis Maximum Temperature (°C)	Percentage In Product (%)					
	Phases of Silicon (SiO_2)			Barium Mineral Formed		
	Silicon Fd-3m	Tridymite Low	Cristobalite Low	Fresnoite ($Ba_2TiSi_3O_8$)	Barium Titanate ($BaTiO_4$)	Total Identified (%)
1300	55.57	19.03	--	19.63	--	94.23
1400	37.21	--	10.34	52.45	--	100
1450	50.95	--	8.18	31.93	8.94	100
1500	52.62	--	17.70	22.90	6.78	100

samples were analyzed using a Bruker D8 Advance diffractometer from 10° to 20° 2θ and analyzed using Topas 4.0 software.

The PXRD analyses of the powders synthesized from 1300°C to 1500°C (Figure 3) did not indicate the presence of any benitoite phases, but instead a similar fluorescent mineral composition was identified as fresnoite ($Ba_2TiSi_3O_8$). In addition, a second barium-containing mineral, barium titanate ($BaTiO_4$) was also observed in two of the products. Each of the samples also contained various phases of synthetic silicon (SiO_2). At 1300°C, this synthetic SiO_2 was identified as a phase of disordered tridymite low transition, which is also referred to as α-tridymite. The higher temperature reactions (i.e., 1400°C–1500°C) did not produce any tridymite low, but instead yielded the high-temperature silicon by-product, in the cristobalite phase. All four reaction temperatures also indicated the presence of a third silicon by-product that was a member of the diamond space group, Fd-3m. This information is also presented in Table 1.

When comparing the various synthetic maximum temperatures, it can be seen from both Figure 3 and Table 1 that the highest percentage of the fluorescent fresnoite product (52.45%) can be obtained under conditions held at 1400°C. This temperature was then identified as the optimal temperature for any future work utilizing this synthetic route.

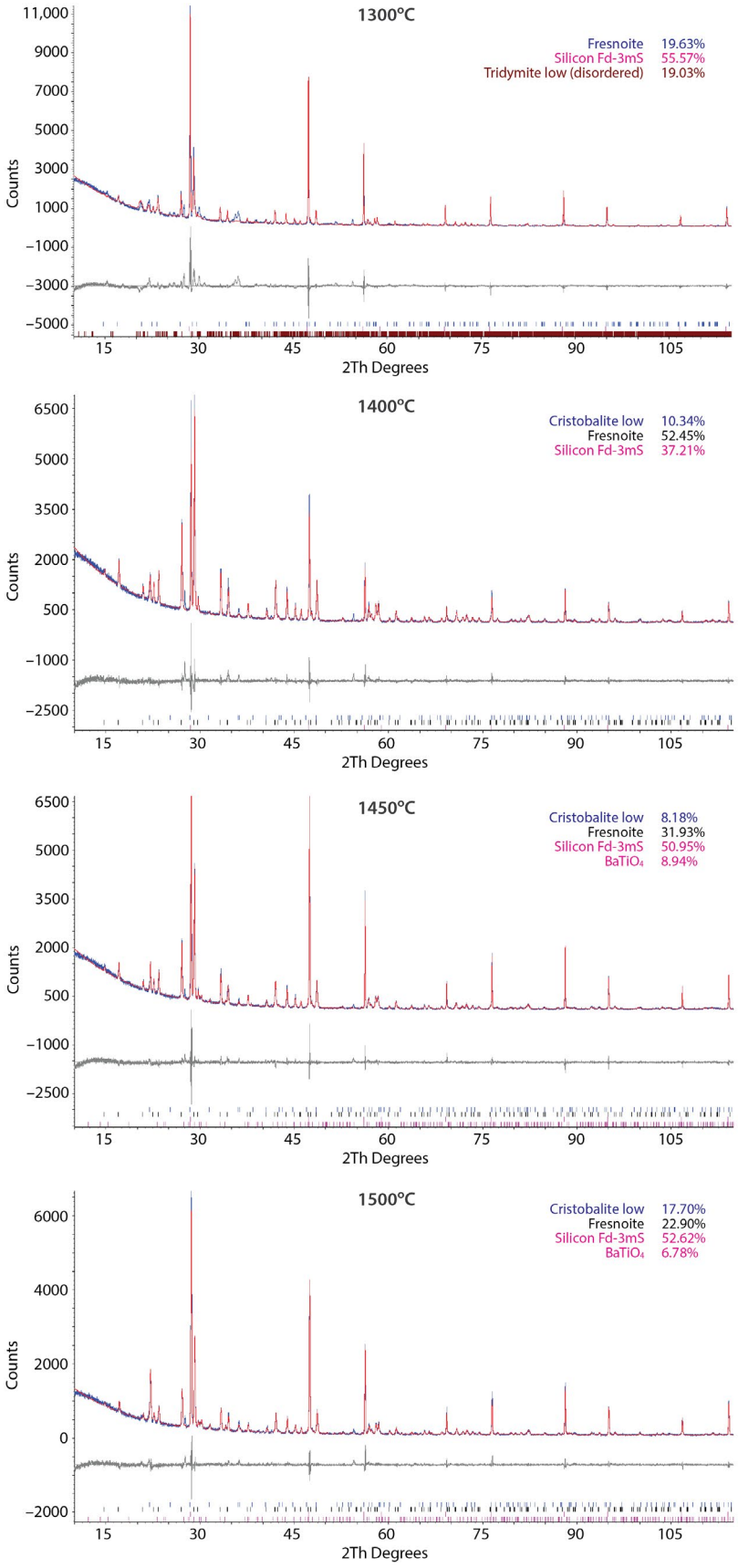

Figure 3. PXRD of products from reactions of BaO_4, TiO_2, and SiO_2 from 1300°C to 1500°C identified that conditions held at 1400°C yielded the highest percentage of the desired product, fluorescent fresnoite. The blue solid curve is the measured pattern, the red solid curve is the refined profile, and the gray curve is the residual between the observation and the refinement. The vertical ticks are defined in the legend of each figure.

Scheelite/Powellite Synthesis and Characterization

Scheelite and powellite can both be synthesized from the solid-state reaction of MO_3 (M = Mo, W) and calcium oxide (CaO) at elevated temperatures (Abdel-Rehim 2001). Scheelite emits as a blue phosphor whereas the powellite is yellow. It has also been shown that the addition of europium (Eu^{3+}) to these mineral forms yields red emitting phosphors (Dutta 2013).

In this work, the scheelite and powellite samples were synthesized using the method described by Abdel-Rehim (2001). Powders of MO_3 (M = Mo, W) and CaO were weighed to obtain a 1:1.25 mol stoichiometry, and then homogenized using a sonicator. Approximately 5 g quantities were then removed from the resulting powder mixture and transferred to the platinum/ceramic reaction crucibles described previously. These samples were reacted either under atmospheric conditions in a box furnace, or under an argon atmosphere in the MTI furnace at 860°C for 2 hours. Each reaction yielded similar products—condensed, semi-hard pucks that fluoresced under the UV lamp (Figure 4). The scheelite samples were noticeably more brittle than the powellite products. As shown in Figure 5, the visible effect of atmosphere on the synthesis of these materials is negligible. When pulverized, the material also fluoresced. This indicates an overall homogeneity within the product (Figure 5). A small quantity of these materials was removed and analyzed by PXRD. The PXRD results displayed that there were remaining unreacted starting materials. The samples produced under air were reground with a mortar and pestle and reacted again at 860°C for

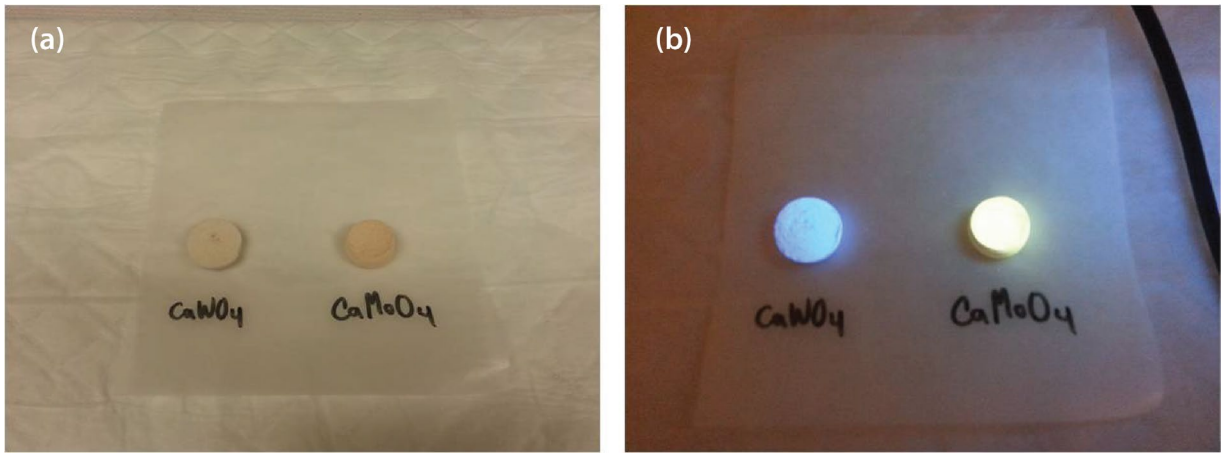

Figure 4. Synthetic scheelite ($CaWO_4$) and powellite ($CaMoO_4$) samples (a) under ambient lighting conditions and (b) under a UV lamp

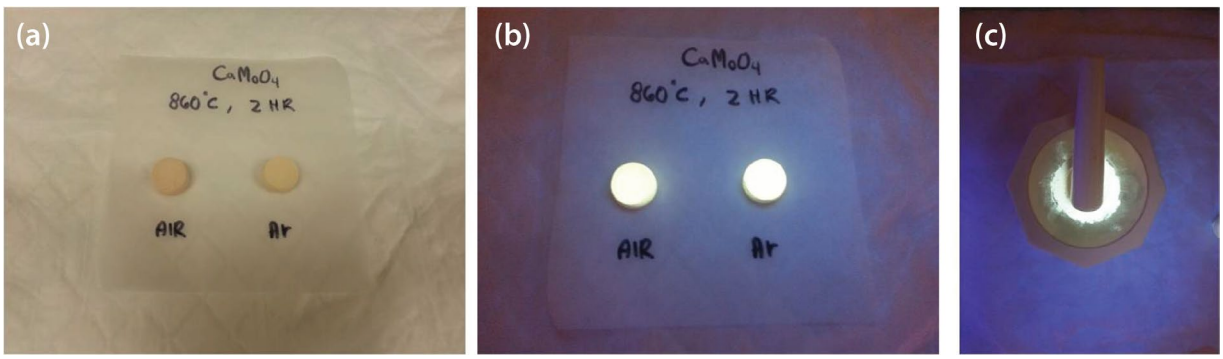

Figure 5. Comparison of synthetic powellite samples produced under air or argon are shown (a) under ambient lighting conditions, (b) under a UV lamp, and (c) as a ground powder under a UV lamp

4 hours. An additional reaction was performed with MoO_3 and CaO (1:1.25 mol ratio) doped with 1% wt Eu_2O_3. The sample was then heated under air at 860°C for 2 hours. The resulting product fluoresced as a bright red phosphor (Figure 6).

Using the same synthesis conditions as described above, smaller samples of $CaMoO_4$ and $CaWO_4$ were prepared. The dry initial mixture of MO_3 (M = Mo, W) and CaO in a 1:1.25 ratio were treated with methanol in a ratio of 1 g of oxides to 100 µL of methanol. When heated to 860°C for 2 hours, the powder from small agglomerations (Figure 7) produced fluorescent particles approximately 2 mm in diameter.

Analyses by PXRD were performed on the $CaMO_4$ (M = Mo, W) that was synthesized under air after a combined total of 6 hours of reaction time. The results (Figure 8) show that both syntheses yield the desired mineral phases as the primary components in the product with small amounts of unreacted starting compounds. The results are also compared in Table 2.

Table 2 shows that the synthesis of both minerals was successful in fairly high quantities; however, powellite was formed with a higher percentage (59.28%) than scheelite (51.18%) and also had less by-product than the scheelite.

Computational Studies

Computational studies were used to investigate the feasibility of incorporating technetium into the various minerals. This step is necessary in order to optimize the amount of technetium that can be incorporated into the selected minerals without altering their desirable properties, such as environmental stability and fluorescence.

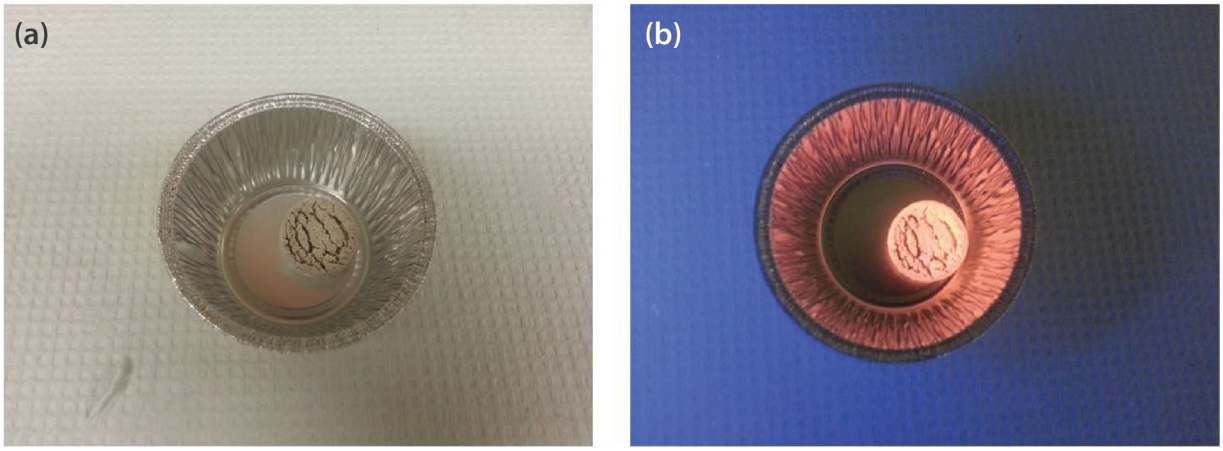

Figure 6. $CaMoO_4$ doped with Eu_2O_3 (a) under ambient lighting and (b) under a UV lamp

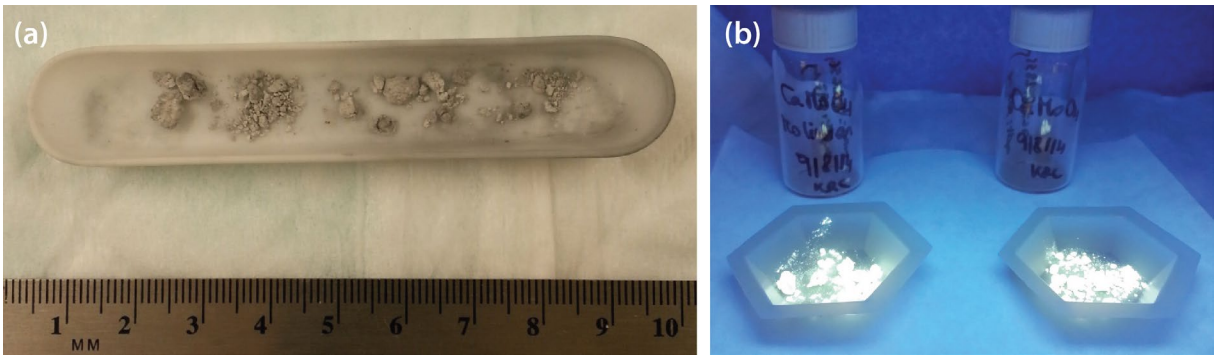

Figure 7. $CaMoO_4$ treated with methanol (a) before and (b) after heating

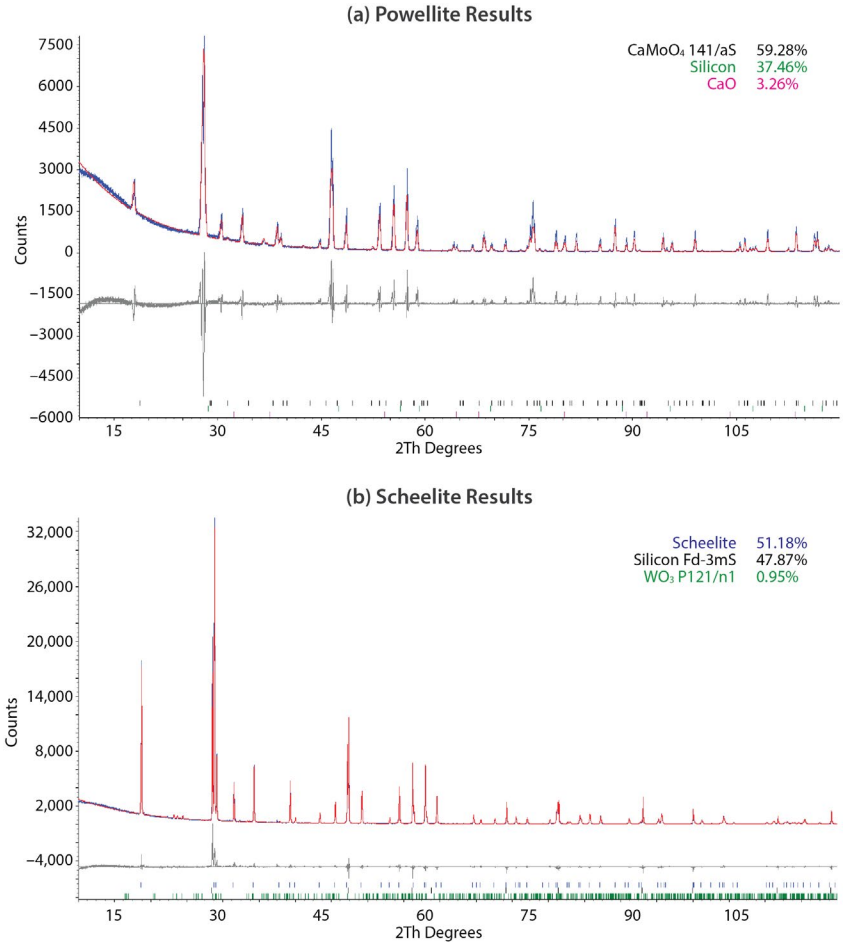

Figure 8. PXRD analysis of reaction products at elevated temperature under air after 6 hours of reaction time indicates successful synthesis of the desired compounds. The blue solid curve is the measured pattern, the red solid curve is the refined profile, and the gray curve is the residual between the observation and the refinement. The vertical ticks are defined in the legend of each figure.

Table 2. Summary of reaction products observed using PXRD analysis from powders synthesized in the reaction of MO_3 (M = Mo, W) and CaO

Product	Percentage In Product (%)					
	Starting/By-product Materials			Product Formed		
	CaO	WO_3	Silicon	Powellite ($CaMoO_4$)	Scheelite ($CaWO_4$)	Total Identified (%)
Powellite	3.26	--	37.46	59.28	--	100
Scheelite	--	0.95	47.87	--	51.18	100

The total energy of the scheelite and powellite structures (Table 3) have been calculated using density functional theory (DFT) implemented in the Vienna *ab initio* simulation package (VASP). The properties and characteristics of the lattice for scheelite and powellite are presented. The structural energies for the incorporation of technetium into $CaWO_4$ and $CaMoO_4$ crystal lattice sites have also been calculated using DFT. The relative energies of each lattice occupied with technetium have been compared and used to determine the relative stability of each lattice. The most probable structure for supporting technetium has also been provided based on the calculated lattice energies and indicates interstitial location for technetium in the

Table 3. Volume, energy, and pressure data calculated by DFT for scheelite and powellite

Lattice	Volume (Å^3)	Energy (eV)	Pressure (GPa)
$CaWO_4$	296.39	–203.09	10.84
	305.46	–203.45	8.81
	314.72	–203.70	6.73
	324.16	–203.75	4.62
	333.79	–203.67	2.46
	343.60	–203.46	0.27
	353.61	–203.19	–1.98
$CaMoO_4$	276.89	–189.23	17.12
	285.28	–190.02	14.97
	293.83	–190.62	12.78
	302.56	–191.03	10.54
	311.46	–191.29	8.26
	320.53	–191.39	5.94
	329.78	–191.37	3.56
	339.20	–191.26	1.15
	348.80	–191.02	–1.31
	358.58	–190.73	–3.82

material. These studies were performed on dedicated clusters at the University of Nevada, Las Vegas (UNLV) by the Radiochemistry Program.

The lattice structures for scheelite-technetium and powellite-technetium compounds were also calculated using DFT and are presented in Table 4. Total energy calculations were performed using VASP, and lattice structures were analyzed by VESTA, a 3-D visualization program. Equilibrium structures and properties for scheelite and powellite were determined by minimizing the total energy with respect to lattice volume. Lattice volume and parameters calculated were in strong agreement with those reported using PXRD. The calculated bulk modulus for scheelite and powellite are 77 GPa and 103 GPa, respectively, in good agreement with experimentally reported results.

The $CaWO_4$ and $CaMoO_4$ compounds have been experimentally examined. The comparable DFT computations from this work are in Table 3. The equilibrium lattice volume for $CaWO_4$ was 325.52 Å^3 as compared to 312.6 Å^3 reported by Hazen (1985) and 312.2 Å^3 by Grzechnik (2003), an approximately 4% difference. Similarly, we calculated the equilibrium volume for $CaMoO_4$ as 323.55 Å^3, while Hazen (1985) reported a value of 311.5 Å^3, a deviation of less than 4%. The calculations performed by DFT in VASP were expected to overestimate due to the limited accuracy applied for each calculation. Regardless, the experimental and calculated results still share excellent agreement.

In scheelite, technetium was found to preferentially occupy interstitial space rather than displace or substitute the calcium and tungstate atoms of the lattice,

Table 4. Total lattice energy and energy difference for the substitution and interstitial occupation of technetium in $CaWO_4$

Atom	Total Lattice Energy (eV)	Initial Energy, E_i (eV)	Final Energy, E_f (eV)	Energy Difference, ΔE (eV)
$Ca_3TcW_4O_{16}$	–203.67	–207.05	–203.79	3.26
$Ca_4TcW_3O_{16}$	–197.07	–207.05	–201.43	5.61
$Ca_4TcW_4O_{16}$ (a)	–207.71	–207.05	–207.71	–0.66
$Ca_4TcW_4O_{16}$ (b)	–207.15	–207.05	–207.15	–0.10
$Ca_4TcW_4O_{16}$ (c)	–206.74	–207.05	–206.74	0.31
$CaWO_4$	–203.75	--	--	--
Ca (atomic)	–0.12	--	--	--
W (atomic)	–4.36	--	--	--
Tc (atomic)	–3.30	--	--	--

based on the lower energy of the system from the DFT calculations. The calculated total energy of the scheelite-technetium lattice was –207.71 eV, lower than the –203.75 eV for the pure scheelite lattice.

The equations of state for $CaWO_4$ and $CaMoO_4$ were derived from

$$P = -\frac{\partial E}{\partial V}, \quad (1)$$

where P is pressure, E is energy, and V is velocity. Calculations were also performed to determine the compression behavior, the bulk modulus (K), for each mineral as

$$K = V_0 \frac{\partial^2 E}{\partial V^2}. \quad (2)$$

The compression behavior calculated in this work was compared with experimentally determined bulk behavior for agreement. Technetium atoms were admitted to the $CaWO_4$ and $CaMoO_4$ lattices by atomic substitution, interstitial placement, and displacement of calcium, tungstate, and molybdenum atoms to interstitial positions. The energy difference (ΔE) for the final lattice states were calculated while treating calcium, tungsten, and molybdenum as atomic species. A comparison of the energy difference for each lattice was used to determine the most probable lattice structure with technetium (Tables 4 and 5).

Technetium was substituted for calcium or the respective metal ion of the equilibrium lattices for $CaWO_4$ and $CaMoO_4$; then the lattice energies were calculated using DFT. In Table 4, the entries for $Ca_4TcW_4O_{16}$ (a), (b), and (c) correspond to the lattice cells provided in Figure 9. The energies for atomic technetium, tungsten, molybdenum, and calcium were also calculated using DFT and used appropriately to determine the energy difference for each final state in Tables 4 and 5.

The most probable structure in which technetium occupied the $CaWO_4$ lattice required that technetium be placed among the interstitial lattice space without displacing calcium or tungsten from their atomic positions. Figure 9a shows the lattice arrangement for this most likely inclusion of technetium in $CaWO_4$, which had the lowest energy difference of –0.66 eV, reported in Table 4. The $CaMoO_4$ lattice required additional time to perform calculations,

Table 5. Total lattice energy and energy difference for the substitution and interstitial occupation of technetium in $CaMoO_4$

Atom	Total Lattice Energy (eV)	Initial Energy, E_i (eV)	Final Energy, E_f (eV)	Energy Difference, ΔE (eV)
$Ca_3TcMo_4O_{16}$	–190.69	–194.69	–190.81	3.88
$Ca_4TcMo_3O_{16}$	–182.93	–194.69	–185.08	9.61
$CaMoO_4$	–191.39	--	--	--
Ca (atomic)	–0.12	--	--	--
Tc (atomic)	–3.30	--	--	--
Mo (atomic)	–2.15	--	--	--

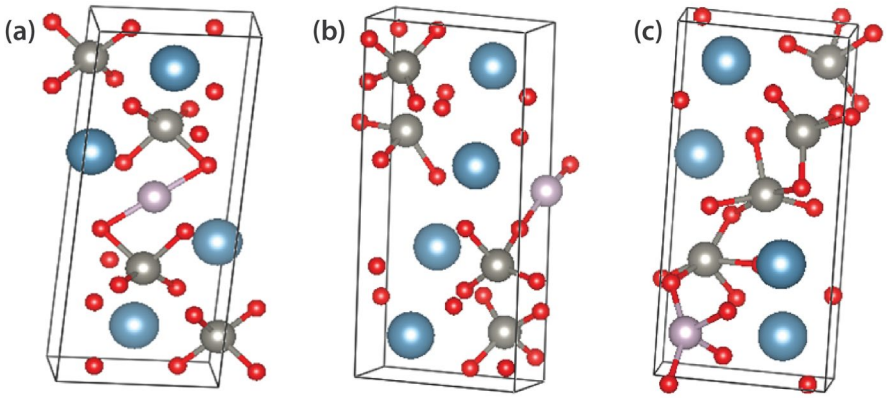

Figure 9. (a) Lattice for technetium occupying the middle of the lattice interstitial space. (b) Lattice for technetium substituting calcium while calcium occupies interstitial space. (c) Lattice for technetium substituting tungsten while tungsten occupies interstitial lattice space.

and a probable structure was not yet determined. However, the energy differences calculated for $CaWO_4$ and $CaMoO_4$ follow similar trends in relative energies. Therefore, it has been predicted that the most likely placement of technetium with $CaMoO_4$ would be interstitial amid the lattice.

Conclusion

This was the first year of a proposed 3-year project. During the studies performed this year, the synthesis of fluorescent material suitable for technetium incorporation was successfully evaluated. Based on synthesis conditions, particularly material formation under 1000°C, the compounds $CaMoO_4$ and $CaWO_4$ appear to be the optimal selections for future research. During this work, both of these compounds were produced in 2 g samples as well as 2 mm particles. The large and small samples demonstrated fluorescent properties when exposed to UV light.

Computational studies were also performed to predict the best path forward for incorporation of technetium into the minerals studied this year. Those calculations indicated that technetium will be most stable in the $CaWO_4$ lattice when placed interstitially amid the calcium, tungsten, and oxygen atoms. From the similarities in the total energies for $CaWO_4$ and $CaMoO_4$

technetium species, it was predicted that technetium would also be found most stable amid the interstitial space of the $CaMoO_4$ lattice. Further calculations of the equilibrium lattice parameters and total energy for the interstitial technetium species will be required to obtain higher accuracy.

In 2015, technetium will be incorporated into the fluorescent materials as NH_4TcO_4 or TCO_2. The resulting compounds will then be evaluated for efficiency of the technetium incorporation into the sample matrix. In 2016, the resulting technetium compound will be used in an exercise at the NNSS.

References

Abdel-Rehim, A. M., "Thermal analysis and x-ray diffraction of synthesis of scheelite," *Journal of Thermal Analysis and Calorimetry* **64** (2001) 1283–1296.

Dutta, P. S., A. Khanna, "Eu^{3+} activated molybdate and tungstate based red phosphors with charge transfer band in blue region," *ECS Journal of Solid State Science and Technology* **2**, 2 (2013) R3153–R3167.

Grzechnik, A., W. A. Crichton, M. J. Hanfland, S. van Smaalen, "Scheelite $CaWO_4$ at high pressures," *J. Phys. Condens. Matter* **15** (2003) 7261–7270.

Hazen, R. M., L. W. Finger, J. W. E. Mariathasan, "High-pressure crystal chemistry of scheelite-type tungstates and molybdates," *J. Phys. Chem. Solids* **46**, 2 (1985) 253–263.

Rase, D. E., R. Roy, "Phase equilibria in the system $BaTiO_3$-SiO_2," *J. Am. Ceram. Soc.* **38**, 11 (1955) 389–395.

Schwochau, K., *Technetium: Chemistry and Radiopharmaceutical Applications*, Wiley-VCH, Weinheim, Germany, 2000, 3.

Takahashi, Y., K. Iwasaki, H. Masai, T. Fujiwara, "Raman spectroscopic study of benitoite-type compounds," *J. Ceram. Soc. Jap.* **116** (2008) 1139–1142.

This page left blank intentionally

Development of an X-Ray Radar Imaging Technique for 3-D Scene Scanning

LAO-09-13 | Continued from FY 2013 | Year 2 of 2

Wendi Dreesen,[1,a] David Schwellenbach,[a] Andrew Smith,[a] Mark Browder,[b] Rick Wood,[b] Carl Carlson,[a] Craig Kruschwitz,[a] Sara Thiemann,[c] and Aric Tibbitts[a]

The x-ray radar imaging concept combines standard radar signal processing methods using the penetration power of x-rays to image scenes. Our project demonstrates the basic principles of the technique using a 2 MeV linear electron accelerator to generate the S-band–modulated x-ray signals. X-ray detectors, including photodiodes and scintillators, are used to detect the signals in backscatter and transmission detection schemes. The S-band microstructure is imposed on the variable-width electron pulse, and this modulation carries over to the bremsstrahlung x-rays after the electron beam is incident upon a copper-tungsten alloy target. Using distance calculations, a low-jitter system, and a short- or long-pulsed electron beam, we expect to detect different object distances by comparing measured phase or time differences. The experimental setup, which meets strict jitter requirements, and experimental transmission and reflection measurement results are presented. Our 1-D reflection measurement distances compared to measured reflection distances show a 9% error over a range of 22 cm.

[1] dreesewm@nv.doe.gov, 505-663-2050
[a] Los Alamos Operations; [b] Lockheed Martin Missiles and Fire Control Systems; [c] Keystone International, Inc.

Background

A U.S. patent on the concept of x-ray radar was recently awarded to Lockheed Martin (Wood 2013). The technology uses radar signal processing techniques on a signal produced by RF-modulated x-rays rather than the standard RF electromagnetic (EM) waves. X-rays can penetrate metal walls, whereas standard EM waves at radio frequencies will reflect off metal walls. This technique's strength lies in its ability to flood a scene with modulated x-rays while the source and detector array are in fixed locations. The signals extracted can produce a 3-D reconstruction of the scene, much like a CT scan, because the phase information extracted from the modulation gives the ranging information. This project will demonstrate the first steps to generate 3-D reconstructions of shielded configurations with fixed x-ray sources and detectors.

Project

Experiment Definition

The goals of this project are to (1) identify candidate sources and detectors, (2) evaluate short-pulse (time domain) and long-pulse (frequency domain) measurement techniques, (3) demonstrate the ability to determine range through transmission and reflection experiments, and (4) experimentally verify implementation of the x-ray radar concept in 1-D. Objects of interest are placed in the field of view of an x-ray pulse from the linac, and the scene is flooded with RF-modulated x-rays. X-ray detectors situated in a fixed position measure the reflected backscatter signal along with phase information, and the range can be calculated using radar signal processing techniques. Ultimately the development of a 2-D image-forming array of

detectors combined with ranging from the phase of the modulated x-rays will provide enough information to form a 3-D image.

Radar uses a ranging and detection algorithm that relies on time delays of a signal reflected off of an object, $d = ct/2$. The radar equation in one dimension gives a distance (d) based on the speed of light (c) and the time of flight (t) divided by two, to compensate for the distance traveled to and from the backscattered object. Because the relative phase of a signal is related to the time of flight, radar techniques include methodologies using time domain and frequency domain analyses. More sophisticated models can be used to extract 2-D and 3-D information.

The NSTec Los Alamos Operations (LAO) linac generates electrons with energies ranging from 100 keV to approximately 2 MeV. Long- and short-pulse bursts of electrons can be generated; however, each type requires a different radar processing technique. For short-pulse electron bursts, a 1 ns pulse is accelerated through the RF cavities, and a 2.856 GHz RF waveform is superimposed on the pulse. A time-based radar ranging technique can be applied to analyze the backscattered waveform. Impulse radar (Azevedo 1996) transmits a short pulse and receives one or more reflections. The delay of each reflection is then correlated with distance. As the phase ambiguity limits distance measurements to one wavelength, impulse radar makes slight time delays on each transmitted pulse, essentially accomplishing a range sweep over the volume of interest. Using photodiodes that are fast enough to detect the reflected x-rays, we can deconvolve the signal and generate a depth map of the scanned volume.

In long-pulse mode, the linac employs a frequency-based radar approach. A 100 ns pulse accelerated through the RF cavity creates a 100 ns pulse with a 2.856 GHz microstructure superimposed on the long pulse. Then, the intra-pulse modulation signal is used to analyze the scanned volume. In long-pulse mode, a frequency domain technique uses an FFT of the x-ray signal generated by the long pulse. The FFT yields the magnitude and phase of the x-ray signal with respect to the frequency domain; phase can be used to calculate the range.

Because distance is calculated from small time or phase differences, minimal system jitter is desirable. The goal for imaging resolution was in the sub-centimeter range; therefore, it was very important to maintain pulse-to-pulse stability on the linac ($\Delta d = c\Delta t/2 = c \times 10$ ps$/2 = 0.15$ cm). We found RF system components to generate the 2.856 GHz RF for the accelerator and the logic pulses synchronized to the RF that met these requirements. At 0.15 cm resolution the calculated maximum acceptable jitter was 10 ps. An additional requirement for a phase-synchronized 219.69 MHz signal, a sub-harmonic of the 2.856 GHz, was included for implementation of the sub-harmonic buncher on the linac for impulse measurements.

Initial System for Running and Triggering the Accelerator

The Tektronix 7122C arbitrary waveform generator (AWG) was chosen because of its sub-picosecond jitter specification between the RF signal and either of the digital output signals, which Tektronix refers to as a digital marker. The AWG also generates two programmable RF waveforms and four digital markers. The AWG RF waveform we programmed shows data acquisition noise imposed on the generated signal, so we added an analog low-pass filter (Picosecond Pulse Labs 5915) before sending the signal to RF amplifiers in the linac system.

Figure 1 shows the schematic diagram of the experimental setup, indicating synchronization of the linac's electron gun with the RF burst. The klystron supplies a fixed 4 µs burst of RF energy to the accelerator, and the electron pulse from the injector must be injected at a stable, flat-topped region within that burst. The injector has considerable volume for installing benchtop amplifiers and delay units for firing the electron gun. The injector has a short-pulse amplifier that fires 1 ns electron pulses triggered by a rising edge, but has a long-pulse amplifier that can produce pulses from 40 ns to 1 µs. The system's master clock is a Quantum

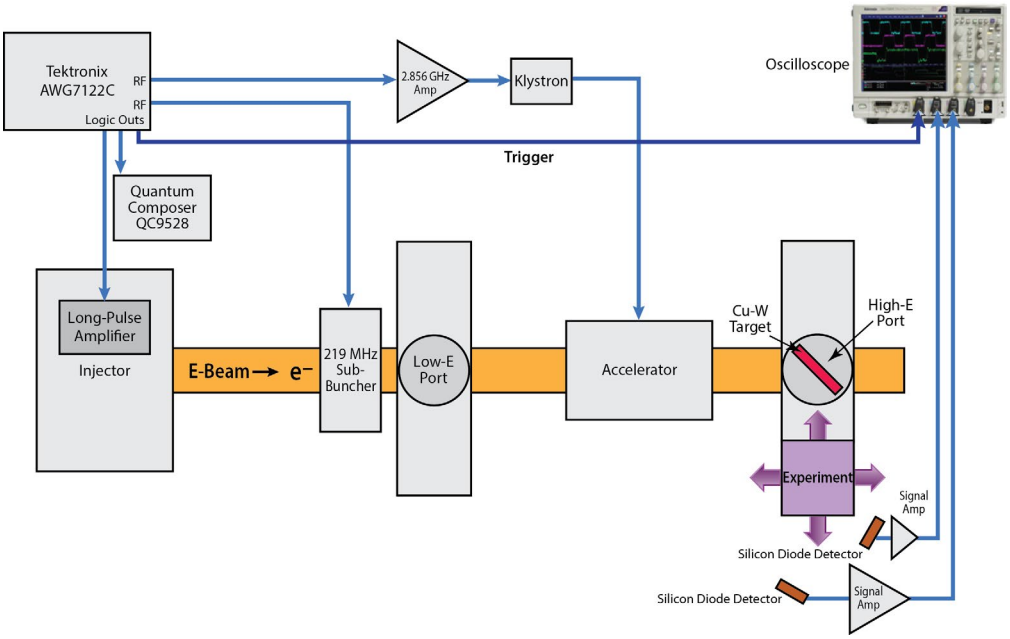

Figure 1. System diagram and experimental setup for accelerator operation includes synchronization of RF with injected electron pulse and with oscilloscope for data acquisition

Composer trigger delay unit capable of triggering up to eight channels with 2 ns of jitter. The Tektronix AWG is controlled by the master clock to generate a 4 µs burst of 2.856 GHz sinusoidal signal to drive the klystron.

Alternate System for Running and Triggering the Accelerator

We also designed, built, and tested an alternate prototype to replace the cost-prohibitive AWG (Figure 2). Although the AWG would be a practical instrument to use on the accelerator, it cannot be permanently installed into the accelerator system. We discovered a Hittite Microwave part, HMC747 RF D-flip-flop, which would provide the synchronization we needed at a much lower cost. The part has a bandwidth of 13 GHz, well within our requirement specification. The new system couples the synchronous circuit to an existing RF generator that can produce a 4 µs long RF burst at 2.856 GHz with a voltage of 5.6 Vpp (0.78 mW). The primary challenges were to bias all the DC voltages to the correct levels and to ensure the correct capacitance coupling in the circuit. The use of the flip-flop is somewhat unconventional; we synchronize it to the trigger signal by sending the 2.856 GHz signal into the clock and the trigger pulse from the master clock into the D input. The Q output has the newly synced RF burst, which is sent to the next RF amplifier stage.

We built the housing for the circuit, and it meets specifications. We compared the performance of the two synchronization mechanisms, finding a trade-off between cost and jitter performance. Our first-generation prototype was approximately $30,000, while the AWG-based system would cost about $160,000. Our prototype measured 35 ps of jitter (including all system jitter), while the AWG measured 10 ps. The loss in jitter performance would decrease system resolution to 0.53 cm from 0.15 cm. Note that the measurements completed for this project used the AWG, and the new prototype will be tested once it has been installed in its new housing during the final weeks of the project.

Detector Evaluation

Photodiode

Using x-ray detectors capable of resolving 3 GHz–modulated x-rays was anticipated as a significant challenge for this project. The fastest commercial x-ray detector identified was the Opto Diode AXUVHS6 coupled with a Picosecond Pulse Labs 5541 bias tee. The detection system rise time, 50 ps, was driven by the Opto Diode detectors. Because the estimated width of the microstructure pulses from the linac is 30 ps, this detection system cannot give full temporal information about the x-ray pulse. However, these

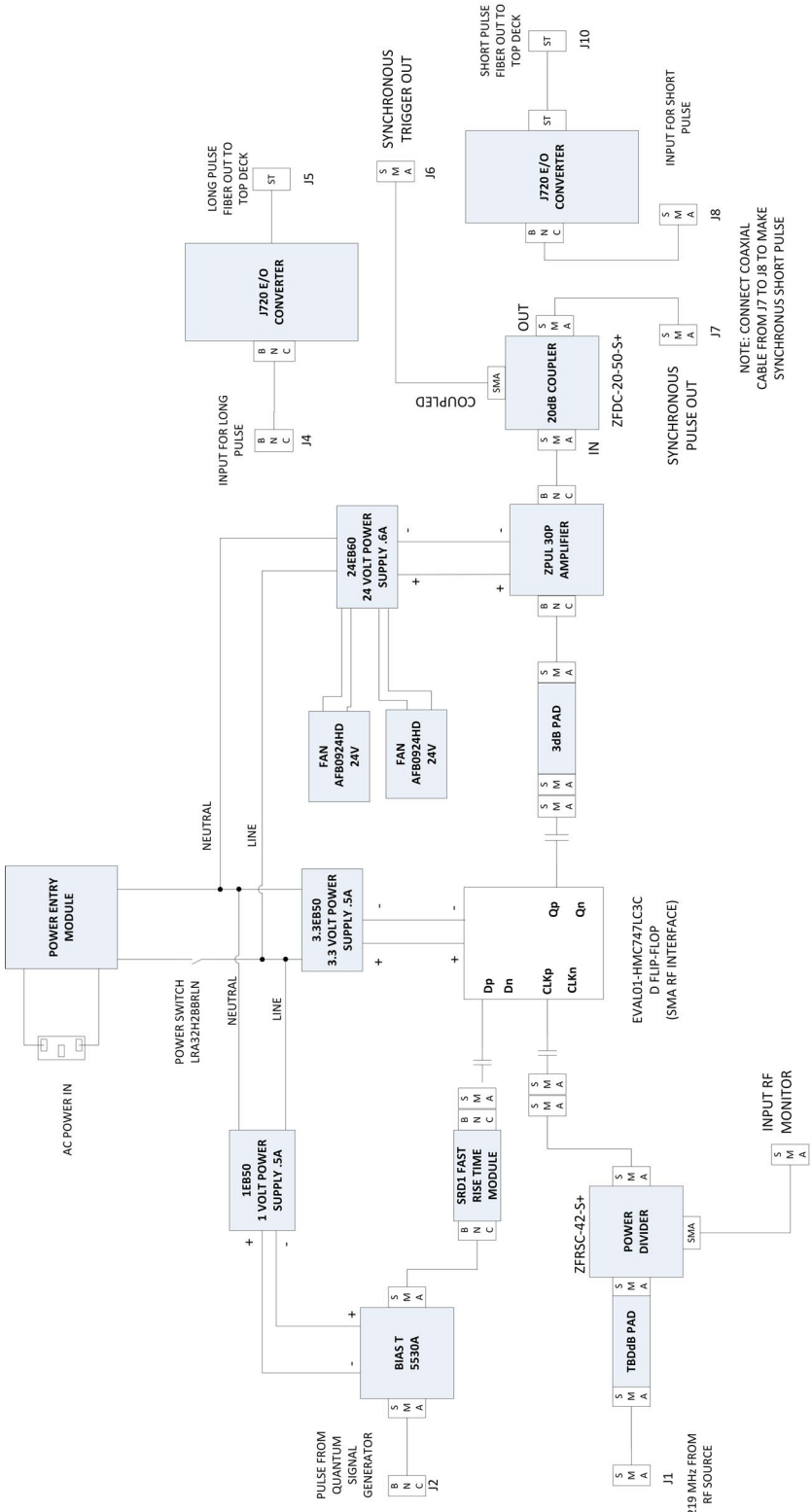

Figure 2. Prototype synchronous circuit diagram for the alternate system

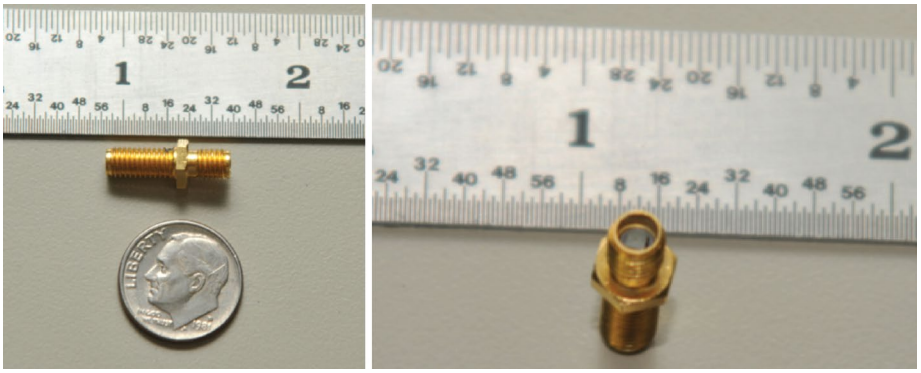

Figure 3. The Opto Diode AXUVHS6 UV silicon diode was used on initial experiments because it was readily available. However, it has low signal strength.

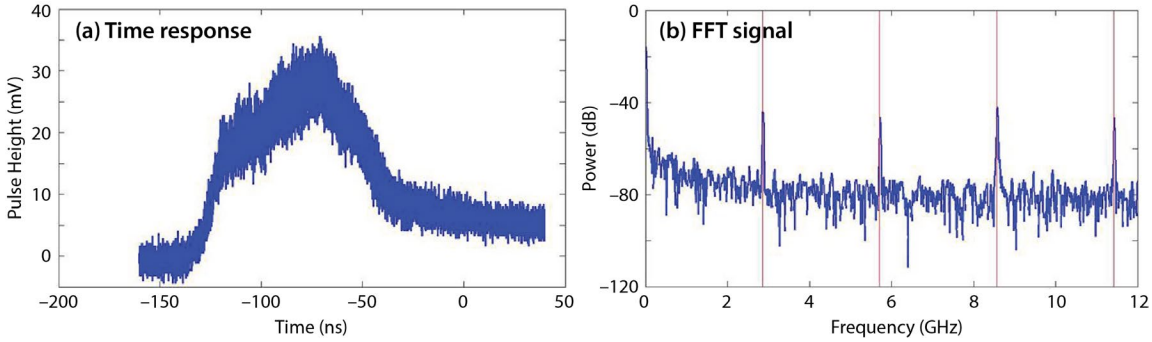

Figure 4. (a) Time response data show the detector's low signal strength, which made it difficult to use for short-pulse time-response measurements. (b) FFT calculation for (a) for the same detector.

detectors can resolve the 350 ps (2.856 GHz) microstructure spacing. Figure 3 shows the size of the Opto Diode detectors with respect to a dime.

As seen in Figure 4a, the oscilloscope is at maximum sensitivity, and the signal strength measured up to 30 mV when the detector was placed facing the x-ray target close to the x-ray window on the beam port. Although the small active area (0.029 × 0.029 mm) increased the frequency response and provided a larger bandwidth, the signal strength is weaker. Therefore, the detector was too small to use for time response measurements with the linac in short-pulse mode. With the linac in long-pulse mode, we used the detector for frequency domain measurements, which provided a larger signal to process. A representative FFT magnitude is shown in Figure 4b.

With the initial experimental setup complete, and without amplification, the diode signals measure from 5 to 30 mV, requiring the highest gain setting on the 20 GHz oscilloscope. In these experiments, we directly measured x-ray intensity as close as possible to the x-ray source. Our results from last year (Dreesen 2014) were inconsistent and showed measurement errors. We determined that because the detector's area is so small, the cross-sectional interaction is very small and therefore receives too few x-rays. The detector acted like an antenna to the RF generated by the accelerator. A better detector was sought out.

Scintillator

We explored the use of a scintillation detector that would give us a larger detection volume (2.36 cm^3) while maintaining acceptable detection bandwidth. The scintillation detector consists of an Eljen Technologies EJ-232Q (0.5%) scintillator rod 10 mm in diameter by 30 mm long with a 110 ps rise time and a 700 ps decay time, coupled to a Photek PMT-210 microchannel plate (MCP) with a 60 ps rise time and a 110 ps FWHM characteristic (Figure 5). We expected the scintillator to pick up the leading edge of the x-ray

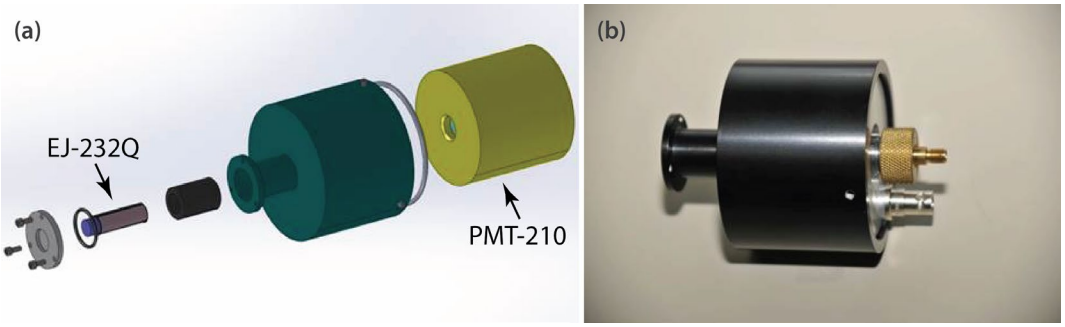

Figure 5. (a) CAD model of the scintillator detector assembly and (b) the assembled detector

pulse, but due to the long decay time, its ability to detect the 2.856 GHz microstructure modulated onto the signal was questionable.

Experiments

Time and Frequency Domain Measurements

Time domain analysis relies on measuring the time delay between a known time marker signal and the detection of the x-ray signal. The delay and the distance are directly related by the speed of propagation of the x-ray: $d = ct$, where d is distance, c is the speed of light, and t is time. The frequency domain approach uses an FFT applied to the signal after it is detected to extract the phase information used to calculate range. These measurements can be performed on the direct x-ray beam to determine source-detector distance or on the reflected x-ray beam to determine the distance from the reflecting object to the detector. We began with the direct mode to test the basic concept and then addressed the more difficult problem of backscatter, where we anticipated the reflected signal would be several orders of magnitude lower in intensity. The low intensity of the reflected signal drives our pursuit of detectors with large signal strengths.

Experimental Setup

Fixed and Moveable Photodiodes

We used a frequency analysis technique to measure phase because of the better signal-to-noise ratio of the phase technique with the Opto Diode detectors in long-pulse mode on the linac. Prior to making derived range measurements in the backscatter mode, we needed to verify the capability to measure basic phase changes as we moved two detectors in a direct-mode setup using the FFT result. One photodiode was set up as a fixed diode placed near the beam port. The second diode was movable, sliding toward and away from the beam port on an optical rail. The diodes were mounted using plastic holders and screws to decrease scatter from the mounting mechanisms.

We placed the fixed diode approximately 16.8 cm from the copper-tungsten target in the electron beam line as a fixed phase reference. The movable diode's position was adjusted in 1 cm increments from 5 to 14 cm relative to the fixed diode. Range can be derived using the following equations:

$$\Delta\theta = \left(\theta_{fixed} - \theta_{movable}\right)_{position\,0} - \left(\theta_{fixed} - \theta_{movable}\right)_{position\,1} \quad (1)$$

$$Range(f) = \frac{c \cdot \Delta\theta}{f \cdot 360.0^{\circ}} \quad (2)$$

We were well within the 10.5 cm range maximum (wavelength = c/frequency) before the point at which we would expect to see phase wrap. At a distance change of 3 cm and 2.856 GHz, one would expect 103° of change using the following formula:

$$\Delta\theta(degrees) = 360^{\circ}\frac{\Delta d}{\lambda}. \quad (3)$$

The phase values we observed were much more stable shot-to-shot than in prior measurements. For each 1 cm increment, we expected a 34.3° relative phase change, but this effect was not clearly seen. We replaced potentially bad cables and connectors and moved the oscilloscope to the accelerator cell

to reduce line attenuation and RF pickup, but still obtained inconsistent results. We also took measurements on the Faraday cup, which is used to measure the temporal behavior of the electron beam directly.

These measurements showed unexpected noise inconsistent with past linac performance. We identified an out-of-phase component between the two traces that would indicate RF leakage or other interference. In addition, we believe there was a problem with the accelerator tuning that caused the electron beam to spiral. An inadvertent stray beam will cause multiple x-ray beams to emanate from the beam pipe and could be the cause of these measurement problems. We measured the phase and calculated the derived range at the first and second fundamentals or harmonics of the FFT. We carefully retuned the accelerator and repeated the experiment, but we found no significant improvement. With small detector volume and low signal, the signal-to-noise ratio is too low for accurate measurements; also, stray RF or scattered x-rays were likely contaminating the phase measurements. Therefore, we sought out a new detector that would provide higher signal strength, although we knew it would have a reduced bandwidth.

Measurements with the Scintillation Detectors

We identified a larger-volume scintillation detector from Eljen Technologies as a more promising approach. The scintillator was coupled to a Photek MCP detector. Figure 6 shows the output from the scintillation detector with an order of magnitude increase in signal compared to the diodes. We ran the accelerator in short-pulse mode with the intention of making time delay measurements using the leading edge of the x-ray pulse. The leading edge is well defined, but RF modulation appeared on the detector's signal. When we calculated the FFT, a peak appeared at 2.856 GHz on the magnitude portion of the transform; this peak indicates the scintillation detector may perform well in frequency mode as well as impulse mode.

We attempted a frequency measurement using the accelerator in long-pulse mode. Unfortunately the detector saturated, and we deemed only timing measurements, using the short-pulse mode, could be accomplished with this detector.

Next we repeated the photodiode measurements with the new scintillator detector; we set up the detector in a transmission mode, moved it different distances from the x-ray port, and verified that the delay in time measured was consistent with the speed of light. Figure 7 shows positioned distance vs. the measured delay; we expected the slope of the fitted line to the measurement would be the speed of light. We collected data for 100, 200, and 500 samples. As we increased the sample count, our fitted line continuously approached the expected value of the speed of light (29.98 centimeters per nanosecond). This built confidence that the detectors were working well, and we could move on to reflection measurements.

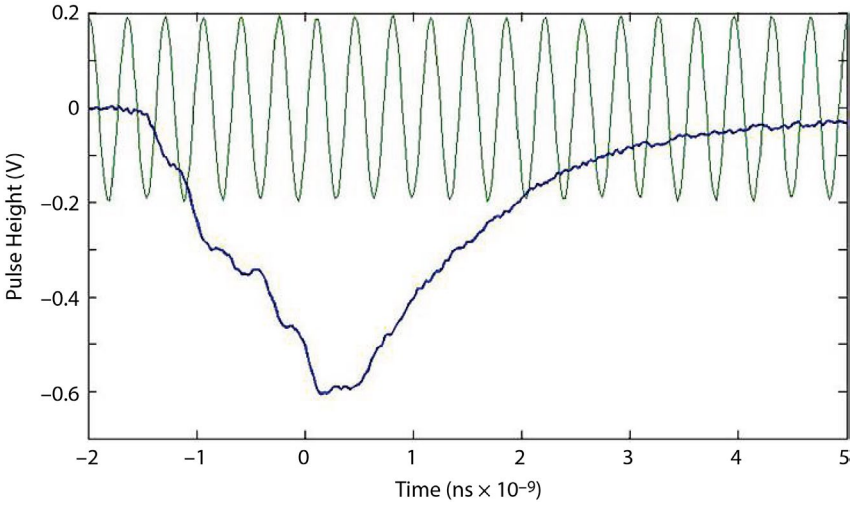

Figure 6. Output of the Eljen/Photek detector. The blue trace shows the detected x-ray signal using the scintillator, two orders of magnitude stronger than the photodiode, and there is some ripple on the signal showing the RF modulation from the accelerator. The green trace shows the RF modulation alone for comparison.

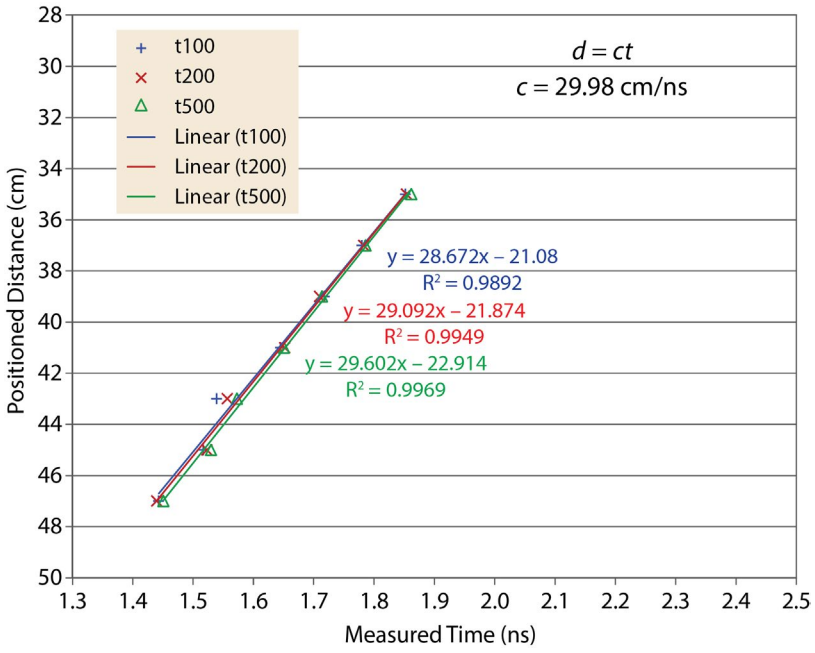

Figure 7. Scintillator delay measurements. Plotting measured position distance vs. time, one would expect to see the slope be the speed of light, *c*. As more samples are collected (sample groups are 100, 200, and 500), the fitted line approaches *c*, improving confidence.

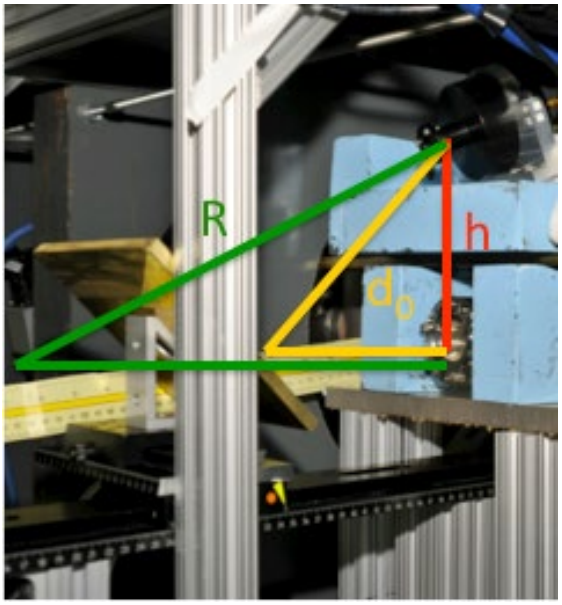

Figure 8. Experimental setup for reflection measurements

Reflection Measurements with the Scintillation Detectors

Once we established a good correlation between the changed position and time delay, we were ready to insert a reflector into the scene and determine if we could predict the change in distance of the reflector to the change in measured system delay. After testing different materials, including aluminum foil and aluminum, steel, and brass plates, we identified a brass plate to be the reflection material. We set up a scene (Figure 8) with a 3/8-inch-thick brass plate mounted at an angle on the optical rail. Above the x-ray port, we mounted the detector pointing down toward the reflection plate. The measurement was completed using an initial distance, d_0, defined as the original reflection distance close to the x-ray window including the transmission and reflection distances. We defined the variable h to be the fixed height between the source port and the detector. Using the Pythagorean theorem, we derived an equation describing the total distance traveled by the x-ray from the port, reflecting off the plate and hitting the detector. We called this variable R and calculated its value in centimeters as a function of the change in delay time, Δt (Equation 4). Our experiments began with the brass reflecting plate approximately 6 cm from the x-ray window, and we measured the time when the x-ray pulse crossed 50% the height of the pulse. We set up a Tektronix DPO4104 20 GHz oscilloscope to measure in averaging mode, using 16 samples, and used a histogram function to make the measurement. Each measurement was made after moving the reflector 1 cm at a time through a total range of 22 cm.

We also calculated weighted error bars for our measurement. The sources of error identified were the measured time difference, height, and distance. We assumed the error in measured height and distance to be negligible compared to the Δt error, so we calculated a partial derivative as a function of Δt (Equation 6) and used this equation to provide our error bars calculated on the data in Gnuplot, the program we used to graph and fit the data. Gnuplot uses the Levenberg-Marquardt least-squares fitting routine.

$$R = \frac{\left(c\Delta t + d_0\right)^2 - h^2}{2\left(\Delta tc + d_0\right)} \quad (4)$$

$$\partial R^2 = \left(\frac{\partial R}{\partial \Delta t}\delta\Delta t\right)^2 + \left(\frac{\partial R}{\partial d_0}\delta d_0\right)^2 + \left(\frac{\partial R}{\partial h}\delta h\right)^2 \quad (5)$$

$$\frac{\partial R}{\partial \Delta t} = \frac{c}{2}\left[1 + \left(\frac{h}{c\Delta t + d_0}\right)^2\right] \quad (6)$$

The data are plotted in Figure 9, where the y-axis represents the calculated range based on the change in time measured between the original position and each of the other 22 positions. The x-axis is the measured position. The error bars were calculated based on Equation 6. The error in the fitted line is reported by Gnuplot to be 8%. The expected slope is 1.0, giving a difference between the expected slope and fit slope of 9%.

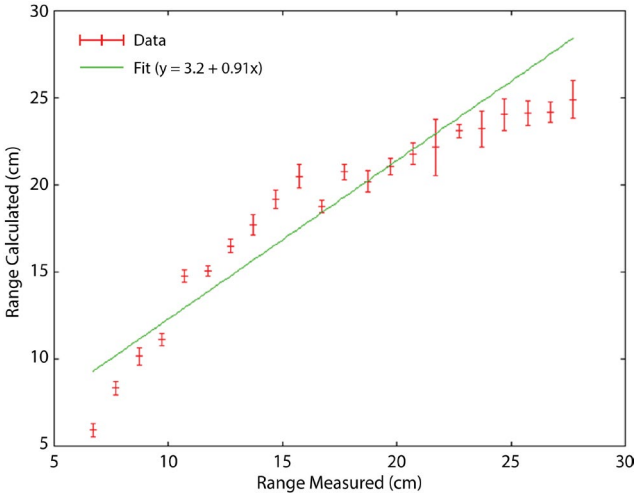

Figure 9. Results of reflection measurements with the scintillation detector that shows approximately 10% error in calculated position over a range of 22 cm

Conclusion

Measurements to demonstrate the x-ray radar concept have proven challenging using photodiode and scintillator detectors. The LAO linac required modifications to improve its stability for making these sensitive measurements. The stability of the injector and the time jitter have been improved to the level required for x-ray radar measurements. Once confidence in the detector and measurement techniques was established, 1-D backscatter studies were performed to validate the performance of x-ray radar. The new scintillator coupled to an MCP detector proved to be an order of magnitude improvement in signal-to-noise ratio, but we had to sacrifice timing at the same time. We changed our measurement scheme to use the time domain, and the transmission measurements showed good results. We completed 1-D reflection measurements and found a good correlation between measured and calculated reflection distances with a roughly 10% error. The 1-D backscatter experiment results show a need for an improvement in detector response time.

Were this research to continue, we would test the system with the 219 MHz, sub-harmonic buncher. The buncher provides a reduction of the pulse width to 250 ps and would achieve a better delay response. A comprehensive study of source (type and energy) vs. detector types should be performed to find the optimum pairing. Finally, we would work to develop the requirements for a fieldable detector using the results of these studies. After improved detectors are designed and built, an array of detectors can test the feasibility of imaging using x-ray radar.

Acknowledgments

The authors acknowledge the outstanding support from the staff at National Security Technologies, LLC, including Brent Davis, Irene Garza, Carl Carlson, and J. Andrew Green.

References

Azevedo, S., T. E. McEwan, "Micropower impulse radar," *Science & Technology Review* (January/February 1996) 16–29.

Dreesen, W., M. Browder, R. Wood, C. Carlson, N. Kallas, C. Kruschwitz, D. Schwellenbach, S. Thiemann, A. Tibbitts, "Development of an x-ray radar imaging technique for 3-D scene scanning," in *Site-Directed Research and Development*, FY 2013, National Security Technologies, LLC, Las Vegas, Nevada, 2014, 69–77.

Wood, J. R., "X-Ray Radar," U.S. Patent 8,433,037 B1, filed October 23, 2009, and issued April 30, 2013.

Novel Deployment of Elpasolites as a Dual Gamma–Neutron Directional Detector

RSLN-06-13 | Continued from FY 2013 | Year 2 of 3

Paul Guss,[1,a] Thomas Stampahar,[a] Alexander Barzilov,[b] Amber Guckes,[c] Jessica Hartman,[b] Sanjoy Mukhopadhyay,[d] Michael Haugh,[e] Joshua Lee,[e] Kanai Shah,[f] William Higgins,[f] and Michael Squillante[f]

The problem of accurately detecting extremely low levels of nuclear radiation is rapidly increasing in importance in nuclear counter-proliferation, verification, and environmental and waste management. Since the ^{239}Pu gamma signature may be weak, for instance, even when compared to the natural terrestrial background, coincidence counting with the ^{239}Pu neutron signature may improve overall ^{239}Pu detection sensitivity. However, systems with sufficient multiple-particle detectors require demonstration that the increased sensitivity be sufficiently high to overcome added cost and weight. We report the results of measurements and calculations to determine sensitivity that can be gained in detecting low levels of nuclear radiation from use of a relatively new detector technology based on Elpasolite crystals. We have performed investigations exploring a new class of scintillator: defined for this report as cerium (Ce^{3+})-doped Elpasolites $Cs_2LiYCl_6:Ce^{3+}_{0.5\%}$ (CLYC), $Cs_2LiLaCl_6:Ce^{3+}_{0.5\%}$ (CLLC), $Cs_2LiYBr_6:Ce^{3+}_{0.5\%}$ (CLYB), $Cs_2LiLaBr_6:Ce^{3+}_{0.5\%}$ (CLLB), and $Cs_2LiLa(Br_6)_{90\%}(Cl_6)_{10\%}:Ce^{3+}_{0.5\%}$ (CLLBC:Ce). These materials can provide energy resolution ($r(E) = 2.35\sigma(E)/E$) as good as 2.9% at 662 keV (FWHM). The crystals show an excellent neutron and gamma radiation response. The results of our studies on the scintillation properties of CLLBC, specifically radioluminescence, energy resolution, light yield, decay times, and nonproportionality, are also discussed.

[1] gusspp@nv.doe.gov, 702-295-8095
[a] Remote Sensing Laboratory–Nellis; [b] University of Nevada, Las Vegas; [c] North Las Vegas;
[d] Remote Sensing Laboratory–Andrews; [e] Livermore Operations; [f] Dynasil Radiation Monitoring Devices, Inc.

Background

Some applications, particularly in homeland security, require detection of both neutron and gamma radiation. Interestingly, the wavelength of thermal neutrons is comparable to atomic distances in the solid state, and their energy is comparable to that of phonons. It is often important to discriminate the thermal neutrons from the gamma rays that may be concurrently present in a field of neutron flux (Reeder 2001, Bessière 2004). Space applications (Bodnarik 2013), non-destructive assay work (Dubi 2013, Henzl 2013), and active interrogation (McFee 2013, Menlove 2013) would all benefit from a detector with neutron/gamma discrimination.

Recently, we have researched a number of scintillators from the Elpasolite crystal family that can detect both neutron and gamma radiation. The most promising are cerium (Ce^{3+})-doped Elpasolites such as $Cs_2LiYCl_6:Ce^{3+}_{0.5\%}$ (CLYC), $Cs_2LiLaCl_6:Ce^{3+}_{0.5\%}$ (CLLC), $Cs_2LiLaBr_6:Ce^{3+}_{0.5\%}$ (CLLB), and $Cs_2LiYBr_6:Ce^{3+}_{0.5\%}$ (CLYB). For our project, all were doped with 0.5% Ce^{3+}. They are capable of providing very high energy resolution. The best values achieved for each material are 3.9%, 3.4%, 2.9%, and 8.5% at 662 keV (FWHM) for CLYC, CLLC, CLLB, and CLYB, respectively. Because ^{6}Li has an acceptable cross section for thermal neutron capture,

these materials also detect thermal neutrons. The full energy thermal-neutron peak typically appears above 3 MeV gamma equivalent energy. Thus, very effective pulse height discrimination (PHD) can be implemented with these materials. The CLLC and CLYC scintillations consist of two main components: core-to-valence luminescence (CVL; 220 to 320 nm) and Ce emission (350 to 500 nm). The former is of particular interest as it appears only under gamma excitation. It is also very fast and decays with a time constant of less than 2 ns. The CVL provides a significant difference to temporal responses under gamma and neutron excitation; thus, it may be used for effective pulse shape discrimination (PSD) (van Loef 2002, Bessière 2004, Glodo 2011). The emission spectra for the CLLB crystal show two peaks, one at 392 nm and one at 419 nm (Mukhopadhyay 2009).

Project

Both undoped and cesium-doped CLYC exhibit CVL under gamma irradiation (van Loef 2002). This luminescence consists of a fast (~2 ns decay time) luminescence produced by radiative recombination of a valence electron with an outermost core hole (Rodnyi 1992). The CVL is observable under gamma excitation and absent under alpha irradiation (Kubota 1986, Glodo 2009a), as observed in $LiBaF_3$ (Knitel 1996), $LiBaF_3$:Ce,Rb, and BaF_2 (Combes 1998, Dinca 2002). CVL, therefore, is a useful property that helps discriminate between alpha and gamma rays. The presence of Li makes both CLYC and $Cs_2LiLa(Br_6)_{90\%}(Cl_6)_{10\%}:Ce^{3+}{}_{0.5\%}$ (CLLBC:Ce) suitable candidates for neutron detection (Bessière 2005). Li-based Elpasolites contain ^6Li with 7.5% natural abundance that capture thermal neutrons and convert them into ionizing particles according to the reaction (Bessière 2004):

$$ {}^{6}_{3}\mathrm{Li} + {}^{1}_{0}\mathrm{n} \rightarrow {}^{3}_{1}\mathrm{H} + {}^{4}_{2}\alpha + 4.78\ \mathrm{MeV}, \qquad (1) $$

where the reaction products ionize the material. The α and triton share a kinetic energy of 4.78 MeV. The particles create ionization tracks, and subsequent trapping of the free charges in the luminescence center Ce^{3+} leads to a scintillation light pulse. Roughly 22%, 18%, and 60% of the captured thermal neutrons are captured by ^6Li, ^{133}Cs, and $^{35,37}Cl$ in CLLC, respectively. The numbers are 40%, 34%, and 26% for ^6Li, ^{133}Cs, and $^{79,81}Br$ in $Cs_2LiLaBr_6:Ce^{3+}$ (Bessière 2004).

A new scintillation material $Cs_2LiLaBr_{6-x}Cl_x:Ce^{3+}{}_{y\%}$ (CLLBC:Ce), doped with y% Ce^{3+}, has been investigated. The ^6Li detects thermal neutrons and the ^{35}Cl detects fast neutrons. Figure 1 shows that at 10 MeV the neutron total cross section for ^{35}Cl is over twice that of either ^3He or ^4He and is higher than that of either ^6Li or ^{10}B. CLLBC:Ce's response to fast neutrons via $^{35}Cl(n,p)^{35}S$ reaction was tested using $^{241}AmBe$, ^{252}Cf, and ^{239}Pu sources. The differences in the decay times of neutrons and gammas allowed PSD to differentiate between the two types of radiation. For $Cs_2LiLaBr_{6-x}Cl_x:Ce^{3+}{}_{2\%}$, that is with 2% Ce^{3+} doping, the neutron peak centroid was observed to move linearly with neutron energy. Therefore, CLLBC:Ce would be an excellent detector for combined gamma ray and neutron (thermal and fast) spectroscopy (Shirwadkar 2012). If pulse shape differences depending on the type of radiation are also observed in CLLBC:Ce, this material could be used with a PSD technique (Knitel 1996, Bessière 2005) to distinguish neutrons from gamma rays.

Experimental Approach

A 12 × 18 × 3 mm^3 CLLBC:Ce sample and a 25 × 25 mm CLYC (Figure 2) sample, with calculated densities of 4.13 and 3.31 g/cm^3, respectively, were grown as single crystals by the melt-based, vertical Bridgman technique (van Loef 2002). The Ce^{3+} doping concentration was 0.5%. $Cs_2LiLa(Br_6)_{90\%}(Cl_6)_{10\%}:Ce^{3+}{}_{0.5\%}$ has a cubic Elpasolite structure and crystallizes in the space group $Fm\bar{3}m$. Both crystals contain natural Li, which has a natural abundance (7.5%) of the ^6Li isotope. The compounds are hygroscopic, so all experiments were performed on samples sealed in a metal housing with one optical window. The crystals were mounted on a 2" diameter super bialkali (SBA) R6231-100-01HA (Hamamatsu) photomultiplier tube (PMT), which is a 51 mm diameter, head-on type, SBA photocathode, 8-stage PMT. Its effective area is 46 mm in diameter. It has a spectral response from 300 to 650 nm,

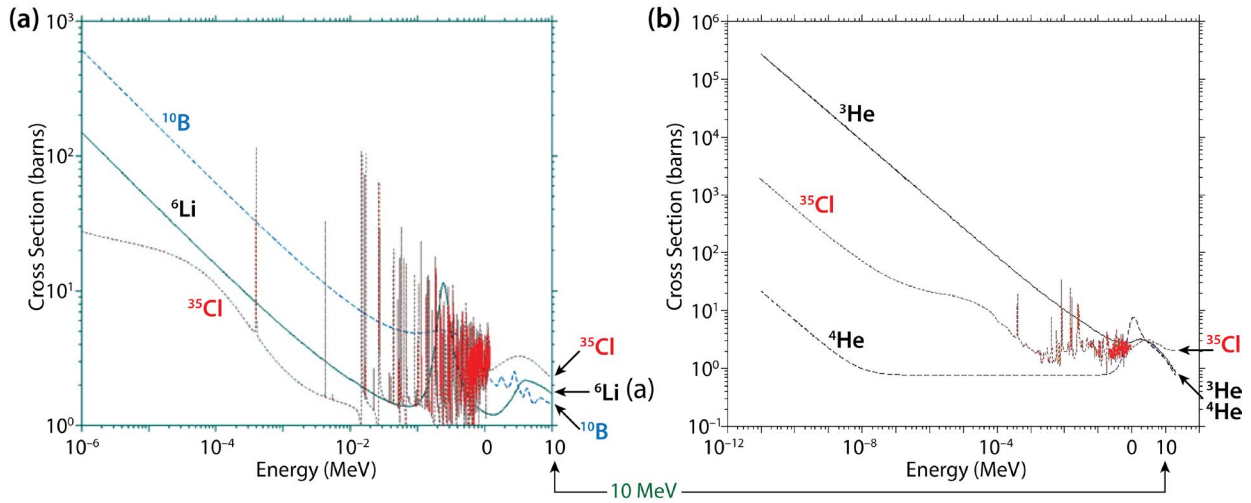

Figure 1. (a) Neutron total cross sections for ^{6}Li, ^{10}B, and ^{35}Cl; (b) neutron total cross sections for ^{3}He, ^{4}He, and ^{35}Cl

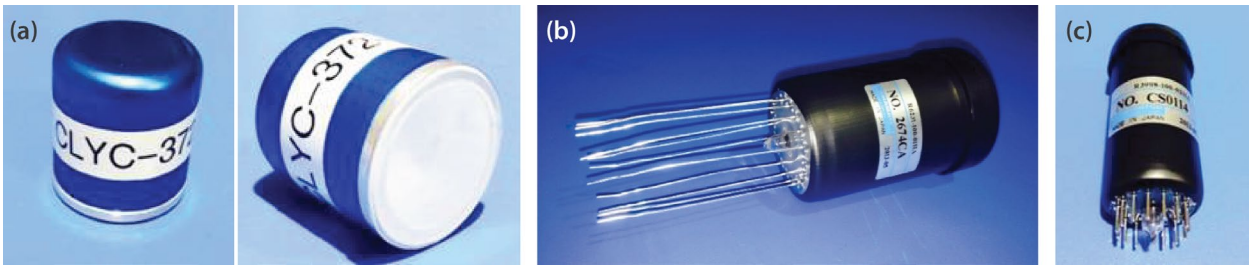

Figure 2. Components of the Elpasolite detector: (a) packaged CLYC scintillator crystal, (b) 2" diameter PMT R6231-100-01HA, (c) 1" diameter PMT R3998-100-02HA

peaking at 350 nm, and it has a gain of 2.3 × 10^5. For some of the characterization done at the University of Nevada, Las Vegas, we also used their 1" diameter SBA R3998-100-02HA (Hamamatsu) PMT, which has an identical spectral response. It is a 28 mm diameter, head-on type, SBA photocathode, 9-stage PMT with an effective area of 25 mm in diameter. Even though its gain is 1 × 10^6, there was little difference observed in the response between using either PMT. Coupling fluid and Teflon tape were used to optimize light collection. The high voltage was set to −700 V. The crystals were irradiated with gamma rays from ^{60}Co, ^{133}Ba, ^{137}Cs, ^{152}Eu, ^{228}Th, ^{235}U, ^{239}Pu, ^{241}Am, and depleted uranium (DU) sources, and were neutron-response tested using ^{241}AmBe, ^{252}Cf, and ^{239}Pu sources. Spectra were measured with a 4 µs shaping time, and the numbers for scintillation light yield were obtained from the single photoelectron response (Guillot-Noël 1999, Bessière 2004).

CLYC Detector

The CLYC scintillator/PMT system achieved at least the 8% energy resolution at 662 keV, the 20,000 ph/MeV for gammas, and the 70,000 photons/n that were reported by Bessière (2004). It achieved better than the 1-to-1000 neutron/gamma energy discrimination reported earlier (Glodo 2009b).

CLLBC Detector

Two neutron interactions exist: one with the ^{6}Li atom (thermal neutrons) and a second with the chlorine atom (fast neutrons). The CLLBC scintillator/PMT system shows an excellent response to gamma ray irradiation, with energy resolution of ~3.0% at 662 keV, 180,000 photons/n, and 50,000 ph/MeV for gammas (Bessière 2004) as well as at least a 1-to-10 neutron/gamma energy discrimination.

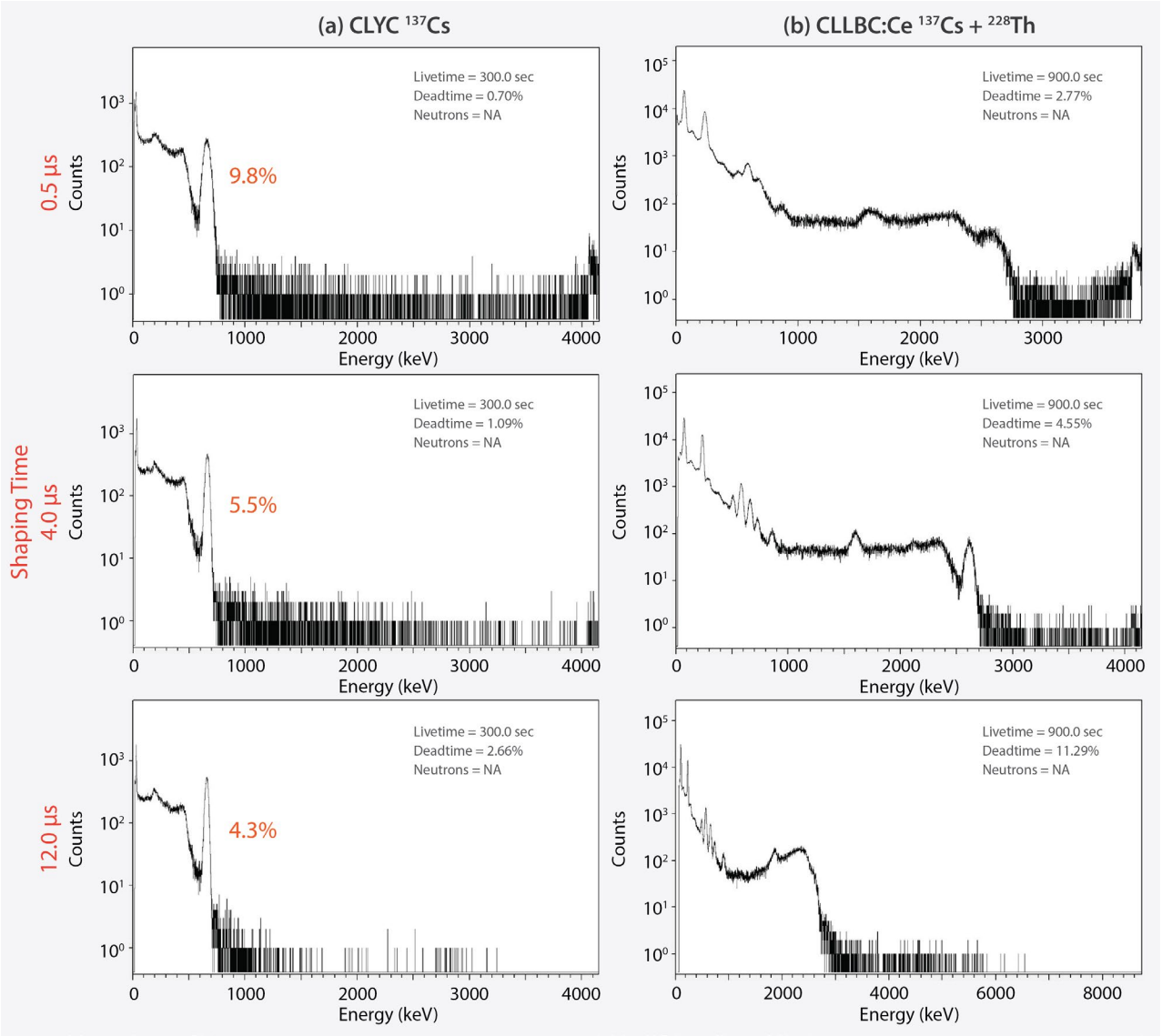

Figure 3. (a) CLYC ^{137}Cs and (b) CLLBC:Ce ^{137}Cs and ^{228}Th energy spectra for shaping times of 0.5, 4, and 12 µs

Experimental Results

We report on the scintillation response to gamma rays and thermal neutrons. When irradiated by ionizing radiation, CLYC has shown a doublet emission band at 404 and 376 nm, and $Cs_2LiYBr_6:Ce^{3+}_{0.1\%}$ a doublet emission at 423 and 389 nm. These emissions are caused by transitions from the lowest $\overline{5}d$ excited state of Ce^{3+} to the two spin-orbit split $^2F_{7/2}$ and $^2F_{5/2}$ ground state levels. Time components measuring 1–10 µs long, caused by slow energy transfer to Ce^{3+} centers, were also observed in CLLBC:Ce as well as in CLYC. CLYC crystals exhibit a 4 ns fast CVL under gamma ray excitation. Similar CVL was observed with gamma irradiation of $LiBaF_3$ (Knitel 1996), $LiBaF_3$:Ce,Rb (Combes 1998), and BaF_2 (Laval 1983); however, it is absent under alpha particle or thermal neutron irradiation (Kubota 1986, Rodnyi 1992). CVL is also absent in CLLB (van Loef 2002, Bessière 2004).

In Figure 3, we demonstrate the importance of selecting the shaping time, shown here in gamma ^{137}Cs and ^{228}Th spectra for CLYC. Different shaping times present different linearities and energy resolutions.

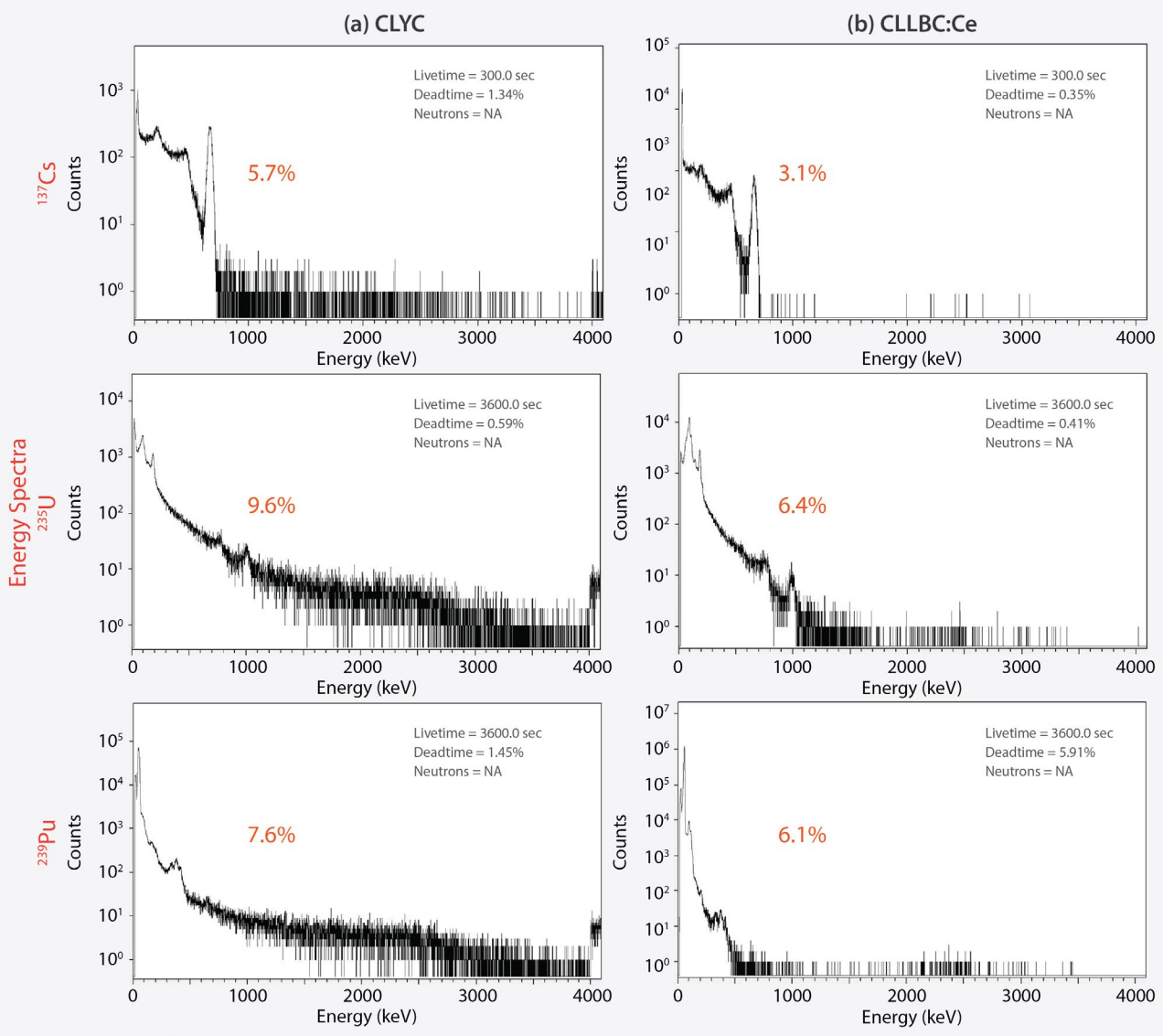

Figure 4. ^{137}Cs, ^{235}U, and ^{239}Pu energy spectra for a shaping time of 4 µs for (a) CLYC and (b) CLLBC:Ce, which has a slightly better energy resolution

The best solution is to use a 4 µs shaping time for both CLYC and CLLBC:Ce. Figure 4 presents our ^{137}Cs, ^{235}U, and ^{239}Pu energy spectra for a shaping time of 4 µs compared with CLYC (Figure 3a) and CLLBC:Ce (Figure 3b). CLLBC:Ce has a slightly better energy resolution.

Figure 5 presents spectra for the CLLBC:Ce sample. The energy resolutions of CLLBC:Ce and CLYC are compared in Figure 6. One sees, in general, a slightly superior performance for the CLLBC:Ce with regard to energy resolution. CLYC is also sensitive to thermal neutrons via the ^{6}Li(n,α)t reaction, and to fast neutrons via the ^{35}Cl(n,p) reaction (Shirwadkar 2012, D'Olympia 2013). Figure 7 displays a similar behavior exhibited by the CLLBC:Ce sample.

Analysis

The gamma-equivalent factor, F_γ, can be defined as

$$F_\gamma = \frac{GEE_n(4.78\ MeV)}{(4.78\ MeV)}, \quad (2)$$

where $GEE_n(4.78\ MeV)$ is the gamma equivalent energy of the neutron peak when 4.78 MeV energy

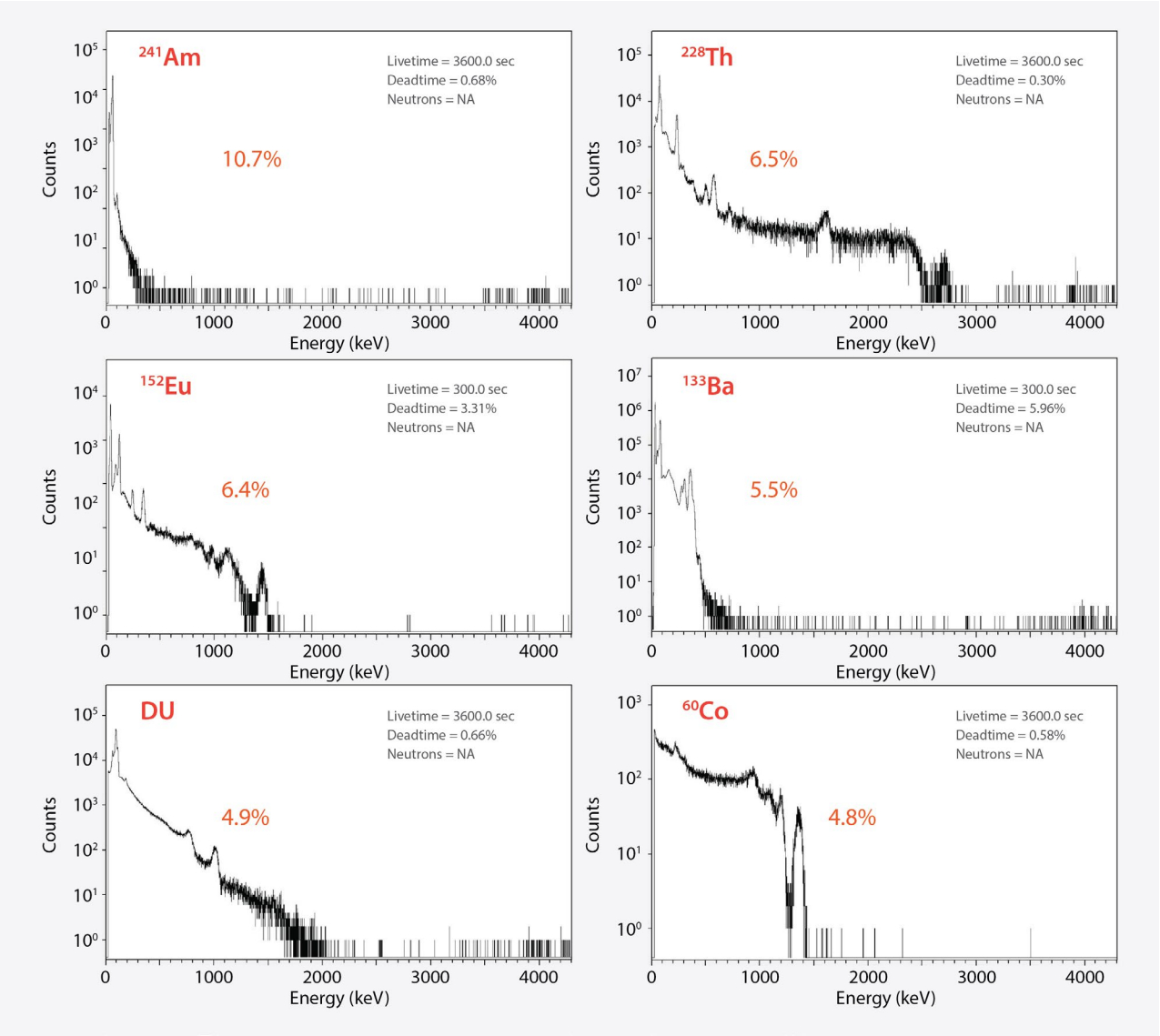

Figure 5. ^{241}Am, ^{152}Eu, DU, ^{228}Th, ^{133}Ba, and ^{60}Co energy spectra for a shaping time of 4 µs for CLLBC:Ce

is deposited in the scintillator (Bessière 2004). F_γ for CLLBC:Ce is higher than for CLYC (Table 1). We measured a figure of merit for pulse shape discrimination, $\mathrm{FOM}_{\mathrm{PSD}}$, of 2.3 and 1.73 for CLYC and CLLBC:Ce, respectively, where

$$\mathrm{FOM}_{\mathrm{PSD}} = \frac{\mathrm{centroid}_{\mathrm{neutron}} - \mathrm{centroid}_{\gamma}}{\mathrm{FWHM}_{\mathrm{neutron}} + \mathrm{FWHM}_{\gamma}}. \quad (3)$$

Resolution is a key element in looking for specific isotopes. Quarati (2013) has shown that a figure of merit (FOM_γ) may be constructed, such as

$$\mathrm{FOM}_{\gamma} = \frac{\left[s\,\varepsilon(E)t\right]}{\sigma_{\mathrm{Nbkg}}(E,t)}, \quad (4)$$

where s is the source strength, $\varepsilon(E)$ is the detection efficiency, t is the acquisition time, and $\sigma_{\mathrm{Nbkg}}(E,t)$ is the standard deviation of the intrinsic background activity count $N_{\mathrm{bkg}}(E,t)$ of the detector as a function of energy. Quarati (2013) reduces this FOM_γ into terms that relate it to the energy resolution $r(E)$ and the intrinsic background $f_{\mathrm{bkg}}(E)$ rate:

$$FOM_{\gamma} = \left[s\,\varepsilon(E)\right]\sqrt{\frac{t}{\left(f_{bkg}(E)\,r(E)\right)}}. \quad (5)$$

Figure 6 shows energy resolution obtained as a function of gamma ray energy for the CLYC and CLLBC:Ce scintillators. The data may be fit to Equation 6, composed of the photon statistics term and a "B" factor that accounts for all non-idealities in the measurement (Cherepy 2010).

$$R = \sqrt{\sqrt{\frac{A}{E}}^{2} + B^{2}}. \quad (6)$$

In Equation 6, A is a constant, E is the gamma energy, and B is required when there is deviation from pure photon statistics. Values for B obtained from fits to resolution data are shown in Table 2. A large value of B for sodium iodide (NaI:Tl) is thought to be due to its intrinsic non-proportionality. The much smaller value for $SrI_2:Eu^{2+}$ likely results from light trapping, which may be addressed by careful optical design (Glodo 2010, Sturm 2011). Using the Cherepy (2010) results for E = 200 keV, the resolution is an important factor in reduction of the false alarm rate (FAR):

$$FAR \sim \frac{r(E)^{3.4}}{\left(\frac{S_{PP}}{B_{TOT}}\right)^{0.54}}, \quad (7)$$

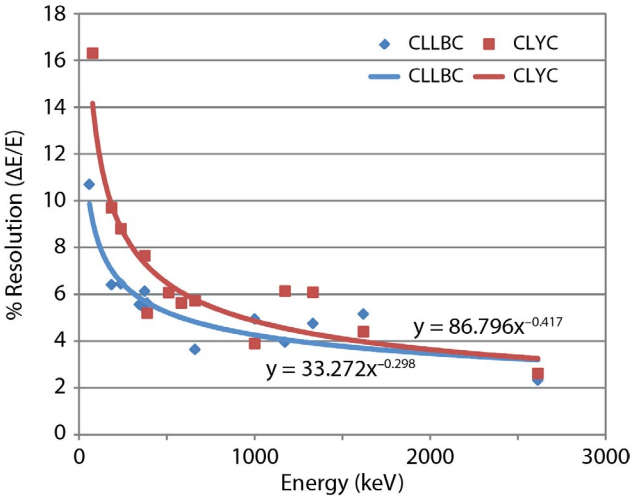

Figure 6. Energy resolutions of CLYC and CLLBC:Ce

where S_{PP} is the photopeak efficiency (product of the stopping power and the photofraction), and B_{TOT} is the sum of the natural background (B_{NAT}) and the self-radioactivity (B_{SELF}) of the scintillator (i.e., B_{SELF} is the product of the acquisition time and $f_{bkg}(E)$). FAR results, relative to the NaI:Tl $FAR_{NaI:Tl}$, for several Elpasolites are presented at the bottom of Table 2 for comparison with other scintillators (Cherepy 2010).

Conclusion

Qualities of a good detector for detection of ^{239}Pu include high resolution (i.e., better than the resolution of NaI:Tl), and low intrinsic self-activity (i.e.,

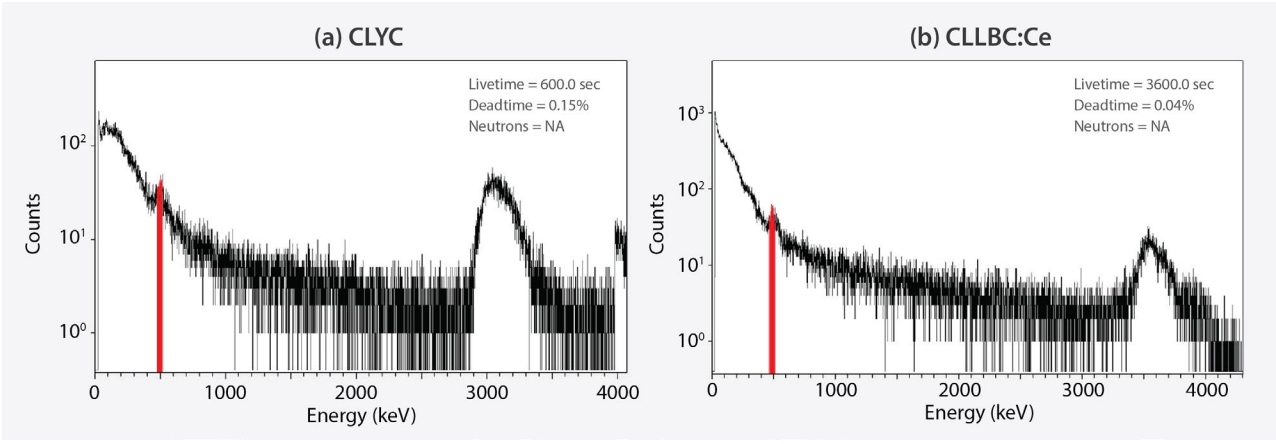

Figure 7. $^{241}AmBe$ energy spectra for both the (a) CLYC and (b) CLLBC:Ce samples. Energy windows used to determine the best fit parameters, including energy resolution (FWHM), are indicated by the red areas of integration.

Table 1. Spectrum parameters of CLYC and CLLBC

Material	Light Yield (ph/Mev)	Energy Resolution at 662 keV R_{662kev} (%)	Light Yield (ph/n)	Gamma Equivalent Factor, F_γ	Energy Resolution of neutron peak R_n (%)	Gamma Equivalent Energy, GEE_n (MeV)
CLYC	21,600	4.1	70,000	0.66	3.5	3.2
CLLBC	50,000	4.1	180,000	0.74	4.8	3.6

Note: R_n is the energy resolution of the thermal neutron peak located at the gamma equivalent energy GEE_n. It is the FWHM divided by the centroid value for this neutron Gaussian peak.

lower than that of cerium-doped lanthanum bromide, $LaBr_3$:Ce). Coincidence counting with the ^{239}Pu gamma and neutron signature may improve the overall ^{239}Pu detection sensitivity (Reilly 1991). Elpasolite detectors offer neutron and gamma detection at the same time. The directionality algorithms (Guss 2013) using arrays of Elpasolite detectors will require the best-resolution Elpasolite detectors. The ability for performing neutron and gamma detections and neutron and gamma directionality algorithms at one time improves the confidence level of the detection.

Results are summarized in Tables 1 and 2. We found photon yields for CLLBC:Ce of ~50,000 ph/MeV under gamma irradiation and ~180,000 ph/n. In that respect, CLLBC:Ce has better light yield than the well-known scintillator for neutron detection, LiI:Eu^{2+} (51,000 ph/n), and is even higher than for the best current neutron detector, LiF/ZnS:Ag^+ (160,000 ph/n) (Crawford 1993). Note that the maximum emission wavelength (419 nm) slightly exceeds by 5% the maximum sensitivity of the super bialkali PMTs. Due to a large difference in light yields depending on the type of excitation (gamma or neutron), CLLBC:Ce may be used simultaneously for neutron and gamma detection based on a simple amplitude differentiation. One may distinguish gamma rays from neutrons by PSD. CLLBC:Ce does enable fast counting rates as a neutron detector. The decay time τ = 300 ns makes CLLBC:Ce competitive with LiI:Eu^{2+} (with a 1.2 µs decay time) (Leo 1994) or LiF/ZnS:Ag^+ (with a pulse pair resolution of ~2 µs) (Rhodes 1996, Bessière 2005).

The radiation detection hardware and the data analysis software for the experiments have been set up and tested. The Monte Carlo simulations of the thermal neutron–induced photons within the volume of the CLYC and CLLBC:Ce Elpasolite detectors have been carried out. Preliminary experiments with the 25 × 25 mm CLYC and a 0.65 cc CLLBC:Ce sample were performed. Typically, the CLLBC:Ce sample presents a superior energy resolution. The energy resolutions achieved with the CLYC detector with the gamma ray sources were ~5% FWHM at 662 keV, 3.86% FWHM at 1173 keV, and 3.6% FWHM at 1332 keV. The energy resolutions achieved with the CLLBC:Ce detector with the gamma ray sources were ~3% FWHM at 662 keV, 4% FWHM at 1173 keV, and 4.8% FWHM at 1332 keV.

The preliminary PSD experiments with CLLBC:Ce using the ^{241}AmBe source were also performed. Elpasolites can be used in PHD mode to do neutron/gamma discrimination (limited by neutron peak). Elpasolites can also be used in PSD mode to do neutron/gamma discrimination. Elpasolites have good energy resolution for gamma rays. Additionally, we have determined specifications of the detectors for a directional detector array (Guss 2013). We also determined the material content to use as a hybrid CLLBC:Ce for improved sensitivity to neutrons.

Acknowledgments

The authors acknowledge the professional staff of Radiation Monitoring Devices, Inc., (RMD) Watertown, Massachusetts, for the production of the detectors, for providing these detectors to the Remote Sensing Laboratory, and for their support and advice. RMD

Table 2. Comparison of scintillator properties to consider when detecting ^{239}Pu

Scintillator	Light Yield (ph/MeV)	Energy Resolution at 662 keV (R, %)	B (Equation 6)	Energy Resolution at 200 keV (R, %)	Density (g/cc)	Photopeak Efficiency (S_{pp})	Background (B_{TOT})*	False Alarm Rate (FAR) Calculation for $FAR_{NaI:Tl}$
NaI:Tl	40,000	7%	5.3	9%	3.67	0.30	B_{NAT}	1
$LaBr_3:Ce^{3+}$	63,000	3%	0.003	5.4%	5.1	0.34	$B_{NAT} + B_{SELF}$	0.24
$CeBr_3$	63,000	4%	0.003	7%	5.2	0.34	B_{NAT}	0.40
$CeBr_3:Ca^{2+}$	---	3.2%	---	6%	5.2	0.34	B_{NAT}	0.24
$SrI_2:Eu^{2+}$	90,000	3%	1.1	4.3%	4.55	0.36	B_{NAT}	0.07
$(Gd,Y)_3(Al,Ga)_5O_{12}:Ce^{3+}$	50,000	4.8%	1.3	7.3%	6	0.38	B_{NAT}	0.43
Standard PVT	15,000	8%	---	25%	1.03	0.0006	B_{NAT}	1000
Bi-loaded polymer	10,000–30,000	8%	6.4	15%	1.2	0.08	B_{NAT}	12
CLYC	21,600	4%	0.014	8.8%	3.31	0.28	$B_{NAT} + B_{SELF}$	1.39
CLLB	50,000	3%	0.037	6.4%	4.2	0.32	$B_{NAT} + B_{SELF}$	0.44
CLLBC:Ce	50,000	3%	0.037	6.4%	4.13	0.32	$B_{NAT} + B_{SELF}$	0.44

* PVT = polyvinyl toluene; B_{NAT} = natural background; B_{SELF} = self-radioactivity

data were quoted. We would like to thank Norman Richardson, Benjamin Kaiser, John O'Donoghue, Ki Park, and Michael Mohar for their contributions to this work.

References

Bessière, A., P. Dorenbos, C. W. E. van Eijk, K. W. Krämer, H. U. Güdel, "New thermal neutron scintillators: Cs_2LiYCl_6:Ce and Cs_2LiYBr_6:Ce," *IEEE Trans. Nucl. Sci.* **51**, 5 (2004) 2970–2972.

Bessière, A., P. Dorenbos, C. W. E. van Eijk, K. W. Krämer, H. U. Güdel, "Luminescence and scintillation properties of Cs_2LiYCl_6:Ce for gamma and neutron detection," *Nucl. Instrum. Methods Phys. Res. A* **537** (2005) 242–246.

Bodnarik, J. G., D. M. Burger, A. Burger, L. G. Evans, A. M. Parsons, J. S. Schweitzer, R. D. Starr, K. G. Stassun, "Time-resolved neutron/gamma-ray data acquisition for in situ subsurface planetary geochemistry," *Nucl. Instrum. Methods Phys. Res. A* **707** (2013) 135–142.

Cherepy, N. J., et al., "Comparative gamma spectroscopy with SrI_2(Eu), GYGAG(Ce) and bi-loaded plastic scintillators," *Nucl. Sci. Symp. Conf. Record (NSS/MIC) 2010 IEEE* (2010) 1288–1291.

Combes, C. M., P. Dorenbos, R. W. Hollander, C. W. E van Eijk, "A thermal-neutron scintillator with n/γ discrimination LiBaF: Ce,Rb," *Nucl. Instrum. Methods Phys. Res. A* **416** (1998) 364–370.

Crawford, R. K., "Position-sensitive detection of slow neutrons – survey of fundamental principles," *Proc. SPIE* **1737** (1993) 210–223.

Dinca, L. E., P. Dorenbos, J. T. M. De Haas, V. R. Bom, C. W. E. van Eijk, "Alpha–gamma pulse shape discrimination in CsI:Tl, CsI:Na and BaF_2 scintillators," *Nucl. Instrum. Methods Phys. Res. A* **486** (2002) 141–145.

D'Olympia, N., P. Chowdhury, C. J. Lister, J. Glodo, R. Hawrami, K. Shah, U. Shirwadkar, "Pulse-shape analysis of CLYC for thermal neutrons, fast neutrons, and gamma-rays," *Nucl. Instrum. Methods Phys. Res. A* **714** (2013) 121–127.

Dubi, C., T. Ridnik, I. Israelashvili, B. Pedersen, "A novel method for active fissile mass estimation with a pulsed neutron source," *Nucl. Instrum. Methods Phys. Res. A* **715** (2013) 62–69.

Glodo, J., R. Hawrami, E. van Loef, W. Higgins, U. Shirwadkar, K. S. Shah, "Dual gamma neutron detection with $Cs_2LiLaCl_6$," *Proc. SPIE* **7449** (2009a) 74490E-1.

Glodo, J., W. M. Higgins, E. V. D. van Loef, K. S. Shah, "Cs_2LiYCl_6:Ce scintillator for nuclear monitoring applications," *IEEE Trans. Nucl. Sci.* **56**, 3 (2009b) 1257–1261.

Glodo, J., E. V. van Loef, N. J. Cherepy, S. A. Payne, K. S. Shah, "Concentration effects in Eu doped SrI_2," *IEEE Trans. Nucl. Sci.* **57**, 3 (2010) 1228–1232.

Glodo, J., E. V. D. van Loef, R. Hawrami, W. M. Higgins, A. Churilov, U. Shirwadkar, K. S. Shah, "Selected properties of Cs_2LiYCl_6, $Cs_2LiLaCl_6$, and $Cs_2LiLaBr_6$ scintillators," *IEEE Trans. Nucl. Sci.* **58**, 1 (2011) 333–338.

Guillot-Noël, O., J. T. M. De Haas, P. Dorenbos, C. W. E. van Eijk, K. W. Krämer, H. U. Güdel, "Optical and scintillation properties of cerium-doped $LaCl_3$, $LuBr_3$ and $LuCl_3$," *J. Lumin.* **85** (1999) 21–35.

Guss, P., S. Mukhopadhyay, "Dual gamma/neutron directional Elpasolite detector," *Proc. SPIE* **8854** (2013) 885402.

Henzl, V., S. Croft, J. Richard, T. Swinhoe, S. J. Tobin, "Determination of the plutonium content in a spent fuel assembly by passive and active interrogation using a differential die-away instrument," *Nucl. Instrum. Methods Phys. Res. A* **712** (2013) 83–92.

Knitel, M. J., P. Dorenbos, J. T. M. De Haas, C. W. E. van Eijk, "$LiBaF_3$, a thermal neutron scintillator with optimal n-γ discrimination," *Nucl. Instrum. Methods Phys. Res. A* **374** (1996) 197–201.

Kubota, S., M. Suzuki, J. Ruan, F. Shiraishi, Y. Takami, "Variation of luminescence decay in BaF_2 crystal excited by electrons, alpha particles and fission fragments," *Nucl. Instrum. Methods Phys. Res. A* **242**, 2 (1986) 291–294.

Laval, M., M. Moszynski, R. Allemand, E. Cormoreche, P. Guinet, R. Odru, J. Vacher, "Barium fluoride—inorganic scintillator for subnanosecond timing," *Nucl. Instrum. Methods Phys. Res. A* **206**, 1–2 (1983) 169–176.

Leo, W. R., *Techniques for Nuclear and Particle Physics Experiments: A How-To Approach*, 2nd edition, Springer-Verlag, Berlin, Germany, 1994, 157–334.

McFee, J. E., A. A. Faust, K. A. Pastor, "Photoneutron spectroscopy using monoenergetic gamma rays for bulk explosives detection," *Nucl. Instrum. Methods Phys. Res. A* **704** (2013) 131–139.

Menlove, H. O., S. H. Menlove, C. D. Rael, "The development of a new, neutron, time correlated, interrogation method for measurement of ^{235}U content in LWR fuel assemblies," *Nucl. Instrum. Methods Phys. Res. A* **701** (2013) 72–79.

Mukhopadhyay, S., C. Stapels, E. B. Johnson, E. C. Chapman, P. S. Linsay, T. H. Prettyman, M. R. Squillante, J. F. Christian, "Comparison of neutron sensitive scintillators for use with a solid-state optical detector," *Proc. SPIE* **7449** (2009) 74491P.

Quarati, F. G. A., "Scintillation and detection characteristics of high-sensitivity $CeBr_3$, gamma-ray spectrometers," *Nucl. Instrum. Methods Phys. Res. A* **729** (2013) 596–604.

Reeder, P. L., S. M. Bowyer, "Neutron/gamma discrimination in LiBaF scintillator," *J. Radioanal. Nucl. Chem.* **248**, 3 (2001) 707–711.

Reilly, D., N. Ensslin, H. Jr. Smith, S. Kreiner, eds., *Passive Nondestructive Assay of Nuclear Materials*, NUREG/CR-5550, LA-UR-90-732, Los Alamos National Laboratory, Los Alamos, NM, 1991, 447.

Rhodes, N. J., N. W. Johnson, "The role of inorganic scintillators in neutron detector technology," *Proc. Int. Conf. Inorganic Scintillators and Their Applications*, Delft University Press, The Netherlands (1996) 73–85.

Rodnyi, P. A., "Core-valence band transitions in wide-gap ionic crystals," *Sov. Phys. Sol. State* **34** (1992) 1053–1066.

Shirwadkar, U., R. Hawrami, J. Glodo, E. V. D. van Loef, K. S. Shah, "Novel scintillation material $Cs_2LiLaBr_{6-x}Cl_x$:Ce for gamma-ray and neutron spectroscopy," *Proc. Nuclear Science Symposium and Medical Imaging Conference (NSS/MIC)* (2012).

Sturm, B. W., et al., "Effects of packaging SrI_2(Eu) scintillator crystals," *Nucl. Instrum. Methods Phys. Res. A* **652**, 1 (2011) 242–246.

van Loef, E. V. D., P. Dorenbos, C. W. E. van Eijk, K. W. Krämer, H. U. Güdel, "Scintillation and spectroscopy of the pure and Ce^{3+}-doped Elpasolites: Cs_2LiYX_6 (X = Cl; Br)," *J. Phys. Condens. Matter* **14** (2002) 8481–8496.

This page left blank intentionally

High-Resolution Flash Neutron Radiography of Dense Objects

NLV-26-14 | Year 1 of 1

E. Chris Hagen,[1,a] Daniel Lowe,[a] Steve Molnar,[a] Aaron Luttman,[a] Jeremy Chittenden,[b] Brian Applbe,[b] and Frank Kosel[c]

While the concept of how dense plasma focus (DPF) machines operate is simple, the plasma physics of the underlying processes is complex and not well understood, even after five decades of study throughout the world. With the advent of more powerful computational capabilities and the continuing advance of diagnostic instrumentation, modern theory can be advanced by comparing predictions to observations. In turn, new understanding from improved predictive codes may lead to further improvements in DPF performance. In this study, the time evolution of the complex process that results in heated compression of rarified gas in a DPF was imaged with nanosecond resolution and millimeter spatial resolution. A new and novel optical arrangement that enabled simultaneous axial and radial imaging along the z-axis and orthogonal to the z-axis was conceived, developed, and implemented; these experiments employed an intensified commercial framing camera system. Collaboration with plasma theorists at Imperial College was initiated; furthermore, existing NSTec capabilities using magnetohydrodynamic (MHD) codes were also investigated. Data were acquired as a series of 16 images of a single DPF process sequence, in which individual image exposures were as short as 5 ns, separated by intervals as short as 10 ns. Images were taken during the nuclear fusion–producing process using pure deuterium, or deuterium with admixtures of small amounts of krypton. Features of process initiation (plasma sheath formation), plasma sheath transport from the initiation point to the fusion location, and the final portion of the z-pinch process that produces fusion were imaged. In parallel, standard 1-D time-of-flight techniques recorded time histories of fusion neutrons, x-rays, and gamma rays. We present a comparison of theoretical predictions to measurements, the relationship of DPF machine operational data to optical data, and the relationship to neutron diagnostic data in this report. FWHM analyses of the optical pinch size show it to be ~3 mm. This size correlates well with predictions obtained from the GORGON MHD hybrid code used by Imperial College London. It is not fully understood, however, how the optical pinch size correlates to the neutron spot size; thus, further research should be undertaken to understand this correlation. Finally, a time-resolved neutron image sequence of a tungsten block behind a scintillator was demonstrated using the Gemini deuterium-deuterium source in an attempt to estimate the neutron spot size from first principles.

[1] hagenec@nv.doe.gov, 702-295-4712
[a] North Las Vegas; [b] Imperial College; [c] Specialised Imaging

Background

Future subcritical experiments at the NNSS are planned to include neutron-based measurements, including neutron radiography. Because neutrons and x-rays penetrate matter differently, neutron radiography and x-ray radiographic experiments provide distinct yet complementary information. When the

first Neutron-Diagnosed Subcritical Experiment (NDSE) is fielded, it is likely that a neutron image looking down a separate line-of-sight, taken during maximum compression, can be obtained using the same dense plasma focus (DPF) neutron pulse used to cause fission in the NSDE target. The NDSE experiment infers the fission rate by measuring fission photons.

NSTec has built a state-of-the-art DPF machine that produces 14 MeV neutrons as a prototype for the emerging NDSE experimental program. The technologies developed in this SDRD project can be used to optimize the performance of neutron radiographic systems and also to further understand the plasma physics of the DPF itself.

Project

This one-year SDRD project set out to measure the optical pinch size of the deuterium-deuterium (D-D) DPF, compare theory with experimental data, and, if the high-yield DPF under construction were to become operational during this project, estimate the neutron spot size of the beam-target interactions.

The NSTec Gemini 1-megajoule DPF was used to provide the plasma to be photographed. Special hardware was designed to enable optical access to the DPF. Ultra high–speed framing cameras from Specialised Imaging (2015), placed 33 meters from the source, acquired images. Telephoto lenses were used to fill the camera's image plane with the DPF object to be measured. Relay mirrors enabled the camera to be shielded from the direct radiation generated during the short DPF pulses. It was desirable to image the DPF both looking along the z-axis (i.e., axially, or Z view), and looking perpendicular to it (i.e., radially, or R view). To accomplish this, a new optical system was designed, and DPF tubes with large apertures were constructed. To measure the pinch spot size in the optical regime, our optical system used a fully mirrored copper plate placed at a 45° angle at the bottom of the chamber, as shown in Figure 1. This system allows truly simultaneous Z and R images of the DPF shot. Because the mirror is damaged in a single shot, and becomes unusable after several shots, precise mirror-changing procedures were implemented to ensure the machine would pinch on the first shot after the vacuum was broken.

To sufficiently resolve the optical spot size in both time and space, a Specialised Imaging SIMX 16-frame intensified camera (Specialised Imaging 2015) was used to study the sheath formation, pinch collapse, and pinch breakup for over 100 DPF shots. Understanding the dynamics of the imaging system took significant effort. The images we obtained in the first simultaneous

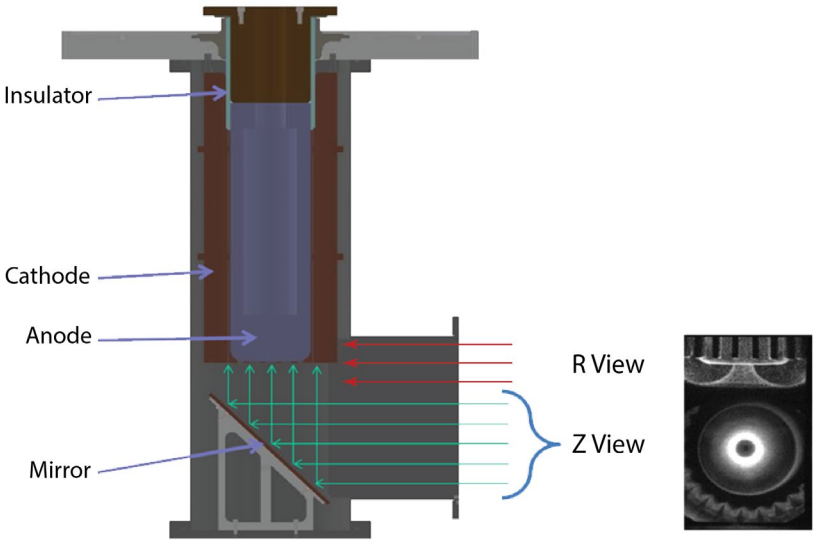

Figure 1. Experimental layout for simultaneous optical imaging in Z and R views

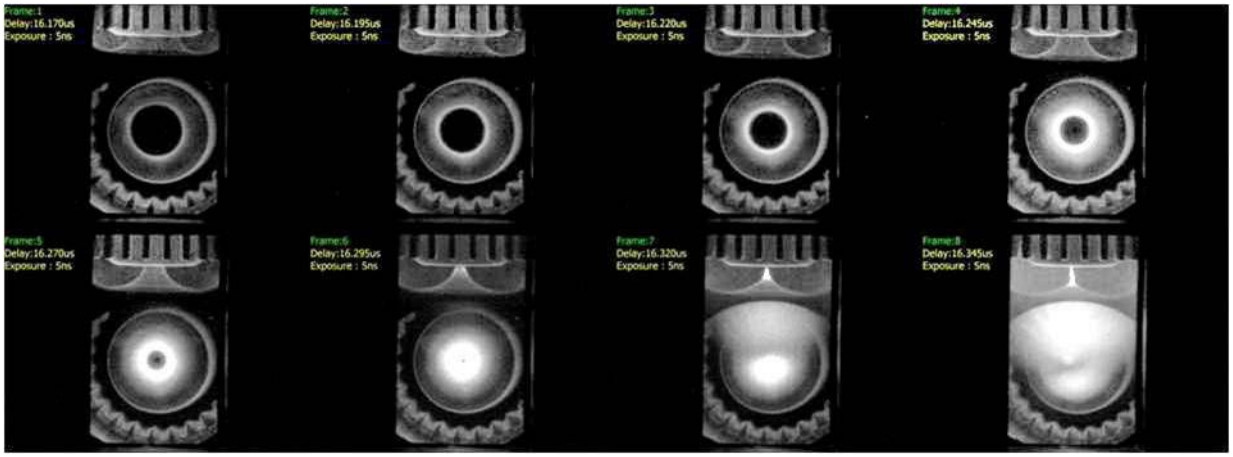

Figure 2. The first 8 of 16 total frames of a successful image sequence were captured while the mirror was clean, the pixel intensity in the pinch region was not saturated, and the machine pinched and produced neutrons on the first shot after vacuum was broken. Each frame has a radial view on the top and a simultaneous axial view below.

Z and R image sequence showed a larger than expected spot size. We then noticed that ~7–8 pixels in the pinch region were overexposed beyond the 4095 levels that could be recorded by the microchannel plate. It was determined that because the camera was an intensified version, phosphor spillover was dominating the spot size. Phosphor spillover occurs when a local area of the phosphor screen is significantly brighter than the surrounding areas. The manufacturer estimates that phosphor spillover can be as large as 5 to 10 pixels, a significant number, compared to typical CCD spillover, which is typically 1 to 2 pixels. For pinch size measurements, a follow-on imaging run was conducted to ensure that all pixels in the pinch region were within the optical system's dynamic range; this is a very difficult task to accomplish. The results from this successful image are shown in Figure 2.

Data in Figure 2 were taken with a 1% krypton mixture with a 99% deuterium backfill forming the plasma. The Gemini D-D machine was charged to 35 kV and filled to a total pressure of 3.0 Torr, which produced a total current maximum of 2.1 MA and neutron yield of 1.5×10^{11}. The top portion of the images clearly show the current sheath run-in, compression, and pinch phase. The total time between frames 1 and 8 is 175 ns, with a 25 ns interframe time and 5 ns exposure time. Analysis of this image is presented in the ***Results*** section.

Results

One of the major goals of this project was to verify the accuracy of the advanced modeling capabilities of predictive codes when used to model the performance of large, megajoule DPF machines. Collaboration between the DPF experimental team, the NSTec modeling team, and Imperial College was formed. The DPF design team provided CAD models and operating parameters for a certain tube design that was fielded on the Gemini system. This system definition was provided to the Imperial College and NSTec modeling teams. DPF parameters such as run-down time, neutron yield, time-dependent neutron yield, plasma jet velocities, and plasma temperatures were simulated. Because ALEGRA (a pure magneto-hydrodynamic [MHD] code) cannot simulate the physics required for beam-target interactions and LSP (a particle-in-cell [PIC] code) executes too slowly to finish a DPF simulation in a reasonable time period, only the Imperial College group, who uses a hybrid MHD-PIC process that they developed, was able to provide insight on the neutron production physics. The basis of their calculation was use of the Gemini physical parameters, with currents in the same range as these data were taken.

Comparison of GORGON Simulations with Optical Observations

Figure 3 shows both qualitative and quantitative comparisons of Imperial College simulations as they compare to optical framing camera data. The images clearly show the general shape of the main plasma sheath is correct, as well as being correct with respect to the first Mach jet stem. Analysis of the framing camera pictures show the Mach jet having a mean velocity of 360 ±60 km/s, and the Imperial College simulation estimates the Mach jet at 390 ±40 km/s, which is in good agreement.

Optical Pinch Size Analysis

An important geometric quantity to be computed from the optical video imagery is the time evolution of the optical pinch size. As seen in Figure 3a, the pinch occurs near the anode; the image is zoomed on the tip of the anode, leaving about 70 mm above the anode in the frame. For each shot, the video is viewed to determine in which frames the pinch begins and ends. Then each zoomed-in frame containing pinch dynamics is smoothed with a Gaussian filter of window size of 11 × 11 pixels and σ = 3 (Figure 4). The optical pinch is extracted from each frame using the k-means clustering algorithm (Lloyd 1982).

The segmented optical pinches are shown for frames 4–6 of Shot 2 (Figure 4) and for frames 7–10 of Shot 4 (Figure 5). The frames were spaced 25 ns apart. The shots were executed on September 29, 2014.

The first moment the pinch formed is shown in frame 4 of Shot 2 (Figure 4a); it can be seen that the pinch forms as a tall tube, potentially with so-called "sausage instabilities" visible in the middle. As time evolves, the pinch detaches from the anode and moves away (up in these images). In frame 4, the pinch is 26.8 mm tall, then 24.0 mm in frame 5 (Figure 4b), and 18.4 mm in frame 6 (Figure 4c). By frame 7 the pinch has essentially dissolved, and length can no longer be extracted.

Shot 4 (Figure 5) is similar, except that the pinch forms (frame 7, Figure 5a) as a short and thick region, then evolves to being long and slender (frame 8, Figure 5b) before evolving back to a short and thick region (frames 9–10, Figures 5c–5d). In frames 9 and 10, the pinch has again detached from the surface of the anode. In frame 7 the pinch is 12.8 mm tall, and then evolves to 24.4 mm, 20.8 mm, and 12.0 mm in frames 8–10, respectively.

Figure 6 shows the widths of the pinch in each frame, as a function of the height above the anode. For Shot 2 (Figure 6a), the pinch at the anode starts at 2 mm

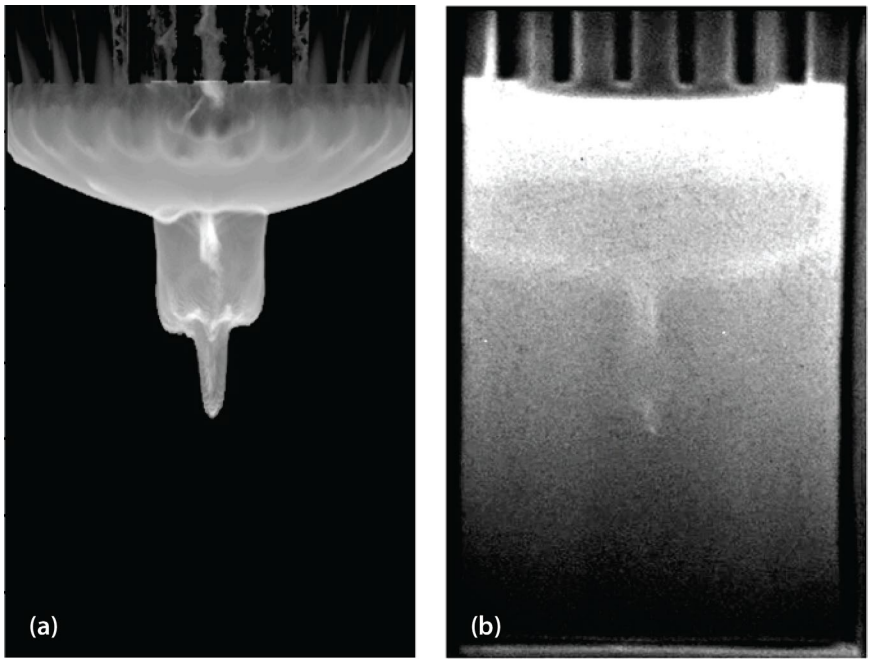

Figure 3. (a) A synthetic image, created by Imperial College, at ~500 ns after the pinch compared to (b) observed framing camera data. The cathode is ~10 inches in diameter across the R dimension.

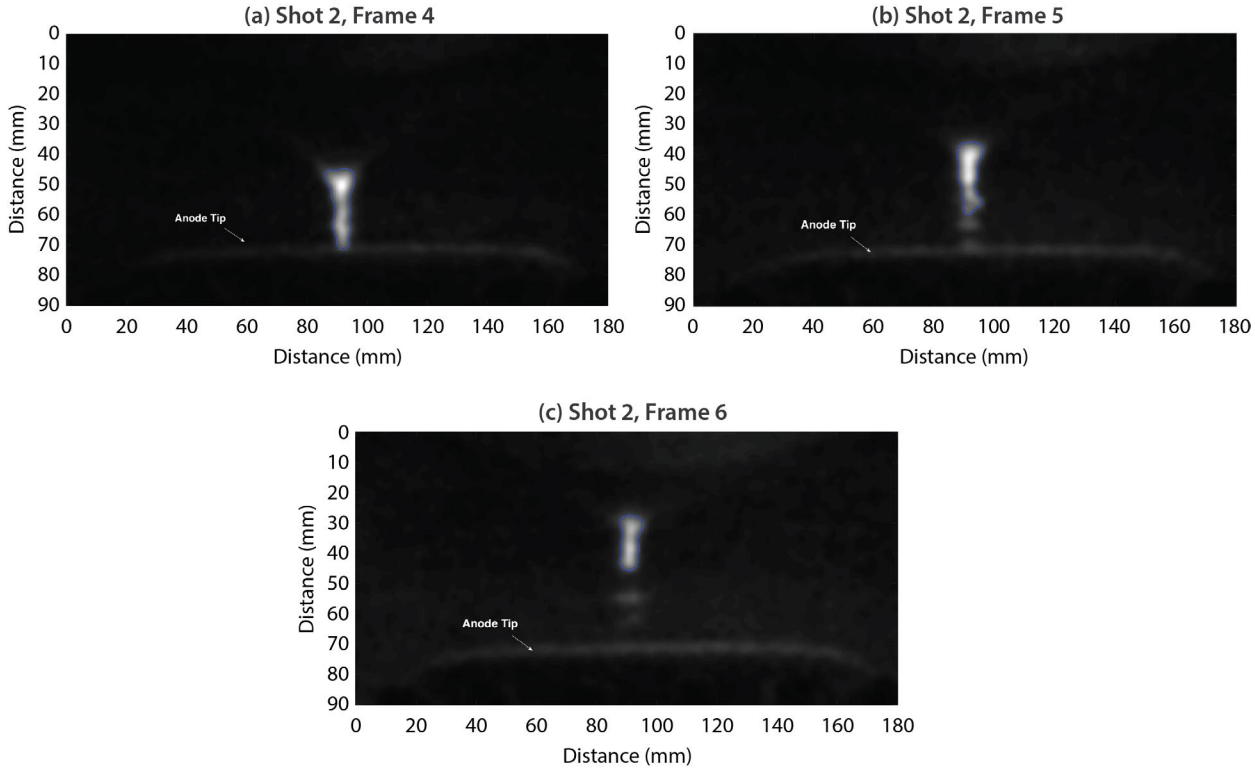

Figure 4. The optical pinch extracted from the images using the k-means clustering algorithm for Shot 2 on September 29, 2014.

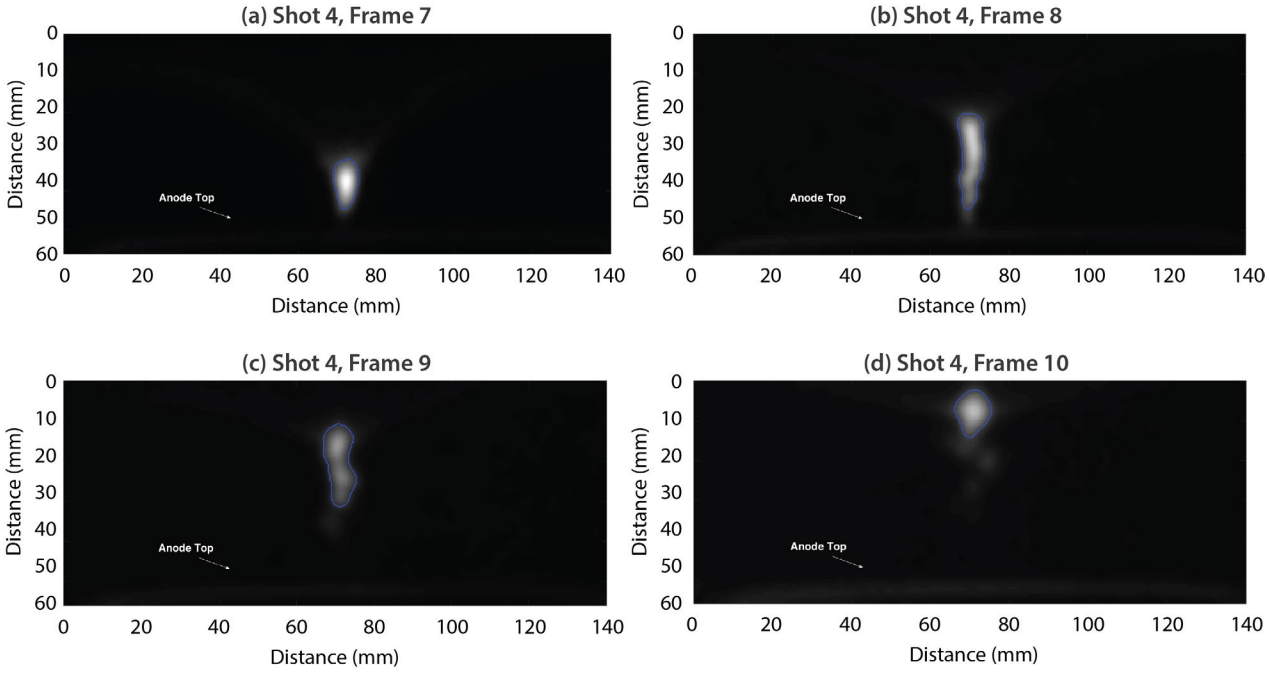

Figure 5. The optical pinch extracted from the images using the k-means clustering algorithm for Shot 4 on September 29, 2014.

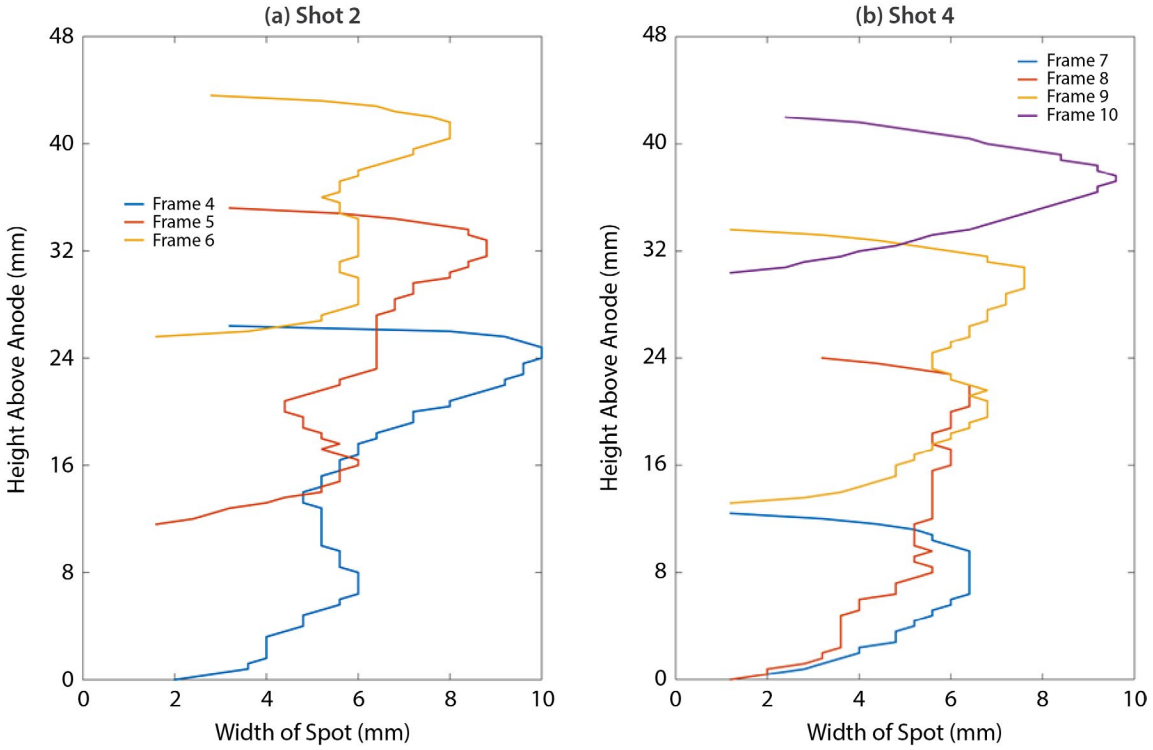

Figure 6. The width of the optical pinch as a function of the height above the anode for each frame containing the pinch in (a) Shot 2 and (b) Shot 4

wide and increases to 10 mm wide at a height of 24 mm above the anode. By frame 6, the optical pinch region ranges from ~2 mm wide at a height of 24 mm above the anode to 8 mm wide when 40 mm above the anode. For Shot 4 the results are nearly the same, with the pinch width ranging from just ~6 mm when 8 mm above the anode to ~10 mm when 40 mm above the anode.

Validating GORGON Simulations Against the Optical Imagery

The time-integrated neutron spot size as predicted by the Imperial College GORGON code is shown in Figure 7. These results are for the beam target–produced neutrons only; it is now widely agreed within the scientific community that DPFs are primarily beam-target devices, and do not produce neutrons via a thermonuclear mechanism.

The beam-target spot size is calculated by a combination of an MHD code (GORGON) and a post-processing routine with PIC capabilities, a specialized in-house code to Imperial College. The hybrid code uses time-dependent information from the MHD simulations (electric field, magnetic field, plasma density) to track deuteron ions through the simulation volume. The beam-target reaction rate can then be calculated by knowing the ion velocity and gas density, to produce a neutron reaction rate. The simulated neutron spectrum is also shown in Figure 7, which shows a significant beam-target contribution. If the directions of the ion velocities were not aligned as they are in a beam, but rather randomly oriented in the center of mass, then the observed "side on" energy distribution would be peaked about the 2.45 MeV escaping neutron energy.

Extracting the Optical Shock Front and Computing Its Velocity

In order to assess the validity of simulations of the DPF, it is necessary to validate the codes against quantities that can be measured directly or computed from the fielded diagnostics. One such quantity is the velocity of the plasma sheath as it "runs in" from the edge

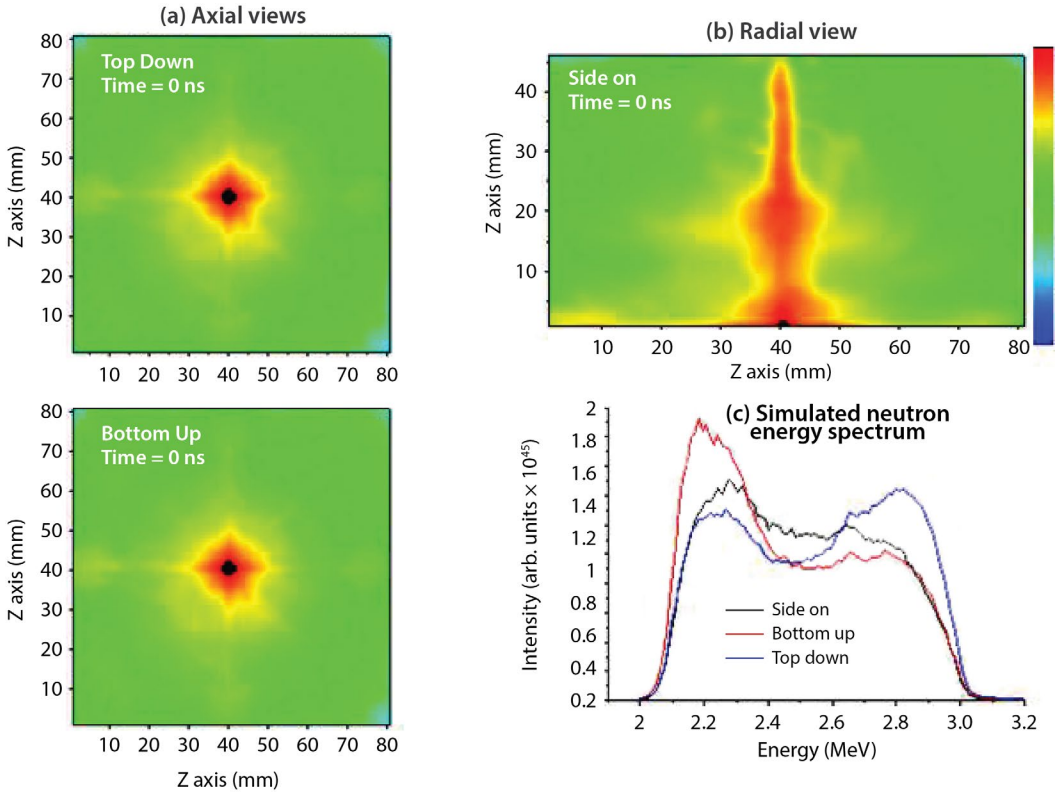

Figure 7. Imperial College hybrid MHD/PIC simulation results for beam target–produced neutrons. Here, the FWHM estimate for beam-target-created neutrons is ~2 mm. The mesh size of the simulation (1 mm) limits the accuracy of the FWHM estimation. (a) Top up and top down are axial views; (b) side-on is the radial view; (c) the graphs shows the neutron energy spectrum as predicted by the simulation.

of the anode to the pinch. This cannot currently be measured directly, but the optical imagery does allow us to extract the optical shock front—which we treat as a surrogate for the true plasma shock front—and compute its velocity.

As with the spot size computation, the first two steps in the optical shock front extraction are to zoom in on the region just above the anode and smooth the images with a Gaussian filter with window size of 11 × 11 pixels and σ = 5. The optical front is defined to be the ridge of local maxima in intensity that moves up from the anode (Figure 8). In order to enhance the ridge, the data are also processed with a Split Bregman (Goldstein 2009) approach to total-variation (Rudin 1992) denoising. This technique calculates the best piecewise constant approximation to the data, in the least squares sense.

Given the total-variation smoothed data, a data mask is drawn around the shock front in each frame before the pinch, and the pixels of maximum intensity in each row are computed. These points are shown as black crosses in Figure 8 for frames 1–6 from Shot 4. The points of maximum intensity are then fit to a cubic smoothing spline, which is shown as the white curve in each of the frames of Figure 8. From the computed curve, the horizontal component of the velocity can be computed.

Figure 9a shows the optical shock running in and four horizontal lines along which the horizontal velocity of the shock front is computed. The velocities are shown in Figure 9b, where the solid curves correspond to the left velocity of the optical shock run-in, and the dashed curves indicate the right velocity of the run-in shock. Figure 9c shows the left and right optical shock

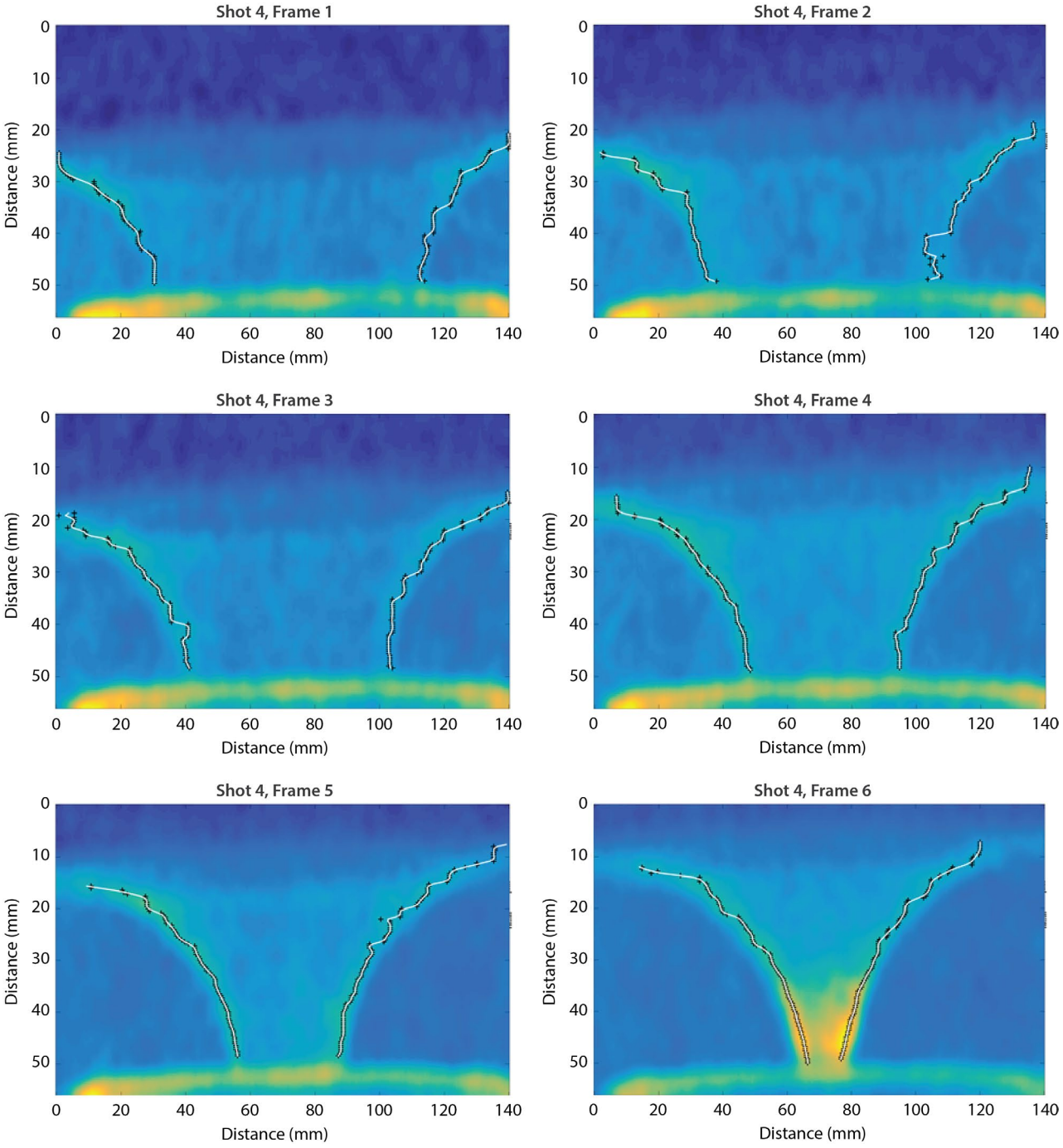

Figure 8. Extraction of the optical shock front for frames 1–6 for Shot 4. The top of the anode is the horizontal region of yellow across the bottom of each frame, the black crosses represent the optical shock front points in each row, and the white curve is a spline fit to the extracted points.

velocities averaged spatially. These images show that, broadly speaking, the velocity increases as the shock gets closer to the pinch and that the left and right sides are running in at close to the same velocities. The shock speeds range from 200 to 400 km/s (20 to 40 cm/ms), which is not enough to generate the pressures needed for thermonuclear fusion at the pinch, further reinforcing the evidence that the primary

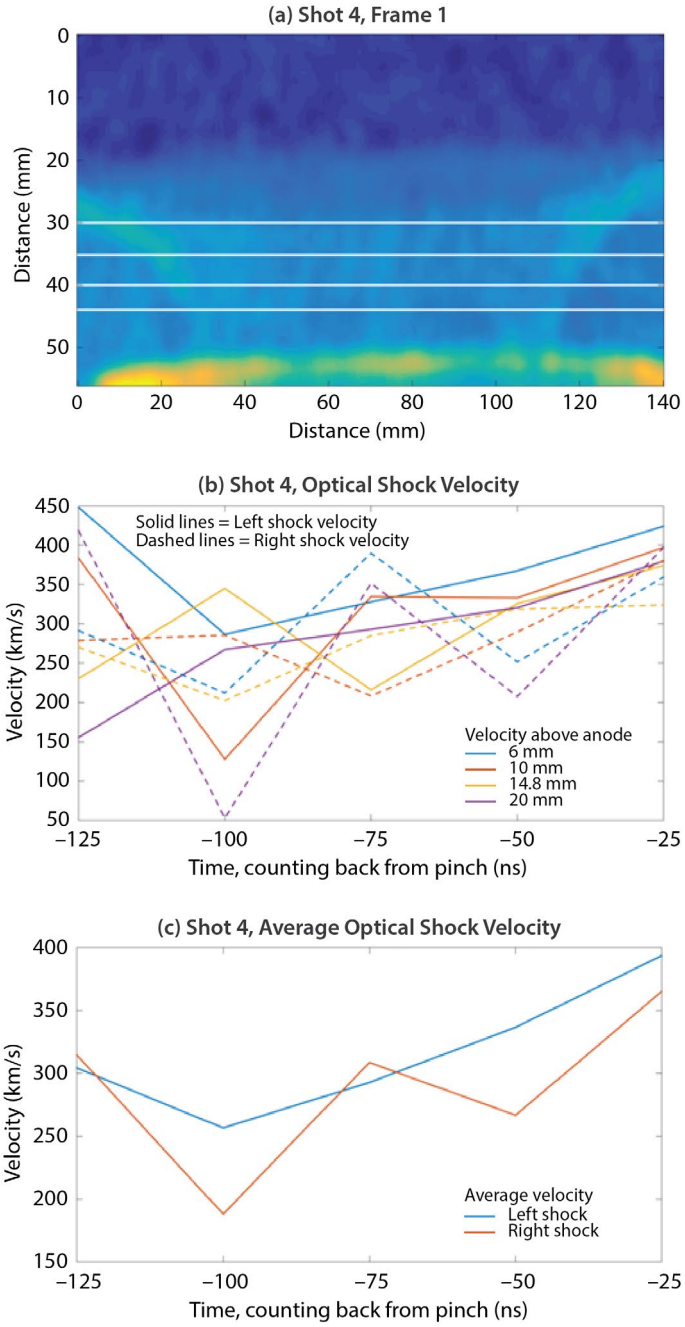

Figure 9. (a) A frame showing the optical front running in towards the pinch and the lines along which the horizontal velocity is computed. (b) A plot of the velocities as a function of time along the four lines. Each white horizontal line in (a) has a corresponding velocity for the front running from the left towards the center (solid) and from the right towards the center (dashed curve). (c) Average optical left and right shock velocities averaged over the horizontal lineouts.

mechanism of neutron creation is beam-target fusion. Note that the temporal resolution is not fine enough to draw conclusions about the fine-scale structures in these velocity calculations.

Shown in Figure 10 are a tungsten cylinder and a neutron image acquired with the high-speed framing camera. As the high-yield programmatic deuterium-tritium (D-T) DPF was not yet available for imaging, this test was performed using the 1-megajoule Gemini D-D DPF, which has a yield approximately 100 times lower than the D-T source. It did provide information to estimate the threshold at which high-speed neutron radiography becomes feasible. As the image illustrates, faint images at the 10^{11} 2.45 MeV neutrons per pulse level can be acquired, but for quantitative work more fluence, use of 14 MeV neutrons, and an optically more efficient optical system must be employed.

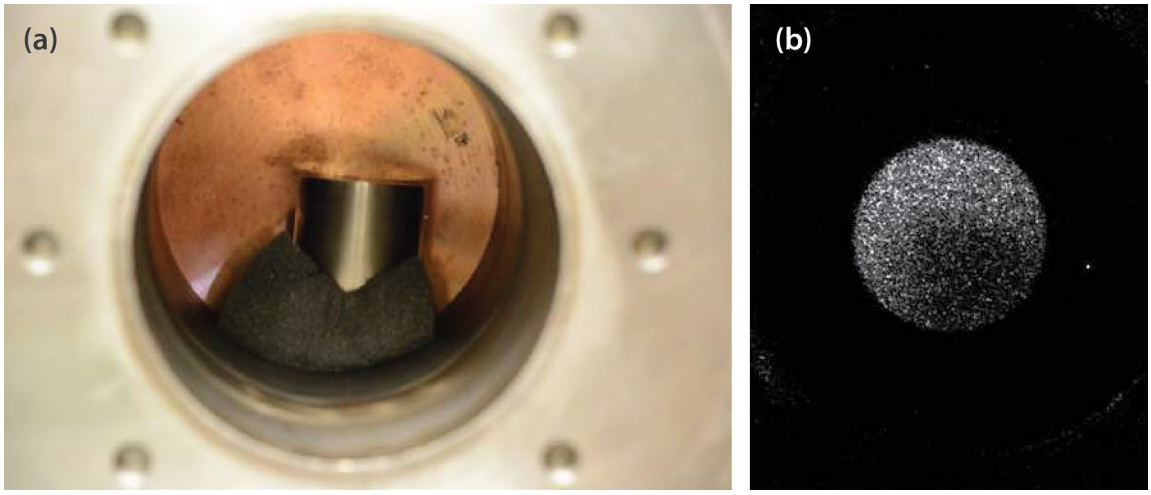

Figure 10. (a) Experimental setup and (b) results of a tungsten block in front of a BC-400 scintillator. Framing camera images were stacked (16 individual frames) and timed for neutron output.

Specific yield levels necessary to quantify a specific experimental variable (presence, shape, density, etc.) vary greatly. They depend on the goals of an experiment, and on many experimental variables. A Los Alamos National Laboratory (Merrill 2013) study concludes that a "DT DPF source, generating 10^{14} neutrons per ~50 ns pulse in a 1 mm source, at the NNSS could provide a remarkable source for flash neutron radiography. This source could provide radiographs with 1 mm uncorrected spatial resolution and 2% density resolution within a spatial resolution element. Standard reconstruction algorithms, such as exist in the BIE, could be implemented to improve the resolution of the imaging system to sub-mm resolution." Thus, some quantitative measurements are already practical with the existing yields being produced with the D-T DPF at the NNSS. When the yield is increased to approach 10^{14} neutrons per ~50 ns pulse, it is believed that very high–resolution data could be obtained.

Conclusion

High spatial–resolution, nanosecond, time-resolution imaging in the equipment-hostile DPF environment has been demonstrated. Predictive calculations made using GORGON show very good agreement with optical data. The threshold of neutron imaging at the 10^{11} yield level (using lens optics with 2.45 MeV neutrons) has been established. Further, as the neutron source when viewed end on is nearly a point source, neutron radiographs with resolutions in the millimeter regime may be acquired, as shown by the optical data and the theoretical predictions. With the recent startup of the NSTec D-T DPF, which has produced yields of $\geq 1 \times 10^{13}$, well-defined shadowgraphs are possible. With planned increases in D-T yield beyond this level, based on use of optimized tube geometry and capacitor banks, possibly augmented further with gas puff and other technologies, detailed radiographs will be possible. Finally, the project has already resulted in two technologies being transferred to programmatic use: (1) NSTec has procured a framing camera that will be used in future radiographic experiments at the NNSS, and (2) our collaboration with Imperial College has established a capability for advanced computational prediction.

Acknowledgments

The authors would like to thank Stuart Baker for a loan of his camera to this project, which allowed acquisition of additional data; we also would like to thank Nathan Sipe for his assistance in the early setup of the imaging experiment. Finally, the assistance and expertise of the Imaging Sciences personnel was invaluable during startup of imaging with the camera we rented from them.

References

Goldstein, T., S. Osher, "The Split Bregman method for L^1 regularized problems," *SIAM J. Imaging Sci.* **2**, 2 (2009) 323–343.

Lloyd, S. P., "Least squares quantization in PCM," *IEEE Trans. Information Theory* **28**, 2 (1982) 129–137.

Merrill, F. E., "Neutron radiography of thick dynamic systems," LA-UR-13-24549, Los Alamos National Laboratory, Los Alamos, New Mexico, 2013, http://www.osti.gov/scitech/biblio/1084508, accessed February 18, 2015.

Rudin, L. I., S. Osher, E. Fatemi, "Nonlinear total variation based noise removal algorithms," *Physica D* **60** (1992) 259–268.

Specialised Imaging, "SIMX - Ultra High Speed Framing Camera," http://specialised-imaging.com/products/simx-ultra-high-speed-framing-camera, 2015, accessed February 12, 2015.

This page left blank intentionally

MPDV Data Analysis and Uncertainty Quantification for Large-Scale Data Sets

NLV-21-12 | Continued from FY 2013 | Year 3 of 3

Rand Kelly,[1,a] Marylesa Howard,[a] Eric Machorro,[a] Aaron Luttman,[a] Jerome Blair,[b] and Melissa Matthes[c]

Photonic Doppler velocimetry (PDV) is a heterodyne laser interferometric technique for computing the velocities of free surfaces moving up to tens of kilometers per second. This information can be used to infer material properties such as equation of state and phase transitions, many of which are unknown even for common materials like steel. Over the last several years, a broad literature has grown up describing methods for computing surface velocity from the measured voltages on an oscilloscope, and it is important to understand how velocities extracted using the different methods relate to each other and how the results relate to measurements from independent diagnostics. This project had two primary goals: (1) developing statistically justified techniques for calculating surface velocity with rigorous uncertainty quantification and (2) benchmarking velocity and displacement results from PDV against independent diagnostics. To this end, we provide a short review of some of the most common analysis techniques as well as a detailed description of local polynomial approximation (LPA), a statistical method developed by the authors that has been extended significantly in FY 2014. We also present computed surface velocities of a flat plate of stainless steel impacted by a projectile traveling approximately 4 km/s from a light gas gun, using several different analysis methods, and we compare the results of the different PDV analyses against high-speed video captured at 5 million frames per second with a hybrid framing-video camera. The results are presented as well as a description of how the different methods for computing velocity—with a focus on LPA—compare to each other and the high-speed imagery.

[1] kellyrp@nv.doe.gov, 702-295-0137
[a] North Las Vegas; [b] Keystone International, Inc.; [c] University of Nevada, Las Vegas

Background

Photonic Doppler velocimetry (PDV) is a kind of Michelson interferometer (Strand 2004, 2006; Holtkamp 2006) used in dynamic material experiments (Holtkamp 2011) to measure free surface velocities up to tens of kilometers per second. PDV works by a laser emitting light with known frequency f_0 along an optical fiber to a probe, with some of the light being diverted directly to an optical detector and some being upshifted by known frequency f_u before being diverted to the detector. The probe focuses the light onto the surface of interest and captures the Doppler-shifted light that is reflected back. The shifted light, with frequency f_d, is mixed with the original light at the detector, and an optical detector converts the light with beat frequency $f_0 - f_d + f_u$ to a voltage measured by a digitizer. (Note that when the surface is not moving, $f_d = f_0$, which gives a measurement of f_u rather than 0 at the detector.) We measure the voltage trace from the digitizer and used that data to compute the beat frequency. The multiplexed version of PDV (Daykin 2011) is capable of capturing the data from multiple probes on a single digitizer, making it a significant improvement over the original configuration.

The mathematical model for the measured voltage trace $y(t)$ is

$$y(t) = A(t)\sin(\phi(t)) + \eta, \quad (1)$$

$$A(t) = A_0 + A_1(t - t_c), \quad (2)$$

$$\phi(t) = \varphi_0 + \varphi_1(t - t_c) + \varphi_2(t - t_c)^2, \quad (3)$$

for constants A_0, A_1, φ_0, φ_1, and φ_2, and additive Gaussian noise η, and the goal is to compute $\phi(t)$. If $A_1 = 0$, this model implies the assumption that the beat frequency at the detector is changing in time linearly, whereas the further assumption $\varphi_2 = 0$ implies that the beat frequency is constant in time. This model results in a nonlinear inverse problem for the signal beat frequency—which is proportional to the surface velocity—that is straightforward to frame but for which there are many different approaches to solving.

The model in Equations 1–3 is not appropriate for all time in nearly any experiment, so it is common to analyze a "windowed" version of the signal, which is equivalent to the assumptions above being approximately true over the time duration of the window used. The most common window is a Hamming window, but some methods require windows with infinite support, like Gaussian windows. The frequency spectrogram is computed by taking the short-time Fourier transform of the windowed signal at selected points (often subsampled to less than 1/100 of the original record length). Different methods for computing the velocity use the spectrogram for different purposes, and the different methods take approaches that diverge from each other after the spectrogram is calculated. There is no universal agreement on which method, or class of methods, gives the best results, and there has been significant work to develop these techniques over the last few years (Schoukens 1992, Ao 2010), including a new class of methods that focuses on statistically motivated formulations designed to compute both $\phi(t)$ and estimates of the uncertainties associated with $\phi(t)$ (Machorro 2013, 2014).

Project

Quantifying Uncertainties in PDV Analysis

The velocity extraction techniques presented here all require the generation of a spectrogram of the Doppler-shifted voltage, upon which the user manually draws a region of interest (ROI) around the signal of interest (Figure 1). Some methods tend to be sensitive to the ROI, and, for example, the ROI should not include the baseline frequency, $f_0 + f_u$, at times when the object in the experiment has nonzero velocity.

Frequency-Based Techniques for Analyzing PDV

The first three techniques presented here are methods that extract velocity in the frequency domain. One computes the absolute value of the Fourier transform of a subset of the data that has been windowed using either a Hamming, Hann, rectangular, or Gaussian window. We denote this transformed data set f_t for a given time t. This is repeated on data subsets at each determined step in time.

Using the transformed data set, a first attempt at extracting the dominant frequency at each time step is to take the frequency at which the maximum signal strength occurs within the ROI. The interpolated fast Fourier transform (IpFFT) method, described by Schoukens (1992), advances this idea. For each t, the location of the maximum peak within the bounds of the ROI is determined, i, and the frequency, $f(t)$, is given by

$$f(t) = f_t(i) + \left(\frac{2\left|\frac{f_t(i+1)}{f_t(i)}\right| - 1}{\left|\frac{f_t(i+1)}{f_t(i)}\right| + 1} \right). \quad (4)$$

If a Gaussian window of the form $w(t) = \exp(-t^2 / 2\tau^2)$ is used, where τ is the window length, the square of the resulting transformed data set f_t is approximately Gaussian (Dolan 2010). The Gaussian fit method fits a Gaussian of the form $g = a \cdot \exp(-(f - b)^2 / c^2)$ to the subset of f_t bound by the ROI, where b is taken to be the peak at time step t.

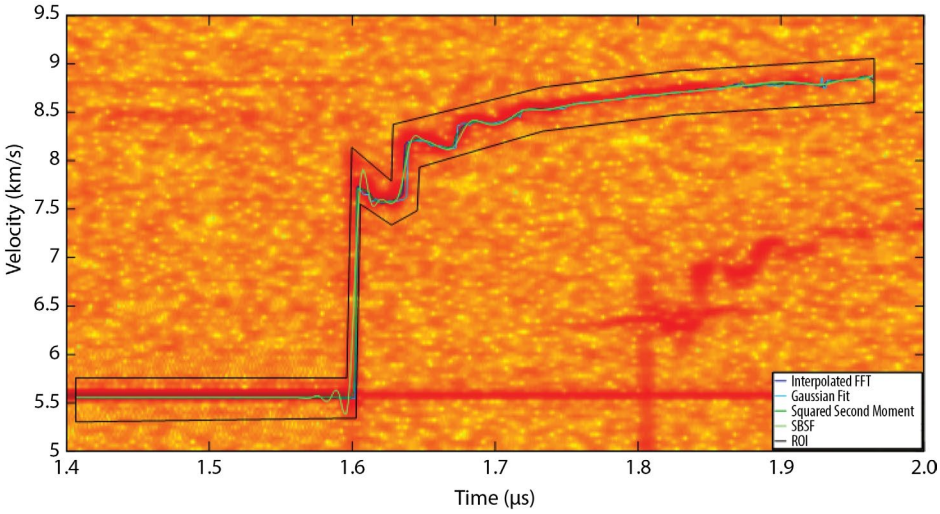

Figure 1. Spectrogram of a multiplexed photonic Doppler velocimetry (MPDV) signal with the different velocity extraction methods overlaid onto one another in the region of interest (ROI)

If we consider the ROI-bounded set of frequencies, f_t, to represent density, the first and second moment represent the mean and variance of the data set, respectively. The ROI-bounded subset of f_t is denoted as f_{t_ROI}, and the corresponding signal strength for that vector is denoted as s_x. By definition, the first moment is calculated as

$$E\left(f_{t\_ROI}\right) = \left\langle f_{t\_ROI}, s_x \right\rangle, \tag{5}$$

and the second central moment is calculated as

$$E\left(\left[f_{t\_ROI} - E\left(f_{t\_ROI}\right)\right]^2\right) = \left\langle \left(f_{t\_ROI} - E\left(f_{t\_ROI}\right)\right)^2, s_x \right\rangle. \tag{6}$$

The squared second moment method mimics this concept but calculates peak frequency at time t to be

$$f(t) = E_{SSM}\left(f_{t\_ROI}\right) = \left\langle f_{t\_ROI}, s_x^4 \right\rangle \Big/ \sum s_x^4, \tag{7}$$

and its corresponding standard deviation at time t to be

$$\sigma(t) = E_{SSM}\left(\left[f_{t\_ROI} - E_{SSM}\left(f_{t\_ROI}\right)\right]^2\right) = \sqrt{\left\langle \left(f_{t\_ROI} - E_{SSM}\left(f_{t\_ROI}\right)\right)^2, s_x^4 \right\rangle \Big/ \sum s_x^4}. \tag{8}$$

Using the fourth power of the signal strength is the same as squaring the power, an attempt to sharpen the peak of the signal strength. The term $\sum s_x^4$ serves the purpose of normalizing the transform of the signal strength vector to simulate a probability density.

Phase-Based Techniques for Analyzing PDV

Rather than working from the Fourier transform of the data, it is also possible to estimate the phase directly, which allows for velocity extractions that are formulated statistically for quantifying the uncertainties in the computed velocities. One such method is statistics-based spline fitting (SBSF) (Blair 2007), which models the Doppler shifted signal, $y(t)$, as

$$y(t) = A_t \sin(\phi_t) + \eta_t, \tag{9}$$

where A_t is the amplitude, ϕ_t is the phase, and η_t is the oscilloscope noise at time t. A Hilbert transform and other approximations, denoted as $\mathrm{H}^+(y(t))$, produce the model $\mathrm{H}^+(y(t)) \approx \phi_t + \varepsilon_t / A_t$, where ε_t is the transformed noise. A cubic spline is fit to the phase estimate using global weighted-least-squares.

Local Polynomial Approximation

As noted above, there has been a significant shift in recent years towards developing methods for computing surface velocities from PDV traces that have statistical formulations, and they are often phase-based approaches, rather than frequency-based approaches.

The goal is to have statistically justified error bars associated with the extracted velocities, and, in particular, to estimate independently the errors due to random noise and errors due to modeling bias. The SBSF technique described above is one such method, and the second approach developed under this project is local polynomial approximation (LPA). This method has been described in Machorro (2013, 2014)—with details of the bias error estimates in Blair (2011, 2013, 2014)—but there are several important improvements that were made to the technique that we describe below.

Phase Noise Background

A mathematical formulation for the PDV that is a slight adaptation of that given in Equations 1–3 is

$$y(t) = A(t)\cos\left(\omega_0 t + \phi_s(t) + \phi_n(t)\right) + \eta(t), \qquad \textbf{(10)}$$

where $y(t)$ is the signal recorded on the oscilloscope, $A(t)$ is the amplitude, ω_0 is the baseline angular frequency, $\phi_s(t)$ is the change in phase of the signal due to the displacement of the target, $\phi_n(t)$ is the random variation in the phase caused by imperfections in the system oscillators, and $\eta(t)$ is the additive noise of the oscilloscope. The term $\phi_n(t)$ is called the phase noise, and it has been neglected in previous PDV analyses, which have all assumed that $\eta(t)$ is the only random noise source. Recent analysis shows, however, that the phase noise term in Equation 10 is a substantial source of error. This is illustrated in Figure 2, which shows the natural logarithm of the ratio of the error from phase noise to the error from the additive oscilloscope noise, as a function of time, in the final estimated velocity for one of the probes from one of the experiments described in the section ***Benchmarking PDV***. When the curve is above the red line, the phase noise dominates; when it is below, the additive noise dominates. For most of the time, the ratio is above 2, so the phase noise contribution to the standard deviation is more than 7.4 (e^2) times larger than the additive noise contribution, which means the phase noise cannot be ignored when quantifying uncertainties.

Phase Noise Effect on Bias Error Estimate

Phase noise affects both the errors due to random noise and the errors due to model bias. Estimating the bias error requires a bound on the third derivative of the phase as a function of time. This estimate fails to represent the bias error correctly when the phase noise component is not taken into account.

The phase noise is assumed to be a stationary random process, which is described by its power spectral density, an assumption made in all analyses of phase noise in other applications of both optical and electrical oscillators. We measured the phase noise by recording signal from the system without a moving target, and the phases were extracted from these records by the same procedure used in the SBSF and LPA analyses of signals, giving $\phi(t) = \omega_0 t + \phi_n(t)$ + constant for the extracted phase. A straight line is fit to the phase data and then subtracted from it to yield $\phi_n(t)$, and the power spectral density is estimated by applying Welch's method (Welch 1967) to $\phi_n(t)$.

Welch's method consists of multiplying the data by a sequence of overlapping windows, calculating the squared absolute value of the Fourier transform for each window, and averaging the results for the various windows. Each window is shifted one-half window length from the previous one. Obtaining highly accurate results requires many windows, and obtaining the required frequency resolution requires long windows. Thus, a very long record is needed, and, because we could not get adequately long records from the system, we averaged the results from ten different records. This allows us to use fewer, longer windows from each record.

Figure 3a shows a typical result for the phase noise power spectral density. The result is shown out to 600 MHz, the Nyquist frequency of the phase extraction (window shift of 16 samples). Note that the power spectral density varies by a factor of more than 10^{11} over this range.

Figure 3b is a zoom of the first 6 MHz from Figure 3a. Over this frequency range, the power spectral density varies by a factor of about 10^6. The fluctuations are

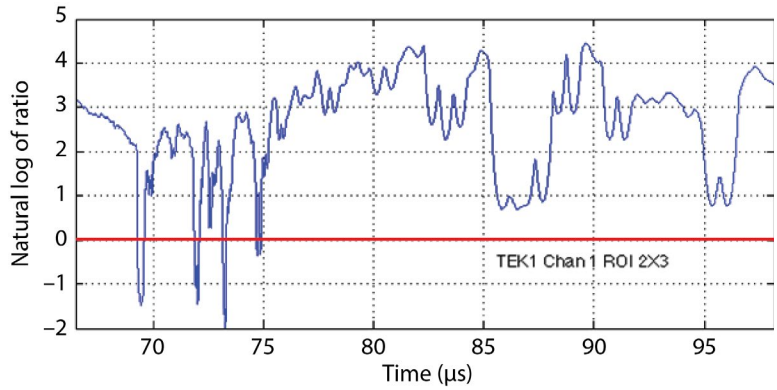

Figure 2. Natural logarithm of the ratio of the phase noise to the oscilloscope noise as a function of time, for one of the gas gun experiments described

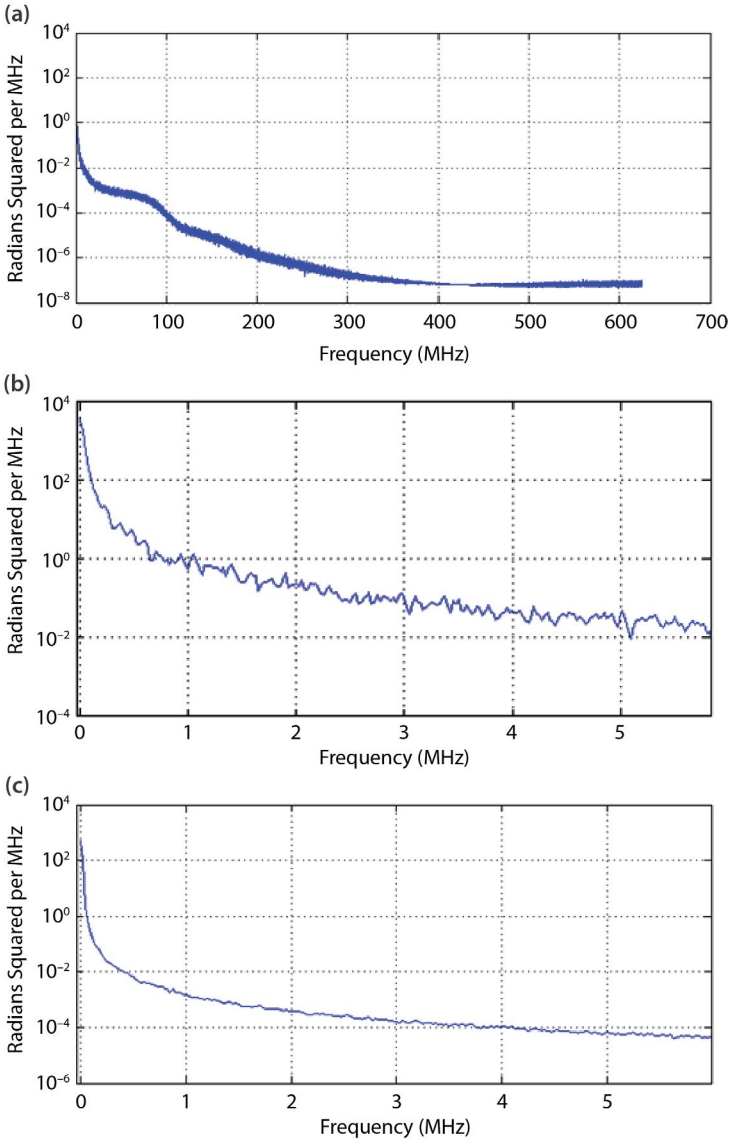

Figure 3. (a) Phase noise power spectral density for a time-multiplexed PDV shot with (b) zoom in at the lowest frequencies. (c) Phase noise power spectral density for a PDV shot that is not time-multiplexed over the same frequencies as (b).

a result of the random errors in the limited data set. Figure 3c is the power spectral density for a shot in this year's experimental campaign that was not time-multiplexed. The general characteristics are the same, but the magnitude was lower for the non-multiplexed shot, by a factor of approximately 1000 at 1 MHz. This is a squared quantity, so the actual standard deviation is about a factor of 30 larger for the multiplexed system.

Time-Varying Fit Interval

The LPA method is based on fitting a polynomial to the data over an interval and evaluating the polynomial (for displacement) or its derivative (for velocity) at the center of the interval. Each polynomial fit gives one output data point. The choice of the length of the interval involves a trade-off between the bias and random errors. The bias error increases as the interval length increases, while the random error generally decreases as the fit interval increases. An estimate of both sources of error is obtained at each data point, and error bars for each source are plotted along with the displacement or velocity curve.

Ultimately, the goal is to automatically choose the fit interval that minimizes the total error at each point. This proved to take an unacceptable amount of time using MATLAB optimization routines, and resources were not available to solve this problem. Instead a program was developed to manually adjust the fit interval as a function of time to get acceptable error bars. Figure 4a shows a velocity curve extraction, and Figure 4b is the corresponding fit interval as a function of time.

The fit interval varies between 0.031 μs and 2.0 μs, a factor of over 64. Spectrogram methods use a constant fit interval (called the FFT interval) throughout. Figure 5a shows the size in meters per second of the error bars as a function of time. The red is the estimated random error (2σ), the blue the estimated upper bound on the bias error, and the black the quadrature sum of the two. The peak near 22 μs is cut off so that the error bounds at other times will be discernable. The bias error estimates are based on an estimated upper bound on the second derivative of the velocity, which is obtained without operator input in an early stage of the analysis. Figure 5b shows the second derivative of the smoothed velocity (red) along with the bound (blue).

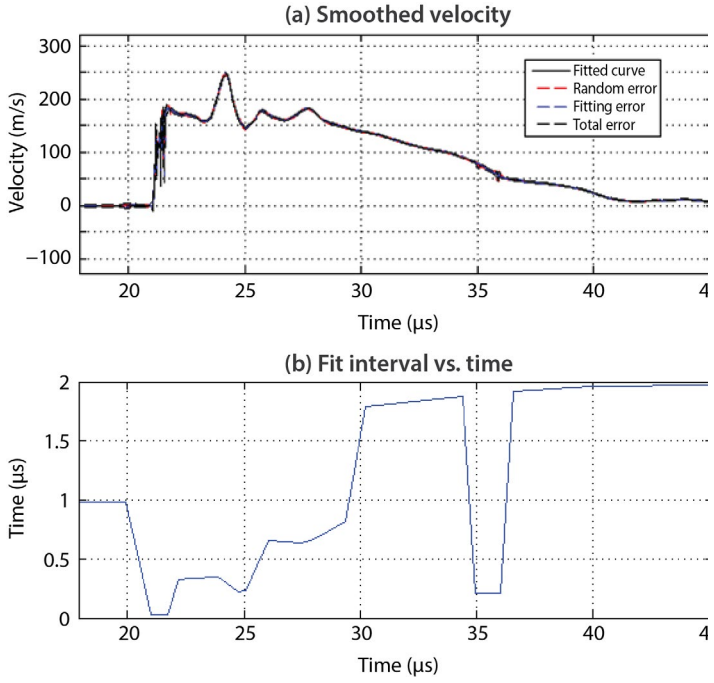

Figure 4. (a) An LPA velocity extraction plot with random and bias error bars for a PDV probe from one of the experiments described in the section on *Benchmarking PDV*. (b) Plot showing the corresponding fit interval length as a function of time. The interval length is manually adjusted by the user.

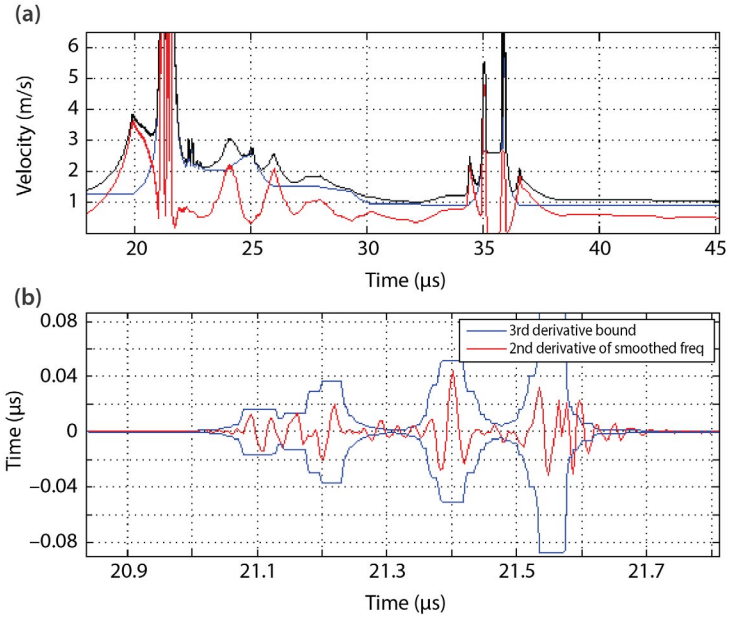

Figure 5. (a) A plot of the estimated random 2σ error (red), estimated upper bound on the bias error (blue), and total error as calculated by the second root of the sum of the squared errors (black) for the velocity extraction in Figure 4a. (b) The second derivative of the smoothed velocity (red) alongside the third derivative bounds (blue).

Benchmarking PDV

The second primary component of this project was to experimentally benchmark PDV methods against an independent diagnostic. To this end, we collected PDV data measuring the deformations of the surfaces of steel plates when impacted by a high-velocity projectile from the two-stage gas gun laboratory at the University of Nevada, Las Vegas (UNLV). The results of the PDV extraction are then compared to high-speed video captured by a hybrid framing-video camera. In the remainder of this section we present the experimental setup as well as a comparison of the displacement and velocity results obtained from the high-speed imaging and the PDV analysis methods described above.

Experimental Setup

A Kirana high-speed hybrid video-framing camera manufactured by Scientific Imaging was fielded; the camera captures 5 million frames per second at 100 ns exposure times to measure the displacement of the metal surface as it was impacted by the projectile. A block diagram of the experimental setup of the camera is shown in Figure 6. To light the back of the bulge as it starts forming due to the impact of the Lexan projectile, two 99.9% reflective mirrors were set at 45°, one with respect to the metal target plate and the other with respect to that mirror, which then partially faced the 9-inch porthole window. On the outside of the porthole, there was another 45° mirror that reflected light from the flash lamp into the gun chamber. A close-up can be seen in Figure 7a. In between the 45° mirror and the flash lamp lies an iris and a set of lenses to collimate the light. As the collimated light backlights the formation of the bulge, the lens on the outside of the chamber looks through the 9-inch porthole towards the target plate. The camera and flash lamp were both triggered by a digital pulse generator (DG-535), which received an initial trigger pulse from the disruption of an optical beam break residing in the drift tube, and a laptop running the camera software recorded the frames from the camera for viewing. The digital delay was altered according to the estimated velocity of the shot based on averages from previous shots boasting similar parameters such as projectile caliber and pressure.

In parallel with the high-speed camera, there was a single MPDV 32-probe array placed normal to the target plate to capture data as the bulge formed in time. The array was arranged in a 4 × 8 grid pattern that was centered on the expected impact location, which can be seen in Figure 7b—a position with a radial

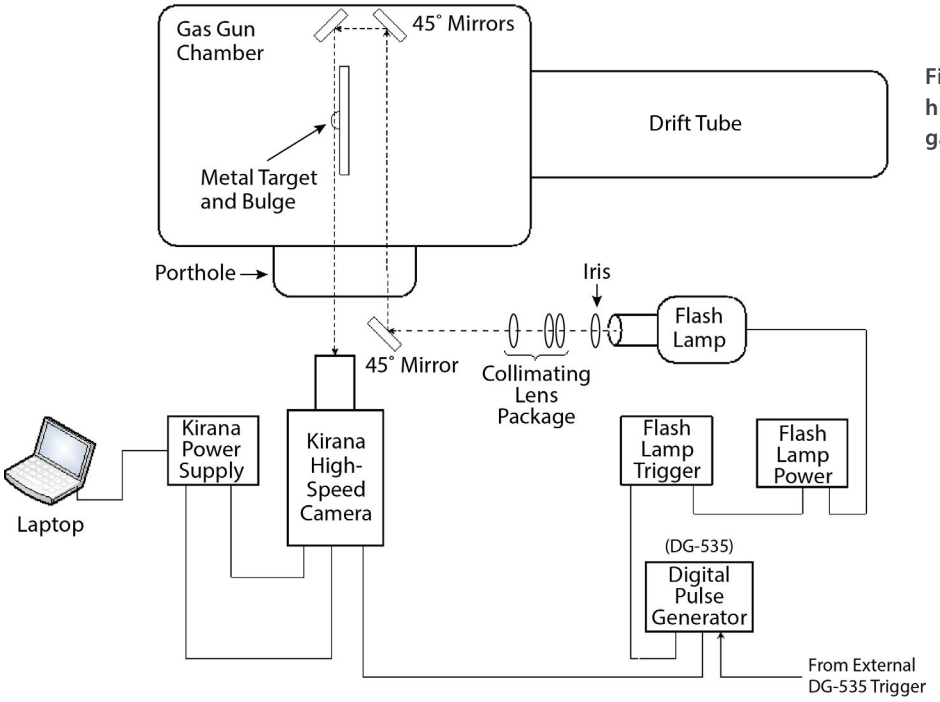

Figure 6. Schematic diagram of the high-speed camera setup at UNLV's gas gun

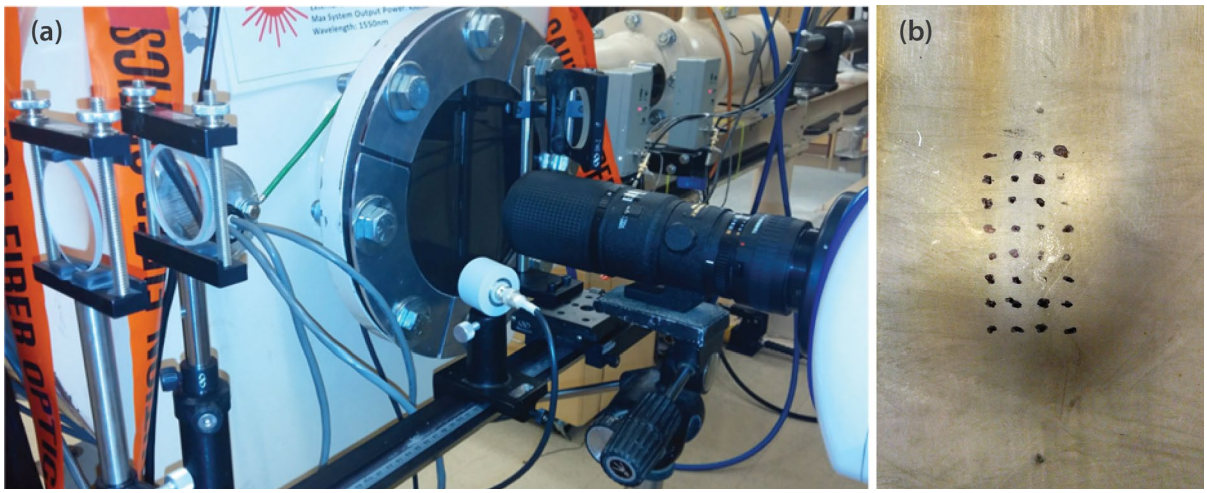

Figure 7. (a) The setup of the high-speed camera viewing the inside of the gas gun chamber, and (b) the 4 × 8, 32-channel MPDV probe array marked on the target plate after a shot

uncertainty of 3 mm. This led to many shots where the Lexan projectile was off center of the expected impact location, which resulted in the 4 × 8 MPDV grid not fully covering the bulge at times. The high-speed camera had its image frame centered and focused to the center MPDV probe so that if the MPDV captured the data, the high-speed camera did as well, and there were several shots where the 4 × 8 grid covered most of the bulge, providing excellent data from both the MPDV and the camera. A typical view of the target plate can be seen in Figure 8b, and PDV data can be seen in Figure 8a.

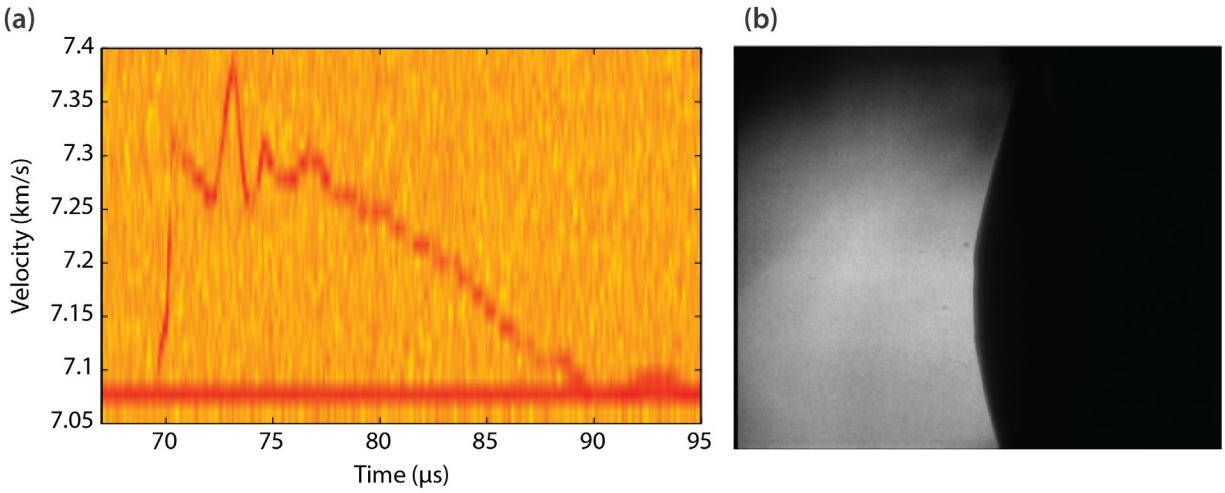

Figure 8. (a) The spectrogram corresponding to a single PDV probe, and (b) a single frame of the high-speed video taken of a deforming HY100 steel plate

High-Speed Hybrid Video Camera Data Analysis Technique

The high-speed hybrid framing-video camera was fielded to serve as an independent diagnostic against which to benchmark the results of the PDV analysis. When the bullet impacts the steel plate, the plate deforms, and the leading edge of the "bump," as seen in Figure 7a and Figure 8b, is extracted from the video.

The Kirana camera captures images 10 at a time, so image 11 is overlaid on image 1, image 12 on image 2, etc. This results in a 10-frame oscillation in the readout intensity of the camera, denoting the intensity at pixel (x,y) at time t by $I(x,y,t)$. Figure 9a shows a plot of $\underset{(x,y)}{\text{median}}\, I(x,y,t)$ as a function of t (blue). In order to offset this anomaly from the camera, the signal $\underset{(x,y)}{\text{median}}\, I(x,y,t)$ is median filtered with a window length of 21, and the resulting "target" median value, M_t, is shown as the green curve in Figure 9a. Each frame is then normalized as

$$I(x,y,t)_{normalized} = I(x,y,t) - \left(\underset{(x,y)}{\text{median}}\, I(x,y,t) - M_t\right). \quad (11)$$

The resulting signal, $I(x,y,t)_{normalized}$, clearly has median value equal to M_t, removing the intensity fluctuations caused by the camera capture.

Once the video frames have been normalized, the leading edge of the deforming surface is extracted from each frame by calculating the norm of the spatial gradient of each frame. Figure 9b shows a grayscale rendering of the magnitude of the gradient of one such frame, along with points in each pixel row of maximum magnitude (red crosses). These points of maximum gradient within the frame are then fit to a cubic spline, which is taken as the extracted surface for that frame. Figure 11 shows three frames with the spline curves (in blue) that represent the leading edge of the bulging surface.

Results of PDV Extractions and High-Speed Imagery in Gas Gun Experiments

We present results from two different experiments. Figures 10a and 10b show the computed bulge displacement at rows in the camera's field of view that corresponds to lines of sight of two PDV probes for an HY100 steel plate experiment. The projectile had a 0.375-inch diameter, and it was propelled at approximately 3.94 km/s. The location corresponding to plot (Figure 10a) is at row 105, and the location corresponding to plot (Figure 10b) is at row 470 in the camera data (see Figure 11). The PDV analysis methods all provide estimates of the surface velocity, whereas the camera data are a direct measure of displacement, so we differentiate the camera data to get velocity and integrate the velocities from the PDV analyses to get displacements. Figures 10a and 10b show that the

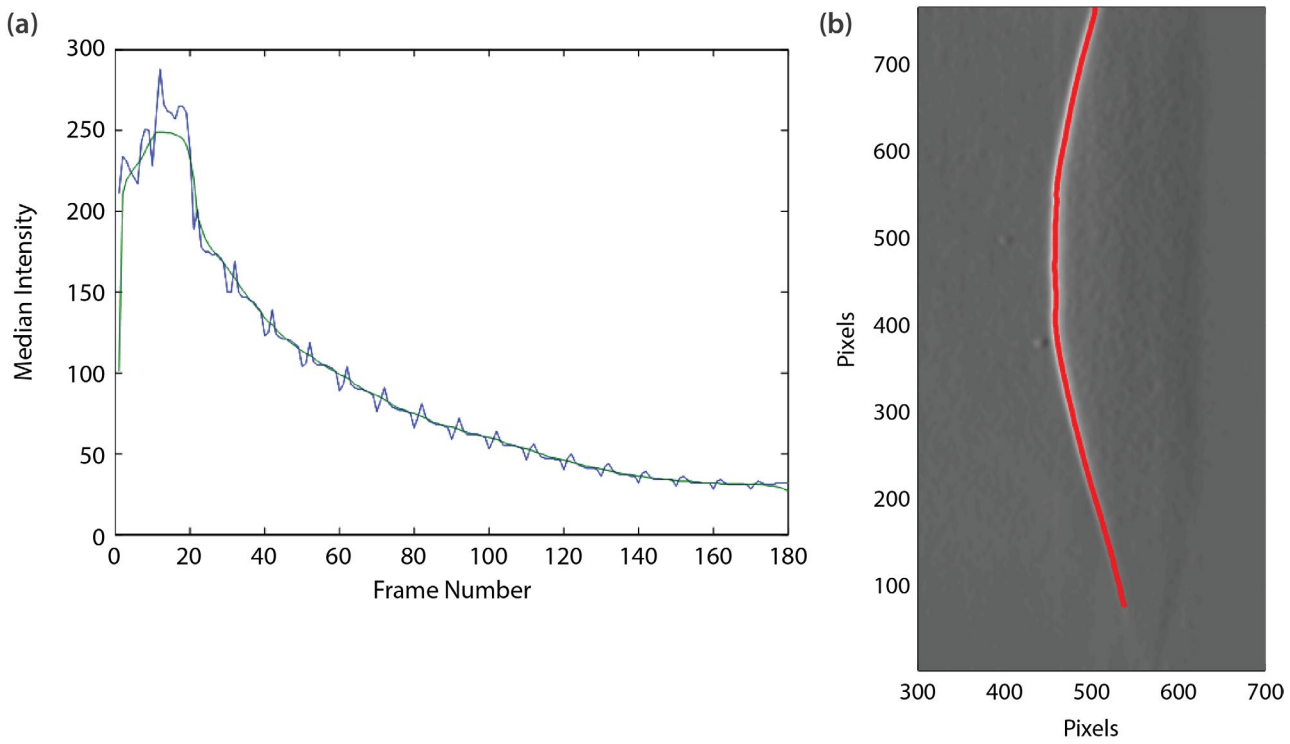

Figure 9. (a) The median intensity of each frame in the video sequence (blue) and the median intensity of the normalized frames (green). (b) The magnitude of the spatial intensity gradient of a frame in the sequence, with red crosses denoting the maximum gradient across the bump.

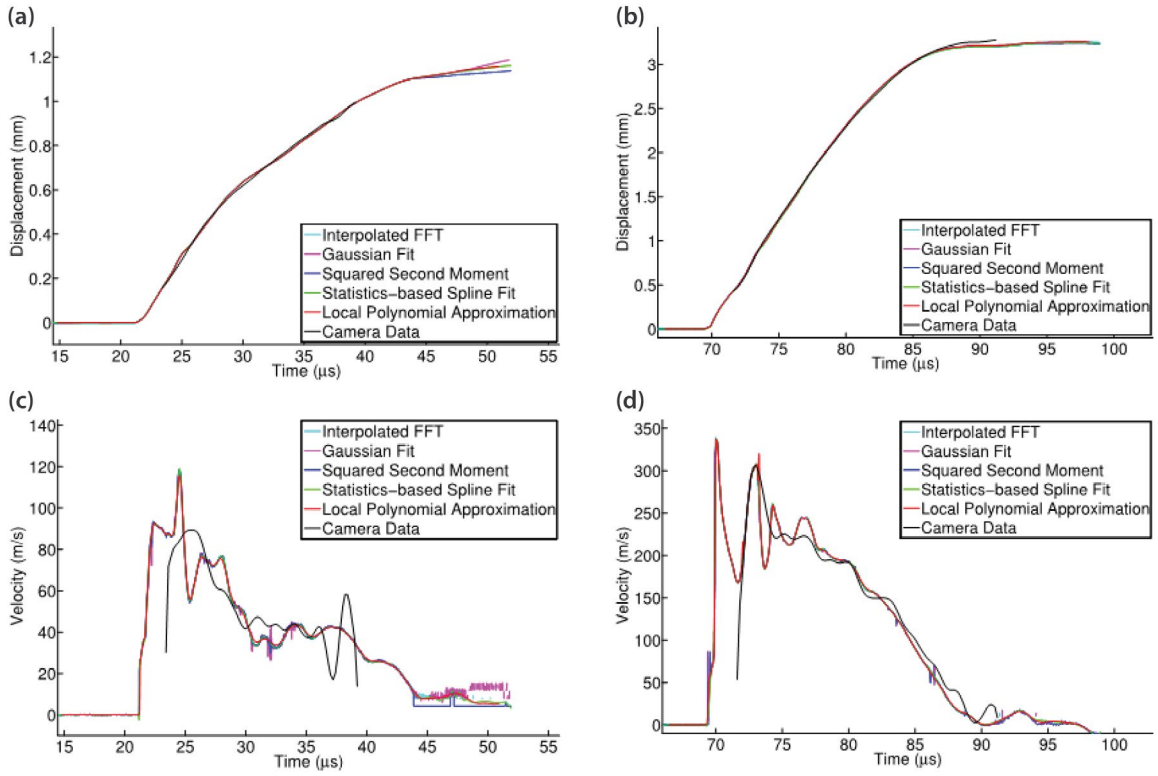

Figure 10. (a) and (b) Plots showing the surface displacement for two PDV probes compared to the extracted camera displacement at the location of the PDV probes. (c) and (d) The respective extracted velocity plots for the two PDV probes. These results are from the HY100 steel plate experiment.

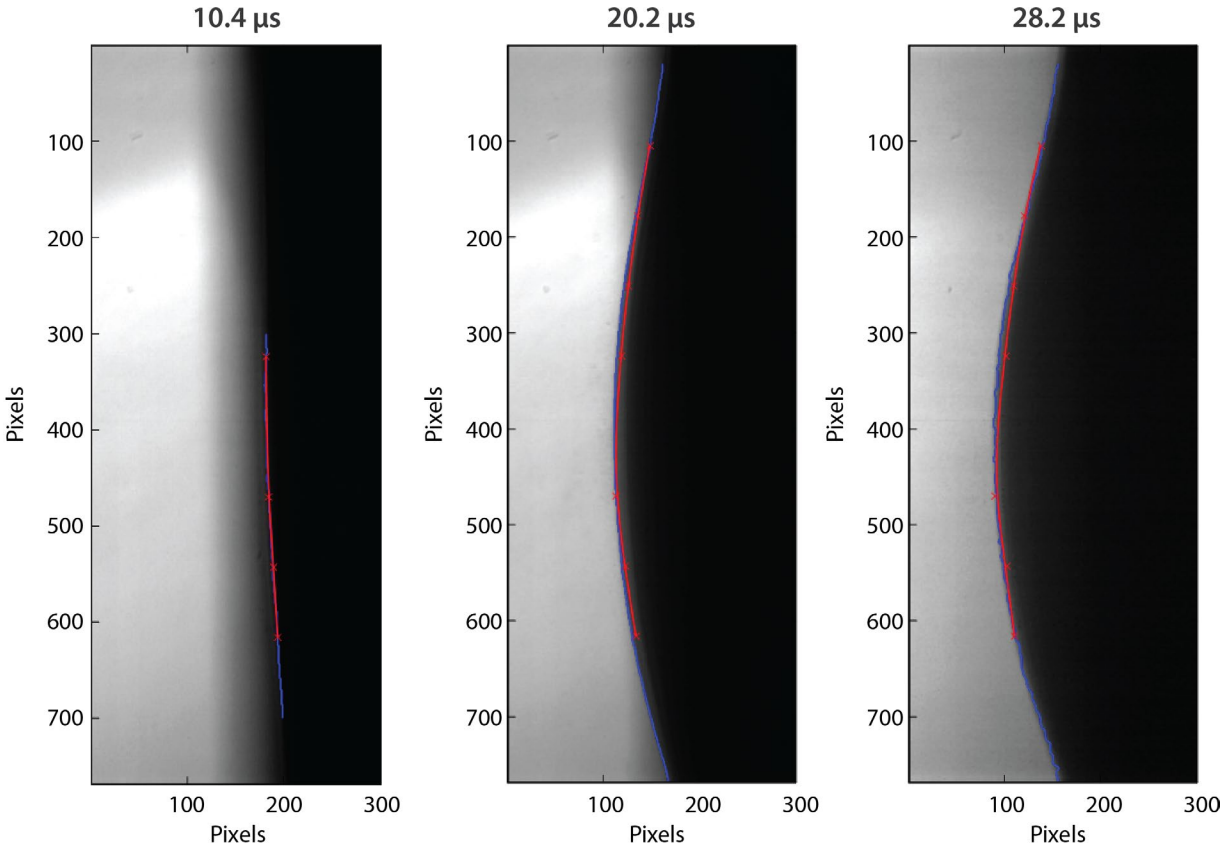

Figure 11. An impacted HY100 metal plate bulging at times 10.4, 20.2, and 28.2 µs after breakout. The blue line indicates the extracted leading edge of the bulge in the camera data, and the red line is the spline interpolation of the red crosses, which indicate the integrated velocity of the mPDV probes (using LPA).

displacements computed from each of the PDV analysis methods and the camera all agree extremely well. The video begins too late to pick up the initial breakout, but from the point the video begins, it shows the same displacement as the PDV extraction methods until it ends, which is before the end of the PDV record.

Note that the PDV extractions begin to diverge near the end of the record. Figure 11 shows three frames from the video with the leading edge of the bulge and the camera (blue) and LPA PDV displacements overlaid (red). The red crosses show the points where the PDV probes are aimed at the surface, and the red curve is a cubic spline interpolation of those points. Displacement computed from the top probe agrees very well with the position computed from the camera, but there are visible discrepancies between the camera and PDV for the other probes. Nonetheless, the overall agreement is quite good. The velocity plots in Figures 10c and 10d would seem to tell a different story, as the PDV analysis techniques no longer agree as well as they appear to for displacement, and the camera-computed velocities are significantly different from the PDV-computed velocities. Because of the late start of the camera, the peak velocity of the surface is not able to be computed, and, due to the much coarser time resolution, the camera does not capture all of the structures that PDV traces show. It is remarkable that the displacement calculations agree as well as they do, given the differences in velocity.

Figure 12 shows the computed bulge displacement and velocities at rows in the camera's field of view that correspond to lines of sight of two PDV probes for an impact experiment on an A36 steel plate. This projectile also had a 0.375-inch diameter, but it was propelled a bit more slowly, at approximately 3.24 km/s. For this experiment the velocities for the PDV and camera

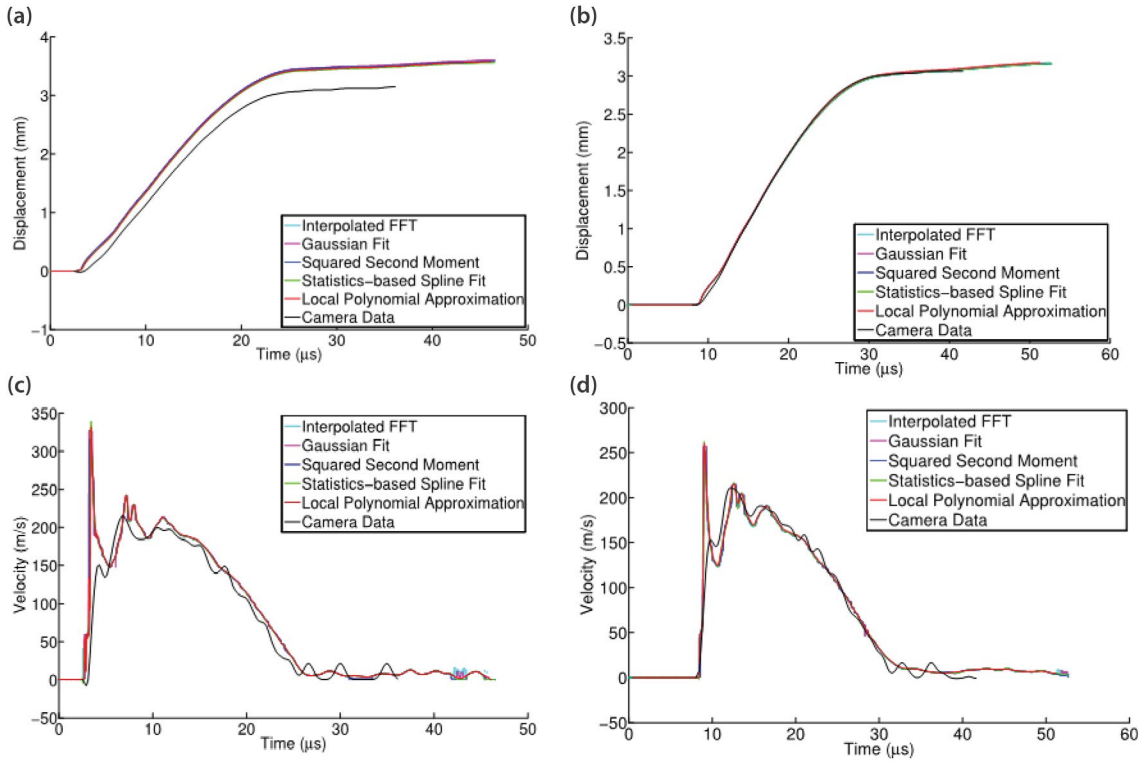

Figure 12. (a) and (b) Integrated velocity, or displacement, for two PDV probes compared to the extracted camera displacement at the location of the PDV probes. (c) and (d) The respective extracted velocity plots for the two PDV probes. These results are from the A36 steel plate experiment.

appear to agree much better than for the previous, but the displacements in Figure 12a show significant disagreement, at least for the probe in Figure 12a, which shows a difference of several hundred microns between the final displacement computed from the camera and that computed from the PDV. The camera and PDV calculations agree quite well for both the displacement and velocity for the probe in Figures 12b and 12d.

Conclusion

The two goals of this project were to develop statistically justified methods for computing surface velocity from PDV voltage data and benchmark these velocity and displacement calculations against other diagnostics. We presented descriptions for some of the common PDV analysis techniques and a detailed discussion of the LPA method, a technique developed by the authors in this project. We fielded a 32-channel PDV system and a high-speed hybrid framing-video camera on experiments at UNLV in which a light gas gun shot a Lexan projectile at a flat steel plate. The diagnostics were placed on the other end of the plate to observe its deformation. Surface velocities were computed using PDV data, and displacements were computed from the camera data. In order to compare the diagnostics, the PDV velocity extractions were integrated to obtain displacement, and the camera displacements were differentiated to obtain comparable velocities. The displacement profiles computed from the camera data and integrated PDV velocities showed good agreement. Any discrepancy seen in resulting displacement is explainable by the inability of the camera to catch peak velocity right after initial movement of the steel plate. The velocity profile comparison showed agreement in large-scale features; however, velocities calculated from camera data showed many different small-scale features than the PDV calculated velocities. While the velocity

extraction comparison of PDV techniques also showed differences in small-scale features, they agreed with one another more than with the velocity computed from camera data.

Acknowledgments

We would like to thank Robert Hixson and Edward Daykin for their technical review and support. We would also like to thank the MPDV fielding team, Michael Peña, Anselmo Garza, and Michael Hanache, as well as the high-speed imaging team, Nathan Sipe and Zachary Fussell, for collecting data in the gas gun lab to use in this project. We would like to thank Drs. Brendan O'Toole and Mohamed Trabia, Richard Jennings, and Shawoon Roy for their assistance and use of the gas gun facility at UNLV.

References

Ao, T., D. H. Dolan, *SIRHEN: A Data Reduction Program for Photonic Doppler Velocimetry Measurements*, SAND2010-3628, Sandia National Laboratories, Albuquerque, New Mexico, 2010.

Blair, J., "Error estimates derived from the data for least squares spline fitting," *IEEE Instrumentation and Measurement Technology Conference Proceedings* (2007) 1–6.

Blair, J., "Filtering error estimates and order of accuracy via the Peano kernel theorem," *Computer Standards and Interfaces* **33**, 2 (2011) 122–127.

Blair, J., E. Machorro, A. Luttman, "Estimating the bias of local polynomial approximation methods using the Peano kernel," *Contemporary Mathematics* **586** (2013) 65–71.

Blair, J., A. Luttman, E. Machorro, "A generalized Peano kernel theorem for distributions of exponential decay," *Mathematical Analysis and Its Applications*, submitted March 2014.

Daykin, E., C. Perez, A. Rutkowski, C. Gallegos, "Advanced PDV techniques: Evaluation of photonic technologies," in *Site-Directed Research and Development*, FY 2010, National Security Technologies, LLC, Las Vegas, Nevada, 2011, 205–214.

Dolan, D. H., "Accuracy and precision in photonic Doppler velocimetry," *Rev. Sci. Instrum.* **81**, 5 (2010) 053905.

Holtkamp, D. B., "Survey of optical velocimetry experiments – Applications of PDV, a heterodyne velocimeter," *Proceedings of the 2006 Conference on Megagauss Magnetic Field Generation*, Santa Fe, New Mexico, 2006.

Holtkamp, D. B., "Photonic Doppler velocimetry for dynamic experiments," *Proceedings of 6-Laboratory Conference on Engineering and Materials at Extreme Conditions*, Barcelona, Spain, LA-UR-11-05797, 2011.

Machorro, E., J. Blair, A. Luttman, E. Daykin, "Uncertainty estimation techniques for high-density 1-D MPDV imaging diagnostic," in *Site-Directed Research and Development*, FY 2012, National Security Technologies, LLC, Las Vegas, Nevada, 2013, 169–176.

Machorro, E., A. Luttman, J. Blair, N. Sipe, M. Peña, "MPDV and large data sets," in *Site-Directed Research and Development*, FY 2013, National Security Technologies, LLC, Las Vegas, Nevada, 2014, 171–182.

Schoukens, R., R. Pintelon, H. Van Hamme, "The interpolated fast Fourier transform: A comparative study," *IEEE Trans. Instr. Measurement* **1**, 2 (1992) 226–232.

Strand, O. T., L. V. Berzins, D. R. Goosman, W. W. Kuhlow, P. D. Sargis, T. L. Whitworth, "Velocimetry using heterodyne techniques," *Proc. SPIE* **5580** (2004) 593.

Strand, O. T., D. R. Goosman, C. Martinez, T. L. Whitworth, W. W. Kuhlow, "Compact system for high-speed velocimetry using heterodyne techniques," *Rev. Sci. Instrum.* **77** (2006) 083108-1.

Welch, P. D., "The use of the fast Fourier transform for the estimation of power spectra: A method based on time averaging over short, modified periodograms," *IEEE Trans. on Audio and Electroacoustics* **AU15**, 2 (1967) 70–73.

This page left blank intentionally

LIBS as a Surrogate for Large-Scale Detonations and Means to Characterize Intermediates

STL-05-14 | Continued in FY 2015 | Year 1 of 2

Clare Kimblin,[1,a] Rusty Trainham,[a] Gene Capelle,[a] Xianglei L. Mao,[b] and Rick E. Russo[b]

Laser-induced breakdown spectroscopy (LIBS) can simulate certain characteristics of detonations and high-temperature combustion. As a diagnostic tool it can complement, inform, and even guide efforts brought to optical diagnostics of high-explosives field tests. In FY 2014 we conducted tabletop LIBS studies of aluminum combustion, collected shadowgraph images of laser-induced shock fronts for various metals, performed stand-off spectroscopy measurements during a series of parametric explosives tests, and explored Cantera chemical kinetics software as a tool for modeling combustion and detonation. We present tabletop LIBS results for aluminum and show relevance to data collected from high-explosives testing. In FY 2015, when this project continues, we will compare plasma properties from LIBS spectra collected in air, argon, and vacuum in FY 2014; we will prepare a manuscript for publication of some of the shock-front data collected in FY 2014; and we will explore the impact of carbon obscurants on the emission spectra of aluminum, and how they pertain to high-explosives testing.

[1] kimblicw@nv.doe.gov, 805-681-2257
[a] Special Technologies Laboratory; [b] Applied Spectra, Inc.

Background

Laser-induced breakdown spectroscopy (LIBS) is a tabletop spectroscopic technique in which a laser surface interaction creates luminous plasma. The plasma's optical emissions are collected by a spectrometer and analyzed for elemental and molecular plasma constituents. Various thermodynamic properties such as temperature, pressure, and density can be inferred from the line profiles, intensity ratios, and molecular band structure. Isotopic abundances can be measured by means of atomic and molecular isotope shifts. The physical conditions of the plasma can be controlled by altering the degree of coupling of the laser energy into the plasma. This can be accomplished via the laser's wavelength, temporal pulse width, pulse power, and focus spot size. By choosing different substrates, gases, and gas pressures, the chemistry of the plasma can also be controlled. For example, chemical combustion can be initiated or suppressed depending on whether the atmosphere is oxidizing, reducing, or inert.

The peak temperatures attainable in laser-induced plasmas can be as high as 50,000 K (Bogaerts 2003), and those temperatures drop to sub-combustion within a few milliseconds. This range of temperatures and timescale is relevant to many combustion and detonation applications, so LIBS can be a complementary technique to traditional explosives testing. Of particular value is the ability of LIBS techniques to very easily perform kinetic scans by means of repetitive laser pulses and gating of the data acquisition. In traditional explosives testing a single shot involves considerable setup time, often measured in hours or days, whereas in LIBS the data are generated at the laser repetition rate, usually measured in milliseconds.

Project

The project was conducted at three separate locales. The first was a laboratory for LIBS studies of aluminum (Al) combustion located at NSTec's Special Technologies Laboratory (STL). The second was a laboratory located at Applied Spectra, Inc. (ASI), in Fremont, California, where studies of laser-induced shock fronts were conducted. The third location was at the Big Explosives Experimental Facility (BEEF) at the NNSS, where stand-off spectroscopy measurements were collected during a series of parametric explosives tests during the High Explosive Testing (HET) campaign in June 2014.

In addition to the experimental work, we also began working with the Cantera (Goodwin 2014) chemical kinetics software package to assess its suitability for modeling combustion and detonation processes relevant to the LIBS and HET applications. Cantera is an open-source software project begun by Dr. David Goodwin at the California Institute of Technology (Caltech) in the 1990s. Dr. Goodwin died in 2012, and the project is currently being managed by his former students and collaborators. The discipline of chemical kinetics is concerned with solutions of coupled rate equations for complicated chemical reactions that can involve dozens, if not hundreds, of species. Cantera can model kinetics for reversible and non-reversible reactions, phase transitions, and transport mechanisms in 0-, 1-, and 2-D geometries. The thermodynamic data needed for Cantera simulations are heat capacity, molar enthalpy, and molar entropy; the required reaction data can be in the form of the Arrhenius equation or Chebyshev parameterization.

STL Results

The work at STL centered upon LIBS plasmas generated by a 1064 nm, 10 ns, 35 mJ/pulse, neodymium-doped yttrium aluminium garnet (Nd:YAG) laser ablating Al samples in atmospheres of air and argon as well as in vacuum. Aluminum is a pyrophoric metal that proceeds though several oxide species during combustion to terminate in aluminum oxide (Al_2O_3). The most spectroscopically active of the molecular Al species is aluminum (II) oxide, AlO, which has strong vibro-rotational bands in the blue-green part of the optical spectrum between 450 and 550 nm for the B $^2\Sigma^+ \rightarrow$ X $^2\Sigma^+$ transition, where five or more band heads are usually observable (Schamps 1973, Parigger 2011). The atomic emissions of elemental Al are also fairly strong, with the most important being the lowest excited state to ground state transition doublet, $3s^24s \rightarrow 3s^23p$, at 394.4 and 396.1 nm, and the next lowest transition doublet, $3s^23d \rightarrow 3s^23p$, at 308.2 and 309.3 nm (Kramida 2014). LIBS spectra of these transitions collected 7 µs after the laser pulse are shown in Figure 1. At this delay the plasma has become diffuse,

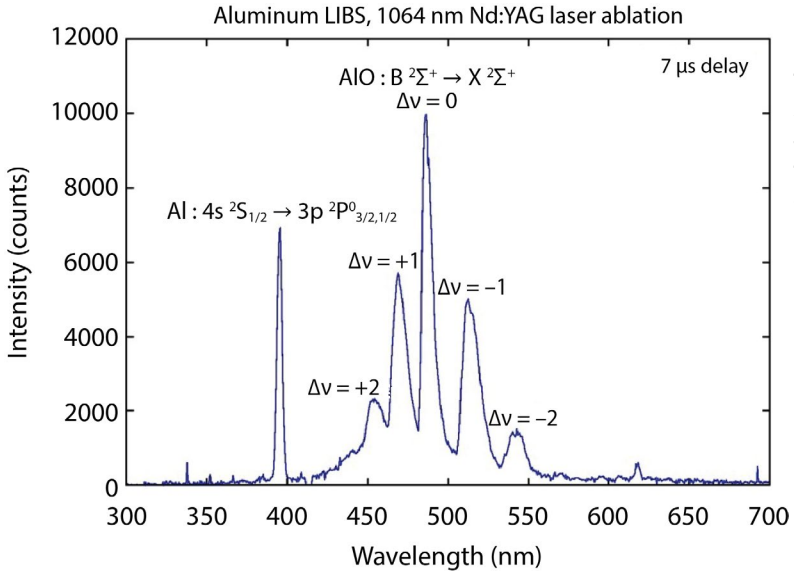

Figure 1. The most important Al emissions are from the B $^2\Sigma^+ \rightarrow$ X $^2\Sigma^+$ transition of molecular AlO, with five vibrational bands seen here from 450 nm to 550 nm, and the neutral atomic Al transition from the lowest excited state to the ground state, $3s^24s \rightarrow 3s^23p$, at 396 nm. In this low-resolution LIBS spectrum, the rotational structure of the vibrational bands and the fine structure of the atomic line are unresolved.

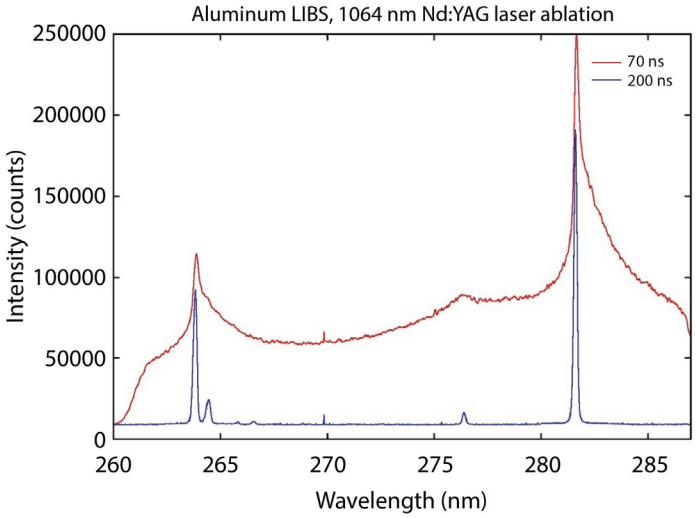

Figure 2. Stark broadening can be recognized by its asymmetry, as long as there are no neighboring lines interfering with the profile. The feature at 281.6 nm is asymmetrically Stark broadened. The feature at 263.8 nm is also broadened, but it is complicated by a neighboring transition.

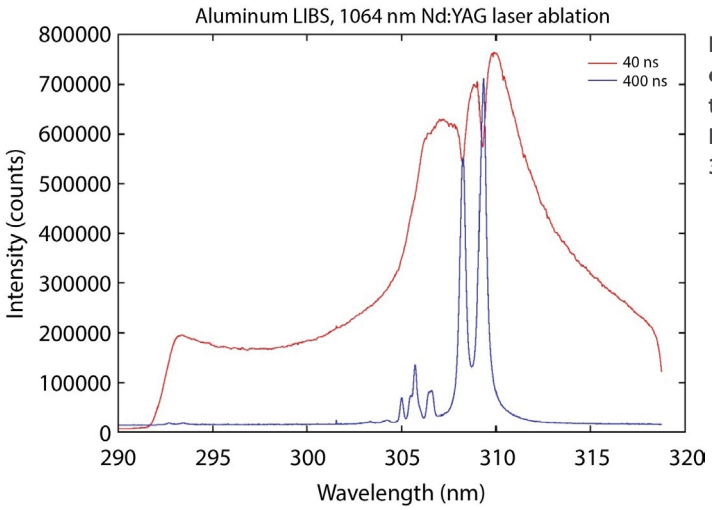

Figure 3. Fraunhofer-type absorptions can be seen in early times of LIBS continuum emissions. At later times those absorptions evolve into line emissions. In the example shown here, the atomic transition is $3s^2 3d \rightarrow 3s^2 3p$ in neutral Al.

and the blackbody background has dropped into the noise, clearly revealing the atomic and molecular transitions.

Plasma formation during the laser ablation phase, while the laser is still on, is very hot and dense. The emitted light is a continuum, and presumably comprises a mixture of continuum-continuum, bound-continuum, and blackbody emissions. The shape of the continuum, even when accounting for the instrument response, is not entirely blackbody. As the spectrum evolves in time, the continuum develops broad features that eventually become recognizable as line spectra. The broadening is due to both Doppler broadening from the high temperature of the plasma, and Stark broadening from the plasma's charge density. Stark broadening can be recognized by its asymmetry and, if quantifiable, can be used to estimate the plasma density. An example of Stark broadening is shown in Figure 2 for the $3s4s\ {}^1S \rightarrow 3s3p\ {}^1P^0$ transition of the Al^+ ion at 281.6 nm.

Another interesting feature observed in the LIBS data is Fraunhofer-type absorptions of the plasma's continuum radiation by a layer of lower-temperature atomic vapor at the periphery of the plasma. In the spectra shown in Figure 3, the data were collected 40 ns after the laser pulse (red curve) and show dips in the continuum at wavelengths corresponding to absorption by the doublet $3s^2 3d \rightarrow 3s^2 3p$ transitions at 308.2 nm and

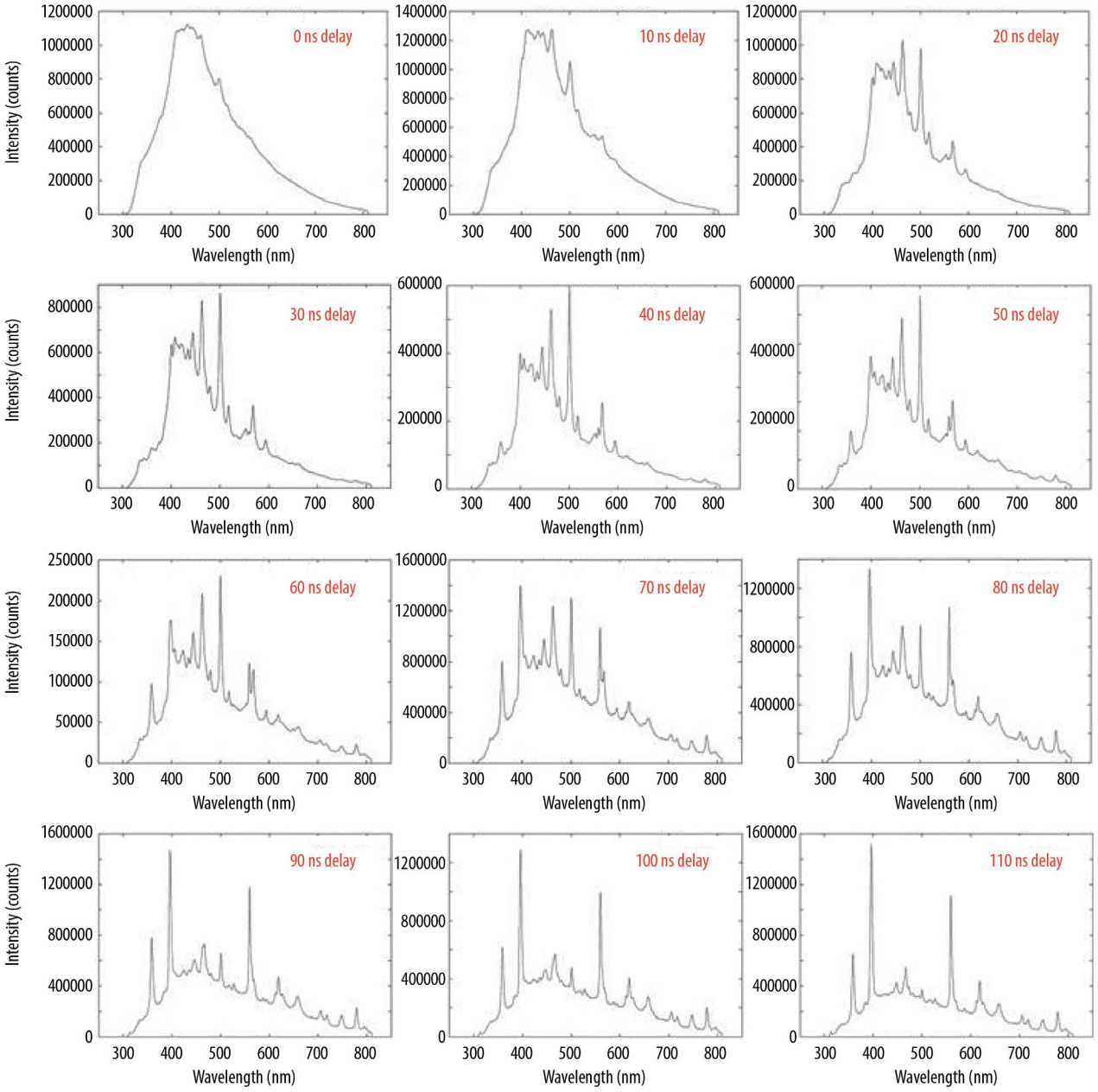

Figure 4. The early-time emissions from the plasma are nearly featureless continua. As the plasma cools and dissipates, atomic and ionic line spectra become recognizable, and at later times, after a few microseconds, molecular band structure becomes visible. The last few frames of this sequence show an atomic line from neutral Al, and the B → X bands of AlO.

309.3 nm of neutral atomic Al. At 400 ns after the laser pulse, those absorptions have evolved into recognizable line emissions. The explanation for the feature is that at early times the plasma is emitting only continuum radiation, and the absorptions occur within a cool shell of neutral atomic vapor surrounding the plasma. At later times, the plasma has cooled sufficiently to emit line spectra, and the atomic vapor shell surrounding the plasma is no longer visible either because it has dissipated or because its absorption of the spectral line is not strong enough to obscure it.

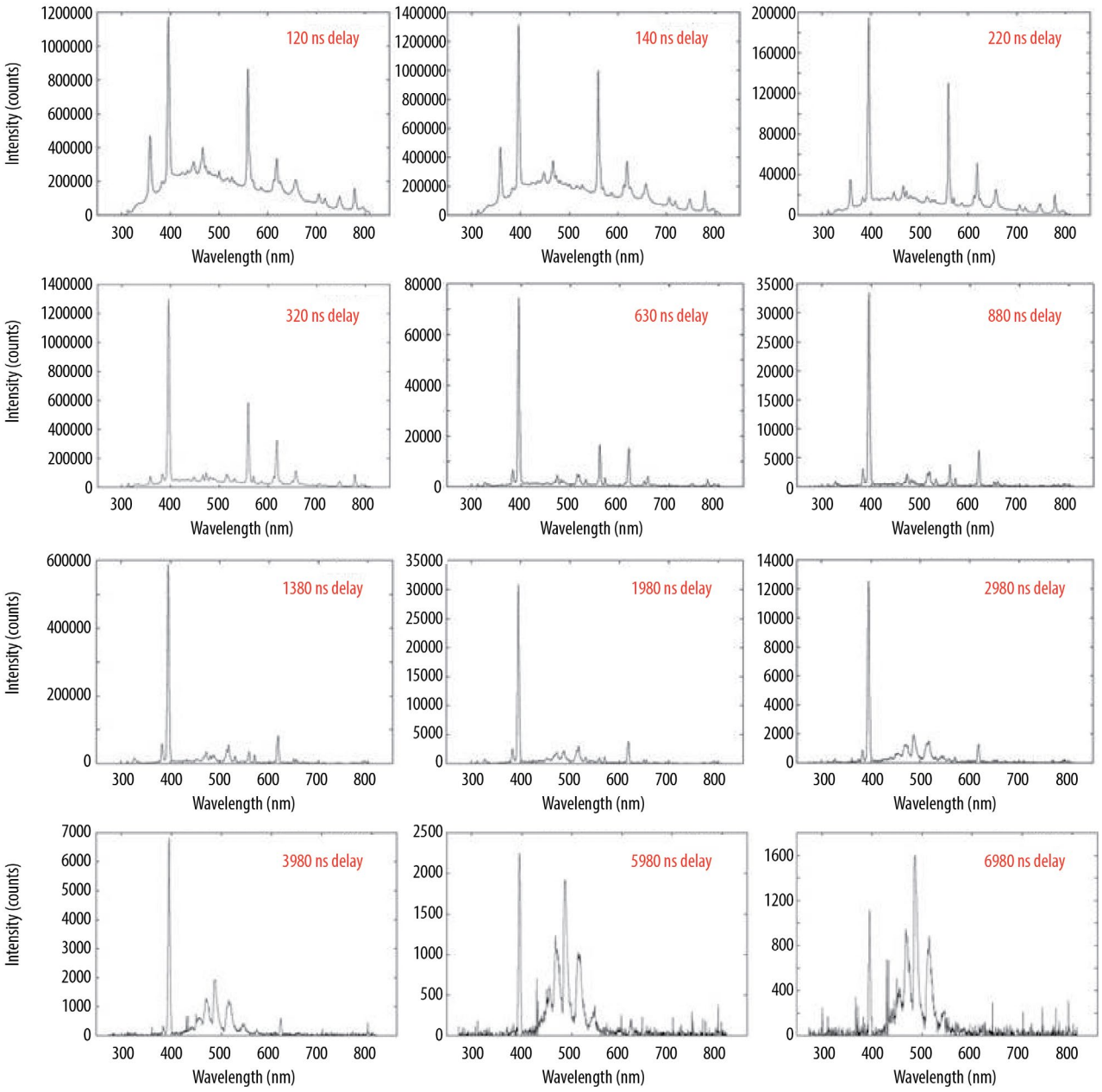

Figure 4. (continued) The early-time emissions from the plasma are nearly featureless continua. As the plasma cools and dissipates, atomic and ionic line spectra become recognizable, and at later times, after a few microseconds, molecular band structure becomes visible. The last few frames of this sequence show an atomic line from neutral Al, and the B → X bands of AlO.

The plasma formed during the laser pulse is very hot, and its emission is typically characterized by a nearly featureless continuum for about the first 100 ns. Then, as the plasma cools and dissipates, atomic and ionic line spectra become apparent. The spectral lines evolve as the temperature and the plasma composition change. The ions neutralize and disappear from the spectra, and ratios of atomic line intensities change as the temperature evolves. In later times, once the plasma temperature has dropped low enough to stop dissociating molecules, molecular band spectra appear in the emissions. Typical spectral evolution for times ranging from the laser ablation, t_0, out to 7 µs are shown in Figure 4.

ASI Results

Experiments were conducted at the ASI laboratory to investigate phenomena of shock fronts generated by LIBS. The ablating laser pulse was the 1064 nm fundamental from a Nd:YAG laser, and the illuminating pulse for Schlieren shadowgraphy was the 532 nm second harmonic from a different Nd:YAG laser. The ablating laser pulse was directed vertically downward onto the sample substrate, and the illuminating pulse was directed horizontally across the substrate at 90° into the optics of a gated framing camera. Snapshots of the laser-ablation shock fronts were collected at variable delays between ablating and illuminating laser pulses. The shock-front velocity showed a rather strong dependence on laser pulse energy and only a weak dependence on the substrate material, unless the substrate was pyrophoric. Data were collected from substrates of aluminum, magnesium, gold, tungsten, and stainless steel. Examples of shock-front shadowgraphs for laser ablation of Al are shown in Figure 5. The vertical shock-front velocity initially was about 45 km/s, and after 200 ns decelerated to approximately 6 km/s. While the ablating laser is still on, the laser pulse feeds energy into the expanding plasma and accelerates the shock front within the laser beam path. Once the laser is off, the horizontal component of the shock front catches up, and the aspect ratio of the shock front changes from a prolate semi-ellipsoid to a more spherical profile. The initial prolate profile may be due to ignition of a laser-supported detonation wave in the ambient atmosphere near the surface of the target.

HET Results

In June 2014, we participated in the HET parametric campaign and collected spectra from shots consisting of 15 kg of Comp B explosive in cases of aluminum, copper, and stainless steel. Our observation post was located 1.3 km from the blast site, and we collected light with a 5" Newtonian reflector telescope fiber-coupled to five Ocean Optics modular spectrometers (USB4000, USB2000+, HR4000, LIBS2500, and QE65000). The spectrometers covered a spectral range from 200 nm to 1200 nm. Each spectrometer was interfaced to a Compulab PC-2i fanless modular computer without monitor or keyboard, and the modular computers were networked as slaves via a gigabit Ethernet switch to a master computer, a Shuttle SA76G2. The master computer had a monitor, keyboard, and mouse, and acted as console for all operations of the slaves and spectrometers. A Globalsat BU-353 GPS receiver was interfaced to the master computer to provide an absolute time reference, and the master computer provided network time protocol (NTP) to discipline the

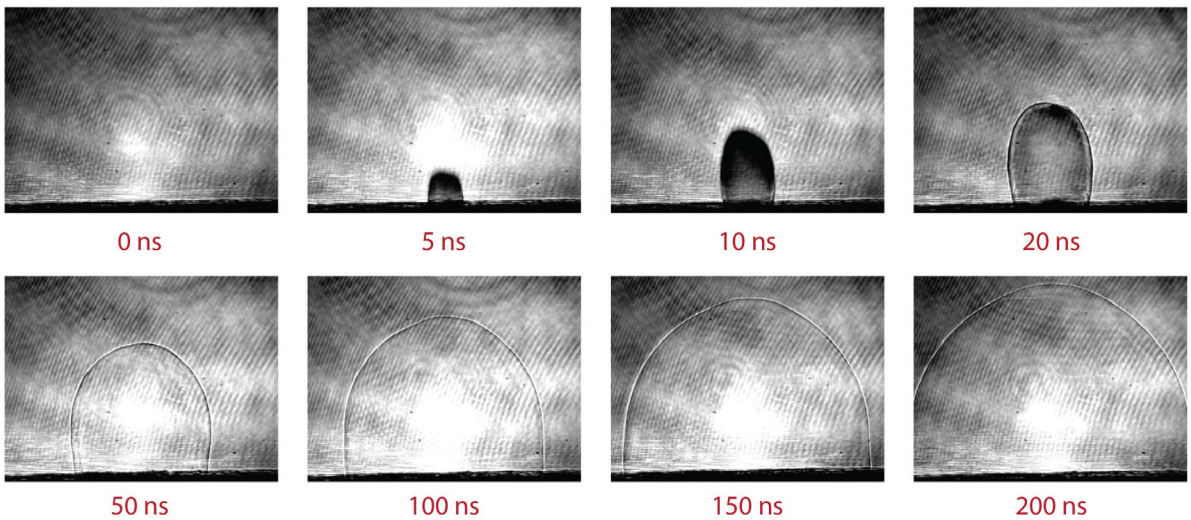

Figure 5. The vertical shock-front velocity generated by a 1064 nm, 10 ns, Nd:YAG laser ablating Al in air starts at approximately 45 km/s, and by 200 ns has slowed to approximately 6 km/s

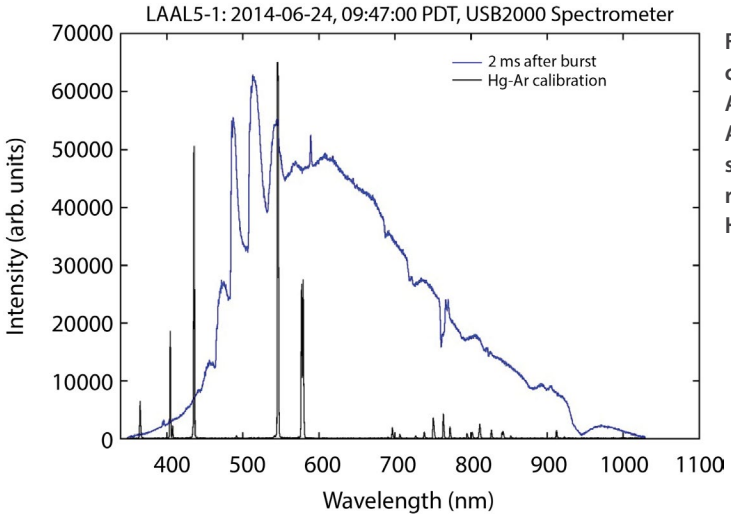

Figure 6. This spectrum from the HET shot with the Al case shows combustion of the Al, as can be seen by the AlO band structure between 450 nm and 600 nm. Atomic Al is also visible at 396 nm. The spectrum shows Na and K contamination at 589 nm and 769 nm, respectively, and Fraunhofer-type absorptions from H_2O and O_2 are also visible.

clocks of all the slaves. The time jitter from the GPS receiver was on the level of 20 ms. GPS time is capable of sub-microsecond precision, but a more precise GPS reference was not readily available to us at the time of the campaign. In any case, more precision would have been irrelevant since the Ocean Optics spectrometers are not capable of sub-millisecond timing.

Of the data collected at HET, the most interesting are from the shots with the Al cases. The spectra from those shots are brighter and hotter than those from the copper and stainless steel cases, and the Al shots show clear spectral evidence of Al combustion. The other shots do not contain any spectral evidence of the container material. The blue curve in Figure 6 shows a spectrum of an Al shot collected within 2 ms after the burst. Six vibrational bands of the B $^2\Sigma^+ \rightarrow$ X $^2\Sigma^+$ transition of AlO are clearly visible above the black-body background. The atomic transition $3s^24s \rightarrow 3s^23p$ of neutral Al is also visible, but it is small. Other features in the spectrum are line emissions from the sodium doublet at 589 nm (unresolved fine structure) and the potassium (K) doublet at 766.5 nm and 769.9 nm. Fraunhofer-type absorptions are also visible from water (H_2O) at 720 nm, 820 nm, and 940 nm, and from molecular oxygen (O_2) at 686 nm and 760 nm. The black curve in Figure 6 is a calibration spectrum from a mercury-argon (Hg-Ar) lamp collected by the same USB2000+ spectrometer. It is included in Figure 6 to illustrate the resolution of the spectrometer and to emphasize that the broadness of the emission bands between 450 nm and 600 nm is molecular in nature. The atomic lines from atomic Al, sodium (Na), and K in the HET spectrum are as narrow as the calibration lines.

Finer details of the spectra from an HET shot with an Al case, but from a different spectrometer, are shown in Figure 7. Na and K were not nominal components in the explosive charge or the case, but those elements are omnipresent in nature, and their spectral emissions are very strong. Thus, Na and K spectra were seen in all of the HET tests irrespective of the case material. Fraunhofer-type absorptions from H_2O and O_2 are also visible in the spectra because the emission light from the blast had to traverse 1.3 km of air before reaching our telescope.

Emissions from atomic Al are clearly visible in HET spectra for the $3s^24s \rightarrow 3s^23p$ transition in the ultraviolet, as seen in Figure 8. What is curious about the ultraviolet emissions is that they maximize after the initial burst, during the second burn phase. There is some uncertainty in the timing of the LIBS2500 spectrometer that collected these spectra, since its integration time was 5 ms, but the Al features do appear to maximize after the initial burst. In Figure 8, the doublet at 394 nm and 396 nm is from the $3s^24s \rightarrow 3s^23p$ transition, and the small doublet at 308.2 nm and 309.3 nm is from the $3s^23d \rightarrow 3s^23p$

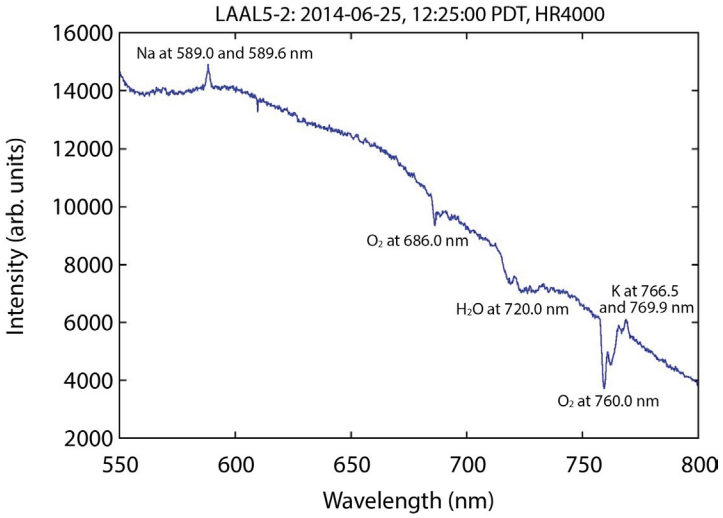

Figure 7. Na and K contamination emissions, along with Fraunhofer-type absorptions from H_2O and O_2, are seen in all of the HET spectra, irrespective of casing material

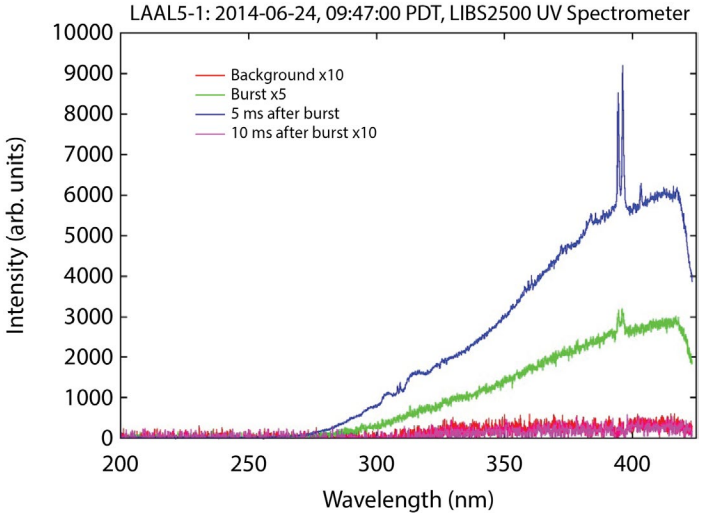

Figure 8. In the ultraviolet part of the spectrum, atomic Al and molecular AlO emissions become apparent a few milliseconds after the explosive burst

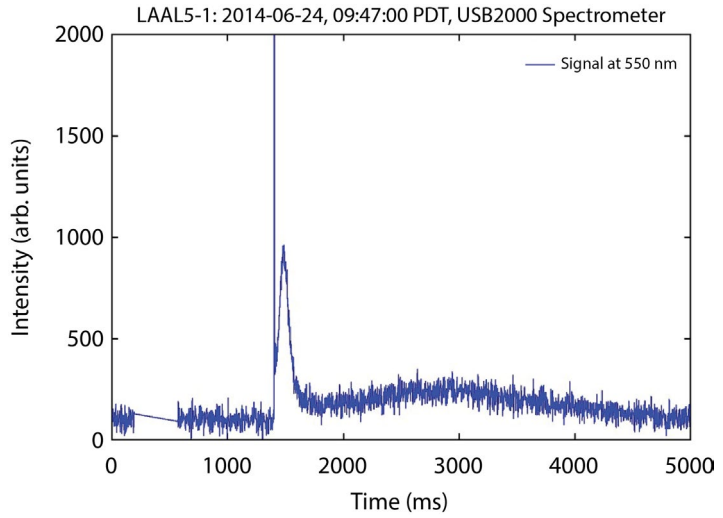

Figure 9. The radiance of the explosive burst is very bright, and it persists on the order of a millisecond, or less. Then, a few milliseconds later, a second radiance peak about an order of magnitude less intense is emitted, and it persists for more than 100 ms. This plot has the burst peak going off scale in order to show the secondary radiance peak.

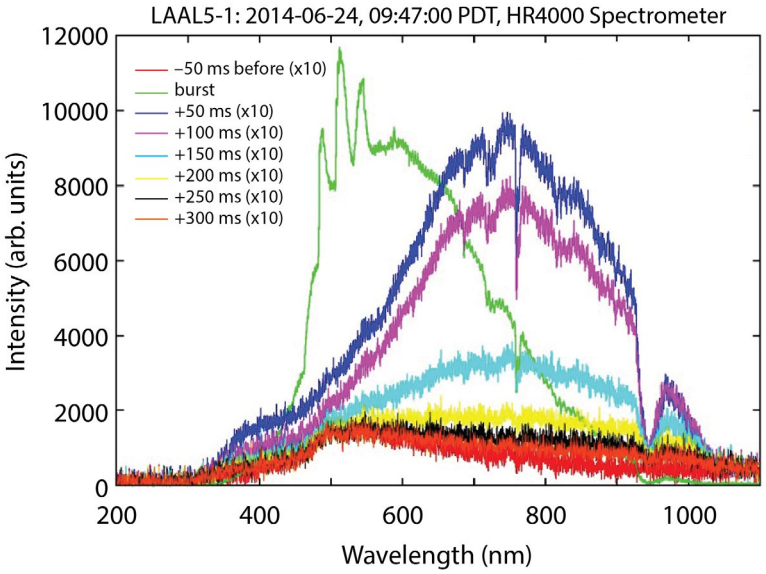

Figure 10. The green curve is the spectrum of the explosive burst. Its temperature is about 6000 K. The dark blue and magenta curves are from the second temporal radiance peak, and the temperature at that time was on the order of 4500 K.

transition. There are also small bumps in the spectra at 302 nm and 311 nm. These are the locations where one would expect to see the C $^2\Pi_r \rightarrow$ X $^2\Sigma^+$ (0-0) and (0-1) vibrational bands of AlO.

The temporal behavior of the majority of the HET blasts shows a curious rebound effect, as can be seen in Figure 9. Initially, there is a very bright burst lasting for a millisecond or less, which dies away to nearly ambient light levels. Then, after a couple of milliseconds, the radiance rises again to another peak about an order of magnitude weaker in intensity and persists between 100 and 200 ms, then dies away. The light collected after the second peak die-away is primarily reflected solar radiance. Sometimes it is brighter than pre-shot ambient light because of smoke reflection, and sometimes it is dimmer because of smoke obscuring the ambient light.

There is some debate about the origin of the second radiance peak, but it would appear to be from a second burn phase after the initial blast. Perhaps oxygen depletion during the blast extinguishes combustion and then turbulent in-welling of fresh air restarts the combustion. The spectral character of the initial burst of the Al shot indicates a burst temperature of about 6000 K. The second radiance peak has a temperature on the order of 4500 K. Examples of the burst and second peak spectra are shown in Figure 10. The burst spectrum, shown in green, has a blackbody component around 550 nm to 600 nm. The spectra for the second peak, shown in dark blue and magenta, have a blackbody component maximizing in the vicinity of 750 nm, indicating a cooler burn environment. Ultimately, the late-time spectra return to the ambient solar, or sky radiance, background (shown in yellow, black, and orange). The solar blackbody temperature is 5800 K.

Modeling Results

To better understand the information contained within spectra, we have attempted to model various aspects of the chemistry of the combustion environment and the physics of the optical emissions. In Figure 11 we show results from calculating molecular AlO emissions in a blackbody background. The vibrational and rotational states, as well as the blackbody background, were set in thermodynamic equilibrium at 6000 K. The molecular model assumed Hund's coupling case (b) for the molecular states. Franck–Condon vibrational overlap factors were taken from Londhe et al. (2010). These are consistent with the Franck–Condon factors found in Linton and Nicholls (Linton 1969) and in Coxon and Naxakis (Coxon 1985). Hönl-London formulae for angular momentum amplitudes were taken from Herzberg (1950). The instrument resolution is 100 cm^{-1}, and an approximate spectrometer roll-off at short wavelengths was included in the model.

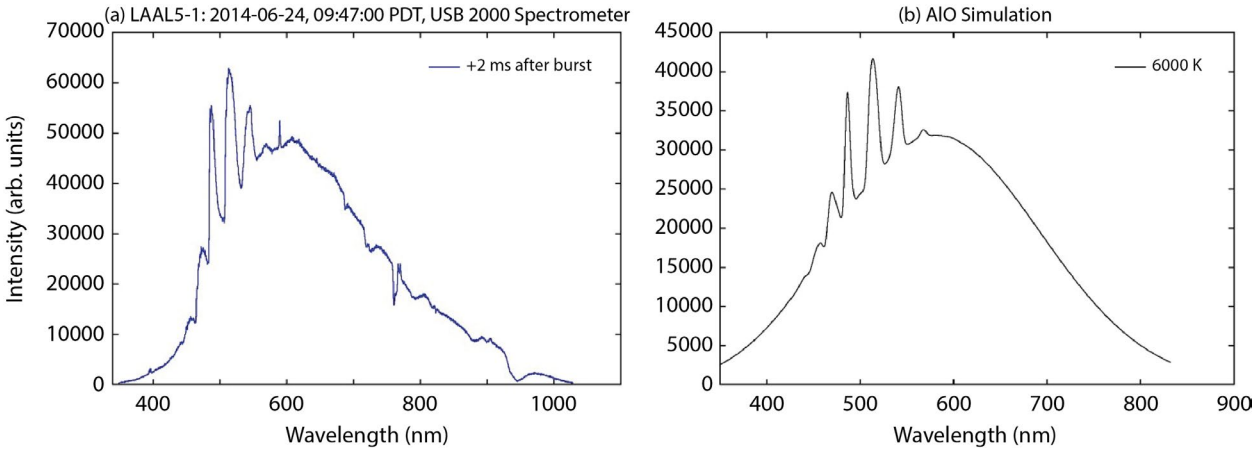

Figure 11. This comparison of (a) data and (b) simulation of AlO molecular band structure includes a blackbody background, assumes global thermodynamic equilibrium at a temperature of 6000 K, and includes a spectrometer response function. The simulation does reproduce the AlO bands convincingly, but the characterization of the spectrometer response and the convolution with the blackbody background need refinement.

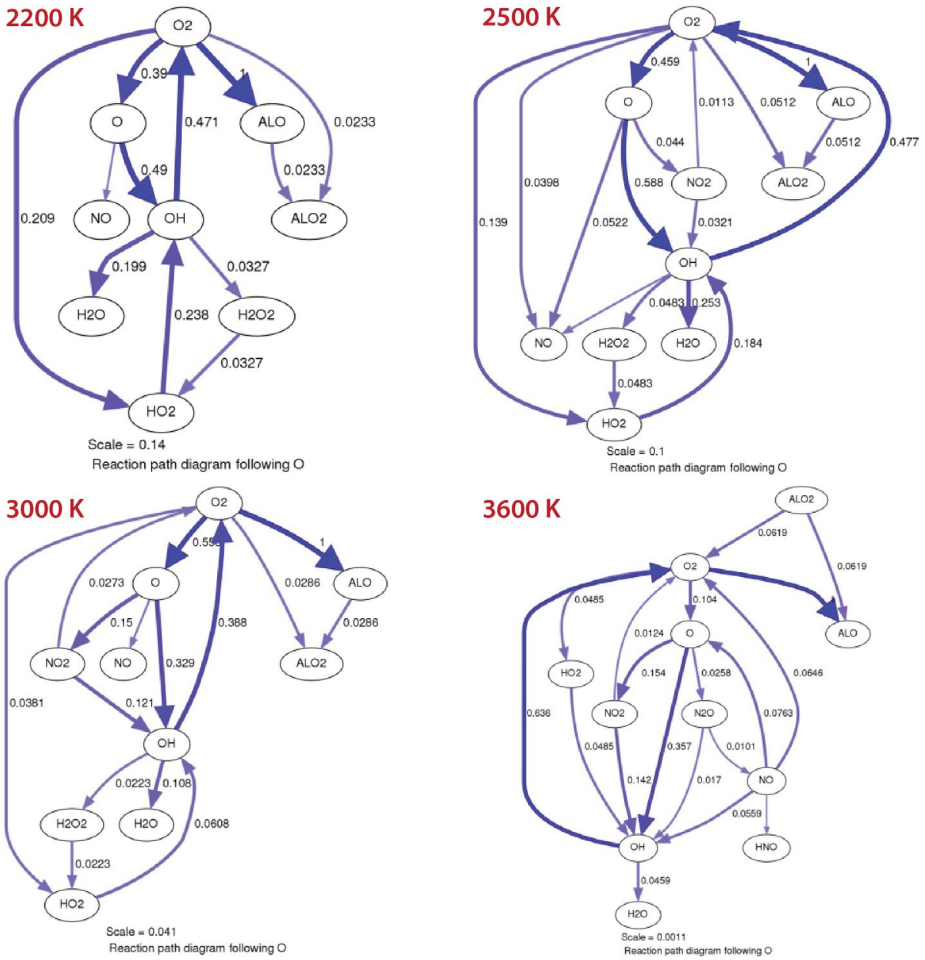

Figure 12. Reaction path diagrams for Al reacting with air to reach equilibrium at the temperatures 2200 K, 2500 K, 3000 K, and 3600 K

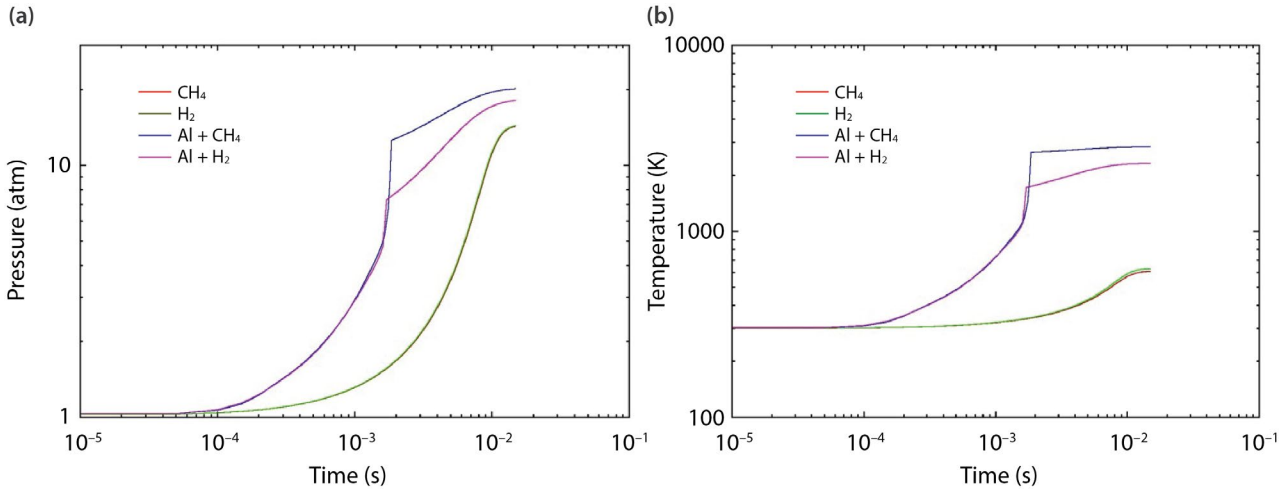

Figure 13. This Cantera simulation demonstrates that mixtures of either hydrogen (H_2) or methane (CH_4) with air undergoing adiabatic compression do not detonate for pressures up to 10 atm. Seeding the mixture with a small amount of Al vapor, however, causes the air-gas mixture to detonate once the pressure reaches just under 5 atm.

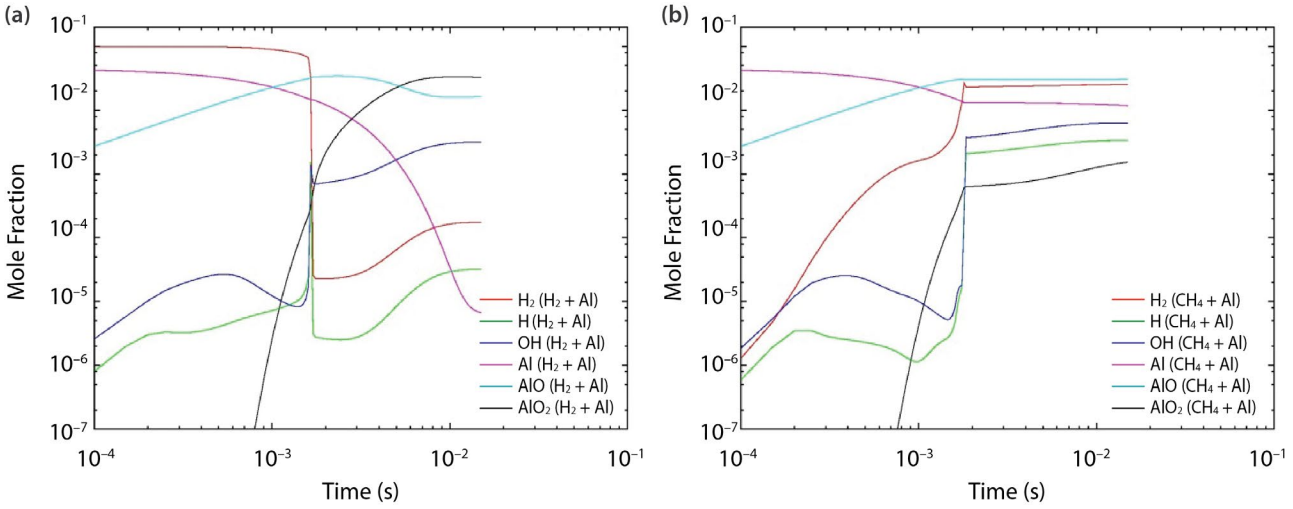

Figure 14. The same Cantera simulation for adiabatic compression of hydrogen mixed with air, with and without Al vapor seeding, shows the abrupt transition of chemical reaction constituents when detonation occurs

In addition to calculating molecular radiative transitions, we have also begun modeling the chemistry of detonation and combustion using the Cantera chemical kinetics software package (Goodwin 2014). An initial test simulation was of elemental Al reacting with air to reach equilibrium at several temperatures. The reaction path diagrams in Figure 12 show the various reaction species' fluxes from initial conditions to equilibrium at the temperatures 2200 K, 2500 K, 3000 K, and 3600 K. The model contained reasonably complete air chemistry, but it was incomplete for Al chemistry due to lack of relevant reaction data. For example, the model did not include reaction paths to Al_2O_3, which precipitates.

Another test simulation was of adiabatic compression of hydrogen gas (or methane) mixed with air, with and without seeding of elemental Al. Without the Al seeding, the air-gas mixture simply compresses and heats up (Figure 13). With the Al seeding, however, the mixture detonates when the pressure reaches 5 atm. The abrupt increase of temperature and

pressure signal rapid reaction of detonation. Similarly, the abrupt change in the mole fractions of the reaction products upon detonation is shown in Figure 14.

Conclusion

LIBS is a very flexible and powerful bench-top technique for exploring plasma phenomena related to explosives testing. Temperatures, pressures, and temporal evolution are largely tunable with laser settings, and our laboratory bench-top results anticipated much of what we saw in the field at the HET parametric campaign. Bench-top LIBS can be useful for preparing and calibrating instrumentation before going to the field, and analytical techniques developed for and tested on LIBS data can be valuable for processing and understanding data from explosives testing.

In FY 2015, we will compare plasma properties from LIBS spectra collected in air, argon, and vacuum in FY 2014; we will prepare a manuscript for publication of some of the data collected in FY 2014; and we will explore the impact of carbon obscurants on the emission spectra of aluminum and how they pertain to high-explosives testing.

Acknowledgments

We gratefully acknowledge Glen Anthony, Ben Valencia, and Wayne Lenhard for their assistance during the construction of the LIBS apparatus at STL. Additionally, we wish to thank Chunyi Liu for his assistance during the shock-front measurements at the ASI lab in Fremont, California. We are also grateful to Mike Madlener and the team at BEEF for accommodating us during the HET parametric campaign. Finally, we would like to thank Ian McKenna and Steve Jones for their hands-on assistance during the field work at BEEF.

References

Bogaerts, A., Z. Chen, R. Gijbels, A. Vertes, "Laser ablation for analytical sampling: What can we learn from modeling?" *Spectrochim. Acta, Part B: Atomic Spectroscopy* **58**, 11 (2003) 1867–1893.

Coxon, J. A., S. Naxakis, "Rotational analysis of the B $^2\Sigma^+ \rightarrow$ X $^2\Sigma^+$ system of the aluminum monoxide radical, AlO," *J. Mol. Spectrosc.* **111**, 1 (1985) 102–113.

Goodwin, D. G., H. K. Moffat, R. L. Speth, "Cantera: An object-oriented software toolkit for chemical kinetics, thermodynamics, and transport processes," (version 2.2.0) http://www.cantera.org, accessed September 30, 2014.

Herzberg, G., *Molecular Spectra and Molecular Structure I. Spectra of Diatomic Molecules*, 2nd edition, Van Nostrand Reinhold Company, New York, New York, 1950.

Kramida, A., Y. Ralchenko, J. Reader, NIST ASD Team, "NIST Atomic Spectra Database," version 5, National Institute of Standards and Technology, Gaithersburg, Maryland, http://physics.nist.gov/asd, accessed September 30, 2014.

Linton, C., R. W. Nicholls, "Relative band strengths for the AlO blue-green system," *J. Quant. Spectros. Radiat. Transfer* **9**, 1 (1969) 1–11.

Londhe, C. T., K. Sunanda, M. D. Saksena, S. H. Behere, "Franck–Condon factors and *r*-centroids of B–X, C–X, and C–A band systems of AlO molecule," *J. Mol. Spectrosc.* **263**, 2 (2010) 178–182.

Parigger, C. G., J. O. Hornkohl, "Computation of AlO B $^2\Sigma^+ \rightarrow$ X $^2\Sigma^+$ emission spectra," *Spectrochim. Acta, Part A: Molecular and Biomolecular Spectroscopy* **81**, 1 (2011) 404–411.

Schamps, J., "The energy spectrum of aluminium monoxide," *Chem. Phys.* **2**, 3 (1973) 352–366.

Solid-State Neutron Detectors Using Uranium Oxides

LAO-22-13 | Continued from FY 2013 | Year 2 of 3

Craig Kruschwitz,[1,a] David Schwellenbach,[a] Sanjoy Mukhopadhyay,[b] Thomas Meek,[c] and Brandon Shaver[c]

In this project we pursue the development of a new type of solid-state neutron detector fabricated from uranium compounds. It has been known for many years that uranium dioxide (UO_2), triuranium octoxide (U_3O_8), and other uranium compounds exhibit semiconducting characteristics with a broad range of electrical properties. We seek to exploit these characteristics to make a direct-conversion semiconductor neutron detector. In such a device a neutron interacts with a uranium nucleus, inducing fission. The fission products deposit energy, producing detectable electron-hole pairs. The high energy released in the fission reaction indicates that noise discrimination in such a device has the potential to be excellent. We fabricated Schottky devices from polycrystalline UO_2 thin films a few microns thick on a sapphire substrate and from single-crystal UO_2 samples approximately 1,500-microns thick. Neutron pulse height spectra have been simulated using GEANT4, and neutron sensitivity for the Schottky devices was tested experimentally using ^{252}Cf sources. Results, while far from perfect, indicate that UO_2 holds promise as a potential direct-conversion neutron detector material. In FY 2015, we will focus on improving the quality of the uranium oxide samples, improving the quality of the Schottky junctions, and possibly fabricating a p-n junction.

[1] kruschca@nv.doe.gov, 505-663-2023
[a] Los Alamos Operations; [b] Remote Sensing Laboratory–Andrews; [c] The University of Tennessee, Knoxville

Background

Highly efficient neutron detectors are required for a wide variety of applications ranging from homeland security to astronomy. The well-known shortage of ^3He gas has recently driven a search for new neutron detector materials to replace ^3He-based detectors. Solid-state devices are one such alternative, as they are more compact and require smaller voltages to operate compared to ^3He gas detectors. Solid-state neutron detection devices are classified as one of two types: indirect-conversion devices and direct-conversion devices.

In an indirect-conversion device, a layer of a neutron-reactive substance (usually ^{10}B or ^6Li) is placed in contact with a separate detector material, typically a silicon diode. A neutron interacting in the reactive layer produces energetic reaction products, some of which deposit energy in the detector material, generating electron-hole pairs and hence a signal. Devices of this type have been produced by a variety of groups recently. A key shortcoming of such devices is that only some of the reaction energy can be deposited in the detecting medium; the rest is either absorbed in the reactive material or moves away from the detecting medium to conserve momentum in the reaction. Use of etching technologies to create complex structures in the silicon detector, in which the neutron-reactive material is then embedded, have led to significant increases in the neutron sensitivity for such devices (McGregor 2009, Bellinger 2010, Nikolic 2010). However, improvements could be made upon such devices with the discovery of a suitable direct-conversion device material.

In a direct-conversion device, the neutron-reactive material and the detector material are one and the same—virtually all of the reaction energy is available for detection. But materials suitable for direct-conversion devices are relatively rare, and their properties are often poorly understood. In the past, much research has been conducted into boron-based compounds, such as boron carbide and boron nitride. More recently, groups at Fisk University, Y-12, and Radiation Monitoring Devices have investigated lithium indium diselenide ($LiInSe_2$) (Kargar 2011, Tupitsyn 2012). However, none of these materials have yet proven viable as direct-conversion detector materials.

The goal of this project, which continues work started in FY 2013 (Kruschwitz 2014), was to evaluate the feasibility of using uranium dioxide (UO_2) as a candidate material for a direct-conversion semiconductor neutron detector. Until recently, UO_2 and other uranium oxides have been largely overlooked as neutron detector materials, despite being known to have semiconducting properties and to be neutron reactive. In this initial work we used depleted uranium (DU), which consists primarily of ^{238}U. The cross sections for neutron-induced fission as a function of neutron energy for both ^{238}U and ^{235}U are plotted in Figure 1. The data are from the ENDF/B VII tables (Chadwick 2006). The fission cross section of ^{238}U for slow neutrons is small, unlike that of ^{235}U; for >1 MeV energy neutrons, however, the ^{238}U fission cross section approaches that of ^{235}U, making a DU-based detector suitable for fast neutron detection. A fast neutron incident on a ^{238}U nucleus induces fission, releasing >165 MeV of energy. This energy is deposited locally, creating copious electron-hole pairs, which are detectable as an electrical signal in the detector.

The large amount of energy released as a result of the fission of a uranium nucleus, especially when compared to that released in the transmutation of ^{10}B or ^{6}Li nuclei, raises the possibility of developing a neutron detector with exceptional noise and gamma discrimination. Though UO_2 has a high effective Z-number and a high density, and is therefore more sensitive to gamma rays than other semiconductor materials, the energy deposited by gammas is still likely to be much less than that deposited by fission, and indeed in most cases, gamma backgrounds would likely be less than the natural background in the UO_2 due to emission of 4.3 MeV and 4.7 MeV α-particles from the decay of ^{238}U and ^{235}U, respectively. The one exception to this would be gamma rays with sufficient energy (>6 MeV) to induce photofission in ^{238}U and ^{235}U. Photofissions from such gammas would produce signals that are indistinguishable from neutron-induced fissions.

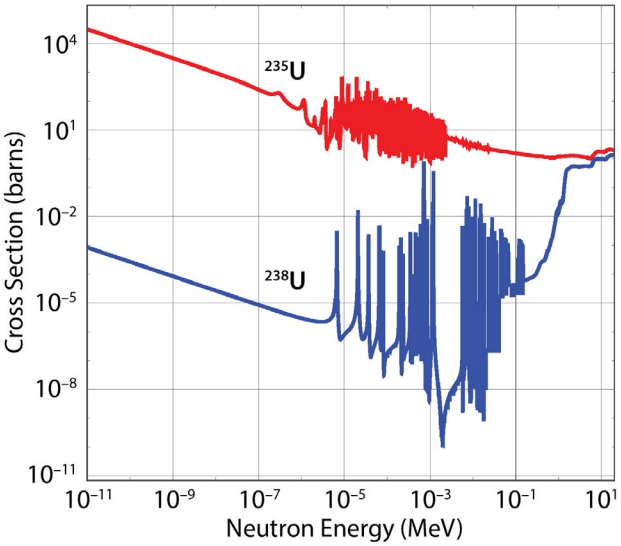

Figure 1. Neutron-induced fission cross sections vs. neutron energy for ^{235}U and ^{238}U. ^{235}U has a relatively high cross section for thermal and low-energy neutrons, while ^{238}U is sensitive primarily to neutrons with energies greater than 1 MeV.

Semiconductive Properties of UO_2

UO_2 has some fascinating properties, which make it an interesting material not only for radiation detection, but also as a general-purpose semiconductor material. While we refer to UO_2 as a semiconductor here, and it was long assumed to be one, it is not a semiconductor according to traditional band theory. Indeed, band theory actually predicts UO_2 to be a conductor. Instead, due to strong correlations arising from interactions between electrons, UO_2 is a Mott insulator (Mott 1949, Roy 2008). The band gap, according to theoretical modeling (He 2013), is around 2 eV, though

the precise stoichiometry and dopant profile can affect this (Meek 2005). This value has been verified by optical absorption measurements (Ruello 2004).

The electrical and thermal properties of UO_2 have also been studied extensively, due largely to its use as a nuclear fuel (An 2011). The resistivity of intrinsic UO_2 is about 1.5×10^3 Ω-cm at room temperature, which is similar to Si and GaAs. The resistivity, however, is highly sensitive to the stoichiometry of the sample, such that hypostoichiometric compositions are insulating and hyperstoichiometric compositions are more conductive (Meek 2001). The conduction mechanism in UO_2 has also been studied and has been determined to be p-type and due to small polaron hopping (Devreese 1966, De Coninck 1969). The carrier mobilities in materials exhibiting small polaron hopping transport are typically very low, and UO_2 appears to be no exception, with most measurements of the mobility being around 10^{-2}–10^{-1} $cm^2/(V{\cdot}s)$ (Nagels 1963, Devreese 1966, De Coninck 1969). There has, however, been wide variation in measurements of UO_2 carrier mobility, with some early experiments yielding values as high as 10 $cm^2/(V{\cdot}s)$ (Hartmann 1936). Such high values are the exception though, and it is generally accepted that the carrier mobility in UO_2 is on the order of 10^{-2}–10^{-1} $cm^2/(V{\cdot}s)$.

Recently, there has been interest in exploring the use of UO_2 and other oxides of uranium to fabricate electronic devices (Meek 2001, 2005), and as a possible material to use for neutron detection (Caruso 2010). In work described by Meek (2008), Schottky diodes were fabricated from UO_2 deposited in thin films using the sol-gel process, and a simple p-n-p transistor was successfully fabricated from a single crystal of UO_3. Meek (2005) also studied the effects of various dopants on the electrical properties of UO_2. In addition to their semiconductive characteristics, uranium oxides offer other potential advantages as semiconductor materials. For example, UO_2 and triuranium octoxide (U_3O_8), being ceramic oxides, can withstand much higher temperatures than other semiconductor materials (Meek 2005). Uranium oxides may also be expected to be more resistant to radiation damage than many other materials. These characteristics make them potentially attractive candidates for detectors in high-temperature or high-radiation environments.

Project

GEANT4 Simulations

In FY 2013, we performed simulations of neutron-induced fission efficiency of UO_2-based devices using MCNP. However, MCNP does not track fission fragments and thus is of limited use for our study of UO_2-based neutron detectors. GEANT4 (Agostinelli 2003), however, does have this capability and therefore we used this package to study the fission fragment energy deposition in the UO_2. The GEANT4 simulations modeled samples with thicknesses as thin as 1 µm with source neutron energies of thermal, 1 MeV, and 10 MeV.

Simulated pulse height spectra from fission product energy deposition in UO_2 samples with 1, 2, and 100 µm thicknesses are plotted in Figure 2. The source neutron energy for all of these pulse height spectra is 10 MeV. It is clear that not all of the fission fragment energy is deposited in the 1 and 2 µm thick samples, leading to much broader spectra for these samples. This is expected, as the range of a fission fragment in UO_2 is on the order of 6–10 µm. It is encouraging to note, however, that even for the 1 µm sample, the smallest value of deposited energy is ~20 MeV. We expect this to be well above the inherent α-particle–induced background, as well as any background from gammas. For the 100 µm sample, a well-defined peak at around 165 MeV is seen, indicating essentially all of the fragment energy is deposited in the UO_2 at this sample thickness.

Fabrication of UO_2 Samples

Fabrication and preparation of UO_2 samples was performed by the Meek group from the University of Tennessee, Knoxville, Materials Science and Engineering Department. Samples have been fabricated using two different techniques. Thin film, depleted UO_2 samples were formed by a chemical

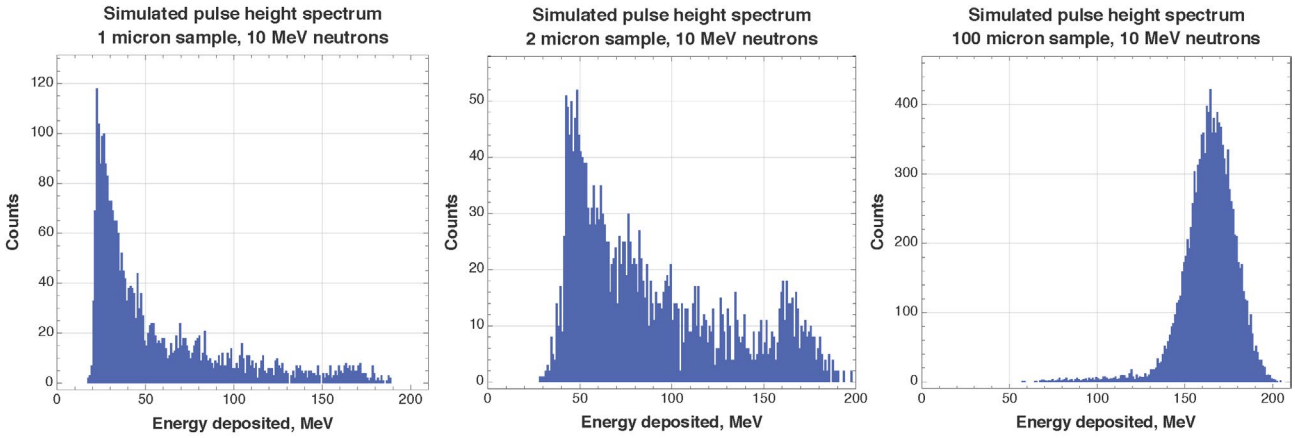

Figure 2. Simulated energy deposition pulse height spectra for 10 MeV neutrons incident on 1, 2, and 100 µm UO_2 samples. Significant fission fragment energy escapes the thinner samples, while essentially full energy deposition is obtained for the 100 µm sample.

solution deposition technique. This technique is an inexpensive and effective way of fabricating thin films. Uranyl acetate precursors are deposited onto sapphire substrates. The sapphire substrates are first plasma cleaned, and then a 50 nm layer of Au is sputtered onto a third of the surface to be used as a rectifying contact. The solvent is then evaporated and the thin film annealed in an argon atmosphere. Upon cooling, a 50 nm layer of Ag is sputtered onto the top surface to create an ohmic contact. A schematic of the thin film samples is shown in Figure 3b. The maximum film thickness obtainable with this method is on the order of a few microns. While this is most likely too thin to be of much practical use for neutron detection, it is sufficient for testing the concept. Indeed, the GEANT4 simulations presented earlier indicate that even though substantial fission fragment energy will escape such a thin sample, a clearly distinguishable fission pulse height spectrum should be obtainable. Thus far, however, the thin film samples have primarily served as a method of studying the effects of stoichiometry on UO_2 thin film electrical properties. In FY 2015, we will attempt to use the thin film samples to detect neutrons.

The Meek group provided several single-crystal UO_2 samples, which were available from earlier research and some of which were used in our FY 2013 work. A typical single-crystal sample is pictured in Figure 3a. The samples varied in size, but most were approximately

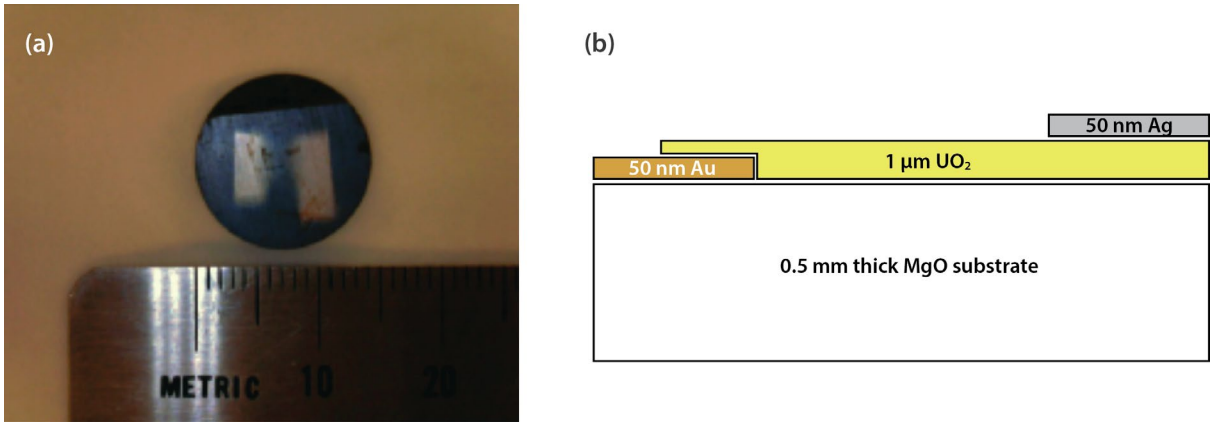

Figure 3. UO_2 samples used in experimental tests. (a) Single-crystal sample with Au and Ag contacts deposited on a surface; (b) schematic of a typical thin film sample.

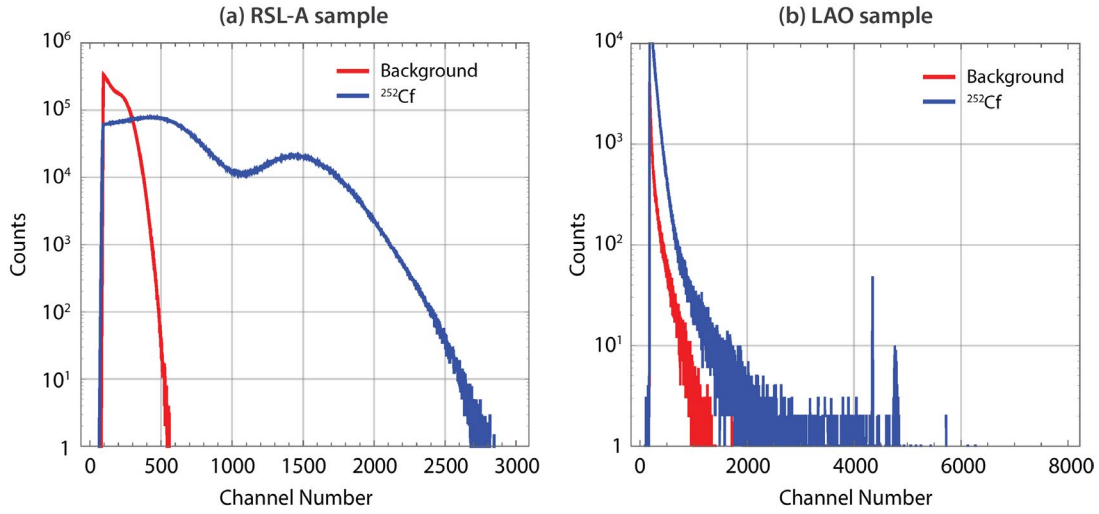

Figure 4. Measured background and ^{252}Cf source pulse height spectra. (a) Results from RSL-A tests and (b) subsequent tests at LAO with different electronics. RSL-A results show a change in the noise spectrum. LAO results exhibit some clearly distinguishable high-energy pulses in the source spectrum.

0.5" in diameter and 1.0 to 1.5 mm thick. The majority of the single-crystal samples were doped with different dopant materials in varying concentrations at each of the sample faces. The dopants were deposited using ion beam implantation and were generally confined to a layer near the sample surface. Thin coatings (50 nm) of Au and Ag were sputtered onto each surface of the samples to attempt to make Schottky and ohmic contacts, respectively. Use of a sputterer to first clean the surface and then deposit the electrode coatings was a major improvement over our FY 2013 procedures, which used Au and Ag conductive paint to make electrodes. Current-voltage characteristics were measured for some of the samples using a Keithley Semiconductor Characterization System. Ongoing problems with the Keithley station have limited our ability to measure current-voltage characteristics, but the few current-voltage characteristics obtained so far verify that a few of the samples exhibit Schottky diode behavior, albeit with high leakage currents. Most of the samples, though, exhibit relatively little rectification, perhaps due to the dopants near the sample surface. Several samples were tested as potential neutron detectors.

Experimental Tests

Preliminary tests on neutron sensitivity have been performed on some of the single-crystal samples mentioned above. These were tested in laboratory facilities at the Remote Sensing Laboratory–Andrews (RSL-A). The experiments used a 67 µCi ^{252}Cf source in two different configurations: (1) moderated to produce thermalized neutrons and (2) bare to give a raw fission neutron spectrum. No shielding was used to eliminate gammas in the tests. A high-voltage power supply was used to supply a reverse voltage bias to the samples. An ORTEC preamplifier (Model 142), ORTEC amplifier (Model 527A), and ORTEC multichannel analyzer were used to obtain pulse height spectra.

Data from an intrinsic (undoped) sample tested at RSL-A are shown in Figure 4a. Background spectra were collected away from the ^{252}Cf source. Then spectra were taken with the sample as close as possible to the ^{252}Cf source—approximately 4–5 cm when thermalized, less when bare. The background spectrum and the spectrum collected near the source for the phosphorous-doped sample are shown in Figure 4a. Spectra for other samples tested look similar to that shown in Figure 4a, and the spectra were consistent across several integrations. There is clearly a

significant difference between the two spectra, with the ^{252}Cf source spectrum exhibiting higher energy pulses, but the general shape of the spectra are similar. We expected a clear high-energy fission peak well separated from the background signal as in the simulation results shown in Figure 2, but no such feature appears in the spectra. Also absent are clear features corresponding to the 4.3 and 4.7 MeV decay α-particles. After the experiments were completed, we discovered a problem with the electronic circuit we used to apply the voltage to the sample. This problem was such that the applied reverse bias was of a much smaller magnitude than we desired and intended. This may explain why the RSL-A tests only succeeded in seeing changes in the background spectrum.

Follow-up tests were performed at Los Alamos Operations (LAO) using a non-thermalized 5.2 µCi ^{252}Cf source. In the LAO experiments, some changes were made to the electronics used to bias the samples. These changes permitted us to apply much higher voltages than in the RSL-A tests. Figure 4b shows typical source and background spectra using the LAO setup. It is evident that the source spectrum exhibits pulses at high energy well above background. The number of high-energy counts is very small, however, due to the relatively small activity of the source and short integration time. Nevertheless, we view this as an encouraging improvement. The quality of the diodes presents problems, as high leakage currents resulting from the relatively low resistivity of the material and poor rectification properties of the Schottky contact are a hindrance to fission-induced pulse detection. We will actively seek to improve sample quality in FY 2015. The thin film samples hold some promise in that they show better rectification at the Schottky junction and have much higher resistance, which should help reduce leakage currents.

Conclusion

In FY 2014, we continued our exploration of uranium oxides, in particular UO_2, as a potential direct-conversion semiconductor neutron detector material. Our primary focus has been on improving the quality of the UO_2 devices we are using. We improved electrode quality by using a sputterer to deposit the electrode materials on the UO_2 samples, rather than using conductive paints for the contacts as we did in FY 2013. We also made high purity thin film samples (approximately 1 µm thick), although these have not yet been tested for neutron sensitivity. Additionally, in FY 2014 we improved upon FY 2013 MCNP modeling efforts by instead using GEANT4 to simulate pulse height distributions. The GEANT4 results indicate that for UO_2 samples as thin as 1 µm, a pulse height spectrum with a fission feature clearly separable from background may be obtainable.

Preliminary neutron sensitivity tests using a ^{252}Cf source have been performed on some simple Schottky devices fabricated from single crystals of UO_2. The samples themselves were not ideal, suffering from poor rectification despite the aforementioned improvements in the techniques used to deposit the electrode coatings. Furthermore, problems with the electronics in our initial experimental setup were discovered. Nevertheless, we saw clear differences between background and ^{252}Cf source pulse height spectra. Follow-up experiments, which improved upon some of the electronics issues, exhibited clear high-energy pulses in the presence of a ^{252}Cf source that are absent in the background spectrum. The results indicate that UO_2 holds some potential as a direct-conversion neutron detector material.

The principal investigator was asked to present an invited paper at the SPIE Hard X-ray, Gamma-Ray, and Neutron Detector Physics conference. The conference occurred in August of 2014 and the talk was well received. Collaborators at the University of Tennessee presented posters at the Gordon Research Conference on Inorganic Chemistry in June of 2014.

In FY 2015, the final year of this project, our focus will be on improving the quality of the samples and on performing a definitive test of the concept of using uranium oxides for a direct-conversion neutron detector. We will have alternative fabrication techniques available to us such as tape casting and vapor phase deposition. These will allow us

to improve the purity of the samples and possibly make heterojunctions from different oxides using different techniques. We will also pursue making a p-n heterojunction by depositing UO_2 on a silicon substrate.

References

Agostinelli, S., et al., "GEANT4—a simulation toolkit," *Nucl. Instrum. Methods Phys. Res. A* **506**, 3 (2003) 250–303.

An, Y. Q., A. J. Taylor, S. D. Conradson, S. A. Trugman, T. Durakiewicz, G. Rodriguez, "Ultrafast hopping dynamics of 5*f* electrons in the Mott insulator UO_2 studied by femtosecond pump-probe spectroscopy," *Phys. Rev. Lett.* **106**, 20 (2011) 207402.

Bellinger, S. L., R. G. Fronk, W. J. McNeil, J. K. Shultis, T. J. Sobering, T. J., D. S. McGregor, "Characteristics of the stacked microstructured solid state neutron detector," *Proc. SPIE* **7805** (2010) 78050N.

Caruso, A. N., "The physics of solid-state neutron detector materials and geometries," *J. Physics Cond. Matter* **22** (2010) 443201.

Chadwick, M. B., et al., "ENDF/B-VII.0: Next generation evaluated nuclear data library for nuclear science and technology," *Nuclear Data Sheets* **107**, 12 (2006) 2931–3060.

De Coninck, R., J. Devreese, "The thermoelectric power and the conduction mechanism in nearly stoichiometric uranium dioxide single crystals," *Phys. Status Solidi B* **32**, 2 (1969) 823–829.

Devreese, J., R. De Coninck, H. Pollak, "On the conduction mechanism in uranium dioxide," *Phys. Status Solidi B* **17**, 2 (1966) 825–829.

Hartmann, W., "Elektrische Untersuchungen an oxydischen Halbleitern," *Zeitschrift für Physik* **102**, 11–12 (1936) 709–733.

He, H., D. A. Andersson, D. D. Allred, K. D. Rector, "Determination of the insulation gap of uranium oxides by spectroscopic ellipsometry and density functional theory," *J. Phys. Chem. C* **117**, 32 (2013) 16540–16551.

Kargar, A., J. Tower, H. Hong, L. Cirignano, W. Higgins, K. Shah, "Lithium and boron based semiconductors for thermal neutron counting," *Proc. SPIE* **8142** (2011) 81421P.

Kruschwitz, C. A., D. Schwellenbach, S. Mukhopadhyay, T. Meek, J. Auxier, B. Shaver, T. Cunningham, "Solid-state neutron detectors using uranium oxides," in *Site-Directed Research and Development*, FY 2013, National Security Technologies, LLC, Las Vegas, Nevada, 2014, 97–102.

McGregor, D. S., W. J. McNeil, S. L. Bellinger, T. C. Unruh, J. K. Shultis, "Microstructured semiconductor neutron detectors," *Nucl. Instrum. Methods Phys. Res. A* **608**, 1 (2009) 125–131.

Meek, T., M. Hu, M. J. Haire, "Semiconductive properties of uranium oxides," *Waste Management Symposium* **10**, 6 (2001), http://www.wmsym.org/archives/2001/14/14-3.pdf, accessed October 1, 2014.

Meek, T., B. Von Roedern, P. Clem, R. Hanrahan, Jr., "Some optical properties of intrinsic and doped UO_2 thin films," *Materials Letters* **59**, 8–9 (2005) 1085–1088.

Meek, T. T., B. Von Roedern, "Semiconductor devices fabricated from actinide oxides," *Vacuum* **83**, 1 (2008) 226–228.

Mott, N. F., "The basis of the electron theory of metals, with special reference to the transition metals," *Proc. Phys. Soc. A* **62**, 7 (1949) 416–422.

Nagels, P., M. Denayer, J. Devreese, "Electrical properties of single crystals of uranium dioxide," *Solid State Commun.* **1**, 2 (1963) 35–40.

Nikolic, R. J., et al., "Nine element Si-based pillar structured thermal neutron detector," *Proc. SPIE* **7805** (2010) 78050O.

Roy, L. E., T. Durakiewicz, R. L. Martin, J. E. Peralta, G. E. Scuseria,C. G. Olson, J. J. Joyce, E. Guziewicz, "Dispersion in the Mott insulator UO_2: A comparison of photoemission spectroscopy and screened hybrid density functional theory," *J. Comput. Chem.* **29**, 13 (2008) 2288–2294.

Ruello, P., K. D. Becker, K. Ullrich, L. Desgranges, C. Petot, G. Petot-Ervas, "Thermal variation of the optical absorption of UO_2: Determination of the small polaron self-energy," *J. Nucl. Mat.* **328**, 1 (2004) 46–54.

Tupitsyn, E., P. Bhattacharya, E. Rowe, L. Matei, M. Groza, B. Wiggins, A. Burger, A. Stowe, "Single crystal of $LiInSe_2$ semiconductor for neutron detector," *Appl. Phys. Lett.* **101**, 20 (2012) 202101.

This page left blank intentionally

An Experimental and Theoretical Investigation into the Chemical Properties of Uranium and Thorium Ions in the Gas-Phase and on Surfaces

STL-19-13 | Continued in FY 2015 | Year 2 of 3

Manuel J. Manard[1,a]

The continued development of an instrument that embeds a variable-temperature, high-pressure drift/reaction cell between two quadrupole mass analyzers for the purpose of investigating gas-phase interactions of uranium (U) and thorium (Th) ions with neutral reactant species is discussed. This is the second year of a three-year collaborative effort involving the Special Technologies Laboratory and the University of California, Santa Barbara. Our overall aim is to probe the interactions of U and Th ions both in the gas phase and deposited on surfaces. The primary focus this year was assembly of an instrument that will be used to generate data for gas-phase, ion-neutral reactions. The system is designed to mass-select ions with the first quadrupole for injection into the drift/reaction cell. The cell, which measures 4 cm in length, has a uniform electric field supplied by eight ring electrodes situated inside the cell body. The cell pressure is variable up to 5 Torr, and the temperature of the cell can range from 80 to 800 K. Ions exiting the cell are mass-selected by the second quadrupole and detected by an electron multiplier. Thermodynamic and kinetic properties of U and Th ions when reacting with ligands of interest that occur in the cell will be studied. This effort will also utilize density functional theory to theoretically model the systems studied to elucidate the complex factors involved with these bonding interactions. The experiments described will be the primary focus of the project in FY 2015.

[1] manardmj@nv.doe.gov, 805-681-2121
[a] Special Technologies Laboratory

Background

A deeper understanding of the chemical properties of uranium (U) and thorium (Th) compounds could lead to advancements in techniques used to detect these compounds for the purposes of nuclear nonproliferation. Here, a detailed investigation into the fundamental chemical interactions that occur, for example, when these materials are exposed to the atmosphere or are spilled on the ground, could unearth new proliferation signatures or generate new methodologies for remote detection. Additionally, by generating metal or mixed-metal cluster ions in addition to U and Th, the potential of observing reactions that occur when shocked materials are ejected into the surrounding environment exists. These studies could result in new or improved diagnostics for the shock physics community. In all cases, by comparing or contrasting the experimental data collected on species of interest in the gas phase and on surfaces and combining these findings with theoretical calculations using density functional theory, we expect to further our knowledge about the fundamental chemical properties of these systems.

Studies involving mass-selected ion-neutral interactions have the potential to elucidate some of the complex factors involved with the bonding processes of these species. By experimentally determining the fundamental physical properties of these molecules, such as bond dissociation energies, association entropies, molecular geometries, and reaction energetics (to name a few), a deeper understanding of these processes will be gained, leading to the possibility of manipulating their chemistry for a specific outcome. The results of these studies can also be used as an experimental point of reference to verify the accuracy of theoretical methods used to predict these properties for more complicated systems.

Project

A schematic representation of the instrument, as well as an illustration of the type of data that will be generated by the system, are shown in Figure 1. The design details of the components that make up the various regions of the instrument were described in the final report for the first year of the project (Manard 2014). The mechanical design of the system was generated using the SolidWorks software package, and ion trajectory simulations were performed using Simion 8 to determine the optimal configuration of electrodes and electric field strengths to efficiently guide the ion beam through the system. This year, the primary focus of the project was construction of the instrument. This process involved fabrication of the parts and components that make up the system; acquisition and modification of numerous commercially available components that are incorporated into the design of the instrument; and the development of the electronic control modules that supply the various electric fields to each region of the instrument to control the kinetic energy and trajectories of the ions being studied. Thus, the instrument is made up of several subassemblies that combine to generate the ion-neutral reaction data. These subassemblies consist of the ion sources, the ion source focusing assembly, the first quadrupole assembly, the reaction cell, and second quadrupole/detector assembly. A detailed discussion of the various subassemblies is provided in the following sections. A picture of the assembled instrument is shown in Figure 2.

Ion Sources

As stated in last year's report (Manard 2014), the instrument was designed to allow for the use of various types of ionization sources, depending on the nature of analytes being studied. The ion sources that will be used with the system are shown in Figure 3. These ion sources share similar design aspects. Specifically, the source bodies can be floated to a desired potential so that ions formed within the region have a known kinetic energy when exiting the source. The ion kinetic energy is variable up to 100 eV. Additionally, an extraction potential can be applied to the exit orifice of each source (measuring 0.5 mm) to aid in "pulling" the ions out of the source. The exit orifice of each source also serves as a conductance-limiting orifice that restricts the flow of the inert bath gas that cools the ions by collision, after they are formed, so that the kinetic energy of the beam is well defined by the source bias.

The electron impact source will provide diagnostic information to optimize the experimental conditions used to guide the beam through the instrument. Once these parameters have been established, the laser vaporization source will generate the Th and U ions. Here, metal ions will be generated using pulsed laser vaporization of a translating/rotating metal rod in a high-pressure argon (Ar) bath gas. The desorbed metal plasma will be entrained in the Ar to collisionally cool the plasma and, if desired, generate clusters. The laser light enters the vacuum chamber via a laser window positioned perpendicular to the axis of the instrument. A pulse valve generates the Ar pulse, which is synchronized with the laser pulses by a delay generator.

Source Focusing Assembly

Ions exiting the source are focused in the ion source chamber by an Einzel lens through a 0.3" conductance-limiting orifice into the vacuum chamber housing the

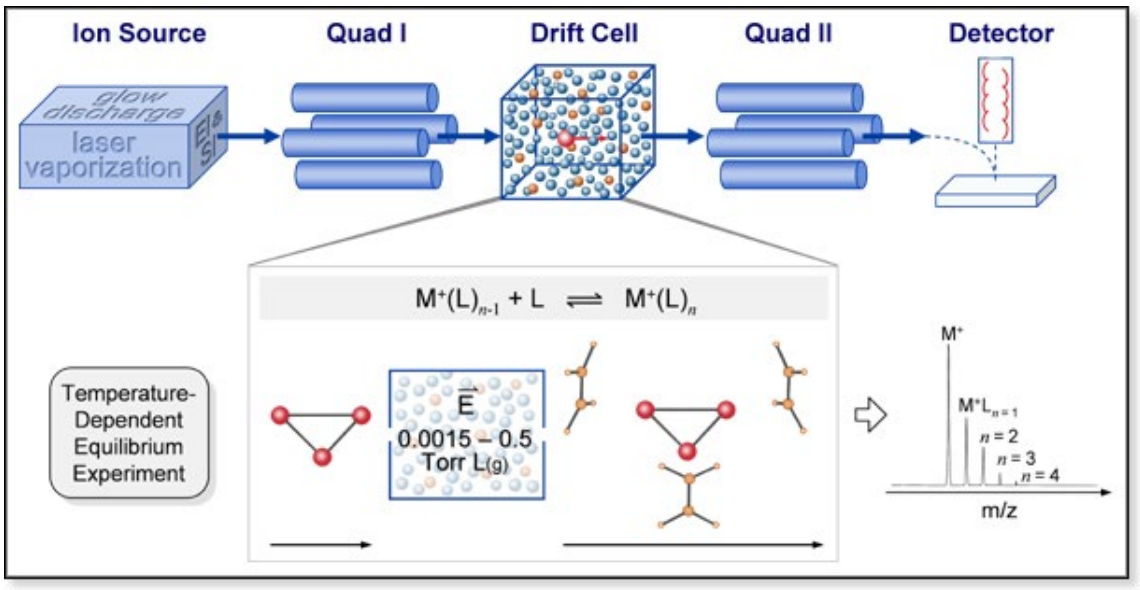

Figure 1. Schematic representation of the quadrupole-cell-quadrupole mass spectrometer

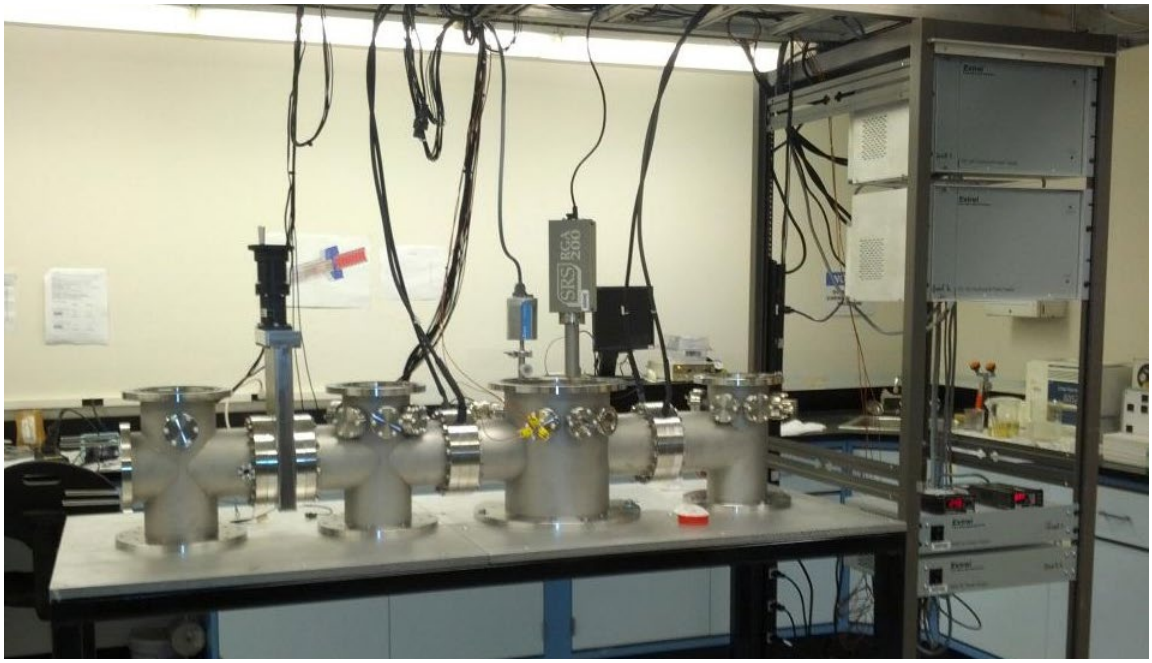

Figure 2. The assembled quadrupole-cell-quadrupole instrument. The chambers shown (left to right) are the ion source chamber, the first quadrupole chamber, the main chamber, and the second quadrupole/detector chamber. The various subassemblies are housed within these vacuum chambers.

first quadrupole. An *xy*-steering electrode is situated directly following the source Einzel lens to correct the trajectory of the ion beam prior to introduction to the first quadrupole, if needed. An additional electrode is positioned directly after the steering element, which is connected to an electrometer as a diagnostic to measure the total ion current generated by the ion source. Finally, an isolation valve positioned between the source chamber and the rest of the instrument allows samples to be changed without needing to vent the entire system.

Figure 3. The three ionization sources developed for use with the instrument. The sources shown (left to right) are an electronic impact source, a DC-discharge source, and a laser vaporization source.

First Quadrupole and Transfer Lenses

The entrance half of the first quadrupole assembly is shown in Figure 4. Two electrostatic tube lenses focus the ion beam into the first quadrupole. The quadrupole (made by Extrel Core Mass Spectrometers) is made up of ¾-inch rods and has a mass range of 4–4000 amu. The quadrupole shroud has been modified to include venting slots to improve pumping efficiency. Ion kinetic energy through the quadrupole is a function of the potential applied to the source body and the quadrupole bias. The kinetic energy of the beam is variable, with higher ion energies leading to higher sensitivity and ion transmission through the quadrupole, while lower kinetic energies maximize the mass resolution. A similar section of steering/focusing elements are positioned directly after the first quadrupole. These electrodes focus the mass-selected ion beam into the drift/reaction cell. The assembly utilizes two $^{5}/_{16}$-inch ceramic rods to ensure proper alignment of the individual components.

Drift/Reaction Cell

The drift/reaction cell is shown in Figure 5. The cell is based on the design of Kemper and Bowers (Kemper 1990), which consists of a cylindrical copper shroud that contains the heating/cooling passages, an end cap that is electrically isolated from the shroud, and eight ring electrodes that provide the uniform drift field through the cell. A precision resistor chain delivers the proper potentials to the individual drift rings. Ions are drawn though the cell under the influence of the electrical field. The field will be weak enough so that the thermal energy of the ions is not significantly perturbed. The drift volume is 4 cm long by 1.5 cm in diameter, with entrance and exit orifices measuring 0.5 mm in diameter. The maximum operating pressure of the cell is 5 Torr. The pressure in the cell is monitored using a capacitance manometer. Separate gas inlet connections are made to the helium (He) buffer gas, the reactant gas, and to the pressure monitor.

The experimental temperature range of the cell can be varied from 80 to 800 K. Temperatures greater than 300 K are achieved by resistive heating of tantalum resistors embedded in the cell body, while temperatures below 300 K are reached by flowing cooled liquid nitrogen through channels that are also present in the cell body. The temperature is monitored by three thermocouples, placed at various locations on the cell,

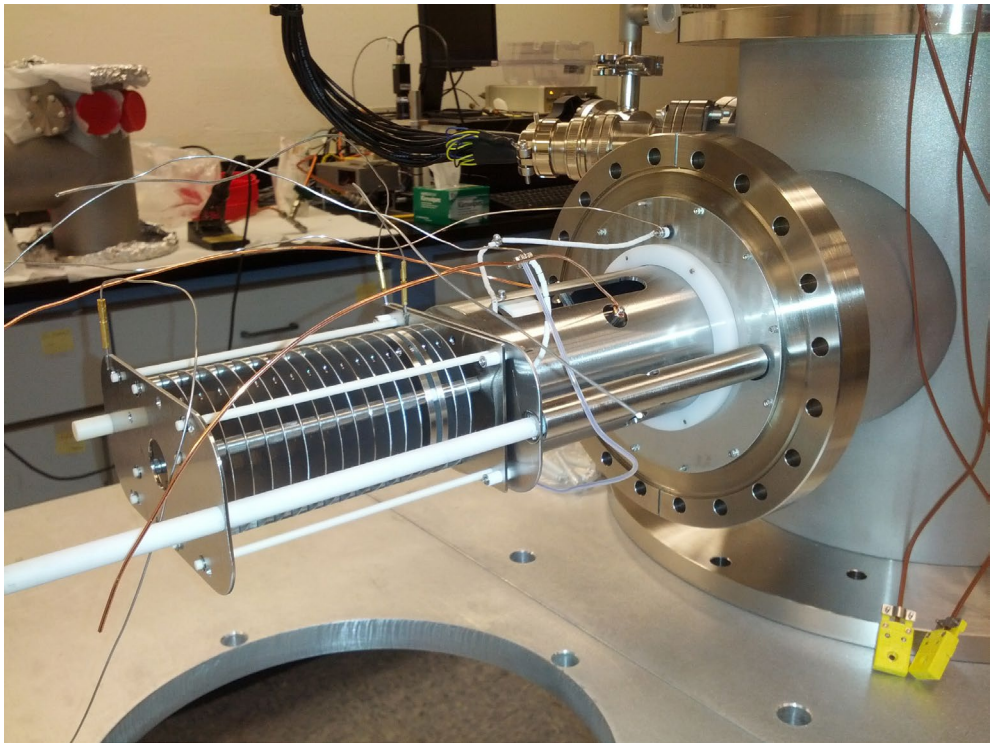

Figure 4. The entrance half of the first quadrupole assembly shown mounted to the main vacuum chamber of the instrument

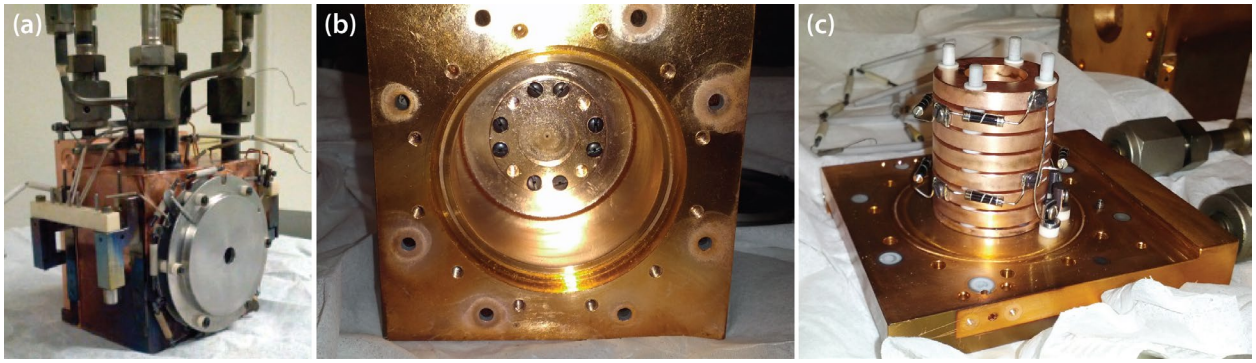

Figure 5. (a) The assembled reaction cell, (b) the copper shroud that houses the drift ring electrodes, and (c) the drift ring electrodes shown mounted to the end cap of the reaction cell. The end cap is electronically isolated from the copper shroud housing using a Macor spacer.

in order to determine whether significant temperature gradients exist across the cell and if errors in the temperature reading are present.

The reaction cell is housed in the main chamber between the first and second quadrupole assemblies (Figure 6). The cell rests on the ceramic rods that are used to align the assemblies, allowing the cell to be removed from the system for periodic maintenance without needing to disassemble the other components of the instrument.

Second Quadrupole/Detector Assembly

The quadrupole/detector assembly is shown in Figure 7. Ions exiting the cell are accelerated and focused into a second quadrupole using a set of transfer lenses identical to the steering/focusing elements situated prior to the first quadrupole. The second quadrupole is identical to the first (Extrel Core Mass Spectrometers), again consisting of ¾-inch rods and having a mass range of 4–4000 amu. Upon exiting

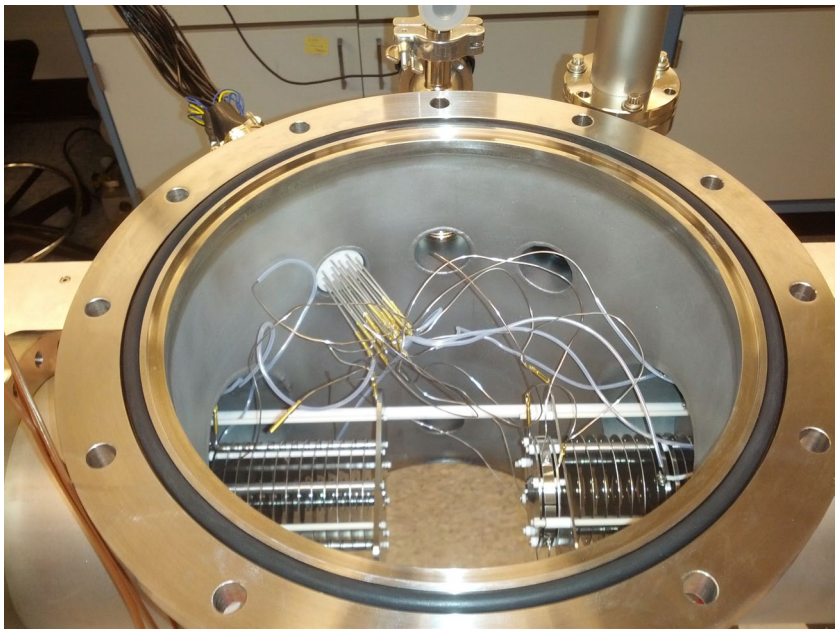

Figure 6. Inside the main vacuum chamber of the instrument. The reaction cell (not shown) is positioned in the space between the two ion focusing assemblies.

Figure 7. The second quadrupole/detector assembly

the second quadrupole, the ions pass through a final steering/focusing lens combination and are detected using a conversion dynode and an electron multiplier. The resulting quadrupole mass scans are collected on an Ortec multichannel scaler having 100 ns resolution (Ortec MCS Plus).

Experimental Methods

Testing of the instrument will begin in early FY 2015, the third year of the project. Thus, to date, no experimental data are available. However, a brief description of the experimental methods that will be used to analyze the type of data we expect to be generated by the system follows, as an example of some of the physical properties that can be measured with the system.

Equilibrium Reactions

Equilibria will be rapidly established in the cell for successive association reactions of neutral ligands to the core ions (Equation 1).

$$M_m^{+/-}L_{n-1} + L \rightleftarrows M_m^{+/-}L_n \quad \textbf{(1)}$$

Integrated peak areas of the various $M_m^{+/-}L_n$ ions will be recorded and these values, along with the pressure

of the ligating gas (P_L) in Torr, are used to determine an equilibrium constant (K_p°) for each reaction, using Equation 2.

$$K_p^\circ = \frac{\left[M_m^{+/-}L_n\right]}{\left[M_m^{+/-}L_{n-1}\right]} * \frac{760}{P_L} \quad (2)$$

The equilibrium constants can then be used to calculate the standard Gibbs free energies for the reactions,

$$\Delta G_T^\circ = -RT\,ln\left(K_p^\circ\right), \quad (3)$$

and the values obtained for ΔG_T° plotted versus the temperature, to obtain ΔS_T° and ΔH_T° for each reaction, using Equation 4.

$$\Delta G_T^\circ = \Delta H_T^\circ - T\Delta S_T^\circ \quad (4)$$

The resulting plots will be linear over the experimental temperature range. A least-squares fitting procedure will be used to obtain slopes and intercepts of each line. The slopes will be used to determine the association entropy (ΔS_T°) for Equation 1, and the intercepts will give the corresponding ΔH_T° values.

Ion Mobility

In order to obtain the mobility data, a pulse of mass-selected ions are injected into the He-pressurized cell. A weak, homogeneous electric field is applied across the cell, causing the ion packet to drift toward the small exit orifice. The ion packet is rapidly thermalized by collisions with the buffer gas. Ions exiting the cell are then detected as a function of time in order to establish an arrival time distribution (ATD). The mobility of the ions, $K_\circ$, is given by Equation 5 (Mason 1988),

$$K_\circ = \left(l^2 \frac{273}{760T} \frac{p}{V} \frac{1}{t_a - t_\circ}\right), \quad (5)$$

where l is the length of the drift cell, T is the temperature in Kelvin, p is the pressure of the He buffer gas in Torr, V is the drift voltage, t_a is the arrival time of the ions acquired from the center of the ATD peak, and $t_\circ$ is the time the ions spend outside of the cell. A plot of t_a versus p/V has a slope inversely proportional to $K_\circ$, which yields the collision cross section from Equation 6 (Mason 1988),

$$\sigma = \frac{3e}{16N_\circ}\left(\frac{2\pi}{\mu\, k_b\, T}\right)^{1/2} \frac{1}{K_\circ}, \quad (6)$$

where $N_\circ$ is the number density of He at standard temperature and pressure, e is the charge of the ions, μ is the ion-He reduced mass, k_b is Boltzmann's constant, and T is temperature.

Conclusion

An instrument that embeds a variable-temperature, high-pressure reaction cell in between two quadrupole mass analyzers for the purpose of studying the gas-phase, ion-neutral reactions/interactions of U and Th ions has been described. The instrument has been designed and developed to examine the thermodynamic and kinetic properties of U and Th ions when reacting with ligands of interest in the gas phase. Initial testing of the instrument is scheduled to begin in early FY 2015. Additionally, a collaboration that was previously established between Special Technologies Laboratory and the University of California, Santa Barbara, will be used to begin acquiring data to examine the interactions of Th and U ions with select surfaces next year.

References

Kemper, P. R., M. T. Bowers, "A hybrid double-focusing mass spectrometer—high-pressure drift reaction cell to study thermal energy reactions of mass-selected ions," *J. Am. Soc. for Mass Spectrom.* **1**, 3 (1990) 197–207.

Manard, M. J., "An experimental and theoretical investigation into the chemical properties of uranium and thorium ions in the gas phase and on surfaces," in *Site-Directed Research and Development*, FY 2013, National Security Technologies, LLC, Las Vegas, Nevada, 2014, 103–107.

Mason, E. A., E. W. McDaniel, *Transport Properties of Ions in Gases*, John Wiley and Sons, New York, 1988.

This page left blank intentionally

Ionospheric Plasma Coupling to Low-Frequency Electromagnetic Radiation

LAO-04-14 | Continued in FY 2015 | Year 1 of 2

Alfred Meidinger,[1,a] Daniel Clayton,[a] Derek Aberle,[a] Kelsey Kramer,[a] and William Zimmerman[b]

The advent of the modern dual- and tri-frequency Global Navigation Satellite System (GNSS) offers improved and emerging opportunities for probing the earth's ionosphere as a sensitive sensing medium. The concept of monitoring for concealed nuclear detonation is reinvestigated using the combined GNSS-ionosphere system as a nuclear detonation detection mechanism. Conceptual studies and targeted analysis techniques indicate the system will provide tangible information on concealed detonations by applying appropriate analysis techniques to GNSS carrier signals. This technique potentially offers an additional method for monitoring clandestine nuclear development efforts. Second-year activities will focus on developing a fluid-plasma model of the ionosphere and conducting experiments to compare modeling and simulation results to field data.

[1] meidina@nv.doe.gov, 505-663-2018
[a] Los Alamos Operations; [b] Voss Scientific, LLC

Background

The Preparatory Commission for the Comprehensive Nuclear-Test-Ban Treaty Organization (CTBTO), founded in 1996, is tasked with promotion of the Comprehensive Test Ban Treaty (CTBT) and implementation of a verification regime ahead of full treaty ratification. The verification regime is designed to detect any nuclear explosion conducted on earth—underground, underwater, or in the atmosphere. The verification regime relies on four monitoring technologies: seismic, hydroacoustic, infrasound, and radionuclide (CTBTO 2014).

Despite CTBTO's claim of being able to detect any nuclear explosion conducted on earth, there remains some skepticism regarding evasive testing, that is, seismically decoupled underground nuclear proliferation experiments (UNPEs), as well as small-scale atmospheric tests. In either case, no seismic signal would be detected and infrasound signatures could lie below background noise. In the case of UNPEs, adequate containment could prevent release of fission-produced radionuclides.

Seismic detection experts postulate 10% detection thresholds of 6 tons for fully coupled events with regional detection (event-station distances less than 1600 km) to 6.2 kilotons for fully decoupled events in salt domes with teleseismic detection (event-station distances greater than 1600 km) (National Research Council 2012). The prediction for a fully decoupled event is based on the measured decoupling factor of 70 for the 380-ton Sterling nuclear explosion (1966) conducted in a salt cavity created by the larger 5.3-kiloton Salmon nuclear explosion (1964) in Lamar County, Mississippi (National Research Council 2012).

The challenge presented by seismic decoupling led early researchers to seek alternate detection mechanisms. Since the time of the earliest nuclear tests, weapons researchers were aware of the electromagnetic pulse (EMP) generated during a nuclear detonation; in fact, numerous underground tests at the Nevada Test Site (later renamed the Nevada National

Security Site) as well as one test (the Joint Verification Experiment) at the Soviet test site Semipalatinsk were instrumented to determine the suitability of monitoring nuclear explosion–induced EMPs as a treaty verification technology (Sweeney 1989). The hypothesis was that nuclear explosion–induced EMPs would excite the earth-ionosphere cavity, thus exciting the well-known Schumann resonances in a fashion similar to lightning-induced resonances. Unfortunately, the signals generated during nuclear detonation are of longer duration (unlike the short burst of a lightning strike), thus limiting useful magnetic field monitoring to within 10 km of the event.

Recent modeling efforts have rekindled interest in exploiting this effect. Researchers with the Russian Zababakin Institute of Technical Physics (Karlykhanov 2004) found that, based on a comprehensive numerical model, a fully seismically decoupled nuclear detonation in air at atmospheric pressure would increase the magnetic dipole moment by more than a factor of 200 over the magnetic dipole moment resulting from a fully tamped detonation. (Karlykhanov's calculations for a 1-kiloton device result in a magnetic dipole moment of 4.4×10^4 $A{\cdot}m^2$ for a fully tamped detonation vs. ~10^7 $A{\cdot}m^2$ for a detonation in a cavity with radius of 80 m.) Karlykhanov's model is based on expanding plasma, which creates a "bubble" due to initial heating caused by the nuclear detonation followed by high pressure and temperature associated with the expanding shock front and expanding fireball, an effect often termed the magnetic bubble effect. The effect is present in both coupled and uncoupled events, where coupling to solid material like surrounding rock severely limits the extent of bubble growth. The growing ionized bubble, which is immersed in the geomagnetic field, creates a circulating current on the bubble surface as a result of the Lorentz force acting on the plasma. Assuming the plasma is a perfect conductor, this circulating current creates a circulating current surface and consequent magnetic dipole that exactly cancels the geomagnetic field inside the bubble. Because magnetic flux is conserved, the geomagnetic field outside the bubble is compressed, creating a magnetic perturbation that propagates spherically at the speed of light. Although a direct comparison is not valid, it is interesting to note the magnetic flux density calculated using Karlykhanov's results compares favorably with the measured magnetic flux density associated with lightning strikes.

Jhavar (2005) measured the magnetic flux density for 103 lightning strikes at a distance of 30 m. The average flux density for the 103 strikes was 104 µT (1.04 G) compared to the peak flux density of 930 µT (9.3 G) for Karlykhanov's 1-kiloton decoupled calculation. This result is an order of magnitude greater than the earth's magnetic field (≈0.5 G). Another interesting, albeit qualitative, comparison is the Hunter's Trophy underground nuclear detonation. The Hunter's Trophy experiment was conducted September 18, 1992, at the Nevada Test Site. Hunter's Trophy was a <20-kiloton device detonated in a tunnel at a depth of 385 m. Sweeney instrumented Hunter's Trophy at slant distances of 490 m and 1.25 km. The measured peak vertical magnetic flux density at 490 m was greater than 2 nT (Sweeney 1996). Sweeney's measurement compares to a calculated range of magnetic flux densities at 490 m for a 1-kiloton detonation in atmosphere of 107 nT at dipole equator to 214 nT at dipole zenith. The degree of seismic decoupling for Hunter's Trophy is not known, but considering it was a tunnel-emplaced, weapon-effect experiment, some small amount of seismic decoupling is possible. Even with this consideration, an increase in magnetic signature by a factor of ~100 would be a reasonable approximation if Hunter's Trophy were to be conducted in a fully decoupled cavity. This brings the potential dipole moment of Hunter's Trophy (if fully decoupled) to the magnitude of that measured for lightning strikes.

Recent research points to a connection between global thunderstorm activity and spectral resonant structures in the earth-ionosphere cavity (Bösinger 2008, Schekotov 2011). In addition to the well-documented Schumann resonances, field data show resonant structures below the fundamental Schumann resonance of ≈8 Hz (Bösinger 2009). These resonances are attributed to the ionospheric Alfvén resonator (IAR), which consists of two resonant modes, shear Alfvén waves

propagating along geomagnetic field lines and fast Alfvén waves propagating transverse to the geomagnetic field lines. These low-frequency plasma waves are observed as magnetic pulsations at the earth's surface, typically in the range of a few pT. Fraser-Smith (2014) shows thunderstorms generate surface magnetic pulsations on the order of 10 $pT \cdot Hz^{-1/2}$, which is an order of magnitude above background levels. The data were recorded at a frequency range of 0.01 to 10.00 Hz in eight frequency bands. Fraser-Smith goes on to suggest these pulsations induce hydromagnetic waves in the ionosphere above the source that travel outward, producing pulsations at distant locations; models suggest these pulsations can travel to several thousand kilometers (Pilipenko 2012). Communications/Navigation Outage Forecasting System data verify that Schumann frequencies do indeed couple to the ionosphere as dissipative evanescent waves, and the data indicate a strong coupling to frequencies below the lowest Schumann frequency (Simões 2011), suggesting the lightning impulse–generated, coupled, low-frequency IAR resonances produce concurrent oscillations in the ionosphere electron density.

Project

Hypothesis

As noted in in the prior section, tamped underground nuclear detonations generate magnetic fields that are measurable at the earth's surface at slant ranges up to 10 km. Also noted are numerical calculations that indicate a fully seismically decoupled detonation will result in more than a 200-fold increase in magnetic dipole moment compared to the fully tamped case, which casts the magnetic flux density of the fully decoupled case into the same order of magnitude as that measured for lightning strikes. Combining these observations and a seemingly accurate decoupling model with observations of ionospheric disturbances resulting from thunderstorm activity, it is reasonable to speculate that fully seismically decoupled nuclear detonations in the 1-kiloton and lower-yield range will magnetically couple to the ionosphere, creating localized perturbations in the ionosphere electron density. The magnetic impulse generated by decoupled nuclear detonations will likely produce (possibly periodic) oscillations in the IAR, which will be observable in Global Navigation Satellite System (GNSS) carrier signals.

Technical Approach

The project is divided into three components: source terms consisting of the time-dependent electric dipole (Compton diode) resulting from asymmetries in device configuration, currents induced in surrounding conductive structures, and magnetic bubble effects; signal propagation through the lithosphere, troposphere, and ionosphere; and GNSS signal propagation through the ionosphere.

Compton Diode Results

Wouters (1989) provides an equation for nuclear detonation local gamma flux in the form

$$\frac{d\Phi(\mathrm{r,t})}{dt}\left(MeV/m^2 \cdot s\right) = \frac{\left(\Phi_a \cdot Y_{KT}\right) \cdot f(t)}{4\pi r^2}, \quad (1)$$

where Φ_a is average flux, Y_{KT} is yield in kilotons, r is the cavity radius, and $f(t)$ is the dimensionless forcing function

$$f(t) = \frac{e^{-\beta_1 t_P} + e^{\beta_2 t_P}}{e^{-\beta_1 (t-t_0)} + e^{\beta_2 (t-t_0)}}, \quad (2)$$

where t_P is the time when the function is at peak value. Choosing $\beta_1 = \frac{0.3}{ns}$, $\beta_2 = \frac{0.06}{ns}$, and $t_P = 4.47$ ns, the forcing function takes the form illustrated in Figure 1.

Noting that a nuclear explosion yields approximately 1.3×10^{23} fissions/kiloton with approximately 200 MeV/fission, and assuming a conservative gamma conversion efficiency of 10%, the total fission yield is approximately 2.6×10^{24} MeV/kiloton. Dividing the total yield by the integrated forcing function value results in an average energy flux of approximately 9.2×10^{32} MeV/kiloton·sec, where we note the peak

current is approximately an order of magnitude greater. Ignoring time-delay transient effects, the Compton current can be expressed as (Messier 1975)

$$J_C = \frac{d\Phi(\mathrm{r,t})}{dt} \cdot \frac{-eR_e}{E_\gamma R_\gamma}, \quad (3)$$

where e is electron charge, E_γ is gamma energy, and R_e and R_γ are the respective electron and gamma mean free paths. The ratio $\frac{R_e}{E_\gamma R_\gamma}$ varies only slightly across the Compton energy range of 1 to 5 MeV; therefore, we choose the value corresponding to E_γ = 1 MeV, resulting in

$$J_C\left(A/m^2\right) = \frac{1.02 \times 10^{-21}}{MeV} \cdot \frac{d\Phi(\mathrm{r,t})}{dt}. \quad (4)$$

The Compton dipole moment is determined by integrating over the volume of the current distribution in the cavity. Using the relationship between volume current density and electric dipole moment, where ρ is the total charge inside the volume and $\boldsymbol{p}$ is the general form for the total dipole moment of charge within the volume,

$$\int_V \boldsymbol{J}\, d^3\boldsymbol{r} = \int_V \boldsymbol{r}\frac{\partial \rho}{\partial t}\, d^3\boldsymbol{r} = \frac{d\boldsymbol{p}}{dt}, \quad (5)$$

the Compton dipole is expressed as

$$\frac{d\boldsymbol{p}}{dt} = \iiint \boldsymbol{J}_c r^2 dr d\Omega. \quad (6)$$

Note the Compton dipole vanishes for spherically symmetric explosions because the current distribution will be spherically symmetric, but in the small angle limit (gamma jetting) the dipole moment will reach its maximum value. Substituting the average energy flux for a 1-kiloton event, the total dipole moment becomes

$$\boldsymbol{p} = 2\pi \cdot \frac{1.02 \times 10^{-21}}{MeV} \cdot 9.2 \times 10^{32}\ {}^{MeV}/_{\sec} \cdot \int r^2 dr. \quad (7)$$

Assuming a decoupling radius of 100 m, the upper (peak) limit of the electric dipole moment is proportional to 10^{18} *A·m*. This estimate is the extreme; any detonation would be more symmetric than this estimate provides; furthermore, the calculation ignores gamma attenuation. Based on Zablocki's (1966) estimate of ~10^5 *A·m* for the close-coupled Gnome event and the $\int r^2\, dr$ geometric decoupling factor, it is reasonable to assume ~10^8 *A·m* for a fully decoupled 1-kiloton device. Surface azimuthal magnetic field distribution for a vertically oriented Compton dipole is calculated using the relationship

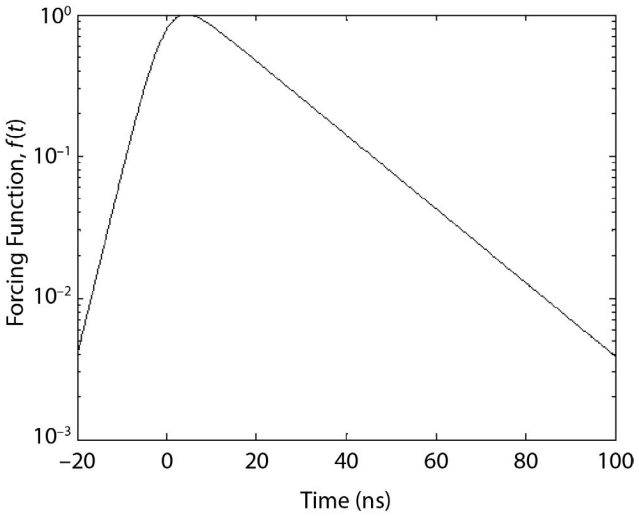

Figure 1. A plot of the normalized time history for a prompt nuclear explosion gamma source. The integral from –20 to 100 ns is determined numerically to be 27.3 ns.

$$\boldsymbol{H}_\varphi = \nabla X \frac{d\boldsymbol{p}}{dt} = \frac{dp}{dt}\frac{\sin(\varphi)}{4\pi\sigma r^2}\hat{\boldsymbol{\varphi}}, \quad (8)$$

where φ is the angle measured from zenith, σ is the electrical conductivity in *S/m*, and *r* is the slant distance to the surface. Figure 2 illustrates the peak surface distribution for a vertical dipole of 10^8 *A·m* buried 200 m in material with bulk conductivity for dry sediment of 0.01 *S/m*. Using these parameters, Figure 2 indicates a peak surface field of 0.012 *A/m*, corresponding to a flux density of 1.5 × 10^4 G. Substituting the bulk conductivity for dry granite of 0.001 *S/m*, the flux density increases by one order of magnitude, which remains two orders of magnitude below the geomagnetic flux density.

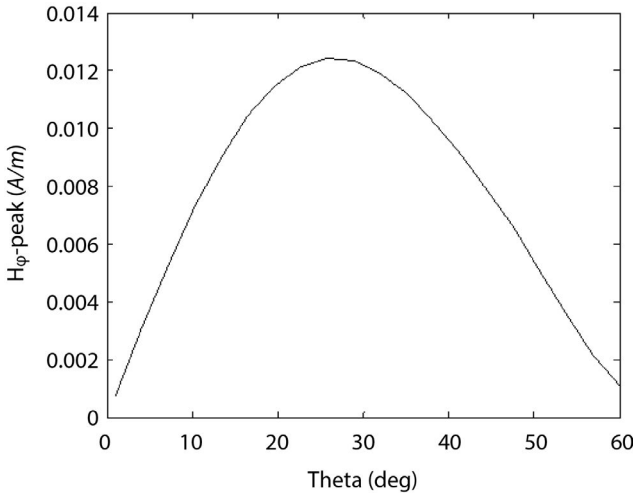

Figure 2. Approximate bound of the peak transverse magnetic field at the surface as a function of polar angle for a Compton diode of $p = 10^8$ *A·m*, a depth of burial of 200 m, and a ground conductivity of 0.01 *S/m*

Induced Current Results

An adversary conducting seismically decoupled nuclear tests will likely avoid electrical detonation and signal cables to minimize electromagnetic signals resulting from EMP propagation along such cables. Other possible conduction pathways are stem pipe, cable trays, or rail tracks, which are continuously grounded to earth. Considering the 1-kiloton example given above, the peak Compton dipole current is $I = 10^8$ *A*. Models show that current in grounded conductors falls off at an approximate rate of one order of magnitude per 100 m. This suggests currents near the surface for a 200 m overburden will be $I_s \approx 10^6$ *A*. The effective electric dipole moment at the surface will be proportional to the skin depth, where the skin depth can be approximated by

$$\delta \approx \left(\frac{\tau_p}{\mu_0 \sigma}\right)^{1/2}, \tag{9}$$

which is approximately 60 m and 200 m for dry sediment and dry granite, respectively, using a pulse with of τ_p = 50 µs. The peak surface electric dipole moment can be approximated by

$$P_s \approx \frac{1}{2} I_s \delta \approx 10^7 A \cdot m. \tag{10}$$

Comparing this to Jhavar's (2005) lightning mean peak current of 15.3 kA and average length of 8 km, the typical lightning stroke has an electric dipole moment ~10^8 *A·m*. Using the far-field approximation, electric field strength scales as $1/\tau_p$. Because lightning strikes typically have a duration of 1 µs, the surface dipole field strength in the ionosphere for a 1-kiloton nuclear detonation will be up to three orders of magnitude lower than that for a typical lightning strike; hence stem materials, cable tray, rails, etc., will provide little contribution to ionospheric fluctuations.

Magnetic Bubble Results

Development of a kinematic model for the expanding plasma bubble falls beyond the scope of this project; instead, an analytic form is derived. As a consequence of the Lorentz force acting on the plasma, expansion of the bubble through the geomagnetic field creates an electric current on the bubble surface layer. Assuming the plasma is a perfect conductor, the current generates a magnetic field that exactly cancels the geomagnetic field inside the bubble. Conservation of magnetic flux dictates that magnetic flux density must increase outside the bubble to compensate for the reduction inside. The instantaneous magnetic field outside the bubble can be expressed as a superposition of the locally uniform geomagnetic field and magnetic dipole field for a dipole at the sphere's center (Haus 2008). Setting the z axis parallel to the local geomagnetic field, the total magnetic field outside the sphere in spherical coordinates is given by

$$\boldsymbol{H} = H_E \left(\cos(\theta)\hat{\boldsymbol{r}} - \sin(\theta)\hat{\boldsymbol{\theta}}\right) + \frac{m}{4\pi}\left(\frac{2\cdot\cos(\theta)}{r^3}\hat{\boldsymbol{r}} + \frac{\sin(\theta)}{r^3}\hat{\boldsymbol{\theta}}\right), \tag{11}$$

where H_E is the local geomagnetic field strength and m is the magnetic dipole moment of the spherical current. Noting the field approaches ambient conditions as $r \to \infty$, the magnetic dipole moment is found by solving at the bubble surface, R_b, where the normal component of the magnetic field vanishes. Solving for the magnetic dipole moment, $m = -2\pi H_E R_b^3$, which indicates the magnetic dipole moment is proportional to the sphere volume and is aligned antiparallel to the

ambient field, meaning the dipole moment magnitude is greatest at maximum bubble expansion. Using the maximum fireball expansion value of 100 m at ⅓ second (Needham 2010) and an average geomagnetic field value of B_E = 0.5 G → H_E = 39.8 A/m, the maximum magnetic moment is –2.5 × 10^8 $A{\cdot}m^2$, corresponding with magnetic field energy ~10^3 J. This result for the magnetic moment is an order of magnitude greater than Karlykhanov's numerical result, which can possibly be explained by the perfect conductor assumption for the plasma surface. Nonetheless, the results of the analytic analysis do appear plausible, suggesting the effects of the magnetic bubble for a fully decoupled 1-kiloton detonation will result in an ionospheric signature.

Ionosphere Interaction Model

A 1-D model of the ionosphere was constructed using the kinematic particle-in-cell Large-Scale Plasma Suite, a plasma modeling and simulation code by Alliant Techsystems Operations, LLC. The code tracks charged plasma particles by calculating the interaction between charged particles and external and self-generated electric and magnetic fields. Based on the 1-D simulations, extrapolation to a full 3-D model proves intractable with available computer systems; hence the kinematic model was abandoned in lieu of combined fluid and electromagnetic modeling for FY 2015. Although exhibiting some expected properties, the 1-D model lacks sufficient physical content for predicting ionospheric response to the expected geomagnetic perturbations.

GNSS Signal Analysis

GNSS data are archived in the Receiver Independent Exchange (RINEX) format, a standardized data interchange format for raw satellite navigation system data using ASCII file types. All global navigation systems broadcast three constant observables: beat frequency, navigation code, and observation times. Earth-based control stations and ground stations sample and archive these observables and store the sampled data in RINEX format. Sample rates are once per second and once per 30 seconds depending on the receiver. The magnetic signals recorded by Zablocki (1966) and Sweeney (1989) for underground nuclear explosions (UNEs) indicate nuclear detonation EMP frequencies comparable to IAR frequencies of a few hertz, which places the RINEX sampling rate below the Nyquist limit for the detection of EMPs resulting from nuclear detonations. This fact forces hypothesis testing via surrogate studies or experiments that mimic nuclear detonations, which are planned for FY 2015.

Although RINEX data at higher sampling rates are available for limited applications, for example crustal monitoring along the San Andreas fault, only lower sampling rates are available for GNSS receiving stations in the vicinity of the Democratic People's Republic of Korea (DPRK) nuclear tests. We developed RINEX analysis routines this year and applied them to the DPRK tests data from receiving stations in Japan, South Korea, and China along with geomagnetic conjugate sites in Australia. Although EMP signatures are not evident in the analysis, signatures stemming from acoustic gravity waves (AGWs) associated with ground motion resulting from the detonations are evident at numerous receiver locations. Analyses were conducted on the three known DPRK tests conducted in 2006, 2009, and 2013. AGW signatures are seen for all DPRK tests; sample AGW results for the 2013 test using data from the Chinese receiving station SHAO are provided in this report.

The ionosphere is susceptible to acoustic perturbations without prejudice; hence any event that generates an infrasound signature in the lower atmosphere will propagate to the ionosphere, coupling to the ionospheric plasma, thus inducing electron density perturbations. This leads to a noisy background that requires signal processing techniques able to identify the structure of source signatures. For the case of seismically coupled underground explosions, we expect the surface to first rise then relax into compression with subsequent rebound, essentially a piston effect (Imtiaz 2012). This type of motion will produce a compression wave followed by rarefaction and subsequent return to ambient atmospheric condition. Several filtering techniques are available,

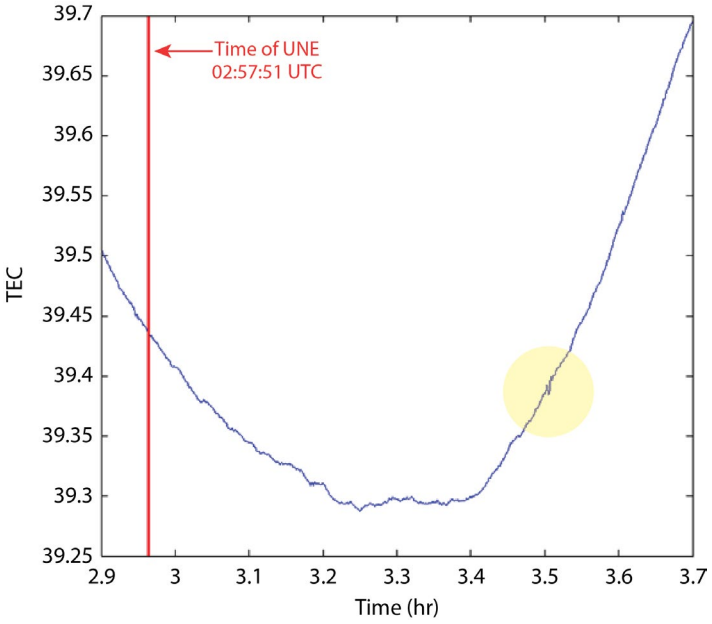

Figure 3. Plot of vertical TEC seen between station SHAO and satellite 8 between 2.9 and 3.7 hours UTC on February 12, 2013, the day of the third DPRK nuclear test. Evidence of an acoustic signature is seen in the yellow highlight.

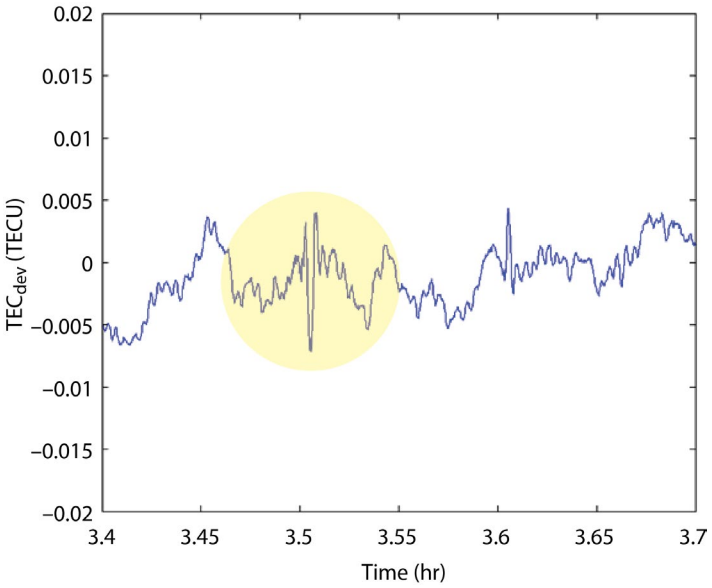

Figure 4. Plot of TEC_{dev}, where the average is taken over 5 minutes of data split before and after each epoch, seen between station SHAO and GPS satellite 8 between 2.95 and 3.25 hours UTC on February 12, 2013. The AGW signature of the detonation is highlighted in yellow.

including use of derivatives as a pseudo high-pass filter (which results in added high-frequency noise), wavelet analysis, and difference averaging.

For the difference averaging technique, the relative phase between two GNSS carrier signals is analyzed to determine total electron content (TEC) along the path between satellite and receiver, termed the slant TEC. Geometric corrections are then applied to determine the vertical TEC for a given epoch at every pierce point between the satellite and receiver; these points are typically calculated at a height 350 km above the surface. Figure 3 illustrates the resulting vertical TEC for the path between station SHAO and GPS satellite 8. A feature demonstrating a perturbation in TEC is highlighted in yellow; this feature shows characteristics that are associated with the type of piston effect noted above. Note that the data trend to greater TEC values with time; this is a result of the overall increase in TEC as sunlight ionization increases TEC (the time offset for Korean time is UTC + 9 hours, indicating local time of detonation is approximately noon).

A better understanding of the feature seen between 3.5 and 3.6 hours is gained by applying the averaging technique. This is done by averaging over some length of time and differencing with the instantaneous value, in the case of Figure 4, 5 minutes spanning 2.5 minutes on either side of each data point. Defining $\langle TEC_V \rangle$ as this average in vertical TEC, the data are smoothed by taking the difference $TEC_{dev} = TEC_V - \langle TEC_V \rangle$. Figure 4 illustrates the result of this smoothing where the signature of the piston effect is highlighted in yellow. Noting the data are sampled at 1-second intervals and smoothing is the difference between the instantaneous vertical TEC minus the average vertical TEC, the process can be viewed as a type of numerical differentiation, such that the signature is no longer the actual waveform of the density perturbation. Inspection of the signature reveals that the integral of the waveform will take the form of an increase in vertical TEC followed by a decrease with overshoot and subsequent return to ambient density. The duration of this waveform is approximately 35 seconds, suggesting some amount of dispersion during travel from the source epicenter to the pierce point. Also of interest is the feature at 3.6 hours, approximately 6 minutes later. This feature shows the characteristics of subsidence with an overshoot (compression) and rebound effect.

Conclusion

A literature review of prior magnetic bubble research and current ionosphere research was conducted to determine feasibility of using GNSS carrier signals as a probe for measuring UNPE-induced electron density perturbations in the ionosphere. Efforts to model the interaction using a kinematic software package proved intractable; therefore, a fluid approach will be used for FY 2015 modeling efforts. Based on data from several UNEs conducted during the second half of the 20th century, waveforms containing frequency components of a few hertz are expected, but RINEX data are sampled and archived at a maximum of 1 Hz. Due to this limitation, analysis of the three DPRK events was limited to lower-frequency AGW signatures resulting from ground motion.

FY 2015 research will include conducting surrogate pulsed power experiments and data acquisition at sampling rates greater than available in GNSS data archives. Conceptual analysis of this technique suggests the magnetic signal strength for a 1-kiloton seismically decoupled UNE is on the order of that induced by atmospheric lighting. As lightning activity is routinely observed in ionospheric electron density fluctuations, it is reasonable to assume UNPEs of 1-kiloton can be observed as well, although separation of the UNPE signature from the noisy background will require sophisticated analysis techniques. Prior research indicates magnetic signatures resulting from underground nuclear detonations are unique, exhibiting characteristics that will facilitate feature separation from noisy backgrounds.

Acknowledgments

The authors thank Timothy Neese for developing the vertical TEC analysis routine and the SDRD External Advisory Board for helpful discussions and recommendations.

References

Bösinger, T., S. L. Shalimov, "On ULF signatures of lightning discharges," *Space Sci. Rev.* **137** (2008) 521–532.

Bösinger, T., E. N. Ermakova, C. Haldoupis, D. S. Kotik, "Magnetic-inclination effects in the spectral resonance structure of the ionospheric Alfvén resonator," *Annales Geophysicae* **27** (2009) 1313–1320.

CTBTO, Preparatory Commission for the Comprehensive Nuclear-Test-Ban Treaty Organization, http://www.ctbto.org, accessed September 3, 2014.

Fraser-Smith, A. C., S. N. Kjono, "The ULF magnetic fields generated by thunderstorms: A source of ULF geomagnetic pulsations," *Radio Sci.*, accepted for publication, 2014, doi10.1002/2014RS005566.

Haus, H. A., J. Melcher, M. Zahn, M. Silva, "Magnetoquasistatic fields in the presence of perfect conductors," in *Electromagnetic Fields and Energy, Spring 2008*, Haus, H. A., J. R. Melcher, eds., MIT Hypermedia Teaching Facility, http://ocw.mit.edu/resources/res-6-001-electromagnetic-fields-and-energy-spring-2008, accessed December 9, 2014.

Imtiaz, N., R. Marchand, "Modeling of ionospheric magnetic field perturbations induced by earthquakes," *J. Geophys. Res.: Space Physics* **117** (2012) A04320.

Jhavar, A. B., "Triggered-lightning properties inferred from measured currents and very close magnetic fields," Master's Thesis, University of Florida, 2005, http://etd.fcla.edu/UF/UFE0013160/jhavar_a.pdf, accessed October 1, 2014, 36–37.

Karlykhanov, N. G., A. A. Kondrat'ev, Y. I. Matvienko, V. N. Nogin, "Magnetic dipole moment from a one-kiloton underground nuclear explosion in a cavity," *J. Appl. Mech. Tech. Phys.* **45**, 3 (2004) 311–315.

Messier, M. M., K. S. Smith, R. M. Hamilton, "Development and testing of DAVID: A close-in EMP coupling code for arbitrarily shaped objects," DNA 3923T, Mission Research Corporation, Santa Barbara, California, November 1975.

National Research Council, *The Comprehensive Nuclear Test Ban Treaty—Technical Issues for the United States*, The National Academies Press, Washington, D.C., 2012, 104–117.

Needham, C. E., "Blast Waves" in *Shock Waves and High Pressure Phenomena*, R. A. Graham, L. Davidson, Y. Horie, G. Ben-Dor. F. K. Lu, N. Thadhani, eds., Springer-Verlag, Berlin, Heidelberg, 2010, 23–33.

Pilipenko, V. A., "Impulsive coupling between the atmosphere and ionosphere/magnetosphere," *Space Sci. Rev.* **168** (2012) 533–550.

Schekotov, A., V. Pilipenko, K. Shiokawa, E. Federov, "ULF impulsive magnetic response at mid-latitudes to lightning activity," *Earth Planets and Space* **63** (2011) 119–128.

Simões, F., R. Pfaff, H. Freudenreich, "Satellite observations of Schumann resonances in the earth's ionosphere," *Geophys. Res. Lett.* **38**, 22 (2011) L22101, http://onlinelibrary.wiley.com/doi/10.1029/2011GL049668/pdf, accessed October 1, 2014.

Sweeney, J. J., "An investigation of the usefulness of extremely low-frequency electromagnetic measurements for treaty verification," UCRL-53899, Lawrence Livermore National Laboratory, Livermore, California, January 1989.

Sweeney, J. J., "Low-Frequency Electromagnetic Measurements as a Zero-Time Discriminant of Nuclear and Chemical Explosions – OSI Research Final Report," UCRL-ID-126780, Lawrence Livermore National Laboratory, Livermore, California, December 1996, http://www.iaea.org/inis/collection/NCLCollectionStore/_Public/37/073/37073983.pdf, accessed October 1, 2014.

Wouters, L. F., "The Underground Electromagnetic Pulse: Four Representative Models," UCID-21720, Lawrence Livermore National Laboratory, Livermore, California, January 1989, https://www.etde.org/etdeweb/servlets/purl/5829556/5829556.pdf, accessed October 1, 2014.

Zablocki, C. J., "Electrical transients observed during underground nuclear explosions," *J. Geophys. Res.* **71**, 14 (July 1966) 3523–3542.

This page left blank intentionally

Secure Sensor Networks Using Direct-Sequence Spread-Spectrum

STL-33-13 | Continued from FY 2013 | Year 2 of 2

Kelly Painter[1,a] and Duane Gardner[b]

The initial goal for this project was to develop a secure, direct-sequence spread-spectrum modulation physical layer for national security applications. During the course of the year, focus was shifted to developing a fully operational software-defined radio platform. Starting with the state of the system as of last year, improvements were made to the Costas demodulator, an RF automatic gain control was implemented, the system was phase-locked to GPS, and a control user interface was developed.

[1] paintekd@nv.doe.gov, 805-681-2476
[a] Special Technologies Laboratory

Background

In last year's work, a technique was investigated to mathematically determine the despread code for a direct-sequence spread-spectrum (DSSS) receiver (Fay 2014). This technique was of interest because it could be used to implement a spread-spectrum system that would utilize a non-stationary spread code, thereby incorporating a very high degree of security. In FY 2014, we continued the effort with the goal of implementing the algorithm in a field-programmable gate array (FPGA). A state-of-the-art digital radio platform was developed last year (Fay 2014). However, it was decided this year that it would be beneficial to make an operational radio system out of this board with a narrowband waveform.

Project

At the conclusion of last year's work, the Eigenvalue despreader algorithm we investigated seemed feasible (Fay 2014). The investigation was simulated exclusively in MATLAB. However, the procedural nature of programming in MATLAB does not always represent a real-world environment. Thus, we decided it would be ideal to also evaluate performance of the algorithm in a fading channel, with Doppler shift. This can be done using Simulink, which provides a low-level way of coding where each process runs independently of other processes in the system. This is the manner in which the same processes would behave in the FPGA. Significant effort was put toward implementing the Eigenvector algorithm in Simulink using Level-2 S-Functions. This proved to be a problem, however, as Simulink cannot manage multidimensional arrays. Functions that are relatively easy to implement in MATLAB are very difficult to implement in Simulink. After a period of time in which no headway was made in implementing the algorithm in Simulink (and since the goal was to get the algorithm implemented in the FPGA), the pure Simulink analysis approach was abandoned.

We then attempted to implement the algorithm using Xilinx's System Generator for DSP. System Generator for DSP connects highly optimized parametric FPGA building blocks using Simulink to form a larger module that is then instantiated inside the FPGA. We have used this tool to develop multiple complex communications systems, but this was the first time we attempted

complex linear algebra. In particular, we needed to find the Eigenvalues of a matrix. Unfortunately, there was a lack of support for multidimensional arrays in System Generator for DSP. We explored another product, Vivado High-Level Synthesis, that we determined could provide better multidimensional array support, but the tools also were weak in this area.

Facing these limitations, we refocused the project goals. We set the Eigenvector algorithm problem aside and worked on hardware operability and achieving over-the-air, unit-to-unit communications with the board designed last year. Our basic transceiver design from last year had some remaining deficiencies that prevented over-the-air operations. Specifically, there was no mechanism for controlling the RF gain in the Lime Microsystems LMS6002 multi-band transceiver other than manually setting it by issuing Python commands. Also, there was an error between the temperature-compensated crystal oscillator (TCXO) frequency between the two units. Finally, we made some improvements to the Costas Loop and the receiver in general. These efforts are further described in the sections below.

Costas Loop Improvements

To improve weak signal performance, we made changes to the Costas Loop and demodulator design that did not yield the performance level we desired. We discovered that when using a raised-root cosine (RRC) pulse-shaping filter to achieve optimal bandwidth, the ringing at low noise levels caused the loop to lose lock. This problem has proven to be persistent. During the year, we were able to attend a short class offered at the University of California, Los Angeles Extension, where we learned that the Costas Loop is not the most optimal demodulator to use for weak signal performance. What is missing in most of the literature, and in our demodulator, is an estimate of signal-to-noise ratio (SNR) at each frequency-lock correction sample being used to weight the effect the correction has on the system. Without this weighting, poor SNR frequency updates will throw the loop out of lock. Our work confirmed this observation; incorporating this knowledge will improve our future receiver designs immensely. In spite of the fact that our receiver does not approach theoretical levels of operation, it does in fact work quite well.

Digital RF Automatic Gain Control

All digital radios suffer from a common problem: any fading of the signal can either drop below the useful range of analog-to-digital (A/D) converters or overload them. We implemented an automatic gain control (AGC) circuit inside the FPGA that estimates the amplitude of the received signal. Two things are done with this amplitude estimate: (1) the inverse of the signal is computed and is used to normalize the signal level to unity as the signal proceeds through the rest of the receiver chain; (2) the amplitude estimate is compared against a set point and a correction factor is determined. This correction factor is ultimately converted into gain settings for the variable gain receiver amplifiers inside the LIME receiver (Figure 1). The set point we used translates to two-thirds of full scale on the A/D converter. The error between this set point is integrated and converted to decibels, and this measurement is exported to a Verilog module that formulates commands to the LIME.

With the LIME completely configured, control of the command serial peripheral interface (SPI) bus is transferred from the computer over to the FPGA so it can control the gain of the RF amplifiers and thereby close the feedback loop.

Phase Lock of VCTCXO to GPS

Another issue we addressed was frequency synchronization between the two units. The protocol we used has to achieve timing and frequency synchronization within the 128-bit preamble. This is achievable provided the frequency error between the two units is small. The voltage-controlled TCXO (VCTCXO) will have a short-term stability of ±1.5 ppm or ±60 Hz at 40 MHz. When this reference frequency is multiplied up to 1.5 GHz, this error becomes ±2.25 kHz. The maximum differential error between the two units is 4.5 kHz. This is a lot of error to deal with in the

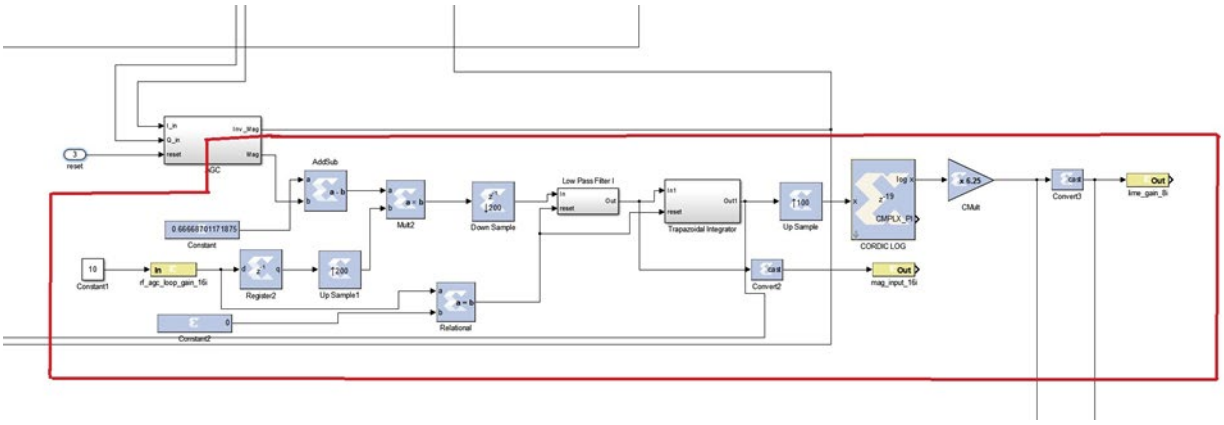

Figure 1. System generator portion of the digital RF AGC

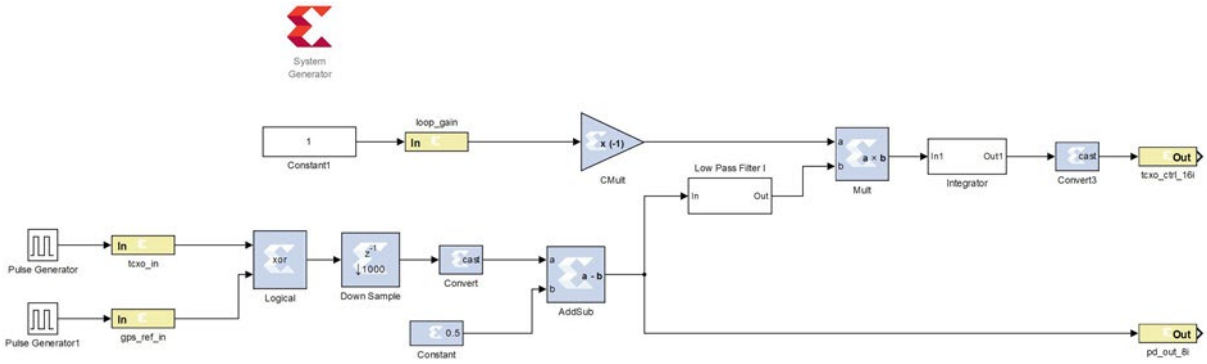

Figure 2. System generator portion of the VCTCXO phase lock to GPS

demodulator within the 128-bit preamble. One way to address this is to synchronize our VCTCXO to the frequency reference generated from our GPS receiver.

The system generator for the DSP block diagram shown in Figure 2 implements a phase-locked loop that compares the reference from the GPS against a frequency derived from the VCTCXO. The GPS reference frequency is 100 kHz, which we empirically determined works given that it periodically resets when the GPS receives updated time estimates. The output of the phase-locked loop block goes to a Verilog module that writes the control signal to a serial digital-to-analog converter. When operating with a valid GPS fix, the VCTCXO error was measured to be less than 0.001 Hz, the limit of our equipment's ability to measure frequency error. The frequency error at 1.5 GHz was less than our capability to measure.

Over-the-Air Testing

With the RF AGC and VCTCXO phase lock in place, we began over-the-air tests. Weak signal tests over a cable determined that error-free communications were achievable down to a received power of −125 dBm, which is still about 9 dB worse than what should be possible. As previously mentioned, the primary issue is the receiver becoming unlocked at low levels due to the ringing of the RRC matching filter.

Radio Control GUI

The radio control code is currently implemented in Python. This code base is composed of several hundred functions that are called from a command line terminal. The actual operation of the radio can be quite complex. In an effort to simplify operation, we have worked on a graphical user interface (GUI) implemented with PySide to improve the operation

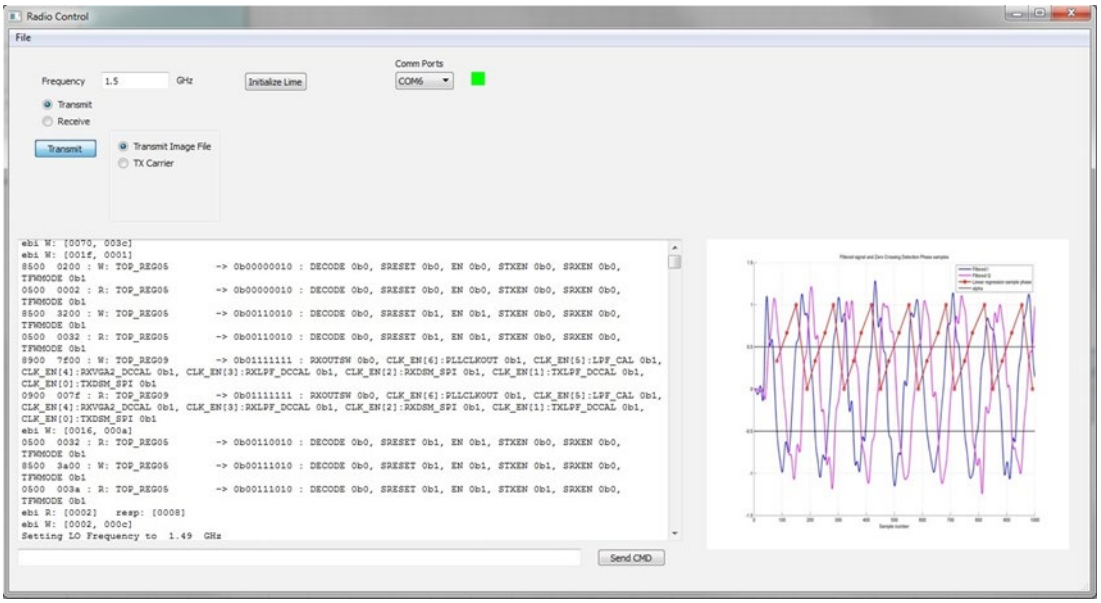

Figure 3. Screen capture of the radio control GUI setting up the LIME transceiver for transmit. The image to the right is the payload to be transmitted.

of the radio with a focus on demonstrating the radio. The intent was to be able to transmit a photo from one radio using a computer running the GUI and receive the photo on another radio with a computer also running the GUI. The second unit would display in the terminal window low-level operations the radio performed during reception, and would ultimately display the received photo. A screenshot of the GUI is shown in Figure 3. Ultimately, multithreading issues interfered with GUI operation.

Conclusion

While the Eigenvalue despreader algorithm was not successfully implemented in hardware, we were successful in transferring files between two units over the air. In FY 2014 we improved the Costas demodulator, implemented an RF automatic gain control, phase-locked the system to GPS, and developed a control user interface. The project as a whole has been successful in generating interest from other sponsors with custom communications system needs. As a direct outcome of this work, several projects have been funded, with more prospective efforts in the process. In effect this project has helped develop a new capability in software-defined radios and created a pathway for enhanced mission in secure communications.

Reference

Fay, M., K. Painter, S. Gordoni, S. Lyon, “Secure sensor networks using direct-sequence spread-spectrum,” in *Site-Directed Research and Development*, FY 2013, National Security Technologies, LLC, Las Vegas, Nevada, 2014, 79–84.

Power Automation System (PAS) Cyber Vulnerability Assessment

RSLN-04-13 | Continued from FY 2013 | Year 2 of 2

Ki Park[1,a] and Yoohwan Kim[b]

Key theft and malware injection attacks in the electrical power grid, which are controlled by Supervisory Control and Data Acquisition (SCADA) control devices, are very dangerous because attackers can inject malicious commands that can bring down the power grid or propagate malware to other SCADA devices or the control center. To guard against such attacks, a prototype of new SCADA controller architecture is implemented in a field-programmable gate array. In this second year of our research, we implemented a proof of concept on a Xilinx ML605 board utilizing a MicroBlaze soft-core processor. The new SCADA control software functionality compares the cryptographic values derived from the seed value for the cryptographic operation and the keyed hash value stored in the flash storage. When the integrity of each key value matches, the code is executed properly. Any unauthorized change of the executable code in the storage invalidates the hash value and fails to operate the SCADA facility properly. No keys are stored in the flash storage; thus, the system is not vulnerable to key theft attack. The security of the new system was demonstrated with simulated SCADA control software in a simulated SCADA facility. The new architecture will reduce the vulnerability from threats of key theft and malware injection at the substation level.

[1] parkkh@nv.doe.gov, 702-295-8022
[a] North Las Vegas; [b] University of Nevada, Las Vegas

Background

This report details the second of two years of Power Automation System (PAS) Cyber Vulnerability assessment research. During the first year (Park 2014), we proposed a new scheme to protect key material and firmware manipulation. To demonstrate key theft mitigation on Supervisory Control and Data Acquisition (SCADA) systems, we used a Xilinx ML605 board (Virtex-6 XC6VLX240T-1FFG1156 field-programmable gate array [FPGA]) (Xilinx 2014) as our hardware platform. In our initial design, a Joint Test Action Group (JTAG) mode was used to accommodate additional configuration changes on the board as needed. As our design matured, we switched to a Master byte peripheral interface (BPI)-up to configure the FPGA. While there are many functional modules in the ML605 board, the ones we used are listed in Table 1.

The ML605 board supports configuration in the following modes:

- Slave SelectMAP: Using platform flash XL with the onboard 47 MHz oscillator
- Master BPI-up: Using linear BPI flash device
- JTAG: Using the included USB-A to Mini-B cable and CompactFlash (CF) card for boundary scan

In BPI flash mode, the FPGA can be configured automatically and quickly, which helps when developing and debugging the software. A linear BPI flash memory on the ML605 provides 32 MB of non-volatile storage available for configuration and software storage. The Xilinx System Advanced Configuration Environment

Table 1. ML605 functional modules used in this project

Module	Notes
Virtex-6 FPGA	XC6VL240T-1FFG1156
Linear BPI flash	Numonyx JS28F256P30T95
System ACE CompactFlash controller and connector	Xilinx XCCACE-TQ144I
JTAG cable connecter (USB Mini-B)	USB JTAG download circuit
USB Mini-B, USB-to-UART bridge	Silicon Labs CP2013GM bridge
FPGA INIT, DONE	Init (red), Done (green)
System ACE CF status	Status (green), Error (red)

(ACE) CF configuration controller allows a Type I or Type II CF card to program the FPGA through the JTAG port. Both hardware and software data can be downloaded through the JTAG port. The Xilinx System ACE CF controller supports up to eight configuration images on a single CF card. The System ACE CF microprocessor unit (MPU) port is connected to the FPGA. This connection allows the FPGA to use the System ACE CF controller to reconfigure the system or access the CF card as a generic FAT file system. In our design, the CF card simulates the storage devices that store our software and communicate with the firmware in the FPGA.

We chose a soft-core processor because it is more flexible and suitable for prototyping than a hard-core one. The MicroBlaze soft-core processor is a 32-bit reduced instruction set computing (RISC) Harvard architecture soft processor core (MicroBlaze 2013) included in our FPGA package. The MicroBlaze processor communicates with the rest of the system over an on-chip peripheral bus.

Project

Key theft and malware injection attacks in electrical power grids controlled by SCADA devices (Wei 2011) are very dangerous because attackers can inject a malicious command to close down the entire power grid. This project demonstrates SCADA system key theft mitigation with a Xilinx ML605 board as the FPGA platform and a MicroBlaze soft-core processor in a simulated SCADA control environment. When the integrity of each key value matches, the onboard LED blinks and the comparison result is displayed on the development console.

Prototype System Architecture and Design

To implement the hardware components (invisible non-volatile memory [I-NVM] and visible non-volatile memory [V-NVM]) within the CPU and related machine instructions, we first created a working computing system on the FPGA board. It should be noted that any design that includes a processor increases its complexity significantly. Although we can incorporate the Set and Gen functions in hardware, we cannot run the application code in that mode. Therefore, we needed to implement the processor to execute the application code. Moreover, within the FPGA, multiple components were created including the processor, non-volatile memory, RAM, data, and address buses as well as arbiter, interface, and the drivers for external devices. Figure 1 identifies the main components of the computing system designed on the FPGA.

The major components are:

- **I^2C EEPROM:** Electronically erasable programmable read-only memory (EEPROM) based on inter-integrated circuit (I^2C) protocol, a multi-master, serial, single-ended computer bus used for attaching low-speed peripherals to a motherboard.

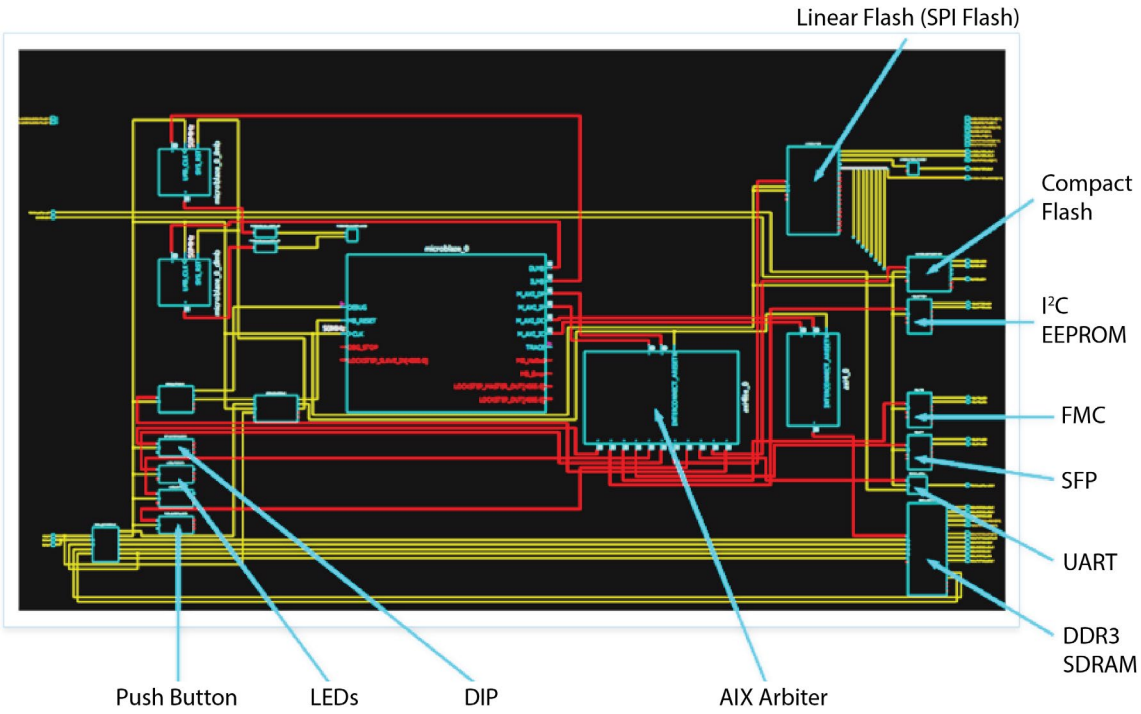

Figure 1. Components on the FPGA

- **FMC:** The FPGA mezzanine card (FMC) is an ANSI/VITA standard that defines input/output (I/O) mezzanine modules with connection to an FPGA or other device with reconfigurable I/O capability. The card has a low profile and is therefore suitable for standard slot card, blade, and low-profile motherboards.
- **SFP:** Small form-factor pluggables (SFPs) are a new generation of optical modular transceivers specially designed to work with small form-factor connectors. Besides being compact, the SPFs are capable of data speeds of 5 Gbps or higher.
- **UART:** Universal asynchronous receivers/transmitters (UARTs) translate data between parallel and serial forms. UARTs are commonly used in conjunction with communication standards such as Electronic Industries Alliance (EIA) RS-232, RS-422, or RS-485.
- **AXI Arbiter:** The advanced eXtensible interface (AXI) arbiter accepts memory access commands from the AXI slave interface and the memory manager.

The FPGA system architecture is shown in Figure 2. The CPU has 8 KB instruction cache and 8 KB data cache. Both caches are embedded in MicroBlaze processor. The high-speed device (DDR3 memory) is connected to AXI bus, while the low-speed devices are connected to AXI_Lite bus. To store the key material and process the cryptographic functions, a "keymem" module was developed.

Prototype System Development and Configuration

The software was developed on the Xilinx ISE development system. We used Verilog to create the firmware code segment for keymem operation and configuration modules. Figure 3 shows a portion of the keymem operation codes and configuration module segment. As for the configuration of bus interfaces for various hardware components, we leveraged the Xilinx FPGA development environment. Figure 4 lists the type of bus interfaces for various components. Figure 5 shows a block diagram of the MicroBlaze configurations on processor, buses, memory, and peripherals for our application.

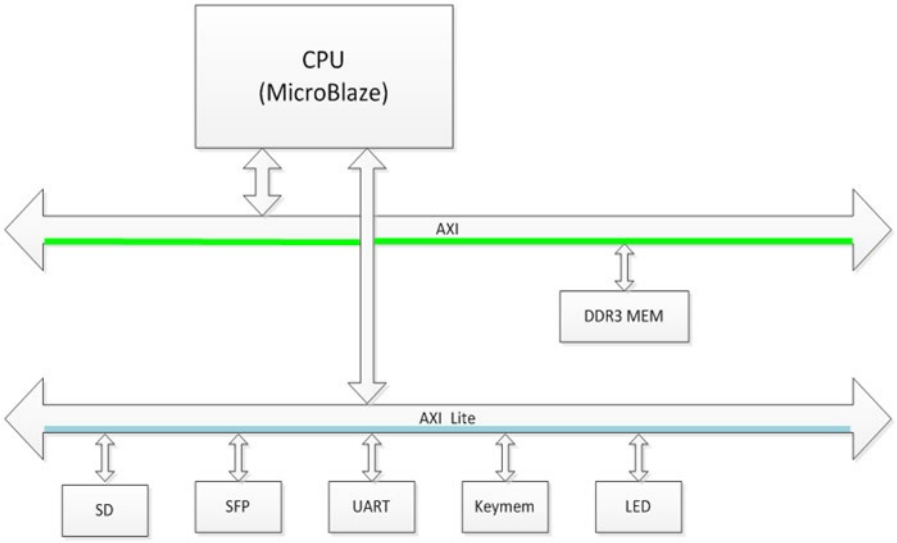

Figure 2. FPGA system architecture

```
// USER logic implementation added here

always @( posedge Bus2IP_Clk)
begin
    if (Bus2IP_Reset == 1'b0)
    begin
        IP2SD_Enable <= 1'b0;
    end
    else begin
        if (Key_Match)
        begin
            IP2SD_Enable <= 1'b1;
        end
        else begin
            IP2D_Enable <= 1'b0;
        end
    end
end


// Write the Key to the Key registers
always @( posedge Bus2IP_Clk)
begin
    if (BusIP_Reset == 1'b0)
    begin
        Key_Match <= 1'b0;
    end
    else
    begin
        if (Key_Register[KEY_LENGTH-1 : 0] == Key_Register_Match[KEY_LENGTH-1 : 0])
        begin
            Key_Match <= 1'b1;
        end
        else
        begin
            Key_Match <= 1'b0;
        end

    end
end


// Write the Calculated Key into Key Register
always @( posedge Bus2IP_Clk)
begin
    if (BusIP_Reset == 1'b0)
    begin
        Key_Register_Match[KEY_LENGTH-1 : 0] <= 128'H5a5a5a5a5a5a5a5a5a5a5a5a5a5a5a5a5
a;
    end
end

always @( posedge Bus2IP_Clk)
begin
    if (BusIP_Reset == 1'b0)
    begin
        Key_Register[KEY_LENGTH-1 : 0] <= 128'b0;
    end
    else if (Bus2IP_WrCE)
    begin
        case (Bus2IP_Addr)
            C_BASEADDR + 0x0  :
                Key_Register[31 : 0] <= Bus2IP_Data[C_SLV_DWIDTH-1 : 0];
            C_BASEADDR + 0x4  :
                Key_Register[63 : 32] <= Bus2IP_Data[C_SLV_DWIDTH-1 : 0];
            C_BASEADDR + 0x0  :
                Key_Register[95 : 64] <= Bus2IP_Data[C_SLV_DWIDTH-1 : 0];
            C_BASEADDR + 0x0  :
                Key_Register[127 : 96] <= Bus2IP_Data[C_SLV_DWIDTH-1 : 0];
            default:
                Key_Register[KEY_LENGTH-1 : 0] <= Key_Register[KEY_LENGTH-1 : 0];
        endcase
    end
end
```

```
    .s_axi_arqos ( axi4_0_M_ARQOS ),
    .s_axi_arvalid ( axi4_0_M_ARVALID[0] ),
    .s_axi_arready ( axi4_0_M_ARREADY[0] ),
    .s_axi_rid ( axi4_0_M_RID[0:0] ),
    .s_axi_rdata ( axi4_0_M_RDATA ),
    .s_axi_rresp ( axi4_0_M_RRESP ),
    .s_axi_rlast ( axi4_0_M_RLAST[0] ),
    .s_axi_rvalid ( axi4_0_M_RVALID[0] ),
    .s_axi_rready ( axi4_0_M_RREADY[0] ),
    .s_axi_ctrl_awaddr ( net_gnd32[0:31] ),
    .s_axi_ctrl_awvalid ( net_gnd0 ),
    .s_axi_ctrl_awready (  ),
    .s_axi_ctrl_wdata ( net_gnd32[0:31] ),
    .s_axi_ctrl_wvalid ( net_gnd0 ),
    .s_axi_ctrl_wready (  ),
    .s_axi_ctrl_bresp (  ),
    .s_axi_ctrl_bvalid (  ),
    .s_axi_ctrl_bready ( net_gnd0 ),
    .s_axi_ctrl_araddr ( net_gnd32[0:31] ),
    .s_axi_ctrl_arvalid ( net_gnd0 ),
    .s_axi_ctrl_arready (  ),
    .s_axi_ctrl_rdata (  ),
    .s_axi_ctrl_rresp (  ),
    .s_axi_ctrl_rvalid (  ),
    .s_axi_ctrl_rready ( net_gnd0 )
  );

(* BOX_TYPE = "user_black_box" *)
keymem_0_wrapper
  keymem_0 (
    .S_AXI_ACLK ( clk_100_0000MHzMMCM0 ),
    .S_AXI_ARESETN ( axi4lite_0_M_ARESETN[13] ),
    .S_AXI_AWADDR ( axi4lite_0_M_AWADDR[447:416] ),
    .S_AXI_AWVALID ( axi4lite_0_M_AWVALID[13] ),
    .S_AXI_WDATA ( axi4lite_0_M_WDATA[447:416] ),
    .S_AXI_WSTRB ( axi4lite_0_M_WSTRB[55:52] ),
    .S_AXI_WVALID ( axi4lite_0_M_WVALID[13] ),
    .S_AXI_BREADY ( axi4lite_0_M_BREADY[13] ),
    .S_AXI_ARADDR ( axi4lite_0_M_ARADDR[447:416] ),
    .S_AXI_ARVALID ( axi4lite_0_M_ARVALID[13] ),
    .S_AXI_RREADY ( axi4lite_0_M_RREADY[13] ),
    .S_AXI_ARREADY ( axi4lite_0_M_ARREADY[13] ),
    .S_AXI_RDATA ( axi4lite_0_M_RDATA[447:416] ),
    .S_AXI_RRESP ( axi4lite_0_M_RRESP[27:26] ),
    .S_AXI_RVALID ( axi4lite_0_M_RVALID[13] ),
    .S_AXI_WREADY ( axi4lite_0_M_WREADY[13] ),
    .S_AXI_BRESP ( axi4lite_0_M_BRESP[27:26] ),
    .S_AXI_BVALID ( axi4lite_0_M_BVALID[13] ),
    .S_AXI_AWREADY ( axi4lite_0_M_AWREADY[13] )
  );

IOBUF
  iobuf_0 (
    .I ( SysACE_MPD_O[7] ),
    .IO ( SysACE_MPD[7] ),
    .O ( SysACE_MPD_I[7] ),
    .T ( SysACE_MPD_T[7] )
  );

IOBUF
  iobuf_1 (
    .I ( SysACE_MPD_O[6] ),
    .IO ( SysACE_MPD[6] ),
    .O ( SysACE_MPD_I[6] ),
```

Figure 3. Keymem operation codes and configuration module

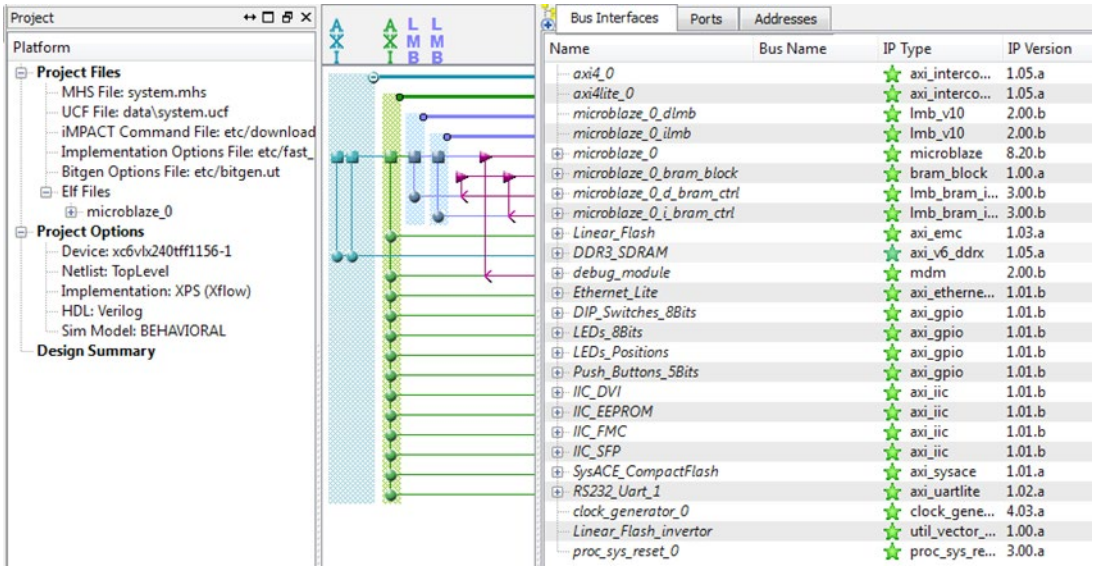

Figure 4. Types of bus interfaces for various components

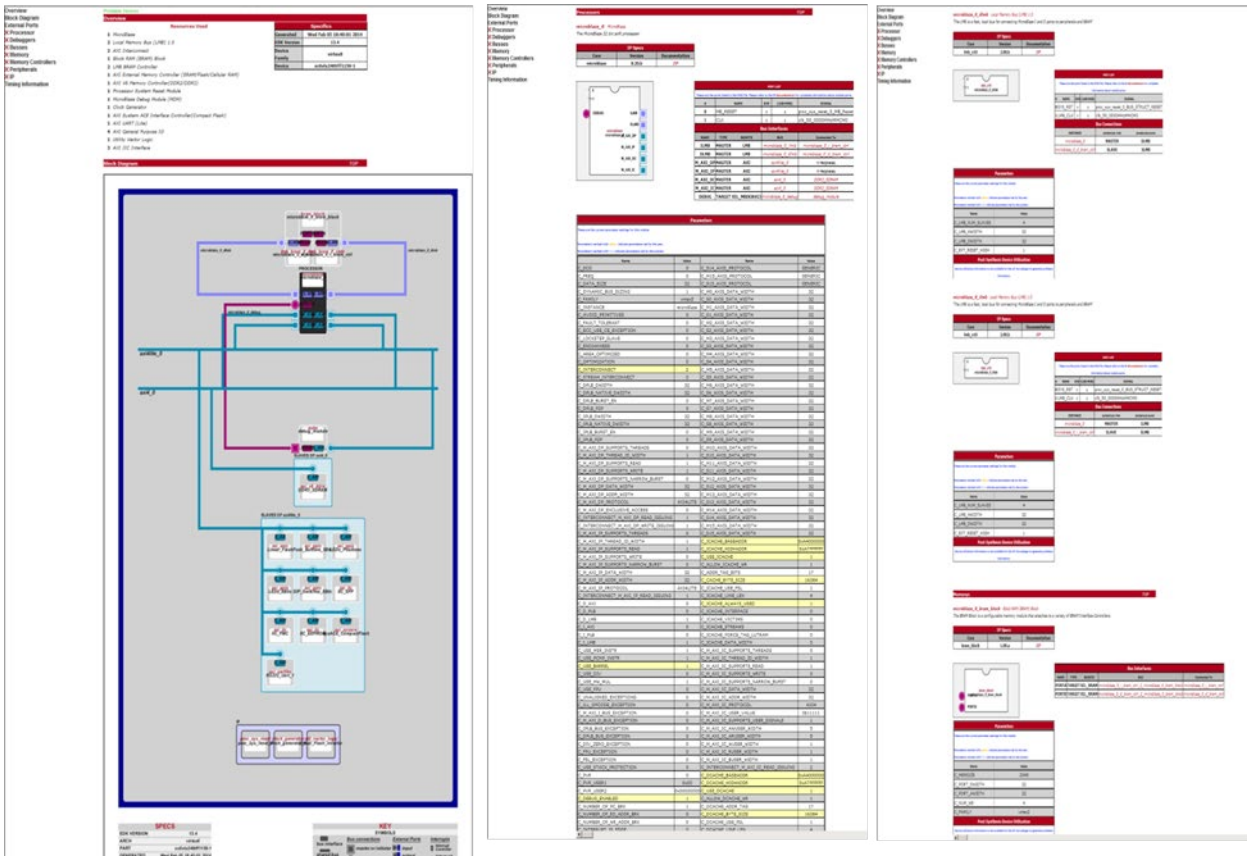

Figure 5. Block diagram of the MicroBlaze soft-core processor system

Implementation of Secure Architecture

The secure digital (SD) card external memory stores the application program that will demonstrate SCADA operation. Our proposed scheme requires storing various functions and programs in non-volatile memory within the CPU. We dedicated a few blocks of read-only memory in the FPGA to accommodate this requirement. The data in our emulated read-only memory are downloaded from the development machine and stored in the FPGA. When the board is powered on, data are copied to the main memory. The I-NVM should not be accessible from any application program and can be accessed only by the Gen function. By designating a block of memory with write access only and without read access in the keymem module, the memory appears as if it does not exist for the application program.

The keymem module handles the verification process by comparing the key value stored in key_match and the seed value stored in the key_factor that is transformed into the verification value in the key_result section. If the two keys match, the system enables the flash memory module so that the CPU will load the whole software into memory and start executing it.

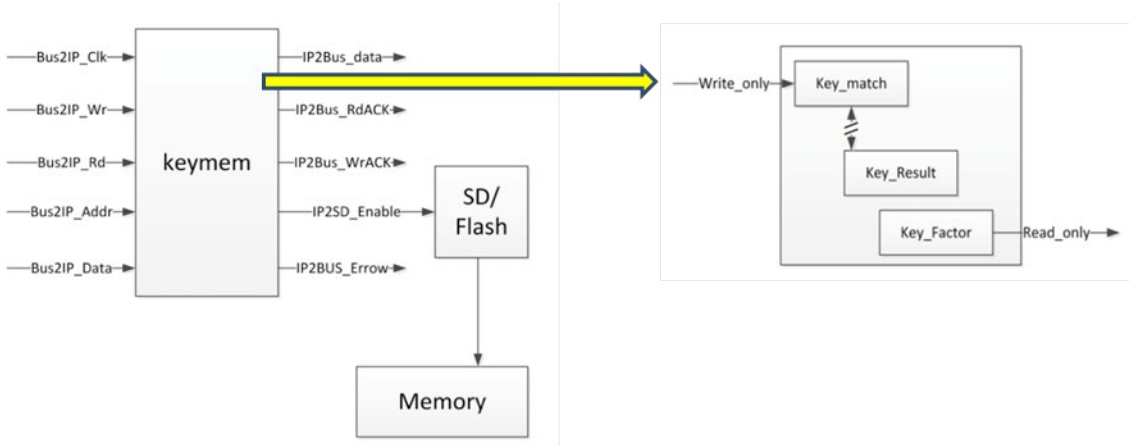

Figure 6. Memory module implementation

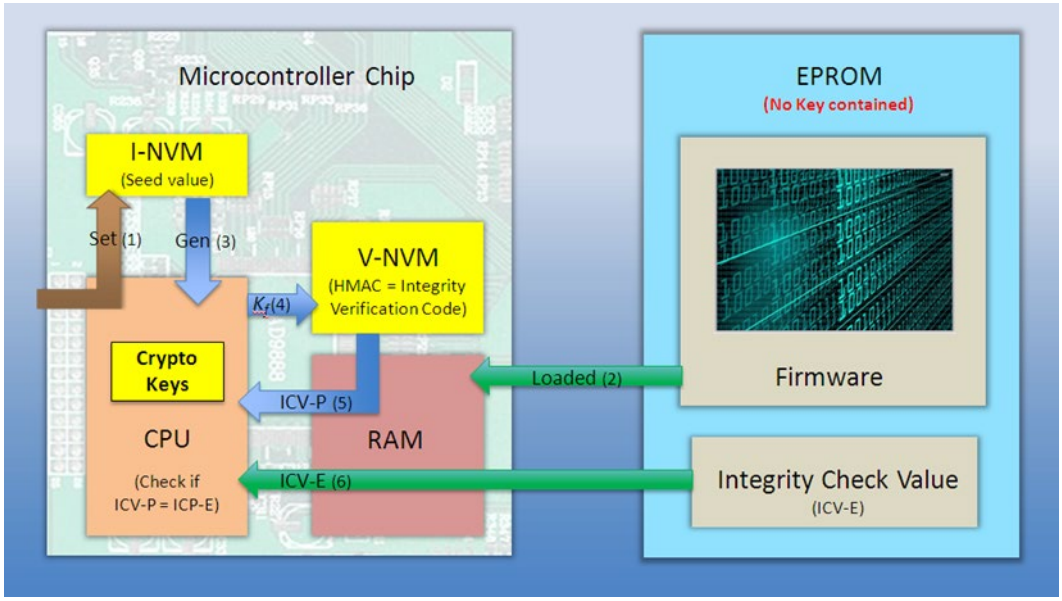

Figure 7. Application software loading process (EEPROM represents any storage unit, which may be EEPROM, Flash ROM, or an SD card)

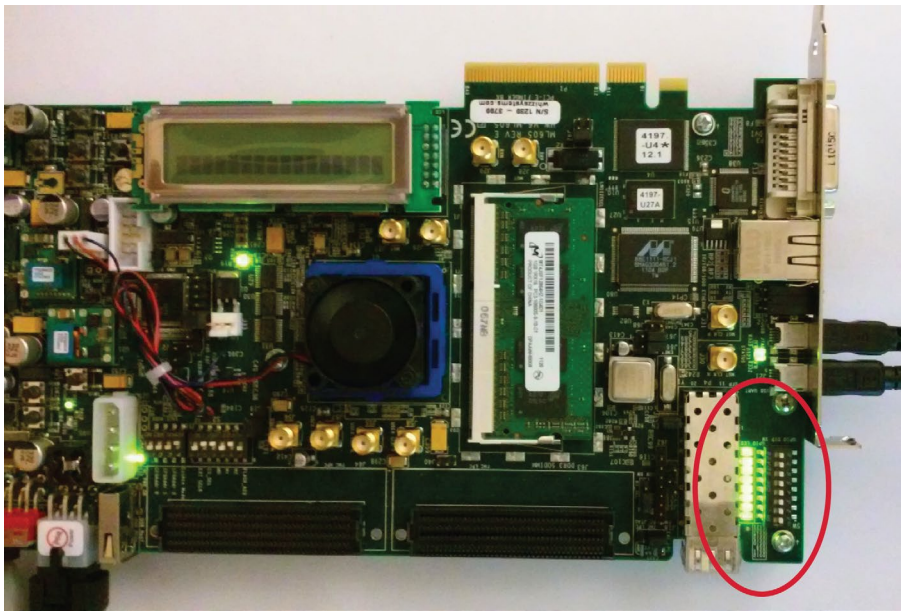

Figure 8. Simulated SCADA operation as an LED blinks active on the FPGA board

Figure 6 shows three independent memories in the keymem: key_match, key_result, and key_factor. The Set function operates on the write-only space. The seed for the algorithm is stored in key_factor (read_only).

System Operation and Evaluation via Simulated SCADA Control Software

The seed value is stored in the I-NVM module (i.e., keymem). The seed value derives a key, and the key is used for application software verification via an LED blinking program. When the board is powered up, the software embedded in the hardware reads the verification key from the software stored in SD memory. Then it reads the seed from keymem, calculates the key out, and puts the hashed key back into keymem. If the key matches, then the keymem module will set up the SD enable bit as part of the status register, allowing the software to be loaded into memory. Figure 7 describes the software loading sequence; the loading is stopped if the comparison fails, thus blocking the execution of any malware.

Our test code simulates controlling the SCADA facility by turning on and off the LEDs. The set of LEDs on the lower right corner of the FPGA board are controlled through the GPIO ports in the hardware system we built before. When the LEDs are turned on, they simulate the successful SCADA operations as shown in Figure 8. The test program also produces print output on the console. Because the FPGA does not have a monitor, the output is forwarded to the development platform over the UART cable.

Conclusion

Cyber security is a serious and ongoing challenge for the energy sector. The electric grid was not designed with modern interconnected networks in mind and will encounter significant new risks (Flick 2011). The SCADA device in the electrical power grid is vulnerable to physical attack that leads to key theft attack and malware injection. To guard against the key theft attack, a prototype of a new SCADA controller architecture was demonstrated as a proof of concept. Major components of our system are a Xilinx ML605 board, as the FPGA platform, along with the MicroBlaze soft-core processor.

All firmware must pass the integrity verification process by comparing the cryptographic values derived from the seed value for the cryptographic operation and the keyed hash value stored in the flash storage,

ensuring a high level of security. When the integrity value matches, the code is executed properly. Any unauthorized change of the executable code in the storage invalidates the hash value and fails to operate the SCADA facility properly. Because no keys are stored in the flash storage, the system would not be vulnerable against key theft attack. By designating a block of memory with write access only and without read access in the keymem module, the memory appears as if it does not exist for the application program. The benefits of the new architecture were previously described (Park 2014).

This project will allow us to determine methods to prevent, resist, and recover from cyber threats, thus attaining better risk management and resilience (Radvanovsky 2013). The new architecture will reduce the vulnerability from threats of key theft and malware injection at the substation level (O'Halloran 2013).

References

Flick, T., J. Morehouse, *Securing the Smart Grid: Next Generation Power Grid Security*, Elsevier, Burlington, Massachusetts, 2011, 14–18.

"MicroBlaze," 2013, http://www.xilinx.com/tools/microblaze.htm, accessed October 9, 2014.

O'Halloran, S., "Improving SCADA and industrial control systems," http://www.foodengineeringmag.com/articles/print/90314-improving-scada-and-industrial-control-systems, accessed February 26, 2013.

Park, K., Y. Kim, "Power automation system (PAS) vulnerability assessment in smart grid," in *Site-Directed Research and Development*, FY 2013, National Security Technologies, LLC, Las Vegas, Nevada, 2014, 191–200.

Radvanovsky, R., J. Brodsky, *Handbook of SCADA / Control Systems Security*, CRC Press, Boca Raton, Florida, 2013, 69–71.

Wei, D., Y. Lu, M. Jafari, P. M. Skare, K. Rohde, "Protecting smart grid automation systems against cyberattacks," *IEEE Trans. Smart Grid* **2**, 4 (2011) 782–795.

Xilinx, Virtex-6 FPGA Configuration, User Guide, UG360 (v3.8) August 28, 2014, http://www.xilinx.com/support/documentation/user_guides/ug360.pdf, accessed October 9, 2014.

Advanced Modeling and Uncertainty for the Aerial Measurement System

RSLA-02-14 | Continued in FY 2015 | Year 1 of 2

Johanna Turk,[1,a] John D. Hague,[a] Marylesa Howard,[b] Aaron Luttman,[b] Michael Mazur,[a] and Thomas McCullough[a]

The development of functional data analysis techniques for gamma ray mapping and search with aerial, vehicular, pedestrian, and maritime-based data collection methods are described. The algorithms and techniques are especially suitable for use by emergency response teams. We pursued the following parallel—and interrelated—research tracks for all of the data collection methods: search- and mapping-path optimization, minimum discernable difference in activity for realistic detector platforms, statistically robust data mapping, superior spectral anomaly detection, and "quick-look" data visualization, analysis, and classification. Effort in the second year of the project will focus on finalizing the techniques for use in air, ground, and pedestrian-based data collection; publishing the results; and socializing the techniques with the emergency response programs that could most benefit from them.

[1] turkjl@nv.doe.gov, 301-817-3333
[a] Remote Sensing Laboratory–Andrews; [b] North Las Vegas

Background

Decisions for the nation's nuclear emergency response actions are heavily dependent on reliable data analysis and radiation visualization techniques. In the past, radiological emergency response programs, such as the Aerial Measuring System (AMS), the Radiological Assistance Program (RAP), and the Nuclear/Radiological Advisory Team (NRAT), have proven successful in the event of disasters; however, the data analysis methods used have not been advanced to the current or next-generation techniques in the field of mathematics and analysis and fail to extract all usable information from the data. Sodium iodide gamma ray detectors are the most common radiation detection systems for emergency response, due to their advantageous properties; they are scalable, highly efficient, non-cryogenic, and inexpensive. Due to the ubiquitous use of this detector medium, likely for decades to come, a fruitful and cost-effective way to improve radiation detection for emergency applications lies in data handling and analysis.

The goals of this project are to reduce noise and variance at different steps in the data collection and analysis process, in order to collect the highest quality data we can, with the goal of the mission in mind; detect the presence of non-naturally occurring isotopes at low thresholds, while not triggering on natural variations in the natural background; perform statistically robust data interpolation to understand the uncertainties in the results; and visualize the data in new and meaningful ways.

Project

Path Optimization and Positional Uncertainties

We have developed a modeling framework to simulate the response of the detectors flown on the AMS aircraft. This framework has allowed us to study how various systematic uncertainties, especially those related to aircraft position and orientation, affect the

data collected. Our models show that most GPS errors and deviations from idealized aircraft flight—drifting off a survey line or rotating away from level flight—lead to negligible changes in the detection sensitivity and to very small (less than 1%) changes in the calculated total exposure rate. The largest uncertainties are due to the radar altimeter and to extreme pitch angles of the aircraft, and these may contribute up to 10% uncertainties. We are also using these models to optimize AMS flight parameters in order to either maximize ground coverage or to maximize the sensitivity to changes in ground deposition during radiological mapping missions. We have studied the canonical AMS rule-of-thumb that recommends flying grids with the line spacing equal to twice the altitude. This pattern can be well suited to a point-source search mission, where the maximum detection distance can easily be calculated to ensure that the source can be found even when it is located between two flight lines. However, this pattern leads to very non-uniform sensitivity on the ground, which may not be ideal for radiological mapping missions, especially if high fidelity is required. We have studied the ground coverage as a function of line spacing for various energy gamma rays, and found that closer line spacing, up to a 1:1 ratio with altitude, is preferred, especially for low-energy sources.

We are continuing the study of response patterns on the ground by simulating deposition patterns and corresponding overflights, with accurately convolved detector response, for a large ground area. From this we conclude that, at higher altitudes or larger line spacing, the ability to resolve fine details at ground level is diminished. A primary goal for FY 2015 is to quantify the trade-offs between resolution and flight time, and to optimize flight parameters accordingly.

Spectral Anomaly Detection

The current standard default method for detecting anomalous radiation signals in time-series data compares the deviation of the gross counts of the most recent measurement(s) with the expected gross counts based on the mean and variance of previous, but recent, measurements. This "Golf Alarms" approach is straightforward to interpret in the presence of stochastic (normally distributed) data, but the natural environment is inherently non-Gaussian, and, therefore, this alarm algorithm can lead to a high false alarm rate. Furthermore, this algorithm makes no attempt to use the information contained in the energy spectra collected by the instrument. For example, it is preferred to ignore a strong source of naturally occurring radioactive material but to alarm in the presence of a weak source of, say, special nuclear material. To this end, we have developed and studied two new spectrum-based anomaly detection algorithms, and compared them with both the Golf (non-spectral) algorithm and the Nuisance-Rejection Spectral Comparison Ratio Anomaly Detection (NSCRAD) algorithm, which is based on spectral windowing.

The Kolmogorov-Smirnov test is a well-established statistical method for testing the probability that two distributions are drawn from the same parent. The test uses the maximum difference between the cumulative distribution functions of two observed data sets to analytically calculate a *p*-value. This test does not make assumptions about the parametric form of the parent distribution, but is only sensitive to the overall *shape* of the distribution.

The Wavelet Assisted Variance Reduction for Anomaly Detection (WAVRAD) algorithm was developed at the NSTec Remote Sensing Laboratory–Andrews in order to compare spectra at different energy scales. In this algorithm, the background and foreground spectra are compared at different energy scales by transforming the channel data into a non-standard topological vector space (the specific l^p-norm can be adjusted). The metric distance between the spectra in the transformed space enhances the difference in *shape* between the spectra and can be used to robustly differentiate a signal from typical background variations.

Comparing the performance of these four algorithms based on representative data sets, we can conclude that Kolmogorov-Smirnov outperforms the Golf algorithm and that WAVRAD outperforms both

Table 1. True and false alarm rates of the four different alarm algorithms, for various source configurations. The data sets (no source, ^{133}Ba, ^{60}Co, and uranium ore) were collected at the same location by driving past the known source five times. The data set from Washington, D.C., was taken by driving throughout the area without emplacing sources. Natural and man-made sources were present, in addition to variable background profiles, but were not known to the measurement team. For this reason, alarms cannot be categorized as false or true, and only total alarm number is reported.

Data	# Sources	# True Alarms / # False Alarms			
		Golf	Kolmogorov-Smirnov	WAVRAD	NSCRAD
No source	0	0 / 6	0 / 0	0 / 0	0/0
^{133}Ba	5	1 / 0	3 / 0	5 / 0	0/0
^{60}Co	5	0 / 1	2 / 0	5 / 0	5/0
Uranium ore	5	2 / 0	5 / 0	5 / 0	4/0
Washington, D.C.	Unknown	**140**+ total alarms	**3** total alarms	**9** total alarms	**9** total alarms

Kolmogorov-Smirnov and NSCRAD. Although NSCRAD and WAVRAD appear to perform similarly, the fact that NSCRAD missed all of the ^{133}Ba exposures reveals its primary weakness. Alarms in NSCRAD are based on windows of the energy spectra, which are tuned by the developers (not users) to be sensitive to the isotopes they believe to be of interest. For isotopes for which this is done well, NSCRAD does indeed provide effective alarms, but as we see, it can fail spectacularly for a common isotope. Neither the WAVRAD nor the Kolmogorov-Smirnov algorithms are trained for a specific isotope library, which can be a strength.

Spatial Analysis and Uncertainty Quantification

Standard data-visualization techniques for AMS data typically use an interpolation scheme. Among other drawbacks, such methods may not lend themselves to estimating the error in the interpolated values.

Kriging is a method of interpolation that naturally provides error estimates, assuming a Gaussian process and foreknowledge of spatial covariance (Cressie 1993). When the assumptions are met, the Kriging procedure produces the best linear unbiased estimator. It is a lengthy process, however, to verify that the assumptions are met. With the possibly arduous task of data manipulation involved in the Kriging procedure, we sought an adaptation that would allow for faster results while retaining sufficient statistical rigor. We call this method "quick Kriging." To compare and contrast the typical interpolation method with canonical Kriging and quick Kriging, the methods were applied to a data set and are shown in Figure 1. The data set consisted of 1027 points obtained during an AMS flight in Maryland, over a field with a radiation source near the center of the sampling area.

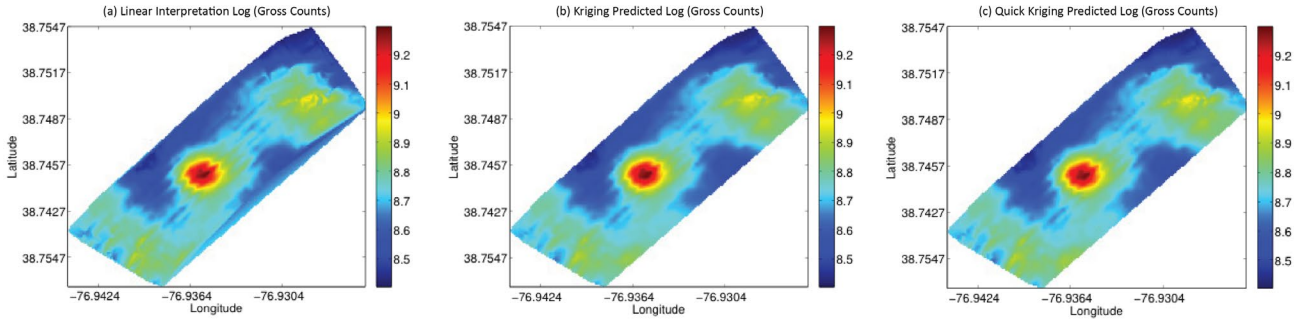

Figure 1. Interpolated maps of the logarithm of gross counts for a field in Maryland that contains a radioactive source by (a) linear interpolation, (b) Kriging estimation, and (c) quick Kriging estimation

We see that linear interpolation struggles to extrapolate data, that is, compute estimates outside of the boundaries in which data was taken (e.g., see bottom right-hand corner of Figure 1). Furthermore, both Kriging approaches demonstrate less striation in the data than linear interpolation, a result of the process in which data are collected via flight path lines. Lastly, the two Kriging estimate maps are nearly identical, with the largest absolute log difference being 0.0272, or about 3%.

Computed error estimates for both Kriging approaches are shown in Figure 2. We see that the computed errors for quick Kriging is, on average, about 1% higher than the estimated errors for Kriging.

"Quick-Look" Data Analysis, Visualization, and Classification

A fundamental method of data analysis relevant to the emergency response mission is conversion from count rate to exposure rate. Exposure rate maps are of vital significance in an emergency involving public health and safety. However, this reveals nothing about the underlying source of the radiation. Often, the source of the radiation (namely isotopic constituents) is of interest.

The current method for classifying data based on isotopic constituents is to extract the counts present in a fixed spectral region, generally around a photopeak of interest. This method assumes a priori knowledge of isotopes of interest, which is not always reasonable. This spectral stripping approach provides especially poor results in the presence of down-scatter (energy is largely deposited well below the photopeak) and/or in the situation of isotopic conflicts, where other isotopes contribute meaningfully to the utilized energy region. We have developed an alternative approach to accommodate isotopic analysis for gamma spectra that is particularly relevant when the data are "challenging," that is, acquired at 1 Hz and of low count rate/statistical fidelity.

From a large ensemble of spectral measurements, effective determination of measurements that naturally "go together" is a powerful tool. This simultaneously allows immediate reduction in complexity of the problem by reducing the number of spectra to be specifically analyzed, strengthens spectral analysis efforts by increasing the statistical quality (variance reduction) of the spectra, and reveals potentially very subtle spatial or temporal trends. This is a singular, but powerful, first step in the isotopic analysis effort, which can be used to understand the isotopic makeup of the data without a priori knowledge of the source(s), make cuts on data to increase signal-to-noise ratio by including only those data points relevant to the spectral analysis being conducted, and display how the isotopic composition is structured spatially, to name a few.

Our proposed approach was to use novel application of existing tools in non-linear dimension reduction (Belkin 2003) and apply data clustering to spectral

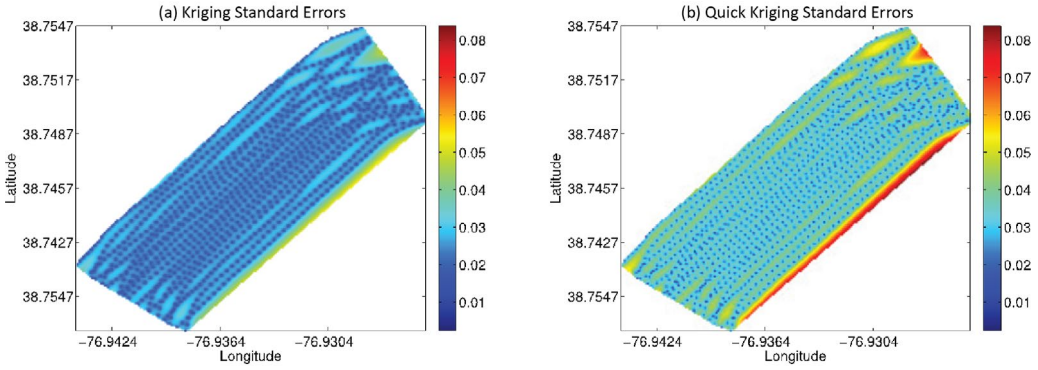

Figure 2. Standard errors for the (a) Kriging estimates and (b) quick Kriging estimates

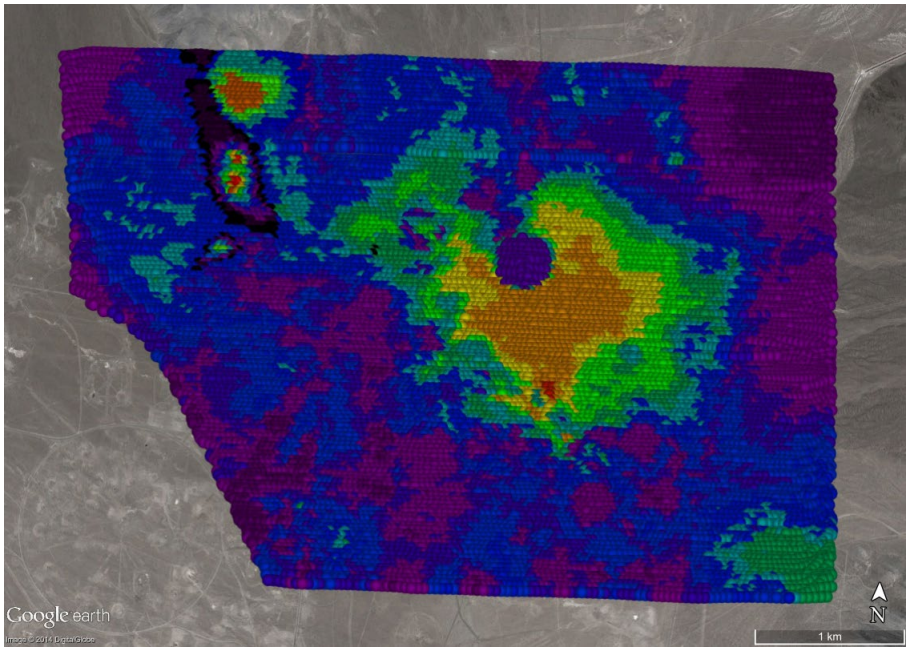

Figure 3. The Sedan Crater and surrounding area, with spectral clustering into 50 classes applied. Each cluster class corresponds to a color in the plot. Notice three disparate regions of interest: the large orange region in the center shows ^{137}Cs and ^{57}Co around the Sedan Crater; the smaller orange region in the upper left shows the neutron activation ring from a tower shot; the red region just below that shows ^{241}Am from a safety shot.

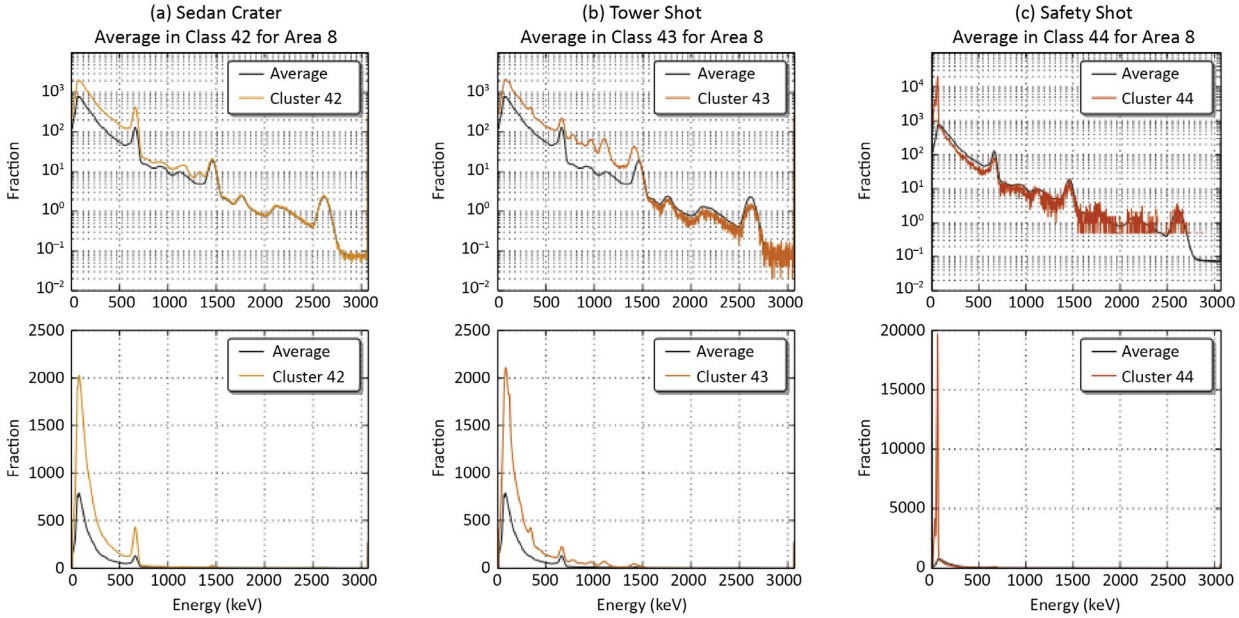

Figure 4. Mean spectra of three classes shown in Figure 3. The top plots show the normalized spectra of the mean of the entire data set (black) and the individual class (colored) on a log scale. The bottom shows the same but on a linear scale. One class corresponds to the (a) Sedan Crater, one class corresponds to the (b) tower shot, and one class corresponds to the (c) safety shot. Note that while the mean gross counts for each of these spectra are coincidentally similar, the spectral shapes are notably different. Clustering can be a very powerful analysis tool in cases where regions with similar gross counts have dissimilar spectral shapes. Without it, identifying these three distinct regions would be very time consuming.

measurements. Numerous approaches to this problem have been attempted on existing data, to great success. The visual representation of clustering applied to aerial data taken over the Sedan Crater and two neighboring shots is shown in Figure 3. Examples of the spectral classes found by the clustering technique are shown in Figure 4.

Immediate benefits of the efforts are that it (1) informs the application of the spectral stripping approach, both by revealing feasibility and shortcomings; (2) provides effective visualization of spatial trends in spectral measurements; and (3) reveals subtle spatial trends, which will be missed or poorly quantified using spectral analysis methods on individual measurements. Particularly for spectral complex data sets, for which spectral windowing is not an effective tool for reducing the data, clustering provides a valuable tool to the scientist for understanding the spectral information.

Future work mainly consists of iterative improvements and developing use guidance for this method. The final method cannot be fully automated, as it is fundamentally a resource for the scientist analyzing the data, rather than a step of the analysis process. However, guidance for use will be developed to address the technical application of the tool, and the scientific value of the information resulting from its use.

Conclusion

In the first year of this project, we completed the preliminary studies of search- and mapping-path optimization, minimum discernable difference in activity for realistic detector platforms, statistically robust data mapping, superior spectral anomaly detection, and quick-look data visualization, analysis, and classification. In each of these areas, we have worked to decrease noise and variance in the data collection and analysis processes. In the second year of the project, the algorithms will be finalized; methods for their use by air, ground, and pedestrian data collection teams developed; and those methods socialized with the stakeholders for different emergency response teams. Implementation of these methods by the emergency response programs is outside the scope of this SDRD project. Therefore, other programs, such as the Technology Integration program, will be required to take the final step of implementation. Some of these results may also be of interest to a wider community, and will also be published and presented at conferences accordingly.

References

Belkin, M., P. Niyogi, "Laplacian Eigenmaps for dimensionality reduction and data representation," *Neural Computation* **15**, 6 (2003) 1373–1396.

Cressie, N. A. C., *Statistics for Spatial Data, Revised Edition*, Wiley-Interscience, New York, 1993, 105–210.

Chemically Activated Quiescent Persistent Sensors for Semantic Networks

STL-25-13 | Continued from FY 2013 | Year 2 of 2

Stephan Weeks,[1,a] Shayla Sawyer Armand,[b] Yasashi Ono,[c] and James Kornell[a]

The target application is autonomous, persistent remote sensing for chemical, biological, radiological, nuclear, and explosives (CBRNE) threats. Last year, we evaluated low-power sensor types and studied nanomaterials to provide specific surface chemistries, toward the goal of creating passive, chemically activated sensors (Weeks 2014). In this year's work, a sensor-agnostic hardware platform, "Urchin," was designed, fabricated, and tested for ultra-compact, ultra low–power persistent monitoring. Commercial chemical sensors using CCFET (capacitive-coupled field-effect transistor) technology were integrated onto the Urchin platform for the detection of nitrogen dioxide, ammonia, hydrogen, and volatile organic compounds. Operations were performed using Android algorithms within the Special Technologies Laboratory's NanoRaptor software platform. The next step would be to incorporate distributed semantic sensing, which will be required for advanced, next-generation, ubiquitous, remote detection of CBRNE threats and situational awareness. To further chemical sensor development, research on nanosensing materials and ultra low–power devices was continued. Reduced graphene oxide nanocomposites provide many chemically active defect sites, as well as high surface area and conductivity; plus, they can be used at room temperature and are amenable to different device structures.

[1] weekssj@nv.doe.gov, 805-681-2262
[a] Special Technologies Laboratory; [b] Rensselaer Polytechnic Institute; [c] Keystone International, Inc.

Background

Autonomous, persistent monitoring for low-level chemical transients is an unsolved problem. There are mission-relevant observations of intermittent, transient, and very low–level chemical emissions that can only be detected by persistent, in situ sensors. Robust chemical, biological, radiological, nuclear, and explosives (CBRNE) sensor networks for unattended and remote operations require ultra low–power sensors and sensor platforms together with global situational awareness software platforms and computational ontologies to support semantic sensing. This allows the development of autonomous persistent sensing (e.g., unattended remote sensing in denied areas). Continuous monitoring using distributed CBRNE sensor semantic networks can sample remote areas, autonomously perform scenario-confirming measurements, then exfiltrate information. These chemical sensor networks must be persistent over months or years, capable of sensing continuously without breaks, able to rapidly relay important detections, flexible enough in design to support multiple missions and needs, cost-effective, and stealthy enough for use in restricted areas. In addition, the network should be able to work as a "team": it must be self-organizing, and sensor field productivity should be more important than any individual device.

The development of technologically innovative sensors is critical for enhanced remote sensing capabilities. Understanding of surface chemistry and structure effects at the nanoscale level; developing chemically functionalized, application-specific materials; and integrating these materials into device substrate surfaces for efficient signal extraction are required. The nanofabrication of robust, low-cost, ultra low–power, selective, and sensitive chemical sensors is needed to develop field prototypes to validate wearable and wide-area, distributed wireless monitoring applications. Then, integration into ultra low–power sensor platforms with mission-specific semantic sensing logic (i.e., sensors that decide when to exfiltrate data) enables the deployment of "smart" and autonomous persistent sensing networks for situational awareness.

Project

This is an autonomous remote sensing project. The project fundamentally began with chemistry at the nanoscience level to identify specific and/or selective gas/surface interactions. Materials science integrated chemically active defect sites in an architecture that would provide high surface area and conductivity to enhance detectability. Our research sought to understand the charge transfer within the chemically functionalized materials at the nanoscale level, then integrate these chemically selective sensing materials into device structures capable of ultra low–power operation with efficient signal transduction. Then, selective chemical sensors were tested for robust operation. Electrical and system engineers then developed and optimized the hardware for robust remote sensing applications. The addition of firmware and integration into a software situational awareness sensor system platform allowed the sensors to be tested. The hardware platform named Urchin achieved ultra low–power operation of the chemical and additional environmental sensors.

Autonomous operation for large-area remote sensing requires semantic algorithms for smart sensor networks. Developing this structure would enable R&D projects from conceptual phase (TRL 1) to fairly advanced system prototypes capable of being expeditiously performed, allowing technology-enabling (e.g., new materials and devices) as well as programmatic applications (e.g., demonstrated in relevant environments [TRL 6]) development. The target application is persistent CBRNE monitoring in denied areas. We describe herein the hardware and software platform approach, which allowed us to develop chemical-specific "trigger" sensors and select sensor suites that would appropriately monitor the scenario and provide analysts with information.

Hardware Platform Development—Urchin

The Urchin hardware platform was developed as a proof of concept of zero-power chemical sensing. With this in mind, the platform was specifically designed to run without batteries, to push the limits of what is capable with current technology. All electronics and sensing components were chosen with the concept that no battery will be available. Because the data needed to be extracted from the device with minimal power, Bluetooth low energy (BLE) was chosen as the wireless link, and the Nordic Semiconductor nRF51822 multilink protocol system with built-in BLE was an ideal match. Additionally, it runs at low power levels and is highly flexible, allowing the wireless transceiver to run custom protocols (such as a low-power mesh network).

The chemical sensors were researched from a previous SDRD study (Weeks 2014) and were integrated into the design. In addition to the chemical sensors, several other low-power sensing capabilities were added: acceleration, magnetism, infrared heat, RGB light, humidity, pressure, temperature, and voltage levels. A 4 MB magnetic memory was added to persist data, if needed. Lastly, an expansion port was added to allow more sensors to be attached in the future. This port contained an inter-integrated circuit (I^2C), a serial peripheral interface (SPI), an analog-to-digital converter (ADC), general-purpose input/output (GPIO), and power.

For the platform to operate without batteries, a super capacitor was used to store enough energy to run for

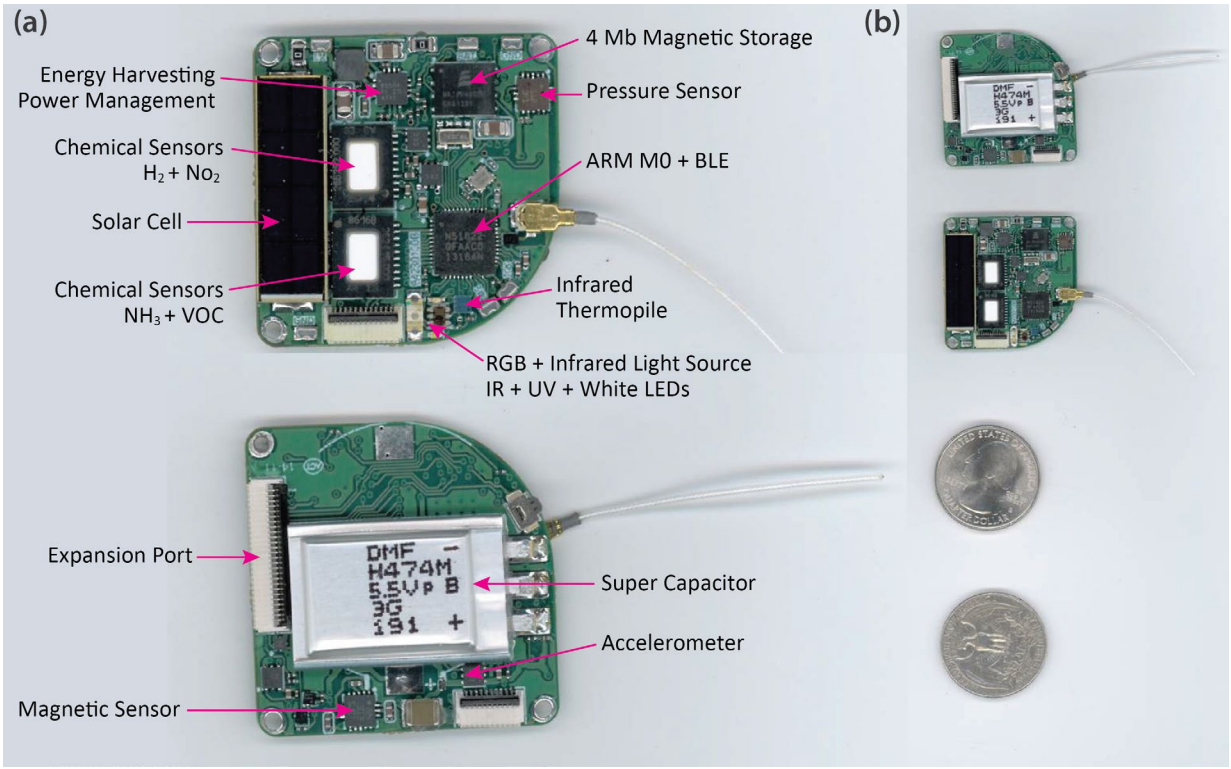

Figure 1. (a) The Urchin PCB showing placement of components. (b) As-built photo showing relative size.

about 12 hours. Adding a power-harvesting circuit and a small solar cell allows for potentially unlimited run times without a battery. Next, a PCB was designed in-house and tested. Testing revealed minor issues, and modifications were made. Using the improved design, we built ten units to be used in experiments as well as develop a firmware and software framework. Figure 1 shows the Urchin PCB design and components.

The software that runs on the device was written in the C programming language, and uses the open-source GNU compiler collection (GCC) tool chain. Firmware was written to read the sensors and wirelessly transmit data over the BLE link. Heavy optimization was done to the firmware to minimize power consumption, especially during sleep, as this is the dominant power draw. We designed the units so that the target power draw in sleep mode was less than 10 µA; in the final design, the measured sleep currents were typically around 6 µA.

The sensor platform is quite capable and can be integrated into a number of different applications without hardware modifications. The expansion port can be used for future applications development, or for conveniently testing innovative R&D ultra low–power devices or sensors. Additionally, the design is straightforward enough that smaller and lower-cost variants can be made with minor effort.

Software Platform Integration—NanoRaptor

Because the sensors send data via BLE, a natural choice for receiving the data was a cell phone—newer models provide BLE communications.[1] For this project, an Android platform was chosen. First, a small Android application was developed to receive data, convert the binary data to actual units, and then graph the data. Then, the Urchin sensor platform was integrated into Special Technologies Laboratory's (STL's) NanoRaptor situational awareness software.

[1] Few PCs yet include BLE; the installed base for RaptorX does not.

Persistent Monitoring with Distributed Semantics Context

The driving hypothesis for this project was that extremely low-powered sensor fields can use domain semantics to *decide when to exfiltrate data*. We were motivated by the recognition that most of what the sensors report will be uninteresting—"Nothing happened. Nothing happened, again." The goal was to have randomly distributed sensors work together, report important events, discard unimportant collections, and have reasonable false negative rates, depending on the detection. "Semantics" refers to meaning: we wanted a way whereby the energy and operational lifetime cost and risk of exfiltration was assessed by the sensor field against the best guess of the current value of the collected information, i.e., the sensors assign meaning to the collected data and decide whether to exfiltrate, taking power consumption into consideration.

Four assumptions were made: (a) extremely low power implies no GPS or real-time clock and no master with respect to network organization, (b) placement was random, as if dropped from a drone or spread by hand, (c) domain experts would be able to define events of interest and say what they mean for a particular mission, and (d) mission semantics can vary widely and the same events could have different meanings according to mission. Assumptions (c) and (d) drove the architecture, while assumptions (a) and (b) influenced the implementation. The key concepts to this four-layer architecture are:

- Domain semantics (the top layer), which represent the meaning of the events, including both context (day/night, for instance) and history ("We already saw this event; it's only interesting the first time we see it."). A computational ontology, represented via state machines,[2] was used to represent the semantics.
- Virtual events, which represent things of interest that happen in the domain. Key to virtual events is that multiple sensor detections and sequences can combine into a single event.

The two supporting layers are virtual digital signal processors at Level 2, which are used to tune and normalize sensing data and the sensors themselves at the foundation level.

In the nuclear domain, some virtual events seem commonsensical (e.g., detection of kerosene and tributyl phosphate [TBP] together). While this is a very simple virtual event, one could still foresee false positives if the wind were blowing from the direction of a nearby airfield. It is easy to imagine virtual events that (for example) combine chemical, acoustic, and vibrational sensing where relative timing (how long is "at the same time"?) or selectivity (how sure is the detection?) might result in complex virtual events that unintentionally misrepresent domain expertise. The fundamental problem of finding the balance between too much and too little communication is non-predictive, even within a single mission. The architectural goal for this project was to accommodate the widest possible range of deployment decisions (Figure 2).

Too much data can flood a system, driving a low-power sensing field to early battery death (much the way that, at higher levels, too much data can drive users of situational awareness software/tools to "attention death").

Systems Integration and Applications Development Approach

Providing both hardware and software platforms, as well as being able to code semantics into the operations, allows quick-response engineering solutions. The feasibility of developing an application-specific sensor node can also be tested prior to the cost of full design, fabrication, and packaging. New sensors, whether commercial or developed in-house or by collaborators, can be efficiently tested using the

[2] State machines are common in industrial applications and control systems (like automobiles). Generally they comprise small blocks of code that monitor the status of one or more "lines," then produce defined outputs when the status of an input line changes. For instance, a state machine might monitor the oil pressure in your car and cause a light to go on in the instrument panel if it drops below a set threshold.

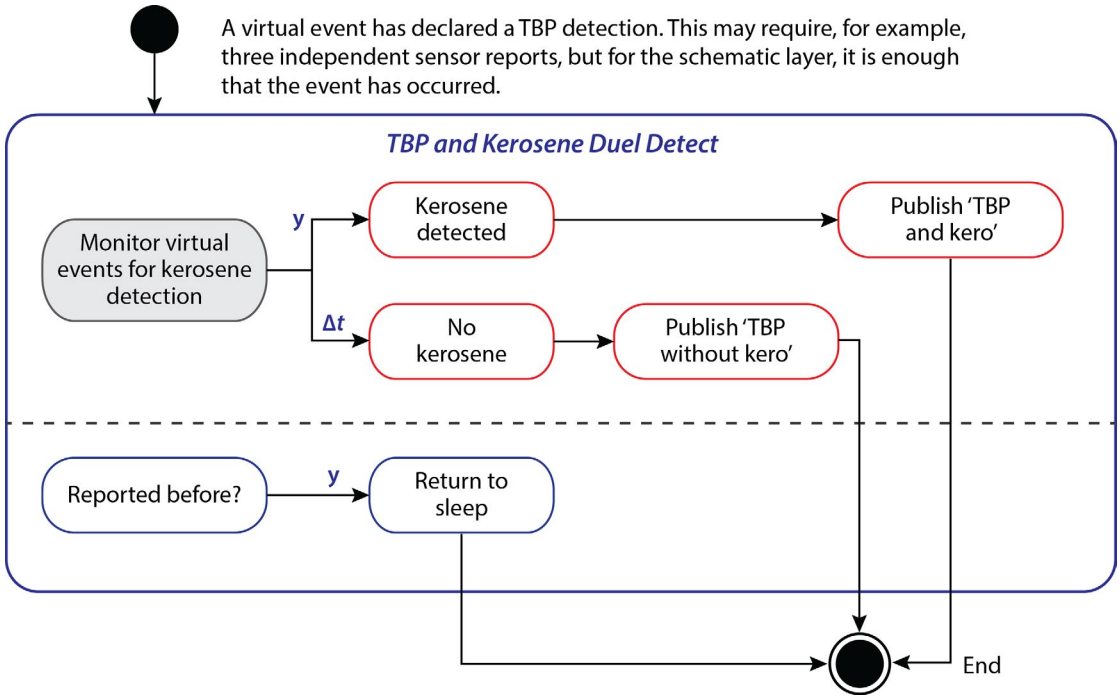

Figure 2. The state machine runs parallel paths. On entry, a monitor flips on a timer and waits for the virtual event "kerosene detected." Concurrently, the state machine "remembers" whether it has published TBP before. If it has, it exits without doing anything further (since there is nothing to do); the exit turns off the monitor as well. If it has not been published, either there is a detection or the time delta expires, and publication is made accordingly. A separate state machine might then make a decision about whether to exfiltrate the information, save it for later exfiltration, or discard it.

hardware expansion port. The hardware platform also may be used to develop and test energy harvesting–technology innovations.

Materials and Device Research

An approach to creating new sensors was explored to address meeting the difficult requirements including low-power operation, selectivity, sensitivity, room-temperature operation, and a relatively fast response. There are currently no sensors available that achieve even a combination of three of these. Research in this area is important to the impact of sensor node systems and what, where, and how they monitor spaces.

In this project, we employ a graphene-based nanocomposite to explore its potential for chemical sensing. Graphene is a unique nanomaterial with a single flat atomic layer of carbon with atoms arranged in a 2-D honeycomb configuration (Ghosh 2013). Reduced graphene oxide (rGO) is an alternative to graphene that has additional sensing properties due to its chemically active surface defect sites. Chemical sensors have been researched for gases such as hydrogen (H_2), carbon monoxide, ammonia (NH_3), chlorine, nitrogen dioxide (NO_2), and oxygen (Kuila 2011). Recent work by Fowler (2009) reported the detection of NO_2, NH_3, and 2,4-Dinitrotoluene (DNT). In this device, rGO demonstrated an increase in resistance when NH_3, due to its n-type dopant characteristics, depleted holes from the conduction band. Conversely, NO_2, a p-type dopant, increased hole conduction and therefore decreased resistance. The response time of this resistance-based device was about an hour.

In previous work, a novel tungsten oxide-reduced graphene oxide (WO_3-rGO) nanocomposite was created for ultraviolet sensing (Figure 3). As a result of synergistic effects, the detector performance improved significantly (Shao 2013). The responsivity was more

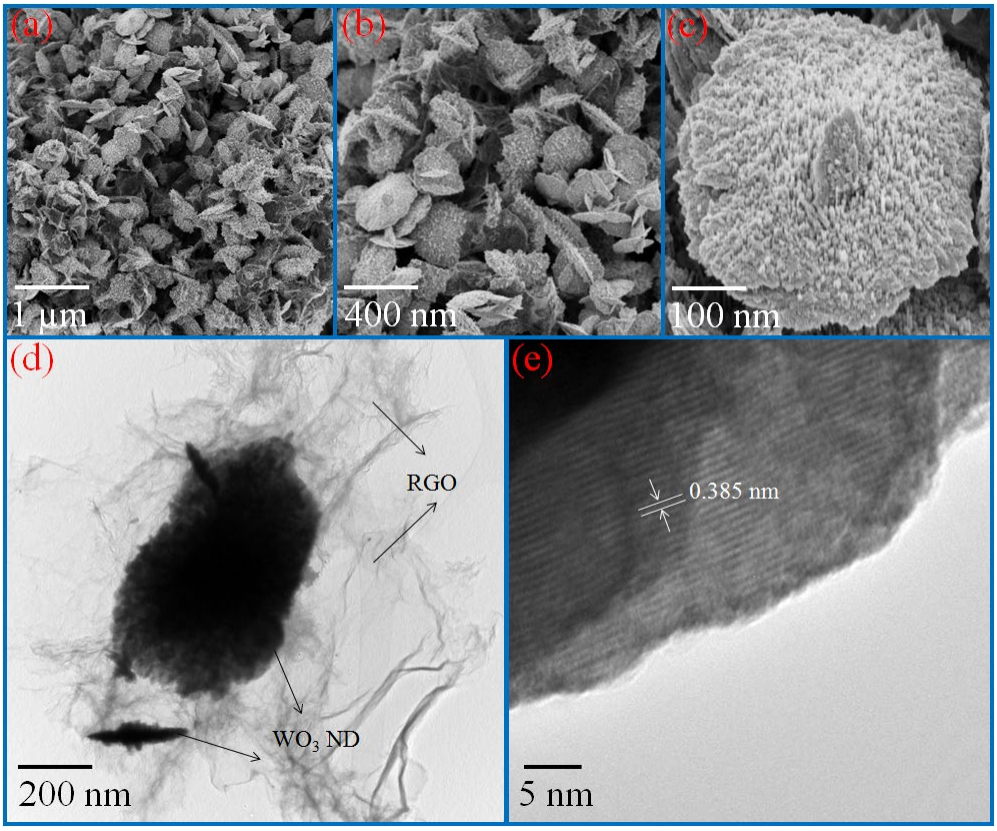

Figure 3. (a–c) High-resolution scanning electron microscopy images of the WO_3 nanodisks (NDs)-rGO composite material, (d) transmission electron microscopy (TEM), and (e) high-resolution TEM image of the WO_3 NDs-rGO composite material (Shao 2013)

than 30 times greater than commercial devices and 17 times greater than the reference device (without rGO) (Shao 2013). Most pertinent to this project, the time response demonstrated marked improvement with faster response by three orders of magnitude. Due to the faster response time, the chemical sensing properties of rGO, and the inherently large surface area from nanostructure device architectures, the resistive device was developed and tested for chemical sensing. The fabrication process can be found in Shao (2013).

The resistance of the rGO as it is exposed to ammonia over a time span of 5 minutes is depicted in Figure 4. The chemical response seems to begin to saturate at approximately 3 minutes. Though initial tests looked promising, a more thorough investigation must be done to confirm that the resistance change is due to ammonia and its adsorption on the surface on the device.

Future work would include the creation of a field-effect transistor (FET) device structure using the rGO nanocomposite as the conducting channel. The sensitivity of FET-based chemical sensors depends on their transconductance, g_m,

$$g_m = \partial I_D / \partial V_G = C_G V_D \mu, \quad (1)$$

where C_G and μ are the gate capacitance and field effect mobility, respectively (Ohno 2010). The measurement of the capacitance change due to adsorbed molecules is more sensitive and may induce a faster response. Furthermore, the porous nature of the rGO-WO_3 nanocomposite increases the surface area of the overall active area significantly. Improvements in sensitivity and time response due to both the nanocomposite material properties and the FET device structure are expected. Using nanocomposite hybrid materials including rGO is just the beginning. Functionalization

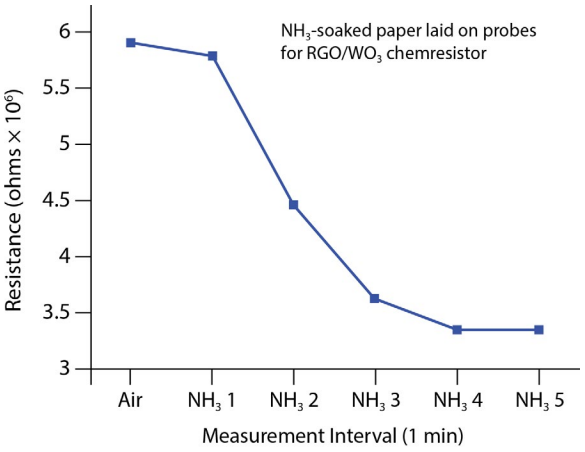

Figure 4. Initial testing of rGO nanocomposite as a resistive device. The device was exposed to ammonia for 5 minutes, and measurements were taken every minute.

of the materials must be pursued to add selectivity. A non-enzymatic approach can be taken to reduce the high cost of using enzymes, circumvent the complexity of immobilization on the surface of rGO, and reduce temperature, pH, and unwanted chemical interference. Water-soluble, conducting graft co-polymers have been used in literature for electrochemical detection without affecting the intrinsic conductivity of rGO (Zhang 2010). In this hybrid nanocomposite configuration, the capture of carriers in the conductive path happens when the target attaches to the conductive co-polymer. The appropriate polymer depends on the target chemical.

Conclusion

The ultra-compact and ultra low–power Urchin hardware platform was developed, optimized for low-power operation, and tested using a commercial gas sensor chip. Integration into NanoRaptor began, and the prototype Urchin PCB was tested. Design features allow the use of the sensor nodes in a semantic distributed sensor network.

The primary goal of the project, which was to use a chemical sensor to activate additional CBRNE and environmental sensors in the sensor node, was achieved. The overall research efforts occurred over several R&D areas: remote sensing, chemistry, materials and device engineering, electrical engineering and system development, and software engineering. We developed a capability that will make autonomous, persistent remote sensing at the NNSS or in denied areas possible.

We also researched continuous analog monitoring with digital wake-up on detection and developed chemical processes and approaches for functionalizing nanomaterials for selective chemical/biological sensing. Nanomaterials providing high surface area and chemically active surface defect sites were examined for developing devices capable of ultra low–power operation, efficient signal transduction, and fast response times. The Urchin sensor platform demonstrated a 6 µA sleep state and the ability to self-charge (energy harvest) in dim light.

Our software engineering effort included completing the Urchin firmware and Android programming for testing and evaluation. We demonstrated a semantic sensing approach and began integrating the Urchin into the situational awareness software platform NanoRaptor.

Depending on the availability of specific ultra low–power chemical sensors or sensor arrays, prototype sensor nodes can be developed in wearable or distributed formats for persistent gas-phase monitoring.

Acknowledgments

We would like to thank Arlene Budiardjono (University of California, Santa Barbara) and Andrew Ellis and James Davis (Rensselaer Polytechnic Institute) for their contributions to this work. In particular, we acknowledge Eric Nystrom (STL) for his support of the project and valued comments on systems engineering and applications.

References

Fowler, J. D., M. J. Allen, V. C. Tung, Y. Yang, R. B. Kaner, B. H. Weiller, "Practical chemical sensors from chemically derived graphene," *ACS Nano* **3**, 2 (2009) 301–306.

Ghosh, R., A. Midya, S. Santra, S. K. Ray, P. K. Guha, "Chemically reduced graphene oxide for ammonia detection at room temperature," *ACS Appl. Mater. Interfaces* **5**, 15 (2013) 7599–7603.

Kuila, T., S. Bose, P. Khanra, A. K. Mishra, N. H. Kim, J. H. Lee, "Recent advances in graphene-based biosensors," *Biosens. Bioelectron.* **26**, 12 (2011) 4637–4648.

Ohno, Y., K. Maehashi, K. Matsumoto, "Chemical and biological sensing applications based on graphene field-effect transistors," *Biosens. Bioelectron.* **26**, 4 (2010) 1727–1730.

Shao, D., M. Yu, J. Lian, S. Sawyer, "An ultraviolet photodetector fabricated from WO_3 nanodiscs/reduced graphene oxide composite material," *Nanotechnology* **24**, 29 (2013) 295701.

Weeks, S., S. Sawyer Armand, H. McHugh, "Chemically activated quiescent persistent sensors," in *Site-Directed Research and Development*, FY 2013, National Security Technologies, LLC, Las Vegas, Nevada (2014) 149–159.

Zhang, J., J. Lei, R. Pan, Y. Xue, H. Ju, "Highly sensitive electrocatalytic biosensing of hypoxanthine based on functionalization of graphene sheets with water-soluble conducting graft copolymer," *Biosens. Bioelectron.* **26**, 2 (2010) 371–376.

Computational and Information Sciences

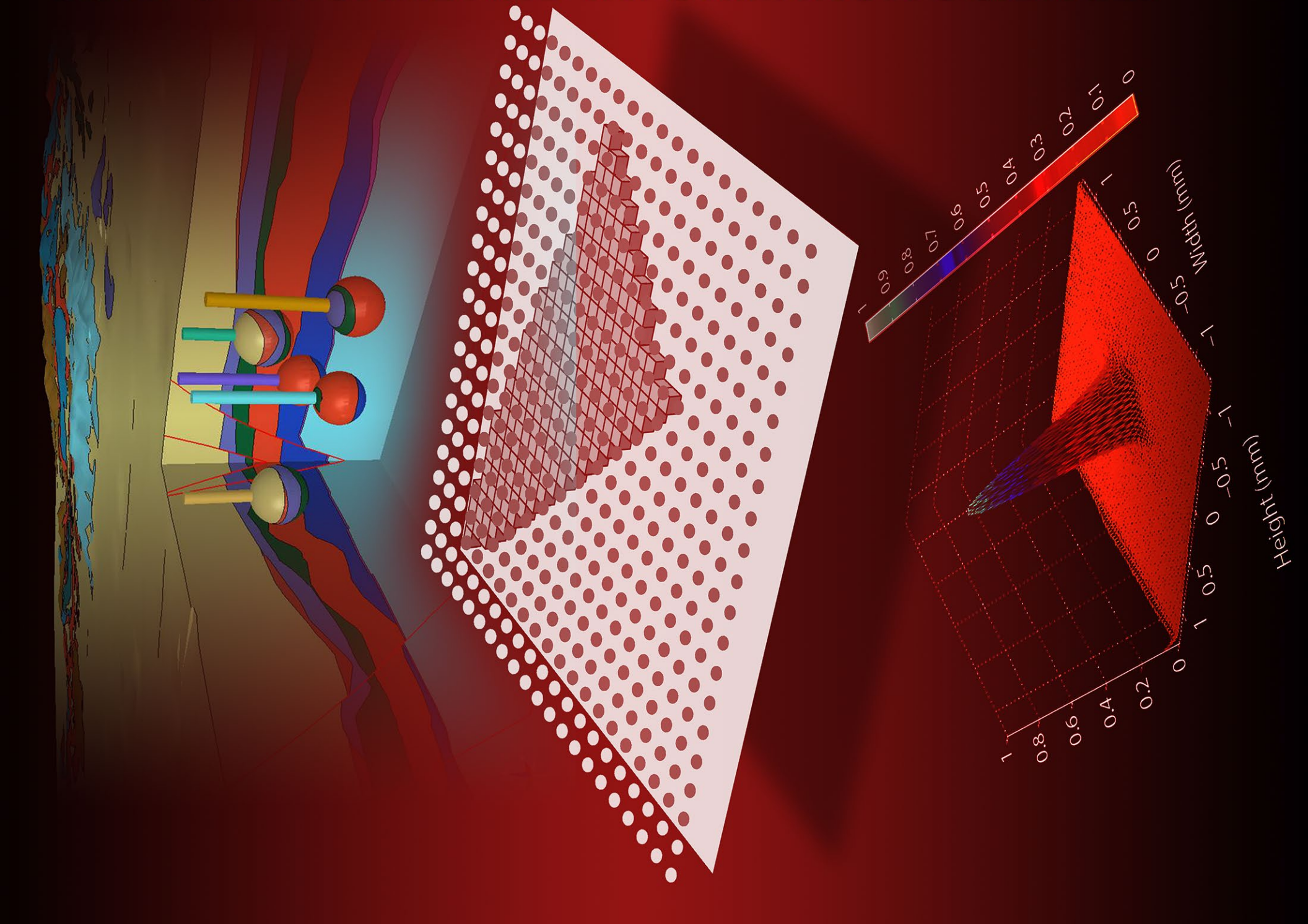

Reduced Order Modeling for Real-Time Monte Carlo Simulations with Applications to Radiation Detection

NLV-01-14 | Year 1 of 1

Aaron Luttman,[1,a] Brian Helenbrook,[b] Indika Udagedara,[b] Stephen Mitchell,[a] and Michael Fowler[a]

Monte Carlo (MC) methods are the most popular for simulating radiation transport due to the fact that they work very well. Nonetheless, they have substantial drawbacks in that they require significant computational resources and often prohibitively long computation times. There is extensive literature on techniques for increasing the statistical efficiency of MC modeling, but there are other possible approaches to accelerating simulations for specific radiation transport problems. In this work we designed methods for developing reduced order models (ROMs) for radiation transport applications. Proper orthogonal decomposition (POD) is adapted for use with radiation transport, and we show that this can accelerate some MC simulations by several orders of magnitude. The details of POD, the generation of the training data, and how the ROM is constructed from the training data are presented, as well as the results from a simulated radiation detection scenario. The second research track of this work was to develop nonlinear model reduction methods that can be applied to radiation transport, and we extend a nonlinear decomposition from image processing—known as the "cartoon-texture" decomposition—as a ROM for fluid flow. Because most model reduction methods come from the fluids literature, this is a natural first step towards applying the technique to radiation transport.

[1] luttmaab@nv.doe.gov, 702-295-0303
[a] North Las Vegas, [b] Clarkson University

Background

Numerical approaches to simulating radiation transport essentially fall into two categories: (1) deterministic methods based on partial differential equations (PDEs) and (2) stochastic methods based on ray tracing and the probabilities of particle interactions. Deterministic approaches (Olson 2000) tend to be difficult to implement and require sophisticated numerical methods to solve the associated PDEs. Stochastic methods are more straightforward to implement but can be computationally demanding. Among the stochastic techniques, the Monte Carlo (MC) method (Kalos 1986, Robert 2004) is the most common approach to radiation transport (Carter 1975, Dupree 2002), and there are several radiation transport codes that implement MC techniques, including MCNP from Los Alamos National Laboratory (Goorley 2013) and GEANT4 from CERN (Amako 2006, Asai 2012).

The primary drawback to modeling radiation transport with MC methods is that the error in the simulation is a function of the number of particle histories simulated, which means that for many applications the approach can be computationally prohibitive. There is extensive literature on variance reduction (Saidi 2013) methods that increase the statistical efficiency of MC simulations, but, given applications where multiple simulations are run with few changes among them, it is also possible to use reduced order models (ROMs)

to accelerate the calculations. The focus of this project was to design a ROM-based approach to improving MC simulations, and we developed a linear approach based on proper orthogonal decomposition (POD) as well as a nonlinear technique for model reduction adapted from image processing.

Project

Our primary task was to develop a POD-based approach to reduced order modeling for radiation transport. The section titled ***POD-Based Model Reduction for Radiation Transport Simulations*** details the construction of the training data used, the generation of the ROM from the training, and the results showing that POD can be used to accelerate some MC simulations up to four orders of magnitude. A complete description of the method is detailed in Udagedara (submitted 2014). The second task was to explore nonlinear model reduction techniques that could be implemented within our ROM framework for radiation transport. This led to our adapting a signal processing method, known as "cartoon-texture" decomposition in the image processing literature, to model reduction for fluid flows, which is the first step in adapting it to radiation transport. The ***Nonlinear Model Reduction–Cartoon-Texture Decomposition*** section details this variational approach to computing a ROM and shows the corresponding results for simplifying computational fluid dynamics simulations of flow across an airfoil (Luttman in preparation 2014).

POD-Based Model Reduction for Radiation Transport Simulations

In this section we present the details of POD, the generation of the training data used to demonstrate the approach, and the results for a radiation detection scenario.

General Formulation of POD

The primary goal of model reduction is to construct a basis for the data space such that a sufficient proportion of the variation in the training data is captured in the fewest possible basis functions. In the first application presented here, we wish to reconstruct the normalized photon number distribution, $n(x,e)$, where x is the location of a photon detector in some simulation domain and e is the photon energy. A ROM for the source spectrum is then a collection of basis functions, $\{\phi_1, \phi_2,\ldots, \phi_N\}$, such that

$$n(x,e)_N = \sum_{j=1}^{N} a_j(x)\,\phi_j(e), \tag{1}$$

where $a_j(x)$ are weighting coefficients and N is the number of functions—also called modes—used in the model. In principle, any technique for constructing such a basis can be used, but, in this project, we focused on using the well-known POD (Lumley 1967, Peterson 1983, Rathinam 2003). Given the training data, $n(x,e)_{training}$, the first POD basis function is the solution of the optimization problem

$$\phi_1 = \underset{\tilde{\phi}\in L^2(\Omega)}{\operatorname{argmax}} \left\langle \left(\int_\Omega \tilde{\phi}(e)\, n(x,e)_{training}\, de \right)^2 \right\rangle \tag{2}$$

subject to $\int_\Omega \phi_1(e)^2\, de = 1$ where <·> denotes spatial average and Ω is the range of energies over which the photons are detected. The second POD basis function, ϕ_2, is calculated by solving the corresponding optimization problem over the subspace of $L^2(\Omega)$ orthogonal to the span of ϕ_1, and, similarly, the n^{th} POD basis function is computed as the solution to the corresponding optimization problem on the subspace of $L^2(\Omega)$ orthogonal to span $\{\phi_1, \phi_2,\ldots, \phi_{n-1}\}$. In this way, the spectra from the training data can be represented by the fewest basis functions possible, in the sense of capturing L^2 variation.

The optimization problem in Equation 2 can be recast as the Fredholm eigenvalue problem

$$\int_\Omega R(e,e')\,\phi_1(e')\,de' = \lambda_1\,\phi_1(e), \tag{3}$$

where $R(e,e')$ is the data correlation tensor. In practice this alternate form of the problem is solved for ϕ_1, because of the relationship between eigenvalues to the error in the ROM representation. Denote by E^2 the squared $L^2(\Omega)$ norm of the difference between the data $n(x,e)$ and the N-dimensional POD representation, $n(x,e)_N$,

$$E^2(x) = \int_{\Omega} \left(n(x,e)_N - n(x,e) \right)^2 de. \quad (4)$$

The average value of E^2 over the spatial domain is given by

$$\langle E^2 \rangle = \sum_{i=N+1}^{\infty} \lambda_i, \quad (5)$$

which implies, when the problem is discretized, that the eigenvalues of the data correlation matrix correspond to the accuracy of the POD representation.

Generating Training Data for Constructing a ROM

The first step is to generate training data of a radiation transport scenario in order to demonstrate that such problems are amenable to reduced order modeling. We simulated a 21 × 21 rectangular array of sodium iodide (NaI) photon detectors, as shown in Figure 1 (gray dots). Steel boxes (dark gray) are placed in a quasi-triangular configuration to act as shielding of the radiation source, which is placed on the ground in the center of the domain. The shape of the shielding has no axis of symmetry through the center of the domain to avoid symmetries in the simulated radiation intensities at each detector.

The detectors, which have a radius of 1.5 inches, were placed 1 m above the ground and are spaced on a 1 m grid, so that the spatial domain is 20 × 20 m. A ^{60}Co source, a ^{137}Cs source, and a ^{99}Tc source were each placed individually at the center of the domain, and the radiation from the source was simulated with MCNP using 10^{10} particle histories. A radiation background consisting of potassium (K), uranium (U), and thorium (Th) was also simulated. The simulations of the three sources plus the background result in "data" that are histograms of normalized particle counts at each location in space. Each histogram has 200 energy bins, equally partitioned from 59.7 keV to 2 MeV.

Figure 2 shows $n(x,e)$ integrated over energy for the radiation background and the three radiation sources. The sources are shown in the figures as the peaks of the radiation intensity contours (yellow regions). The peak is brightest for ^{60}Co, which had emission peaks at 1.17 and 1.33 MeV. Following in brightness are ^{137}Cs and ^{99}Tc, which have emission peaks at 661.6 keV and 140.51 keV, respectively. In all four images, the shielding configuration is clear, as the background is shielded as well as the sources.

Using POD for Radiation Transport Model Reduction

The first question that must be addressed is whether radiation transport simulations can provide sufficient data compression to result in useful model reduction. Given the 200 energy bins, we combine the simulated spectra into a 200 × 1764 (21 × 21 detectors for the four sources) data matrix, M. This is referred to as the "coagulated data." Following Equation 5, the most straightforward assessment of the viability of using POD to construct a ROM from the training data

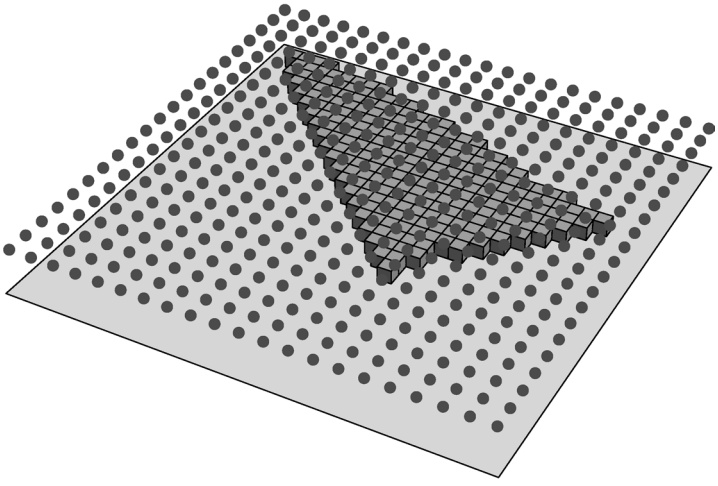

Figure 1. Cartoon schematic of the radiation transport scenario being simulated. The computational domain is a rectangle with NaI detectors (dots) spaced at 1 m grid points. Steel boxes (dark gray) are placed on a portion of the domain as shielding.

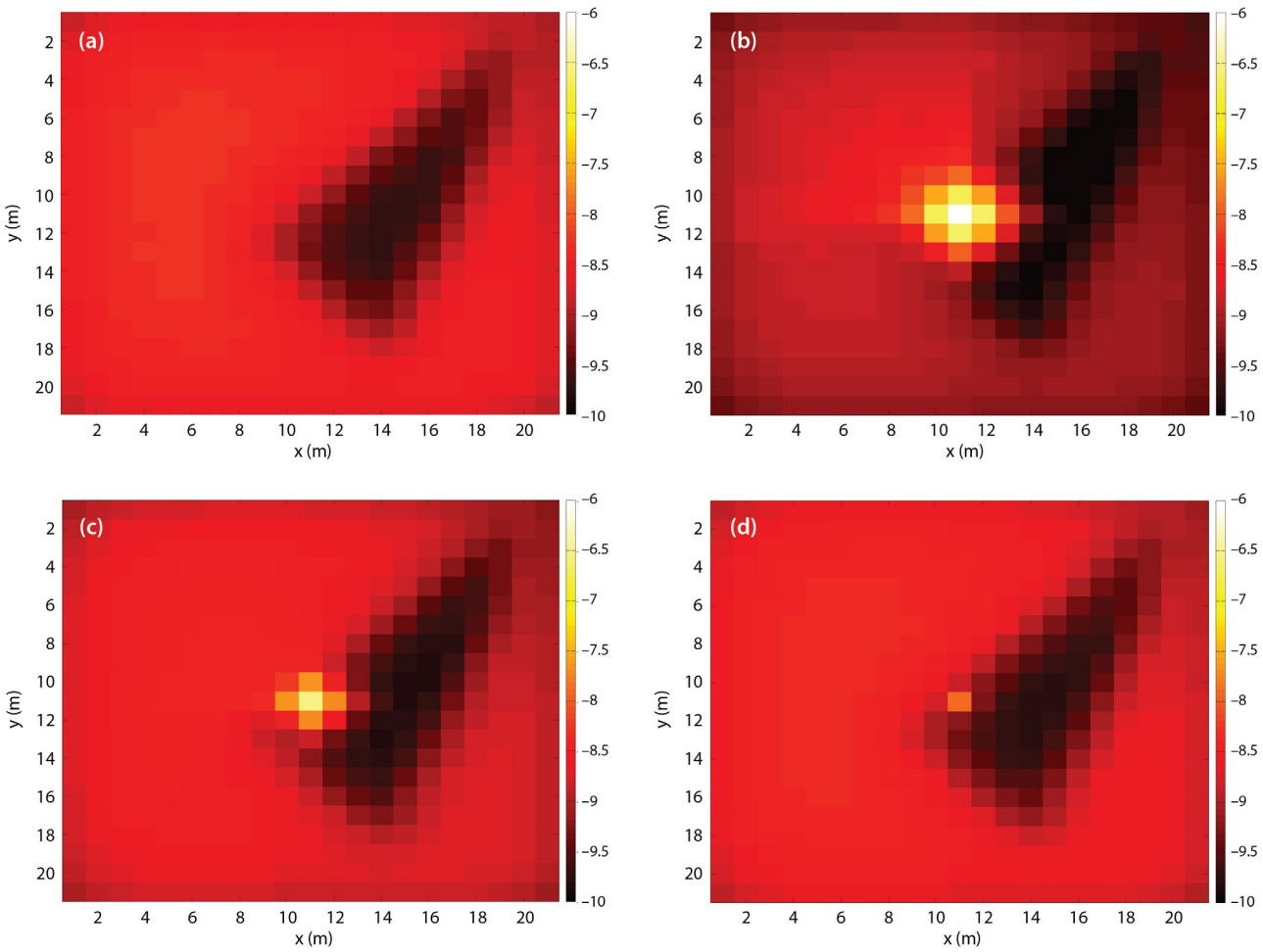

Figure 2. The logarithm of radiation intensity for (a) the KUT background and the (b) ^{60}Co, (c) ^{137}Cs, and (d) ^{99}Tc sources

described above is then to evaluate the decay of the eigenvalue spectrum of the data correlation matrix, $C = MM^T$.

Figure 3a shows the decay of the eigenvalues of C (black line) as well as the decays of the data correlation matrices constructed from each of the three primary radiation sources individually. The eigenvalues of the individual source data correlation matrices decay more than four orders of magnitude over the first four modes, then they decay slowly thereafter. This indicates the first four modes of the individual sources capture the radiation transport behavior, and the remaining modes represent MC noise in the simulations. For the coagulated data, the first six modes are required for four orders of magnitude decay, which shows that there are approximately two more degrees of freedom in the coagulated than in the individual source data. In all cases, however, the eigenvalue spectra decay very quickly, indicating that the POD approach to data compression will likely work well. Figure 3b plots the first four modes of the coagulated data correlation matrix. The third and fourth modes show the characteristic peaks for ^{60}Co, ^{137}Cs, and ^{99}Tc, but the first mode is dominated by features from the radiation background.

There are other factors that impact the quality of a ROM generated from training simulations. For example, the number of particle histories used in the training simulations is an important factor, as too few particle histories in the training data will result in POD

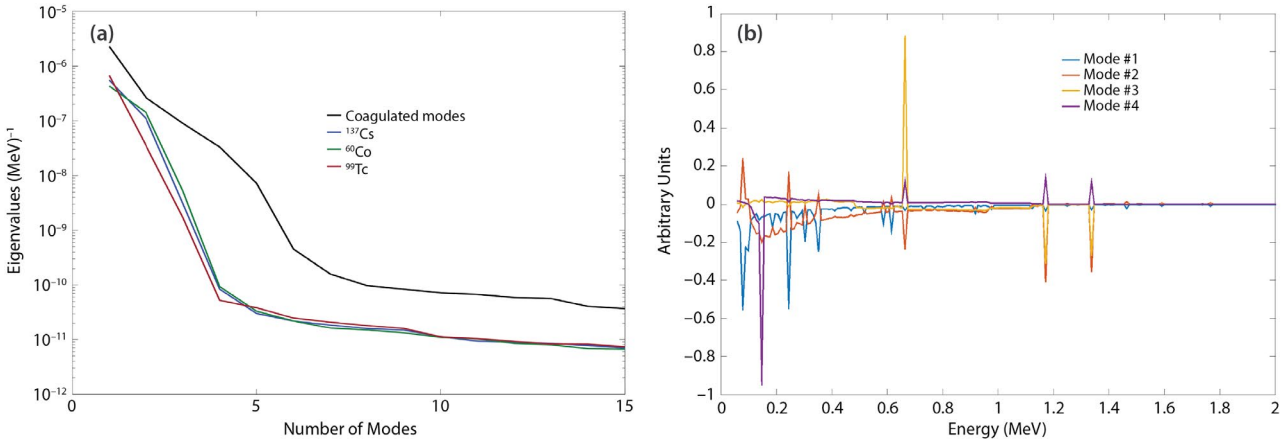

Figure 3. (a) The decay of the correlation matrix eigenvalues for each radiation source individually and the coagulated data. (b) The first four POD modes (basis functions) for the coagulated data.

modes that primarily represent MC noise, rather than the radiation transport dynamics. The geometry of the spatial domain and the shielding configuration are also important factors to consider, and future work will include detailed studies of the impact of radiation shielding. Another factor that can impact ROM quality is the simulated radiation sources. Each of these factors is explored in more detail in Udagedara (submitted 2014).

Monte Carlo Acceleration

The primary goal of reduced order modeling for MC simulations is to accelerate future simulations. In this section we reconstruct the spectrum of a radiation source that is a mixture of ^{60}Co, ^{137}Cs, and ^{99}Tc, using the ROM constructed from the coagulated data. Note that the training data do not contain any mixtures of the "pure" sources, so that the source reconstructed here is not a component of the training data.

Figure 4 shows the radiation spectrum of the mixed source, as simulated at the center of the domain, using 10^6, 10^8, and 10^{10} particle histories. The simulation with 10^{10} particle histories (black line) shows the two emission peaks from cobalt, the peak from cesium, and the peak from technetium. Even with 10^{10} histories, there are very few counts above the Compton edge of cobalt (to the right of the 1.33 MeV peak). The 10^8 simulation (red line) also shows the primary peaks, though the signal is much noisier, and there are essentially no counts at all above the Compton edge. This corresponds to the gaps in the red curve. The 10^6 simulation (green line) contains virtually no information about the radiation source, as nearly all of the energy bins detected no counts and none of the primary emission peaks is discernible. Due to the statistical independence of the particle histories (from each other), the computation time scales directly with the number of particle histories, so the 10^6 simulation is roughly four orders of magnitude faster than the 10^{10} simulation.

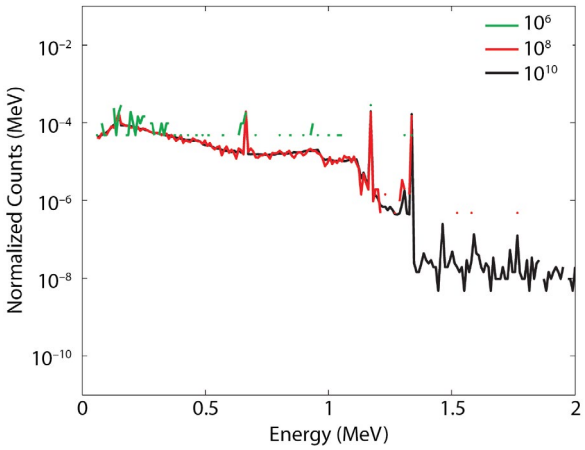

Figure 4. Mixed source radiation spectrum simulated with 10^6, 10^8, and 10^{10} particle histories

Figure 5 shows the projection of the mixed source simulation with 10^6 particle histories onto the first two modes of the ROM constructed from the pure sources, as described in the sections above. Whereas the 10^6 simulation alone (green line in Figure 4) contained essentially no information about the radiation source, the projection of the 10^6 simulation (green line in Figure 5) onto only two POD modes represents the cobalt, cesium, and technetium emission peaks as well as the 10^{10} simulation (black dotted line in Figure 5). The projection and the full-scale simulation deviate from each other significantly only above the higher cobalt emission peak, where even the full-scale simulation suffered from few particle counts. Thus, given the ROM computed offline, the mixed radiation source can be simulated four orders of magnitude faster than is required without the ROM.

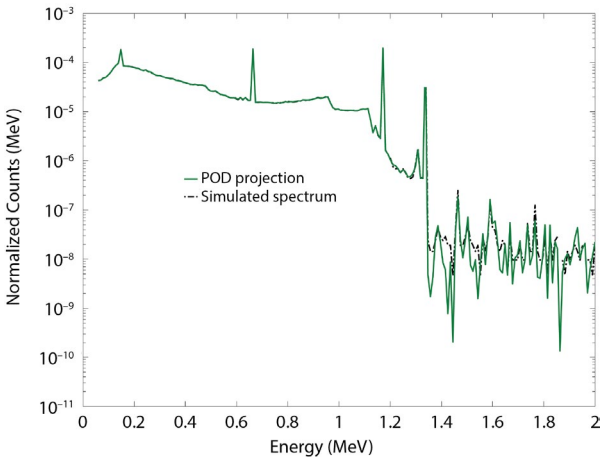

Figure 5. The mixed radiation source spectrum (black, dashed line) simulated with 10^{10} particle histories and the projection of the simulation with 10^6 particle histories onto two POD modes

Nonlinear Model Reduction—Cartoon-Texture Decomposition

While above we used POD for our model reduction, it is also possible to combine POD with nonlinear techniques to reduce the dimensionality of the data space. Nonlinear model reduction methods are virtually non-existent in the radiation transport literature, so we begin with an example of model reduction for fluid flow across an airfoil by adapting a technique from image processing, known as the cartoon-texture decomposition (Vese 2003, 2006).

The data from which the ROM is calculated are simulated using a computational fluid dynamics approach to solving the incompressible Navier-Stokes' equations for the flow across a NACA0015 airfoil with an *hp*-adaptive finite element method (FEM) on the unstructured triangular mesh shown in Figure 6; Helenbrook (2001) includes further details on the simulations. The magnitude of the flow for a single time step is shown in Figure 7, where it can be seen that there are vortices being shed off the airfoil and propagating through the simulation domain.

It is well known that POD fails to capture structures that are temporally but not spatially coherent—like vortices that maintain their shape but travel across the domain—so it is necessary to perform an additional model reduction. In this work we adapt the vector-valued cartoon-texture decomposition (Vese 2003, 2006) from image processing for use with fluid flow data. First, we remap the horizontal and vertical components of the original flow onto a regular rectangular grid at approximately 5 mm resolution. As in Vese (2003), the goal is to decompose the flow field f into two components, $f = a + b$, such that a—the cartoon component—is a function of bounded variation, and b—the texture component—is the divergence of a vector field whose components are elements of a space of oscillatory functions that is, in some sense, the dual of the space of functions of bounded variation. See Vese (2006) for the mathematical formalism of the cartoon-texture decomposition.

Each of a and b are thus vector fields that solve the optimization problem

$$\arg\min_{\vec{a},\vec{b}} \lambda \sum_{k=1}^{2} \int_{\Omega} \left| f_i - a_i - \mathrm{div}\left(g_i\right) \right|^2 d\Omega + \int_{\Omega} \left|\nabla \vec{a}\right| d\Omega + \mu \left[\int_{\Omega} \left(\sqrt{\left|\vec{g}_1\right|^2 + \left|\vec{g}_2\right|^2} \right)^p d\Omega \right]^{1/p}, \quad (6)$$

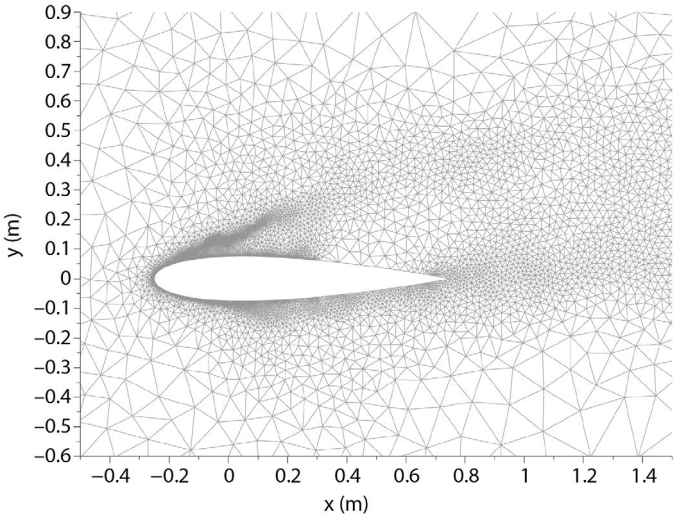

Figure 6. The finite element method mesh used to simulate the flow across a NACA 15 airfoil

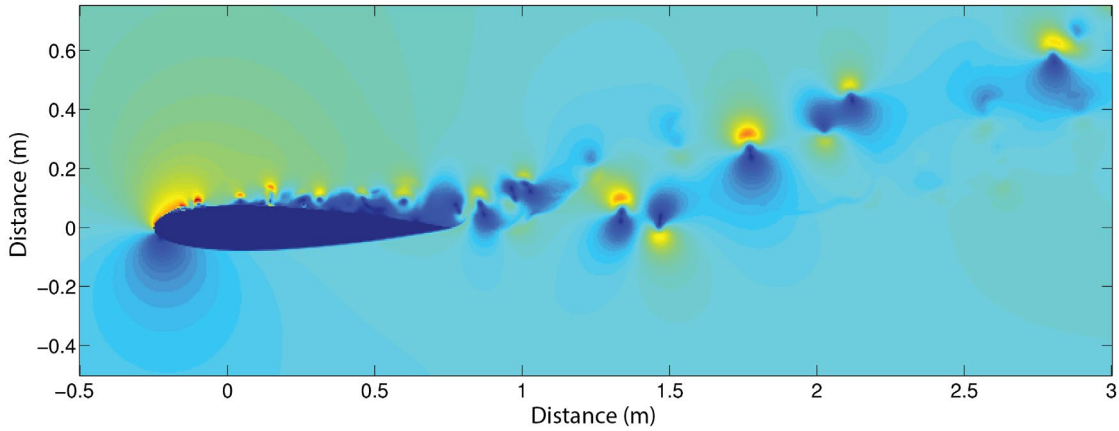

Figure 7. The magnitude of the flow field across the airfoil at a single time instance

where $b_i = div(g_{i1}, g_{i2})$, Ω is the spatial domain, λ and μ are parameters that balance the weighting between the data fidelity and the regularization, and, in practice, $p = 1$. In this context

$$\left|\vec{g}_1\right|^2 = g_{11}^2 + g_{12}^2. \quad (7)$$

Figure 8 shows the cartoon component and the logarithm of the texture component of the flow shown in Figure 7. As can be seen, the cartoon component captures the large-scale structures of the flow but misses the fine-scale details. The texture component retains the fine features of the flow, including the structures of the vortices as they are shed from the airfoil and propagate through the spatial domain.

Decomposing the flow into the cartoon and texture components is not, of itself, model reduction, as it results in twice as much data as the original simulation. As described above, however, POD can be applied to the cartoon and texture components. From this we construct the data matrices A_{Cart} and A_{Text} of size 351902 × 800 (corresponding to the 251 × 701 × 2 spatial grid for the horizontal and vertical components and to the 800 time steps at which the flow is simulated). As with the radiation transport example above, the POD modes are then computed as the left singular vectors of the data correlation matrices of size 800 × 800.

A common application of simulations such as this is to determine the simulation parameters at which

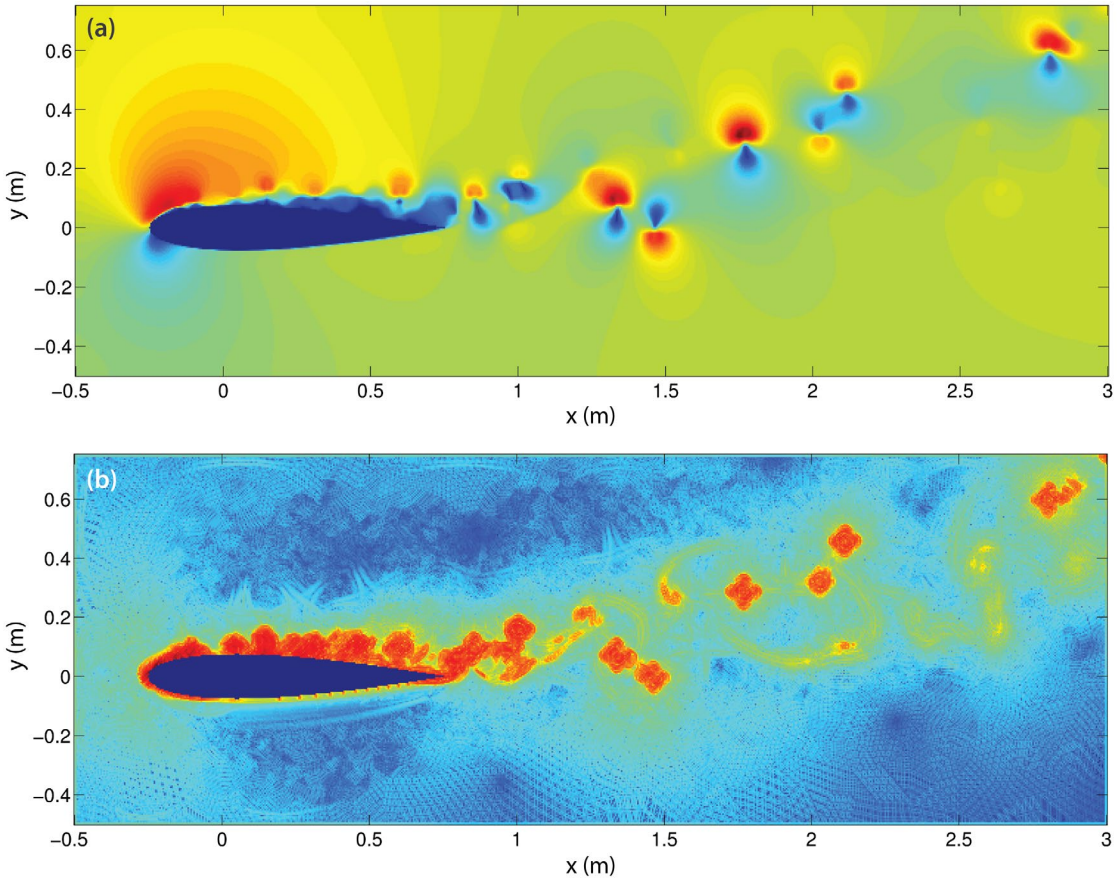

Figure 8. The magnitudes of the (a) cartoon and (b) texture components of the flow. (The texture component is shown in the log scale, and the horizontal and vertical axes are both meters.)

the flow becomes unsteady and separates from the airfoil, shedding vortices. In this case, the texture component captures that information very well (note the magnitude of the flow in the vortices around the airfoil in Figure 8 is significantly higher than elsewhere in the flow). In fact, a five-mode POD reconstruction of the texture component around the wing retains the structure of the flow separation, as can be seen for a single time step in the Figure 9b. The cartoon component—which corresponds to the total-variation regularized (Rudin 1992) smoother version of the flow—fails to retain the fundamental structures of the flow, even though smoothing of this type is the most common form of model reduction. This work shows that it is not the smooth, average flow but rather the "remainder" after subtracting the smoothed flow that is best suited for flow model reduction.

The long-term goal of this work is to further extend the cartoon-texture decomposition for use with radiation transport simulations in the same way that it has been demonstrated here for use with fluid flow simulations.

Conclusion

The primary goal of this work is to develop model reduction techniques for the purpose of accelerating MC methods for radiation transport simulations. In addition to classical variance reduction methods, we have developed a POD approach to constructing application-specific ROMs. Such ROMs, constructed using full-scale MC simulations, can then be used for further fast simulations, and we showed that in a mixed-source radiation detection scenario one could achieve four orders of magnitude acceleration for simulations using the POD-based ROM.

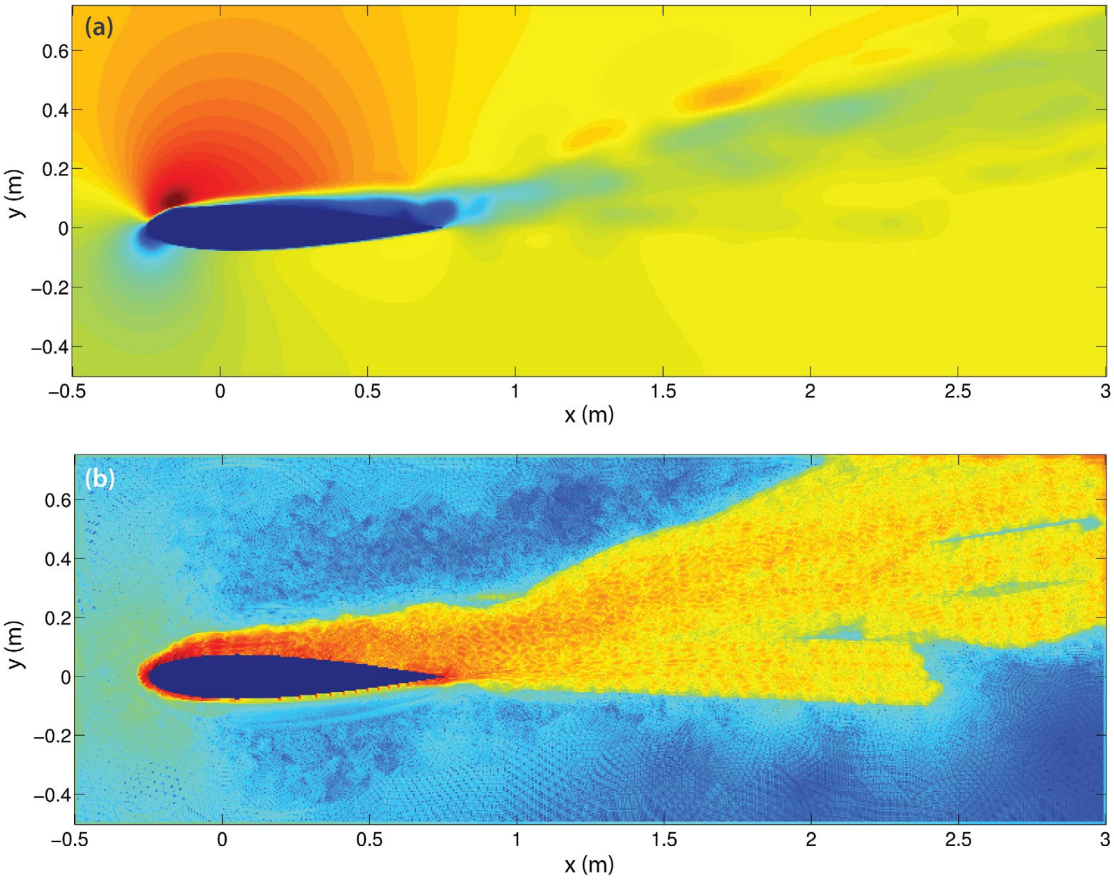

Figure 9. The five-mode POD reconstruction of the (a) cartoon and (b) texture components of the flow

In order to further improve the POD-based approach, in this project we also explored nonlinear model reduction methods and adapted the cartoon-texture decomposition approach developed in the image processing community to capture the important structures of fluid flow. Because the fluids community develops most model reduction methods, this is an important first step before extending the approach to radiation transport.

These two parallel research tracks are the first steps in developing tools that can be used by the radiation transport community for enhanced modeling and simulation, and there is important future work to be done, including formal studies of the impact of geometry and shielding on the construction of a ROM, applications to live radiation detection, Bayesian model selection for choosing which modes best represent the data, and radioactive material identification. We intend to pursue external funding to support these research tracks.

Acknowledgments

The authors would like to thank B. T. Meehan for generating Figure 1 and Larry Zajac for administering the contract with Clarkson University.

References

Amako, K., et al., "GEANT4 and its validation," *Nucl. Phys. B - Proc. Suppl.* **150** (2006) 44–49.

Asai, M., "A roadmap for GEANT4," *J. Phys. Conf. Ser. B* **396** (2012) 052007.

Carter, L. L., E. D. Cashwell, "Particle transport simulation with the Monte Carlo method," TID--26607, Los Alamos Scientific Laboratory, Los Alamos, New Mexico, 1975.

Dupree, S. A., S. K. Fraley, *A Monte Carlo Primer: A Practical Approach to Radiation Transport*, 2nd edition, Kluwer Academic, New York, 2002.

Goorley, J. T., et al., *Initial MCNP6 Release Overview - MCNP6 Version 1.0*, LA-UR-13-22934, Los Alamos National Laboratory, Los Alamos, New Mexico, 2013.

Helenbrook, B. T., "A two-fluid spectral element method," *Comp. Meth. Appl. Mech. Eng.* **191**, 3–5 (2001) 273–294.

Kalos, M. H., P. A. Whitlock, *Monte Carlo Methods. Volume I: Basics*, John Wiley-Interscience, New York, 1986.

Lumley, J. L., "The structure of inhomogeneous turbulent flows," in *Atmospheric Turbulence and Radio Wave Propagation*, A. M. Yaglom, V. I. Tatarski, eds., 1967, 166–178.

Luttman, A., B. Helenbrook, E. M. Bollt, "A cartoon-texture decomposition for air flow model reduction," in preparation, 2014.

Olson, G. L, L. H. Auer, M. L. Hall, "Diffusion, P_1, and other approximate forms of radiation transport," *J. Quant. Spectros. Radiat. Transfer* **64**, 6 (2000) 619–634.

Peterson, J. S., *High Reynolds number solutions for incompressible viscous flow using reduced basis technique*, Tech. Rep. TCMA-83-49, Institute for Computational Mathematics and Applications, University of Pittsburgh, 1983.

Rathinam, M., L. R. Petzold, "A new look at proper orthogonal decomposition," *SIAM J. Numer. Anal.* **41**, 5 (2003) 1893–1925.

Robert, C. P., G. Casella, *Monte Carlo Statistical Methods*, 2nd edition, Springer, New York, 2004.

Rudin, L. I., S. Osher, E. Fatemi, "Nonlinear total variation based noise removal algorithms," *Physica D: Nonlinear Phenomena* **60**, 1–4 (1992) 259–268.

Saidi, P., M. Sadeghi, C. Tenreiro, "Variance Reduction of Monte Carlo Simulation in Nuclear Engineering Field," in *Theory and Applications of Monte Carlo Simulations*, W. K. (V.) Chan, ed., 2013, InTech, http://www.intechopen.com/books/theory-and-applications-of-monte-carlo-simulations/variance-reduction-of-monte-carlo-simulation-in-nuclear-engineering-field, accessed December 17, 2014.

Udagedara, I., B. Helenbrook, A. Luttman, S. E. Mitchell, "Reduced order modeling for accelerated Monte Carlo simulations in radiation transport," *Applied Mathematics and Computation*, submitted October 2014.

Vese, L., S. Osher, "Modeling textures with total variation minimization and oscillating patterns in image processing," *J. Sci. Comput.* **19**, 1–3 (2003) 553–572, http://www.math.ucla.edu/~lvese/PAPERS/JSC_VeseOsher.pdf, accessed December 17, 2014.

Vese, L., S. Osher, "Color texture modeling and color image decomposition in a variational-PDE approach," in *Proceedings of the Eighth International Symposium on Symbolic and Numeric Algorithms for Scientific Computing* (2006) 103–110.

Predictive Radiological Background Distributions from Geologic Data

RSLN-23-14 | Continued in FY 2015 | Year 1 of 2

Russell Malchow,[1,a] Pamela Burnley,[b] Elisabeth Hausrath,[b] Kara Marsac,[b] Daniel Haber,[b] and Christopher Adcock[b]

Aerial radiological surveys have a decades-long history of use in prospecting, consequence management, and search applications. Recent experience during the Fukushima nuclear power plant accident exposed the need for better knowledge of the normal radiological landscape before a radioactive release occurs, and modern search algorithms are increasingly making use of a priori data to estimate anticipated background radiation distributions. This project is using available information in the form of existing geochemical data, geologic maps, remote sensing data, and sparse radiological data to create high-resolution maps of estimated background radiation levels. In FY 2014, we developed a successful method for creating high spatial resolution background predictions by extrapolating low spatial resolution background radiation data using radiological background units that we defined based on geologic information. In FY 2015 we will continue to investigate the best method to construct a background model using potassium, uranium, and thorium contents of bedrock and soils measured by standard geochemical techniques, combined with chemical weathering and photon transport models.

[1] malchorl@nv.doe.gov, 702-295-8770
[a] Remote Sensing Laboratory–Nellis; [b] University of Nevada, Las Vegas

Background

Our goal is to devise a method to use existing geologic data to predict gamma ray background levels as measured during aerial radiological surveys. Foreknowledge of the background will be valuable for a variety of homeland security and disaster response purposes. Important components of the gamma ray background come from the rocks and soil within the first 40 cm of Earth's surface and should therefore be predictable based on an understanding of the geochemistry of the surface rocks. We use geologic maps, remote sensing imagery, the National Uranium Resource Evaluation (NURE) national airborne gamma ray spectrometry survey (Duval 2005) database, and bedrock and soil geochemical data from existing databases and the scientific literature combined with reactive transport modeling to create surface geochemical models. Monte Carlo N-Particle (MCNP6, version 1.0) code is used to predict the background exposure rates. By comparing predicted with observed background values, we are refining our modeling strategies to produce a protocol that can be used by others.

During an actual consequence management mission, knowledge of pre-contamination background may be limited. The ability to estimate pre-release backgrounds will improve data products that are produced for customers. Benefits for radiological search include providing a location-specific map of natural radiation anomalies to help rule out false positives in direct radiation measurements and delineating spatial variability of radiation to help select optimized search techniques and parameters (Kock 2014).

Project

The correlation between spatial variations in geology and changing radiation backgrounds measured during aerial surveys has long been recognized (International Atomic Energy Agency 1991) but never exploited to a great degree. The correlation has been hard to quantify because geologic maps alone do not provide enough information about the geochemistry of mapped bedrock units or surface materials. Although rock types delineated on geologic maps have chemical similarities, specific detailed geochemical information is not given. In addition, aerial measurements are most sensitive to radioisotopes residing at or very near the surface, but geologic maps elucidate the bedrock exposed at the surface, not loose materials (regolith) on top of the bedrock. Furthermore, many regions are not mapped with a high enough spatial resolution to match the requirements of an aerial radiological survey produced for consequence management or search missions. A variety of remote sensing imagery types with comparable and even higher spatial resolutions and techniques exist that use a variety of spectral bands to map rock types. However, a unique correlation between spectral bands and rock geochemistry is not made, for example, for potassium (K), uranium (U) and thorium (Th), which account for the vast majority of the terrestrial component of natural background radiation. In light of this, we proposed that it should be possible to combine remote sensing imagery with bedrock geologic maps and publicly available geochemical data to build a surface geochemistry model for predicting background in areas that have not been previously characterized and to help interpret aerial background measurements when they are made.

Over the last 75 years, a significant fraction of the bedrock units exposed in the U.S., as well as soils resting on them, have been chemically analyzed for major and trace element content. Extensive research on the relationship between soil chemistry and parent bedrock chemistry as a function of climate (Egli 2003, Riebe 2004, Thompson 2007, Rasmussen 2010) has been undertaken. These chemical data are available (Max Plank Institute of Chemistry [MPIC] 2014) in the scientific literature and increasingly in online geochemical databases. Thus, the specific geochemistry of bedrock exposed in a target area and soil chemistry (especially from the NURE program) can often be obtained through a literature search. In cases where no specific chemical data are available, constraints can be placed on the bedrock geochemistry by using regional or global averages for the given lithology (rock type).

The radioisotope content of the loose and weathered materials at the surface that give rise to aerial spectra is not identical to that of the bedrock because exposure to water and gasses in the atmosphere alters the chemistry. In cases where chemical analyses of regolith are not available, the chemistry can be modeled. Specifically, we are using CrunchFlow (Steefel 2009), a reactive transport modeling code that utilizes fully kinetic mineral dissolution and precipitation reactions that incorporate erosion, burial, and adsorption kinetics of uranium series isotopes.

Data from multispectral remote sensing systems such as NASA's Earth Observing System and U.S. Geological Survey (USGS) Landsat spacecraft can be applied to constrain or otherwise inform modeling efforts. The data from these and similar instruments provide information about mineralogy, lithology, alluvial source area, water content, clay content, or other aspects of the terrestrial surface that can influence naturally occurring gamma radiation. For example, Landsat 8 band combinations of 7-5-3 RGB (equivalent to Landsat 7, 7-4-2 RGB) are routinely used to investigate soil moisture content variations and clay abundance, as well as other variations in geologic materials (Abdelsalam 2000, Peña 2006, Sabins 2007). The Advanced Spaceborne Thermal Emission and Reflection Radiometer (ASTER) package on Earth Observing System Terra is also commonly used in geologic remote sensing applications and has more discrete sensors in the shortwave infrared, improving the possibility of remotely investigating specific lithologies (Galvão 2005, Rowan 2005, Mars 2006, Janati 2014). With the availability of the USGS Digital Spectral

Library 06 (and similar databases) that contain laboratory-based IR spectra for hundreds of minerals, band combinations or ratios specific to a set of relevant mineralogical characteristics can potentially be developed (Rowan 2005), making multiband remote sensing data a powerful tool to aid in modeling efforts.

Results

Test areas for this project were chosen from previous U.S. Department of Energy Aerial Measuring System (AMS) surveys, which were made available to us. These areas are Cameron, Arizona; Government Wash, Nevada; and the AMS calibration line along the shore of Lake Mohave, Nevada (Figure 1). We obtained legacy data that had been collected using an array of thallium-activated sodium iodide (NaI:Tl) detectors mounted on a helicopter. Aircraft position was recorded using differential GPS. The data were analyzed by AMS to produce exposure rates at 1 m (3.3 ft) above ground level. Contributions from cosmic rays and atmospheric radon were removed from the data.

Cameron, Arizona

AMS conducted a radiological survey of the Cameron area in 1997 as part of the Abandoned Uranium Mines Project conducted by the U.S. Army Corps of Engineers and the U.S. Environmental Protection Agency (Hendricks 2001). Exposure rates in this area range from about 2.4 to 67 µR/h, with the majority of the area below 12 µR/h. We were able to obtain geographic information system (GIS) shape files from the most recent state geologic maps (Billingsley 2007), which reasonably captured spatial variation of rock types as seen in the satellite imagery available in Google Earth. We obtained over 1000 geolocated geochemical analyses relevant to the area from national databases (USGS 2008, MPIC 2014) and private industry (Turner 2011). We evaluated the metadata attached to each analysis as well as the geochemical data (USGS 2008, Turner 2011, MPIC 2014) itself for consistency with the mapped rocks types at the reported location (Billingsley 2007). After this culling process, 536 analyses remained. These analyses were grouped according to the bedrock geologic unit that they occurred in (or on) and by whether they were soil or bedrock analyses. The area contains 9 bedrock, 22 alluvial, and 31 paired soil units. The number of geochemical analyses per unit ranged from 0 to 184. Perhaps because of the geologic processes that created ore-quality concentrations of U, the U content drives the observed exposure rate (Figure 2).

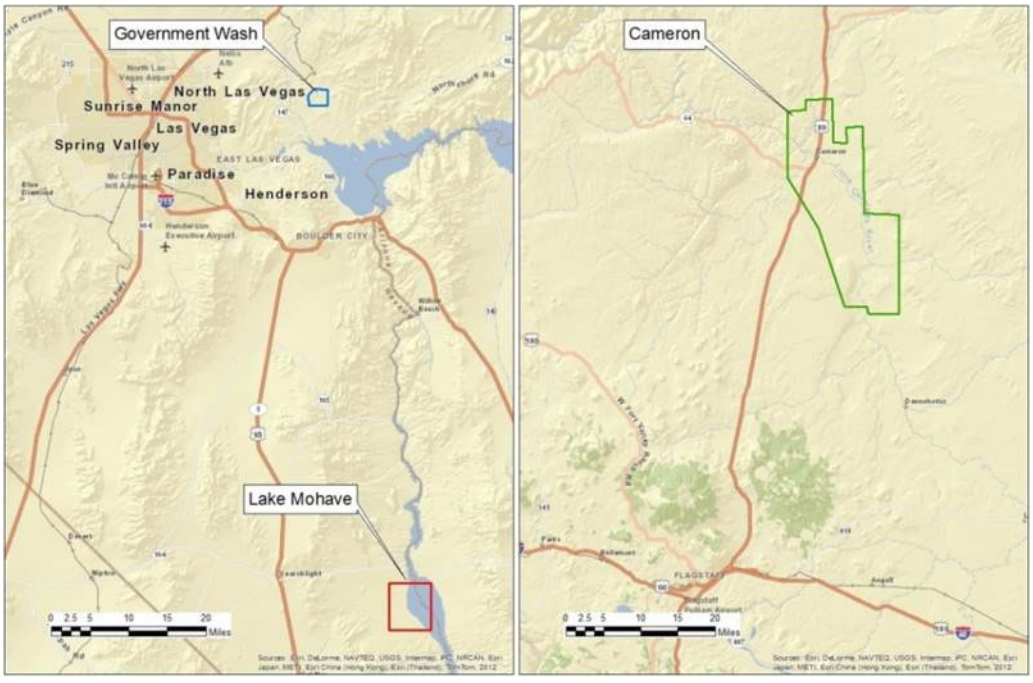

Figure 1. Locations of test areas: Government Wash and Lake Mohave, Nevada, and Cameron, Arizona

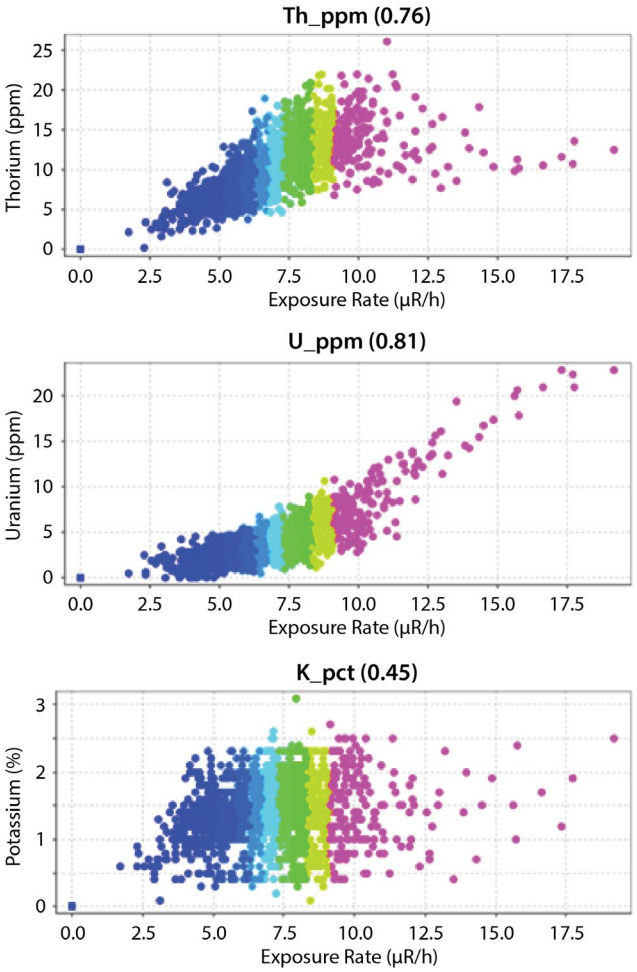

Figure 2. Exposure rates in µR/h for NURE data over the Cameron test area plotted vs. Th, U, and K concentrations

For some units the distribution of U content in bedrock and soil units contained extremely high outliers. Therefore, for bedrock units with multiple analyses, the median values of K, U, and Th were used to calculate an exposure rate for the unit. For soil units the mean values were used. Exposure rates for each geologic unit were calculated using the relationship from Grasty (1984). In order to compare the predicted exposure rates with the measured exposure rates for each geologic unit, we used the GIS shape files to capture the AMS data provided as geolocated exposure rate values. The mean exposure rate for each unit was calculated and chosen to represent that unit. The predicted exposure rate yielded generally good spatial correlation for highs and lows (Figure 3); however, differences between predicted and observed exposure rates exceeded the levels required for the strategy to be useful; in some cases the rates were outside the range where we anticipate corrections derived from CrunchFlow and MCNP analysis to account for the lack of correlation.

Lithologic and geochemical variations within units have related, but not identical, issues. Lithologic variations arise when a given map unit contains several different lithologies; for example, the Harrisburg Member of the Kaibab Formation contains gypsum, siltstone, sandstone, and limestone (Billingsley 2007). The K, U, and Th content of each lithology may be very different, but they are mapped as a single unit. Another significant source of lithologic variations within geologic units is found in Quaternary alluvial units; this is discussed in more detail below. Even within a given rock type within a single unit, there may be variations in the K, U, and Th content. Although we expect these geochemical variations to be much smaller than those caused by variations in lithology, they are expected to exist and may be somewhat more difficult to predict by the tools available to us.

The Radiological Background Unit (RBU)

To manage lithologic variations we developed the concept of a radiological background unit (RBU): an RBU is a definable geographical area chosen to exhibit the smallest possible variation in exposure rate. Initially we assigned an RBU status to geologic formations as defined on a geologic map, as discussed above. However, an RBU could be defined using remote sensing band math, drainage basins, or some combination of both. We considered an RBU to be valid in relation to the standard deviation of the exposure rates of AMS data captured by the RBU. For example, by looking at the distribution of radiation over the Cameron area, we determined that an RBU for that region that has no correlation with the distribution of background radiation will have a standard deviation of 2.4 µR/h.

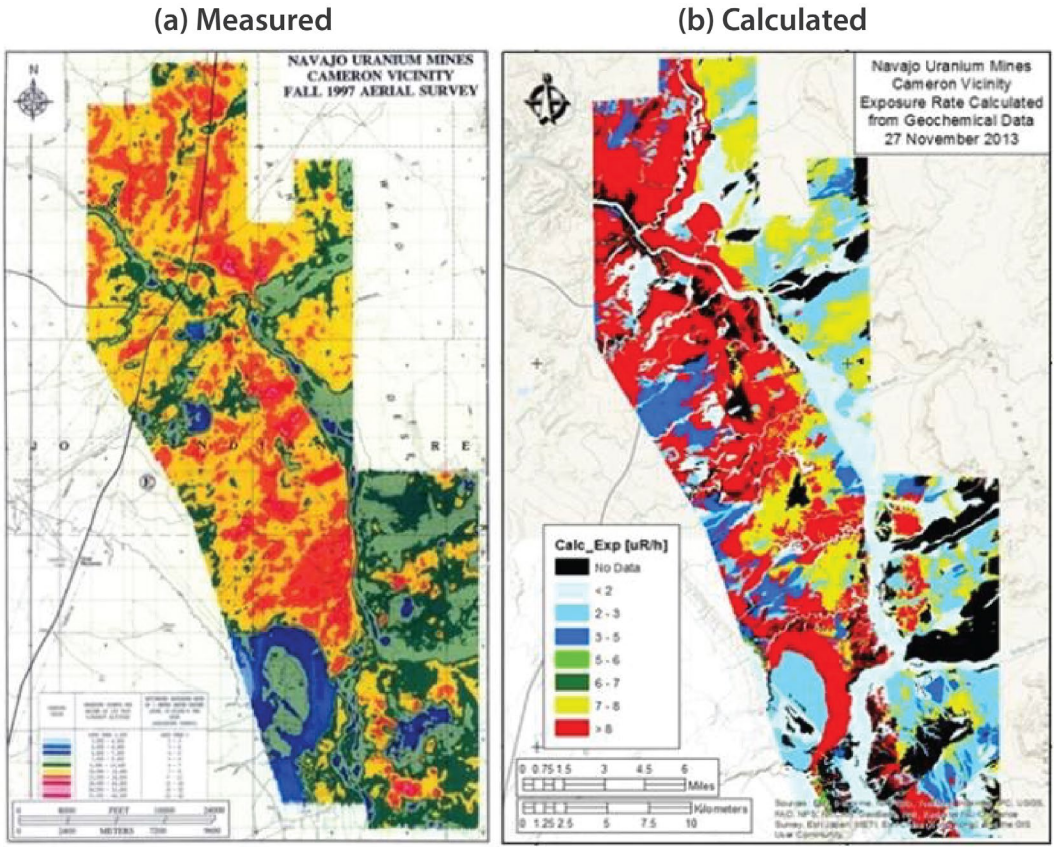

Figure 3. (a) AMS measured exposure rates for the Cameron area and (b) predicted exposure rates; differences between predicted and observed exposure rates exceeded the levels required for the strategy to be useful

Lithologic Variations

Lithologic variations are most pronounced for Quaternary (<3 Ma) alluvial units. Alluvial units are classified and mapped by geologists based on their age of deposition. However, their mineralogy and chemistry are more closely related to their upstream source rock than to alluvial units of similar ages in different watersheds. This can be observed in the field and is also clearly seen in multispectral images based on bands that are sensitive to the mineralogy of surficial materials (Sabins 2007). In the Cameron area we used a map of tributaries of the Little Colorado River calculated in ArcMap, digital elevation models, and topographic maps to draw drainage basins. Figure 4 shows the outlines of 19 drainage basins (light blue) that intersect the test area. The alluvial units within each drainage basin were then grouped together to form a single RBU.

The AMS exposure rate data were then resampled using RBUs. To avoid uncertainty due to geolocation issues, we filtered AMS data that fell within 50 m of each RBU boundary. The standard deviations of the AMS data captured by these RBUs is on average 1.3 µR/h, as opposed to 1.5 µR/h for alluvial units as defined on the geologic map. We see this as a promising approach especially for small drainage basins containing a limited number of bedrock lithologies, as well as a component of remote sensing strategies for defining RBUs that we are developing.

Lithologic variations within sedimentary bedrock units can be detected using multispectral imaging. In this case, a single geologic map unit would be broken down into a number of RBUs based on classification of remote sensing band math images. The band math can be chosen to maximize the anticipated differences in lithologies within a unit. Although lithological

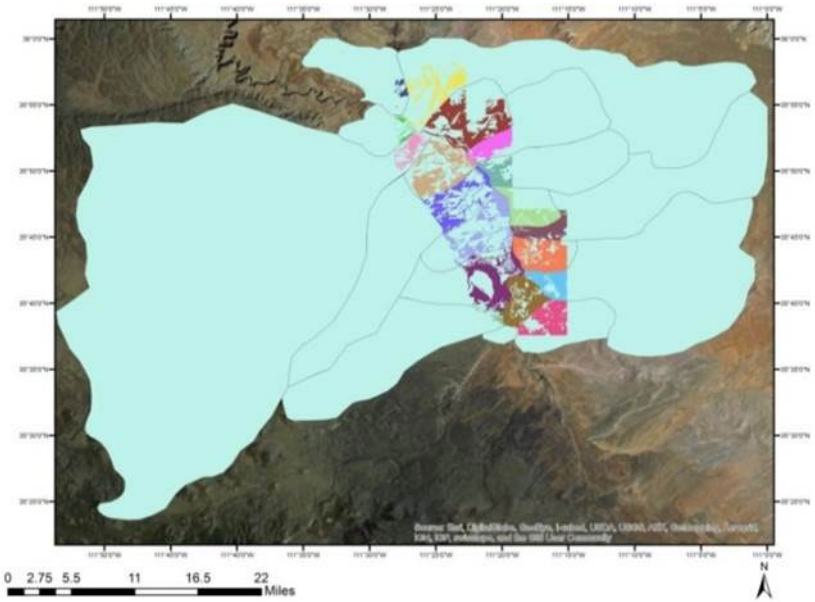

Figure 4. Drainage basins in and around the Cameron test area (light blue). Alluvial units in distinct basins within the test area are shown in various shades.

differences within sedimentary units are sometimes not mapped, the geologic unit description will give a list of the lithologies observed within the unit. Thus, the band math can be tuned to select the expected lithologies.

Applying the Grasty Equation to Geochemical Analyses

Grasty (1984) proposed a relationship between K-U-Th concentrations and exposure rate based on work by others. In Duval (2005) this takes the form

$$D = 1.32K + 0.548eU + 0.272eTh. \quad \textbf{(1)}$$

With the concentrations of K in percent potassium and of eU and eTh in ppm of equivalent uranium and equivalent thorium, respectively, D will be in µR/h. Here, "equivalent" means that U and Th are assumed to be in equilibrium with their progeny. Aerial measurements of radiation from U are significantly lower than lab measurements [in the case of Grasty (1984), about 40%] because radon escapes from the ground. In the desert where the radon trapping effect of soil moisture is exceptionally low, this effect will be exacerbated. The issue of radon escape was of minimal concern to Grasty (1984) because in the Canadian Shield (a region of ancient rocks at the core of the North American continent) U only accounted for ~10% of the exposure rate. In the Cameron area U contents are driving exposure rates (Figure 2); thus, Equation 1 may not be completely appropriate. In addition, geochemical databases have values of K, U, and Th measured by x-ray fluorescence (XRF) or inductively coupled plasma mass spectrometry. At the moment, we do not fully understand how closely the two different analytical techniques (gamma ray spectrometry vs. geochemical) reproduce each other or if there are systematic biases.

In the second year of this project, we will compare chemical analyses, lab-based gamma ray spectroscopy, and ground-based measurements made with an NaI:Tl detector for soil samples collected from the Cameron area. We have characterized the mineralogy of these soils using polarized light microscopy and will conduct x-ray diffraction and XRF measurements to further constrain the mineralogy and determine the K, U, and Th content. These data will allow us to check the efficacy of using Equation 1 in a desert environment. Another issue with Equation 1 is that it assumes that all rocks have the same screening factor and soil moisture level. To evaluate the level of uncertainty generated by these assumptions, we have begun making models of exposure rates using MCNP6 codes. We have successfully modeled single soil layers

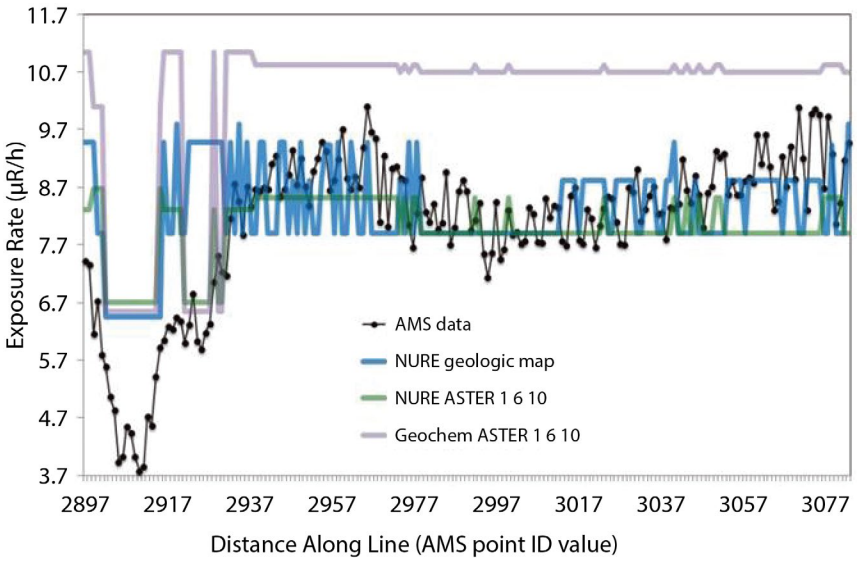

Figure 5. Exposure rates (measured and predicted) for the Lake Mohave calibration line. Available geochemical data, distributed according to ASTER imagery (grey line) overpredicts exposure rates measured by AMS (black dots and line). Using NURE KUT values, distributed according to geologic units (blue line) or ASTER imagery (green line), produces a closer prediction of measured exposure rates.

and validated our models using data collected over concrete calibration pads at Walker Field in Grand Junction, Colorado (USGS 2008).

Extrapolating NURE Data

Another route to generating high-resolution predictive background radiation maps is to devise a means for extrapolating low spatial resolution NURE national airborne gamma ray spectrometry survey data. The dataset gives K and equivalent U and Th values. If appropriate RBUs can be defined, then we can use the existing NURE measurements made over each RBU to extrapolate to the entire aerial extent of the RBU. We calculated exposure rates using Equation 1 for NURE data measured in the Cameron area and used ArcGIS to capture the NURE data into the RBUs. For the alluvial RBUs based on drainage basins discussed above, we found that the mean of the AMS data was within one standard deviation of the mean of the NURE data and in most cases differed by less than 1 µR/hr.

Government Wash and Lake Mohave Calibration Line

Government Wash lies just east of Las Vegas, Nevada. The wash area is used for AMS training flights. The Lake Mohave calibration line lies on the western shore of Lake Mohave, which is located on the Nevada-Arizona state line south of Lake Mead. The calibration line is also regularly flown by AMS. In these areas we have followed the same strategy that we took with Cameron. Geochemical data for bedrock and soil was acquired from databases (USGS 2008), culled for internal consistency, and associated with geologic units. For Government Wash, the GIS shape file with the geologic boundaries (Duebendorfer 2003) was corrected such that it better followed lithologic boundaries as observed on satellite images from Google Earth. As with the Cameron area, we found that the geochemical data significantly overpredicted the background radiation as observed in the survey data. RBUs used to date are based on bedrock geologic units in Government Wash. The alluvial unit in the wash is sourced from several smaller basins upstream, which produces variations in the radiological background measured by AMS that clearly correlate with variations in multispectral imagery. We are in the process of finding the right band math combinations to define RBUs within this large alluvial unit.

The Lake Mohave calibration line crosses only alluvial units. As with the other study areas, the geochemical data overpredict the background as measured by AMS (Figure 5). NURE measurements combined with RBUs based on mapped alluvium (House 2008) compared similarly with RBUs built from ASTER remote sensing images (using a 1-6-10 band combination for classification) to AMS data. A joint AMS and University of

Nevada, Las Vegas (UNLV) field campaign in January 2014 collected soil samples and ground level radiation data with a high-purity germanium detector and pressurized ionization chamber. In the case of Lake Mohave, the calibration line was flown on the same day as the field work, ensuring that soil moisture conditions were the same for all data. The soil samples have been sent to an independent laboratory (TestAmerica Laboratories, Inc., 13715 Rider Trail North, Earth City, Missouri 63045) for counting. We have used polarized light microscopy to characterize the mineralogy of the soils. In the second year of the project, we will chemically analyze the soil with XRF after the gamma ray spectroscopy is completed.

Conclusion

In the first year of our project, we have determined that applying geochemical (Riebe 2004, Thompson 2007, Rasmussen 2010) data from the literature to predict background radiation using Equation 1, while qualitatively similar, does not constrain backgrounds quantitatively at the desired levels. We are in the process of further investigating the best method for using K, U, and Th contents measured by standard geochemical techniques for background prediction. We have, however, demonstrated a successful method for extrapolating low-resolution NURE background radiation survey data using RBUs based on a combination of geologic maps, drainage basins, and remote sensing. We will continue to refine this strategy as well as our work based on geochemical data.

Acknowledgments

We gratefully acknowledge the assistance of Ralf Sudowe of UNLV, Jez Stampahar of the Remote Sensing Laboratory–Nellis, and the U.S. Department of Energy's Aerial Measuring System for the use of their data. We would also like to acknowledge technical support by the UNLV High Pressure Science and Engineering Center (funded through the National Nuclear Security Administration/Stewardship Science Academic Alliances program under DOE Cooperative Agreement #DE-NA0001982). Lastly, we are grateful to the U.S. Department of the Interior National Park Service and the Lake Mead National Recreation Area for their cooperation under permit LAKE-2014-SCI-0002.

References

Abdelsalam, M. G., R. J. Stern, W. G. Berhane, "Mapping gossans in arid regions with Landsat TM and SIR-C images: The Beddaho Alteration Zone in northern Eritrea," *Journal of African Earth Sciences* **30**, 4 (2000) 903–916.

Billingsley, G. H., S. S. Priest, T. J. Felger, Geologic Map of the Cameron 30' x 60' Quadrangle, Coconino County, Northern Arizona, U.S. Geological Survey Scientific Investigations Map 2977, scale 1:100,000, 2007, http://pubs.usgs.gov/sim/2007/2977/, accessed October 7, 2014.

Duebendorfer, E. M., Geologic Map of the Government Wash Quadrangle, Clark County, Nevada, Map 140, Nevada Bureau of Mines and Geology, Reno, Nevada, 2003, http://www.nbmg.unr.edu/freedownloads/m/m140.zip, accessed October 7, 2014.

Duval, J. S., J. M. Carson, P. B. Holman, A. G. Darnley, "Terrestrial radioactivity and gamma-ray exposure in the United States and Canada," U.S. Geological Survey Open-File Report 2005-1413, 2005, http://pubs.usgs.gov/of/2005/1413/, accessed September 19, 2014.

Egli, M., A. Mirabella, G. Sartori, P. Fitze, "Weathering rates as a function of climate: Results from a climosequence of the Val Genova (Trentino, Italian Alps)," *Geoderma* **111**, 1–2 (2003) 99–121.

Galvão, L. S., R. Almeida-Filho, Í. Vitorello, "Spectral discrimination of hydrothermally altered materials using ASTER short-wave infrared bands: Evaluation in a tropical savannah environment," *International Journal of Applied Earth Observation and Geoinformation* **7**, 2 (2005) 107–114.

Grasty, R. L., J. M. Carson, B. W. Charbonneau, P. B. Holman, *Natural Background Radiation in Canada*, Geological Survey of Canada Bulletin 360, Ottawa, Canada, 1984.

Hendricks, T. J. *An Aerial Radiological Survey of Abandoned Uranium Mines in the Navajo Nation*, DOE/NV/11718--602, Bechtel Nevada, Las Vegas, Nevada, 2001, http://www.nv.doe.gov/library/publications/Environmental/DOENV11718_602.pdf, accessed October 7, 2014.

House, P. K., J. E. Faulds. Preliminary Geologic Map of the Spirit Mtn. NW Quadrangle, Clark County, Nevada and Mohave County, Arizona, Nevada Bureau of Mines and Geology, Reno, Nevada, 2009, http://www.nbmg.unr.edu/freedownloads/of/of2009-06.zip, accessed October 7, 2014.

International Atomic Energy Agency, *Airborne Gamma Ray Spectrometer Surveying, Technical Reports Series 323*, International Atomic Energy Agency, Vienna, Austria, 1991.

Janati, M. El, A. Soulaimani, H. Admou, N. Youbi, A. Hafid, K. P. Hefferan, "Application of ASTER remote sensing data to geological mapping of basement domains in arid regions: A case study from the Central Anti-Atlas, Iguerda inlier, Morocco," *Arabian Journal of Geosciences* **7** (2014) 2407–2422.

Kock, P., C. Rääf, C. Samuelsson, "On background radiation gradients—the use of airborne surveys when searching for orphan sources using mobile gamma-ray spectrometry," *J. Environ. Radioact.* **128** (2014) 84–90.

Mars, J. C., L. C. Rowan. "Regional mapping of phyllic- and argillic-altered rocks in the Zagros magmatic arc, Iran, using Advanced Spaceborne Thermal Emission and Reflection Radiometer (ASTER) data and logical operator algorithms," *Geosphere* **2**, 3 (2006) 161–186.

Max Planck Institute for Chemistry (MPIC), Georoc, Geochemistry of Rocks of the Oceans and Continents, May 2014, http://georoc.mpch-mainz.gwdg.de/georoc/, accessed October 7, 2014.

Peña, S. A., M. G. Abdelsalam, "Orbital remote sensing for geological mapping in southern Tunisia: Implication for oil and gas exploration," *Journal of African Earth Sciences* **44**, 2 (2006) 203–219.

Rasmussen, C., R. A. Dahlgren, R. J. Southard, "Basalt weathering and pedogenesis across an environmental gradient in the southern Cascade Range, California, USA," *Geoderma* **154**, 3–4 (2010) 473–485.

Riebe, C. S., J. W. Kirchner, R. C. Finkel, "Erosional and climatic effects on long-term chemical weathering rates in granitic landscapes spanning diverse climate regimes," *Earth and Planetary Science Letters* **224** (2004) 547–562.

Rowan, L. C., J. C. Mars, C. J. Simpson, "Lithologic mapping of the Mordor, NT, Australia ultramafic complex by using the Advanced Spaceborne Thermal Emission and Reflection Radiometer (ASTER)," *Remote Sensing of Environment* **99**, 1–2 (2005) 105–126.

Sabins, F. F., *Remote Sensing: Principles and Interpretation*, 3rd edition, Waveland Press, Long Grove, Illinois, 2007, 361–380.

Steefel, C. I., *CrunchFlow, Software for Modeling Multicomponent Reactive Flow and Transport, User's Manual*, Lawrence Berkeley National Laboratory, Livermore, California, 2009, http://www.csteefel.com/CrunchFlowManual.pdf, accessed October 7, 2014.

Thompson, A., J. Ruiz, O. A. Chadwick, M. Titus, J. Chorover, "Rayleigh fractionation of iron isotopes during pedogenesis along a climate sequence of Hawaiian basalt," *Chemical Geology* **238**, 1–2 (2007) 72–83.

Turner, L. D., DIR Exploration, Inc., Palisade, Colorado, 2011, http://www.dirxploration.com, accessed October 7, 2014.

U.S. Geological Survey (USGS), Geochemisty of Rock Samples from the National Geochemical Database, U.S. Geological Survey, Reston, Virginia, 2008, http://mrdata.usgs.gov/metadata/ngdbrock.html, accessed October 7, 2014.

This page left blank intentionally

Optimizing DPF Neutron Output Using Particle-In-Cell and MHD Models

NLV-18-14 | Continued in FY 2015 | Year 1 of 2

Tim Meehan[1,a] and Michael Berninger[b]

This project sought to optimize the neutron output from a dense plasma focus by using a magneto-hydrodynamic (MHD) simulation program to speed up the time evolution of a particle-in-cell (PIC) code. While PIC codes are best able to represent the physics present in the plasma, they require a high cost in computing resources, taking long times to run. MHD codes are much faster but are unable to represent many of the physically interesting phenomena in the plasma. This research seeks to leverage the best of both codes. Collaboration with Imperial College London allowed us access to their MHD hybrid code, GORGON. An investigation of existing methods was performed, and the results were compared. In FY 2015 this project will continue as "Modeling Technique Applicable to High Plasma Densities and Long Time Scales" (SO-03-15).

[1] meehanbt@nv.doe.gov, 702-295-0490
[a] North Las Vegas; [b] Los Alamos Operations

Background

Simulating the neutron yield from dense plasma focus (DPF) machines has proven to be challenging since their discovery. Presently, two types of simulation codes are used: particle-in-cell (PIC) codes, such as LSP (Welch 2009), and magneto-hydrodynamic (MHD) codes, such as ALEGRA (Robinson 2008, ALEGRA 2014). The benefit of the PIC code is that it is best able to represent the physics present in the plasma. The drawback is that its high cost in terms of computing resources makes it prohibitively expensive. MHD codes are much faster but are unable to represent many of the physically interesting phenomena in the plasma. The purpose of this project is to leverage the strengths of each type of code to provide an accurate, timely answer to the neutron yield estimate for a DPF in order to design a neutron-yield-optimized DPF.

Previous efforts to simulate DPF pinch physics (Welch 2010, Schmidt 2012) focused on 2-D PIC simulations, and even then the simulations took hundreds to thousands of CPU hours. This work leverages MHD code to provide an accurate initial condition for the PIC code at the point in the plasma development when it begins to become non-MHD. Our collaborators have employed two methods of addressing this issue. The group at Imperial College London uses a hybrid approach, based on an MHD code, GORGON, which they developed. The group at Lawrence Livermore National Laboratory (LLNL) uses the HYDRA MHD code to initialize the PIC simulation. Of the two methods, the hybrid approach is by far the faster method. If it can be shown that the hybrid simulation method gives results that are "close enough" to experimental data in some sense, this would be the best method of optimizing the electrodes for maximizing neutron dose.

Project

Start Condition

Recent framing camera images of the plasma shock starting on the DPF show that the plasma shock does not move as would be expected from an MHD simulation. Previous to this, MHD models had assumed that the plasma started as a conductive skin on the insulator; however, the framing camera images indicate that something rather different was happening when the plasma forms in the breach of the DPF. Other "conventional wisdom" gleaned from observing MHD models led researchers to assume that the shape of the field enhancements in the breach of the DPF did not dramatically affect the plasma shock formation. This assumption turned out to be wrong, although it was well known that MHD physics did not accurately describe the breakdown of the working gas (deuterium in our case). An example simulation of the formation of a plasma shock in a DPF is shown in Figure 1. Based on large-scale plasma (LSP) PIC simulations done by Nichelle Bennett of NSTec, the shape of the electrodes near the breach of the DPF has a large effect on the distribution of ions in the breach. This phenomenon was also simulated in GORGON; the GORGON results were reasonably similar to those obtained using ALEGRA, also an MHD code (shown later in Figure 5).

File Conversion

The process of transforming the output of one program into a state suitable for use in another program is a mundane but vital task. When the data have to be moved into or out of unstructured finite element meshes, the software doing the conversion becomes necessarily more complex. This phase of the

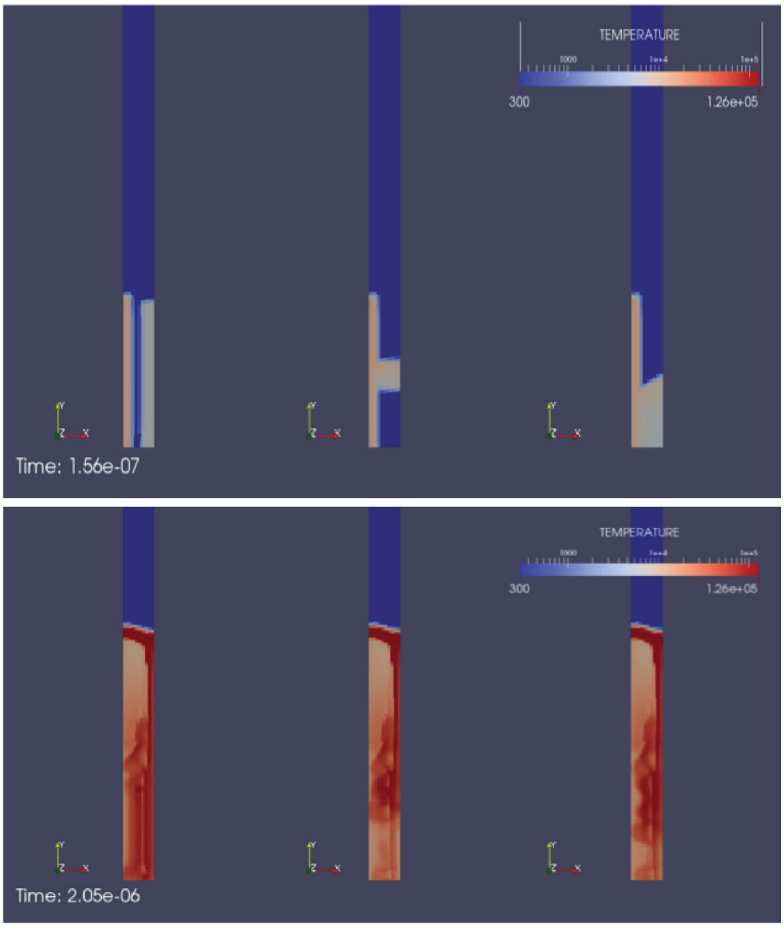

Figure 1. Three initial conditions for the plasma in the DPF as modeled with ALEGRA are compared. There are no significant changes in the timing of the shock front, but there are some differences in the hot plasma left behind the shock.

project went through a number of iterations as more was learned about the requirements for both ALEGRA and LSP.

ALEGRA to LSP

Originally, for the conversion from ALEGRA to LSP, we were restricted to a subset of the possible ALEGRA simulation meshes, namely, the internal mesh format. This meant that the mesh had to be a brick, a generic cylinder section, or a generic sphere section. For many geometries, this results in wasted space in the simulation mesh, which in turn results in longer run times.

All DPF simulation meshes have wasted space where the current does not flow, such as the interior of the copper anode. (An example is shown later in Figure 4; note the hole in the center where the unused copper in the anode would be.) Additionally, if the output was to be exported to an LSP input deck format, the portion that was selected for export either had to be an axis-aligned 2-D slice, or the entire simulation had to be done in a brick-shaped mesh. There are good reasons for not doing the simulation in a brick-shaped mesh, the most obvious of which is the wasted space issue. The most general solution to the problem of exporting input decks to LSP would require us to handle the conversion of scalar and vector, cell-based and node-based quantities, in an unstructured hexahedral mesh to an axis-aligned structured mesh input deck format in LSP.

The primary output of ALEGRA is the Exodus II format (Schoof 1992). There is a C-library for manipulating these files at a low level, but we needed a much higher level of abstraction in order to convert the files to an LSP-readable format. The process of finding a means of manipulating the Exodus II files was simplified when we realized that the recommended post-processing utility, ParaView (Kitware, Inc. 2012), was written using an open-source toolkit, namely, the Visualization Toolkit (VTK) (Schroeder 2006, Kitware, Inc. 2010). The VTK has the ability to read Exodus II files, and made the process of mapping the ALEGRA output to LSP input relatively painless. The VTK is extremely powerful and flexible, and has the capability to interpolate between time steps, as well as an intuitive and extensible pipeline data manipulation paradigm. Because this project also aims to determine where the MHD models begin to fail and how to diagnose or mediate the problems, we will continue to make use of the VTK for data analysis due to its ability to represent mathematical operations on data in a natural manner.

The ALEGRA-to-LSP conversion utility was demonstrated to be automatic and robust. We were able to supply LLNL with input data from ALEGRA early on by carefully processing the data by hand, but now we have a rapid and fully configurable means of supplying LSP input decks in 2-D or 3-D. We believe that the unstructured grid projection algorithm, vtkShepardMethod, is superior to the earlier ad-hoc manual method. Figure 2 is an example of this algorithm in action.

LSP to ALEGRA

The process of converting LSP to an ALEGRA-acceptable format is not well studied. Ordinarily, the simulation in ALEGRA was started with no magnetic field, and with the bulk of the gas at room temperature, and at a pressure of about 3 Torr. The plasma shock is started by artificially initializing a region of gas in the immediate vicinity of the DPF anode insulator to be extremely hot—and therefore conductive. ALEGRA would then pass the current from the externally connected circuit through the conductive gas and start the simulation. Within a handful of nanoseconds of simulation time, the shock would stabilize and the artificially high temperature of the initial condition would reach the expected temperature of the plasma shock.

Ideally, LSP would export a file format that could be easily imported into ALEGRA, and a simulation would start from LSP-provided initial conditions. LSP does indeed write an Exodus II–formatted output; however, the internal structure is very different from that suited to ALEGRA. This was to be expected, as Exodus II is really a geometry database format. When this project continues in FY 2015 (SDRD project SO-03-15, Modeling Technique Applicable to High Plasma Densities and

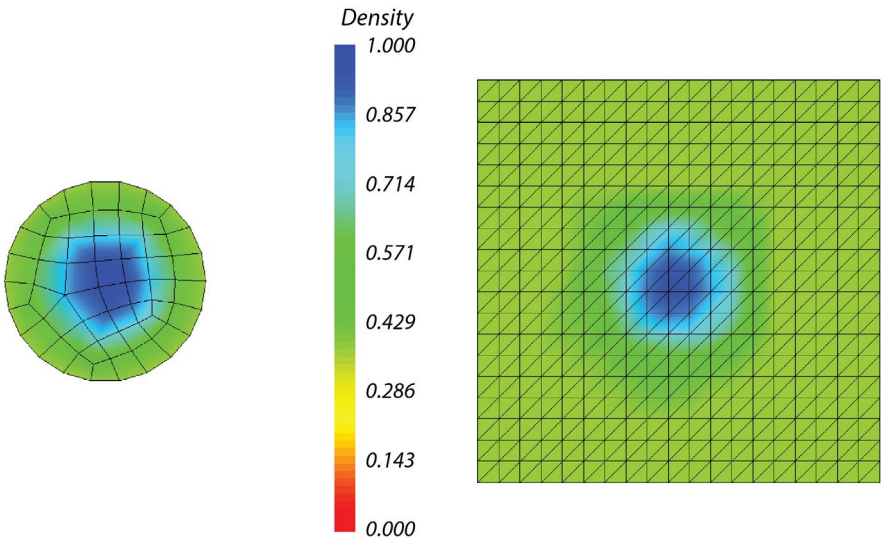

Figure 2. (left) An example of an unstructured quadrilateral mesh, such as would be used by ALEGRA, is shown with (right) a representation of how the data in the unstructured mesh would be mapped onto a structured grid that LSP would take as an input

Long Time Scales), we will again be required to perform extensive post-processing of the LSP output for it to be importable as an initial condition for ALEGRA, using a process similar (but requiring more "hands-on" effort) to that used to export ALEGRA to LSP. The variables to be mapped onto the initial mesh will be density, temperature, and magnetic flux density ($\vec{B}$).

LLNL Results

Using the ALEGRA output we provided, LLNL ran several PIC simulations on their own designs to the z-pinch phase, and they were able to compare the neutron yields for various designs (Figure 3). LLNL identified a design that showed large increases in neutron yield and demonstrated that LSP is capable of giving good estimates of the neutron yield. LLNL is presently investigating ways of improving the speed of the simulations in a high-performance computing environment. Presently, 2-D runs can take months to complete, making optimization an expensive and time-consuming process.

Sandia National Laboratories (SNL) Findings

The mesh-generation software CUBIT (2014) and the modeling software ALEGRA are both SNL products. NSTec and SNL staff engaged in a significant effort to tune both the DPF mesh and the DPF ALEGRA model for this project; the effort is described below.

CUBIT DPF Model

The DPF geometry has evolved into specialized electrodes designed to both maximize neutron yield as well as maximize experimental access to the neutron flux at the top of the anode. The geometry typically exists in CAD drawings in the company drawing database. In order to provide maximum fidelity to the machine, we desired to use the CAD drawings themselves as input geometry for the meshes that were going to be generated for ALEGRA. For this purpose, we used CUBIT, which was able to read in and manipulate the CAD drawings and export quadrilateral and hexahedral meshes in the Genesis format (right-most image in Figure 4). Early in this project, we generated acceptable-quality meshes for ALEGRA as well as simplified geometry files to supply to Imperial College for use in their GORGON code (middle image in Figure 4).

ALEGRA Input Deck Improvements

Because the plasma in the MHD simulation is a rapidly moving shock wave, there were some necessary options that were left out of the original input deck that caused instability during initial runs. These were addressed by adding tensor artificial viscosity and De Bar advection. These options are interrelated, and impose an artificial viscosity on the mesh that serves to reduce instabilities in shocked physics models.

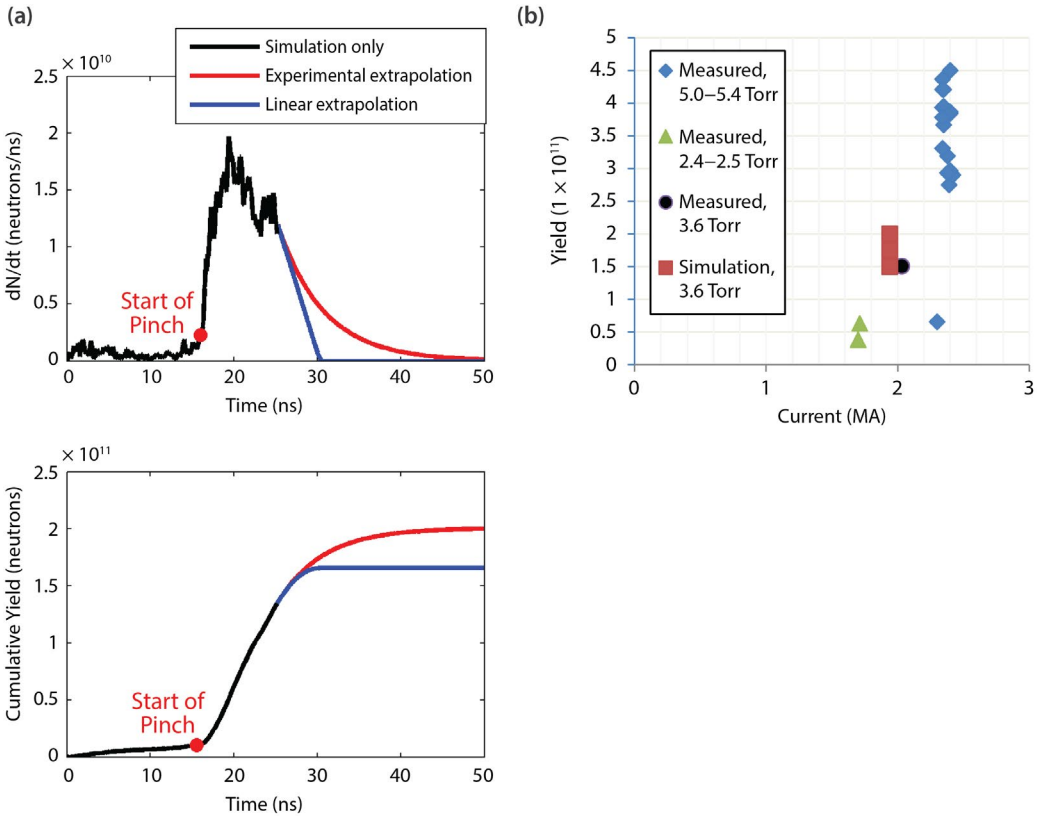

Figure 3. (a) The estimated neutron yield for an LLNL LSP simulation of the DPF initialized by output from ALEGRA is shown with (b) a comparison between the yield of the DPF measured experimentally and that simulated by LSP

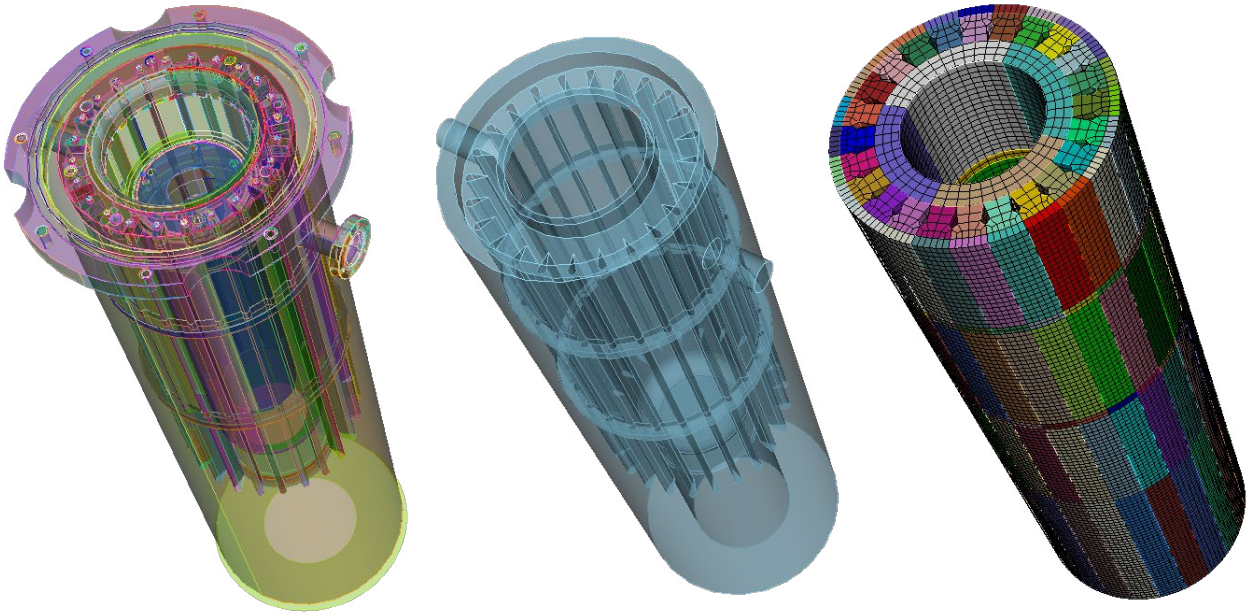

Figure 4. This figure illustrates the meshing process. The image on the far left is the actual CAD drawing. The middle image is a simplified representation of the geometry, ready for meshing. The image on the far right is the finished 3-D hexahedral mesh.

Neutron production is handled by the *tnburn* and *two temperature* cards. These cards are only available in the ALEGRA-HEDP version of the code. The *two temperature* option is added to the physics description part of the input deck, and *tnburn* is added as a material model. Special equation-of-state (EOS) tables are required to get these to work, and these tables are not ordinarily distributed with ALEGRA, nor is the HEDP version of the code distributed outside of SNL, which means that all of these models must be run on SNL computing resources.

A significant amount of time was spent tracking down instabilities in the model that were believed to be related to boundary conditions. ALEGRA has options for handling arbitrary planar boundary conditions for a given side set in an input mesh, but curved surfaces were not specifically handled other than hemispheres and tori. A work-around was proposed and implemented by putting a metallic backing on curved surfaces so that the exterior of the metallic backing could be over constrained and not cause numerical problems in the various solvers in ALEGRA. A future release of ALEGRA may fix this issue.

Imperial College Results

The Imperial College hybrid MHD program, GORGON, has long been used to model z-pinch plasma physics. The hybrid approach allows a user to estimate yield by running a small-scale PIC simulation in coordination with the MHD physics being simulated in GORGON. As fast run times and numerous runs are implicit in any optimization scheme, GORGON's results are certainly useful. GORGON was also used to model asymmetries in the plasma shock formation (Figure 5a) in order to determine if it were possible for an asymmetric shock to be generated. Asymmetric shocks modeled in GORGON could explain why some DPF shots do not z-pinch.

The Imperial College results showed how the knife-edge bars interfere with the formation of the sheath, though we do not know if they altered their design based on this information. Of interest here is that the model showed results—they predicted the yield of the DPF (albeit underestimating it).

Conclusion

The simulation of plasmas and the estimation of neutron and photon yields is an extremely complicated effort. All serious attempts at predicting experimental results require the most powerful computers, advanced graphics and parallel-processing routines, and multi-disciplinary physics models. It is rare to find expertise in all of these fields within any single organization. Presently, we have had some success

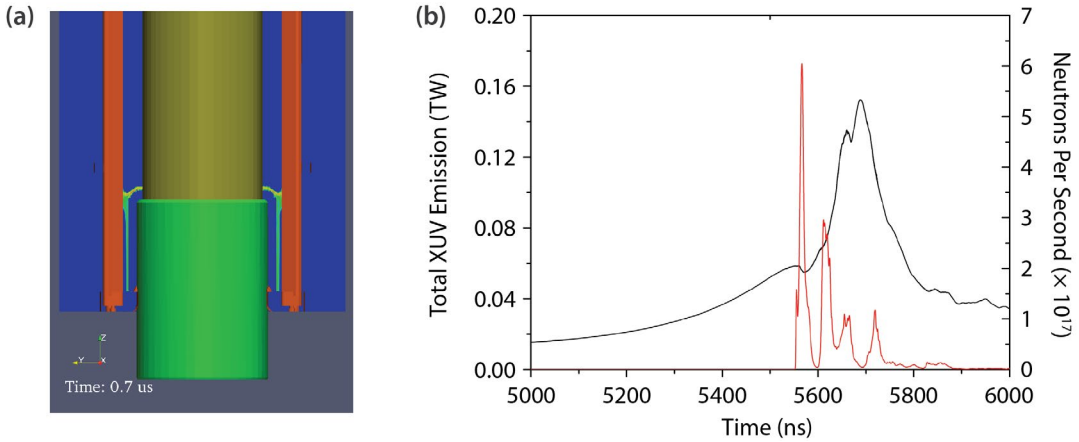

Figure 5. (a) A density slice through a GORGON simulation, courtesy of Imperial College. Notable in this simulation is the asymmetric attachment of the plasma sheath to the cathode bars. (b) The neutron (red curve) and UV emissions (black curve) from the simulation.

using ALEGRA as a source of initial conditions for LSP as evidenced by the LLNL work, as well as some internal results.

Based on interactions with other researchers interested in plasma physics, we may be able to provide some novel insight on the physics of the formation of the plasma shock, as well as being able to come up with diagnostics for the MHD simulations that indicate when the simulation may be running into the limits of what it is capable of simulating. The results of this present collaboration between NSTec, LLNL, and SNL were recently published in *Physics of Plasmas* (Schmidt 2014). This would allow for simulations to be run in MHD mode for as long as is practical. The 3-D simulations of plasmas in LSP will likely be enormously expensive in computing resources, which means that we have to be careful to ensure that any 3-D simulations we start will provide us with information that will be of value comparable to the time and money put into them.

Acknowledgments

We would like to thank Chris Hagen and Daniel Lowe from the NSTec DPF Group for supplying data and images. We also benefited from the insight and expertise of Chris Kuney and the ALEGRA developers from SNL, Nichelle Bennett from NSTec's Sandia Operations, and Andrea Schmidt and Tony Link from LLNL. We would also like to thank the members of the CUBIT and VTK mailing lists for helping us get numerous bugs and conceptual errors fixed.

References

ALEGRA, The Shock and Multiphysics Family of Codes, Sandia National Laboratories, http://www.cs.sandia.gov/ALEGRA/Alegra_Home.html, 2014, accessed February 9, 2015.

CUBIT, Sandia National Laboratories, https://cubit.sandia.gov/, 2014, accessed February 9, 2015.

Kitware, Inc., *The ParaView Guide eBook*, Kitware, Inc., http://kitware.stores.yahoo.net/paraviewebook.html, 2012, accessed December 15, 2014.

Kitware, Inc., *The VTK User's Guide*, 11th edition, Kitware, Inc., 2010.

Robinson, A. C., et al., "ALEGRA: An arbitrary Lagrangian-Eulerian multimaterial, multiphysics code," *Proc. 46th AIAA Aero. Sci. Meeting*, Reno, Nevada, January 7–10, 2008, AIAA20018-1235, http://www.cs.sandia.gov/ALEGRA/Publications/ALEGRA_Overview_AIAA2008.pdf, accessed December 15, 2014.

Schmidt, A., V. Tang, D. Welch, "Fully kinetic simulations of dense plasma focus z-pinch devices," *Phys. Rev. Lett.* **109** (2012) 205003.

Schmidt, A., A. Link, D. Welch, T. Meehan, V. Tang, C. Halvorsen, M. May, E. C. Hagen, "Fully kinetic simulations of megajoule-scale dense plasma focus," *Phys. Plasmas* **21** (2014) 102703.

Schoof, L. A., V. R. Yarberry, "EXODUS II: A finite element data model," Sandia National Laboratories, SAND92-2137, 1992, http://prod.sandia.gov/techlib/access-control.cgi/1992/922137.pdf, accessed December 15, 2014.

Schroeder, W., K. Martin, B. Lorensen, *The Visualization Toolkit: An Object-Oriented Approach to 3D Graphics*, 4th edition, Kitware, Inc., 2006.

Welch, D. R., D. V. Rose, R. E. Clark, C. B. Mostrom, W. A. Stygar, R. J. Leeper, "Fully kinetic particle-in-cell simulations of a deuterium gas puff z pinch," *Phys. Rev. Lett.* **103** (2009) 255002.

Welch, D. R., D. V. Rose, C. Thoma, R. E. Clark, C. B. Mostrom, W. A. Stygar, R. J. Leeper, "Kinetic simulation of thermonuclear-neutron production by a 10^7-A deuterium z pinch," *Phys. Plasmas* **17** (2010) 072702.

This page left blank intentionally

Maximum Likelihood Estimation and Uncertainty Quantification for Signals with Poisson-Gaussian Mixed Noise

LO-03-13 | Continued from FY 2013 | Year 2 of 2

Michał Odyniec,[1,a] Aaron Luttman,[b] and Marylesa Howard[b]

The goals of this project were to develop new algorithms, refine the existing ones for analyzing signals with Poisson-Gaussian mixed noise, and apply them to relevant NNSA projects. During the first year, the project focused on the development of theory and on cultivating NNSA-relevant applications, including x-ray radiography, radiance measurements, and more aspects of neutron time of flight (NToF), including its application to the dense plasma focus project. During the second year, we continued algorithm development and, at the same time, pursued the new applications. Most notable were the applications in edge localization, x-ray radiance reconstruction and uncertainty quantification, generalization of NToF results, and nonhomogeneous Poisson applied to radiance analysis.

[1] odyniem@nv.doe.gov, 925-960-2630
[a] Livermore Operations; [b] North Las Vegas

Background

Signal reconstruction from contaminated measurements is relevant to many NNSA applications such as neutron time of flight (NToF) (for Lawrence Livermore National Laboratory [LLNL] and Sandia National Laboratories), radiance (for Special Technologies Laboratory), and radiography (for LLNL, NNSA, and Los Alamos National Laboratory). The processes that we are modeling and analyzing are particle measurements captured by electrical systems, which means that the signals are contaminated by two sources: (1) a Poisson stochastic process of particle counting and (2) the Gaussian instrumentation noise.

Thus, the problem is modeled as

$$z = H \cdot Poiss(x(u)) + N(0,\sigma^2), \quad \textbf{(1)}$$

where z denotes the measured data, and H is a linear (convolution) operator modeling the measurement system. The term $x(u)$ is the mean of the Poisson process that models the "true" signal $x(u)$ with unknown parameters u.

Our aim was to design numerical techniques to recover these parameters within a statistical framework that accounts for the compound Poisson-Gaussian nature of the noise.

We also considered an important special case, where the parameter dependence is linear:

$$z = Poiss(Au) + N(0,\sigma^2). \quad \textbf{(2)}$$

Within NSTec there are many projects that require this kind of signal reconstruction. Our work provided the first Poisson maximum likelihood estimation signal reconstruction algorithms for NSTec applications, and we believe they are the first to provide systematic uncertainty quantification (UQ) through the reconstruction process.

Project

We developed computational and statistical methods tailored to the Poisson-Gaussian mixed-noise environment to improve signature, signal, and image

reconstructions from mixed-noise data. We also mathematically modeled the propagation of uncertainty through the mixed-noise reconstruction process.

Specifically, we developed the following:

a. Poisson-based method for deconvolution with sampling and edge enhancements, which focused on a new technique for boundary artifacts in inverse problems (Bardsley 2009, 2014a, 2014b)

b. Poisson-based Markov chain Monte Carlo (MCMC) sampling and uncertainty quantification, with non-negativity constraints, applied to x-ray radiography (Fowler 2014; Howard 2014, 2015; Joyce 2014)

c. True Poisson-based sampling method using a Metropolis-Hastings MCMC algorithm for uncertainty quantification (Bardsley 2014c)

d. Explicit results for NToF measurements that provide an insight into measurement setup (Odyniec 2013, 2014a, 2014c)

e. Nonhomogeneous Poisson and Compound Poisson processes applied to radiance analysis (Odyniec 2014b)

Boundary Artifacts in MCMC-Based Deconvolution

Many numerical methods for deconvolution problems are designed to take advantage of the computational efficiency of spectral methods, but classical approaches to spectral techniques require particular assumptions to be applied uniformly across all boundaries of the signal. These boundary conditions (traditionally periodic, Dirichlet, Neumann, or related) are essentially methods for generating data values outside the domain of the signal, but they often lack physical motivation and can result in artifacts in the reconstruction near the boundary. In this project, we developed a new approach to dealing with the boundary artifacts that allows the data itself to locally drive how the boundaries are treated, focusing on the deconvolution of images. The deterministic convolution model is

$$z(s) = Au(s) := \int_{\tilde{\Omega}} a(s-t)u(t)dt, \tag{3}$$

where a is the imaging point spread function (PSF) or measurement system impulse response function, $s \in \Omega$ (the 2-D image domain, commonly referred to as the field of view [FOV]), and $t \in \tilde{\Omega}$. In this setting, $\Omega \subset \tilde{\Omega}$ (i.e., the domain of integration is an extension of the FOV). Because the domain of integration is larger than the FOV, Equation 3 corresponds to a problem of reconstructing a signal u that is larger than the measured data z (i.e., the problem is underdetermined).

The discrete, matrix-vector model for Equation 3 is $\boldsymbol{z} = \boldsymbol{Au}$ (using bold to denote discrete entities), given in Equation 4 (below), with empty spaces indicating a value of 0. Note that the PSF is of discrete size $2k + 1$ and is assumed to be known and symmetric, and the measured data is of size m. The reconstructed signal, $\boldsymbol{u}$, is then of size $m + 2k$. As was noted above, the lack of measured data is usually overcome by making blanket assumptions about the values of $\boldsymbol{u}$ outside of the FOV. For example, a zero boundary condition would imply that $u_j = 0$ for $j < 1$ and $j > m$, which would result in an $m \times m$ system to be solved.

$$\begin{bmatrix} z_1 \\ z_2 \\ \vdots \\ z_m \end{bmatrix} = \begin{bmatrix} a_k & \cdots & a_0 & \cdots & a_{-k} & & & & \\ & a_k & \cdots & a_0 & \cdots & a_{-k} & & & \\ & & \ddots & \ddots & \ddots & \ddots & \ddots & & \\ & & & a_k & \cdots & a_0 & \cdots & a_{-k} & \\ & & & & a_k & \cdots & a_0 & \cdots & a_{-k} \end{bmatrix} \begin{bmatrix} u_{-k+1} \\ \vdots \\ u_1 \\ \vdots \\ u_m \\ \vdots \\ u_{m+k} \end{bmatrix} \tag{4}$$

Rather than making a single assumption to be applied uniformly across the entire boundary, we instead work directly with the underdetermined system in Equation 4, and formulate the solution within a Bayesian framework, with the Bayesian prior adding sufficient constraints to the system. First, we extend the PSF by zero padding, giving the extended matrix $\boldsymbol{A'}$, which is $(m + 2k) \times (m + 2k)$. Then we define the restriction operator $\boldsymbol{D}$ as the $m \times (m + 2k)$ matrix whose i^{th} row is equal to $k + i^{\text{th}}$ row of the $(m + 2k) \times (m + 2k)$ identity matrix. Thus, the final system of equations to be solved is

$$\boldsymbol{z} = \boldsymbol{DA'}u. \tag{5}$$

Assuming a Gaussian likelihood and a Gaussian prior with covariance represented by matrix $\boldsymbol{L}$, the posterior probability density function $p(\boldsymbol{u} \mid \boldsymbol{z},\lambda,\delta)$ is

$$p\left(\boldsymbol{u}\middle|\boldsymbol{z},\lambda,\delta\right) \propto \exp\left(\frac{-\lambda}{2}\left\|\boldsymbol{DA'u}-\boldsymbol{z}\right\|^2 - \frac{\delta}{2}\boldsymbol{u}^T\boldsymbol{Lu}\right), \tag{6}$$

which can be derived using Bayes' Law. Computing the shape of this posterior, via a measure of center of the posterior such as its mean or mode, gives an estimate to the maximum likelihood estimate (MLE) $\boldsymbol{u}$ that is the optimal solution to Equation 3. Based on the variation in the posterior, we obtain a natural quantification of the uncertainties associated with this estimate. These can both be computed using an MCMC method with hierarchical sampling for the parameters λ and δ, which is detailed in Bardsley (2014b).

Figure 1a shows an x-ray radiograph of a "step wedge" (the darkest region), a calibration object used to determine the radiation transmission of the x-ray system. The image was captured at the Cygnus facility at the NNSS, and the lighter gray portions of the image are the areas within the FOV that have no object at all (i.e., 100% transmission of radiation). The vertical edge of the object is a so-called "rolled edge," which can be used to calibrate the spatial resolution of the imaging system, and a horizontal lineout (cross section) of the image across that rolled edge is shown in Figure 1b (in blue). On the left side the intensity is high, because there is no object attenuating the radiation, and on the right side the intensity is low, as the step wedge significantly attenuates the radiation.

The reconstruction shown in Figure 1b shows the efficacy of our deconvolution approach, as it shows the deconvolved lineout (using a standard PSF used in Cygnus image deconvolution) along with 95% credible intervals for the solution. We use periodic boundary conditions on the extended domain, but, due to the fact that the extended boundaries are not near the FOV boundaries, the impacts of periodicity are not seen in the image, as the intensity is around 110

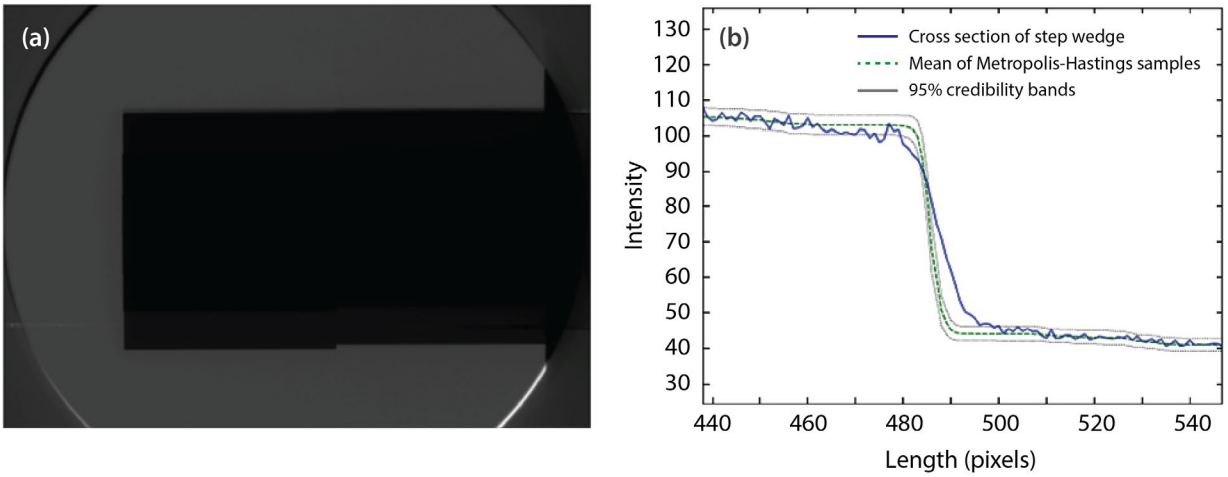

Figure 1. (a) A Cygnus radiograph of a step wedge with a rolled edge on the left vertical side. (b) A horizontal lineout from the image, along with the deconvolved edge reconstruction and 95% credible intervals.

on the left and around 40 on the right. Thus, we are able to gain the computational efficiencies of using periodic boundary conditions, which lend themselves well to spectral approaches, without our solution being impacted by the assumption that our solution is actually periodic.

The method described here has been detailed for deconvolution, but it is applicable to any linear inverse problem whose forward operator includes a boundary condition.

A Statistical Sampling Method for Radiation Source Shape Reconstruction with Non-Negativity Constraints

Many high-energy x-ray imaging systems have a pulsed-power, flash x-ray source that emits radiation through a scene, with any photons that are not attenuated by the scene being absorbed by a scintillator that emits visible light in response. The visible light is focused through an optical system onto a CCD array or imaging plates, producing the measured image data (Figure 2). To characterize images captured with such a system, it is essential to be able to understand the size and spatial profile of the radiation source, or "spot," which is a primary source of system blur due to its finite extent. Blur is also caused by other mechanisms in the system, such as x-ray scatter in the scene, the response of the scintillator used to convert x-rays to visible light, optical effects, and the response of the CCD array recording the visible light, but the spot size and shape are especially important to quantify because they provide a spatially varying lower bound on the overall system resolution. A penumbral imaging technique for reconstructing the spot shape was introduced in Barnea (1994) and formulated statistically in Luttman (2014), but both of those approaches suffer from the pathology that the reconstructed spot could have negative values. Because the spot, in those cases, is essentially a probability distribution, this is non-physical. In this project, we extended the statistical formulation for that problem to include non-negativity constraints and demonstrated its usefulness on real data (Fowler 2014).

The mathematical model for spot shape reconstruction is

$$z(s,t) := A(u)(s,t) = k \int_{s'}^{s''} \int_{t'}^{t''} u\,(\eta,\mu) d\eta d\mu, \qquad \textbf{(7)}$$

where k is a constant that depends on the geometry and (s_c,t_c) are the coordinates of the center of the aperture. The magnification is $m = l_d/l_s$, where the conjugate distances, l_s and l_d, are the distances from the source to the aperture and from the aperture to

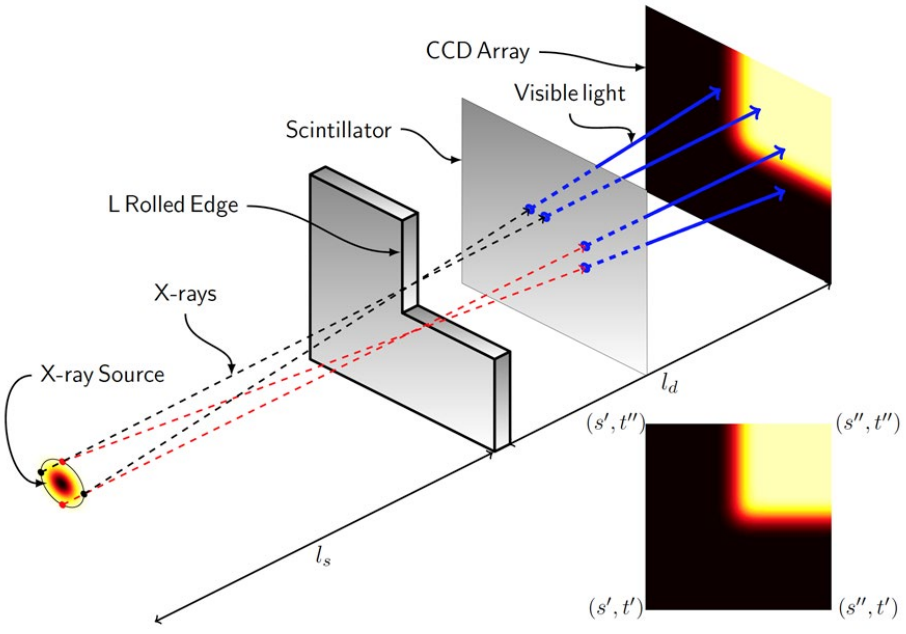

Figure 2. A schematic of the capture of an L rolled edge image from an x-ray imaging system, such as Cygnus at the NNSS

the detector, respectively. The limits of integration define the image domain and are known functions of m and (s_c,t_c).

The spot shape we wish to reconstruct is the maximum of the discrete posterior probability density function given by

$$p(\boldsymbol{u}|\boldsymbol{z}) \propto \exp\left(-\frac{1}{2}\left\|\boldsymbol{C}^{-\frac{1}{2}}(\boldsymbol{A}\boldsymbol{u}-\boldsymbol{z}+\boldsymbol{g})-\frac{\delta}{2}\boldsymbol{u}^T\boldsymbol{L}\boldsymbol{u}\right\|^2\right), \quad (8)$$

where, as above, δ is a scale parameter, $\boldsymbol{g}$ is the vector of background counts (or dark field) in the image, and $\boldsymbol{L}$ is the matrix corresponding to the Gaussian prior covariance. For example, $\boldsymbol{L}$ is the discrete Laplacian in the case of a smoothness prior. The matrix $\boldsymbol{C}$ is a diagonal matrix whose elements are the entries of $\boldsymbol{z}$, which, as above, is the weighted least squares approximation to the Poisson likelihood.

In order to avoid having to select the scale parameter δ manually, we use hierarchical sampling and impose a gamma hyperprior on it, thus assuming

$$p(\delta) \propto \delta^{\alpha-1}\exp(-\delta\beta), \quad (9)$$

where α and β are called hyperprior parameters, which results in a conditional distribution for $\boldsymbol{u}$ of

$$p(\boldsymbol{u}|\delta) \propto \delta^{n/2}\exp\left(-\frac{\delta}{2}\boldsymbol{u}^T\boldsymbol{L}\boldsymbol{u}\right). \quad (10)$$

Thus, the full joint posterior for $\boldsymbol{u}$ and δ is

$$p(\boldsymbol{u},\delta|z) \propto p(\boldsymbol{z}|\boldsymbol{u})\,p(\boldsymbol{u}|\delta)\,p(\delta) \quad (11)$$

$$\propto \delta^{n/2+\alpha-1}\exp\left(-\frac{1}{2}\left\|\boldsymbol{C}^{-1/2}(\boldsymbol{A}\boldsymbol{u}-\boldsymbol{z}+\boldsymbol{g})\right\|^2-\frac{\delta}{2}\boldsymbol{u}^T\boldsymbol{L}\boldsymbol{u}-\beta\delta\right).$$

The full conditional distributions for $\boldsymbol{u}$ and δ are then

$$\begin{aligned}(\boldsymbol{u}|\delta,\boldsymbol{z}) &\sim \mathcal{N}\left(\boldsymbol{\mu},\boldsymbol{A}^T\boldsymbol{C}^{-1}\boldsymbol{A}+\delta\boldsymbol{L}\right)\\ (\delta|\boldsymbol{u},\boldsymbol{z}) &\sim \Gamma\left(\frac{n}{2}+\alpha,\frac{1}{2}\boldsymbol{u}^T\boldsymbol{L}\boldsymbol{u}+\beta\right),\end{aligned} \quad (12)$$

where $\boldsymbol{\mu} := \left(\boldsymbol{A}^T\boldsymbol{C}^{-1}\boldsymbol{A}+\delta\boldsymbol{L}\right)\boldsymbol{A}^T\boldsymbol{C}^{-1}(\boldsymbol{z}-\boldsymbol{g})$.

Note that this formulation does not, of itself, impose non-negativity on the mean of the full joint posterior; however, constraints can be incorporated into the MCMC Gibbs sampler. The Gibbs sampler steps for this problem are:

1. Choose an initial value for δ_0, set a maximum number of samples N, and set k = 0.

2. Compute a non-negatively constrained sample from Equation 12 as

$$\begin{aligned}\boldsymbol{u}^k = \operatorname{argmin}_{\boldsymbol{u}\geq 0}\{&\tfrac{1}{2}\boldsymbol{u}^T(\boldsymbol{A}^T\boldsymbol{C}^{-1}\boldsymbol{A}+\delta_k\boldsymbol{L})\boldsymbol{u}\\ &-\boldsymbol{u}^T(\boldsymbol{A}^T\boldsymbol{C}^{-1}(z-g)+\boldsymbol{w})\}\end{aligned} \quad (13)$$

   where $\boldsymbol{w} \sim \mathcal{N}(0,\boldsymbol{A}^T\boldsymbol{C}^{-1}\boldsymbol{A}+\delta_k\boldsymbol{L})$.

3. Compute a sample from

$$\delta_k \sim \Gamma\left(\frac{n_k}{2}+\alpha,\frac{1}{2}\boldsymbol{u}_k^T\boldsymbol{L}\boldsymbol{u}_k+\beta\right), \quad (14)$$

   where n_k is the number of nonzero entries in $\boldsymbol{u}_k$.

4. Set $k = k + 1$. If $k < N$, return to Step 2.

Figure 3 shows the results of the non-negatively constrained spot shape reconstruction for an L rolled edge image captured by Cygnus at the NNSS. Plot (a) shows the actual image (in false color), with the square aperture in the middle. Plot (b) shows the reconstruction, which is taken to be the mean of the samples computed using the algorithm above. The greatest amount of radiation is emitted in the red region, and the blue indicates regions from which little radiation is emitted. Plot (c) shows the same reconstruction, as a 3-D view to better visualize the shape, and plot (d) shows the pointwise standard deviation of the computed samples, giving an estimate of the uncertainties in the calculation, which vary from very nearly 0% in the central blue regions to approximately 5% in the middle region of highest intensity.

One of the most important quantities used to assess the size of the radiation source is the FWHM of a lineout (cross section) through the middle of the spot. Horizontal and vertical cross sections are shown in Figure 4, along with 95% credibility intervals for the spot. The horizontal lineout gives a spot of 316 µm with a credibility interval of (298 µm, 338 µm). The vertical lineout gives a slightly smaller spot of 298 µm

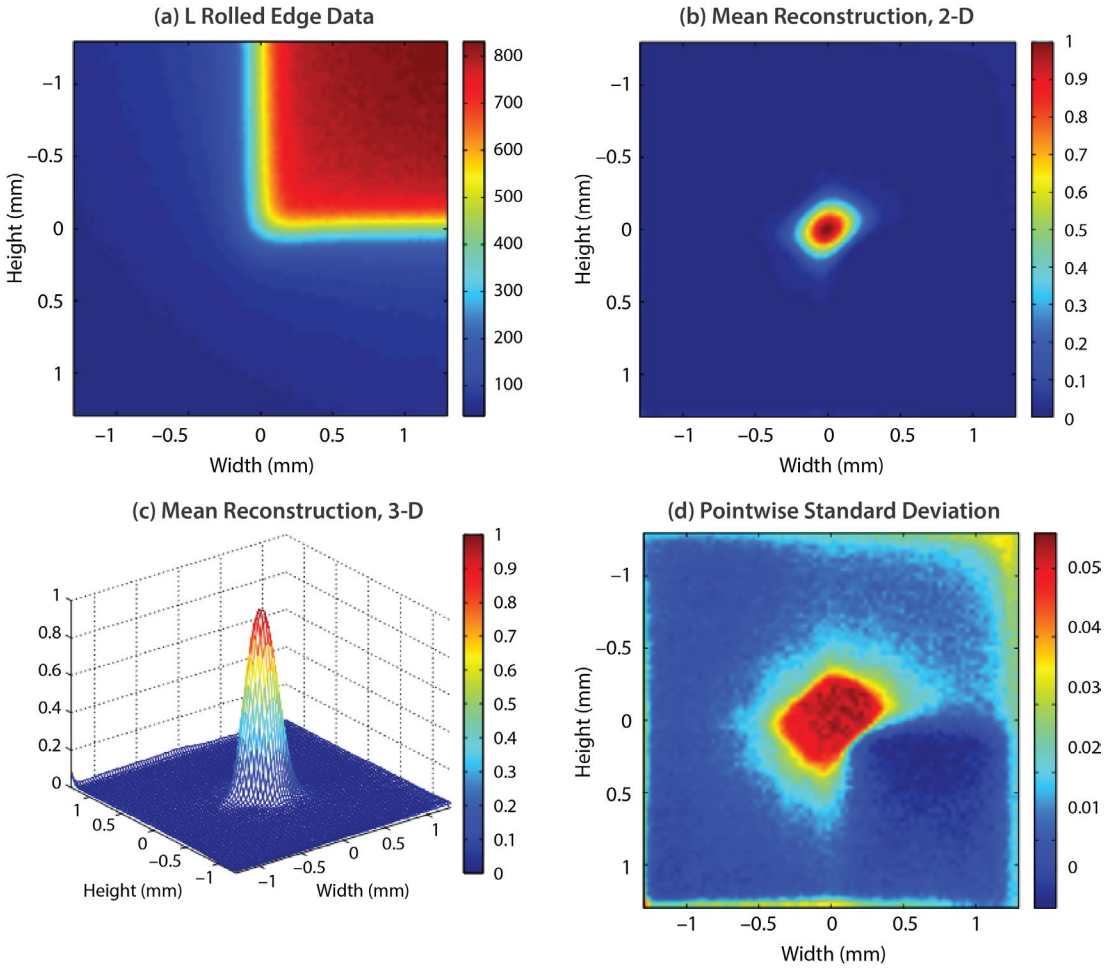

Figure 3. (a) A false-color image of an L rolled edge from the Cygnus x-ray radiography facility at the NNSS. (b and c) The reconstructed radiation source, computed as the mean of the samples from the posterior distribution, shown in 2-D and 3-D. (d) The pointwise standard deviation of the samples, giving a quantification of the uncertainty in the estimate.

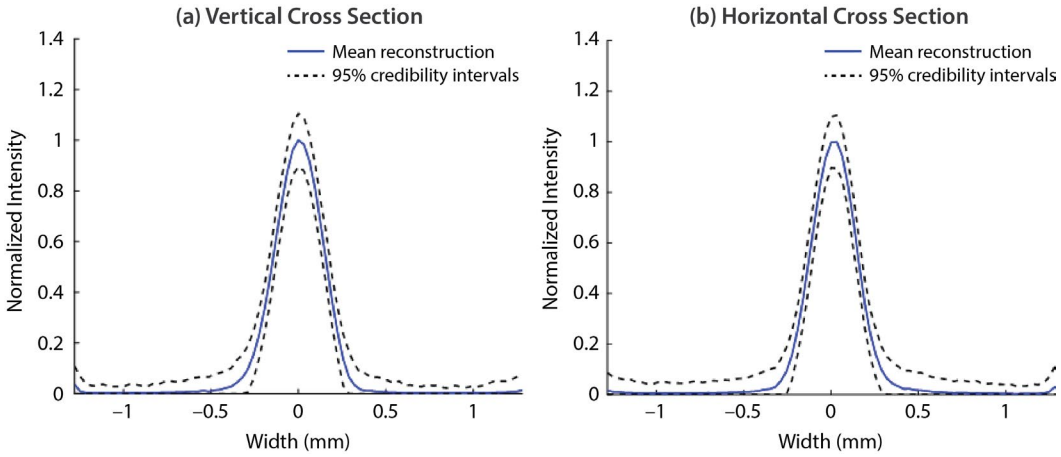

Figure 4. (a) Horizontal and (b) vertical lineouts (cross sections) from the L rolled edge image shown with the 95% credibility intervals

with a 95% credibility interval of (277 µm, 317 µm). Given that the two intervals overlap significantly, and the two means are within each other's credibility intervals, this calculation does not suggest significant asymmetry.

The primary contribution of this project to the spot reconstruction problem is that we have developed a technique to incorporate the non-negativity constraints into the sampling. This approach is not just applicable to the radiation source reconstruction problem; it can also be applied to any linear inverse problem where non-negativity constraints are appropriate.

Poisson-Based Sampling for Quantifying Uncertainties in X-Ray Radiographs

The primary advance demonstrated in the previous sections was a theoretically justified approach to dealing with boundary artifacts in linear inverse problems and a sampling scheme for non-negatively constrained inverse problems, but the final signal reconstructions and uncertainty quantifications were still computed assuming a Gaussian likelihood (Equation 6 or 7). It is common for signals whose noise is dominated by the Poisson component to use a Gaussian approximation to the Poisson likelihood, which allows for an approximate Poisson solution within the Gaussian framework. While this works in some applications, such as the spot reconstruction problem above, there are others for which a true Poisson solution is required, and another of our primary advances in this project was the development of a true Poisson likelihood sampling scheme for solving linear inverse problems.

The basic, discrete Bayesian formulation for a Poisson reconstruction problem with Gaussian prior is given by

$$p(\boldsymbol{u}\,|\,\boldsymbol{z},\delta) \propto \exp\left(-\sum_{j=1}^{m}\left\{\left([\boldsymbol{Au}]_j + g_j\right) - z_j \log\left([\boldsymbol{Au}]_j + g_j\right)\right\} - \frac{\delta}{2}\boldsymbol{u}^T\boldsymbol{L}(\boldsymbol{u}_\delta)\boldsymbol{u}\right), \tag{15}$$

where δ is a scale parameter for the prior, $\boldsymbol{g}$ is the vector of background counts, and $\boldsymbol{L}(\boldsymbol{u}_\delta)$ is the matrix representing the Gaussian prior. The scale parameter, δ, must be estimated, so we define the quantity

$$L_\delta^{\text{wls}}(\boldsymbol{u}_\delta|\boldsymbol{z}) = \frac{1}{2}\left\|\frac{\boldsymbol{Au}_\delta - (\boldsymbol{z}-\boldsymbol{g})}{\sqrt{\boldsymbol{Au}_\delta + \boldsymbol{g}}}\right\|^2, \tag{16}$$

which will be required for the sampling algorithm described below.

Rather than using a Gaussian approximation to the likelihood—equivalent to using the weighted least squares approximation to the Poisson likelihood in the deterministic setting—and using a Gibbs sampler (as is done in Howard 2014), one can instead formulate a full Metropolis-Hastings (MH) MCMC sampler. The full MH algorithm requires a so-called "proposal distribution," and for that we use the density

$$p_{\boldsymbol{u}_\delta}(\boldsymbol{u}\,|\,\boldsymbol{z},\delta) \propto \delta^{(N-1)/2} \exp\left(-\frac{1}{2}\left\|\frac{\boldsymbol{Au}-(\boldsymbol{z}-\boldsymbol{g})}{\sqrt{\boldsymbol{Au}_\delta + \boldsymbol{g}}}\right\|^2 - \frac{\delta}{2}\boldsymbol{u}^T\boldsymbol{L}(\boldsymbol{u}_\delta)\boldsymbol{u}\right), \tag{17}$$

which is the weighted least squares approximation to the MLE when $\boldsymbol{u}_\delta$ is chosen to be the MLE. Given the proposal in Equation 17, the following algorithm then gives theoretically correct samples from the true posterior in Equation 15:

1. Compute $\boldsymbol{u}_\delta$; set $k = 0$ and $\boldsymbol{u}_0 = \boldsymbol{u}_\delta$.
2. Compute a candidate sample $\boldsymbol{u}_*$ from $p_{u_\delta}(\boldsymbol{u}|\boldsymbol{z},\delta)$.
3. Compute $r = \min\{1,\exp(-c)\}$, where
   $c = -\log p(\boldsymbol{z}|\boldsymbol{u}_*) + \log p(\boldsymbol{z}|\boldsymbol{u}_k) - \boldsymbol{L}_\delta^{\text{wls}}(\boldsymbol{u}_k|\boldsymbol{z}) + \boldsymbol{L}_\delta^{\text{wls}}(\boldsymbol{u}_*|\boldsymbol{z})$.
   (See Equation 16.)
4. Compute a random draw s from $U(0,1)$. If $s < r$, set $u_{k+1} = u_*$; otherwise set $u_{k+1} = u_k$.
5. Set $k = k+1$ and return to Step 1.

Note that, rather than using the formula in Equation 15, one can also use hierarchical sampling by imposing a hyperprior on the scale parameter δ, a technique that was partially described above for spot reconstruction and is described further, with all of the details of the MH algorithm by Bardsley (2014c).

NToF Reconstruction

In analysis of neutron creation events, important parameters, such as plasma temperature[1] kT and creation profile parameters (time reference t_n and spread w_n), can be obtained from NToF data (Lehner 1967, Brysk 1973, Ballabio 1998). Our aim was to find parameter variances of neutrons created in a deuterium-tritium reaction from the NToF measurements.

Specifically, let us rewrite Equation 1 so that the measured data are modeled by

$$y(\theta) = h * \xi(\theta) + \eta, \qquad \textbf{(18)}$$

where h is the response function of the measurement system. This model has two sources of uncertainties: the measurement uncertainty, modeled by the Gaussian noise η, and the intrinsic uncertainty of neutron creation, modeled by a Poisson process $\xi(\theta)$ with the mean $x(\theta)$.

The mean is modeled as

$$x(t,\theta) = \frac{N_0}{w_n w_g} \int n\left(\frac{t' - t_n'}{w_n}\right) g_t\left(\frac{t - t' - t_g''}{w_g}\right) dt', \qquad \textbf{(19)}$$

where t is the time of arrival of neutrons at the detector, t'' is their time of flight, and t' is their creation time. The $n\left(\frac{t'-t_n'}{w_n}\right)$ is the neutron creation profile with spread w_n and time reference t_n'. The $g_t\left(\frac{t''-t_g''}{w_g}\right)$ is the neutron energy distribution expressed in terms of time of flight, with $t_g'' = D/\sqrt{2E_0/m_n}$ the mean of the time of flight and $w_g := t_g''\sqrt{0.1\cdot kT/E_0}$ the signal spread.

E_0 is neutron mean kinetic energy and m_n is neutron mass. We want to estimate the variances of $\theta = (t_n, w_n, kT)$ with kT hidden in $w_g := t_g'' w_E/2E_0 \approx 0.0535 \cdot D \cdot \sqrt{kT}$.

We found *explicit* formulae for the variances of the parameters $\theta = (t_n, w_n, kT)$, in terms of measurement settings and the parameter values, such that would apply even before the measurements are performed. Consequently, the formulae would serve as a measurement planning tool.

We addressed two problems: (1) an estimate of the relative effect of the counting vs. the instrument uncertainty and (2) an estimate of parameter uncertainties in our model.

Counting vs. Instrument Uncertainty

The first result presents explicitly in Equation 20 the ratio of the counting (Poisson) vs. the measurement (Gaussian) uncertainties in terms of the oscilloscope and detector parameters:

$$\frac{\sigma^2_{P\max}}{\sigma^2} \approx \frac{5\sqrt{kT}}{N_0} \cdot \frac{2^{2\cdot ENOB}}{\Delta t} \cdot \frac{D^3}{\alpha \cdot A} \times C_{h\max}\left(0.0535 \cdot D \cdot \sqrt{kT}/\Delta t\right). \qquad \textbf{(20)}$$

Note that the first ratio of Equation 20 describes plasma properties (temperature kT and the number of neutrons N_0) that we know approximately even before measurements are performed, the second the properties of the oscilloscope (the effective number of bits $ENOB$ and time step Δt), and the third the properties and placement of the detector (distance D, size A, and efficiency α). The coefficient $C_{h\max}$ (shown in Figure 5) represents the effect of the measurement system $h(t)$. Because the coefficient $C_{h\max}$ (as we show in Odyniec 2014a) is bounded, we know how to choose the oscilloscope and how to choose and place the detector without performing measurements and having only rough values of the parameters of interest. Consequently, Equation 20 allows us to plan the measurement setup.

In FY 2013 (Odyniec 2014d), we analyzed the case of an ideal measurement system ($h(t) = \delta(t)$), for which $C_{h\max} = 1$ and Equation 20 has reduced to

$$\frac{\sigma^2_{P\max}}{\sigma^2} \approx \frac{5\sqrt{kT}}{N_0} \cdot \frac{2^{2\cdot ENOB}}{\Delta t} \cdot \frac{D^3}{\alpha \cdot A}. \qquad \textbf{(21)}$$

When the measurement system's bandwidth is wider than that of the signal, then the impulse response

[1] Here k denotes the Boltzmann constant and T the absolute temperature, so that formally speaking kT is the energy, but we will follow the common habit of calling it temperature.

changes much faster than the signal does (Odyniec 2014a). That results in the value of $C_{h\max}$ being close to 1 for $D > 2\ m$. For a typical system response, $h(t) := b \cdot exp(-bt) \cdot 1(t)$ (where $1(t)$ equals one for $t > 0$ and equals zero for $t < 1$); see Figure 5.

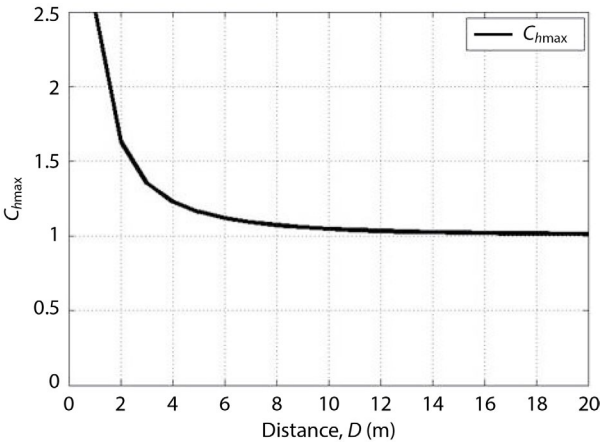

Figure 5. Dependence of $C_{h\max}(D)$ on distance to the detector for $kT = 16$ keV, $\Delta t = 0.01$ ns, and $h(t) := b \cdot exp(-bt) \cdot 1(t)$ with $b = 2$ GHz

Parameter Uncertainties

We further developed explicit formulae for parameter variances obtained independently of the calculation of the parameter values and expressed in terms of the measurement setup. Specifically, we proved that in a causal measurement system of wide enough bandwidth, the parameters are uncorrelated and their covariance matrix equals

$$V(\theta) = z_{\max}^2 \sigma^2 \Delta t \cdot \begin{bmatrix} \left\langle z_{|t0}, z_{t0} \right\rangle^{-1} & 0 \\ 0 & \left\langle z_{|w}, z_{|w} \right\rangle^{-1} \end{bmatrix}, \quad (22)$$

where $z := h * x$ and $K(u) := \int_{-\infty}^{+\infty} h(t)h(t+u)dt$,

so that

$$\left\langle z_{|i}, z_{|j} \right\rangle = \left\langle h * x_{|i}, h * x_{|j} \right\rangle = \\ = \iint K(s-u)x_{|i}(s)x_{|j}(u)dsdu. \quad (23)$$

Diagonality of the covariance matrix results from the fact that $K(u)$ is an even function $K(-u) = K(u)$ for arbitrary $h(t)$.

Consequently, the time delay and signal width are uncorrelated, and their variances are

$$\sigma_{t0}^2 = \kappa_{t0} \cdot \sigma^2 \Delta t \\ \sigma_w^2 = \kappa_w \cdot \sigma^2 \Delta t, \quad (24)$$

where the parameters κ_{t0}, κ_w (calculated in Odyniec 2014a) depend only on signal's shape and system response scaled by signal width.

We can now derive the explicit formulae of their uncertainties (standard deviations):

$$\sigma_{t_n} = \sigma_{t_0} \approx 0.246 \cdot kT^{1/4} \cdot D^{1/2} \cdot \Delta t^{1/2} \cdot \sigma \cdot \kappa_{t_0}^{1/2}, \quad (25)$$

$$\sigma_{w_n} = \frac{0.0117}{w_n} kT^{3/4} \cdot \sigma \cdot \kappa_w^{1/2} \cdot \Delta t^{1/2} \cdot D_1^{3/2} \\ \times f_{w_n}(D_2/D_1), \quad (26)$$

$$\sigma_{kT} = 7.5 \cdot kT^{3/4} \cdot \sigma \cdot \kappa_w^{1/2} \cdot \Delta t^{1/2} \cdot D_1^{-1/2} \\ \times f_{kT}(D_2/D_1). \quad (27)$$

As before, they are expressed in terms of the choice, settings, and placement of the detector and the oscilloscope. *Consequently, the method serves as a tool in planning a measurement setup*.

Indeed, we prove (Odyniec 2013, 2014d) that the optimum placement requires the maximum feasible ratio of D_2/D_1 (in practice $D_1 \approx 2$ m, $D_2 \approx 8$ m). This is intuitively convincing because we want to disentangle the creation time and the time of flight. Thus, we need one detector to be "least" affected by the time of flight (i.e., placed "close" to the source) and the other detector the "most" affected (i.e., placed "far" from) the source.

Moreover, Equations 25–27 tell us that for the present state of the art, the measurement variance dominates the intrinsic variance of neutron production as long as the detector is placed at a distance of a few meters and the reaction yield is of the order of $N_0 = 10^{14}$ neutrons.

Example (Odyniec 2013, 2014d)

For an ideal measurement system, $h(t) = \delta(t)$, we have

$$K(t) := \int_{-\infty}^{+\infty} h(t_1)h(t+t_1)dt_1 = \delta(t) \quad \textbf{(28)}$$

and $K(wt) = \delta(wt) = w^{-1} \cdot \delta(t)$, which results in the following coefficients

$$C_{h\max} := \max_l \sum_{i=0}^{\infty} h_i \cdot e_{l-i} = 1$$

$$\kappa_\tau = w\left(\int t_1^2 \cdot \exp\left(-t_1^2\right) dt_1\right)^{-1} = 2w/\sqrt{\pi} \quad \textbf{(29)}$$

$$\kappa_w = w\left(\int \left(t_1^2 - 1\right)^2 \cdot \exp\left(-t_1^2\right) dt_1\right)^{-1} = 4w/3\sqrt{\pi}.$$

Summary of NToF Reconstruction

We have provided explicit formulae that serve as a tool in planning a measurement setup. One set of the formulae (Equations 20 and 21) provides the relative impact of the intrinsic noise versus the measurement noise. As its corollary we obtain the detector placement range over which the intrinsic noise is negligible. Interestingly, when yield is of the order of $N_0 = 10^{14}$ neutrons, this range proves to be the most practical for detector placement. The other set of the formulae (Equations 25–27) provides uncertainty estimates of the parameters of interest. They provide reasonable uncertainties even for the parameters that are an order of magnitude smaller than the measured data. Therefore, this effort, which aimed at developing methods of analysis for the neutron time of flight, is finished with the results that surpassed our expectations.

Generalized Poisson Process

Another interesting application of UQ in the Poisson process comes from radiance measurements (La Lone 2013). In this case the particles' creation is modeled by the Poisson process with a *time-varying* rate. The particles arrive at a photomultiplier whose output we measure.

In order to apply our methods to this case, two problems should be solved: (1) how to find variance in the time-varying Poisson process and (2) how to recover the counting process from the photomultiplier data.

Finding Variance in the Time-Varying Poisson Process

We showed that this can be done by considering the process described by the distribution

$$P_k(t_l,t_{l+1}) = m(t_l,t_{l+1})^k e^{-m(t_l,t_{l+1})} / k!, \quad \textbf{(30)}$$

where $P_k(t_l,t_{l+1})$ denotes the probability of k particles arriving in the (t_l,t_{l+1}) time interval, $\lambda(u)$ denotes the (time-varying) particle arrival rate, and $m(t_l,t_{l+1}) = \int_{t_l}^{t_{l+1}} \lambda(u)\,du$ denotes the expected value of particles arriving in the (t_l,t_{l+1}).

Note that when the arrival rate $\lambda(u) = \lambda$ and the interval length $t_{l+1} - t_l = \delta$ are both constant in time, we obtain the standard Poisson distribution, namely the probability of k particles arriving in the time interval of length δ equals $P_k(\lambda\delta) = (\lambda\delta)^k e^{-\lambda\delta} / k!$.

This process's variance, over an interval (t_l,t_{l+1}), is equal to its mean value $m(t_l,t_{l+1})$. Therefore, we choose the intervals ("bins"), whose length may vary, in such a way that each interval (t_l,t_{l+1}) contains a positive number of counts. This gives us an estimate of its mean $m(t_l,t_{l+1})$ and the corresponding standard deviation $\sqrt{m(t_l,t_{l+1})}$.

Recovering the Counting Process from the Photomultiplier Data

To this end we devised an algorithm and wrote a MATLAB program that recovers the original particle count from the measured data. Its application is shown in Figure 6.

This effort, as the NToF analysis above, consisted of developing methods for variance estimation for the time-varying radiation phenomena. We have proven the concept, in the process discovering increased complexity of the problem and developing proof of concept of the new expanded (which seems at this

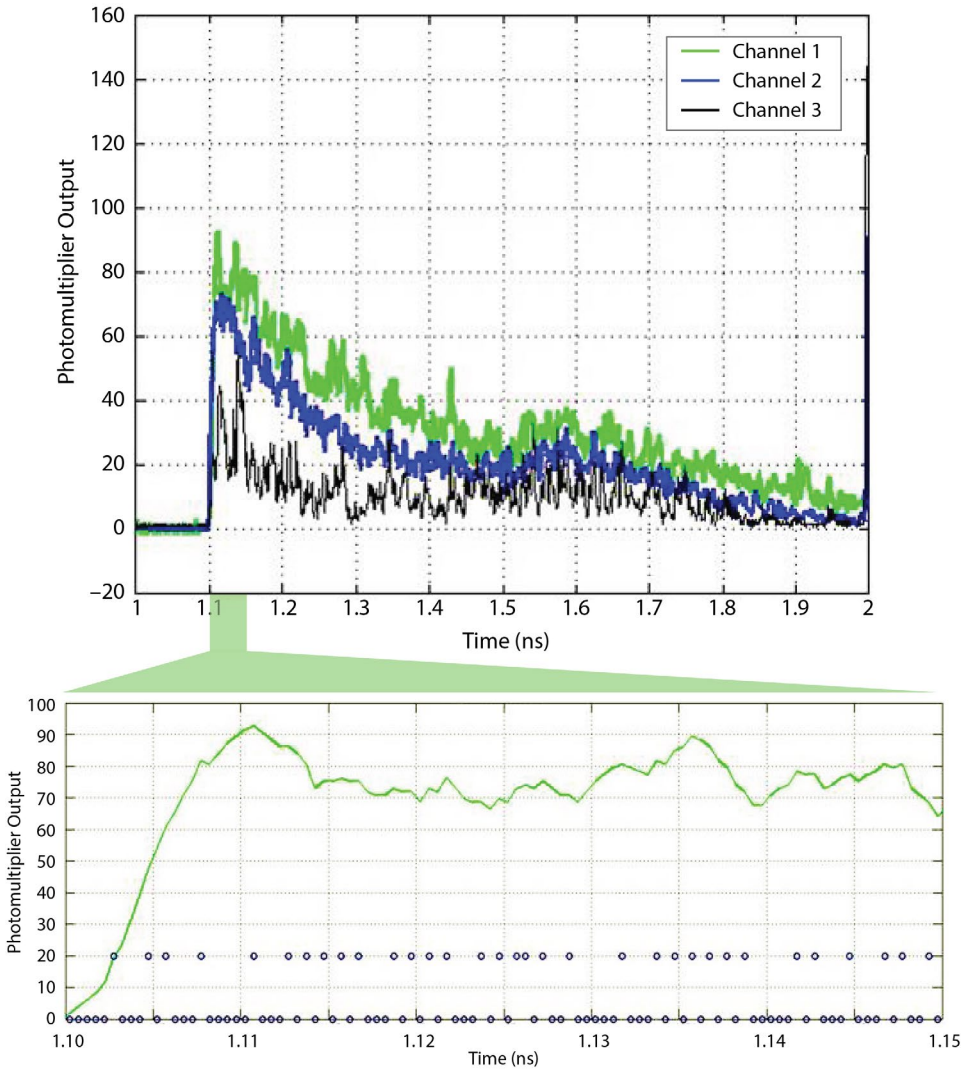

Figure 6. The measured data shown here for three channels are the photomultiplier output. We recover from them particle count, shown for channel 1 in the lower plot, zoomed for better visibility to the interval 1.10–1.15 ns.

point to be) full problem. Thus, having proven that the problem is tractable, we intend to return to it when possible.

Conclusion

We have developed computational and statistical methods for UQ in the presence of mixed Poisson-Gaussian noise and have applied them to several NNSA projects. Specifically, we developed Poisson-based methods for deconvolution with sampling (full Poisson) and edge enhancements, which included a new technique for boundary artifacts in inverse problems (Bardsley 2009, 2014a, 2014b). In this work we presented a data-driven technique for computing boundary values by solving a regularized and well-posed form of the deconvolution problem on an extended domain. Further, a Bayesian framework was constructed for the deconvolution, and we presented an MCMC method for sampling from the posterior distribution. There are several benefits to this approach, including that it still takes advantage of the efficiency of spectral methods, that it allows the boundaries of the signal to be treated in a non-uniform

manner (thereby reducing artifacts), and that the sampling scheme gives a natural method for quantifying uncertainties in the reconstruction.

We also developed a Poisson-based MCMC sampling and uncertainty quantification applied to x-ray radiography (Fowler 2014; Howard 2014, 2015; Joyce 2014). We solved the deconvolution problem within a Bayesian framework for edge-enhancing reconstruction with uncertainty quantification. The likelihood was a normal approximation to the Poisson likelihood, and the prior was generated from a classical total variation regularized Poisson deconvolution. Samples from the corresponding posterior distribution were computed using an MCMC approach, giving a pointwise measure of uncertainty in the reconstructed signal. We demonstrated the results on real data used to calibrate a high-energy x-ray source and showed that this approach gives reconstructions as good as classical regularization methods, while mitigating many of their drawbacks.

We furthermore presented explicit formulae for variances of plasma parameters recoverable from NToF measurements (Odyniec 2013, 2014b, 2014c). Our results, obtained independently of calculation of the parameter values from measured data, can serve as a tool in planning a measurement setup. They are valid for a general measurement system (causality and wide enough bandwidth are our only limitations). Consequently, our formulae allow us to plan measurement setup and provide an insight into available tradeoffs. In particular, they prove that for the present state of the art, the measurement variance dominates the intrinsic variance of neutron production as long as the detector is placed at a distance of a few meters and the reaction yield is on the order of $N_0 = 10^{14}$ neutrons. We also found out that, for an arbitrary measurement system, the signal delay and spread are decorrelated.

We addressed fundamentals of nonhomogeneous and compound Poisson processes (Odyniec 2014b) and provided tools that allow finding the counting process from radiance data. The latter includes system response analysis, which will allow us to compare our results with real experiments.

Acknowledgments

It is our pleasure to acknowledge the fundamental contributions of J. Bardsley (The University of Montana), J. Blair (NSTec), M. Fowler (The MathWorks, Inc.), and K. Joyce (The University of Montana), all well attested by the reference list. We would like to thank B. La Lone (NSTec, Special Technologies Laboratory) for very helpful comments and for sharing the data on radiance, and H. Haario (Lapeenranta University of Technology) for helpful comments and sharing his MCMC programs.

References

Ballabio, L., J. Källne, G. Gorini, "Relativistic calculation of fusion product spectra," *Nucl. Fusion* **38**, 11 (1998) 1723.

Bardsley, J. M., A. Luttman, "Total variation-penalized Poisson likelihood estimation for ill-posed problems," *Adv. Comput. Math* **31**, 1–3 (2009) 35–59.

Bardsley, J. M., A. Solonen, H. Haario, M. Laine, "Randomize-then-optimize: a method for sampling from posterior distributions in nonlinear inverse problems," *SIAM J. Sci. Comput.* **36**, 4 (2014a) A1895–A1910.

Bardsley, J. M., A. Luttman, "Dealing with boundary artifacts in MCMC-based deconvolution," *Linear Algebra and Its Applications* (2014b) doi:10.1016/j.laa.2014.09.023.

Bardsley, J. M., A. Luttman, "A Metropolis-Hastings method for linear inverse problems with Poisson likelihood and Gaussian prior," *SIAM/ASA Journal on Uncertainty Quantification*, submitted July 2014 (2014c).

Barnea, G., "Penumbral imaging made easy," *Rev. Sci. Instrum.* **65** (1994) 1949–1953.

Brysk, H., "Fusion neutron energies and spectra," *Plasma Phys.* **15**, 7 (1973) 611–617.

Fowler, M., M. Howard, A. Luttman, S. Mitchell, T. Webb, "A stochastic approach to quantifying the blur with uncertainty estimation for high-energy x-ray imaging systems," *Inverse Problems in Science and Engineering*, in production, 2014.

Howard, M., A. Luttman, M. Fowler, "Sampling-based uncertainty quantification in deconvolution of x-ray radiographs," *J. Comput. Appl. Math.* **270** (2014) 43–51.

Howard, M., M. Fowler, A. Luttman, S. Mitchell, M. Hock, "Bayesian Abel inversion in quantitative x-ray radiography," *SIAM J. Sci. Comput.*, submitted March 2015.

Joyce, K., "Point spread reconstruction in radiography," *SIAM Conference on UQ*, April 2014.

La Lone, B. M., G. D. Stevens, W. D. Turley, D. B. Holtkamp, A. J. Iverson, R. S. Hixson, L. R. Veeser, "Release path temperatures of shock-compressed tin from dynamic reflectance and radiance measurements," *J. Appl. Phys.* **114**, 6 (2013) 063506–063506-14.

Lehner, G., F. Pohl, "Reaktionsneutron als Hilfsmittel der Plasmadiagnostik," *Zeitschrift für Physik* **207** (1967) 83–104.

Luttman, A., M. Howard, M. Fowler, S. Mitchell, "Quantifying uncertainty and error propagation in radiography image processing," in *Site-Directed Research and Development*, FY 2013, National Security Technologies, LLC, Las Vegas, Nevada, 2014, 161–170.

Luttman, A., M. Odyniec, N. Shlayan, J. Blair, E. Machorro, P. Kachroo, "A model-based approach to fusion neutron spectroscopy," *IEEE Trans. Plasma Sci.*, submitted October 2013.

Odyniec, M., J. Blair, "Effect of the measurement vs. the counting errors on parameters' covariance in neutron tomography analysis," *Proc. SOFE Conf.*, Symposium on Fusion Engineering (SOFE) 2013, San Francisco, California, 2013, 1–6.

Odyniec, M., J. Blair, "Parameters' covariance in neutron time of flight analysis–Explicit formulae," *IEEE Trans. Plasma Sci.* **42**, 12 (2014a) 4031–4037.

Odyniec, M., J. Blair, "Rigorous analysis of Poisson process detection," *CASIS 2014, 18th Annual Signal and Image Sciences Workshop*, Livermore, California, May 21, 2014b.

Odyniec, M., J. Blair, "Uncertainty in Poisson process measurements," *IMS 2014, International Microwave Symposium*, Tampa Bay, Florida, June 1–6, 2014c.

Odyniec M., A. Luttman, J. Blair, "Maximum likelihood estimation and uncertainty quantification for signals with Poisson-Gaussian mixed noise," in *Site-Directed Research and Development*, FY 2013, National Security Technologies, LLC, Las Vegas, Nevada, 2014d, 183–189.

This page left blank intentionally

Three-Dimensional Seismic-Attribute Model for Yucca Flat

NLV-24-14 | Continued in FY 2015 | Year 1 of 2

Lance Prothro,[1,a] Margaret Townsend,[a] Heather Huckins-Gang,[a] Sig Drellack,[a] Dawn Reed,[a] Todd Kincaid,[b] and Kevin Day[b]

Our first year of research indicates that an existing 3-D hydrostratigraphic framework model of Yucca Flat that was developed for groundwater modeling shows considerable promise as a 3-D seismic-attribute model. Based partly on data collected during underground nuclear testing that occurred at Yucca Flat, and with relatively minor modifications, the existing framework model can be modified to function as a 3-D seismic-attribute model. Our FY 2015 efforts will focus on model modifications and enhancements, including constructing an associated velocity model and incorporating subsurface features related to underground nuclear testing that likely influence seismic wave propagation.

[1] prothrlb@nv.doe.gov, 702-295-7745
[a] National Security Technologies, LLC; [b] GeoHydros, LLC

Background

The United States has a significant national security interest in improving its ability to detect, locate, and characterize underground nuclear explosions (UNEs), particularly low-yield UNEs, that may be conducted anywhere in the world (Snelson 2013). One of the primary methods of monitoring for UNEs is to analyze seismic waves generated by the explosions, which propagate outward through the earth from the detonation point to seismic recording sensors located around the globe (Auer 2014). Seismic waves, whether generated by UNEs, or other man-made or natural events, propagate through different rock types at differing speeds and with different characteristics that depend largely on various rock properties and presence of other geologic features. The earth is a very heterogeneous geologic medium, and the 3-D geologic structure of the earth strongly affects how seismic waves propagate both locally and regionally as they encounter various rock types, faults, and other geologic features, and how they interact with the variable topography of the earth's surface.

The Source Physics Experiment (SPE) is currently being conducted in Yucca Flat of the NNSS by the U.S. DOE, NNSA to develop predictive capabilities that will enhance the United States' ability to model and characterize low-yield nuclear tests anywhere in the world (Snelson 2013). The approach of the SPE is to conduct well-characterized chemical explosions at different depths and in different geologic media to improve the understanding of how seismic waves are produced and how they propagate in different geologic settings.

Yucca Flat is an excellent site for studying seismic wave propagation from controlled explosive experiments like those conducted for the SPE. The geologic setting of Yucca Flat is diverse, but well understood, with an abundance of geologic and geophysical data from more than 50 years of subsurface characterization activities associated with the U.S. underground weapons testing program (WTP). In addition, and important for improving seismic wave propagation modeling, a 3-D geology-based computer framework model constructed for a different purpose and under another program already

exists for Yucca Flat. We believe that with minimal modifications, this existing hydrostratigraphic framework model (HFM) can function as a seismic-attribute framework model and thus become a valuable tool for improving seismic wave propagation modeling in and around Yucca Flat. Furthermore, this model will be used by ongoing NNSS projects designed to improve our understanding of seismic wave propagation, and contribute to improvements of the nation's ability to detect, locate, and characterize underground nuclear explosions conducted anywhere in the world.

Project

This project leverages existing seismic property data collected during the WTP in Yucca Flat and an existing 3-D HFM for Yucca Flat to develop a 3-D seismic-attribute framework model and an associated seismic properties database. We are also testing the hypothesis that with minimal modifications the Yucca Flat HFM can function as a seismic-attribute model.

The Yucca Flat Hydrostratigraphic Framework Model (HFM)

The Underground Test Area (UGTA) Activity was initiated by the NNSA Nevada Field Office (NFO) to assess the effects of underground nuclear tests on groundwater at the NNSS (Navarro-Intera 2013). The UGTA strategy requires the development of sophisticated groundwater flow and contaminant transport computer models to estimate the lateral and vertical movement of radionuclide-contaminated groundwater over the next 1,000 years. Because groundwater flow is mainly controlled by certain physical properties of the rocks through which it flows, the development of 3-D computer framework models of the distribution of subsurface units according to their abilities to transmit groundwater was a critical first step in the development of groundwater flow and contaminant transport models. These 3-D HFMs are the foundation for subsequent numerical flow and transport modeling, and have been successfully utilized by UGTA for more than 10 years.

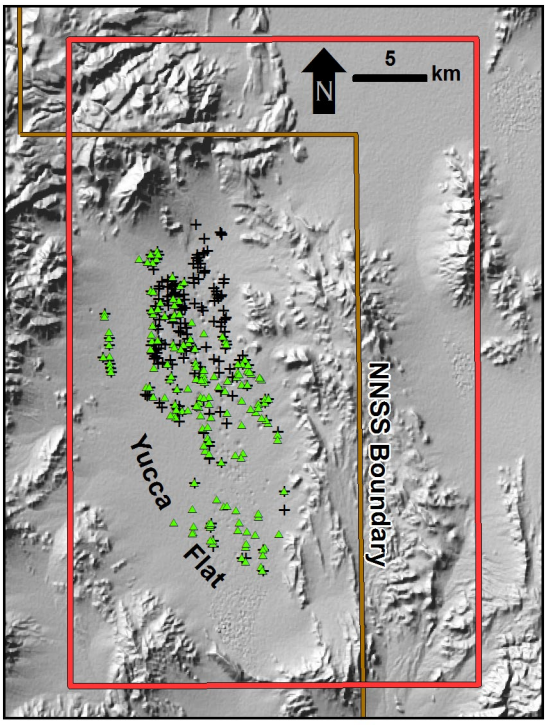

Figure 1. Shaded relief map of Yucca Flat showing the boundaries of the Yucca Flat HFM (red rectangle) and drill holes with working point (WP) medium characteristics (black plus signs) and down-hole geophone data (green triangles)

The Yucca Flat HFM was constructed for UGTA in 2006 (Bechtel Nevada 2006). It covers 1,250 square kilometers in the northeastern portion of the NNSS and includes all of Yucca Flat proper and portions of the adjacent highlands (Figure 1).

Vertically, the Yucca Flat HFM extends from the land surface to 5 kilometers below sea level. The HFM is geology-based and incorporates stratigraphic principles and rock properties to group the various rock layers beneath Yucca Flat into hydrostratigraphic units (HSUs) based on their ability to transmit groundwater. Thus, HSUs form the main 3-D model volumes, or layers, in the HFM. The Yucca Flat HFM includes 25 HSUs as well as 178 faults that cut and offset the HSUs (Figure 2).

Many of the properties and characteristics that influence a rock's ability to transmit groundwater, such as density, porosity, and propensity to fracture, also

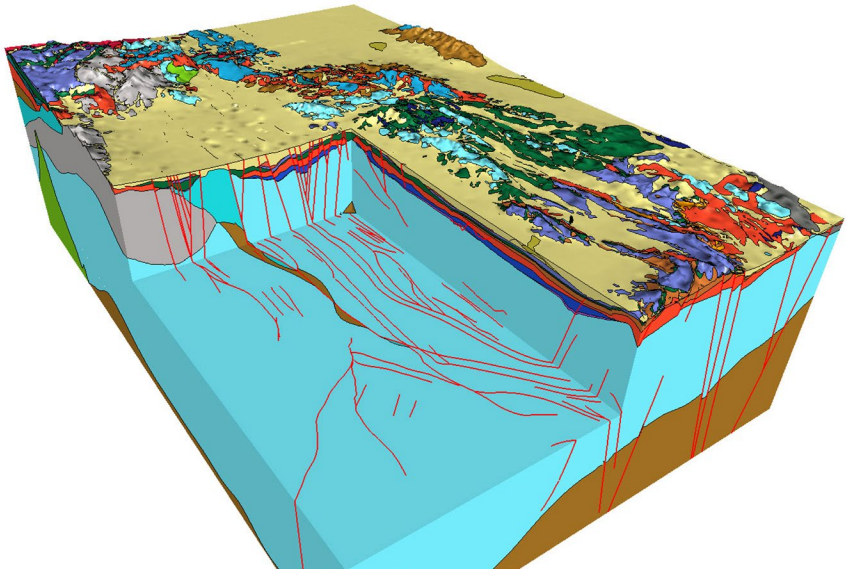

Figure 2. Looking northeast at a cutaway 3-D perspective view of the Yucca Flat HFM. Colored layers are HSUs; red lines are faults.

influence the transmission of seismic waves through the rock. Thus, the Yucca Flat HFM is expected to be applicable for use in modeling of seismic wave propagation in and around Yucca Flat.

Yucca Flat Site-Characterization Data from the Weapons Testing Program

From 1957 to 1992, 747 UNEs were conducted in the Yucca Flat area (Navarro-Intera 2013). The individual sites for these detonations were typically the subject of intense geological and geophysical characterization. More basin-wide geological and geophysical investigations were also commonly conducted and, together with individual site characterization data, resulted in a detailed understanding of the geological and geophysical character of Yucca Flat. After 1992, environmental restoration work associated with the NNSA/NFO's UGTA activity added significantly to this institutional knowledge.

Extensive characterization studies by the WTP and environmental restoration activities in Yucca Flat have produced a diverse set of geological and geophysical data for the basin, including laboratory measurements of rock characteristics (e.g., density, water content, mineralogy), borehole geophysical logs (e.g., bulk density, acoustic impedance, seismic velocity), and field surveys (e.g., seismic reflection and refraction, gravity, resistivity, magnetotelluric, and aerial and ground magnetics).

From this large, diverse assemblage of data, we chose two specific datasets to interrogate and evaluate the applicability of the Yucca Flat HFM to function as a seismic-attribute model. Both datasets provide field-scale seismic velocity data for distinct subsurface intervals of rock sections beneath Yucca Flat. The first data of interest were extracted from detailed site characterization reports from 150 UNE emplacement holes in Yucca Flat (Figure 1). Of particular interest were data tables that list various physical properties of the rocks within the region of the working point (WP; i.e., depth of detonation). These data tables provided seismic compressional-wave (P-wave) velocity for a specified interval of rock around the WP. In addition they listed other important interval-specific rock properties such as bulk density and porosity.

We also compiled the results from down-hole seismic surveys conducted in many of the emplacement holes drilled to site UNEs in Yucca Flat. To conduct these down-hole seismic surveys, a seismic receiver (i.e., geophone) was lowered down the hole and clamped against the borehole wall at a specified depth. A seismic source located at the surface near the

borehole initiated a seismic signal that was recorded by the down-hole geophone. The geophone was then moved to another depth in the hole, and the process was repeated at each geophone station, typically at 50-foot intervals. From these data, an interval seismic velocity was calculated for the rock section between each down-hole receiver depth. This yielded seismic velocity data at 50-foot intervals throughout the depth of the hole. More than 5,400 interval velocity measurements from 188 holes in Yucca Flat were compiled (Figure 1).

Both WP interval data and down-hole seismic data were originally collected and reported prior to the early 1990s. Unfortunately, no WTP electronic database compilations of the data were found for this investigation. Thus, we had to go back to the original WTP reports and down-hole paper logs to extract the required data and compile it into a spreadsheet format. Because all the velocity and other data of interest were for specific depth intervals tied to individual holes, information such as hole name, location, and surface elevation were extracted from existing UGTA databases and included with each interval velocity record. The depth of the water table was also determined for each hole in the spreadsheet, and each velocity interval measurement was assigned a descriptor that indicated whether the entire interval was fully saturated (i.e., below the water table), unsaturated (i.e., above the water table), or partially saturated (i.e., the water table is within the interval). This information allowed us to evaluate the effect of water saturation on the seismic velocity data.

A critical step in the compilation of the Yucca Flat seismic velocity dataset was to correlate each interval velocity in the database with geologic parameters of the interval. These parameters included stratigraphic unit, lithology (i.e., rock type), mineral alteration, and, most importantly, the HSU that the interval represented in the Yucca Flat HFM. Drill hole geologic data were extracted from various WTP-era reports, logs, and data compilations. HSU assignments were determined from Appendix C of the report prepared by Bechtel Nevada (2006).

Data Analyses and HFM Evaluation

Linking each of the 5,526 interval velocity measurements within the seismic velocity drill hole database to geologic parameters allows us to sort, evaluate, and statistically analyze the velocity data relative to stratigraphic unit, lithology, alteration mineralogy, and HSU (Figure 3). Our initial analyses show expected seismic heterogeneity within the rocks beneath Yucca Flat, and a general correlation between seismic properties and HSUs. Thus, most HSUs in the Yucca Flat HFM can function as seismo-stratigraphic units (SSUs). As expected, HSUs composed of denser rock types tend to have higher P-wave velocities. These higher velocity rocks typically compose two types of HSUs: dense fractured aquifer HSUs and tuff confining unit HSUs. Slower velocity rocks are typically defined by HSUs composed of highly porous, low-density, and poorly fractured aquifer HSUs, such as the alluvial aquifer and various vitric-tuff aquifer HSUs. Seismic velocity increases with depth in some rock types, especially alluvium, and likely represents compaction of less consolidated units by increasing overburden pressures as these units become more deeply buried.

Using a subset of the down-hole interval velocity data, we constructed a separate preliminary velocity model independent of the HFM to explore its potential to aid in evaluating the HFM, particularly whether lateral velocity changes occur in some HSUs (Figure 4). Initial assessments of the preliminary velocity model indicate that it can provide an additional and efficient method to evaluate visually and analytically the 3-D distribution of velocities beneath Yucca Flat and the seismic character of HSUs.

Faults

Faults are profound, ubiquitous geologic features in the NNSS region, and the Yucca Flat HFM includes 178 faults as distinct model elements. Not only can faults offset and juxtapose rocks with different seismic properties, but they can also damage adjacent rocks (Caine 1996), potentially altering their seismic properties. Because the faults in the Yucca Flat vicinity have a strong

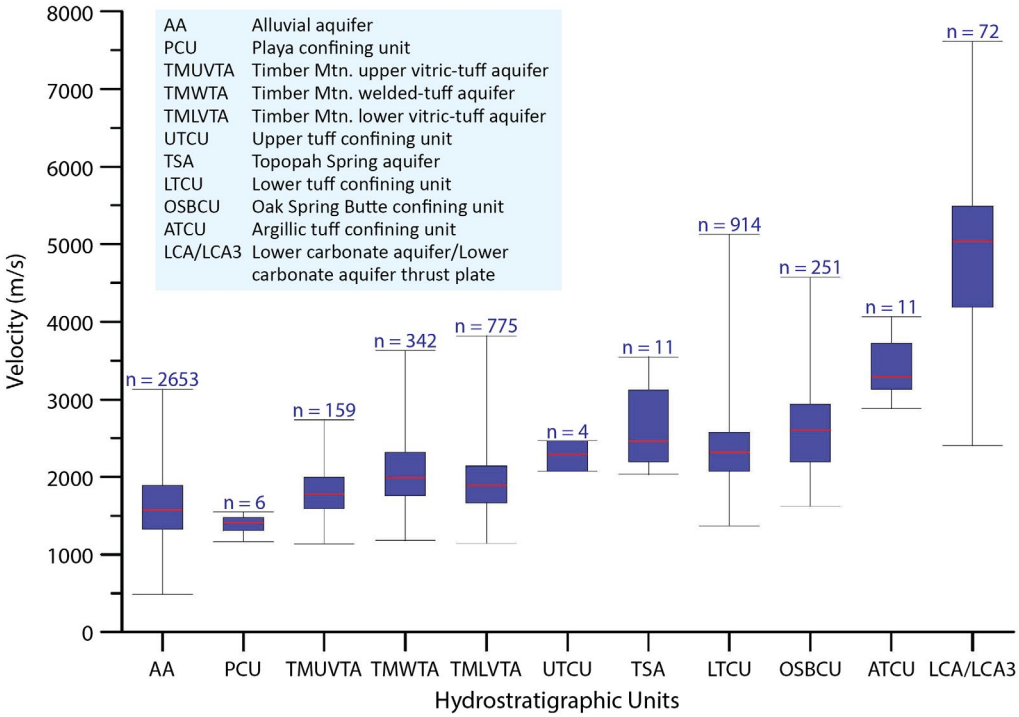

Figure 3. Box-whisker plot of selected HSUs from the Yucca Flat HFM showing velocity heterogeneity within the rocks beneath Yucca Flat; n values indicate measurement counts for particular HSUs

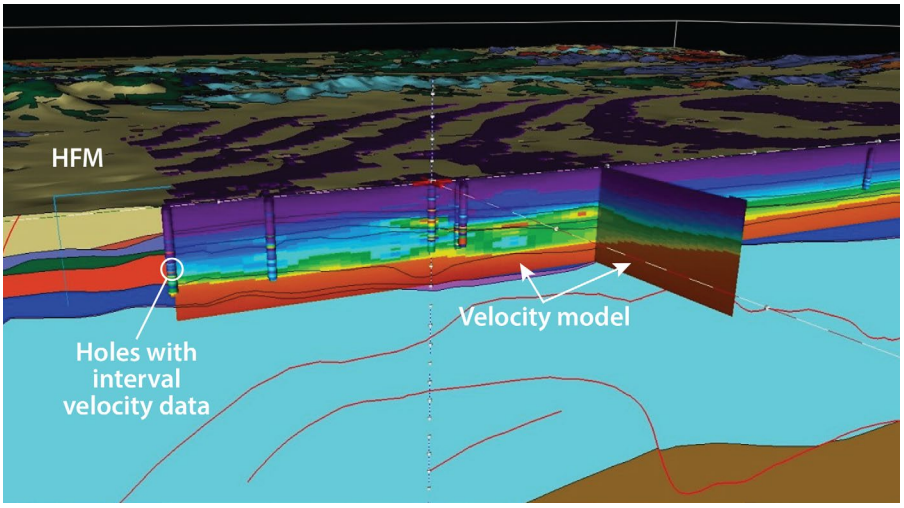

Figure 4. Profiles of the preliminary velocity model superimposed onto the Yucca Flat HFM indicate that this method will be useful in evaluating 3-D distribution of velocities beneath Yucca Flat. For reference, the velocity model panels are 1000 m tall.

north-south preferred orientation, they also have the potential to create anisotropy with respect to some aspects of seismic-wave propagation. The inclusion of 178 faults in the Yucca Flat seismic-attribute model will allow modelers to test the effects of these important and common geologic features on seismic wave propagation.

Collapse Chimneys and Damage Zones

Another potential complicating factor in modeling seismic wave propagation in Yucca Flat is the presence of features associated with individual UNEs that may contain locally altered or damaged rocks, resulting in local zones with seismic properties different than those same rocks in their undamaged state.

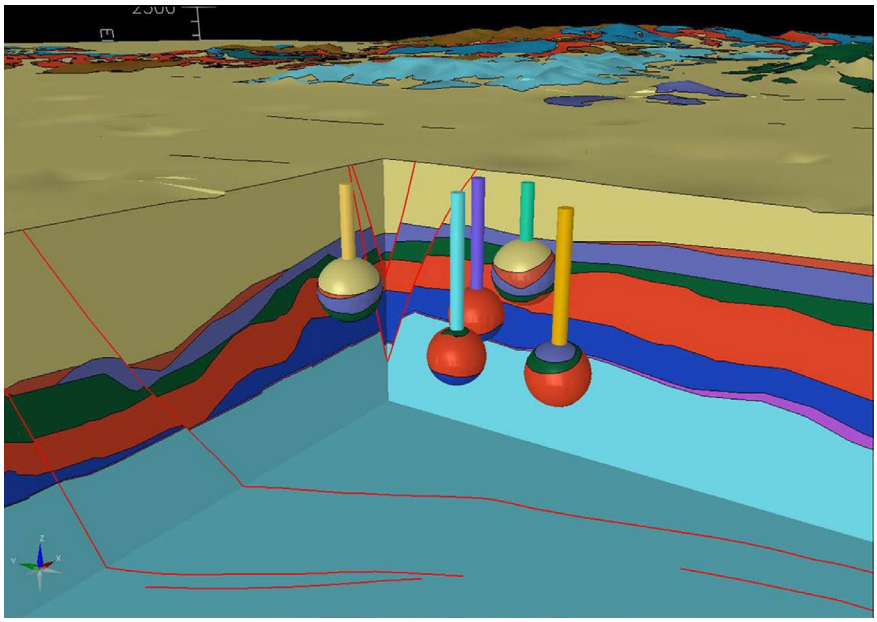

Figure 5. Cutaway 3-D perspective view of the Yucca Flat HFM showing how collapse chimneys (vertical columns) and damage zones (colored spheres) will appear in the Yucca Flat seismic-attribute model. For reference, the light-blue column is ~500 m tall.

The rubble chimneys that form above the WP region when the cavity created by a UNE collapses, and the damage zones that surround the WP region can affect the character of seismic waves as they pass through these features. Carroll (1983) discussed the measured changes in velocity associated with damage to the rock from passage of the stress wave from a UNE. Reductions in shear wave velocities are primary indicators of this damage, but changes in P-wave velocity may also be observed very close to the collapse chimney. Carroll (1983) mainly worked in volcanic tuff, but it may be that similar changes occur in alluvium and other rock types beneath Yucca Flat.

Because sites of expended UNEs are densely clustered in many places in Yucca Flat, the demarcation of individual collapse chimneys and WP-region damage zones associated with Yucca Flat UNEs could be an important addition to any framework model used for seismic wave propagation modeling. Fortunately, all the specifications necessary to digitally construct in 3-D each of these individual elements for all the UNEs in Yucca Flat are publicly available (Figure 5).

Conclusion

Analyses of the field-scale seismic data collected for this investigation indicate that most HSUs in the Yucca Flat HFM directly correspond to SSUs. Therefore, with relatively minor modifications, the UGTA Yucca Flat HFM should function as a 3-D seismic-attribute framework model, and be a valuable tool for studying more precisely seismic wave propagation in Yucca Flat. Modifications to some HSUs by splitting them into more than one unit and restricting some HSUs to include only certain portions (e.g., the interior portion) will result in more precise SSUs and a better seismic-attribute framework model. Developing a 3-D velocity model using the down-hole seismic data within the framework of the current HFM will allow identification of lateral velocity changes in HSUs across Yucca Flat. Modifications of HSUs that show significant lateral velocity changes into separate SSUs will also improve the framework model. Modeling collapse chimneys and damage zones associated with past UNEs in Yucca Flat as separate model elements that can be independently parameterized will improve the framework model, particularly in areas with dense clusters of UNEs.

In the second year of this project, we will construct the velocity model using the interval velocity data we compiled this year. Based on the analysis of the velocity model and FY 2014 results, we will modify the Yucca Flat HFM so that it functions as a seismic-attribute

framework model. We will then incorporate the collapse rubble chimneys and WP damage zones to enhance the functionality of the model.

Acknowledgments

We would like to thank Cathy Snelson and Steve Molnar for their contributions to this work.

References

Auer, M., M. K. Prior, "A new era of nuclear test verification," *Physics Today* **67**, 9 (September 2014) 39–44.

Bechtel Nevada, *A Hydrostratigraphic Model and Alternatives for the Groundwater Flow and Contaminant Transport Model of Corrective Action Unit 97: Yucca Flat–Climax Mine, Lincoln and Nye Counties, Nevada*, DOE/NV/11718--1119, Bechtel Nevada, Las Vegas, Nevada, January 2006.

Caine, J. S., J. P. Evans, C. B. Forster, "Fault zone architecture and permeability structure," *Geology* **24**, 11 (1996) 1025–1028, http://geology.gsapubs.org/content/24/11/1025, accessed October 1, 2014.

Carroll, R. D., "Seismic velocity and postshot properties in and near chimneys," in *Proceedings of the Monterey Containment Symposium, Monterey, CA, August 26–28, 1981*, B. C. Hudson, E. M. Jones, C. E. Keller, C. W. Smith, eds., LA-9211-C, Vol. 1, Los Alamos National Laboratory, Los Alamos, New Mexico, February 1983, 379–396.

Navarro-Interra, *Phase I Flow and Transport Model Document for Corrective Action Unit 97: Yucca Flat/Climax Mine, Nevada National Security Site, Nye County, Nevada*, N-I/28091-080. Navarro-Interra, LLC, Las Vegas, Nevada, September 2013.

Snelson, C. M., R. E. Abbott, S. T. Broome, R. J. Mellors, H. J. Patton, A. J. Sussman, M. J. Townsend, W. R. Walter, "Chemical explosion experiments to validate a new paradigm for nuclear test monitoring," *Eos, Trans., American Geophysical Union* **94**, 27 (July 2013) 237–239.

This page left blank intentionally

PHOTONICS

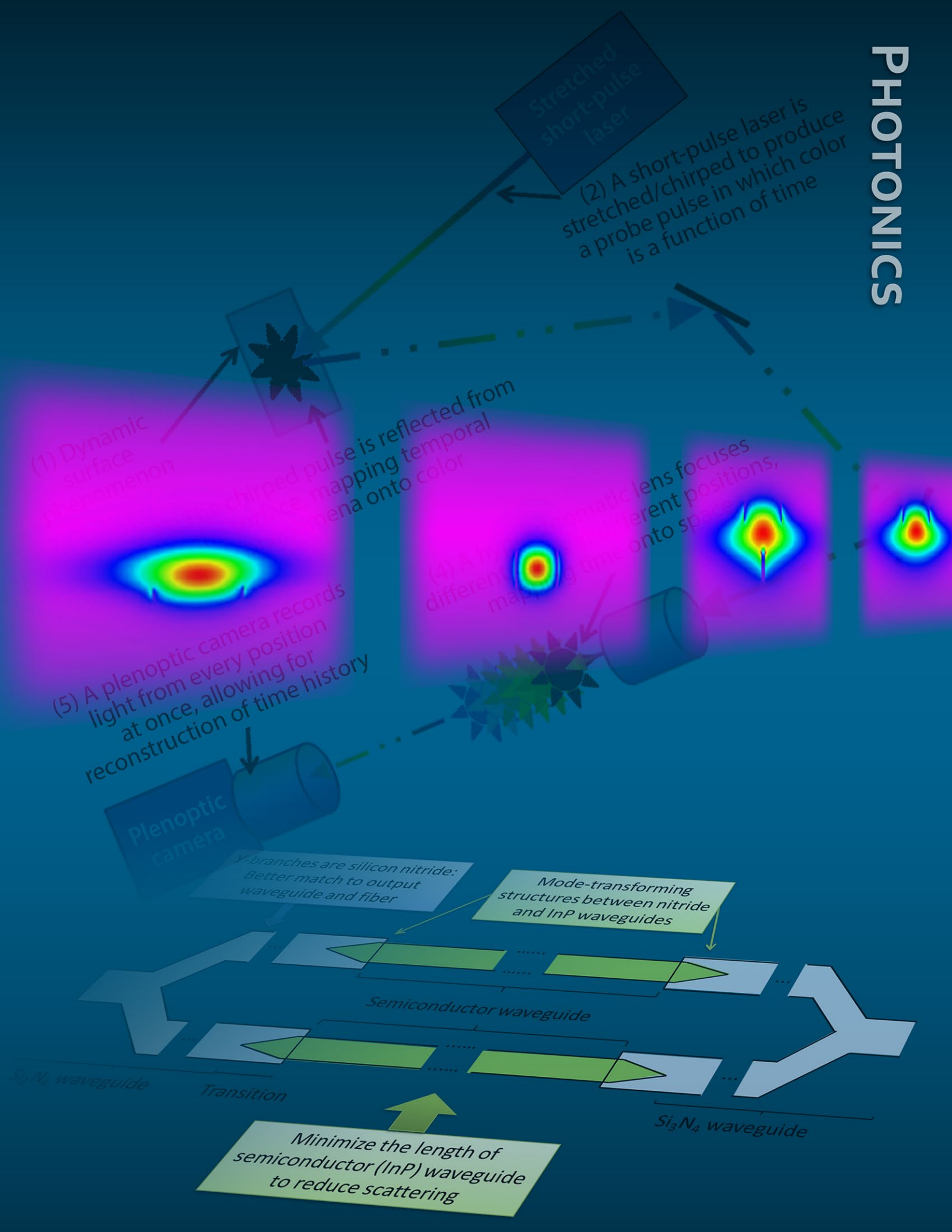
Stretched short-pulse laser
(2) A short-pulse laser is stretched/chirped to produce a probe pulse in which color is a function of time
(1) Dynamic surface phenomenon
chirped pulse is reflected from
mapping temporal
ena onto color
matic lens focuses
erent positions,
onto sp
(5) A plenoptic camera records light from every position at once, allowing for reconstruction of time history
Plenoptic camera
Y-branches are silicon nitride: Better match to output waveguide and fiber
Mode-transforming structures between nitride and InP waveguides
Semiconductor waveguide
Si_3N_4 waveguide
Transition
Si_3N_4 waveguide
Minimize the length of semiconductor (InP) waveguide to reduce scattering

Ultrafast All-Optical Framing Technology

LAO-02-13 | Continued in FY 2015 | Year 2 of 3

Daniel Frayer,[1,a] Gene Capelle,[b] and Aaron Bernstein[c]

Current methods of recording multiple-frame images at short timescales are limited by electro-optic tube physics and radiometry. We developed a novel all-optical methodology for the capture of a high number of quasi-continuous effective frames of 2-D data at very short timescales (from less than 10^{-12} to more than 10^{-8} seconds), with potential improvement over existing framing camera technology in terms of short recording windows and effective number of frames. Our concept combines a chirped laser pulse that encodes temporal phenomena onto wavelength, a strong hyperchromatic lens to map wavelength onto axial position, and a recording technology, such as holography or plenoptic imaging, to capture the resultant focal stack in both spatial (imaging) and longitudinal (temporal) axes. A subcontract for modeling and experimentation was completed with The University of Texas at Austin, and a procurement issued to Raytrix GmbH for modification of their plenoptic algorithm. The lens designed and fabricated in our first year was further characterized and employed to capture simulated data. A separate method for creating a discretized chirped pulse of arbitrary duration was invented. The work will continue in FY 2015 via experimental work with the new chirped-pulse methodology, algorithm development, and experimentation. If these efforts are successful, we will combine this methodology with the Lawrence Livermore National Laboratory's grating-actuated transient optical recorder (GATOR) scheme for imaging soft x-ray radiation.

[1] frayerdk@nv.doe.gov, 505-663-2090
[a] Los Alamos Operations; [b] Special Technologies Laboratory; [c] Center for High Energy Density Science, The University of Texas at Austin

Background

A number of methodologies are currently available for capturing optical phenomena at ultra-short timescales (less than 1 ns), but they suffer from a number of limitations. The temporal resolution of framing cameras employing electro-optic tubes is limited by tube physics, in the case of single-tube imaging, and radiometry, in the case of multiple-path configurations utilizing either tubes or microchannel plates. The temporal resolution of electro-optic streak cameras can be substantially higher, but with the loss of an entire dimension of spatial data. Recent innovations using different phenomena offer improvements over these methods. Time-resolved imaging of non-repeating events with a megahertz frame rate, using a broad-spectrum illumination source and dispersive optics, has been demonstrated by Goda (2009); time-resolved imaging of repeating phenomena with picosecond resolution, using an ultra-fast streak camera in a time-of-flight configuration, has been demonstrated by Velten (2011). The viability of a methodology for recording a pair of frames with 50 fs spacing has been demonstrated by Günther (2011). As of the beginning of the second year of this project, we were unaware of any method for obtaining multiple-frame 2-D optical information at better than nanosecond timescales. However, in August

2014 Nakagawa (2014) published a methodology that employs a discretized chirped laser in combination with beam splitters and an imaging sensor to actively illuminate and record multiple frames of femtosecond phenomena.

We have developed a novel all-optical methodology for the capture of a high number of quasi-continuous effective frames of 2-D data at very short timescales (from less than 10^{-12} to more than 10^{-8} seconds), with potential improvement over existing technologies in terms of short recording windows and number of frames, for specific application in light-matter interaction studies and potential application in focused studies of dynamic materials. This methodology combines three essential components: (1) A chirped laser pulse actively illuminates dynamic phenomena, mapping temporal information onto wavelength. (2) A strong hyperchromatic lens, designed to maximize the change in the position of its focus as a function of incident illumination wavelength, images this laser light to create a focal stack of images of the experiment, such that each narrow slice along the optical axis contains an image from a narrow slice of time. (3) A 3-D recording technology captures the resultant focal stack with axial position information in toto; this technology may be a plenoptic camera or a hologram (digital or film), as imaging such a focal stack with a standard intensity-recording camera would result in substantial loss of temporal resolution. The lens and recording mechanism are here envisioned as, over the length of the recorded phenomena, agnostic to time, as the temporal characteristics are dependent only on the illumination source. The scheme is illustrated in Figure 1.

Although our methodology bears resemblance to that developed by Nakagawa, our use of a diffraction-limited hyperchromatic lens (rather than high-f-number optics and beam splitters) is expected to result in potentially improved spatial resolution, and the employment of a 3-D recording mechanism (rather than either multiple image sensors or a single long sensor) in potentially improved temporal resolution. In the last decade, optical systems in which wavelength is correlated with axial position have been employed in several fields, including confocal microscopy (Garzón 2004, Carrasco-Zevallos 2011, Hillenbrand 2012a), topography (Mikš 2007), and hyperspectral imaging (Hillenbrand 2012b). However, to our knowledge, our methodology is the first to employ hyperchromats in ultrafast imaging. Additionally, published work in the area of hyperchromatic lenses has tended to employ fairly simple optical designs with, for our purposes, low longitudinal chromatic aberration. As such, we expected a final design of substantially higher complexity.

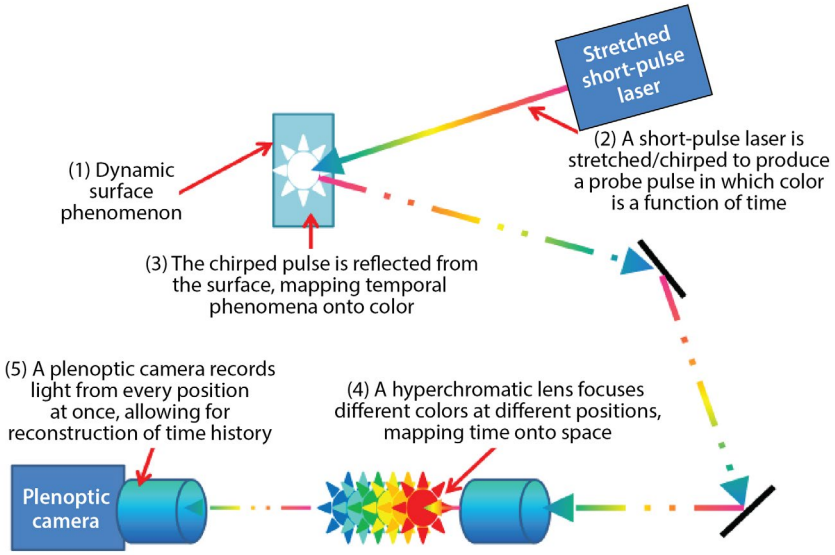

Figure 1. The described experimental and recording methodology for the ultrafast all-optical system

Project

During this project's first year (Frayer 2014a), the three described components of the technology (hyperchromatic lens, chirped laser, and recording system) followed three separate, parallel paths of inquiry: (1) Design and fabrication of the hyperchromatic lens resulted in a final system design with a peak longitudinal chromatic aberration of nearly 9 mm/nm, more than 30 times higher than that achievable with glass dispersion alone, and a high degree of linearity at the peak. This very high dispersion means that the system only requires 5 nm of input illumination bandwidth; as a point of reference, the optical system will image an object illuminated by the entire visible spectrum along more than 1.5 meters of distance on the optical axis. A complete description, including the dispersion curve for the final system and the complex optical design, are available (Frayer 2014b). (2) Investigation into the availability of laser sources with appropriate center wavelength, spectral shape, and spectral width concluded that no commercial systems are available with the required characteristics, but these requirements could be met by a large research-grade laser facility already employing pulse chirping in chirped-pulse amplification. (3) Investigation into recording methods found four possibilities: focusing plenoptic imaging, non-focusing plenoptic imaging, digital holography, and film holography. Of these, we determined that both sorts of holography would require substantial effort to develop hardware and reconstruction algorithms, and that non-focusing plenoptic imaging (such as that employed by cameras produced by Lytro, Inc., of Mountain View, California) would not allow for quantitative depth estimation or single-frame reconstruction, rendering temporal sequencing in the reconstruction algorithm challenging at best. Focusing plenoptic imaging, as employed in cameras produced by Raytrix GmbH of Kiel, Germany, was determined to offer the shortest and most likely path to whole focal-stack capture and quantitative temporal sequencing. We purchased a custom R29 camera from Raytrix in the same year.

The second year of this project saw investigation along the following parallel lines: (1) We worked with laser physicists and manufacturers to investigate alternatives for laser sources and also developed a novel technique for producing discretized quasi-chirped pulses. (2) We investigated modes of extending our methodology into non-active illumination experiments. (3) We initiated a collaborative effort with The University of Texas at Austin (UTA), and conducted preliminary experiments towards validation of the methodology. (4) We worked intensively with Raytrix GmbH in enabling modification of their reconstruction algorithm to allow for determining single axial (read: temporal) slices out of the recorded focal stack for temporal sequencing.

Early in FY 2014, we began communications with a network of laser manufacturers and subject matter experts in laser physics to determine a path forward for an active illumination source having >5 nm of bandwidth, a chirped pulse duration of >1 ns, and >10 µJ/pulse, with as low a repetition rate as feasible. These requirements were derived from the hyperchromatic lens design and R29 camera specifications. We iteratively refined requirements and proposed new lasing and chirping schemes to the experts and manufacturers. Two especially promising new schemes were proposed: (1) chirping 1550 nm pulses using high-dispersion optical fiber, followed by nonlinear tripling and then amplifying the chirped pulses, and (2) chirping 1064 nm pulses using specialized high-dispersion fiber, followed by nonlinear doubling and then amplifying the pulses. It should be noted that neither scheme has ever, to the best of our knowledge, been used in an actual laser system. The first option was ruled out; although the chirping would be the most straightforward, as telecom components are widely available at this wavelength, energy requirements could not be met using available amplification technology. The second option, however, resulted in a statement of viability and estimate from Calmar Laser of Palo Alto, California. Calmar proposed a new system resulting in single-shot 532 nm center-wavelength

pulses with a duration of approximately 5 ns, 100 μJ of energy per pulse, and a mode profile of approximately 1.4.

Along with these efforts, we developed a novel method for producing quasi-chirped pulses with the additional advantage of discretization. In this scheme, a short-pulse pump laser is focused with a lens into a line on an optically transparent vessel filled with a dye solution in a solvent at the appropriate concentration for lasing; the dye is chosen to give the desired output wavelength range, and the pump wavelength is chosen accordingly for efficient dye pumping. This dye laser operates in an untuned mode such that its spectral line width is broad. Output from the dye laser is optically focused onto the slit of an imaging spectrograph. A linear fiber array positioned at the spectrograph output image plane is adjusted to center the light on the array. At the other end of the fiber bundle, each fiber is separately terminated and connectorized. Fiber extensions of varying lengths are connected to each of the fibers such that each fiber along the linear array is incrementally longer than the previous fiber; thus, the transit time of light in each successive fiber is longer than that in its previous neighbor. The discrete fibers of varying lengths mimic a high-dispersion element while producing sub-pulses that are discrete in both time and wavelength. Alternately, the fiber array may be composed of fibers of varying lengths arranged similarly. At their output end these fibers are bundled in a close-packed or similar arrangement, possibly in a single connector or mounting fixture. Optical output from the output bundle can then be used to actively illuminate a dynamic experiment, with or without additional optics, or the bundle can be butt-coupled to a short length of large-core (large enough to accept the outputs of all the fibers) fiber to mix the outputs and transport the quasi-chirped pulse train. The single, final output is the desired chirped pulse. This scheme is illustrated in Figure 2.

We sustained a small effort to extend the usefulness of the ultrafast recording technology into regimes of passive illumination. We investigated the possibilities of using nonlinear optical components to map a passive optical onto the described chirped pulse, and using the radoptic effect to map a passive soft x-ray signal onto the pulse. Although the first option is similar to a technique demonstrated at Lawrence Livermore National Laboratory (LLNL) to map a time-varying signal, employing it while preserving spatial information would require nonlinear crystals and laser fluxes substantially above what is physically possible. The second option is conceptually similar to the grating-actuated transient optical recorder (GATOR) technology developed by LLNL under an LDRD project as a potential diagnostic for the National Ignition Facility (Meissner 2010, Baker 2011). GATOR uses the radoptic effect to modulate the refractive index of a thin semiconductor slab through a machined grating, producing a modulation in the material index corresponding to x-ray image information; illumination

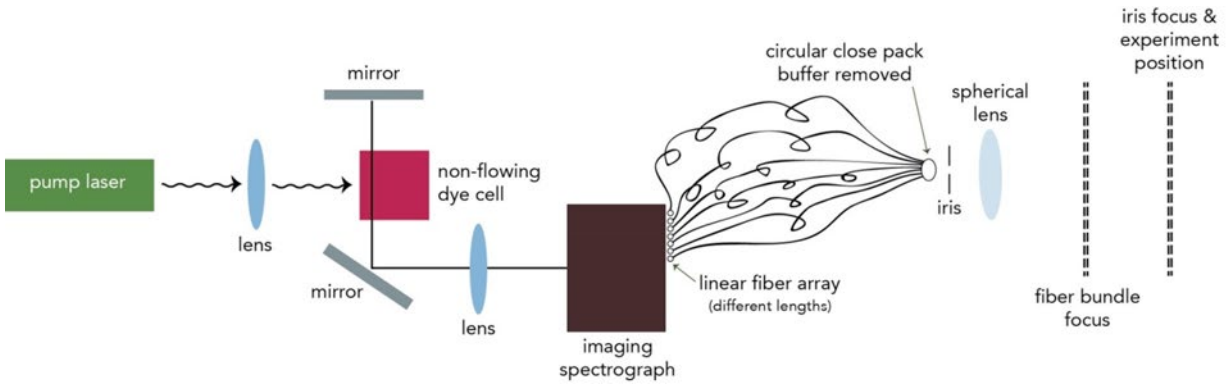

Figure 2. A novel scheme for discretized chirped pulses uses a broad dye source, a grating to separate wavelengths, and a linear fiber array with fibers of different lengths, thereby creating a discretized pulse train

light incident on the back of the induced grating is then diffracted to a recording device, which is, in our scheme, the hyperchromatic lens and Raytrix camera. We believe that should our current methodology prove viable, it should be possible to extend this scheme into ultrafast soft x-ray imaging via combination with a GATOR front-end, and Steve Vernon's group (who developed GATOR) has expressed interest in collaboration.

Throughout the course of FY 2014, we worked continually with the Center for High Energy Density Science at UTA and Raytrix GmbH to establish needs and requirements and conduct research under the aegis of these collaborations. Early in the year, needs, requirements, and capabilities were communicated sufficiently to establish non-disclosure agreements between NSTec and each entity. As mentioned previously, the Raytrix technology was determined to offer the best and most likely course to project success. Raytrix's developed reconstruction software assumes that the recorded scene is opaque and spatially unique (i.e., each point in (x,y) contained data only at a unique (z) position); although company representatives expressed confidence that modifying the algorithm to enable use of the hyperchromat should be possible, the path to success required a substantial rewrite of their reconstruction algorithm. Although we initially expected delivery in FY 2014, as of this writing, the company is still working on the algorithm.

We chose to collaborate with UTA due to their expertise in lasers and high energy–density science, and the operation of several high-energy configurable lasers on-site. These lasers are used to generate pump beams that cause materials to undergo expansion under extreme temperatures and pressures, as well as probe beams to interrogate these dynamic materials. It should be noted that UTA considers the possible applications for our methodology as an exciting prospect, given the persistent significant challenge to obtain highly time-resolved and multiframe 2-D information of dynamic experiments in the laboratory. Investigators currently must repeat experiments, changing the delay of a single probe pulse, in hopes of performing experiments sufficiently consistently to determine repeatable temporal dynamics of the system. This approach is only as effective as the repeatability of the system, and because measurements are of dynamics initiated using laser-plasma interactions, shot-to-shot variations in the laser pulse significantly increase errors. Multiframe 2-D information over a nanosecond timescale would immediately improve laser experiment measurements.

Because UTA's two primary laser facilities were undergoing routine maintenance and were unavailable, we focused on experiments to obtain representative data on their Texas High-Intensity Optical Research Laser (THOR) beam line operating at 800 nm, rather than collecting ultrafast physics data. Here, we recorded data with light from THOR, as well as using a 532 nm laser and a 10 nm bandwidth LED centered at 532 nm. Experiments were performed in the THOR laser room. Several experiments were performed with this setup. For the purposes of this report, we describe the dedicated probe beam developed to examine laser-plasma interactions initiated by the fully amplified THOR laser beam. This probe line was developed specifically for experiments using the hyperchromat lens, and it has a ~1 ns duration and bandwidth up to 50 nm, essential due to the hyperchromat's chromatic inefficiency at 800 nm. The pulse for this line was taken as a portion of the energy of the beam just after a Ti:Sapphire 6-pass amplifier stage, where the beam has the smoothest spatial profile and lowest energy fluctuation in the system. The probe beam was picked off from the laser without perturbing the rest of the beam, so that full amplification of the laser to full energy is still possible for conducting full-energy laser-plasma experiments.

In the final optical configuration, both lasers were aligned colinearly using a dichroic beam splitter, focused onto a 1951 USAF resolution target, collimated using a Nikon photographic lens and directed onto a diffraction grating, refocused onto the object plane of the hyperchromatic lens, and finally imaged using the R29 camera. The diffraction grating was rotated to align 800 nm light or 532 nm light into the

hyperchromat as needed. An image of the final experimental configuration (minus the THOR system) is shown in Figure 3, and images captured using the two visible illumination sources are shown in Figure 4. The THOR laser was not optimized and did not produce sufficient light to overcome the lower dispersion of the hyperchromat and the lower quantum efficiency of the R29 camera and produce good data. The captured data were relayed to Raytrix for the algorithm development effort.

In 2014 UTA developed a solid-target interaction chamber and beam line with a designated diagnostics area. A region has been set aside for including the hyperchromat among other key experimental diagnostics. The THOR laser and this target chamber is an optimal testing ground for the hyperchromat, as UTA is initiating a variety of laser-target interaction experiments that will probe high temperature and pressure dynamic material expansion experiments over a 1 ns timescale. The setup currently in the laser room is staged for eventually diagnosing experiments in the laser-solid interaction chamber. However, even in its present configuration in the laser lab, the hyperchromat could in fact be used to interrogate an ultrafast experiment, even if executed in air, of expanding laser plasma plumes in interactions driven by the uncompressed energetic THOR laser pulse.

FY 2013 and FY 2014 efforts resulted in one publication at SPIE (Frayer 2014b). The project was awarded a third year of funding for FY 2015. We hope to finalize

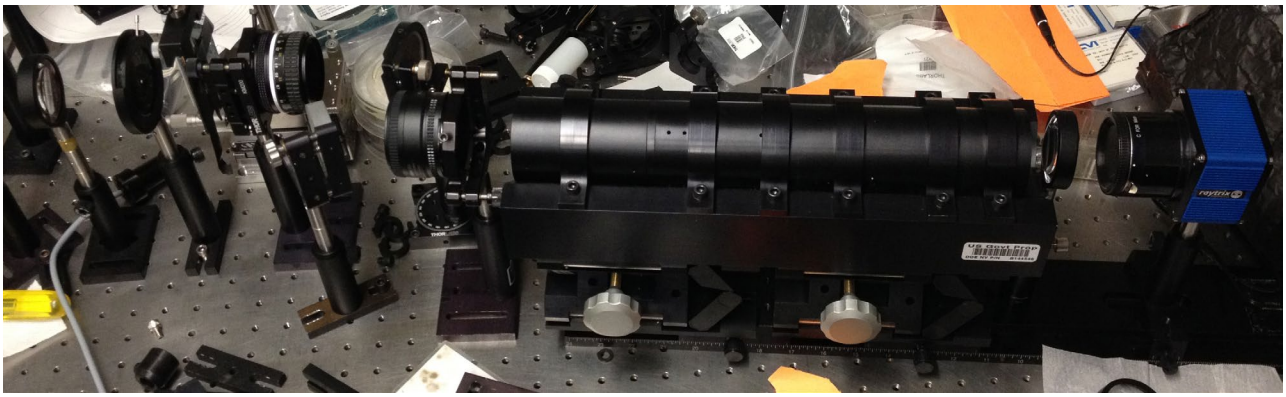

Figure 3. Optical system configuration at UTA. 800 nm light enters from bottom left and ends at the R29 camera on the right. The system is shown with an additional relay optic between the hyperchromat and the R29 camera.

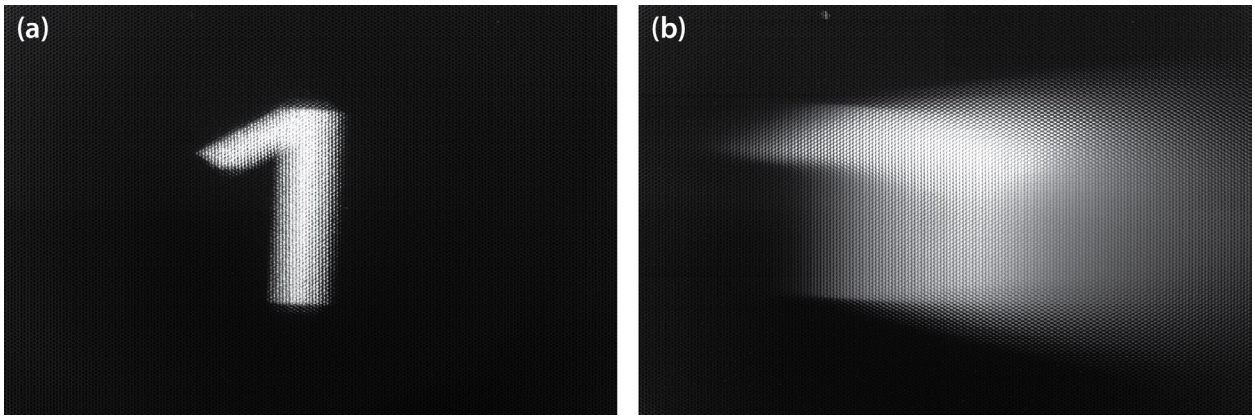

Figure 4. Representative data: (a) image of the number 1 under illumination at a single wavelength at UTA and (b) under 10 nm of incident illumination. Not apparent is recorded depth for images of discrete wavelengths in the broad-spectrum image.

algorithm development with Raytrix, demonstrate the methodology, and record physics data at Special Technologies Laboratory and in collaboration with UTA, and potentially collaborate with LLNL in a time-resolved soft x-ray imaging system experiment, using our system for data collection.

Conclusion

During the second year of this project, we investigated alternatives for laser sources and developed a novel technique for producing discretized quasi-chirped pulses. We explored ways to extend the described methodology into non-active illumination experiments. A collaborative effort with UTA was initiated, and preliminary experiments towards validation of the methodology were conducted. Finally, we worked closely with Raytrix GmbH to enable modification of their reconstruction algorithm, which is essential for temporal sequencing. Investigation in FY 2015 will wrap up these individual efforts as well as seek demonstration of the discretized pulse technique at STL.

Acknowledgments

We would like to thank Christian Perwass of Raytrix GmbH; Kristina Brown, Alden Curtis, and Morris Kaufman of NSTec, Los Alamos Operations; and Rachel Haynes of NSTec, Special Technologies Laboratory, for their significant contributions to this effort.

References

Baker, K., R. Stewart, P. Steele, S. Vernon, W. Hsing, S. Haynes, "An ultrafast x-ray diagnostic suite for burning plasmas," *APS Meeting Abstracts* **1** (2011).

Carrasco-Zevallos, O., R. L. Shelton, C. Olsovsky, M. Saldua, B. E. Applegate, K. C. Maitland, "Exploiting chromatic aberration to spectrally encode depth in reflectance confocal microscopy," *Proc. SPIE* **8086** (2011) 80861D.

Frayer, D., "Ultrafast all-optical framing technology," in *Site-Directed Research and Development*, FY 2013, National Security Technologies, LLC, Las Vegas, Nevada, 2014a, 207–213.

Frayer, D. K., M. I. Kaufman, G. A. Capelle, "A hyperchromatic lens for recording time-resolved phenomena," *Proc. SPIE* **9193** (2014b) 91930X.

Garzón R. J., J. Meneses, G. Tribillon, T. Gharbi, A. Plata, "Chromatic confocal microscopy by means of continuum light generated through a standard single-mode fiber," *J. Opt. A: Pure Appl. Opt.* **6**, 6 (2004) 544.

Goda, K., K. K. Tsia, B. Jalali, "Serial time-encoded amplified imaging for real-time observation of fast dynamic phenomena," *Nature* **458** (2009) 1145–1149.

Günther, C. M., et al., "Sequential femtosecond x-ray imaging," *Nature Photonics* **5** (2011) 99–102.

Hillenbrand, M., B. Mitschunas, C. Wenzel, A. Grewe, X. Ma, P. Feßer, M. Bichra, S. Sinzinger, "Hybrid hyperchromats for chromatic confocal sensor systems," *Advanced Optical Technologies* **1**, 3 (2012a) 187–194.

Hillenbrand, M., A. Grewe, M. Bichra, B. Mitschunas, R. Kirner, R. Weiß, S. Sinzinger, "Chromatic information coding in optical systems for hyperspectral imaging and chromatic confocal sensing," *Proc. SPIE* **8550** (2012b) 8550D.

Meissner, C., "High-speed imager for fast, transient events at NIF," *Sci. Tech. Rev.* Oct./Nov., 2010, https://str.llnl.gov/OctNov10/hsing.html, accessed October 1, 2014.

Mikš, A., J. Novák, P. Novák, "Theory of chromatic sensor for topography measurements," *Proc. SPIE* **6609** (2007) 66090U.

Nakagawa, K., et al., "Sequentially timed all-optical mapping photography (STAMP)," *Nature Photonics* **8** (2014) 695–700.

Velten, A., R. Raskar, M. Bawendi, "Picosecond camera for time-of-flight imaging," *Imaging Systems Applications*, July 10–14, 2011, Optical Society of America, Toronto, Canada (2011).

This page left blank intentionally

Ultra-High-Sensitivity Electro-Optic Links

STL-32-14 | Continued in FY 2015 | Year 1 of 2

E. Kirk Miller,[1,a] Kevin Lee,[a] and Eric Larson[a]

The goal of this project is development of fieldable electro-optic data links with enhanced sensitivity to small analog voltage inputs. As our first approach, we made progress this year on reducing the optical insertion loss of ultra-sensitive electro-optic modulators being developed at the University of California, Santa Barbara. For these devices, optical mode-transforming structures effectively reshape the optical mode to improve coupling from the optical fiber through to the semiconductor waveguide with its high aspect–ratio mode. Our second approach involved conventional modulators, in which we used frequency domain techniques to demodulate the phase shift of the carrier light; such a phase shift can result from a voltage input into a conventional phase modulator or from radiation incident on the fiber during a radiation-generating experiment. We further present existing state-of-the-art detection limits and our ongoing efforts to detect smaller signals at bandwidths suitable for pulsed-power experimentation.

[1] millerek@nv.doe.gov, 805-681-2237
[a] Special Technologies Laboratory

Background

Current fiber-optic links commonly use Mach-Zehnder (M-Z) modulators, for which drive voltages are typically 3–5 V. Recent processing developments, such as those by Professor Nadir Dagli's group at the University of California, Santa Barbara (UCSB), have demonstrated drive voltages below 0.5 V, opening up a new regime of sensitivity to small signals. However, these modulators have neither been used commercially nor for experimentation in the complex.

Diagnostics currently struggling with small signals in noisy environments include electrical conductivity measurements at the Joint Actinide Shock Physics Experimental Research (JASPER) facility, gamma and x-ray measurements at the National Ignition Facility (NIF) and the Sandia National Laboratories' Z machine, and RF recording systems used on high-explosives experiments at the NNSS. All of these measurements and experiments would benefit from the significant increase in sensitivity from a new generation of optical modulators for long-distance data transmission along low-cost, lightweight, fiber-optic cable systems.

Our ultimate goals are to be able to detect small voltages output from detectors of various types and relay those signals via fiber-optic cables to remote digitizers. The current systems employed at various sites across the complex are capable of noise floors of ~2 mVpp at 100 MHz up to 20 mVpp at 10 GHz. A diagram of noise-floor values plus associated applications is shown in Figure 1.

Project

In the first year of this project, we pursued two approaches to improving sensitivity to small signals. First, we teamed with UCSB to accelerate development of high-sensitivity M-Z modulators based on a novel

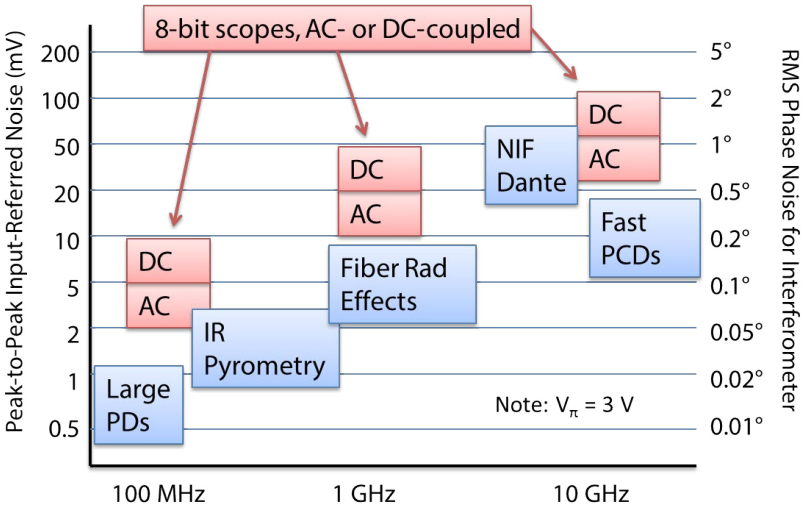

Figure 1. Current noise-floor values for M-Z systems, and associated applications

design, with the goal of transitioning this technology out of the lab for experimental use. Second, as a separate but complementary effort, we investigated demodulation schemes that use frequency domain detection techniques often used in radar systems to recover very faint signals. This report details both of these efforts.

UCSB Collaboration on High-Sensitivity M-Z Modulators

Electro-optic modulators based on interferometers, such as M-Z modulators, are characterized by the voltage required to go from off to on (i.e., through π radians of phase); this on-off voltage is traditionally called V_π. Professor Dagli and his research group at UCSB have developed ultra low–V_π modulators with on-off voltages of <0.5 V, which is encouraging for transducing small voltages to modulated light levels that can be recorded. Practically, however, the modulators suffer from high optical-insertion loss of ~25 dB, meaning that very high optical-input power would have to be used, which limits the fieldability of the system. The measurement of the transfer function for a low-V_π modulator fabricated in Professor Dagli's group is shown in Figure 2. Driving only one arm of the interferometer gives V_π of 0.8 V; the device can also be driven differentially, thus reducing V_π to 0.4 V.

Collaborating with Professor Dagli's group, we worked on strategies to reduce the insertion loss. The first area for design improvement had previously been identified: coupling light from the delivery fiber to the semiconductor waveguide. This is a common hurdle for devices made from high-index semiconductors, as the waveguides tend to be much smaller than the cores of optical fibers used to couple light in and out. The common solution is to develop a structure that transforms the mode geometry from the input mode to the waveguide mode. Figure 3 shows the bench-test setup in Professor Dagli's lab at UCSB for characterizing M-Z performance. This setup is used primarily for low-frequency testing, but high-frequency test stands are also available at UCSB.

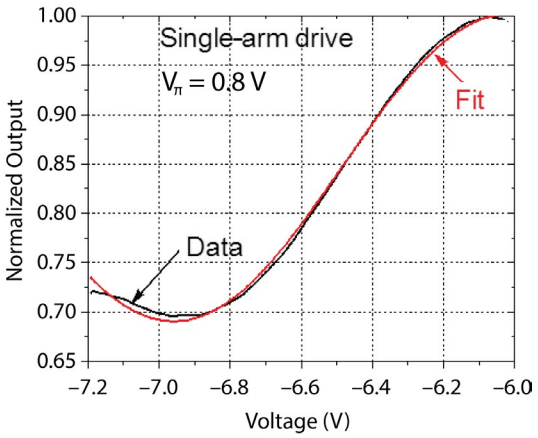

Figure 2. Transfer function measurement for a low-V_π M-Z modulator from UCSB

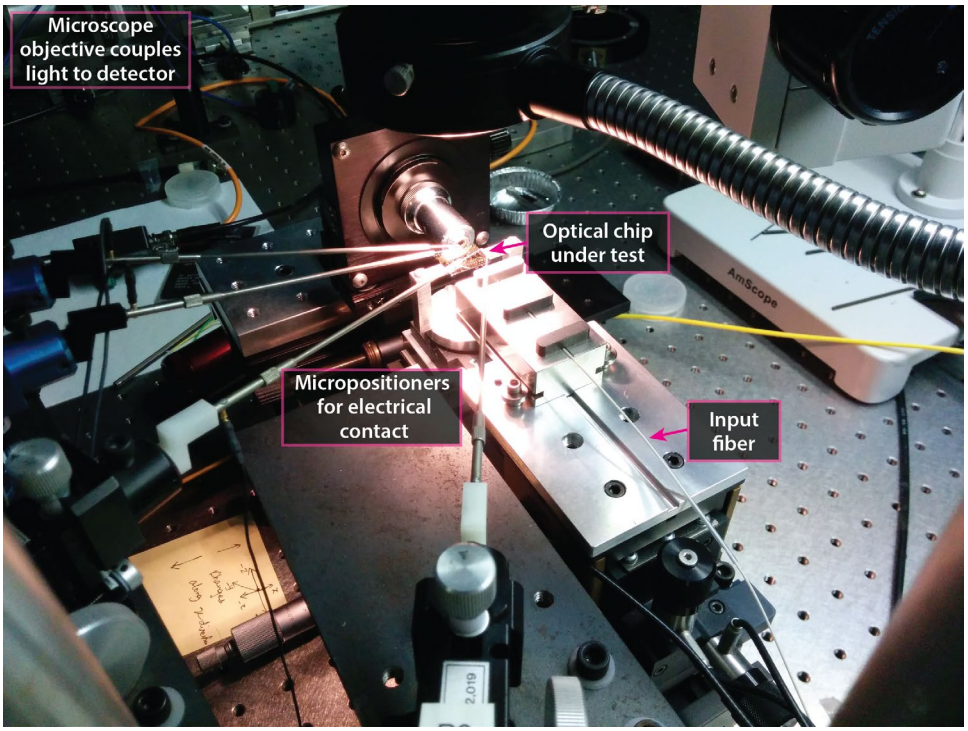

Figure 3. Bench-test setup at UCSB for characterizing M-Z performance

The mode-transformation from a high aspect–ratio indium phosphide (InP) semiconductor waveguide (green) to a silicon-nitride (SiN) waveguide (blue) is shown in Figure 4. The bisbenzocyclobutene (BCB) material is a polymer used to support the semiconductor structures after they are removed from their parent wafer, and the SiN is used to deliver light from the fiber to the electro-optically active semiconductor. Professor Dagli's group computed the mode-field distribution using the RSoft software package running on a dual-core Xeon workstation, with the goal of optimizing the geometry of the tapered semiconductor structure that would most efficiently couple the energy between the semiconductor and the lower index SiN.

We conceived of a second area for design improvement of the UCSB devices during the course of this year's effort: minimizing the path length in the semiconductor waveguide and reducing it to only that length required for electro-optic modulation. The loss in the semiconductor waveguide itself is a sensitive function of sidewall roughness, due to the high index refraction–contrast between the semiconductor and the BCB. While sidewall roughness can be reduced during processing, this often involves expensive electron-beam lithography rather than standard photolithography. Professor Dagli's group developed the idea of splitting and then transporting the light across the substrate using more forgiving waveguides made from SiN. Y-branches and waveguides made from SiN are known to be less lossy, in terms of dB/cm, than the semiconductor waveguides. The proposed structure in an M-Z modulator is shown in Figure 5.

Work on the UCSB M-Z design is ongoing, and we plan to package a fieldable device for testing in FY 2015.

Demodulation Using RF Techniques

In parallel with the effort at UCSB, we also developed techniques to measure very small optical phase shifts, because such phase shifts can be used to encode voltages from a radiation detector using an electro-optic phase modulator. Phase shifts can also result from ionizing radiation depositing energy in the transport fiber; the magnitude of the dynamic effect in SMF-28 fiber was measured at 1.54 radians/kRad/m (Miller 2007), so measuring effects on installed fibers

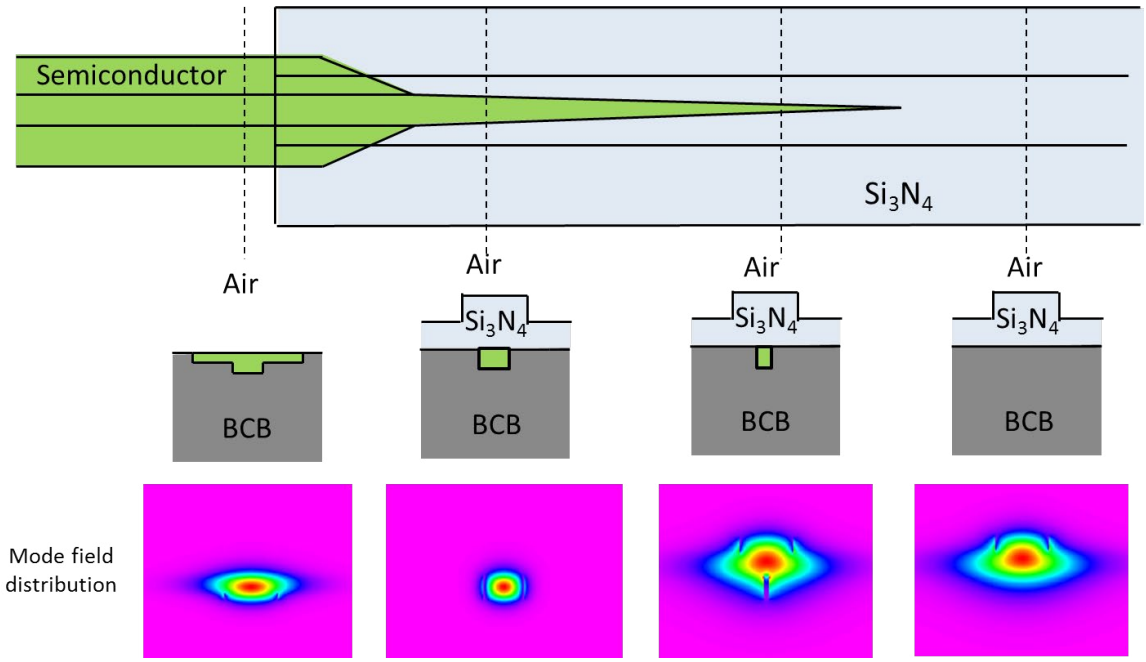

Figure 4. Mode transformation between a high aspect–ratio semiconductor waveguide (green) and a SiN waveguide (blue), together with the computed mode-field distribution patterns as calculated by the UCSB group

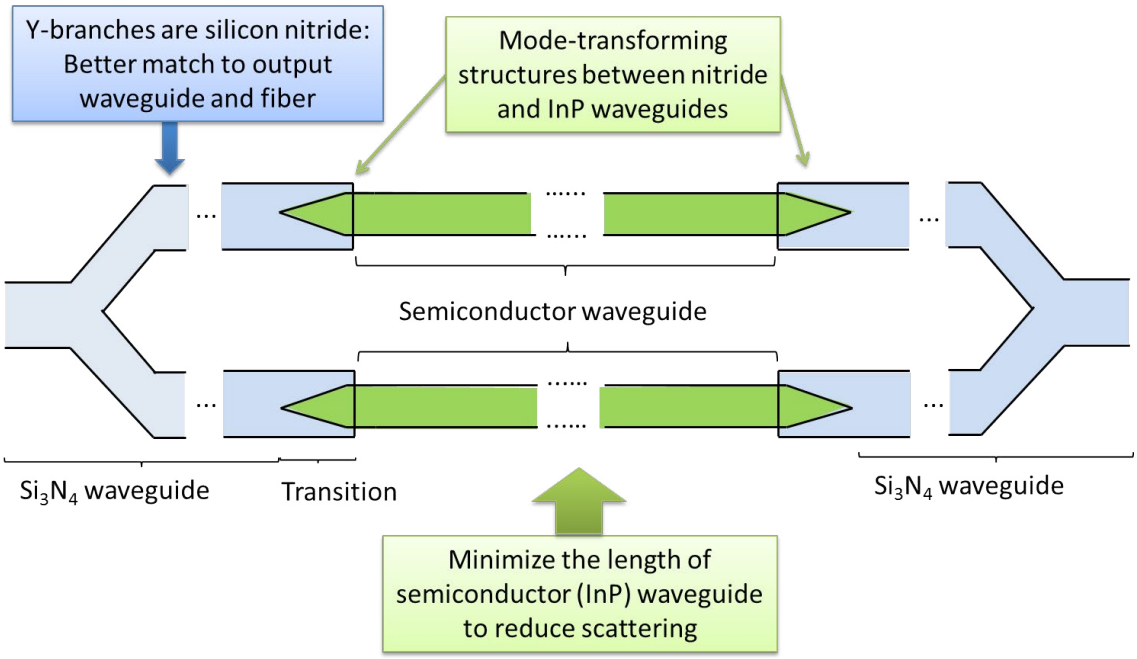

Figure 5. SiN waveguides coupled to semiconductor (InP) waveguides would reduce overall optical loss in this M-Z modulator configuration

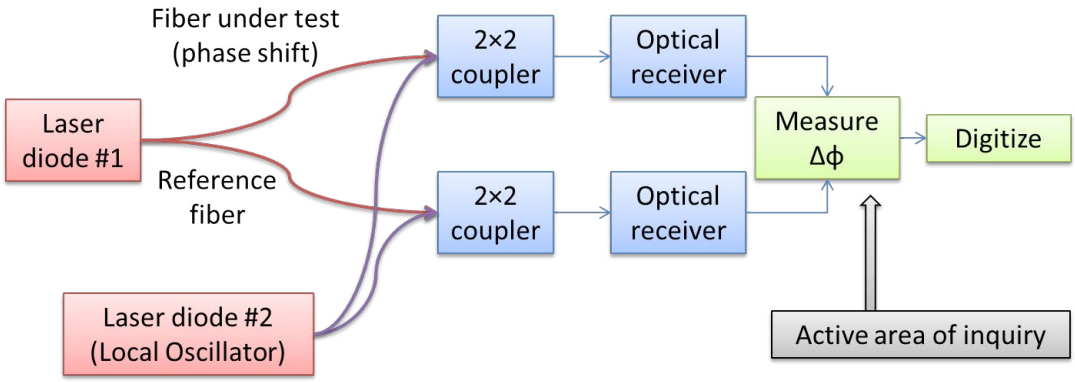

Figure 6. Heterodyne interferometer setup for measuring small phase shifts

at modern experimental facilities will require measurements of very small phase shifts in the milliradians range.

Each of the techniques we explored use heterodyne interferometers to transpose the DC signal up to RF frequencies ranging from 80 MHz up to many GHz. In one approach, we measured the phase difference between two interferometers: a reference interferometer and a "device-under-test" interferometer, which would include a phase modulator or a fiber in which we are testing for radiation effects. The basic configuration is shown in Figure 6, where the two laser diodes are tuned to create a beat frequency of typically 1–8 GHz. The crucial measurement is the heterodyne phase measurement, which is subsequently digitized.

We explored three devices for this heterodyne phase measurement: a conventional double-balanced mixer, a metal-semiconductor field effect transistor (MESFET) mixer, and a dedicated phase detector chip from Analog Devices, Inc. The operation of mixers as phase detectors is described in an application note from Mini-Circuits (2008) and in a tutorial by Enrico Rubiola (2008). The results of our preliminary tests are shown in Table 1.

The dedicated phase detector, AD8032 from Analog Devices, is robust to variation in the RF power. However, this detector has a noise floor that is not spectacular, and the output small-signal bandwidth is only 30 MHz. While transition times of ~10 ns are potentially useful for radiation-effects studies and lower-bandwidth diagnostics, the noise floor of the phase measurement precludes further pursuit at this time.

The two mixers, a Mini-Circuits ZMX-10G+ double-balanced mixer and a Hittite HMC483 MESFET mixer, showed more promise. The double-balanced mixer is a simple diode ring with an output (IF) bandwidth of 2 GHz in unsaturated mode. When run in saturation mode as a phase detector, the output bandwidth is reduced somewhat but is still much higher than other options we have considered. The MESFET mixer has a nominal output bandwidth of 350 MHz, though its RF/LO bandwidths are lower than the double-balanced mixer. In general, a higher RF/LO frequency should allow phase measurement with a given accuracy in a shorter time.

Another approach we considered for using RF techniques to improve sensitivity was log-amplifier detectors, using an M-Z modulator biased near its minimum light transmission. We looked at two log-amp detectors from Analog Devices: AD8310 (DC to 440 MHz) and AD8318 (1 MHz–8 GHz). For the AD8310, we looked at DC light levels near minimum bias with no filtering on the receiver output. In this case, the low-frequency noise created a noise floor that made the technique not particularly useful. With the higher frequencies accessible with the AD8318, we were able to access noise-floor regimes well below what is otherwise achievable.

Table 1. Results of phase measurement techniques

Phase Detector	Input (RF/LO) Frequency	Nominal Output (IF) Bandwidth	Test Conditions and Comments	Phase Noise Floor (rms)
Analog Devices AD8032 Phase detector	Low frequency to 2.7 GHz	30 MHz	1.2 GHz input from dual interferometer. Easy to use and largely independent of RF input levels.	0.12°
Mini-Circuits ZMX-10G+ Double-balanced mixer	3.7–10 GHz	2 GHz	5.6 GHz input from dual interferometer, 200 MHz recording bandwidth, no amplifier. Possibly could have better small-signal performance with pre-amplifier on IF.	0.3°
Hittite HMC483 MESFET Mixer	0.75–1.5 GHz	350 MHz	Electrical only; not yet tested with an optical system. One of a family of mixers that also includes higher frequency models. Includes on-board amplification for LO.	0.01°

LO = local oscillator; IF = intermediate frequency

For the high-frequency operation, the laser light was pre-modulated using one M-Z at full on-off operation at 5 GHz. That light then passed through the signal-transducing M-Z, which was biased near its minimum. The transmitted light was detected as an RF signal at 5 GHz, pushing away from the low-frequency noise inherent in most detector systems. A crucial parameter for the signal-transducing M-Z is its extinction ratio, expressed in dB, since the true minimum bias point will always have some residual transmission. Modern telecommunications M-Zs typically have extinction ratios of 25–45 dB. In Figure 7, the transmission through M-Zs with 30 dB and 40 dB extinction ratios is plotted. It is clear that the higher extinction ratio gives a steeper slope for transducing small signals.

As an alternative, in Figure 8, the sensitivity of the system is plotted as a function of the input voltage away from the minimum bias point. For this work, we used the nominal 24 mV/dB sensitivity of the AD8318. For the M-Z with an extinction ratio of 40 dB, the sensitivity peaked at greater than 30 mV per 0.1% V_π, or 6 mV/mV for an M-Z with V_π of 5 V. At the lower extinction ratio, the sensitivity was more nearly constant over a wider range of input voltages, but the sensitivity peaked near 10 mV/0.1% V_π, or 2 mV/mV.

We performed preliminary testing on this system, using an M-Z to modulate light and attenuators to reduce the light level at the photoreceiver. We modulated the M-Z with 16 dBm of power (4 Vpp) and attenuated the output to −7 dBm at the receiver, and then bandpass-filtered the receiver signal before the AD8318. In this configuration, we observed noise floors of 9 mVpp at a recording bandwidth of 200 MHz and 4 Vpp at a recording bandwidth of 20 MHz. The AD8318 is specified to have a 10 ns rise time, corresponding to approximately 30 MHz, so if the digitizing is bandwidth-limited appropriately, then peak-to-peak, input-referred noise of 0.05% V_π and 0.02% V_π are to be expected with extinction ratios of 30 dB and 40 dB, respectively. For typical modulators with V_π of 5 V, that means 2.5 mVpp and 1 mVpp, respectively.

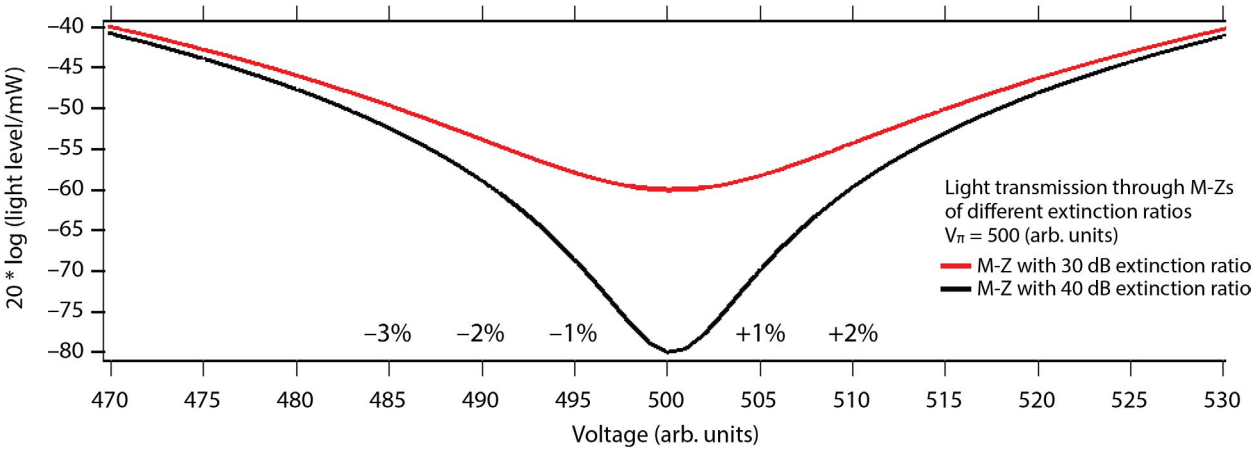

Figure 7. Light transmitted by M-Zs of different extinction ratios near minimum bias, plotted as 20*log (light level/mW)

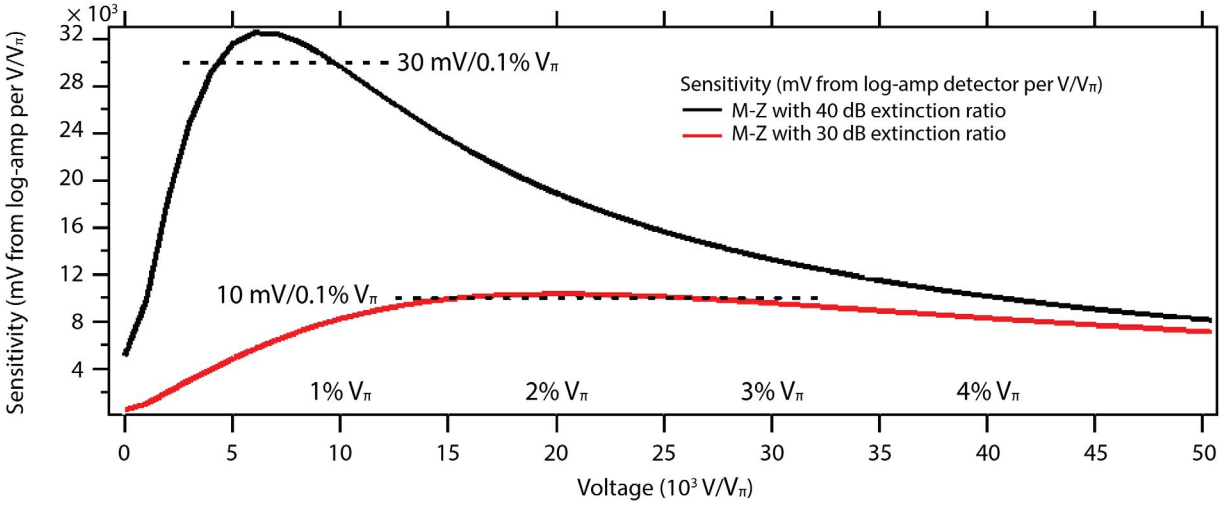

Figure 8. Simulation of log-amp detector outputs using M-Zs of different extinction ratios. Observed noise floors using the AD8318 (10 ns rise time) were 9 mVpp at 200 MHz recording bandwidth and 4 mVpp at 20 MHz recording bandwidth.

Conclusion

During this project, we advanced the effort at UCSB to significantly reduce the optical insertion loss in their ultra low–V_π optical modulators. This will potentially lead to greatly improved sensitivity of fiber-optic recording systems based on M-Z interferometers. In addition, we have developed prototypes of several demodulation schemes that may allow increased sensitivity using existing fiber-optic phase modulators. Phase may be demodulated using mixers and other RF devices when the system is operated as a heterodyne interferometer, and log-amp detectors may provide high sensitivity at useable recording bandwidths.

In the second year of this investigation, we plan to package and test a modulator with the UCSB design. We will pair this effort with our highest sensitivity demodulation scheme and determine the ultimate limit for optical link sensitivity in pulsed-power experimentation.

Acknowledgments

We would like to thank Professor Nadir Dagli of UCSB and his research group for their efforts on modeling and fabricating the electro-optic devices.

References

Miller, E. K., G. S. Macrum, I. J. McKenna, H. W. Herrmann, J. M. Mack, C. S. Young, T. J. Sedillo, S. C. Evans, C. J. Horsfield, "Accuracy of analog fiber-optic links for inertial confinement fusion diagnostics," *IEEE Trans. Nucl. Sci.* **54**, 6 (December 2007) 2457–2462.

Mini-Circuits Application Note AN-41-001, "Frequently asked questions about phase detectors," http://www.minicircuits.com/app/AN41-001.pdf, revised October 21, 2008, accessed October 4, 2013.

Rubiola, E., "Tutorial on the double balanced mixer," http://arxiv.org/abs/physics/0608211v1, February 2, 2008, accessed October 7, 2013.

Site-Directed Research and Development

Appendix

This page left blank intentionally

Appendix: SDRD Performance Metrics

Measuring the performance or output of R&D programs is often the subject of much debate and can vary widely depending on the organization's mission and purpose. In SDRD we have continued to use a suite of basic metrics such as intellectual property, technology needs addressed, and technology transfer to our programs. We also consider the importance of other factors, such as follow-on programmatic or external funding received, new methods developed that effectively save costs, and overall enhanced staff capabilities. These are further indicators of innovation productivity and are also a direct measure of investment return. SDRD provides our staff with opportunities to explore and exercise creative motivations that ultimately lead to new knowledge and realized technologies. The traditional metrics we have used over the past years are tabulated below and are a broad measure of R&D performance.

Invention Disclosures

Invention disclosures are the first step in our intellectual property pursuit and are often followed by patent applications when deemed appropriate. Traditionally, SDRD has generated well over half of all inventions disclosed company-wide since the program began and continues to do so to this day. On average, about one-third of our projects generate new invention disclosures, which is a reasonably high ratio given that projects can vary widely from basic concept, low technical readiness, to much higher, more applied development efforts. In fact, our programs benefit from a high rate of technology utilization precisely due to this diverse mix of projects. A relatively high percentage of projects, roughly 40%, have technology that is subsequently adopted by a direct NNSS program. Another measure of program effectiveness and alignment with missions is how well projects address technology needs as identified in the annual NNSS *Technology Needs Assessment*. The ratio of needs addressed to total projects is also indicative of a trend that aligns efforts strategically with the NNSS mission. In addition, a number of projects, but still a small percentage, are targeting the emerging fields (of the *Needs Assessment*), which are new initiatives intended to incorporate higher risk and seek to explore opportunities for enhanced mission outside of traditional NNSS areas of expertise.

Needs Addressed

The NNSS *Technology Needs Assessment* document continues to be an effective tool for proposal submitters and reviewers. It provides a roadmap and guidance for technology gaps and challenges facing mission areas. As mentioned, our directed research emphasis areas were similar to last year, and they targeted key investment needs, including nuclear security, information security/assurance, high-energy density physics diagnostics, integrated experiments, advanced analysis, and safeguarded energy. The needs assessment is developed from a broad base of input from the national security complex, including laboratories, NNSA, and other external agencies. Significant revisions to the assessment were made again this year; most notably, the "Emerging Areas and Special Opportunities" section was expanded, as were sections on new challenges and "Breaking Barriers" in cyber security, advanced radiography, energy security, and materials in the extremes. In addition, a new preface was provided through our CTO office emphasizing "ground truth and discovery" and new key themes of sense, predict, observe, challenge, and kill (or defeat) threats. The needs assessment itself is now in the eleventh year of revision, and its utility and effectiveness continues to improve year to year.

Publications

Publications are another indicator of R&D output and provide an archival record of the investments made that are then available to the broader scientific and technical community. We have placed a renewed emphasis on high quality, high impact journal publications, and many are highlighted in the annual reports past and present. We are actively targeting about half of all SDRD projects for publication in a given year, and growth in follow-on publications has been noted; expectations are that will improve further in time.

Technology Transfer

We continue to strive to have SDRD effectively contribute new technology into key programmatic efforts as quickly as possible. New strategic efforts are also providing greater emphasis on forward-looking needs and efficient coupling with long-term visionary goals. As always, SDRD looks to be "ahead of our time by design" and push for SDRD innovations to intersect future and evolving missions with the most impact possible.

Acknowledgments

A number of individuals contribute significantly to make SDRD successful year after year. Without their support, much of this would not be possible. My sincere gratitude goes out to Michele Vochosky, Katharine Streeton, and Sierra Cory, for compiling, editing, and publishing this report; to Nancie Nickels for graphic design of the cover and dividers; to the production team under Diana Higgs for printing and distribution; to Linda Flaugher and Emma Gurr for efforts in cost accounting and Tom Graves for project management support; to Newell Ramsey,

SDRD Program Performance Metrics												
Year	FY03	FY04	FY05	FY06	FY07	FY08	FY09	FY10	FY11	FY12	FY13	FY14
Number of Projects	41	57	55	50	37	27	23	25	26	24	24	25
Invention Disclosures	11	12	21	11	9	6	11	9	7	8	7	7
	27%	21%	38%	22%	24%	22%	48%	36%	27%	33%	29%	28%
Technology Adopted by Programs	15	18	12	8	8	8	10	10	9	10	9	10
	37%	32%	22%	16%	22%	30%	44%	40%	35%	42%	38%	40%
Gap or Need Addressed*	11	14	18	17	18	15	15	13	13	11	14	11
	27%	25%	33%	34%	49%	56%	65%	52%	50%	46%	58%	44%
"Emerging Area & Special Opportunity" Effort	--	--	--	--	--	--	--	--	--	--	3	5
	--	--	--	--	--	--	--	--	--	--	13%	20%
Journal Publications	5	5	3	2	7	3	6	6	5	7	9	8

* per NNSS *R&D Technology Needs Assessment*

Kathy Gallegos, and Samantha Hixson for information system support; to Janet Lux for compiling financial data for reporting requirements; to Larry Franks, Rob Hixson, and Lynn Veeser for exceedingly valuable technical guidance and support; and to the SDRD site representatives and review committee, Frank Cverna, Daniel Frayer, Paul Guss, Eric Machorro, Michael Mohar, Sanjoy Mukhopadhyay, Mike Haugh, and Jerry Stevens. Special thanks again to members of our external advisory board, Larry Franks, Carl Ekdahl, Damon Giovanielli, Ralph James, Paul Rockett, and Gerry Yonas, who graciously give their time and provide ongoing, valuable recommendations. Lastly, to our dismay, we acknowledge the passing last year of advisor and colleague Prof. Glenn Knoll—his guidance and wisdom will be missed.

Howard A. Bender III
SDRD Program Manager

This page left blank intentionally

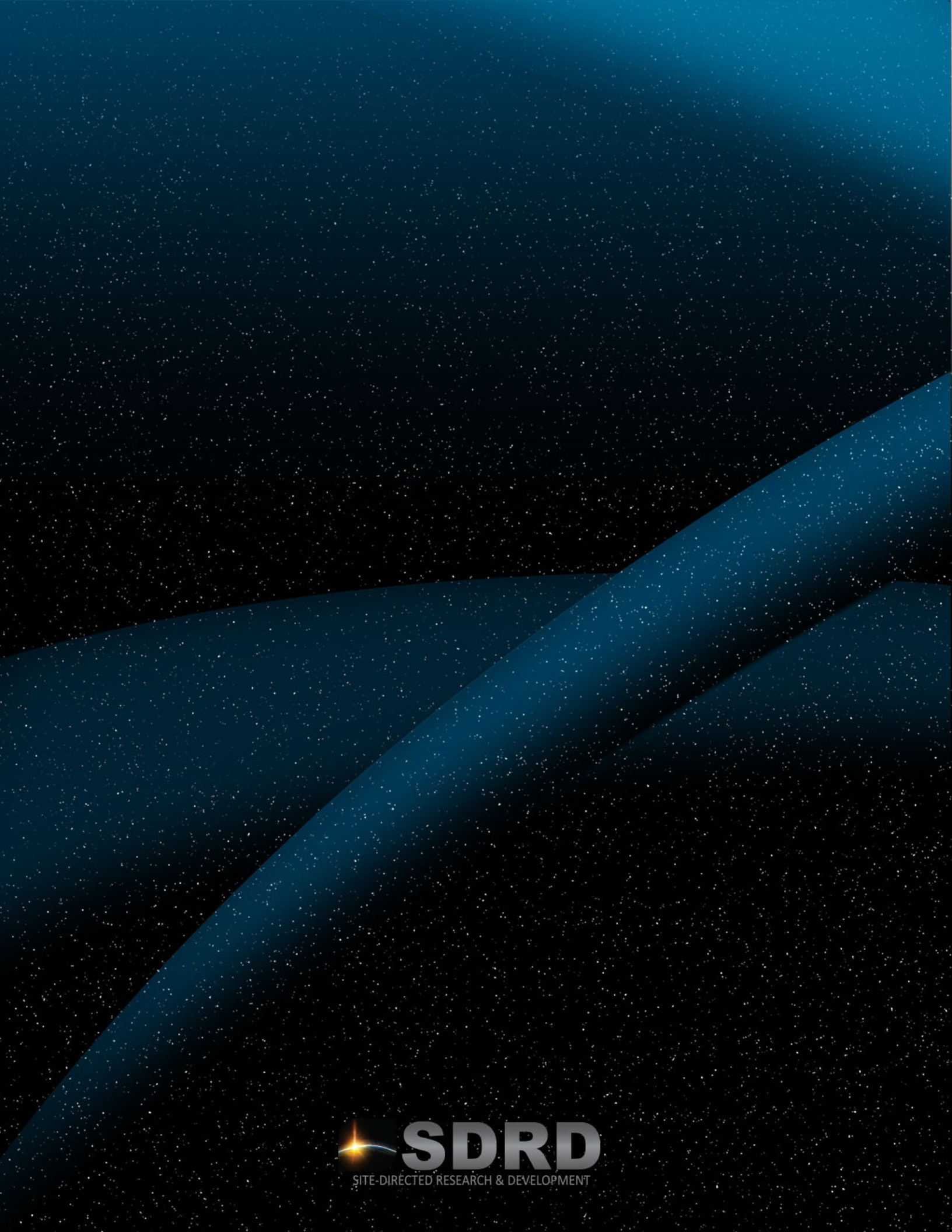
SDRD
SITE-DIRECTED RESEARCH & DEVELOPMENT